

EYE LAND BAND WIDTH,
WHEN THE EARTH
WHISPERED

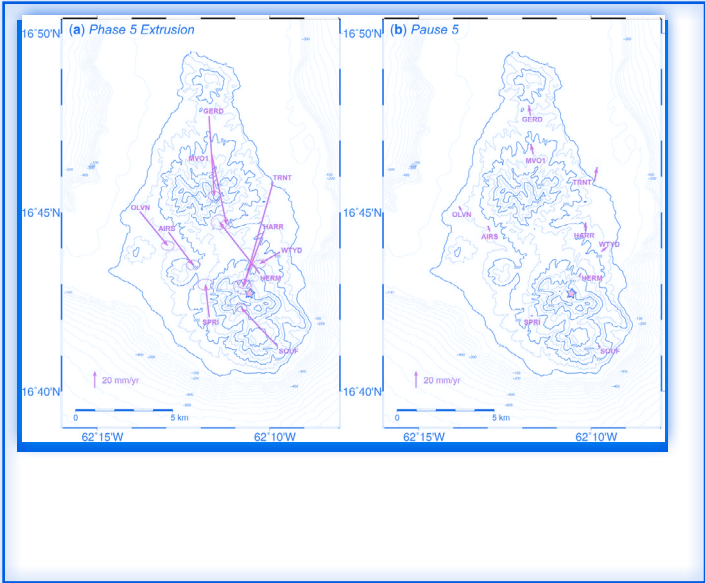
A Shift Register READER for Ilha de São Miguel

THEY ARE OFTEN USED TO MAKE
VERY SMALL MEASUREMENTS
THAT ARE NOT ACHIEVABLE ANY
OTHER WAY

TO SET THE WHOLE WORLD
TALKING

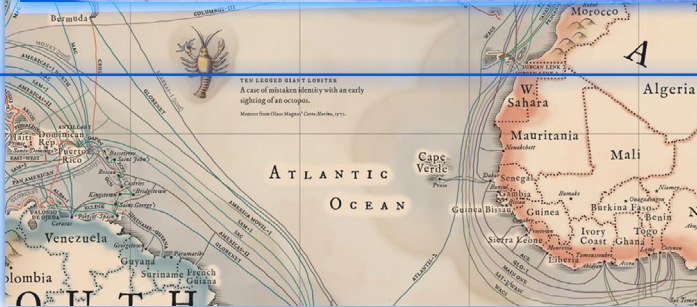
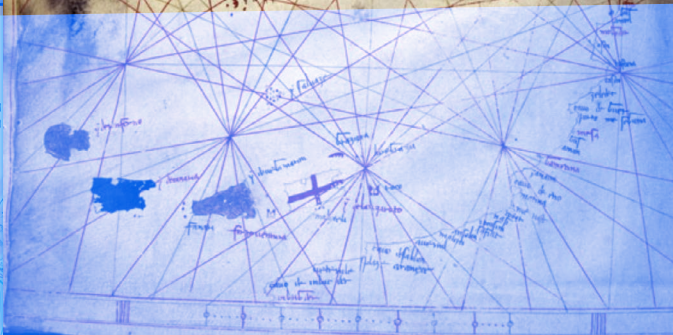
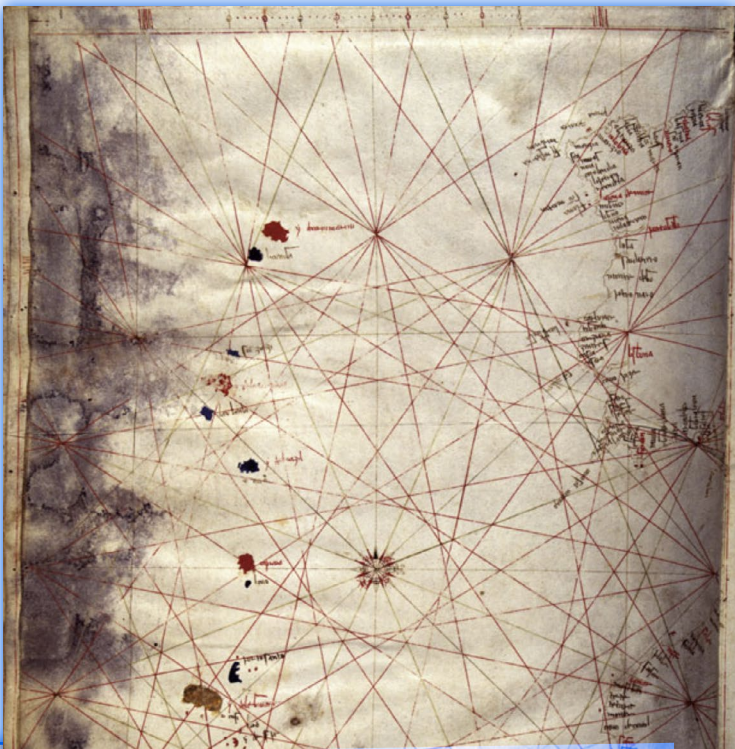
YOU CAN WRITE A POEM WITH
BASALT

ONE PERSON'S NOISE IS
ANOTHER PERSON'S SIGNAL



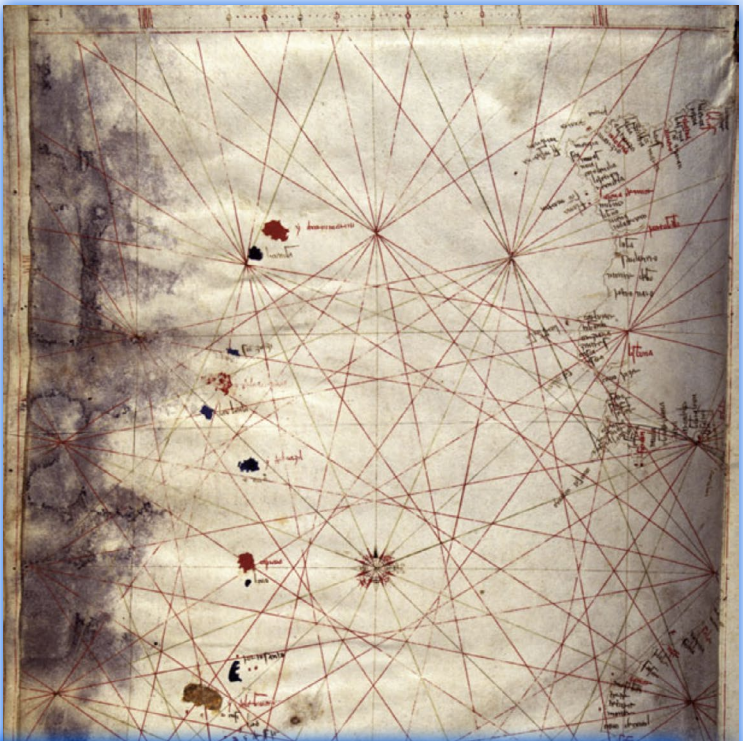
“Planet Earth is solid but viscous; its structure is created by the movement of tectonic plates; submarine currents swirl in the depths of our oceans; the atmosphere derives its stability or instability from the corresponding stability of the winds. More or less slowly, fluxes of every kind transform and conserve the universal order of elements.”

— Michel Serres, *Angels* (1995)

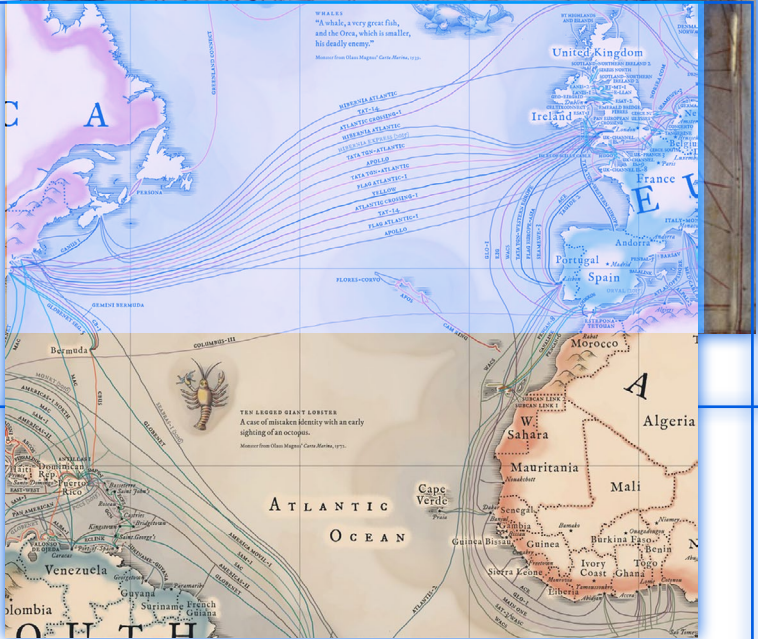


THE LARGEST GIANT LOBSTER
 A case of mistaken identity with an early sighting of an octopus.

Illustration from Oliver Magner's *Cape Verde*, 1711.



WHALES
 "A whale, a very great fish,
 and the Orca, which is smaller,
 his deadly enemy."
Map from Olas Magnus' Carta Marina, 1539.



TEN LEGGED GIANT LOBSTER
 A case of mistaken identity with an early
 sighting of an octopus.
Map from Olas Magnus' Carta Marina, 1539.



interfere

1. To intervene in a situation without invitation or necessity: you promised not to interfere | she tried not to interfere in her children's lives.
2. To prevent a process or activity from continuing or being carried out properly: a holiday job would interfere with his studies.
3. To strike against or impede (something) when working: the rotors are widely separated and do not interfere with one another.
4. To (interfere with) handle or adjust (something) without permission, especially so as to cause damage: he admitted interfering with a van.
5. Law attempt to bribe or intimidate (a witness): they face charges of conspiracy to obstruct justice and interfering with witnesses.
6. To interact with light or other electromagnetic waveforms to produce interference: light pulses interfere constructively in a fibre to emit a pulse.
7. To cause interference to a broadcast radio signal.

interferometer

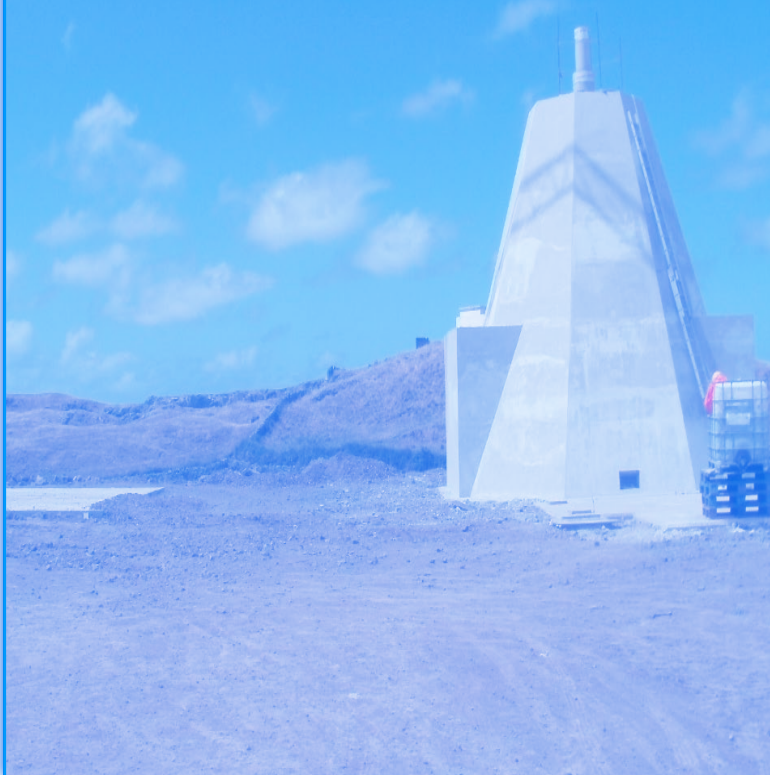
An instrument in which the interference of two beams of light is employed to make precise measurements.

interferogram

A pattern formed by wave interference, especially one represented in a photograph or diagram.

inference

A conclusion reached on the basis of evidence and reasoning.



THEY ARE OFTEN USED
TO MAKE VERY SMALL
MEASUREMENTS THAT ARE
NOT ACHIEVABLE ANY OTHER
WAY

interfere

1. To intervene in a situation without invitation or necessity: you promised not to interfere | she tried not to interfere in her children's lives.
2. To prevent a process or activity from continuing or being carried out properly: a holiday job would interfere with his studies.
3. To strike against or impede (something) when working: the rotors are widely separated and do not interfere with one another.
4. To (interfere with) handle or adjust (something) without permission, especially so as to cause damage: he admitted interfering with a van.
5. Law attempt to bribe or intimidate (a witness): they face charges of conspiracy to obstruct justice and interfering with witnesses.
6. To interact with light or other electromagnetic waveforms to produce interference: light pulses interfere constructively in a fibre to emit a pulse.
7. To cause interference to a broadcast radio signal.

interferometer

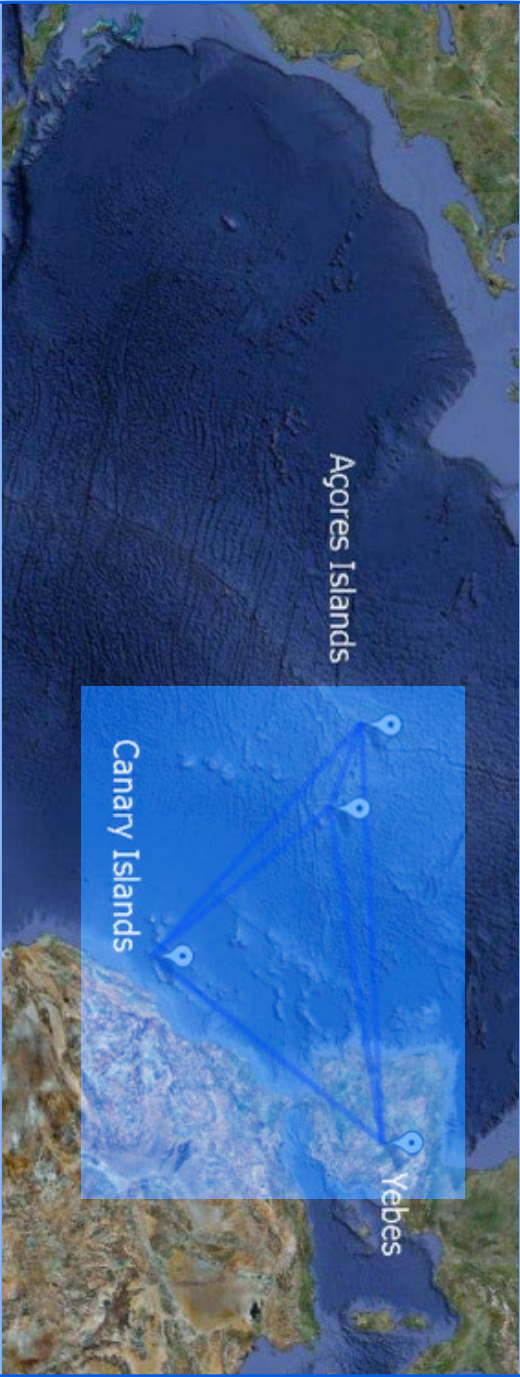
An instrument in which the interference of two beams of light is employed to make precise measurements.

interferogram

A pattern formed by wave interference, especially one represented in a photograph or diagram.

inference

A conclusion reached on the basis of evidence and reasoning.



Agores Islands

Canary Islands

Yebes

Article

Laser-Interferometric Broadband Seismometer for Epicenter Location Estimation

Kyunghyun Lee, Hyungkwan Kwon and Kwanho You *

Department of Electrical and Computer Engineering, Sungkyunkwan University, Suwon 16419, Korea; naman2001@skku.edu (K.L.); ant6565@naver.com (H.K.)

* Correspondence: khyou@skku.edu; Tel.: +82-31-290-7148

Received: 30 August 2017; Accepted: 5 October 2017; Published: 23 October 2017

Abstract: In this paper, we suggest a seismic signal measurement system that uses a laser interferometer. The heterodyne laser interferometer is used as a seismometer due to its high accuracy and robustness. Seismic data measured by the laser interferometer is used to analyze crucial earthquake characteristics. To measure P-S time more precisely, the short time Fourier transform and instantaneous frequency estimation methods are applied to the intensity signal (I_y) of the laser interferometer. To estimate the epicenter location, the range difference of arrival algorithm is applied with the P-S time result. The linear matrix equation of the epicenter localization can be derived using P-S time data obtained from more than three observatories. We prove the performance of the proposed algorithm through simulation and experimental results.

Keywords: seismic wave; laser interferometer; epicenter localization; STA/LTA; range difference of arrival

1. Introduction

The fundamental reasons for earthquakes arise from natural causes and artificial explosions. Natural causes by the movement of tectonic plates bring about energy spouting from the earth's interior, and volcano eruption. Artificial earthquakes are generated by explosions, collapses of large buildings, etc. A seismometer records the vibration caused by natural and artificial earthquakes. Many researchers have used the seismic data measured by seismometer to investigate the features of an earthquake, such as its magnitude, epicenter, and crust pattern. However, despite comprehensive earthquake study, the prediction of earthquake is very difficult since the measurement of seismic wave contains the noise factor during the measurement process [1–4]. The measurement noise occurs inevitably by the imperfection of the measurement environment and the background seismic signals. To investigate earthquake prediction, a precision instrument is needed to measure micro-earthquakes [5–7]. Usually, micro-earthquakes are generated prior to and subsequent to a strong earthquake, and they are termed foreshocks and aftershocks [8], respectively. Therefore, the study of micro-earthquakes is important in seismology. In particular, if a foreshock can be precisely estimated, the damage from a strong earthquake may be lessened.

There have been many efforts to precisely detect and analyze earthquakes. Beyreuther [9] suggested a method to detect and classify earthquakes using hidden Markov modeling, instead of a short-term average over a long-term average (STA/LTA) detector. Botella [10] proposed a real-time earthquake detector with pre-filtering by wavelets. The use of a discrete wavelet transform could increase the detector reliability. Araya [11] suggested a highly sensitive wideband seismometer using a Michelson laser interferometer. This made more exact measurement of the seismic wave than other devices under the noise environment. The epicenter location is very difficult to obtain exactly in spite of its importance [12–14]. Zhu [14] proposed a new estimation algorithm for epicenter location using low frequency seismograms. This is faster than the time domain method, and can also compensate the

error caused by low sampling rate. Gasparini [15] suggested a real-time earthquake location technique for early warning based on an equal differential time formulation and a probabilistic approach for hypocenter estimation.

In this paper, we propose a precision seismometer system with a laser interferometer [16–19]. Contrary to the seismometer based on accelerometers, it can determine the arrival time of a P-S wave and the epicenter location more accurately. The measured seismic wave (I_y) by the heterodyne laser interferometer in the time domain is converted into the time-frequency domain with short-time Fourier transform (STFT) [20–23] and instantaneous frequency (IF) estimation as preprocessing [24,25]. The STFT is a useful tool to analyze non-stationary signals and time-varying systems. In order to more exactly examine the seismic signal with time changes, the IF estimation method is applied to the incoming signal sequences. IF estimation can extract the frequency variation of a seismic wave with time changes. The data in the time-frequency domain is applied and formulated as an STA/LTA ratio to calculate the distance from the epicenter.

In general, the triangulation method is applied to estimate the location of epicenter using three epicentral distances. The triangulation method has weakness about estimation accuracy since it estimates the epicenter location without considering measurement noise. To find the epicenter, the range difference of arrival (RDOA) algorithm [26–29] is used. RDOA method represents the problem in a linear matrix equation and facilitates to apply many kinds of optimization methods. Moreover, the RDOA method has an advantage with the low computational complexity. With the difference of distances that are measured from at least 3 observatories, the origin of the signal spread can be estimated as the epicenter.

This paper is organized as follows. Section 2 describes the seismic wave measurement system with a heterodyne laser interferometer. Section 3 explains P-S time detection with the STFT, IF and STA/LTA method. Section 4 determines the epicenter location with the RDOA algorithm. Section 5 demonstrates the effectiveness of the proposed algorithm through the simulation results, while Section 6 concludes the paper.

2. Heterodyne Laser Interferometer

The measurement of seismic wave is a significant problem since the measurement accuracy is related directly with the accuracy of P-S time computation. In this paper, a heterodyne laser interferometer as a high precision displacement measurement instrument is used for the seismic wave measurement. A heterodyne laser interferometer measures displacement using the orthogonal characteristic of a laser source [30–33]. The laser head emits two polarized beams that have different frequencies. The laser source is divided at the beam splitter (BS) equally into two beams that have the same form. One moves downwards to the detector D_1 , while the other proceeds towards the polarized beam splitter (PBS). The laser sources emitted from the PBS are separated again into two beams. After being reflected by a moving mirror and a fixed mirror respectively, the separated beams are recombined, and collected at the detector D_2 . Figure 1 shows a schematic diagram of seismic detection system based on the heterodyne laser interferometer. The measurement part of seismic detection system needs to be isolated from the seismic wave's effect using the vibration isolation system [34].

The electric fields that are collected at detector D_1 are represented as follows [35]:

$$\begin{aligned} E_{Ap} &= \frac{1}{\sqrt{2}} A e^{j(2\pi f_p t + \phi_A)}, \\ E_{Ao} &= \frac{1}{\sqrt{2}} B e^{j(2\pi f_o t + \phi_B)}, \end{aligned} \quad (1)$$

where A and B are the amplitudes of the electric field, and ϕ_A , ϕ_B are the initial phase values of the given electric field. The laser head emits two-frequency beams of f_p for vertical polarization and f_o for horizontal polarization, respectively. The electric fields measured at detector D_2 are expressed as follows:

$$\begin{aligned} E_{Bp} &= \frac{1}{\sqrt{2}} A e^{j(2\pi f_p t + \phi_A)}, \\ E_{Bo} &= \frac{1}{\sqrt{2}} B e^{j(2\pi f_o t + \phi_B + \Delta\phi)}, \end{aligned} \quad (2)$$

where $\Delta\phi$ is the phase difference occurred by the Doppler effect: $\Delta\phi = 2\pi(f'_o - f_o)t$. f_p and f_o are the frequencies of the two orthogonal polarized beams from a laser head. The intensities of the reference signal and measurement signal that are collected by photo detectors D_1 and D_2 are represented as:

$$\begin{aligned} I_R &\propto (E_{Ap} + E_{Ao})(E_{Ap} + E_{Ao})^* \\ &= \frac{1}{2}(A^2 + B^2) + AB \cos[2\pi\Delta f t + (\phi_B - \phi_A)], \\ I_M &\propto (E_{Bp} + E_{Bo})(E_{Bp} + E_{Bo})^* \\ &= \frac{1}{2}(A^2 + B^2) + AB \cos[2\pi\Delta f t + (\phi_B - \phi_A) + \Delta\phi]. \end{aligned} \quad (3)$$

where Δf means the frequency difference of $f_p - f_o$. The DC components of the measured intensity signals are removed through a high-pass filter. The remaining signals are entered into a lock-in amplifier to obtain the phase value. Then, after passing through a lowpass filter, the intensities of $I_x \propto I_{M,ac} \cdot I_R$ and $I_y \propto I_{M,ac} \cdot I_R e^{j\pi/2}$ are represented as [36]:

$$\begin{aligned} I_x &\propto \frac{AB}{2} \cos(\Delta\phi), \\ I_y &\propto \frac{AB}{2} \sin(\Delta\phi). \end{aligned} \quad (4)$$

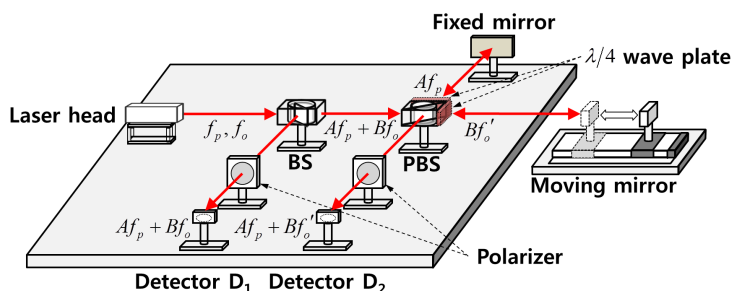


Figure 1. Schematic diagram of seismic wave measurement system using a laser interferometer.

The phase value can then be extracted by solving the trigonometric Equation (4). Moreover, the moving object's displacement can be calculated from the relation between the optical length and the phase value.

3. P-S Time Detection With Instantaneous Frequency

Generally, seismic data that are detected by a seismometer are analyzed in the time-amplitude domain. When an earthquake happens, the seismic signals are measured by observation of the P-wave and S-wave. The P-S time is determined according to the difference of velocity and amplitude between the P-wave and S-wave. However, if the difference of amplitude between the P-wave and S-wave is too small, the measurement of P-S time becomes difficult to calculate. To overcome this problem, we analyze the seismic wave in the time-frequency domain. In order to represent seismic data in the frequency domain, the STFT algorithm is applied. When the seismic signal is transformed into the frequency domain through the STFT, the STFT result represents the frequency change and amplitude value of the seismic signal in frequency with time. Hence, the P-S time is obtained by using the STFT.

With the displacement measurement by the heterodyne laser interferometer, the phase value can be interpreted as proportional to the displacement, as follows:

$$\Delta\phi = \frac{4\pi nD}{\lambda_m}, \quad (5)$$

where n is an air refractive index, and λ_m represents the mean of wavelengths of a laser source. D is the displacement, and $\Delta\phi$ is obtained from Equation (4). The seismic data that are measured by the laser interferometer can be represented as a trigonometric function with the phase information:

$$\begin{aligned} \hat{I}_x &\propto \frac{AB}{2} \cos(\Delta\hat{\phi}), \\ \hat{I}_y &\propto \frac{AB}{2} \sin(\Delta\hat{\phi}), \end{aligned} \quad (6)$$

where \hat{I}_x , \hat{I}_y , and $\Delta\hat{\phi}$ are the measurement values, respectively. With no loss of generality, we use the measured intensity signal (\hat{I}_y) as a seismic data.

Hence, the amplitude change of a seismic signal can be detected with the change of frequency. STFT algorithm is used to represent the detected signal in the time-frequency domain. Fourier transform enables the conversion of a function in the time domain to the frequency domain. However, when data in the time domain is transformed into the frequency domain by the Fourier transform, the time information of the transformed data is lost, and represented in terms of the frequency and amplitude, as the data is calculated for the whole time-interval. The Fourier transform is a function of the angular frequency ω . Therefore, it is impossible to obtain the time-frequency data. To analyze the seismic data in the time-frequency domain, we apply the short-time Fourier transform, which is a modification of the Fourier transform, and has short-term sampling intervals. The STFT of $f(t)$ is defined as follows [37,38]:

$$STFT \{f(t)\} (\tau, \omega) = \int_{-\infty}^{\infty} f(t)h(t-\tau)e^{-j\omega t} dt, \quad (7)$$

where $h(t)$ is a window function for analysis. The shape and the size of the window function affect the resolution of the STFT. When the STFT is applied, the transformed data is represented in time-frequency division as a spectrum, because the STFT is based on the Fourier transform in each time interval. Therefore, we can show the frequency change of the given data as a frequency spectrum. In the STFT method, it is hard to represent the transformed seismic signal in a closed form. To analyze the data as a single value in the time-frequency domain, we use the instantaneous frequency estimation method.

The instantaneous frequency is defined as the derivative of a phase. Generally, the instantaneous frequency is obtained as a single value, by using methods such as counting zero-crossing, and phase differentiation. Other methods for instantaneous frequency estimation are time-frequency distribution with the STFT, wavelet transform, and S-transform. Therefore, the STFT is used for instantaneous frequency estimation to analyze the data in the time-frequency domain. In the time-frequency distribution by the STFT, a single frequency value on time is obtained by an instantaneous frequency estimation. The instantaneous frequency estimation $X(t)$ is defined as follows [39,40]:

$$X(t) = \arg [\max TFD(t, f)], \quad (8)$$

where $TFD(t, f)$ is the time-frequency distribution of a seismic signal that is applied to the STFT. Then, the obtained data is represented in the time-frequency domain, and the arrival time of the P-wave and S-wave can be determined.

STA/LTA is one of the most frequently used methods in seismology to find the P-S time. To determine the arrival time of the P and S wave, the steepness of change rate is an important indicator. STA/LTA uses two moving windows which have different sizes. One has a short-sized window, and the other has a long-sized window. The short-sized moving window is more sensitive to the change of a seismic signal. The long-sized window has a gentle slope. With the characteristic of each window, the variation of seismic data can be detected. The short-term average and the long-term average [41,42] are represented as follows:

$$\begin{aligned}
 A_S(k) &= \sum_{t=k-n_s}^k \frac{X(t)}{n_s}, \\
 A_L(k) &= \sum_{t=k-n_l}^k \frac{X(t)}{n_l},
 \end{aligned}
 \tag{9}$$

n_s and n_l are the short-term window size, and the long-term window size, respectively. Finally, to determine the arrival time of the P-wave and S-wave, we set the threshold value. If v_p, v_s are defined as the velocities of the P-wave and S-wave, respectively, and t_{ps} is the P-S time that is obtained by STA/LTA algorithm, the distance (D_e) from an observatory to the epicenter can be measured by using Equation (10) as follows:

$$D_e = \frac{v_p v_s}{v_p - v_s} t_{ps}. \tag{10}$$

4. Epicenter Localization Based on Range Difference of Arrival

In this section, the RDOA method is used to determine the location of an epicenter. Although the triangulation method has been mostly used for epicenter localization due to its simplicity, there exists a limited accuracy problem caused by not considering the measurement noise. The RDOA method derives the relatively precise location of epicenter with the low computational complexity. The RDOA is the application of the time difference of arrival (TDOA) [43–45]. The TDOA uses the different reaching time from emitter to receiver, and it can be transformed to the RDOA, by multiplying the propagation velocity. The TDOA equation is expressed as follows:

$$t_{ij} = t_i - t_j, \quad i, j \in \{1, 2, \dots, m\}, \tag{11}$$

where t_i is a propagation time, and m is the number of receivers that are considered as observatories. According to the relation between distance and time, the RDOA equation can be expressed as follows:

$$s_i^o = t_i \times v_{sig}, \tag{12}$$

where s_i^o is the distance from the epicenter to each observatory, and v_{sig} is the propagation velocity of the seismic wave.

To determine the epicenter location, we need at least three earthquake observatories. Following the definition of a hyperbola equation, we set the observatory locations as focal points of each hyperbola, and find the point of intersection after depicting two pairs or more hyperbolae. Let us assume that there are m observatories that use the laser seismometer to detect a seismic wave. The measured seismic signals and the arrival time in each observatory are different, because the distances from the epicenter to each observatory are not the same.

RDOA is one of the popular location decision methods. We apply RDOA algorithm based on the least square method. The location of the i -th observatory is defined as $\mathbf{o}_i = [x_i \ y_i]^T, i = 1, 2, \dots, m$. The epicenter location is set as $\boldsymbol{\zeta} = [x \ y]^T$. We set the RDOA measurement value as:

$$\begin{aligned}
 s_i^o &= \|\boldsymbol{\zeta} - \mathbf{o}_i\|, \\
 s_{i1}^o &= s_i^o - s_1^o,
 \end{aligned}
 \tag{13}$$

where s_i^o is the distance between the epicenter and the i -th observatory. s_{i1}^o is the RDOA value between the i -th observatory and the first observatory. Using $s_i^o = \|\boldsymbol{\zeta} - \mathbf{o}_i\|$, the square of the i -th observatory distance from the epicenter can be written as:

$$\begin{aligned}
 (s_i^o)^2 &= \langle \boldsymbol{\zeta} - \mathbf{o}_i, \boldsymbol{\zeta} - \mathbf{o}_i \rangle \\
 &= \|\boldsymbol{\zeta}\|^2 - 2\mathbf{o}_i^T \boldsymbol{\zeta} + \|\mathbf{o}_i\|^2.
 \end{aligned}
 \tag{14}$$

Equation (14) can be rewritten as follows:

$$\begin{aligned}(s_i^o)^2 &= (s_{i1}^o + s_1^o)^2 \\ &= \langle \boldsymbol{\zeta} - \mathbf{o}_1, \boldsymbol{\zeta} - \mathbf{o}_1 \rangle + 2s_{i1}^o s_1^o + (s_{i1}^o)^2.\end{aligned}\quad (15)$$

As Equation (14) is equivalent to Equation (15), we represent the result as a quadratic form:

$$\|\boldsymbol{\zeta}\|^2 - 2\mathbf{o}_1^T \boldsymbol{\zeta} + \|\mathbf{o}_1\|^2 + 2s_{i1}^o s_1^o + (s_{i1}^o)^2 = \|\boldsymbol{\zeta}\|^2 - 2\mathbf{o}_i^T \boldsymbol{\zeta} + \|\mathbf{o}_i\|^2.\quad (16)$$

Then the relation among observatories can be formulated as

$$\|\mathbf{o}_1\|^2 - \|\mathbf{o}_i\|^2 + (s_{i1}^o)^2 = 2 \langle \mathbf{o}_1^T - \mathbf{o}_i^T, \boldsymbol{\zeta} \rangle - 2s_{i1}^o s_1^o.\quad (17)$$

We set the location of the first observatory at the origin of the earthquake coordinate system in order to simplify the equation of epicenter localization. Since the location of the first observatory \mathbf{o}_1 is set as $[0 \ 0]^T$, Equation (17) can be rewritten as the following equation.

$$\bar{\mathbf{A}}\boldsymbol{\zeta} = \mathbf{g}_o + \mathbf{p}_o s_1^o\quad (18)$$

with:

$$\begin{aligned}\bar{\mathbf{A}} &= \begin{bmatrix} \mathbf{o}_2^T \\ \vdots \\ \mathbf{o}_m^T \end{bmatrix}, \quad \mathbf{p}_o = - \begin{bmatrix} s_{21}^o \\ \vdots \\ s_{m1}^o \end{bmatrix}, \quad \mathbf{d} = \begin{bmatrix} \langle \mathbf{o}_2, \mathbf{o}_2 \rangle \\ \vdots \\ \langle \mathbf{o}_m, \mathbf{o}_m \rangle \end{bmatrix}, \\ \mathbf{g}_o &= \frac{1}{2} \begin{bmatrix} \|\mathbf{o}_2\|^2 - (s_{21}^o)^2 \\ \vdots \\ \|\mathbf{o}_m\|^2 - (s_{m1}^o)^2 \end{bmatrix} = \frac{1}{2}(\mathbf{d} - \mathbf{p}_o \bullet \mathbf{p}_o).\end{aligned}$$

where the symbol of (\bullet) means the Hadamard product. However, the epicenter localization formula, denoted by Equation (18), is true only under the ideal condition. In real case, there are some factors that restrict the measurement accuracy.

When we measure the P-S time to calculate the epicenter, STA/LTA algorithm depends on the user selected threshold value for earthquake location. Therefore, the obtained P-S time has a measurement error caused by the limited STA/LTA accuracy. The constrained P-S time data is closely related to finding the epicenter location using the RDOA data. As a result, the RDOA value can be represented as:

$$\begin{aligned}\mathbf{p} &= \text{col} \{s_{k1}^o + \Delta s_{k1}, k = 2, 3, \dots, m\} \\ &= \mathbf{p}_o + \Delta \mathbf{p}, \\ \mathbf{p}_o &= \text{col} \{s_{k1}^o\}, \quad \Delta \mathbf{p} = \text{col} \{\Delta s_{k1}\}, \\ E[\Delta \mathbf{p}] &= 0, \quad \mathbf{Q}_p = E[\Delta \mathbf{p} \Delta \mathbf{p}^T]\end{aligned}\quad (19)$$

where $\Delta \mathbf{p}$ is the epicenter inconsistency error caused by the P-S time measurement error, and $\text{col}\{\cdot\}$ means a column vector. In real environment, the parameter \mathbf{g} is formulated using Equation (19) as follows

$$\mathbf{g} = \mathbf{g}_o + \mathbf{p}_o \bullet \Delta \mathbf{p}.\quad (20)$$

In order to express the formula of the epicenter localization under real environment including the effect of measurement error, the parameters \mathbf{p}_o and \mathbf{g}_o in Equation (18) should be replaced with \mathbf{p} and \mathbf{g} , respectively. Therefore, the epicenter location in real condition can be found as follows [46]:

$$\bar{\mathbf{A}}\zeta = \bar{\mathbf{B}} \quad (21)$$

with:

$$\begin{aligned} \bar{\mathbf{B}} &= \mathbf{b}_o + \mathbf{N}\Delta\mathbf{p}, \\ \mathbf{b}_o &= \mathbf{g}_o + \mathbf{p}_o s_1^o \\ \mathbf{N} &= \text{diag}(\mathbf{p}_o) - s_1^o \mathbf{I} \end{aligned} \quad (22)$$

The vector ζ that denotes the location of epicenter can be obtained using Equation (21). The measurement noise caused by the limited accuracy of STA/LTA method under real environment leads to the discrepancy between the estimated epicenter location and the real epicenter location. By compensating the measurement error using an optimization scheme, the precise location of epicenter (ζ) can be obtained from Equation (21).

5. Simulation and Experimental Results

In this section, we prove the performance of the seismic signal measurement by using a laser interferometer, and obtain the normalized frequency data in the time-frequency domain using STFT algorithm. Moreover, the IF estimation, denoted by Equation (8), is applied to STFT data. Finally, we show the accurate epicenter location detection by using RDOA algorithm from the P-S time that is calculated from IF estimation through STA/LTA algorithm. Figure 2 shows the seismic wave measurement system using a heterodyne laser interferometer. The experiment uses a heterodyne laser interferometer with a He-Ne laser head (Wavetronics: WT-307B). To generate the seismic signal, we use a linear stage driven by a 2-phase stepping motor (Sciencetown: PSA6520) with a 20 mm stroke. Using the linear stage, seismic wave movement is generated to prove the performance of the interferometric seismometer. To compare the performance, we use an accelerometer as a reference since it is currently used as an earthquake motion measurement instrument. The model of JEP-8A3, Mitutoyo, is actively utilized as an acceleration sensor due to its high-performance. The measurement range, dynamic range, and sensitivity of JEP-8A3 are 3000 Gal, 145 dB, and $\pm 3\%$, respectively. The displacement variation caused by the linear stage is measured by the heterodyne laser interferometer. The displacement data can be transformed to the acceleration data using a sample rate (6.7 kHz).

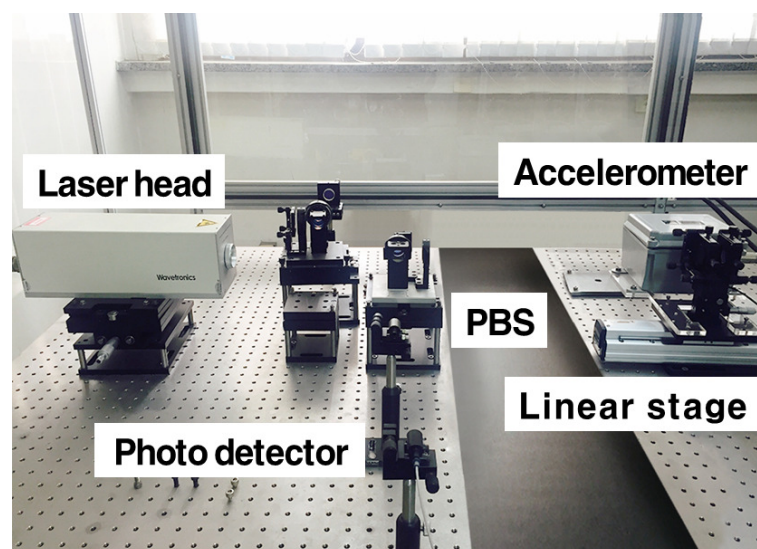


Figure 2. Seismic wave measurement system using a laser interferometer.

We set the mean wavelength (λ_m) from the laser head as 632.9 (nm), and the air refractive index (n) as 1.000000026. Figure 3 shows the seismic wave movement measured by laser interferometer. The amplitude discrepancy in Figure 3 shows the sensitivity to measurement noise.

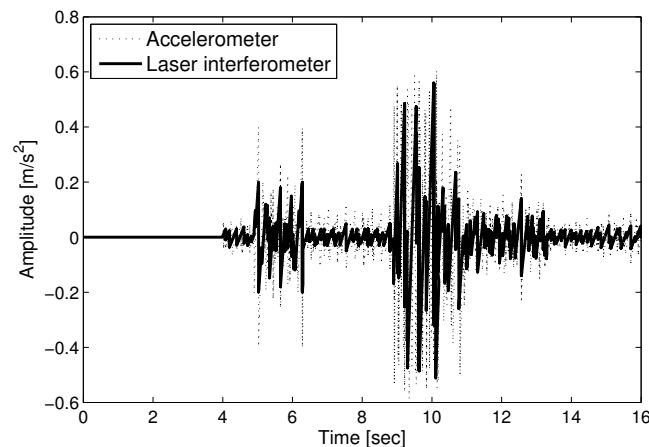


Figure 3. Seismic wave measurement with a laser interferometer.

With the displacement measurement by the heterodyne laser interferometer, the phase value ($\Delta\phi$) is proportional to the displacement (D), as in Equation (5). Figure 4 represents the difference between the true amplitude and the measurement value at each sampling time. The thick solid line and the thin dotted line in Figure 4 denote the root mean square error (RMSE) of the measured seismic wave using a laser interferometer and accelerometer, respectively. The measurement using a laser interferometer is more precise than the accelerometer. Figure 5 shows the intensity signal (I_y) for spectrum analysis with $AB = 2$ in Equation (4). The high-density points of I_y can be interpreted as the arrival time of the P and S waves at 5 and 9 s, respectively. The amplitudes of the P and S waves changing frequently are represented by the highly dense intensities in Figure 5.

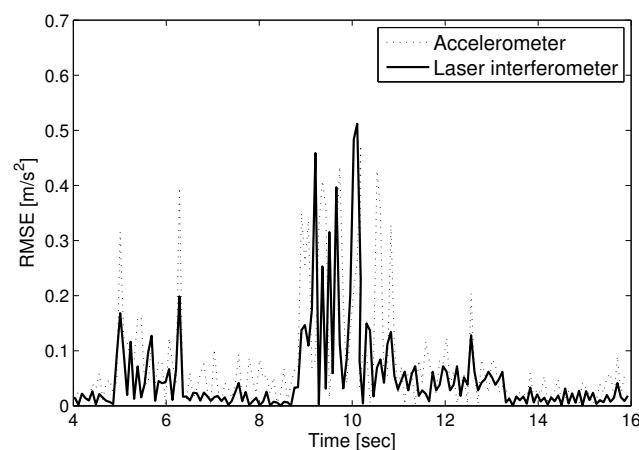


Figure 4. Measurement error comparison between a laser interferometer and accelerometer.

STFT algorithm is used to represent the detected signal in the time-frequency domain. The Fourier transform is adequate to project the data in the time domain into the frequency domain. STFT algorithm is applied to intensity signal (I_y) data that represents high density when P and S wave arrive. The differential phase value is obtained using the STFT data. Figure 6 shows the result of STFT that indicates time, frequency and amplitude distribution. The red color represents a high amplitude value, and the blue color represents a low amplitude value. The figure shows that there are sharp points at 5 and 9 s, respectively. The arrival times of the P-wave and S-wave are confirmed. After the arrival of the P and S waves, the amplitude of the seismic wave changes. Therefore, the peak points at 5 and 9 s mean the arrival time of the P and S waves. With the derived STFT data, IF estimation is performed,

as shown in Figure 7. Using the result of STFT in the time-frequency domain, IF is applied to get the frequency value in each interval time. Similar to the result in Figure 6, the value in Figure 7 represents the arrival time of the seismic signal.

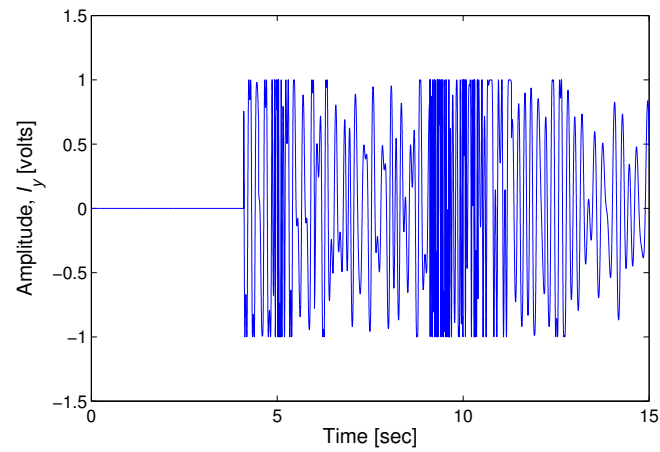


Figure 5. Intensity signal (I_y) for spectrum analysis.

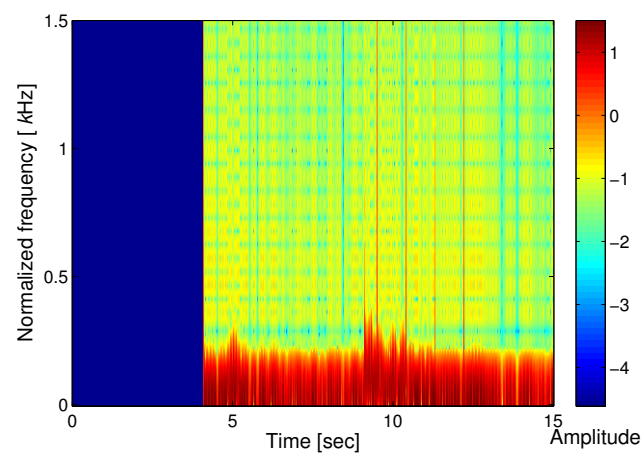


Figure 6. STFT result of the seismic wave.

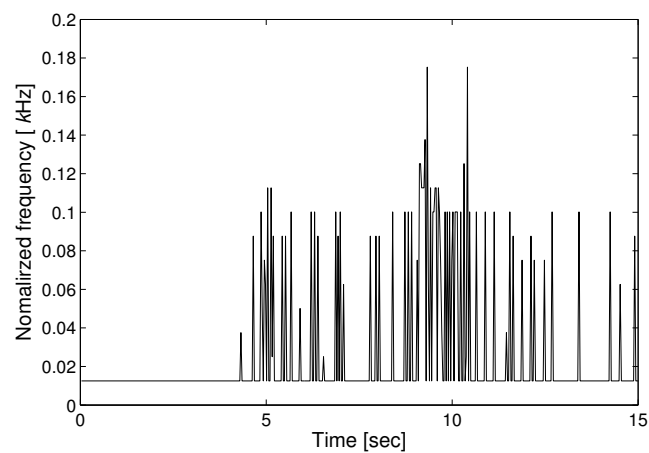


Figure 7. IF analysis of the seismic wave.

Figure 8 shows the seismic wave data with STA/LTA algorithm. We set up the LTA window size with as much as 8 times the STA window size, and set the threshold value as twice the average of the STA/LTA ratio. We can determine the P-S time when the STA/LTA ratio becomes greater than the threshold value. The arrival times of the P-wave and S-wave were measured as 4.65 and 9.12 (s), respectively. If we suppose the velocities of the P-wave and S-wave as 8.2 and 3.7 (km/s) separately, we can calculate the distance to the epicenter as 31.2 (km), according to Equation (10).

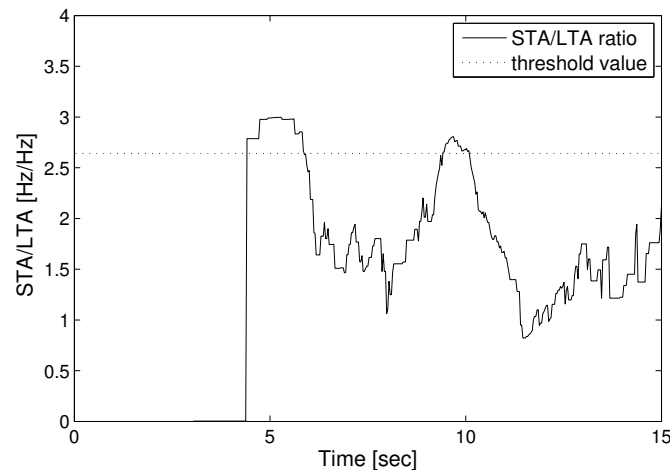


Figure 8. Estimation of the STA/LTA ratio.

Figure 9 shows the estimation of the epicenter location. The circle points represent the observatory locations, while the triangle point represents the epicenter location. We set the epicenter location as (50, 20) (km) when the measurement noise does not exist. We suppose the locations of the observatory as (0, 0), (10, 80), (100, 0), and (100, 80) (km), respectively. The epicenter location found using the RDOA hyperbolae is shown in Figure 9. When the hyperbolae are to be drawn, we set the observatory that is placed at (100, 0) (km) as a reference. With the reference observatory and each separate observatory, the three pairs of hyperbolae were derived. We assume that the measurement noises of epicentral distances at each observatory follow the Gaussian distribution. n_e is the maximum absolute value of the measurement noises. We suppose the parameter n_e as 1 in Figure 9. As a result, we determined the epicenter location using RDOA algorithm as (47.9, 21.2) (km). The asterisk point is the estimated epicenter location using triangulation method that is generally used for location estimation of an epicenter. The estimated result using the triangulation method is (53.7, 17.9) (km). It can be confirmed that the estimated result from RDOA is closer to the actual location. Table 1 shows the RMSE comparison of RDOA based estimation method with the triangulation method for various measurement noises. As the measurement noise represented as n_e increases, the localization accuracy becomes low accordingly. It can be confirmed that the result of RDOA based epicenter estimation is better under the circumstances of measurement noise.

Table 1. RMSE comparison for various measurement noises (n_e).

Methods	RMSE (km)				
	$n_e = 1$	$n_e = 2$	$n_e = 3$	$n_e = 5$	$n_e = 10$
Triangulation	4.25	6.12	7.28	8.92	13.29
RDOA	2.41	3.29	3.93	4.72	7.20

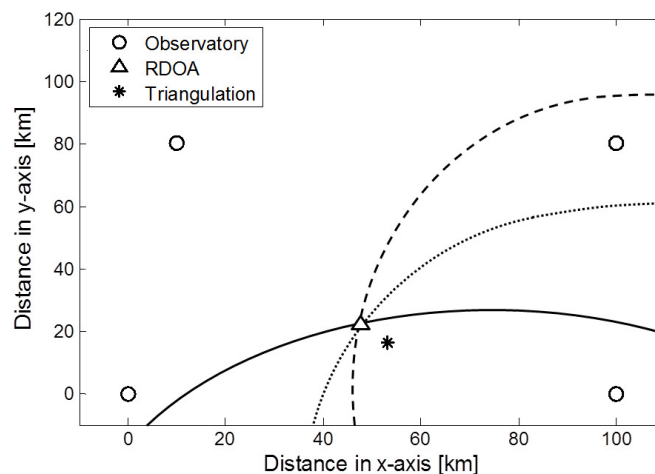


Figure 9. Epicenter location using RDOA algorithm.

6. Conclusions

In this paper, we suggest an epicenter localization method based on RDOA algorithm. The range difference information for RDOA algorithm is obtained from a seismic signal measured by a heterodyne laser interferometer. The laser interferometer uses the Doppler effect to detect movement of the stage. We measure the seismic signal with the use of a laser interferometer. To determine the P-S time, we apply STFT, IF, and STA/LTA algorithms to seismic signal data obtained from the laser interferometer's intensity signal (I_y). Using STFT and IF, the transformed signal of the seismic wave is obtained in the time-frequency domain. With the changes of frequency, we decide the arrival time of the P and S waves. Moreover, we determine the epicenter location with RDOA algorithm. We confirm that RDOA algorithm can more accurately estimate the epicenter location.

Acknowledgments: This work was supported by the National Research Foundation of Korea (NRF) grant funded by the Korea government (MSIP) (NRF-2016R1A2B4011369).

Author Contributions: This paper was accomplished by all the authors with the assignments that Kwanho You and Kyunghyun Lee conceived the idea and performed the analysis and design of the experiment; Kyunghyun Lee and Hyungkwan Kwon carried out the numerical simulation and the experiment; Kyunghyun Lee and Kwanho You co-wrote the manuscript.

Conflicts of Interest: The authors declare no conflict of interest.

References

1. Uyeda, S.; Nagao, T.; Kamogawa, M. Short-term earthquake prediction: Current status of seismo-electromagnetics. *Tectonophysics* **2009**, *470*, 205–213.
2. Zechar, J.; Jordan, T. Testing alarm-based earthquake predictions. *Geophys. J. Int.* **2008**, *172*, 715–724.
3. Keilis-Borok, V.; Ismail-Zadeh, A.; Kossobokov, V.; Shebalin, P. Non-linear dynamics of the lithosphere and intermediate-term earthquake prediction. *Tectonophysics* **2001**, *338*, 247–260.
4. Adeli, H.; Panakkat, A. A probabilistic neural network for earthquake magnitude prediction. *Neural Netw.* **2009**, *22*, 1018–1024.
5. Sileny, J.; Hill, D.P.; Eisner, L.; Cornet, F.H. Non-double-couple mechanisms of microearthquakes induced by hydraulic fracturing. *J. Geophys. Res.-Solid Earth* **2009**, *114*, B08307.
6. Reddy, D.V.; Sukhija, B.S.; Nagabhushanam, P.; Kumar, D. A clear case of radon anomaly associated with a micro-earthquake event in a stable continental region. *Geophys. Res. Lett.* **2004**, *31*, L10609.
7. Collins, D.S.; Pettitt, W.S.; Young, R.P. High-resolution mechanics of a microearthquake sequence. *Pure Appl. Geophys.* **2002**, *159*, 197–219.
8. Ogata, Y.; Utsu, T.; Katsura, K. Statistical discrimination of foreshocks from other earthquake cluster. *J. Geodyn.* **1996**, *65*, 199–217.

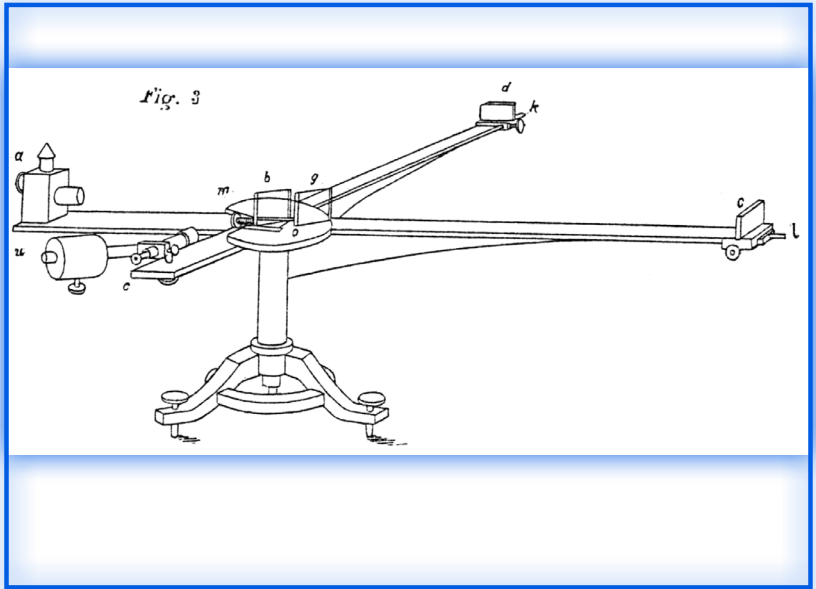
9. Beyreuther, M.; Wassermann, J. Continuous earthquake detection and classification using discrete hidden Markov models. *Geophys. J. Int.* **2008**, *175*, 1055–1066.
10. Botella, F.; Rosa-Herranz, J.; Ginger, J.; Monlina, S.; Galiana-Merino, J. A real-time earthquake detector with prefiltering by wavelets. *Comput. Geosci.* **2003**, *29*, 911–919.
11. Araya, A.; Kawabe, K.; Sato, T.; Mio, N.; Tsubono, K. Highly sensitive wideband seismometer using a laser interferometer. *Rev. Sci. Instrum.* **1993**, *64*, 1337–1341.
12. Du, A.; Huang, Q.; Yang, S. Epicenter location by abnormal ULF electromagnetic emissions. *Geophys. Res. Lett.* **2002**, *29*, 1–3.
13. Zhan, Z.; Wei, S.; Ni, S.; Helmberger, D. Earthquake centroid locations using calibration from ambient seismic noise. *B Seismol. Soc. Am.* **2011**, *107*, 1438–1445.
14. Zhu, W.; Sun, L.; Zhu, X. New estimation algorithm for epicenter location of low frequency seismograms. In Proceedings of the 2012 International Conference on Systems and Informatics (ICSAI), Yantai, China, 19–20 May 2012; pp. 1706–1710.
15. Gasparini, P.; Manfredi, G.; Zschau, J. *Earthquake Early Warning System*; Springer: Berlin, Germany, 2007.
16. Deng, Y.; Li, X.; Wu, Y.; Hu, J.; Yao, J. Analysis of frequency mixing error on heterodyne interferometric ellipsometry. *Meas. Sci. Technol.* **2007**, *18*, 3339–3343.
17. Park, T.; Choi, H.; Han, C.; Lee, Y. Real-time precision displacement measurement interferometer using the robust discrete time Kalman filter. *Opt. Laser Technol.* **2005**, *37*, 229–234.
18. Olyae, S.; Yoon, T.; Hamedi, S. Jones matrix analysis of frequency mixing error in three-longitudinal-mode laser heterodyne interferometer. *IET Optoelectron.* **2009**, *3*, 215–224.
19. Hou, W.; Zhang, Y.; Hu, H. A simple technique for eliminating the nonlinearity of a heterodyne interferometry. *Meas. Sci. Technol.* **2009**, *20*, 105303.
20. Lu, W.; Li, F. Seismic spectral decomposition using deconvolutive short-time Fourier transform spectrogram. *Geophysics* **2013**, *78*, 43–51.
21. Wright, P. Short-time Fourier transforms and Wigner-Ville distributions applied to the calibration of power frequency harmonic analyzers. *IEEE Trans. Instrum. Meas.* **1999**, *48*, 475–478.
22. Lu, W.; Zhang, Q. Deconvolutive short-time Fourier transform spectrogram. *IEEE Signal Process. Lett.* **2009**, *16*, 576–579.
23. Auger, F.; Flandrin, P. Improving the readability of time-frequency and time-scale representations by the reassignment method. *IEEE Trans. Signal Process.* **2002**, *43*, 1068–1089.
24. O’Shea, P. A new technique for instantaneous frequency rate estimation. *IEEE Signal Process. Lett.* **2002**, *9*, 251–252.
25. Aboutanios, E.; Mulgrew, B. Iterative frequency estimation by interpolation on Fourier coefficients. *IEEE Trans. Signal Process.* **2005**, *53*, 1237–1242.
26. Cheung, K.W.; So, H.C.; Ma, W.K.; Chan, Y.T. A constrained least square approach to mobile positioning: algorithms and optimality. *EURASIP J. Appl. Signal Process.* **2006**, *2006*, 1–23.
27. Shin, D.H.; Sung, T.K. Comparison of error characteristics between TOA and TDOA positioning. *IEEE Trans. Aero. Elec. Syst.* **2002**, *38*, 307–311.
28. Dogancay, K. Emitter localization using clustering-based bearing association. *IEEE Trans. Aero. Elec. Syst.* **2005**, *41*, 525–536.
29. Zhu, D.; Yi, K. Localization technology research based on particle filter in underground mines. *J. Comput. Inf. Syst.* **2013**, *9*, 3011–3018.
30. Sutton, C.M. Non-linearity in length measurement using heterodyne laser Michelson interferometry. *J. Phys. E: Sci. Instrum.* **1987**, *20*, 1290–1292.
31. Nozato, H.; Kokuyama, W.; Ota, A. Improvement and validity of shock measurements using heterodyne laser interferometer. *Measurement* **2016**, *77*, 67–72.
32. Fu, H.; Hu, P.; Tan, J.; Fan, Z. Simple method for reducing the first-order optical nonlinearity in a heterodyne laser interferometer. *Appl. Opt.* **2015**, *54*, 6321–6323.
33. McRae, T.G.; Hsu, M.T.L.; Freund, C.H.; Shaddock, D.A.; Herrmann, J.; Gray, M.B. Linearization and minimization of cyclic error with heterodyne laser interferometry. *Opt. Lett.* **2012**, *37*, 2448–2450.
34. Yang, J.; Xiong, Y.; Xing, J. Dynamics and power flow behaviour of a nonlinear vibration isolation system with a negative stiffness mechanism. *J. Sound Vib.* **2013**, *332*, 167–183.

35. Wang, Y.; Shyu, L.; Chang, C. The comparison of environmental effects on Michelson and Fabry-Perot interferometers utilized for the displacement measurement. *Sensors* **2010**, *10*, 2577–2586.
36. Lee, K.; Pyo, Y.; You, K. Lagrange multiplier-based error compensation of heterodyne interferometer. *Electron. Lett.* **2016**, *52*, 1692–1694.
37. Quyang, X.; Amin, G. Short-time Fourier transform receiver for nonstationary interference excision in direct sequence spread spectrum communications. *IEEE Trans. Signal Process.* **2001**, *49*, 851–863.
38. Richard, M. Helium speech enhancement using the short-time Fourier transform. *IEEE Trans. Acoust. Speech* **1982**, *30*, 841–853.
39. Katkovnik, V.; Stankovic, L. Instantaneous frequency estimation using the Wigner distribution with varying and data-driven window length. *IEEE Trans. Signal Process.* **1998**, *46*, 2315–2325.
40. Kwok, H.; Jones, D. Improved instantaneous frequency estimation using an adaptive short-time Fourier transform. *IEEE Trans. Signal Process.* **2000**, *48*, 2964–2972.
41. Hara, T. Measurement of the duration of high-frequency energy radiation and its application to determination of the magnitudes of large shallow earthquakes. *Earth Planets Space* **2007**, *59*, 227–231.
42. Svitek, T.; Rudajev, V.; Petruzalek, M. Determination of P-wave arrival time of acoustic events. *Acta Montan. Slovaca* **2010**, *15*, 145–151.
43. Yu, H.; Huang, G.; Gao, J. Constrained total least-squares location algorithm using time difference of arrival measurements. *IEEE Trans. Veh. Technol.* **2010**, *59*, 1558–1562.
44. Hara, S.; Anzai, D.; Yabu, T. A perturbation analysis on the performance of TOA and TDOA localization in mixed LOS/NLOS environments. *IEEE Trans. Commun.* **2013**, *61*, 679–689.
45. Soliman, M.S.; Morimoto, T.; Kawasaki, Z.I. Three-dimensional localization system for impulsive noise sources using ultra-wideband digital interferometer technique. *J. Electromagn. Waves Appl.* **2012**, *20*, 515–530.
46. Oh, J.; Lee, K.; You, K. Hybrid TDOA and AOA localization using constrained least squares. *IEICE Trans. Fund. Electr.* **2015**, *E98-A*, 2713–2718.



© 2017 by the authors. Licensee MDPI, Basel, Switzerland. This article is an open access article distributed under the terms and conditions of the Creative Commons Attribution (CC BY) license (<http://creativecommons.org/licenses/by/4.0/>).

IS IT POSSIBLE TO
STEREOSCOPICALLY COMBINE
AN INFERENTIAL ACCOUNT
OF THOUGHT AND A
NATURALIST IMAGE OF THE
WORLD?



“Well, gentlemen, we will undertake this, although my conviction is strong that we shall prove only that the earth rotates on its axis, a conclusion which I think we may be said to be sure of already.”

— Albert A. Michelson (1852-1931)

Principles of interferometry

Neal Jackson

University of Manchester, Jodrell Bank Observatory
neal.j.jackson@manchester.ac.uk

In this review I outline the principles of interferometry and describe how these are put into practice in a range of modern interferometric telescopes. The basic philosophy of the review is to emphasise a pictorial approach to the subject, rather than delve into detailed mathematical derivations. Much more rigorous treatment of interferometry can be found in Thompson, Moran & Swenson (2001). In addition, the US National Radio Astronomy Observatory (NRAO) hosts a lecture series every three years in interferometry, published in Taylor, Carilli & Perley (1998).

Throughout, I concentrate on applications of interferometry to interferometers at long (wave-regime) wavelengths, with occasional excursions into methods used in the new generation of optical interferometers. The final section is an overview of current interferometers working in the metre-to-millimetre band. The principles behind interferometers at all wavebands, however, are very similar, including all of section 1 and most of section 2. A recent full and complementary review of optical interferometry is given by Monnier (2003), and other reviews in these proceedings cover the VLT interferometer in detail.

1 Basics: Young's slits and Fourier transforms

1.1 Young's slits

Interferometry begins with the Young's slits fringe pattern (Fig. 1). With a single point source emitting coherent radiation, interference fringes are observed, with constructive and destructive interference observed as the relative delay of the two interfering rays changes; the separation of the fringes is λ/d , the wavelength of the light divided by the slit separation.

If the source is made wider (Fig. 1b), we can think of it as a sequence of point sources each of which emit radiation which is uncorrelated with the emission from the others. It follows that the total interference intensity pattern is the sum of the individual patterns. Since an angular displacement in

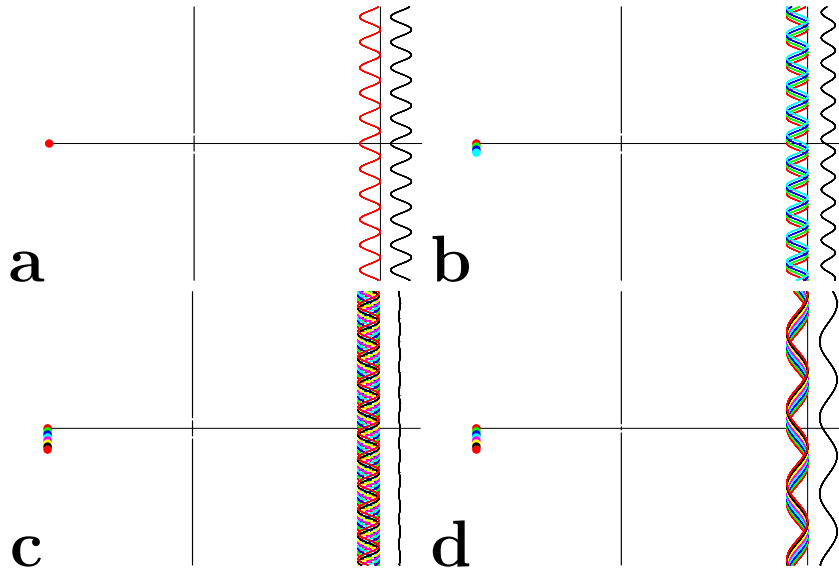


Fig. 1. Young’s slits in various situations. In each panel the source is shown on the left, and on the right of the slit are shown the fringe patterns separately for each part of the source and then the added fringe pattern. a: The basic two-slit pattern, showing fringes an angular distance λ/d apart. b: The effect of increasing the source size. An angular shift of the source position by θ shifts the fringe patterns by θ the other way. Since the patterns come from mutually incoherent sources, the intensity patterns add to give a pattern of reduced visibility. c: When the size of the source reaches λ/d , the fringes add to give zero visibility. d: If the slit spacing is then reduced, the fringe spacing increases, and the same size of source is still able to give visible fringes: the source would need to be increased in size to λ/d_{new} in order to wash out the fringes.

the source produces an equal angular displacement in the fringe pattern, as the source size approaches λ/d the fringe patterns will add to give a constant illumination (Fig. 1c). In this case, the fringe visibility (defined as the difference between maximum and minimum intensity, normalized by the sum of maximum and minimum intensity) drops to zero. Conversely, when the angular size of the source is $\ll \lambda/d$, the fringe visibility is 1; this corresponds to a situation in which the source size is smaller than the angular resolution of the interferometer, and only an upper limit of order λ/d can be obtained on it¹.

Now suppose that the slit spacing d is decreased. For the same size of source, this produces less “washing-out” of the fringes, because the same dis-

¹In practice, the fact that the visibility function begins to decrease as soon as the source extends significantly often allows some information to be derived down to at least $0.5\lambda/d$ and in some cases further.

placement of the source now produces much less displacement of the fringe patterns as a fraction of the fringe separation λ/d (Fig. 1d). The smaller the slit separation, the larger the source size that can be probed using interferometry.

The situation is summarised in Fig. 2. If we plot, for a given source distribution, the way in which visibility varies with slit separation, it can be seen that for small sources the visibility remains high out to large slit separation (in the limit of point sources, to infinite slit separation), whereas large sources produce visibility patterns which fall off quickly as the slit separation increases.

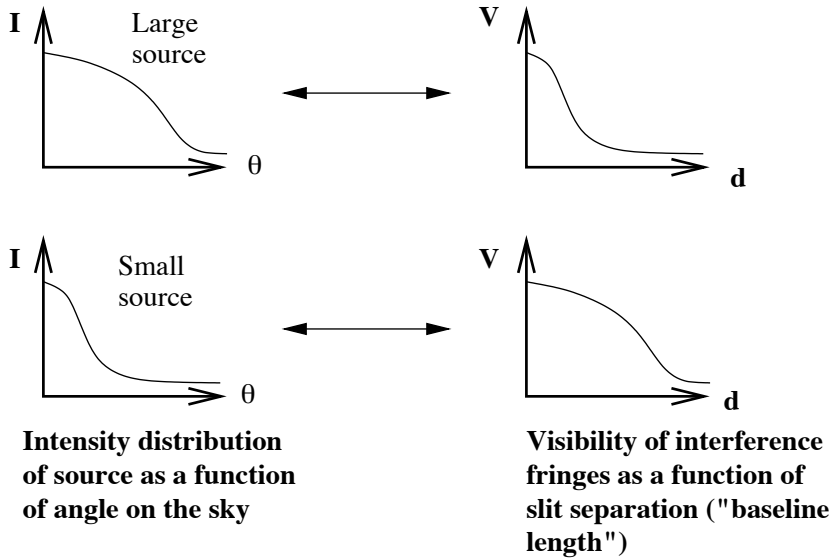


Fig. 2. Relation between source brightness as a function of angular distance and visibility of interference fringes as a function of slit separation (baseline length).

The relation between $I(\theta)$ and $V(d)$ represented here is one which maps a large Gaussian into a small Gaussian, and vice versa, and it is fairly obvious that it is a Fourier transform²; this relationship is the basis of the whole discussion that follows.

This relationship was applied early in the history of radio interferometers to find the sizes of quasars, which were known to be exceedingly small. The method adopted was to use one fixed telescope and one movable telescope, and measure the visibility function using electronic combination of the signals

²This is known as the Van Cittert-Zernicke theorem. Readers requiring a more rigorous derivation are referred to Born & Wolf's (1975) classic textbook on optics, or the introduction to radio astronomy by Burke & Graham-Smith (2002).

over baselines up to ~ 150 km (Adgie et al. 1965). As the telescopes were moved further apart, the visibility finally fell below unity at large separations, allowing the angular size to be calculated as λ/d .

1.2 Application to real interferometers

The Young's slit experiment discussed so far involves sampling two parts of a plane wave generated a large distance away, delaying one wave with respect to the other, and generating the interference pattern as a function of delay. There are many situations in which exactly the same thing is being done. In Fig.3, for example, a plane wave from a source at infinity is sampled by two telescopes separated by a vector \mathbf{B} . The path delay between the two waves is given by $\mathbf{B}\cdot\mathbf{s}$, where \mathbf{s} is the unit vector in the direction of the source, and the phase delay is therefore given by $k\mathbf{B}\cdot\mathbf{s}$, where $k \equiv 2\pi/\lambda$.

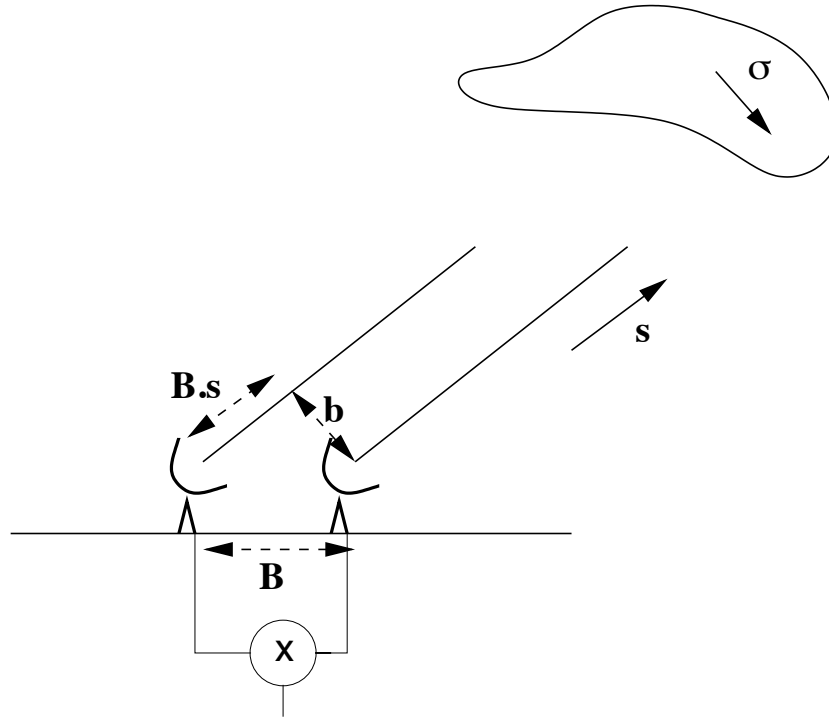


Fig. 3. Basic diagram of an interferometer with baseline vector \mathbf{B} observing a source in a direction with unit vector \mathbf{s} .

Consider a point source. If the electric field received by the first telescope is E , that received by the second is just $Ee^{ik\mathbf{B}\cdot\mathbf{s}}$, because of the phase delay. We can combine these signals, in a way analogous to the screen in Young's

slits, by multiplying them together electronically³ or, in the case of optical systems, by using a Michelson or Fizeau interferometer system to combine the beams. If we then add the fringe patterns over different parts of the source, we obtain the response of the interferometer R as

$$R = \int I(\sigma) e^{ik\mathbf{B}\cdot(\mathbf{s}+\sigma)} d\sigma$$

where $\mathbf{s}+\sigma$ is the vector in the direction of a particular small part of the source with an intensity $I(d\sigma)$. Noting that σ is parallel to the projected baseline vector \mathbf{b} (Fig. 3) and so $\mathbf{B}\cdot\sigma = \mathbf{b}\cdot\sigma$, we then have

$$R = e^{ik\mathbf{B}\cdot\mathbf{s}} \int I(\sigma) e^{ik\mathbf{b}\cdot\sigma} d\sigma,$$

where the $e^{ik\mathbf{B}\cdot\mathbf{s}}$ term is solely dependent on the array geometry and has therefore been removed from the integral.

What we therefore have is a series of fringes, whose amplitude is given by the Fourier transform of the source intensity distribution. In practice, steps are usually taken to get rid of the fringes using a phase rotation whose rate is known (as both \mathbf{B} and \mathbf{s} are known). This is done in optical interferometers by use of accurate delay lines to compensate for the path difference, and in radio interferometers by the insertion of electronic delays. We are then left with the Fourier transform response only, which conveys information about the source. The response is a complex quantity which contains an amplitude and a phase; both are interesting.

Because of the fact that the signal from an interferometer results from the correlation of signals from two telescopes, interferometers have the advantage of much lower sensitivity to interference because most interference does not correlate. Thus the only interference which causes a serious problem is that which saturates or disables the receiver. Such interference can be dealt with by dividing the observing band into spectral channels and removing any channels affected.

1.3 The u, v plane

A further step is to decompose both σ and \mathbf{b} into Cartesian coordinates. The decomposition of σ is easy, as it is just a vector in the sky plane: $\sigma = \sigma_x \mathbf{i} + \sigma_y \mathbf{j}$, where \mathbf{i} and \mathbf{j} are unit vectors in the east-west and north-south directions respectively. This then suggests a decomposition of \mathbf{b} into $u\mathbf{i} + v\mathbf{j}$, so that $\mathbf{b}\cdot\sigma = ux + vy$. The response after fringe stopping then becomes

³This is not exactly the same as the Young's slits screen, which adds the electric fields and then forms the intensity using $I = (E_1 + E_2)^*(E_1 + E_2)$, but the result is almost the same apart from a constant offset term in the addition case. Not having this term is useful because we do not have to worry about the offset term being constant with time.

$$R(u, v) = \iint I(x, y) e^{2\pi i(ux+vy)} dx dy,$$

a much more explicit 2-D Fourier transform. Note that u and v are defined in units of wavelength, hence the k in the previous expressions has become 2π .

The physical interpretation of the decomposition of \mathbf{b} is fairly straightforward. Imagine sitting on the source (Fig.4); then the projected baseline vector appears as a line drawn on the earth. This can be decomposed into a component parallel to the equator at its nearest point to the source, and a component parallel to the line between this point and the north pole. These components are u and v , and they change as the earth rotates. Specifically, they trace out an ellipse in u, v space during one earth rotation (Fig. 4).

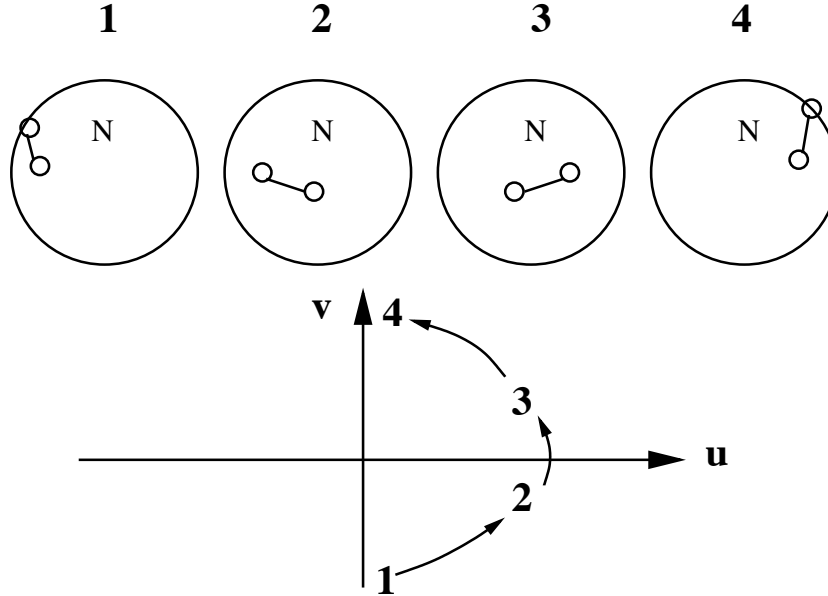


Fig. 4. Schematic diagram showing the baseline between two telescopes as the earth rotates. The E-W and N-S components of this vector give u and v . For an east-west baseline, $v=0$ at source transit.

This change in u and v is useful, as we see if we consider how the response function $R(u, v)$ tells us what is on the sky. Fig. 5 shows the basic Fourier transform relation in a diagram. A double source of separation 1 radian produces stripes in the u, v plane of separation 1 wavelength. Since the Fourier transform gives an inverse relation between distances in the two spaces, a double source of separation a arcseconds gives a series of stripes of separation $206265/a$ wavelengths. Superposed on this is the track of the u, v ellipse, and over a day there are therefore variations in the interferometer response as the interferometer follows the elliptical track over these stripes. Studying

this variation in amplitude (and phase) response over the period, we could work backwards to deduce the separation and orientation of the stripes, and by taking the Fourier transform, recover the source structure.

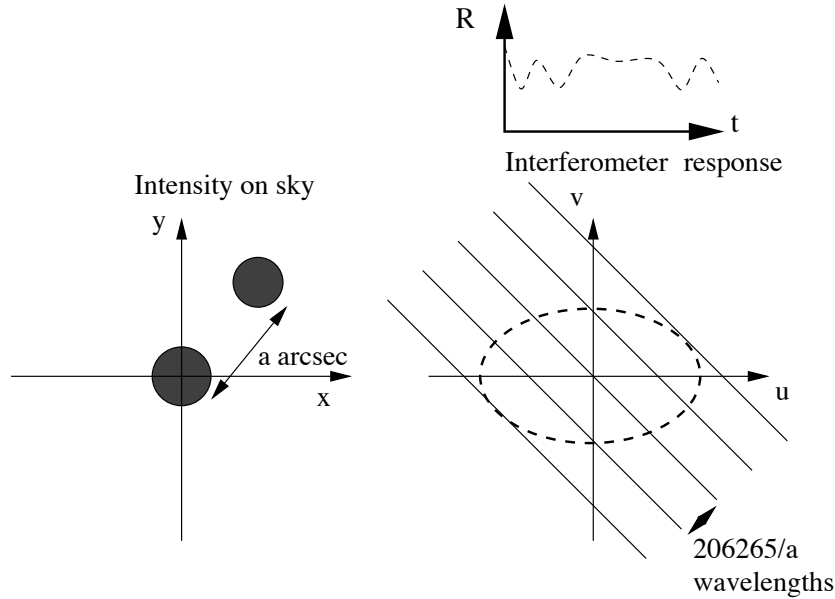


Fig. 5. Diagram showing the interferometer response as a function of u and v for a double source on the sky.

The u, v track has a semimajor axis in the u direction of $\frac{L}{\lambda} \cos \delta$, and a semiminor axis in the v direction of $\frac{L}{\lambda} \cos \delta \sin D$.⁴ In these expressions L is the baseline length, D is the declination of the source, and δ the declination of the baseline; the latter quantity is the declination of the point on the celestial sphere to which the baseline vector points.

The resolution of which a baseline is capable is given by the inverse of the maximum extent of the u, v ellipse, namely λ/L . The point-spread function of an image has dimensions which are the inverse of the spread in the u, v plane of the images being used, which means that for sources close to the equator (where $D \rightarrow 0$ and the ellipses collapse to straight lines) the point-spread function of an interferometer is typically less ideal, although images of the sky can be made with care. Fig. 6 shows the u, v tracks for the MERLIN

⁴Spherical trigonometry can be used to show that the ellipse is parametrised by the equations: $u = \frac{L}{\lambda} \cos \delta \sin(H - h)$, $v = \frac{L}{\lambda} (\sin \delta \cos D - \cos \delta \sin D \cos(H - h))$ (e.g. Rowson 1963). Here, H is the hour angle of the source and h the hour angle of the point on the sky to which the baseline points. For a general baseline, the centre of the ellipse is offset by $\frac{L}{\lambda} \sin \delta \cos D$ from the origin in the v -direction.

interferometer array, which contains baselines from 6 km to 250 km at a range of orientations. Note the gradual change from circular u, v tracks to nearly linear tracks as the source declination decreases.

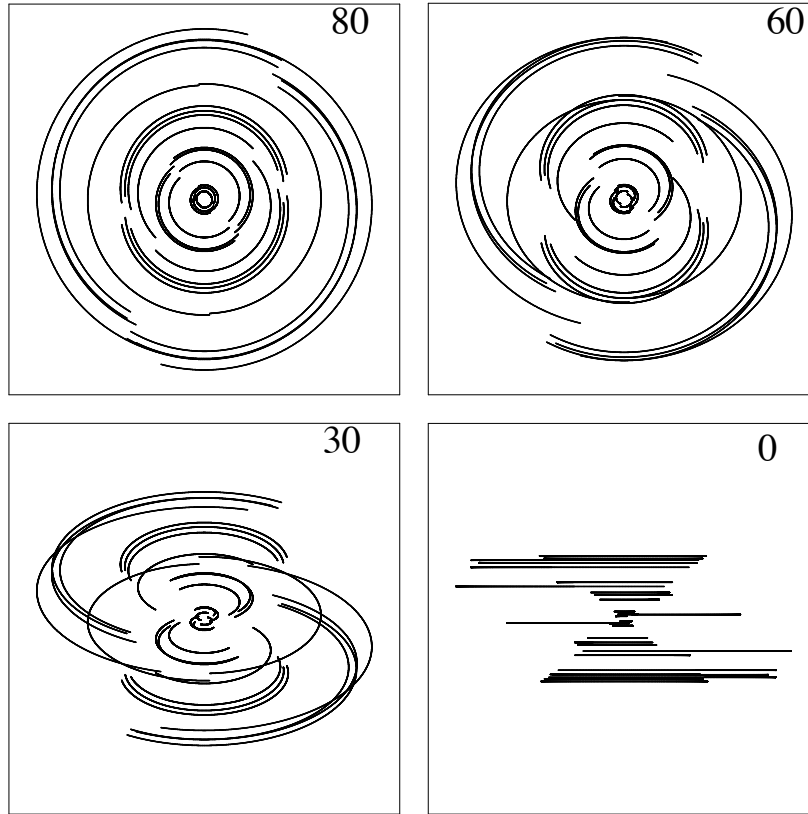


Fig. 6. u, v tracks for the MERLIN interferometer for sources at four different declinations: 80° , 60° , 30° and 0° .

If many baselines are present, many simultaneous measurements can be made in the u, v plane. The more completely the Fourier plane is filled, the easier it is to obtain a faithful reproduction of the sky intensity distribution in an interferometric image.

1.4 A cautionary tale

Interferometric (Fourier) imaging has important differences from direct imaging. The most important difference can be deduced from going back to the Young's slits setup: long baselines record small-scale structure in the source

very well, but are *insensitive* to large-scale structure, because once the source becomes larger than λ/L the fringes wash out and do not return as the source size increases. An example of this is shown in Figs. 7 and 8.

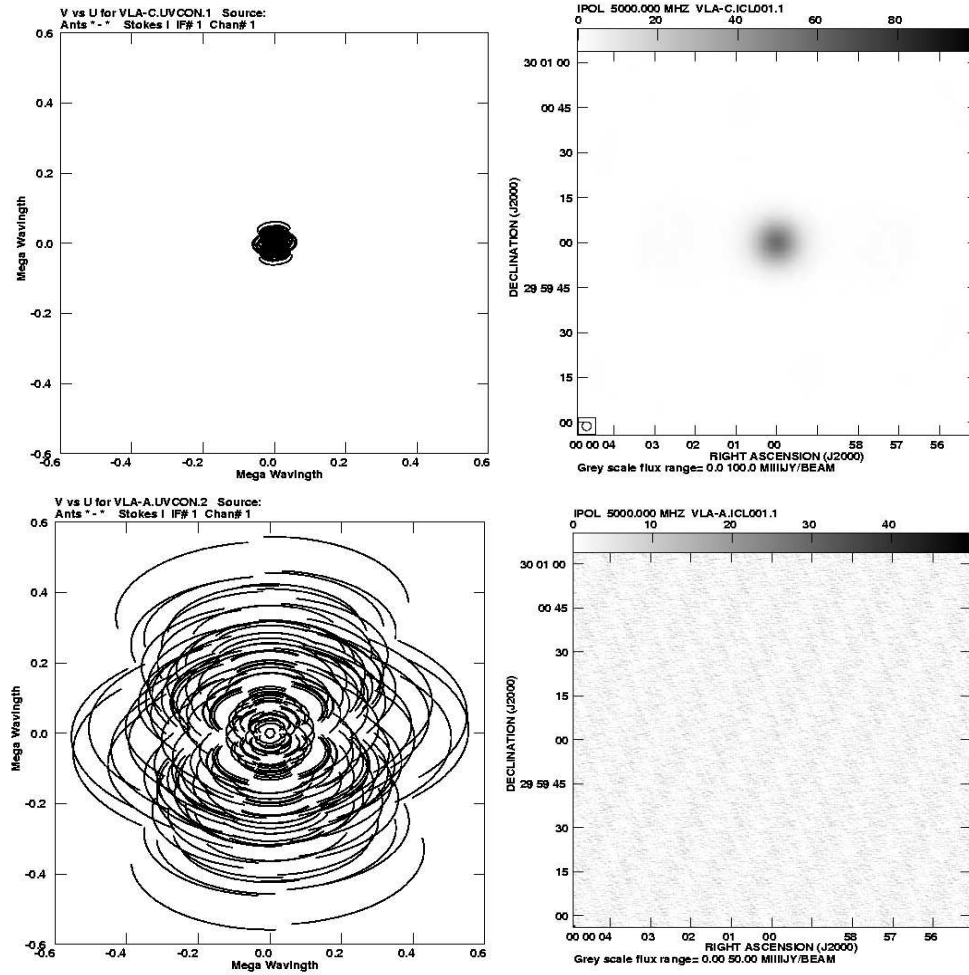


Fig. 7. Simulations of observations of a large Gaussian source with a set of short baselines giving low resolution matched to the size of the source (top left, u, v coverage, top right, resulting image) and a set of long baselines giving higher resolution (bottom left, u, v coverage, bottom right, resulting image).

Fig. 7 (top panels) shows a simulated source of $12''$ extent, mapped using an array whose u, v coverage gives a maximum baseline length corresponding to a resolution of $3''$. The source structure is recovered reasonably well, as

the range of baselines present cover spatial scales from the resolution up to approximately 10 times larger scales. Now suppose that we get greedy, and decide that we would like to observe at ten times higher resolution. This is no problem – we move the telescopes to spacings ten times greater and repeat the observation. This indeed gives a map with 300-mas resolution, on which there is no sign of the source (Fig. 7, bottom panels).

Let us then try to smooth the image and recover the structure. If we try this, what we actually recover is shown in Fig. 8. The awful realisation dawns at this point that by using a long set of baselines, we have not recorded the structure on large spatial scales at all, and have lost it irretrievably. The moral is that interferometer arrays should be chosen carefully to match resolution to the spatial scales required by any particular astrophysical problem⁵.

1.5 Field of view of interferometric images

Primary beam

Once again, we can go back to Young’s double slits to deduce the another fundamental limitation of the interferometric image. If the slits are widened, the aperture distribution no longer consists of two delta-functions, but of two delta functions convolved with a single wide slit. It follows from the convolution theorem that the interference pattern, being the Fourier transform of the aperture distribution, consists of the original two-slit fringe pattern multiplied by the Fourier transform of a wide slit, namely a sinc function. The sinc function has a width inversely proportional to the width (w) of the slits, and the fringes disappear at delays greater than the width of the sinc function, λ/w .

Now in an interferometer, going further away from the centre of the field of view just corresponds to a different delay from that which obtains at the centre. The width of the slits translates directly to the size of each interferometer element, and the field of view in radians is the wavelength of the light being studied divided by the diameter of the elements.

Wavelength ranges

Again going back to Young’s slits, it is easy to see that other effects may intervene before the primary beam limit is reached. The most serious of these

⁵In fact, using resolution higher than required often causes even worse problems. This is because for any given array, higher resolution demands observing at higher frequencies, which in turn imposes penalties in source brightness for typical steep-spectrum radio sources and in generally worse system performance at high frequencies. Some interferometers, in particular the VLA, allow different resolution images at the same frequency by regularly moving the telescopes between different configurations, from compact to more extended.

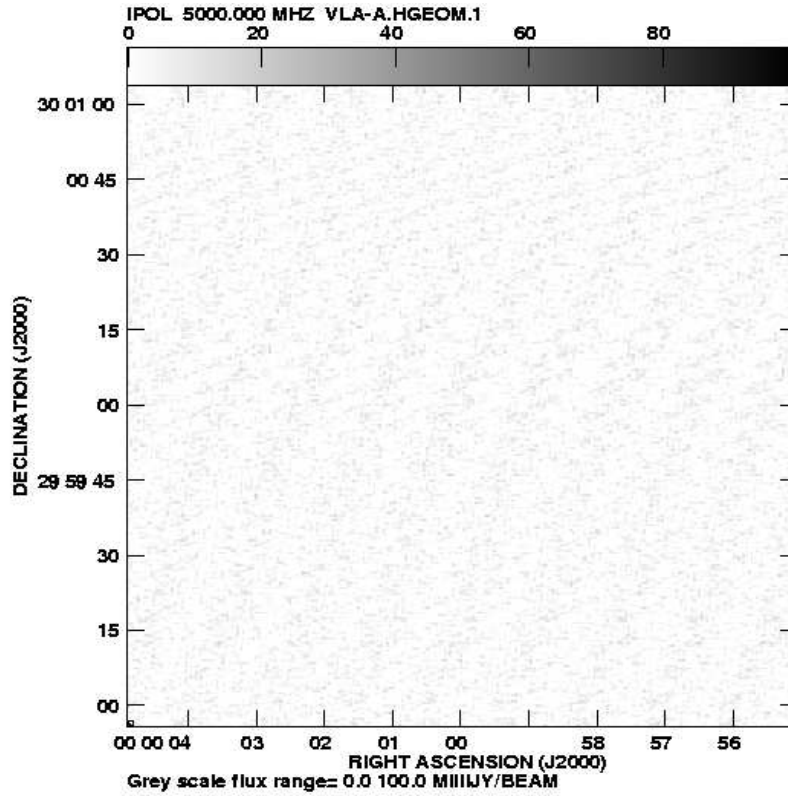


Fig. 8. Smoothed image of a long-baseline observation of a diffuse source. Nothing is visible.

is that the radiation is not monochromatic. We can consider each single frequency separately, and add the resulting fringe patterns which have different separation (λ/d) between maxima. The result is that in the centre of the fringe pattern, full-visibility fringes are seen, since here the delay is zero. At larger values of delay, further up the screen, the interference fringes from different colours add in such a way as to reduce the visibility to zero even for a point source. Once again, the effects at large delay translate directly to the interferometer, and a range of wavelengths in the interferometer causes loss of response at the edge of a field of view where the delay between the interfering waves is different ⁶. If the bandwidth is $\Delta\lambda$, then the field of view is given by

⁶For a large Gaussian-shaped bandwidth, the fringe response as a function of angular distance from the centre is a small Gaussian, and for a small Gaussian-shaped bandwidth, the fringe response varies as a broad Gaussian with angular distance. This completes another “proof” of a Fourier transform relation between these two quantities.

$$\Delta\theta = (\lambda/\Delta\lambda)(\lambda/L),$$

or the beam-size divided by the fractional bandwidth. In order to achieve reasonable signal-to-noise, many interferometers use large fractional bandwidth, implying a very restricted field of view. The solution is simply to divide the signal into many frequency channels and correlate each separately. The cost is greater complexity of the correlator and larger datasets, but in most modern interferometer systems computing and hardware are advanced enough that it is usually possible to image the full primary beam.

Other effects

Two other effects should be mentioned briefly; see Taylor et al. (1998) for further details. The first is that a limitation on the field of view is imposed by the integration time per data point, because the values of u and v change during a finite integration time. This gives a roughly tangential smearing in the u, v plane which becomes worse further out, which Fourier transforms into a tangential smearing in the sky plane which becomes worse further out. The result is that amplitude is lost at the edge of the field. The second effect is that the sky is not flat, and that instead of using a 2-D Fourier transform we should have used a 3-D transform, with an extra phase term of the form $\sqrt{(1-x^2-y^2)}$ added to the transform. Unlike the bandwidth and integration time effects, the effect of non-flatness is curable after the event by additional processing.

2 Producing the image

2.1 Deconvolution

So far we have circumvented the major problem, which is that the interferometer response function has not been measured over the whole u, v plane. To do this at a single frequency would require enough telescopes to provide baselines at all possible separations and orientations, an expensive operation with substantial planning implications. Lack of this information means that the number of different images consistent with the data is infinite, since we could in principle fill in the unmeasured parts of the u, v plane in an infinite number of ways.

The basic problem is that we want the image $I(x, y)$ resulting from the full u, v response function $I(u, v)$,

$$I(x, y) = \iint I(u, v)e^{2\pi i(ux+vy)} du dv$$

but instead have the “dirty image”

$$I_D(x, y) = \iint I(u, v)S(u, v)e^{2\pi i(ux+vy)}dudv$$

which results from the intervention of the sampling function $S(u, v)$ which is 1 in parts of the u, v plane where we have sampled and zero where we haven't.

We recognise the right-hand side of the last equation as a Fourier transform, where the argument is the product of two functions I and S . We can therefore use the convolution theorem to write

$$I_D(x, y) = I(x, y) * B(x, y)$$

where

$$B(x, y) = \iint S(u, v)e^{2\pi i(ux+vy)}dudv,$$

the “dirty beam”, is the Fourier transform of the sampling function. Since we know where the telescopes are and can do spherical trigonometry and Fourier transforms, the sampling function and hence dirty beam are accurately known. Recovering the image $I(x, y)$ is therefore a classical deconvolution problem, in which we need to supply additional information in order to do the deconvolution.

CLEAN

The first way to do this is the algorithm known as CLEAN (Hogbom 1974) which amounts to a brute force deconvolution. The basic algorithm begins by detecting the brightest point in the dirty map, shifting the dirty beam to this point, and scaling and subtracting off the dirty beam⁷. At each subtraction, the flux and position subtracted are noted, until the map from which the dirty beams have been subtracted (known as the residual map) consists only of noise. At this point, the subtracted fluxes are convolved with a restoring beam selected by the user and added back into the field of noise to give a final “CLEAN map” from which the sidelobes of the dirty beam have been removed. The usual procedure is to make the CLEAN beam of the same dimensions as the central spike in the dirty beam. This is a logical procedure, since the dirty beam is the Fourier transform of the sampling function, and the further out in the u, v plane the sampling function has non-zero values, the higher the resolution we are justified in using. It is possible to use a CLEAN beam smaller than the formal resolution (a process known as super-resolution) at increasing risk of introducing incorrect structure in the map. Fig. 9 shows an example of the CLEAN procedure in action.

An important decision in the CLEANing process is the weighting to be applied to the data, as the recorded data is not uniformly distributed across

⁷In practice, a fraction – typically 5–10% – of the dirty beam is subtracted to improve stability. This fraction is known as the ‘loop gain’.

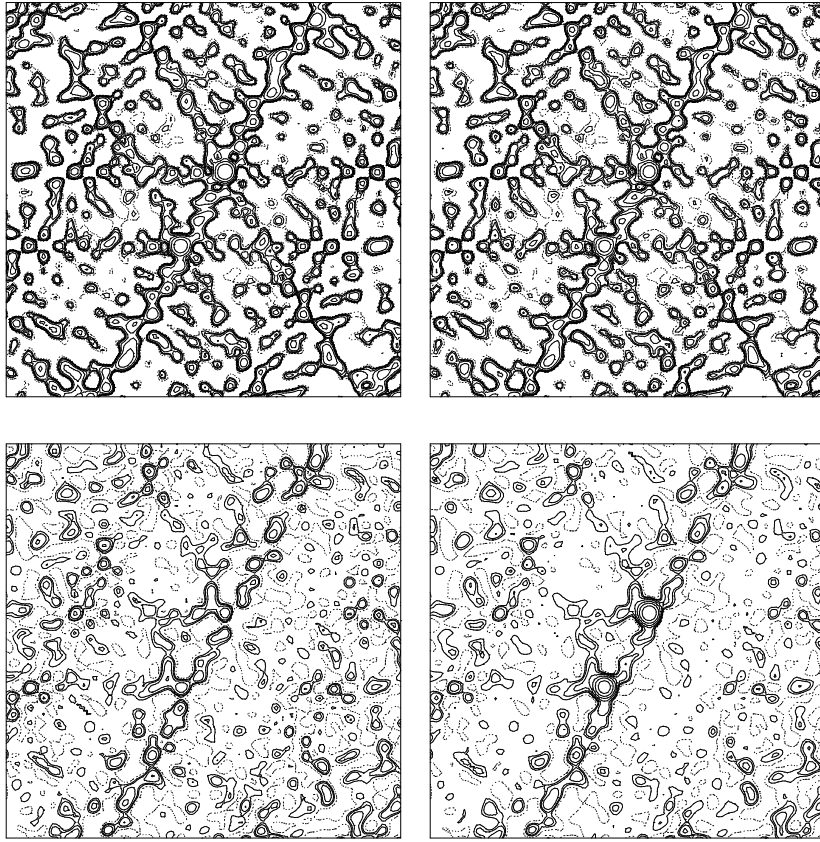


Fig. 9. CLEANing procedure applied to a radio source consisting of two point source components observed with the VLA. All maps are contoured at the same level. Top left: the dirty map. Top right: the residual map after 10 iterations of CLEAN, in which a small amount of flux has been removed at each iteration. Bottom left: the residual map after 100 iterations of CLEAN: note the removal of most of the dirty beam structure. Bottom right: the CLEAN map after some further CLEANing, formed by the addition of the point source components back into the final residual map. Further CLEANing does not give significant improvement; although the basic source structure is visible, there are some clear artefacts remaining. Their causes and cure are addressed in section 3.

the u, v plane and in practice is usually concentrated towards the centre. One option is “natural weighting”, in which all data points are treated equally. Statistically, this provides the best signal-to-noise in the final image, but because of the central concentration of the u, v data the sampling function is more centrally concentrated, and its Fourier transform, the dirty beam in the sky plane, is therefore more extended. The result is worse resolution in the final map. An alternative option is “uniform weighting” in which equal weights are applied to each u, v grid, giving increased resolution at the expense of weighting down data at small u and v and degrading the signal-to-noise.

The additional information that has been supplied to the deconvolution problem by CLEAN is the assumption that the sky consists of a finite number of point sources, or alternatively that most of the sky is empty. Not surprisingly, therefore, CLEAN works very well for simple sources, but can occasionally fail on very large amorphous sources of low surface brightness.

Maximum Entropy

A second deconvolution method is altogether different in philosophy, and is known as the Maximum Entropy Method, or MEM (e.g. Bryan & Skilling 1980). The starting point is to consider possible images of the sky, and prefer those which are more likely. The most preferred image is a completely uniform distribution, which gives the maximum entropy (or minimum information); however, such an image is normally inconsistent with the data. If we consider images which are progressively less likely to be produced by chance, sooner or later we encounter an image which still occurs relatively often, but which is nevertheless consistent with the data. The process therefore corresponds to a joint minimization including the goodness of fit to the data and the maximum effective smoothness (usually parametrised in forms such as $\sum p_i \ln p_i$, where the p_i 's are the individual pixel values).

2.2 Sensitivity

The sensitivity (r.m.s. noise) of a wave-regime (metre-centimetre) interferometer is given by

$$S = \frac{\sqrt{2}k_B T_{\text{sys}}}{A\eta\sqrt{n_b}\Delta\nu t_{\text{int}}}$$

where T_{sys} is the system temperature, A is the area of each antenna, η is the aperture efficiency, n_b is the number of baselines, $\Delta\nu$ is the observing bandwidth and t_{int} is the integration time. The units are $\text{Wm}^{-2}\text{Hz}^{-1}$, but because the Boltzmann constant k_B is uncomfortably small the usual unit is the Jansky, where $1 \text{ Jy} \equiv 10^{-26}\text{Wm}^{-2}\text{Hz}^{-2}$. For extended sources the sensitivity is Janskys per beam area. The sensitivity of many modern interferometers after a few minutes of integration is around $100\mu\text{Jy}/\text{beam}$.

A couple of terms in the equation deserve comment. We can define “temperatures” in this context in terms of the temperature of a black body which would provide the equivalent received power of radiation at the observing frequency⁸. The noise contribution to a radio interferometer is provided mainly by the receivers (contributing typically 30-50K), spillover from thermal emission from the ground, and ultimately by the 3K contribution from the cosmic microwave background. The aperture efficiency η can be varied according to how the aperture is illuminated (i.e. the relative weight given to radiation reaching the feed from different parts of the antenna).

In an optical interferometer the formulas are somewhat different, because we are collecting photons. There are a number of detailed differences. The first is that it is impossible to clone photons in the same way that electrical signals can be reproduced indefinitely, so every time a beam is split, signal-to-noise is lost. For example, if the array consists of eleven elements, the beam from each element must be split ten times, losing signal-to-noise, if we wish to interfere all of the beams to produce fringes on all baselines. Secondly, the practical limit is always imposed by the fact that we need a reasonable number of photons in one isoplanactic patch (the area over which the atmospheric corruption is approximately the same) in one atmospheric coherence time (the timescale of variation of atmospheric corruption). Third, optical interferometers typically contain a large number of reflecting elements, with a some light loss at each reflection.

Although it is probably fair to say that the problems have been more difficult than anticipated, major progress is now being made. The use of adaptive optics on individual telescopes means that the wavefront can be corrected over the whole aperture, increasing the coherence patch to the area of the telescope diameter and hence increasing the potential signal. In an optimum site such as that of the Very Large Telescope Interferometer (VLTI) on Paranal mountain in Chile, images of 14th magnitude objects can be made. A list of current optical interferometer systems is given by Monnier (2003).

3 Dealing with the atmosphere

Electromagnetic radiation travels to us for billions of years through a nearly perfect vacuum as a nearly perfect plane wave. Unfortunately, the Earth’s atmosphere intervenes in the last microsecond to convert a smooth wavefront into a wavefront with phase corrugations which vary over small spatial scales and on potentially small timescales. At some wavelengths, the amplitude of the wavefront is affected as well as the phase.

There are a number of features in the earth’s atmosphere which corrupt the wavefronts. At low radio frequencies, the problem is the ionosphere, con-

⁸In the wave regime, we are in the Rayleigh-Jeans part of the Planck spectrum, and the specific intensity at a given frequency (in units of $\text{Wm}^{-2}\text{Hz}^{-1}\text{sr}^{-1}$) can be written as $2k_B T/\lambda^2$

sisting of a collection of charged particles capable of shifting phases below the plasma frequency (typically a few hundred MHz) and which responds to solar activity, producing most disturbance at times of solar maximum. At higher radio frequencies, the problems are mainly due to water vapour, which produces phase rotations on “coherence timescales” of minutes above 10 GHz. Successively shorter coherence times are seen as the frequency increases, until not only the phase but also the amplitude is affected. Observations at higher radio frequencies, such as the ≥ 30 GHz observations typically used to observe the peak of the CMB radiation, are usually done from high mountains above most of the water vapour; some experiments in this region are planned at the South Pole where the water vapour is frozen out.

In the infrared and optical region of the electromagnetic spectrum, the coherence times are typically much shorter. The transverse length scale of phase fluctuations is given by the Fried parameter r_0 , and these atmospheric fluctuations are blown across any given line of sight by tropospheric winds. The resulting phase and amplitude fluctuations have characteristic timescales of tens of milliseconds, requiring corrections to be applied on short timescales which are now being achieved.

3.1 Closure quantities

Ignoring atmospheric phase fluctuations is not an option, as the response function of the interferometer is directly affected by them and their effect is to wipe out the fringes. The phase on any individual baseline is not a good observable, since atmospheric errors e_1 and e_2 on two telescopes produce a resultant of the form $e_1 - e_2$ in the response function when the signals are correlated⁹.

We can observe, however, that if we have a triangle of three telescopes, and if we measure the interferometer phase response on each baseline, we obtain three phase responses containing the phase error terms $e_1 - e_2$, $e_2 - e_3$ and $e_3 - e_1$. These add to zero, leaving only information on the astronomical structure. Although we have slightly fewer constraints, by modelling these “closure phases” we can obtain constraints on the phases of the response function in the u, v plane and hence deduce the source structure.

A similar quantity can be derived for amplitudes. Since amplitudes are multiplicative, four telescopes are needed in order to use the baseline amplitudes to form the quantity $A_{12}A_{34}/A_{13}A_{24}$. The error on A_{12} is the product of the amplitude error terms, a_1a_2 , and once again the errors cancel out.

Closure mapping has been used for many years. It has successfully been used in optical interferometry, even from sites with considerable phase fluctuations such as the situation of the COAST optical interferometer. Despite the less than ideal atmospheric conditions, maps have been produced of bright

⁹Correlation involves an operation of the form $\langle E_1 E_2^* \rangle = A_1 e^{i\phi_1} A_2 e^{-i\phi_2}$, so amplitudes multiply and phases add or subtract.

stars such as Capella and Betelgeuse (Young et al. 2004). This gives a clue to the main limitation, however; use of this method requires that the sources be bright. This is because what is required is sufficient signal on the source in an atmospheric coherence time to separate atmospheric and source phases.

3.2 Self-calibration

The assumption of closure mapping is that errors in amplitude and phase are separable by telescope, and that no additional errors are introduced into the response function of each baseline separately. This is not precisely true, and in practice the biggest problem is usually mismatched bandpasses in the correlator which gives baseline-dependent errors. Great care is usually taken to minimise these, resulting in such errors being a few tenths of a percent.

The assumption of only telescope-based error is used in the procedure known as self-calibration (Cornwell & Wilkinson 1981) which uses the data, together with a guessed model, to determine the phase and amplitude corrections on each telescope. Suppose we have visibilities V_{ij} on baselines between telescopes i and j , and we call the telescope complex gains g_i and g_j . Suppose also that we have a model whose Fourier transform predicts visibilities V_{ij}^M . Then we write the equation

$$V_{ij} = g_i g_j V_{ij}^M$$

for all i, j , and use a least-squares solution to determine the g_i s. The process is repeated by replacing the original data with $V_{ij}/g_i g_j$, mapping and CLEANing the new data to produce a new model, Fourier transforming to give a new set of model visibilities $V_{ij}^{M'}$, and repeating the process until it converges and the g_i corrections are close to 1.

At first sight this looks an uncomfortably incestuous procedure. A model which may or may not look like the sky has been used to correct the visibility data, and we have then used a model derived from the corrected data to determine further corrections. One answer is that the procedure works. Simulated data can be created, phase and amplitude errors added and the original sky map is recovered by self-calibration. The underlying reason for its success is that the problem is overconstrained, because in any one integration the number of unknowns is proportional to the number of telescopes, n , and the number of constraints is proportional to the larger number of baselines, $n(n-1)/2$. Fig. 10 shows an example of self-calibration in action.

There are a number of caveats in practice. The most important is that the source needs to contain a point source bright enough to be visible on all baselines at $> 3\sigma$ in one coherence time – for many interferometer arrays, this means of the order of 10–20 mJy. The reason is that the least-squares fit in which the g_i s are computed degenerates into a noisy mess if the V_{ij} s are noisy. Because the corrections change over a coherence time, it is not possible to integrate for a long time in order to build up signal-to-noise to do the correction.

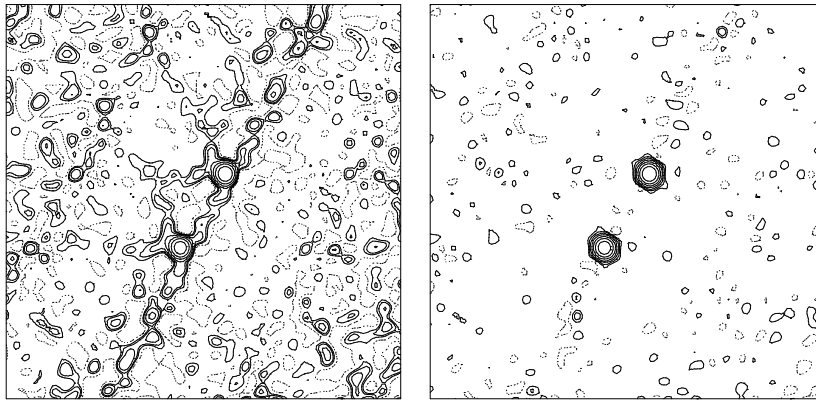


Fig. 10. The same radio source as in Figure 9. The left panel shows the deconvolved map after CLEAN only. On the right is the same map after one iteration of phase selfcalibration and further CLEANing. The maps are contoured at the same level, but the impact of selfcalibration in removing artefacts due to phase corruption is obvious.

A second caution concerns the order in which the phase and amplitude corrections are built up. Since atmospheric effects on phase are nearly always more major than amplitude effects, it is usually better to begin by computing only the phase part of the complex gains, using a time interval shorter than the phase coherence time, and only then to correct the amplitude part. This halves the number of free parameters in the early part of the process and thereby makes it much more stable. Once the phases are determined, the amplitudes can be corrected over a longer timescale as (at least at a few GHz) the amplitude corruption does not change as quickly. Indeed it is often a good idea, particularly in sparsely filled arrays or for relatively weak sources, not to use too short a correction time for the amplitudes. For most VLBI experiments 15-30 minutes is probably safe.

3.3 Phase calibration

A more direct way to correct the atmospheric phase corruption is to calibrate it directly, rather than sort it out after the event. In this approach, a calibrator source of known structure is observed periodically. Because the source structure is known, it can be Fourier transformed and removed from the interferometer response function. Any residual phase structure must be atmospheric and can be interpolated and removed from observations of the target.

This approach is attractive because, provided the calibrator source is strong enough to allow good signal-to-noise per baseline per atmospheric coherence time, there is in principle no limit on the brightness of the target

source. Phase calibration, otherwise known as “phase referencing”, is therefore widely used. There are two caveats: first, the target source must be in the same isoplanactic patch (that is, the target and phase calibrator must be close enough that the atmospheric phase corruption is similar for both), and the switching must be done with a period not greater than the atmospheric coherence time.

4 Interferometers in practice

4.1 Very brief history

Much of the development of connected-element interferometry was done by groups in the UK, USA, the Netherlands and Australia, and a Nobel Prize was awarded to Martin Ryle in Cambridge for development of the technique. This group used arrays of dipoles, and later connected dish antennas together forming the One-Mile Telescope, to discover and investigate radio sources (Ryle 1962). The earliest large radio source catalogue, 3C, contained the first two known quasars, 3C48 and 3C273. The successor to the One-Mile Telescope, the 5-km Telescope (now known as the Ryle Telescope, Ryle 1972) was built soon afterwards.

At the same time, other interferometer arrays were being built, including the Westerbork Synthesis Radio Telescope (WSRT) in the Netherlands (Allen, Hamaker & Wellington 1974), the Bologna Cross, arrays at Molonglo in Australia and Ooty in India. The MERLIN six-telescope interferometer array, based at Jodrell Bank, pioneered the extension of connected-element interferometers to longer baselines of around 200 km giving higher resolution (Davies et al. 1980). Also in the late 1970s, the Very Large Array (VLA, Thompson et al. 1980) was built. This instrument has 27 25-m diameter telescopes, giving high sensitivity, and has a maximum baseline of 36 km. It is arranged in a Y-shape, and the antennas can be moved to four different configurations with baselines shorter by successive factors of 3.

4.2 More current and future interferometer systems

A brief overview of some long-wavelength interferometer systems follows (see also Fig. 11). Again, the new optical systems, such as the VLTI, COAST and Keck interferometers are covered by the article by Monnier (2003).

VLBI

An important subset of interferometer arrays are those operating on very long baselines, known as VLBI (very long baseline interferometer) arrays. The original such collaboration was the European VLBI Network (EVN) whose founding member telescopes included the 76-m Jodrell Bank telescope in the UK,

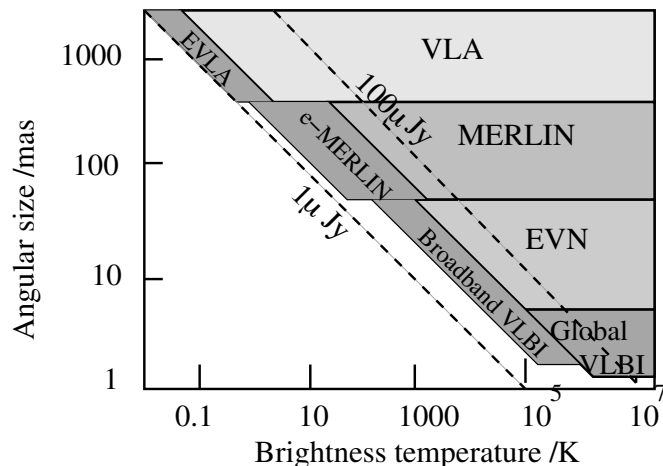


Fig. 11. Range of angular source size (set by the resolution) and brightness temperature of sources, with the northern interferometer array suited to the observation at 5 GHz. The lower limit to each range is set by resolution, and the upper limit by the insensitivity of interferometers to sources larger than that visible to their shortest baselines. The upgrades described in the text are included in the figure. The strength of the sources is plotted as “brightness temperature” which is related to flux density S in Jy by the equation $S = 2k_B T \Omega / \lambda^2$, where Ω is the beam solid angle. Reproduced from the MERLIN website www.jb.man.ac.uk/~merlin.

the WSRT in the Netherlands¹⁰, the 100-m Effelsberg antenna near Bonn, Germany, the Onsala 25-m telescope in Sweden and the 32-m Bologna telescope in Italy. Further telescopes now part of the EVN include the Torun telescope in Poland, and further antennas in Italy, Spain and China. A 10-telescope array, the Very Long Baseline Array (VLBA) was subsequently built in the USA with somewhat higher resolution but lower sensitivity. It is possible to combine the EVN and VLBA into a global VLBI array with high sensitivity (about $10 \mu\text{Jy}/\text{beam}$ after 12 hours) and a resolution of 1 mas, about 50 times higher than that of the Hubble Space Telescope. It is also possible to increase the baseline still further by launching a radio antenna into space. This was done experimentally by use of the TDRSS satellite (Linfield et al. 1989) and later by the dedicated VLBI satellite VSOP/Halca, launched by the Japanese space agency in 1997 and which observed until 2003. A larger mission (VSOP-2) is currently funded, which will feature a larger telescope to be launched in 2012.

¹⁰The WSRT is itself a connected-element interferometer, but it is possible to insert phase delays into the arm of each element in such a way as to use the interferometer as a single telescope with effective area of the sum of the individual telescope areas (a process known as “phasing up”).

VLBI observations are usually not combined into visibilities at the time of observation. Instead, they are often recorded on tape, together with accurate time stamps from a maser clock, and shipped to a central processor for correlating, usually the JIVE facility in the Netherlands or the NRAO correlator in Socorro. Recently, with the availability of increased Internet bandwidths, it has been possible to send the signals to the central correlator online, a process known as e-VLBI. In principle, the only limit on this technique is the speed of the correlator and the availability of the huge Internet bandwidths required.

GMRT

The Giant Metre-wave Radio Telescope (Swarup et al. 1991) is located in India, near the city of Pune. It consists of 30 45-m antennas, and the resulting large collecting area gives very high sensitivity between 50MHz and 1420MHz; the frequency range is limited at the high end by the fact that the antennas are of mesh rather than solid metal. It is particularly suitable for relatively high-resolution, sensitive imaging at low frequencies including the redshifted neutral hydrogen line.

ATCA

The Australia Telescope Compact Array is the most significant long-wavelength interferometer system in the southern hemisphere. It consists of six 22-m antennas over baselines of up to 6 km, with good high-frequency performance.

Fibres and sensitivity: EVLA and e-MERLIN

Important upgrades to Earth-based interferometers are currently under way. The major programmes involve an increase in sensitivity by using higher bandwidth. Currently signals are transmitted using transmission lines or microwave links with a limited bandwidth, typically a few tens of MHz. Both MERLIN and the VLA are being upgraded within the next few years (becoming, respectively, e-MERLIN and the EVLA) by the addition of optical fibre links between telescopes. These links can carry signals of ~ 2 GHz of bandwidth, resulting in a factor of 5–10 in improvement in signal-to-noise, and in both cases for a small fraction of the cost (in current dollars) of the original arrays. The increased bandwidth has another benefit when observing a broadband source, namely an improvement in u, v plane coverage. Since the u, v plane is measured in wavelengths, a wide band means that for a given baseline, a range of positions in the u, v plane are measured simultaneously. This means that even an array with a small number of elements, such as MERLIN with six telescopes, can cover essentially all of the u, v plane and thus deliver very high image fidelity (Fig. 12). With complete aperture coverage, radio interferometers will be able to produce the same level of detail as in current direct optical images.

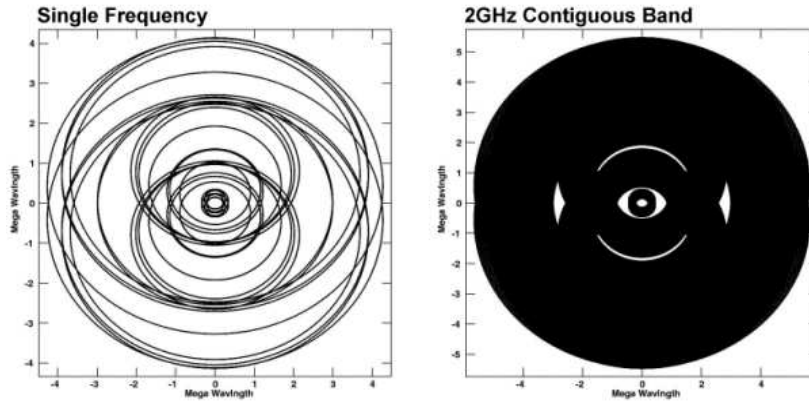


Fig. 12. The difference between u, v coverage of MERLIN, a six-telescope interferometer array, using a single frequency (left) and a 2-GHz bandwidth at 5 GHz (right). The essentially complete coverage of the u, v plane allows extremely high fidelity imaging of much more complex structure than hitherto possible. The processing power needed is considerably greater, because of possible spectral index gradients across the source, but this too is essentially a solved problem. The image is reproduced from the e-MERLIN science case.

LOFAR and the MWA

At the low-frequency end of the radio spectrum, it is possible to increase sensitivity using the fact that huge collecting areas can be achieved relatively cheaply. This is being exploited by the Low Frequency Array (LOFAR, Röttgering 2005) being built in the Netherlands, and by the Mileura Widefield Array (MWA) currently undergoing demonstrator tests in Western Australia. LOFAR will consist initially of about 50 elements, each consisting of a field of 50-m diameter filled with dipole antennas. This will give high sensitivity up to 240MHz and a resolution of a few arcseconds, with a possibility of higher resolution if long baselines are added. At such low frequencies, the field of view is very wide and survey speeds are correspondingly high. It is also possible to manipulate the phases applied to the antennas to form multiple beams on the sky, effectively allowing the telescope to look in a number of directions at once. The major science goals include the detection of the epoch of reionization in redshifted neutral hydrogen, the production of sensitive wide-field surveys and the monitoring of transient sources which becomes possible with rapid sky coverage¹¹. The difficulties include the large amount of process-

¹¹Another widefield telescope at somewhat higher frequencies is the Allen Telescope Array, currently being built at a site in New Mexico, USA. When complete it will consist of 300 6-m dishes and have a large survey speed by virtue of the sensitivity from the large number of elements combined with the large primary beam of the small individual elements.

ing power required, wide-field problems with removing sidelobes from bright sources at large angles, and more seriously the calibration problems associated with dealing with rapidly varying phase corruption from the ionosphere and (particularly in the LOFAR case) the necessity for very efficient excision of radio-frequency interference.

ALMA

At the other end of the frequency range, the Atacama Large Millimetre Array (ALMA) is a new interferometer being built on the Chajnantor plateau in Chile, a dry and high (5000-m) site close to the Bolivian border. The choice of site is due to the effects previously mentioned of the water vapour in the lower atmosphere on the amplitude of radio signals. ALMA will operate between 30 and 950GHz, in the windows permitted by the small quantity of atmospheric water vapour which remains above it. Its strength lies in the wide variety of molecular astrophysics and chemistry which can be probed at these frequencies, due to the huge number of molecular lines in the millimetre and submillimetre bands; it will be able to probe areas of star formation very sensitively, as well as detecting molecular gas on cosmological scales from distant galaxies.

CMB observations

A specialised niche in interferometry is occupied by experiments which are detecting structure in the Cosmic Microwave Background. These experiments tend to use short baselines, because the power in the CMB fluctuations is observed at significant strength on scales from arcminutes up to degrees, and frequencies from a few tens of GHz upwards due to the fact that the CMB radiation has a thermal spectrum with a temperature of 3K and a consequent spectral peak at 300 GHz. Most, like ALMA, operate from high, dry sites such as the Chajnantor plateau itself, the island of Tenerife or the South Pole.

Square Kilometre Array

After the bandwidth of interferometers has been increased to a maximum ($\Delta\nu/\nu \sim 1$) there is only one option for increasing sensitivity, namely increasing the collecting area. In the wave regime, the noise level becomes better as A^{-1} rather than the $A^{-1/2}$ obtained by increasing the collecting area of a photon collector, so increased telescope acreage is rewarded particularly spectacularly in the low-frequency part of the electromagnetic spectrum.

The idea of a very large interferometric telescope arose fifteen years ago (e.g. Wilkinson 1991) and is now under detailed design study with a view to full-scale construction in either western Australia or South Africa in the middle part of the next decade. There are a number of technological challenges,

which are being solved by various parts of the community using existing interferometers, including large-area coverage, multiple beams and large-scale data processing and correlation (e.g. LOFAR), transmission by long distances along optical fibre (e.g. e-MERLIN, EVLA), the possibility of high-resolution imaging using very long baselines and real-time correlation (e.g. eVLBI) and the problems of high frequencies (e.g. ALMA).

Although the SKA is some years in the future, the scientific potential is huge. For example, it will be able to see the faint emission of neutral hydrogen at cosmologically significant distances, give precision tests of cosmology and the star formation history of the universe by galaxy counts, resolve stellar disks and protoplanetary systems, search for extraterrestrial intelligence, and provide very sensitive tests of general relativity using pulsar studies.

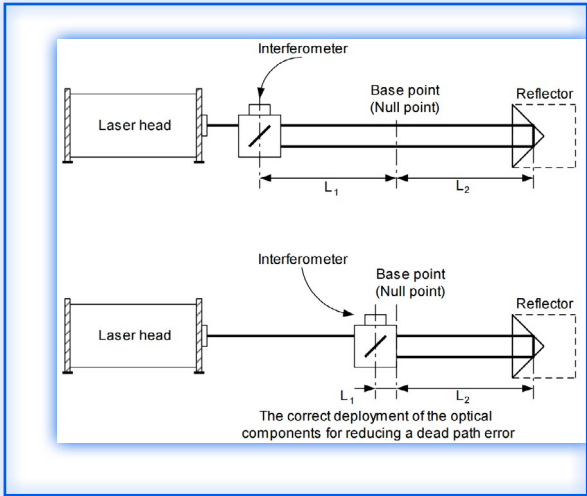
Acknowledgement. I thank the organisers of the workshop for excellent organisation and hospitality. It was supported by the Jetset EU research training network programme MRTN-CT-2004-005592. Work at Jodrell Bank on interferometry and gravitational lenses is supported by the EU network MRTN-CT-2004-505183 “ANGLES”. I thank the Kavli Institute for Theoretical Physics for hospitality during the writing of this review, and Sir Francis Graham-Smith for a careful reading of the manuscript.

References

1. Adgie R.L., Gent H., Slee O.B., Frost A.B., Palmer H.P., Rowson B., 1965. *Nature*, 208, 275.
2. Allen R.J., Hamaker, J.P., Wellington, K.J., 1974, *A&A* 31, 17
3. Born M., Wolf E., *Principles of Optics*, Cambridge University Press. ISBN: 0-521-63921-2
4. Bryan R.K., Skilling J., 1980, *MNRAS* 191, 69
5. Burke B., Graham-Smith F., 2002, Cambridge University Press, ISBN 0-521-00517-5
6. Cornwell T., Wilkinson P.N., 1981, *MNRAS* 196, 1067
7. Davies J.G., Anderson B.A., Morison I., 1980, *Nature* 288, 64
8. Hogbom J.A. 1974, *A&AS*, 15, 417
9. Linfield R.P. et al., 1989, *ApJ* 336, 1105
10. Monnier J. 2003, *Rep. Prog. Phys.* 66, 789
11. Röttgering H, 2005, *IAU Coll. 199*, Shanghai, China, ed. Williams P. et al., Cambridge University Press, p. 281
12. Rowson B. 1963, *MNRAS* 125, 177
13. Ryle M., 1962, *Nature*, 194, 517
14. Ryle M., 1972, *Nature*, 239, 435
15. Swarup G., Ananthakrishnan S., Kapahi V.K., Rao A.P, Subrahmanya C.R., Kulkarni V.K., 1991, *Current Science*, 60, 2
16. Taylor G.B., Carilli C., Perley R.A. (eds) 1998, *Astronomical Society of the Pacific Conf. Ser.* vol. 180
17. Thompson A.R., Clark B.G., Wade C.M., Napier J.R., 1980, *ApJS* 44, 151

18. Thompson A.R., Moran J.M., Swenson G.W. 2001, ISBN 0-471-25492-4, Wiley.
19. Wilkinson P.N., 1991, In "Radio interferometry: Theory, techniques, and applications: Proceedings of the 131st IAU Colloquium, Socorro, Astronomical Society of the Pacific, 1991, p. 428.
20. Young J.S. et al. 2004, Proc National Astronomy Meeting, Milton Keynes, available from www.mrao.cam.ac.uk/telescopes/coast.

“Interferometers are investigative tools used in many fields of science and engineering. They are called interferometers because they work by merging two or more sources of light to create an interference pattern, which can be measured and analyzed; hence "Interfere-ometer". The interference patterns generated by interferometers contain information about the object or phenomenon being studied.



They are often used to make very small measurements that are not achievable any other way.

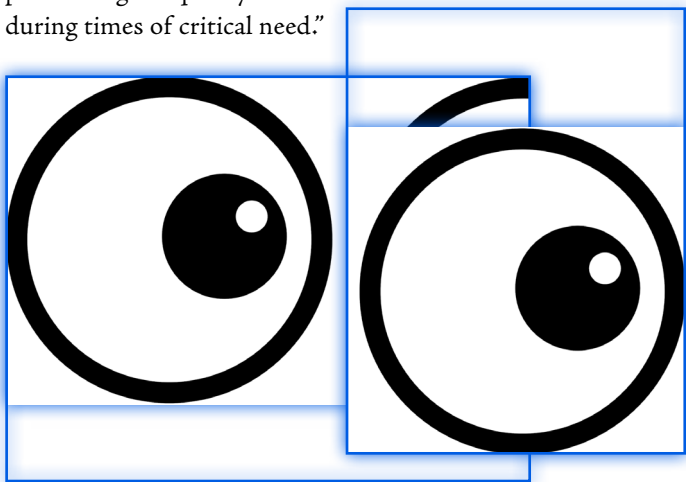
Widely used today, interferometers were actually

invented in the late 19th century by Albert Michelson. The Michelson Interferometer was used in 1887 in the "Michelson-Morley Experiment", which set out to prove or disprove the existence of "Luminiferous Aether"--a substance at the time thought to permeate the Universe. All modern interferometers have evolved from this first one since it demonstrated how the properties of light can be used to make the tiniest of measurements. "

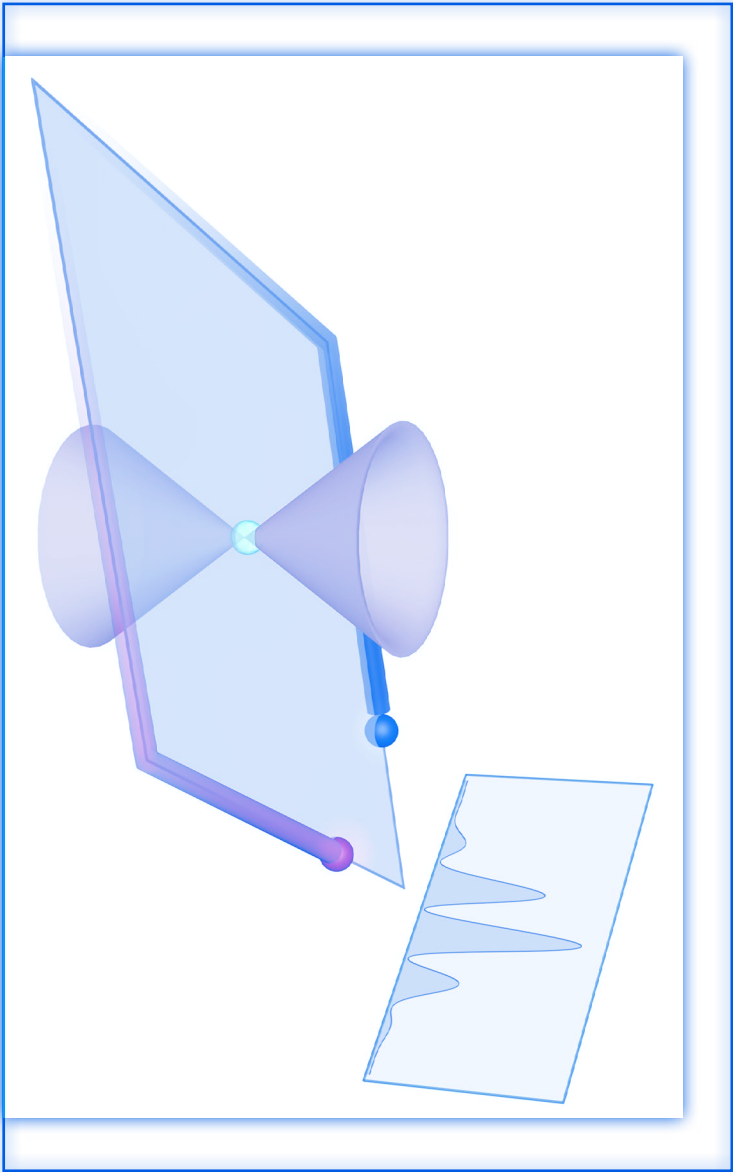
— LIGO Laser Interferometer Gravitational-Wave Observatory National Science Foundation, Operated by Caltech and MIT

(www.ligo.caltech.edu)

“The threat of nuclear proliferation remains a critical issue in our society. Prevention requires knowledge, and there is no greater indicator of the capability and intent of a nation than observation of actual detonation tests being conducted. Ground-based monitoring systems have proven to be very capable in identifying nuclear tests and can provide somewhat precise information on the location and yield of the explosive device. Making these measurements, however, currently requires very expensive and bulky seismometers that are difficult to deploy in places where they are most needed. A high-performance, compact device can enable rapid deployment of large-scale arrays, which can in turn be used to provide higher-quality data during times of critical need.”



— A Laser Interferometric Miniature Seismometer by Dustin W. Carr, Patrick C. Baldwin, Shawn A. Knapp-Kleinsorge, Howard Milburn, and David Robinson

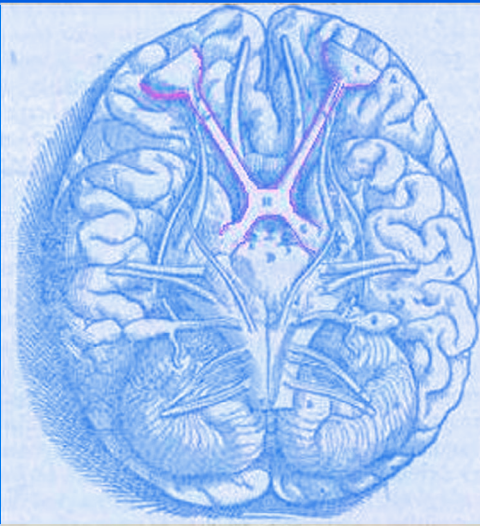


"The optic nerve fibres on the nasal sides of each retina cross over to the opposite side of the brain via the optic nerve at the optic chiasm.

The crossing over of optic nerve fibres at the optic chiasm allows the visual cortex to receive the same hemispheric visual field from both eyes. Superimposing and processing these monocular visual signals allow the visual cortex to generate binocular and stereoscopic vision.

The net result of optic nerve crossing over at the optic chiasm is for the right cerebral hemisphere to sense and process left hemispheric vision, and for the left cerebral hemisphere to sense and process right hemispheric vision.

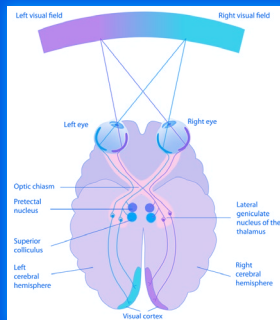
This crossing is an adaptive feature of frontally oriented eyes, found mostly in predatory animals requiring precise visual depth perception. (Prey animals, with laterally positioned eyes, have little binocular vision, so there is a more complete crossover of visual signals)."



CHIASMUS

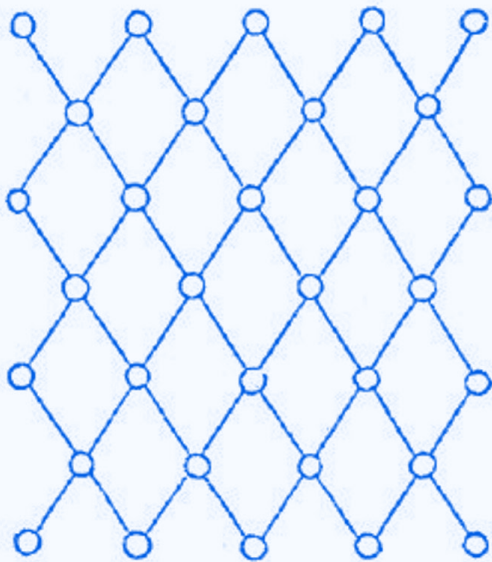
A rhetorical or literary figure in which words, grammatical constructions, or concepts are repeated in reverse order. (From the Greek khiasmos, from khiazein 'mark with the letter chi')

In Plato's *Timaeus*, it is explained that the two bands that form the soul of the world cross each other like the letter 'chi'. Plato's analogy, along with several other examples of chi as a symbol occur in Thomas Browne's discourse *The Garden of Cyrus* (1658). Chi or X is often used to abbreviate the name Christ, as in the holiday Christmas (Xmas).



Xx

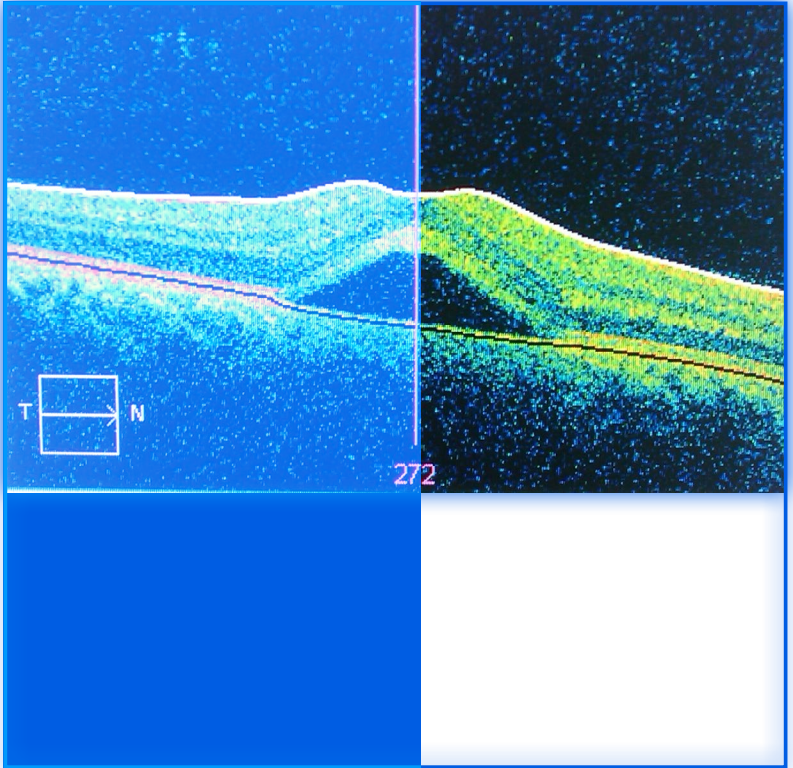
Thomas Browne's interferometer from the frontispiece of "The Garden of Cyrus OR, The Quincuncial, Lozenge, or Network Plantations of the Ancients, Artificially, Naturally, Mystically Considered" (1658). Thomas Browne lived with an an ostrich.



*Quid Quincunce Speciosius, qui, in
quam cunq; partem Spectaueris,
rectus est: Quintilian:¶*

"The smallest cone cells in the fovea have sizes corresponding to 0.4 minarc (minute arc, or minarc, is a unit of angular measurement equal to $1/60$ of one degree) of the visual field, which also places a lower limit on acuity. The optimal acuity of 0.4 minarc or $6/2.6$ can be demonstrated using a laser interferometer that bypasses any defects in the eye's optics and projects a pattern of dark and light bands directly on the retina. Laser interferometers are used routinely in patients with optical problems, such as cataracts, to assess the health of the retina before subjecting them to surgery."

— Visual Acuity, Wikipedia



An occurrence of central serous retinopathy in a retina, imaged using optical coherence tomography with a Zeiss Visante OCT machine. Optical coherence tomography (OCT) is a medical imaging technique using low-coherence interferometry to provide tomographic visualization of internal tissue microstructures, the core of which is a Michelson interferometer.

Due to the position of the eyes, binocular vision creates two slightly different images, and this disparity provides information that the brain uses to estimate depth in the visual scene. Binocular vision has been associated with ecological/behavioral factors such as predatory behavior, nocturnalism, and living in trees. It is functionally related to changes in the visuomotor system, high visual acuity, specializations of visual pathways in the brain, elaboration and differentiation of the visual cortex, and with orbital convergence.



— Binocular vision, the optic chiasm, and their associations with vertebrate motor behavior, Matz Larsson (2015)

TO SET THE WHOLE WORLD TALKING

Géomorphologie : relief, processus, environnement

vol. 13 - n° 3 | 2007 :

Formes de relief volcaniques, processus et risques

Fogo Volcano (São Miguel, Azores): a hazardous edifice

Le volcan Fogo, un édifice générateur d'aléas indirects

NICOLAU WALLENSTEIN, ANGUS DUNCAN, DAVID CHESTER ET RUI MARQUES

p. 259-270

Résumés

Français English

Le volcan Fogo, le plus grand des trois volcans actifs sur l'île São Miguel dans les Açores, montre une variété d'aléas qui sont liés à des processus non éruptifs. Souvent nommés aléas volcaniques indirects, ils sont, sur le Fogo, le produit d'interactions entre l'édifice volcanique instable et les processus contrôlés par des mécanismes sismiques, hydrothermaux, gravitaires et hydrologiques. Il s'avère que de nombreuses maisons, routes et ponts sont en danger si une activité sismique importante se manifestait. Or, depuis que l'île a été colonisée, les tremblements de terre supérieurs à IX sur l'échelle européenne macrosismique (EMS 98) ont frappé en 1522, 1713, 1811 et 1935. Environ 45 000 personnes habitent dans le district de Fogo et, si aucune action pour réduire la vulnérabilité n'est mise en place, des dommages seront inévitables dans le futur. Des gaz sont émis à plusieurs endroits sur le Fogo et, parmi eux, le CO₂ est un gaz dangereux quand il se concentre dans des dépressions. Des concentrations supérieures à 15 % conduisent souvent à l'asphyxie et à la mort, aussi les risques induits par les émissions de gaz représentent-ils un danger important pour les habitants du Fogo. Au cours des cinq derniers siècles, l'île São Miguel a été affectée par plusieurs glissements de terrain destructeurs et des crues soudaines qui ont été provoqués par des tremblements de terre, des éruptions volcaniques et des périodes de fortes pluies. Parmi ceux-ci, un événement de grande magnitude (X, EMS 98) en octobre 1522 a produit une coulée boueuse qui a complètement détruit la ville de Vila Franca do Campo. Environ 5000 habitants furent tués et une surface de 4,5 km² fut recouverte par des millions de mètres cubes de matériel. Les aléas volcaniques indirects sont une menace constante pour les habitants du volcan Fogo, mais ce n'est que récemment que des recherches approfondies leur sont consacrées.

Fogo volcano, the largest of the three active volcanoes of São Miguel Island in the Azores, presents a range of hazards, which are related to non-eruptive processes. Often termed indirect volcano hazards, these are the focus of the present paper and on Fogo volcano are produced by interactions between the unstable volcanic edifice and processes controlled by seismic, hydrothermal, slope instability and hydrological processes. Many houses, roads and bridges are at risk should significant earthquake activity occur. Since the island was settled in the 15th century, earthquakes exceeding IX on the European Macroseismic Scale (i.e. EMS 98) have struck São Miguel in 1522, 1713, 1811 and 1935. An estimated 45,000 people live within the Fogo District

and, without action to reduce vulnerability, future losses are inevitable. Gases are emitted from several locations on Fogo, and CO₂ is a dangerous gas when it ponds in depressions. Concentrations of over 15% often lead to asphyxiation and death, and case studies of the hazards posed by gas discharge are presented. São Miguel has been affected by several destructive landslides and flash floods in the last five centuries, triggered by earthquakes, volcanic eruptions or periods of heavy rainfall. A large (X, EMS 98) earthquake in October 1522 generated a debris flow that buried and completely destroyed the town of Vila Franca do Campo. About 5,000 people were killed and an area of ~4.5 km² was covered by millions of cubic metres of debris. Indirect volcanic hazards are an ever-present threat to people living on the Fogo Volcano, yet until recently they have been little researched.

Entrées d'index

Mots-clés : activité sismique, aléas volcaniques indirects, crues, Fogo, gaz, glissements de terrain, São Miguel des Açores

Keywords : Azores, floods, gases, indirect volcanic hazards, landslides, São Miguel, seismic activity

Errata

Article soumis le 21 novembre 2006, accepté le 1^{er} février 2007.

Notes de la rédaction

Acknowledgements

The authors wish to thank Mrs S. Mather for expertly drafting the figures and Dr F. Marret for translations into French. Most of the fieldwork was supported by the Centro de Vulcanologia e Avaliação de Riscos Geológicos da Universidade dos Açores. We would like to thank Dr K. Nemeth, Professor J.-C. Thouret and the other reviewers whose helpful comments have greatly improved this paper.

Texte intégral

Introduction

- 1 Volcanic eruptions are a major natural hazard and even when inactive a volcanic construct often presents a range of hazards. Volcanic edifices are constructive features that can build up rapidly but are, as a consequence, often unstable. Mount Etna was built to an altitude of around 3,000 m in about 100,000 years (Chester *et al.*, 1985) and the eastern flank has shown instability and episodes of collapse (Calvari *et al.*, 2004). Constructs made up of a high proportion of pyroclastic material are particularly prone to failure. Slope failure can be triggered by heavy rainfall and/or earthquakes. In October 1998 a hurricane in Nicaragua caused avalanches and lahars on Casita volcano, which has no record of historic activity, and around 1600 people were killed (Rodolfo, 2000; Scott *et al.*, 2005). This report is concerned with those hazards posed by non-eruptive processes, which are often termed indirect volcano hazards (Tilling, 2005). Such non-eruptive hazards include seismicity, gas emissions, landslides, flooding and tsunamis. Many indirect hazards are, however, smaller in scale and are associated with interactions between volcanoes, which are essentially rapidly growing-intrinsically unstable landforms, and processes within the subterranean and sub-aerial environments. Examples from volcanoes around the world are listed in table 1 and for the Azores as a whole Malheiro (2006) has recently considered the relationships between potentially unstable volcanoes and human vulnerability. The impact on the coastlines of the Azores of historical tsunami produced by tectonic and others causes has recently been discussed by Andrade *et al.* (2006). Fogo volcano, São Miguel in the Azores, provides good examples of the types of hazards described above. It is the purpose of this paper to provide an analysis of the hazards posed by Fogo volcano when it is not volcanically active.

Table 1 – Examples of volcanoes showing interactions between unstable edifices, and tectonic and geomorphological and hydrological processes.

Tableau 1 – Exemples de volcans montrant des interactions entre les édifices instables et les processus tectoniques, géomorphologiques et hydrologiques.

Processes	Examples
Tectonic	<p>Many volcanoes are located in tectonically active regions where major earthquakes occur. In AD 62, 17 years before the Plinian eruption of AD 79, Pompeii and other Roman cities around the flanks of Vesuvius were damaged by a major earthquake (Guest et al., 2003). In 1693 the city of Catania on the slopes of Mount Etna was devastated by an earthquake in eastern Sicily that left 18,000 people buried in rubble and up to 100,000 dead (Chester et al., 1985). In historic accounts there has often been a blurring of the impacts of seismic and volcanic activity sometimes leading to a misinterpretation of the processes involved. For instance, this has led to some sources attributing deaths from the 1169 Sicilian earthquake to the volcanic activity of Etna (Chester et al., 1985). Examples of tsunami include: Krakatau (1883), when nearly 300 coastal villages were destroyed and more than 30,000 people were killed (Simkin and Fiske, 1983); and the waves generated in 1792 when the Mayuyama dome (Unzen Volcano, Japan) collapsed into the sea generating a tsunami that killed 15,000 people (Tilling, 2005, p. 65).</p>
Hydrothermal/volatiles	<p>Volcanoes which have not been active for hundreds or indeed thousands of years may continue to that release volatiles, in particular CO₂, to the atmosphere. These gases are released, not only through solfataric activity in crater regions but also in leaks from fractures on the flanks of edifices. The Monticchio craters on Vulture volcano in Italy, which were formed around 132 ka ago, discharge CO₂ and Vulture is famous for its naturally carbonated groundwaters (Guest et al., 2003). Discharge of CO₂ may represent a serious hazard because the gas is denser than the atmosphere and ponds in topographic depressions. In 1992 on the island of Graciosa in the Azores two visitors from the Portuguese Navy were asphyxiated by higher than normal levels of CO₂ which collected in the fumarole situated in the intra-caldera Furna do Enxofre lava cave in the Caldera Volcano (Ferreira et al., 2005), which has not been active in the last few thousand years (Gaspar, 1996). The most famous example of the impact of CO₂ discharge from an inactive volcano was at Nyos in Cameroon, where there is a flux of CO₂ into the floor of the crater lake. In 1986 there was a gas burst from the crater lake and CO₂ poured down slope. Over 1,700 people were killed. The exact mechanism that caused the CO₂ to be released from the gas-rich bottom waters of the lake is not yet fully understood (Delmelle and Bernard, 2000).</p>
Sub-aerial	<p>Volcanic edifices are constructive features that build up rapidly but are, as a consequence, immature and unstable. Constructs made up of a high proportion of pyroclastic material are particularly prone to failure. Slope failure may be triggered by heavy rainfall and/or earthquakes. For example: in October 1998 a hurricane in Nicaragua caused avalanches and lahars on Casita volcano, which has no record of historic activity, and around 1,600 people were killed (Rodolfo, 2000; Scott et al., 2005). In 1999 at Cordillera de la Costa Volcano in Venezuela, landslides and debris flows caused the deaths of 30,000 people (Larsen et al., 2001).</p>

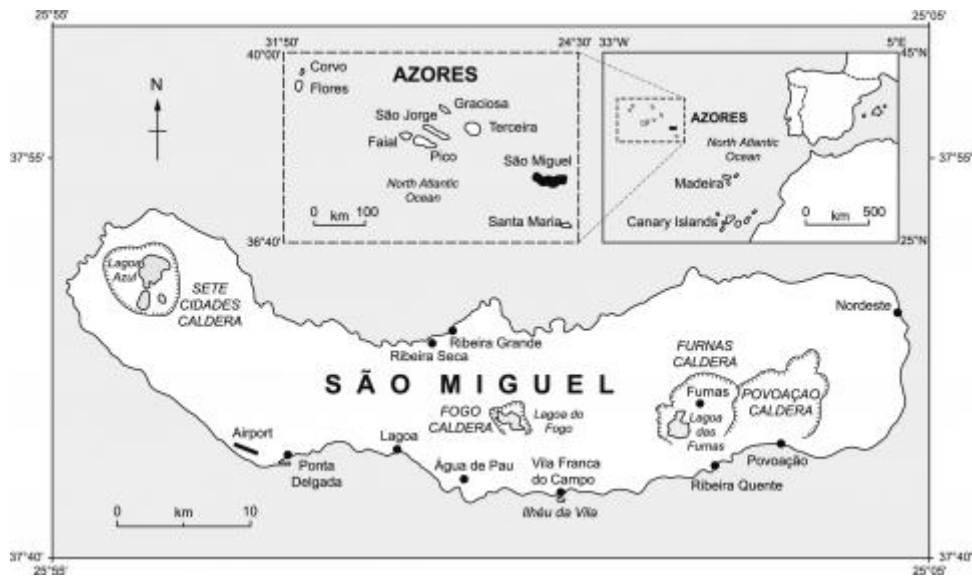
Fogo volcano

- 2 Fogo is the largest of the three central volcanoes on São Miguel and dominates the centre of the island (fig. 1). With a complex morphology the volcano rises to almost 1000 m and a summit caldera has formed as a result of numerous collapses and explosions, the most recent occurring during the sub-plinian eruption of 1563 and the hydromagmatic explosive event of 1564. The northern and southern flanks of the volcano have been extensively dissected by deep valleys that reach the coast, whilst to

the north the volcano has been down-faulted by a northwest to southeast trending graben (Moore, 1990).

Fig. 1 – Location of Fogo volcano within the Island of São Miguel.

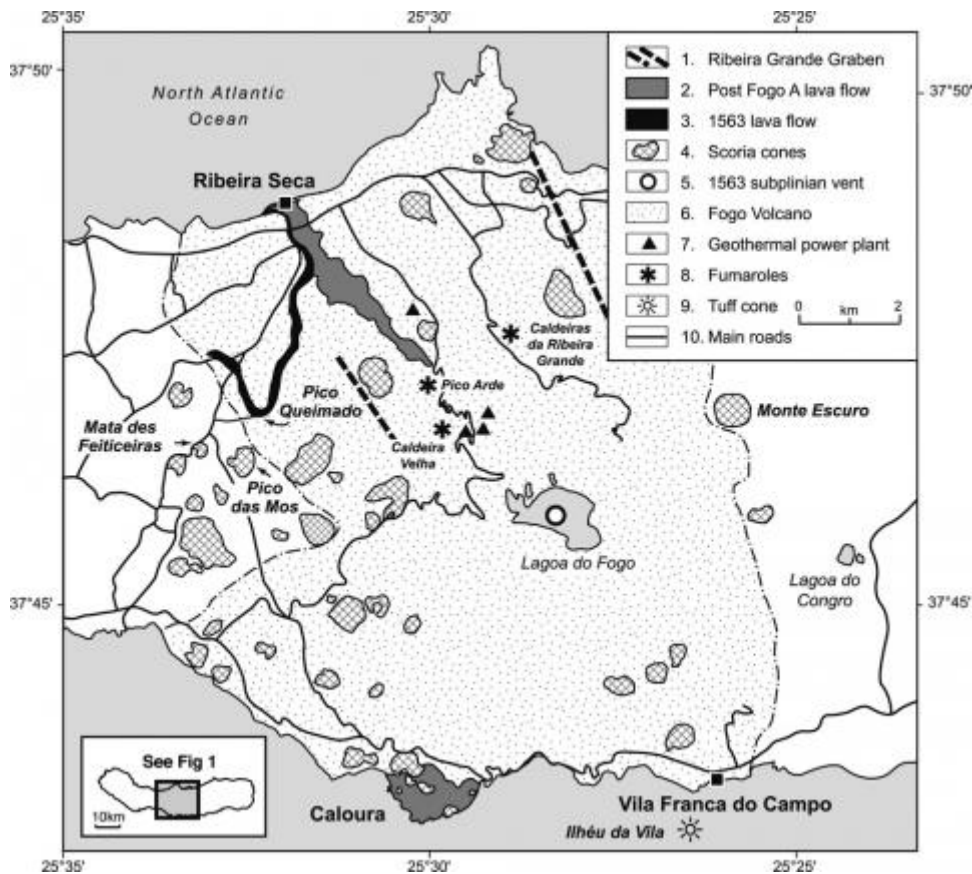
Fig. 1 – Localisation du volcan Fogo au sein de l'île de São Miguel.



cc. - c. et alet al.,

Fig. 2 – Fogo volcano: a morphostructural sketch. 1: Ribeira Grande graben; 2: post Fogo A lava flow; 3: A.D. 1563 lava flow; 4: scoria cones; 5: A.D. 1563 subplinian vent; 6: Fogo volcano; 7: geothermal power plant; 8: fumaroles; 9: tuff cone; 10: main roads.

Fig. 2 – Le volcan Fogo : un schéma morphostructural. 1 : graben de Ribeira Grande ; 2 : coulée de lave postérieure à Fogo A ; 3 : coulée de lave en 1563 AD ; 4 : cônes de scories ; 5 : cratère subplinien de 1563 AD ; 6 : volcan Fogo ; 7 : usine géothermique ; 8 : fumerolles ; 9 : cône de tuf ; 10 : routes principales.



- 3 On Fogo, major hazards are posed through interactions between the unstable volcanic edifice and a number of seismic, hydrothermal, slope instability and fluvial processes. The 2001 census showed that the Fogo District was home for ~45, 000 people and that the island of São Miguel as a whole was becoming an important holiday destination, not only for Azorean expatriates returning home for summer, but also for tourists from

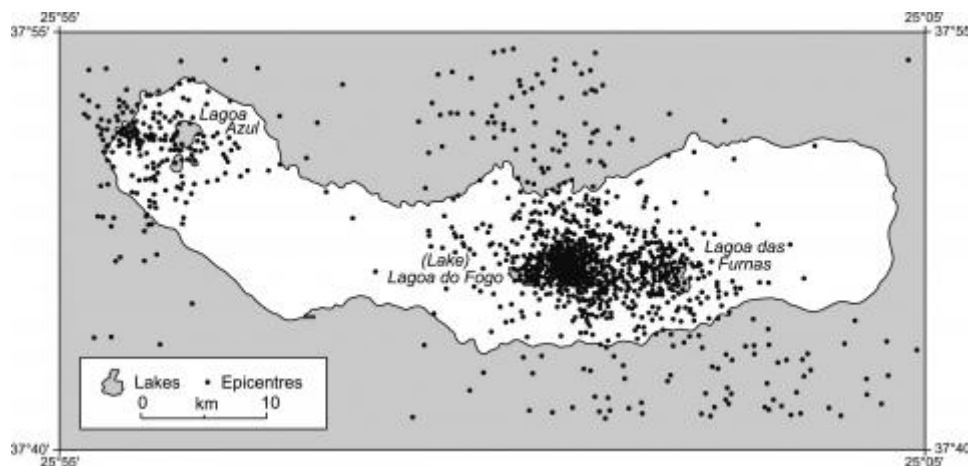
mainland Portugal, the European Union and North America. After decades of decline the population of São Miguel increased by over 4% between the 1991 and 2001 and today stands at over 131,000 (INEP, 2002). Exposure to volcano-related phenomena is increasing. In this paper interactions are first described and then discussed both with reference to the vulnerability of the towns and villages in which the people of Fogo reside and the ability of people to move freely about São Miguel by means of the road network.

Seismicity

- 4 São Miguel is located in a tectonically active region, with the Terceira Rift, which runs from the Mid Atlantic Ridge through Terceira to the Gloria Fault, crossing the western part of the island. There is significant seismicity on São Miguel associated with these NW–SE structures (Queiroz, 1997; Ferreira, 2000) which is typified by the activity that occurred between 1997 and 2003 (fig. 3).

Fig. 3 – Location of earthquake epicentres, 1997-2003.

Fig. 3 – Localisation des épicentres des séismes survenus entre 1997 et 2003.



- 5 Although associated with all São Miguel's active volcanic systems, between 1997 and 2003, seismicity was mainly concentrated in the central part of the island between Fogo and Furnas volcanoes and involved regional tectonic earthquakes as well as seismic swarms associated with the volcanic systems of this region.
- 6 Silveira *et al.* (2003) show that since the island was settled earthquakes exceeding IX (EMS 98) have struck São Miguel in 1522, 1713, 1811 and 1935, with slightly lower intensity events occurring in 1810, 1848, 1852, 1932 and 1952. The largest historic earthquake to have affected São Miguel had a maximum intensity of X (European Macroseismic Scale EMS 98) (Silveira *et al.*, 2003) and occurred on 22 October, 1522 (Frutuoso, 1522-1591[†]; Machado, 1959). It has been suggested that this event had its epicentre on the lower flanks of Fogo, a few kilometres NNW of the town of Vila Franca do Campo (Silveira *et al.*, 2003). The 1522 earthquake caused around 5,000 deaths as a result of building collapse and two devastating landslides. At the time Vila Franca do Campo (fig. 1) was the capital of the island, but after the earthquake the seat of government was moved to Ponta Delgada where it remains to this day. Seismic swarms are very common in the area between Fogo, Congro and Monte Escuro (fig. 2) where a major seismic crisis occurred in 1989. A new series of increasingly energetic seismic swarms began in the same area at the end of 2002 and reached a maximum on September 20, 2005. Several thousand earthquakes were located in the tectonic structures that surround Fogo's geothermal reservoir and in the vicinities of Congro and Monte Escuro volcanoes (fig. 2).
- 7 Some of the principal characteristics of the seismic swarms that have been associated with the Fogo-Congro-Monte Escuro area are typified by the events that occurred between April and July 2003. These events were closely monitored by the permanent seismic stations established by the Azores Seismological Surveillance System (SIVISA), complemented by a network of 14 portable stations and 3 seismic arrays deployed on

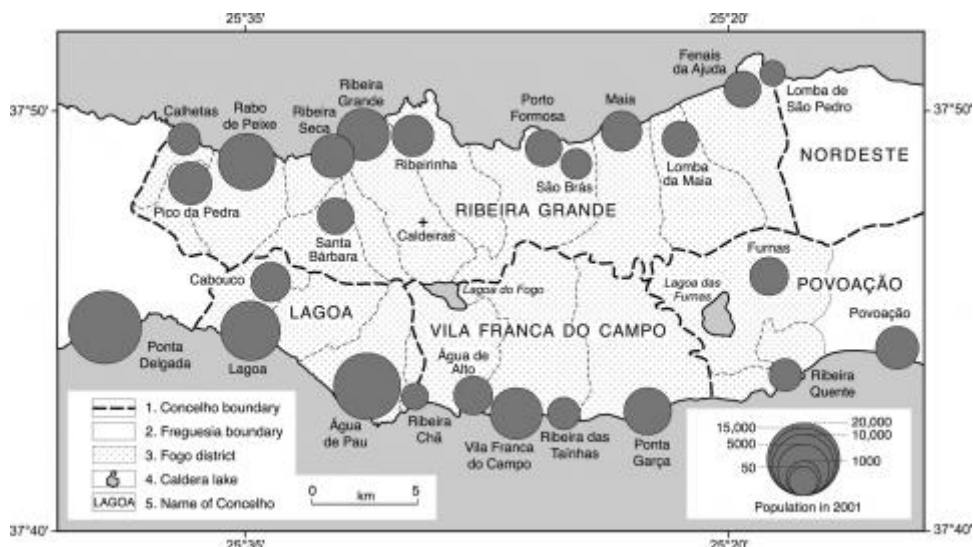
behalf of e-Ruption (a European Union sponsored project) and over 1,000 seismic events were recorded between April and July. During this period of time magnitudes never exceeded 3 (M_L) and focal depths ranged from 2 and 6 km (Silva *et al.*, 2004; Saccorotti *et al.*, 2004). Two main groups of seismic events were identified and occurred north-east of the Fogo Caldera and north-west of Furnas caldera (fig. 1; Saccorotti *et al.*, 2004; Bonagura *et al.*, 2004).

8 Between May and December 2005, more than 46,000 earthquakes were registered by SIVISA. On May 10, 2005 a seismic swarm began in the Fogo-Congro-Monte Escuro area (fig. 2), the two strongest earthquakes occurring on September 20 and 21, 2005, with respective magnitudes of 4.1 and 4.3 (M_L). Epicentres were located in the central part of the island and a maximum intensity of V/VI (EMS-98) was recorded in the closest villages. Despite the magnitude of these earthquakes, they did not cause severe damage or casualties, though they were responsible for extensive slope failure in the central part of São Miguel and some aligned superficial ruptures were observed between Fogo and Monte Escuro volcanoes (Marques *et al.*, 2005, 2006) (fig. 2).

9 Several writers have shown that the traditional 'rubble stone' buildings of São Miguel are extremely vulnerable to earthquake shaking, because they lack resistance to horizontal motions. Gomes *et al.* (2006) have calculated that an earthquake with an EMS-98 intensity of IX would destroy between 57 and 77% of the dwellings located around Sete Cidades volcano in the western part of the island (fig. 1), whilst some 80% of buildings in that part of the Fogo volcano which was surveyed by Pomonis *et al.* (1999) were of similar construction. These findings are confirmed by a study by the present authors into highway stability, evacuation routes and housing types found in what was defined as the Fogo District. Fogo District comprises the municipalities (*concelhos*) and parishes (*freguesia*) that are in close proximity to Fogo. The survey showed similar levels of seismic vulnerability within all the settlements of the Fogo District (fig. 4) and also revealed that many roads and bridges within the district were vulnerable should significant earthquake shaking occur.

Fig. 4 – The location of, and population concentrations within, towns and villages of the Fogo District (Population data from INEP, 2002). 1: *Concelho* boundary; 2: *Freguesia* boundary; 3: Fogo district boundary; 4: caldera lake; 5: name of *concelho*.

Fig. 4 – Localisation de la population dans les villes et villages du District du Fogo (données démographiques d'après INEP, 2002). 1 : limite du Concelho ; 2 : limite de la Freguesia ; 3 : limite du district de Fogo ; 4 : lac de caldera ; 5 : nom du concelho.



10 Many of these routes are also threatened by landslides and flash floods and this aspect of vulnerability is considered later in the paper. Seismic vulnerability is not just a question of building safety and the survey revealed additional dangers within particular settlements. For instance the villages and/or towns of Ribeira Seca, Ribeira Grande, Furnas, Vila Franca do Campo, Ribeira Chã, Água de Pau, Cabouco, and Santa Bárbara (fig. 4) all have narrow streets some of which are also strategic roads serving other parts of the island. These streets would be blocked with rubble following an earthquake, not only impeding escape by the residents of these towns and villages, but also blocking evacuation routes serving other settlements. An estimated 45,000 people live within the

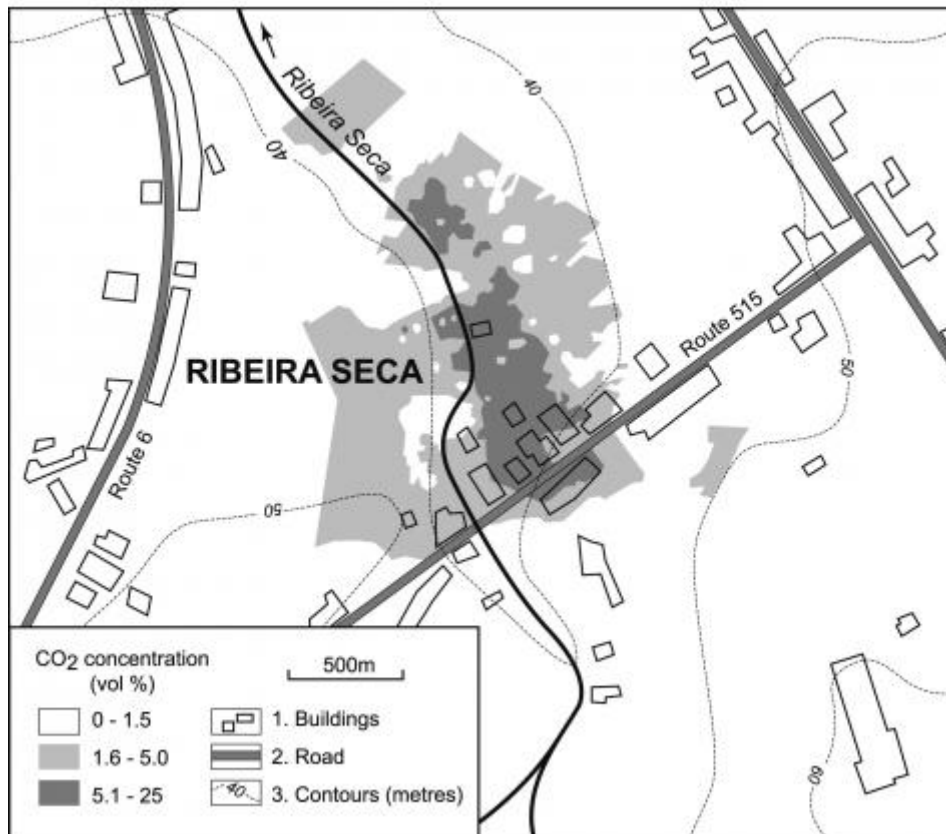
Fogo District (INEP, 2002) and without action to reduce housing vulnerability, future losses to buildings and many of those living in them are inevitable.

Hydrothermal activity and gas emissions

- 11 Volcanoes which have not erupted for hundreds – or indeed thousands – of years can continue to act as conduits releasing volatiles, in particular CO₂, to the atmosphere. These gases are released not only through the crater regions but also leak from fractures on the flanks of volcanic edifices. Discharge of CO₂ can represent a serious hazard as the gas is denser than the atmosphere and ponds in topographic depressions. In the Azores, in 1992, on the island of Graciosa two visitors from the Portuguese Navy were asphyxiated by higher than normal levels of CO₂ in the fumarole situated in the intracaldera Furna do Enxofre lava cave in the Caldera Volcano (Ferreira *et al.*, 2005) which has not been active in the last few thousand years (Gaspar, 1996).
- 12 São Miguel has areas where gases are emitted and related to hydrothermal systems (Ferreira, 2000). Fogo volcano has an active geothermal field on its northern flank and annually over 100 GWh of electricity are generated from geothermal power plants, which represent ~35% of the electricity requirements of the island. Associated with the hydrothermal system are areas of fumarolic activity at Caldeira Velha, Pico Vermelho and Caldeiras da Ribeira Grande (fig. 2) and these are associated with the distensive NW-SE faults of the northern flank (Ferreira, 2000). At Caldeiras da Ribeira Grande a small spa has been developed and, in addition to water, large volumes of CO₂ are emitted. Diffuse emissions of carbon dioxide also leak more generally through faults and fractures on the flanks of the volcano and include cold emissions of CO₂ from a spring in the Lombadas valley (fig. 2), and diffuse soil degassing as in the *freguesia* of Ribeira Seca (Figs. 2 and 4) (Ferreira, 2000; Ferreira *et al.*, 2005).
- 13 CO₂ is a dangerous gas and concentrations of over 15% often lead to asphyxiation and death (Blong, 1984; Baxter *et al.*, 1999). In fact the only deaths attributed to the large-scale explosive eruption of Fogo in 1563 occurred after it had ended when two people are reported to have died when visiting the vent area where they were overcome by gas, almost certainly CO₂ (Wallenstein *et al.*, 2005). The hazard of gas discharge exists even when the volcano is inactive. An area near to the riverbed of the Ribeira Seca is known as a site of high CO₂ discharge and a few years ago the death of a farmer was attributed to CO₂ asphyxiation. There are now warning signs advising people of the hazard. In 1997 the *Centro de Vulcanologia e Avaliação de Riscos Geológicos da Universidade dos Açores* noted vapour discharge in the village of Ribeira Seca (fig. 2) (Ferreira, 2000; Ferreira *et al.*, 2005). During 1998 and 1999 the thermal and CO₂ anomalies associated with these emissions reached a peak of 50 °C and 13.5% concentration, only just below Baxter's asphyxiation danger level (Ferreira *et al.*, 2005). Peak values were only recorded in a localized area of ~1 m², but the general area of anomaly was ~200 m². As this area of anomaly was within a residential area it posed a significant risk and led to the evacuation of four houses. Figure 5 is a hazard map based on this study and points to the need for a systematic investigation of gas emission within other settlements. It is already known, for instance, that high levels of gas discharge occur in Furnas village (fig. 1) where concentrations of over 15% are to be found over an extensive area (Baxter *et al.* 1999, their fig. 2).

Fig. 5 – Hazard posed by the CO₂ gas emission at Ribeira Seca during 1998 and 1999 (Ferreira *et al.* 2005). 1: buildings; 2: roads; 3: contours metres.

Fig. 5 – Aléa engendré par l'émission de CO₂ à Ribeira Seca en 1998 et 1999 (Ferreira *et al.*, 2005). 1 : constructions ; 2 : routes ; 3 : courbes de niveau en mètres.



Landslides and Flash Floods

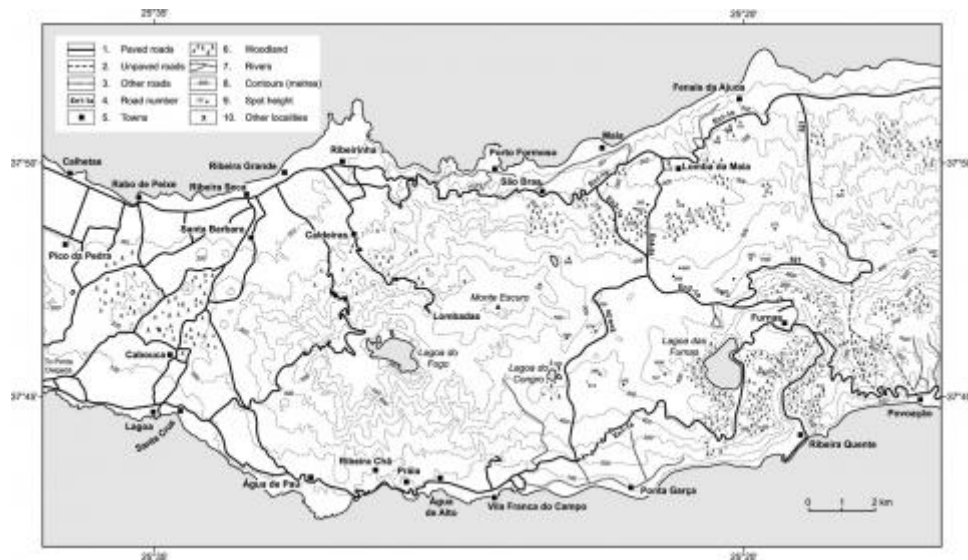
Landslides

- 14 São Miguel has been affected by several destructive landslides in the last five centuries. Triggered by earthquakes, volcanic eruptions and/or heavy episodes of intense rainfall, these have been responsible for many casualties and extensive economic losses. In a study of Povoação *concelho* (fig. 4), it is shown that landslides are highly probable when precipitation exceeds 200 l.m⁻² and that risk is exacerbated by the occurrence of soils composed of volcanic ash, high slope angles and particular landuse and vegetation conditions (Valadão *et al.*, 2002). However, some more recent important landslides have been triggered by lower levels of precipitation, around 120 l.m⁻² (Marques *et al.*, 2005) and with regard to this, Malheiro (2006) has shown that two factors are important. First, areas devoid of vegetation are particularly prone to erosion and, second, the frequent occurrence of storms together with high winds can uproot trees which are shallow-rooted. *Cryptomeria japonica*, an introduced tree now common on São Miguel is particularly prone to being easily uprooted and has often triggered large-scale slope failures.
- 15 One recent example of the effects of rainfall on slope failure occurred on October 31, 1997 on Furnas volcano (fig. 1). Landsliding was triggered by rainfall of up to 220 l.m⁻² (Gaspar *et al.*, 1997) strong southeast winds, volcanic soils and earlier saturation of the ground all being aggravating factors. Landslides were dominated by mobile debris flows, which carried lava blocks with a calibre of up to 3 m. Several roads and bridges were extensively damaged over a wide area and thirty six houses were destroyed, 29 people were killed, 114 residents were left homeless mainly in the village of Ribeira Quente, which was cut off from the rest of São Miguel for more than 12 hours (Gaspar *et al.*, 1997). The total financial loss was estimated at more than €20 million (Cunha, 2003).
- 16 The situation on Fogo is very similar to that described for Povoação *concelho* and for the Azores more generally (Malheiro, 2006). Fogo is an immature, potentially unstable

landform with a significant proportion of pyroclastic materials within its volcanic succession. These pyroclastic deposits are notable for their very low resistant parameters of cohesion and friction angles and high values for permeability, which favour the ready circulation of ground water. In common with Furnas, Fogo's climate is characterized by heavy rainfall (mean value of 1,255 l.m⁻² at 65 m rising to 3,830 l.m⁻² at 947 m) and storms, particularly between the months of September and April (Wallenstein *et al.*, 2005). On Fogo steep slopes, developed on these incoherent materials, are heavily dissected and landslides have been a frequent indirect volcanic hazard, the high density of mapped landslip scars bearing witness to a long history of landslip activity (Valadão *et al.*, 2002). Recent examples include a landslide that destroyed a mineral water plant in the Lombadas valley, just northeast of the summit (fig. 6), and the landslides and flash floods that occurred on the southern flank of Fogo in October 1998 during the passage of tropical storm *Jeanne*.

Fig. 6 – Fogo volcano: roads and drainage (adapted from Wallenstein *et al.*, 2005). 1: paved roads; 2: unpaved roads; 3: other roads; 4: road number; 5: towns; 6: woodland; 7: rivers; 8: contours (metres); 9: spot height (metres); 10: other localities.

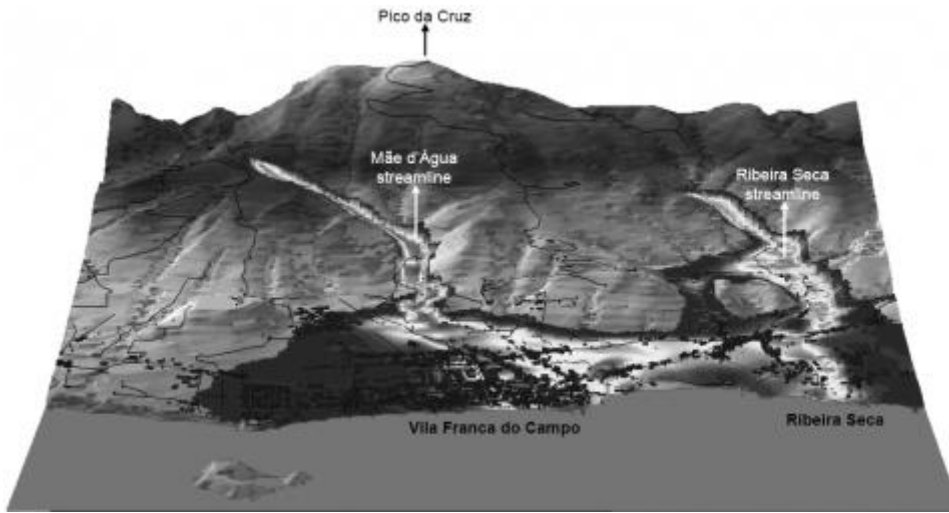
Fig. 6 – Le volcan Fogo : routes et drainage (modifié d'après Wallenstein *et al.*, 2005). 1 : routes asphaltées ; 2 : routes sans revêtement ; 3 : pistes ; 4 : numéro de la route ; 5 : villes ; 6 : forêt ; 7 : rivières ; 8 : courbes de niveau (mètres) ; 9 : altitude du lieu (mètres) ; 10 : autres localités.



17 The most violent example of an earthquake triggering a landslide took place on October 22, 1522. This was the largest such event to have affected the island since it was settled and several landslides were triggered. The most hazardous and spectacular of these was a cataclysmic landslide that was initiated from an altitude of 450 m on the southern flank of Fogo. This event generated a debris flow, which buried and completely destroyed the town of Vila Franca do Campo. About 5,000 people lost their lives and an area of ~4.5 km² was covered by several millions of cubic metres of debris (fig. 7).

Fig. 7 – The estimated area that was flooded during 1522. The area is obtained by the application of a probability model developed by Feltpeto *et al.* (1996) for gravity flows which is superimposed over a three dimensional view of the Vila France do Campo area (adapted from Marques, 2004). Looking north.

Fig. 7 – Estimation de la surface de la région inondée en 1522. Cette surface est calculée en utilisant un modèle de probabilité (Feltpeto *et al.*, 1996), surimposé à une vue 3D du secteur de Vila France do Campo (modifié d'après Marques, 2004). Vue vers le nord.



- 18 The stratigraphic position of the 1522 debris flow deposits are well constrained. In many outcrops in the Vila Franca do Campo area, the sediments directly overly deposits of the Fogo A formation and in some places it is possible to observe the Furnas AD 1630 sub-plinian eruption products resting on top. With thicknesses ranging from a few centimetres to over 2.5 m, deposits from the 1522 debris flows either show a sheet-like morphology or occur as fills within contemporary stream channels. Within stream channels, deposits rest directly on surfaces that were formed by the abrasive erosion of the flow. Four distinct flow units have been identified and interpretation of these has allowed a model of emplacement to be proposed (fig. 7), so allowing the construction of scenarios of future debris flows on Fogo Volcano. A small tsunami was produced by the flow of debris into the Atlantic and destroyed two boats anchored near Vila Franca islet, some 2 km offshore (Fructuoso, 1522-1591⁺). After the Lisbon earthquake of 1755, which killed around 30,000 people (Oliveira, 1986; Chester, 2001), this event represents the largest natural catastrophe to have affected Portugal. More recently and despite their moderate magnitude, the 2005 Fogo-Congro seismic swarms were also responsible for extensive slope failure in the Fogo District, triggering hundreds of slope failures; these being mostly debris flows and shallow soil slips that evolved downslope into debris flows (see fig. 8 and Marques *et al.*, 2006). Some rural roads were temporarily closed and temporary dams were formed in the Ribeira Grande watershed (Marques *et al.*, 2006).

Fig. 8 – View of the Ribeira Grande watershed on the northern flank of Fogo showing extensive landslide scars from the summer 2005 seismic activity. Length of valley about 1 km.

Fig. 8 – Vue du bassin versant de Ribeira Grande sur le flanc nord du volcan Fogo, montrant de nombreuses et grandes cicatrices de glissements de terrain déclenchés par l'activité sismique de l'été 2005. La longueur de la vallée est d'environ 1 kilomètre



Flash Floods

- 19 Flash floods are normally associated with specific geomorphological factors and are triggered by heavy rainfall. On São Miguel catchments are small and this, combined with steep profiles, means that river regimes are characterised by rapid discharge immediately following major rainfall events. As has been recognised for some time (Chester *et al.*, 1999), natural dams produced by sediment and vegetation heighten the danger of flash flooding, and in December 1998 such an event swept through the village of Praia on the lower southern flank of the volcano (fig. 6). Praia is located at the foot of the valley whose catchment extends to just below the southern margin of the Fogo caldera lake. Here the lip of the Fogo Lake is only a few metres high, and even a relatively small landslide from either the steep western or eastern walls could cause a surge of water that would breach the lip and send a catastrophic flood down the Praia valley. Recent building development has occurred on a delta of debris flow deposits, which were emplaced at the mouth of the Praia valley during the 1563 eruption (Wallenstein *et al.*, 1998; Wallenstein, 1999). This is a hazardous location and emphasises the need for risk assessment in planning. Praia village is an extreme example of a populated area which is at risk from flash flooding and other instances are to be found on the northern and southern lower flanks of Fogo (figs. 4 and 6). A survey was undertaken of the landslide and flood risks for that part of the Fogo District, which is located on the slopes of the volcano (i.e. from the settlements of Santa Barbara to Maia on the northern flank, and from Lagoa to Vila Franca do Campo on the southern flank (see fig. 6). The results are summarized in Table 2. This complements a reconnaissance study of volcanic hazard exposure in the Fogo District and an account of the possible effects of an eruption on the settlements of the Fogo District and its roads has already been published (Wallenstein *et al.*, 2005).

Table 2 – Summary of a survey of the exposure of settlements and roads on the northern and southern flanks of Fogo to the effects of landslides and flash floods (population data from INEP, 2002). This table should be read in conjunction with fig. 6.

Tableau 2 – Résumé d'une enquête à propos de l'exposition des constructions et des routes sur les flancs nord et sud du volcan Fogo, face aux effets des glissements et des crues éclair (données démographiques d'après INEP, 2002). Ce tableau devrait être comparé à la fig. 6.

Major landslide and flash flood risks

South Flank: Lagoa, Água de Pau, Ribeira Chã, Agua d'Alto, Vila Franca do Campo and Ribeira das Tainhas. Around 22,000 people (~39% of the population of the *Fogo District*) live

in this area, which is located within a radius of 8 km of the centre of the Lagoa do Fogo.

People are highly exposed to landslides and floods. The risks include:

- a. River valleys that drain the summit region (fig. 6), would be flooded if the walls of the Lagoa do Fogo were to be breached. Landslides would choke valleys with sediment and up-rooted trees would create temporary dams, so exacerbating flooding dangers.
- b. Flood risk was noted in all the valleys that reach the southern coast and is particularly acute at Praia (see main text). Many places were noted along the southern coastal road (i.e. En11a - fig. 6) where, given a combination of circumstances, the route would be blocked. Blocking of this less than secure southern route would severely hamper communications over much of São Miguel.

North Flank: Santa Bárbara, Ribeira Seca, Ribeira Grande, Ribeirinha, Porto Formoso and Maia). Over 15,000 people (~27% of the total for the *Fogo District*) live in these settlements on the north flank. Towns and villages are not as close to the summit as those on the south flanks and have far better road access to the west and to the island's capital, Ponta Delgada (i.e. roads En 1 1a and En 3 1a). Specific concerns are raised by:

- a. The main road (En1 1a) passes close to the town Ribeira Grande and the stream with the same name and has a large catchment reaching almost to the caldera rim. Flash floods are a major risk.
- b. There are many examples where roads and villages could be affected by landslides.
- c. The hazard posed by flash flooding was noted in several north flowing river valleys.
- d. Many bridges could not resist the effects of either flash flooding or large landslides.

Conclusion

- 20 This paper demonstrates that indirect volcanic hazards are an ever present threat to people living on the flanks of the volcano and its immediate environs. Recurrence intervals of extreme natural events are probabilistic and people living on and in the vicinity of Fogo have been extremely fortunate to have not been more adversely affected by indirect hazards. The 1522 landslides, debris flow and tsunami caused the deaths of 5,000 people, but today more than 11,000 people live in the *concelho* of Vila Franca do Campo and would be at risk. Interactions between the volcanic edifice and seismicity, hydrothermal/gas activity, landslides and flash floods all create major hazards and there is a need for a far more detailed and comprehensive study so that appropriate planning and response procedures may be developed. It is pleasing to note that in November 2005, on the final day of the field programme for this paper, a major civil defence exercise was being conducted in Vila Franca do Campo and during 2006 two similar exercises were conducted in the Fogo district. They were focused on the deployment of civil and military teams in response to hypothetical scenarios of devastating earthquakes.

Bibliographie

Andrade C., Borges P., Freitas M.C. (2006) – Historical tsunami in the Azores Archipelago (Portugal). *Journal of Volcanology and Geothermal Research* 156, 172-185.

Baxter P.J., Baubron J.-C., Coutinho R. (1999) – Health hazards and disaster potential of ground gas emissions at Furnas Volcano, São Miguel, Azores. *Journal of Volcanology and Geothermal Research* 92, 95-106.

Blong R.J. (1984) – *Volcanic Hazards. A Sourcebook on the Effects of Eruptions*. Academic Press, Sydney, 424 p.

Bonagura M., Damiano N., Saccorotti G., Ventura G., Vilardo G., Wallenstein N. (2004) – Fault geometries from the space distribution of earthquakes at São Miguel Island (Azores): inferences on the active deformation. *Geophysical Research Abstracts*, 6, 07635. European Geosciences Union, Vienna.

Booth B., Walker G.P.L., Croasdale R. (1978) – A quantitative study of five thousand years of volcanism on São Miguel Azores. *Philosophical Transactions of the Royal Society of London*, Series A 228, 271-319.

Calvari S., Tanner L.H., Gropelli G., Norini G. (2004) – Valle del Bove, eastern flank of Etna volcano: A comprehensive model for the opening of the depression and implications for future hazards. In Bonnacorso A., Calvari S., Coltelli M., Del Negro C., Falsaperla S. (Eds.) *Mt.*

Etna: Volcano Laboratory. Geophysical Monograph Series 143, American Geophysical Union, 65-75.

Chester D.K. (2001) – The 1755 Lisbon earthquake. *Progress in Physical Geography* 25, 363-383.

Chester D.K., Duncan A.M., Guest J.E., Kilburn C.R.J. (1985) – *Mount Etna, anatomy of a volcano*. Chapman and Hall, London, 389 p.

Chester D.K., Dibben C., Coutinho R., Duncan A.M., Cole P.D., Guest J.E., Baxter P.J. (1999) – Human adjustments and social vulnerability to volcanic hazards of Furnas Volcano, São Miguel, Azores. In Firth C.R., McGuire W.J. (Eds.): *Volcanoes in the Quaternary*. Geological Society, London, Special Publications, 161, 189-207.

Cunha A. (2003) – The October 1997 landslides in São Miguel Island, Azores. In Javier H. (Ed.): *Lessons learnt from landslide disasters in Europe*. European Commission Joint Research Centre, ISPRA, Doc 20558EN, 92 p.

Delmelle P., Bernard A. (2000) – Volcanic lakes. In Sigurdsson H. (Ed.): *Encyclopedia of Volcanoes*. Academic Press, San Diego, 877-895.

Felpeto A., Garcia A., Ortiz R. (1996) – Mapas de riesgo. Modelización. In Ortiz, R. (Ed.): *Riesgo volcánico*. Série Casa de los Volcánes 5, Servicio de Publicaciones Cabildo de Lanzarote, Canarias, 67-98.

Ferreira T. (2000) – *Caracterização da actividade vulcânica da ilha de S. Miguel (Açores): Vulcanismo basáltico recente e zonas de desgaseificação. Avaliação de riscos*. Tese de doutoramento no ramo de Geologia, especialidade de Vulcanologia. Universidade dos Açores, Departamento de Geociências, 248 p.

Ferreira T., Gaspar J.L., Viveiros F., Marcos M., Faria F., Sousa F. (2005) – Monitoring of fumarole discharge and CO₂ soil degassing in the Azores: contribution to volcanic surveillance and public health risk assessment. *Annals of Geophysics* 48, 787-796.

Fructuoso G. (1522-1591 †) – Livro Quarto das Saudades da Terra. 1877, vol. I e II, Ed. Instituto Cultural de Ponta Delgada, Ponta Delgada, unknown number of pages.

Gaspar J.L. (1996) – *Ilha Graciosa (Açores. História vulcanológica e avaliação do hazard*. Tese de doutoramento no ramo de Geologia, especialidade de Vulcanologia. Universidade dos Açores, Departamento de Geociências, 256 p.

Gaspar J.L., Wallenstein N., Coutinho R., Ferreira T., Queiroz G., Pacheco J., Guest J., Tryggvason E., Malheiro A. (1997) – *Considerações sobre a ocorrência dos movimentos de massa registados na madrugada de 31 de Outubro de 1997 na ilha de S. Miguel, Açores*. Relatório Técnico-Científico 14/DGUA/97, Centro de Vulcanologia, 28 p.

Gomes A., Gaspar J.L., Queiroz G. (2006) – Seismic vulnerability of dwellings at Sete Cidades Volcano (S. Miguel Island, Azores). *Natural Hazards and Earth System Sciences*, 6, 41-48.

Guest J.E., Cole P.D., Duncan A.M., Chester D.K. (2003) – *Volcanoes of Southern Italy*. Geological Society of London, London, 274 p.

INEP (2002) – *Censos 2001: XIV Recenseamento Geral da População, IV Recenseamento Geral à Habitação*. Instituto Nacional de Estatística, Lisboa, 87 p.

Larsen M.C., Wiczorek G.F., Eaton L.S., Torres-Sierra H. (2001) – The rainfall-triggered landslide and flash-flood disaster in northern Venezuela, December 1999. *Proceedings of the Seventh Federal Interagency Sedimentation Conference*, Reno, NV, IV, 9-16.

Machado F. (1959) – Submarine pits of the Azores plateau. *Bulletin Volcanologique*, 21, 109-116.

Malheiro A. (2006) – Geological hazard in the Azores archipelago: Volcanic terrain instability and human vulnerability. *Journal of Volcanology and Geothermal Research* 156, 158-171.

Marques R. (2004) – *Contribuição para o conhecimento da instabilidade geomorfológica nos Açores: Estudo de movimentos de vertente associados a diferentes mecanismos desencadeantes*. Tese de mestrado em Vulcanologia e Avaliação de Riscos Geológicos. Universidad Dos Açores, Departamento de Geociências, 147 p.

Marques R., Coutinho R., Queiroz G. (2005) – *Considerações sobre a ocorrência dos movimentos de vertente desencadeados pelos sismos de 20 e 21 de Setembro de 2005 no Fogo-Congro (Ilha de São Miguel)*. Caracterização e análise de cenários. Relatório Técnico-Científico 27/CVARG/05, Centro de Vulcanologia, 36 p.

Marques R., Coutinho R., Queiroz G. (2006) - Landslides and erosion induced by the 2005 Fogo-Congro seismic crisis (S. Miguel, Azores). *Geophysical Research Abstracts*, Vol. 8, EGU06-A-06925, SRef-ID: 1029-7006. European Geosciences Union.

Moore R.B. (1990) – Volcanic geology and eruption frequency, São Miguel, Azores. *Bulletin of Volcanology*, 52, 602-514.

Oliviera C.S. (1986) – Some quantitative measurements for calibrating historical seismicity. In *Proceedings of the 8th European Conference on Earthquake engineering*. Laboratório Nacional de Engenharia Civil 1, 2.1/71-2.1/78.

Pomonis A., Spence R., Baxter P. (1999) – Risk assessment of residential buildings for an eruption of Furnas Volcano, São Miguel, the Azores. *Journal of Volcanology and Geothermal Research* 92, 107-131.

Queiroz G. (1997) – *Vulcão das Sete Cidades (S. Miguel, Açores). História eruptiva e avaliação do hazard*. Tese de doutoramento no ramo de Geologia, especialidade de Vulcanologia. Universidade dos Açores, Departamento de Geociências, 226 p.

Rodolfo K.S. (2000) – The hazard from lahars and jokülhlaups. In Sigurdsson H. (Ed.): *Encyclopedia of Volcanoes*. Academic Press, San Diego, 973-995.

Saccorotti G., Wallenstein N., Ibáñez J., Bonagura M.T., Damiano N., La Rocca M., Quadrio A., Silva R., Zandomenighi D. (2004) – A seismic field survey at Fogo Furnas volcanoes, São Miguel island, Azores. *Geophysical Research Abstracts*, Vol. 6, 04493. European Geosciences Union.

Scott K., Vallance J.W., Kerle N., Macias J.L., Strauch W., Devoli G. (2005) – Catastrophic precipitation-triggered lahar at Casita volcano, Nicaragua: occurrence, bulking and transformation. *Earth Surface Processes and Landforms* 30, 59-79.

Silva R., Bonagura M., Damiano N., Zandomenighi D., Saccorotti G., Wallenstein N., Quadrio A., Carmona E. (2004) – Preliminary results of a seismic experiment in Fogo and Furnas volcanoes, São Miguel Island (Azores), Portugal. *Resumos da “4ª Assembleia Luso-Espanhola de Geodesia e Geofísica”*, 343-344.

Silveira D., Gaspar J. L., Ferreira T., Queiroz G. (2003) – Reassessment of the historical seismic activity with major impact on São Miguel Island (Azores). *Natural Hazards and Earth System Sciences*, 3, 615-623.

Simkin T., Fiske, R.S. (1983) – *Krakatau 1883: The volcanic eruption and its effects*. Smithsonian Institution Press, Washington D.C., 464 p.

Tilling R.I. (2005) – Volcanic hazards. In Marti J. and Ernst G. (Eds.): *Volcanoes and the Environment*. Cambridge University Press, Cambridge, 55-89.

Valadão P., Gaspar J.L., Ferreira T., Queiroz G. (2002) – Landslides density map of S. Miguel Island (Azores archipelago). *Natural Hazards and Earth System Sciences* 2, 51-56.

Wallenstein N. (1999) – *Estudo da história eruptiva recente e do comportamento eruptivo do vulcão do Fogo (S. Miguel, Açores). Avaliação preliminar do hazard*. Tese de doutoramento no ramo de Geologia, especialidade de Vulcanologia. Universidade dos Açores, Departamento de Geociências, 266 p.

Wallenstein N., Duncan A.M., Almeida H., Pacheco J. (1998) – A erupção de 1563 do Pico do Sapateiro, São Miguel (Açores). *Proceedings of the 1ª Assembleia Luso Espanhola de Geodesia e Geofísica (electronic format)*. Espanha, Almeria. Fevereiro de 1998, 6 p.

Wallenstein N., Chester D.K., Duncan A.M. (2005) – Methodological implications of volcanic hazard evaluation and risk assessment: Fogo Volcano, São Miguel, Azores. *Zeitschrift für Geomorphologie* NF, Suppl. Band 140, 129-149.

Annexe

Version française abrégée

Le plus grand des trois volcans de São Miguel, le Fogo (fig. 1 et fig. 2) domine le centre de l'île, avec un sommet à presque 1000 m d'altitude. Une caldera sommitale s'est formée à la suite de plusieurs effondrements, le plus récent ayant eu lieu pendant l'éruption de 1563. La formation du Fogo a commencé, il y a plus de 200 000 ans, mais des produits plus anciens, quoique rares, sont préservés sur le flanc nord grâce à l'effondrement d'un graben (Moore, 1990). Une stratigraphie complète a été établie pour les derniers 40 000 ans, fondée en grande partie sur lesaffleurements du flanc sud. Trois grandes éruptions pliniennes de type trachytique, incluant Fogo A, ont eu lieu depuis 15 000 ans (Wallenstein, 1999). L'éruption explosive la plus récente, de type subplinien, a eu lieu en 1563 et a déposé une épaisseur considérable de cendres sur la moitié est de l'île.

Les aléas volcaniques sur le Fogo ont été récemment discutés par Wallenstein et al. (2005). Cet article s'intéresse aux aléas provoqués par les processus non-éruptifs, souvent nommés aléas volcaniques indirects (Tilling, 2005). Ces aléas majeurs sont produits par les interactions entre l'édifice volcanique instable et les processus sismiques, hydrothermaux, gravitaires et hydrologiques.

São Miguel est situé dans une région tectoniquement active (fig. 3) ; environ 80 % des constructions bâties dans la région étudiée du volcan Fogo sont construites en moellons, ce qui les rend extrêmement vulnérables aux secousses sismiques. Ces résultats ont été confirmés lors d'une étude sur la stabilité de l'autoroute, des routes d'évacuation et des types d'habitations dans le District du Fogo. L'investigation a aussi révélé qu'un grand nombre de routes et de ponts sont menacés par l'activité sismique, une grande partie d'entre eux restant aussi sous la menace des glissements de terrain et de crues soudaines d'où la prise en compte de cet aspect de la vulnérabilité. L'étude a révélé des dangers supplémentaires dans certaines régions habitées. Ainsi, un certain nombre de villages et de villes ont des rues étroites, dont certaines sont des routes

stratégiques desservant d'autres parties de São Miguel. Celles-ci seraient bloquées par des éboulements à la suite d'un tremblement de terre.

Gomes et al. (2006) ont démontré que des tremblements de terre supérieurs à IX (Échelle Européenne macrosismique-EMS 98) ont frappé l'île en 1522, 1713, 1811 et 1935 et, avec des secousses de moindre intensité, en 1810, 1848, 1852, 1932 et 1952. Environ 45 000 personnes vivent aujourd'hui dans le District du Fogo (INEP, 2002) ; comme aucune action n'est entreprise pour réduire la vulnérabilité des habitations, des dégâts matériels et des pertes en vies humaines seront inévitables en cas de fortes secousses.

À plusieurs endroits sur São Miguel, des émanations de gaz sont liées aux systèmes hydrothermaux (Ferreira, 2000). Sur le Fogo, ces systèmes coïncident avec les zones d'activité des fumerolles et sont associés aux failles de distension NO-SE sur le flanc nord (Ferreira, 2000). Le CO₂ est un gaz dangereux, car il s'accumule dans les dépressions où les concentrations supérieures à 15 % entraînent souvent l'asphyxie et la mort (Baxter et al., 1999). Une zone proche du lit de la rivière Ribeira Seca (fig. 4) est connue comme le site d'émission importante de CO₂ et il y a quelques années, le décès d'un fermier fut attribué à l'asphyxie par le CO₂.

En 1997, le centre de volcanologie de l'Université des Açores a détecté des émissions de vapeur dans le village de Ribeira Seca (Ferreira, 2000 ; Ferreira et al., 2005). En 1998 et 1999, ces émissions de vapeur ont atteint une température maximale de 50 °C et une concentration en CO₂ de 13,5 %, juste en dessous du niveau dangereux d'asphyxie défini par Baxter (Ferreira et al., 2005). Comme cette anomalie était située dans une zone résidentielle, quatre maisons furent évacuées. La figure 5 représente la carte des risques fondée sur cette étude.

Au cours des cinq derniers siècles, l'île São Miguel a été affectée par plusieurs glissements de terrain destructeurs qui ont été déclenchés par des tremblements de terre, des éruptions volcaniques et par des épisodes de fortes précipitations. Un exemple récent des effets des pluies a eu lieu le 21 octobre 1997 sur le volcan Furnas (fig. 1). Le glissement fut déclenché par des pluies de l'ordre de 220 l/m² : 36 maisons furent détruites, 29 personnes tuées, 114 habitants sont restés sans abri et le village de Ribeira Quente a été coupé du reste de São Miguel pendant plus de 12 heures (Wallenstein et al., 2005 ; Malheiro, 2006). Le volcan Fogo possède une topographie contrastée, potentiellement instable, avec une proportion significative de matériel pyroclastique. Ses pentes raides inscrites dans ce matériau meuble sont fortement disséquées et les glissements de terrain deviennent ainsi un aléa volcanique indirect fréquent, comme le montre le réseau dense des cicatrices dues aux glissements de terrain (Valadão et al., 2002). L'exemple d'un glissement de terrain dû à une secousse sismique et ayant causé un maximum de dommages a eu lieu le 22 octobre 1522, lorsque qu'une coulée boueuse a enterré et complètement détruit la ville de Vila Franca do Campo (fig. 7). Environ 5000 personnes périrent et une surface d'environ 4,5 km² (fig. 7) a été recouverte de millions de mètres cubes de matériaux.

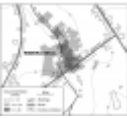
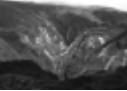
Les crues soudaines, normalement associées à des facteurs hydrologiques spécifiques, sont engendrées par des précipitations intenses. Sur l'île de São Miguel, les bassins versants sont de petite taille, ce qui entraîne, avec leurs profils longitudinaux raides, une montée des eaux fulgurante, consécutive à des abats d'eau abondants. Les barrages naturels créés par les sédiments et la végétation augmentent la menace de crue soudaine et, en décembre 1998, un événement de ce genre a balayé le village de Praia sur la partie basse du flanc sud du volcan (fig. 6). Praia est situé au débouché de la vallée dont le bassin hydrographique s'étend juste en dessous de la limite sud du lac de caldera du Fogo. Praia n'est qu'un exemple extrême d'une zone résidentielle sous la menace de crues soudaines (tab. 2), car de nombreuses implantations similaires à Praia existent sur la partie basse des flancs sud et nord du Fogo (fig. 4 et fig. 6).

Les aléas volcaniques indirects sont une menace constante pour les personnes vivant sur les flancs du volcan et dans certains cas, dans le District du Fogo. Le glissement de terrain de 1522, les coulées boueuses et le tsunami ont provoqué la mort de 5000 personnes, mais aujourd'hui, plus de 11 000 personnes habitant dans le « concelho » de Vila Franca do Campo sont en danger. D'après le recensement de la population en 2001, le District du Fogo abrite environ 45 000 personnes alors l'île São Miguel est devenue une destination touristique de plus en plus populaire (INEP, 2002), ce qui augmente l'exposition à des phénomènes indirectement liés au volcan.

Une recrudescence des précipitations accentuerait les menaces de glissements de terrain et de crues et aggraverait les processus d'érosion des côtes, qui provoquent déjà quelques difficultés sur le flanc sud de Fogo (Malheiro, 2006). Le changement climatique pourrait rendre critique une situation qui, à l'heure actuelle, reste sous contrôle. Les interactions entre l'édifice volcanique et les activités sismiques et hydrothermales (gaz), les glissements de terrain et les crues soudaines créent des risques majeurs et une étude détaillée et intégrée serait nécessaire afin de pouvoir élaborer des plans d'urbanisation appropriés (Wallenstein et al., 2005).

Table des illustrations

	Titre Fig. 1 – Location of Fogo volcano within the Island of São Miguel. <i>Fig. 1 – Localisation du volcan Fogo au sein de l'île de São Miguel.</i>
URL	http://journals.openedition.org/geomorphologie/docannexe/image/2853/img-1.jpg
Fichier	image/jpeg, 344k

	Titre	Fig. 2 – Fogo volcano: a morphostructural sketch. 1: Ribeira Grande graben; 2: post Fogo A lava flow; 3: A.D. 1563 lava flow; 4: scoria cones; 5: A.D. 1563 subplinian vent; 6: Fogo volcano; 7: geothermal power plant; 8: fumaroles; 9: tuff cone; 10: main roads. <i>Fig. 2 – Le volcan Fogo : un schéma morphostructural. 1 : graben de Ribeira Grande ; 2 : coulée de lave postérieure à Fogo A ; 3 : coulée de lave en 1563 AD ; 4 : cônes de scories ; 5 : cratère subplinien de 1563 AD ; 6 : volcan Fogo ; 7 : usine géothermique ; 8 : fumerolles ; 9 : cône de tuf ; 10 : routes principales.</i>
	URL	http://journals.openedition.org/geomorphologie/docannexe/image/2853/img-2.jpg
	Fichier	image/jpeg, 340k
	Titre	Fig. 3 – Location of earthquake epicentres, 1997-2003. <i>Fig. 3 – Localisation des épacentres des séismes survenus entre 1997 et 2003.</i>
	URL	http://journals.openedition.org/geomorphologie/docannexe/image/2853/img-3.jpg
	Fichier	image/jpeg, 288k
	Titre	Fig. 4 – The location of, and population concentrations within, towns and villages of the Fogo District (Population data from INEP, 2002). 1: Concelho boundary; 2: Freguesia boundary; 3: Fogo district boundary; 4: caldera lake; 5: name of concelho. <i>Fig. 4 – Localisation et concentration de la population dans les villes et villages du District du Fogo (données démographiques d'après INEP, 2002). 1 : limite du Concelho ; 2 : limite de la Freguesia ; 3 : limite du district de Fogo ; 4 : lac de caldera ; 5 : nom du concelho.</i>
	URL	http://journals.openedition.org/geomorphologie/docannexe/image/2853/img-4.jpg
	Fichier	image/jpeg, 576k
	Titre	Fig. 5 – Hazard posed by the CO ₂ gas emission at Ribeira Seca during 1998 and 1999 (Ferreira <i>et al.</i> 2005). 1: buildings; 2: roads; 3: contours metres. <i>Fig. 5 – Aléa engendré par l'émission de CO₂ à Ribeira Seca en 1998 et 1999 (Ferreira et al., 2005). 1 : constructions ; 2 : routes ; 3 : courbes de niveau en mètres.</i>
	URL	http://journals.openedition.org/geomorphologie/docannexe/image/2853/img-5.jpg
	Fichier	image/jpeg, 372k
	Titre	Fig. 6 – Fogo volcano: roads and drainage (adapted from Wallenstein <i>et al.</i> , 2005). 1: paved roads; 2: unpaved roads; 3: other roads; 4: road number; 5: towns; 6: woodland; 7: rivers; 8: contours (metres); 9: spot height (metres); 10: other localities. <i>Fig. 6 – Le volcan Fogo : routes et drainage (modifié d'après Wallenstein et al., 2005). 1 : routes asphaltées ; 2 : routes sans revêtement ; 3 : pistes ; 4 : numéro de la route ; 5 : villes ; 6 : forêt ; 7 : rivières ; 8 : courbes de niveau (mètres) ; 9 : altitude du lieu (mètres) ; 10 : autres localités.</i>
	URL	http://journals.openedition.org/geomorphologie/docannexe/image/2853/img-6.jpg
	Fichier	image/jpeg, 460k
	Titre	Fig. 7 – The estimated area that was flooded during 1522. The area is obtained by the application of a probability model developed by Feltpeto <i>et al.</i> (1996) for gravity flows which is superimposed over a three dimensional view of the Vila France do Campo area (adapted from Marques, 2004). Looking north. <i>Fig. 7 – Estimation de la surface de la région inondée en 1522. Cette surface est calculée en utilisant un modèle de probabilité (Feltpeto et al., 1996), surimposé à une vue 3D du secteur de Vila France do Campo (modifié d'après Marques, 2004). Vue vers le nord.</i>
	URL	http://journals.openedition.org/geomorphologie/docannexe/image/2853/img-7.jpg
	Fichier	image/jpeg, 184k
	Titre	Fig. 8 – View of the Ribeira Grande watershed on the northern flank of Fogo showing extensive landslide scars from the summer 2005 seismic activity. Length of valley about 1 km. <i>Fig. 8 – Vue du bassin versant de Ribeira Grande sur le flanc nord du volcan Fogo, montrant de nombreuses et grandes cicatrices de glissements de terrain déclenchés par l'activité sismique de l'été 2005. La longueur de la vallée est d'environ 1 kilomètre</i>
	URL	http://journals.openedition.org/geomorphologie/docannexe/image/2853/img-8.jpg
	Fichier	image/jpeg, 483k

Pour citer cet article

Référence papier

Nicolau Wallenstein, Angus Duncan, David Chester et Rui Marques, « Fogo Volcano (São Miguel, Azores): a hazardous edifice », *Géomorphologie : relief, processus, environnement*, vol. 13 - n° 3 | 2007, 259-270.

Référence électronique

Nicolau Wallenstein, Angus Duncan, David Chester et Rui Marques, « Fogo Volcano (São Miguel, Azores): a hazardous edifice », *Géomorphologie : relief, processus, environnement* [En ligne], vol. 13 - n° 3 | 2007, mis en ligne le 01 octobre 2009, consulté le 22 juin 2018. URL : <http://journals.openedition.org/geomorphologie/2853> ; DOI : 10.4000/geomorphologie.2853

Cet article est cité par

- Pensa, Alessandra. Cas, Raymond. Giordano, Guido. Porreca, Massimiliano. Wallenstein, Nicolau. (2015) Transition from steady to unsteady Plinian eruption column: the VEI 5, 4.6 ka Fogo A Plinian eruption, São Miguel, Azores. *Journal of Volcanology and Geothermal Research*, 305. DOI: 10.1016/j.jvolgeores.2015.09.012
- Martini, Francesca. Bean, Christopher J.. Saccorotti, Gilberto. Viveiros, Fatima. Wallenstein, Nicolau. (2009) Seasonal cycles of seismic velocity variations detected using coda wave interferometry at Fogo volcano, São Miguel, Azores, during 2003–2004. *Journal of Volcanology and Geothermal Research*, 181. DOI: 10.1016/j.jvolgeores.2009.01.015
- Quintela, Ana. Terroso, Denise. Costa, Cristiana. Sá, Henrique. Nunes, João Carlos. Rocha, Fernando. (2015) Characterization and evaluation of hydrothermally influenced clayey sediments from Caldeiras da Ribeira Grande fumarolic field (Azores Archipelago, Portugal) used for aesthetic and pelotherapy purposes. *Environmental Earth Sciences*, 73. DOI: 10.1007/s12665-014-3438-8
- Di Chiara, Anita. Speranza, Fabio. Porreca, Massimiliano. (2012) Paleomagnetic secular variation at the Azores during the last 3 ka. *Journal of Geophysical Research: Solid Earth*, 117. DOI: 10.1029/2012JB009285
- Cabral, L.. Andrade, C.. Coutinho, R.. Cruz, J. V.. (2015) Groundwater composition in perched-water bodies in the north flank of Fogo volcano (São Miguel, Azores): main causes and comparison with river water chemistry. *Environmental Earth Sciences*, 73. DOI: 10.1007/s12665-014-3221-x
- Cruz, J.V.. Andrade, C.. (2015) Natural background groundwater composition in the Azores archipelago (Portugal): A hydrogeochemical study and threshold value determination. *Science of The Total Environment*, 520. DOI: 10.1016/j.scitotenv.2015.03.057
- Hogg, C. Kiyam, D. Rath, V. Byrdina, S. Vandemeulebrouck, J. Revil, A. Viveiros, F. Carmo, R. Silva, C. Ferreira, T. (2018) 3-D interpretation of short-period magnetotelluric data at Furnas Volcano, Azores Islands. *Geophysical Journal International*, 213. DOI: 10.1093/gji/ggx512

Auteurs

Nicolau Wallenstein
Angus Duncan

Articles du même auteur

Formes de relief volcaniques, processus et risques [Texte intégral]

Volcanic landforms, processes and hazards on volcanoes

Paru dans *Géomorphologie : relief, processus, environnement*, vol. 13 - n° 3 | 2007

Volcanic landforms, processes and hazards on volcanoes [Texte intégral]

Paru dans *Géomorphologie : relief, processus, environnement*, vol. 13 - n° 3 | 2007

David Chester

Articles du même auteur

Formes de relief volcaniques, processus et risques [Texte intégral]

Volcanic landforms, processes and hazards on volcanoes

Paru dans *Géomorphologie : relief, processus, environnement*, vol. 13 - n° 3 | 2007

Volcanic landforms, processes and hazards on volcanoes [Texte intégral]

Paru dans *Géomorphologie : relief, processus, environnement*, vol. 13 - n° 3 | 2007

Rui Marques

Droits d'auteur

© Groupe français de géomorphologie

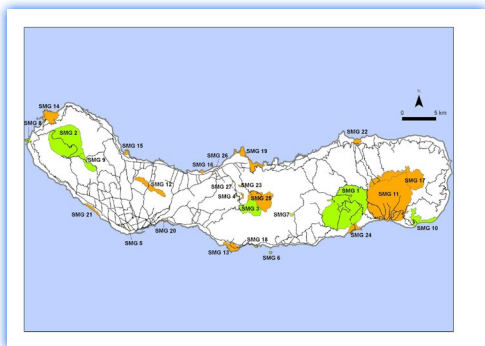
IT HAS BEEN THE COMMON
AMBITION OF MANKIND TO SET
THE WHOLE WORLD TALKING.

What was it happened? Neither Malone nor I was in a position to say, for both of us were swept off our feet as by a cyclone and swirled along the grass, revolving round and round like two curling stones upon an ice rink. At the same time our ears were assailed by the most horrible yell that ever yet was heard. Who is there of all the hundreds who have attempted it who has ever yet described adequately that terrible cry? It was a howl in which pain, anger, menace, and the outraged majesty of Nature all blended into one hideous shriek. For a full minute it lasted, a thousand sirens in one, paralysing all the great multitude with its fierce insistence, and floating away through the still summer air until it went echoing along the whole South Coast and even reached our French neighbours across the Channel. No sound in history has ever equalled the cry of the injured Earth.

Then came the geyser. It was an enormous spout of vile treacly substance of the consistency of tar, which shot up into the air to a height which has been computed at two thousand feet. An inquisitive aeroplane, which had been hovering over the scene, was picked off as by an Archie and made a forced landing, man and machine buried in filth. This horrible stuff, which had a most penetrating and nauseous odour, may have represented the life blood of the planet, or it may be... that it is a protective secretion, analogous to that of the skunk, which Nature has provided in order to defend Mother Earth from intrusive Challengers.

And

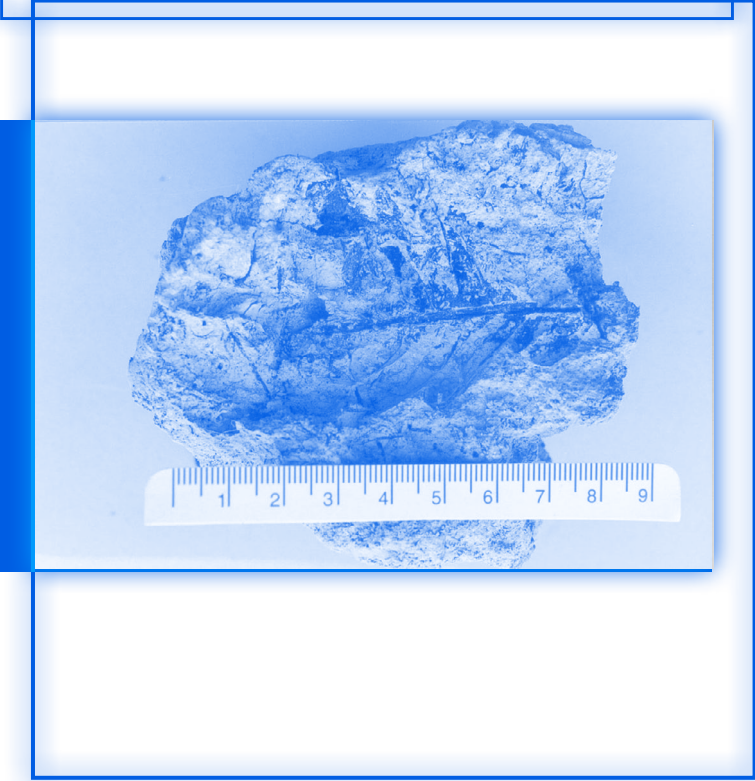
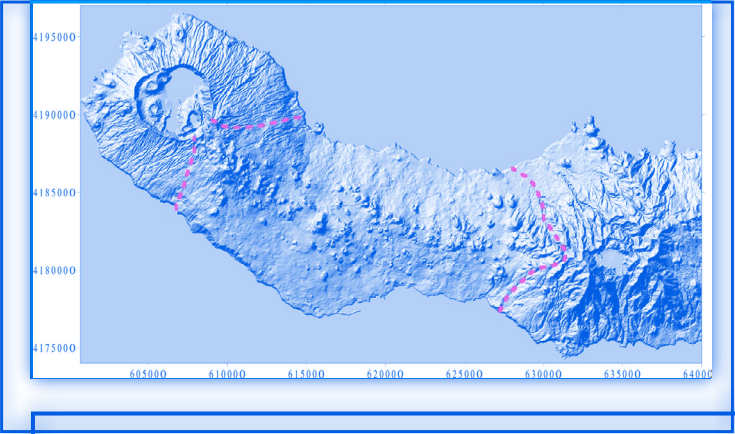




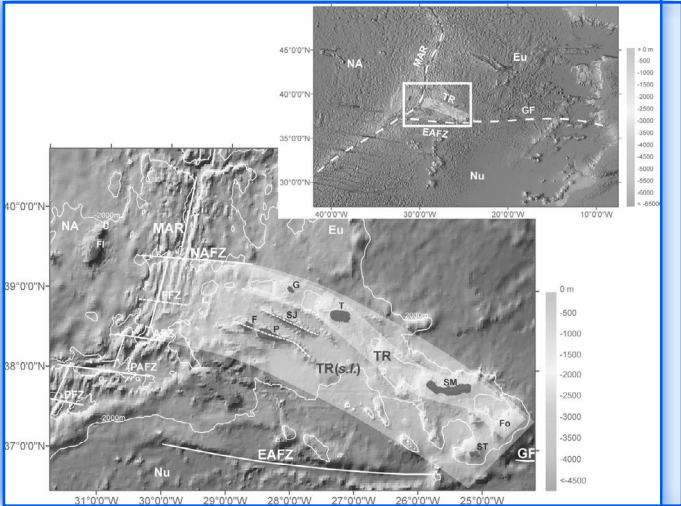
then came the closing of the pit. As Nature slowly closes a wound from below upwards, so does the Earth with extreme rapidity mend any rent which is made in its vital substance. There was a prolonged high-pitched crash as the sides of the shaft came together, the sound, reverberating from the depths and then rising higher and higher until with a deafening bang the brick circle at the orifice flattened out and clashed together, while a tremor like a small earthquake shook down the spoil banks and piled a pyramid fifty feet high of debris and broken iron over the spot where the hole had been.

It is of course well known that the effect of the experiment was a world-wide one. It is true that nowhere did the injured planet emit such a howl as at the actual point of penetration, but she showed that she was indeed one entity by her conduct elsewhere. Through every vent and every volcano she voiced her indignation... It has been the common ambition of mankind to set the whole world talking. To set the whole world screaming was the privilege of Challenger alone.

— When the World Screamed. Strand Magazine, Arthur Conan Doyle (1928)



CHALLENGER THE SUPER
SCIENTIST, CHALLENGER THE
ARCH-PIONEER, CHALLENGER



THE FIRST MAN OF ALL
MEN WHOM MOTHER EARTH
HAD BEEN COMPELLED TO
RECOGNIZE.

When the World Screamed

A Professor Challenger Adventure

by

Arthur Conan Doyle

Published 1928

I had a vague recollection of having heard my friend Edward Malone, of the Gazette, speak of Professor Challenger, with whom he had been associated in some remarkable adventures. I am so busy, however, with my own profession, and my firm has been so overtaxed with orders, that I know little of what is going on in the world outside my own special interests. My general recollection was that Challenger has been depicted as a wild genius of a violent and intolerant disposition. I was greatly surprised to receive a business communication from him which was in the following terms:

“14 (Bis),
Enmore Gardens,
Kensington.

“Sir,--

“I have occasion to engage the services of an expert in Artesian borings. I will not conceal from you that my opinion of experts is not a high one, and that I have usually found that a man who, like myself, has a well-equipped brain can take a sounder and broader view than the man who professes a special knowledge (which, alas, is so often a mere profession), and is therefore limited in his outlook. None the less, I am disposed to give you a trial. Looking down the list of Artesian authorities, a certain oddity--I had almost written absurdity--in your name attracted my attention, and I found upon inquiry that my young friend, Mr. Edward Malone, was actually acquainted with you. I am therefore writing to say that I should be glad to have an interview with you, and that if you satisfy my requirements, and my standard is no mean one, I may be inclined to put a most important matter into your hands. I can say no more at present as the matter is of extreme secrecy, which can only be discussed by word of mouth. I beg, therefore, that you will at once cancel any engagement which you may happen to have, and that you will call upon me at the above address at 10.30 in the morning of next Friday. There is a scraper as well as a mat, and Mrs. Challenger is most particular.

“I remain, Sir, as I began,

“George Edward Challenger.”

I handed this letter to my chief clerk to answer, and he informed the Professor that Mr. Peerless Jones would be glad to keep the appointment as arranged. It was a perfectly civil business note, but it began with the phrase:

“Your letter (undated) has been received.”

This drew a second epistle from the Professor:

“Sir,” he said and his writing looked like a barbed wire fence-- “I observe that you animadvert upon the trifle that my letter was undated. Might I draw your attention to the fact that, as some return for a monstrous taxation, our Government is in the habit of affixing a small circular sign or stamp upon the outside on the envelope which notifies the date of posting? Should this sign be missing or illegible your remedy lies with the proper postal authorities. Meanwhile, I would ask you to confine your observations to matters which concern the business over which I consult you, and to cease to comment upon the form which my own letters may assume.”

It was clear to me that I was dealing with a lunatic, so I thought it well before I went any further in the matter to call upon my friend Malone, whom I had known since the old days when we both played Rugger for Richmond. I found him the same jolly Irishman as ever, and much amused at my first brush with Challenger.

“That’s nothing, my boy,” said he. “You’ll feel as if you had been skinned alive when you have been with him five minutes. He beats the world for offensiveness.”

“But why should the world put up with it?”

“They don’t. If you collected all the libel actions and all the rows and all the police-court assaults--”

“Assaults!”

“Bless you, he would think nothing of throwing you downstairs if you have a disagreement. He is a primitive cave-man in a lounge suit. I can see him with a club in one hand and a jagged bit of flint in the other. Some people are born out of their proper century, but he is born out of his millennium. He belongs to the early neolithic or thereabouts.”

“And he a professor!”

“There is the wonder of it! It’s the greatest brain in Europe, with a driving force behind it that can turn all his dreams into facts.

They do all they can to hold him back for his colleagues hate him like poison, but a lot of trawlers might as well try to hold back the Berengaria. He simply ignores them and steams on his way.”

“Well,” said I, “one thing is clear. I don’t want to have anything to do with him. I’ll cancel that appointment.”

“Not a bit of it. You will keep it to the minute--and mind that it is to the minute or you will hear of it.”

“Why should I?”

“Well, I’ll tell you. First of all, don’t take too seriously what I have said about old Challenger. Everyone who gets close to him learns to love him. There is no real harm in the old bear. Why, I remember how he carried an Indian baby with the smallpox on his back for a hundred miles from the back country down to the Madeira River. He is big every way. He won’t hurt if you get right with him.”

“I won’t give him the chance.”

“You will be a fool if you don’t. Have you ever heard of the Hengist Down Mystery--the shaft-sinking on the South Coast?”

“Some secret coal-mining exploration, I understand.”

Malone winked. “Well, you can put it down as that if you like. You see, I am in the old man’s confidence, and I can’t say anything until he gives the word. But I may tell you this, for it has been in the Press. A man, Betterton, who made his money in rubber, left his whole estate to Challenger some years ago, with the provision that it should be used in the interests of science. It proved to be an enormous sum-- several millions. Challenger then bought a property at Hengist Down, in Sussex. It was worthless land on the north edge of the chalk country, and he got a large tract of it, which he wired off. There was a deep gully in the middle of it. Here he began to make an excavation. He announced”-- here Malone winked again--“that there was petroleum in England and that he meant to prove it. He built a little model village with a colony of well-paid workers who are all sworn to keep their mouths shut. The gully is wired off as well as the estate, and the place is guarded by bloodhounds. Several pressmen have nearly lost their lives, to say nothing of the seats of their trousers, from these creatures. It’s a big operation, and Sir Thomas Morden’s firm has it in hand, but they also are sworn to secrecy. Clearly the time has come when Artesian help is needed. Now, would you not be foolish to refuse such a job as that, with all the interest and experience and a big fat cheque at the end of it--to say nothing of rubbing shoulders with the most wonderful man you have ever met or are ever likely to meet?”

Malone’s arguments prevailed, and Friday morning found me on my way to Enmore Gardens, I took such particular care to be in time that I found myself at the door twenty minutes too soon. I was waiting in the street when it struck me that I recognized the Rolls- Royce with the silver arrow mascot at the door. It was certainly that of Jack Devonshire, the junior partner of the great Morden firm. I had always known him as the most urbane of men, so that it was rather a shock to me when he suddenly appeared, and standing outside the door he raised both his hands, to heaven and said with great fervour: “Damn him! Oh, damn him!”

“What is up, Jack? You seem peeved this morning.”

“Hullo, Peerless! Are you in on this job, too?”

“There seems a chance of it.”

“Well, you find it chastening to the temper.”

“Rather more so than yours can stand, apparently.”

“Well, I should say so. The butler’s message to me was: “The Professor desired me to say, sir, that he was rather busy at present eating an egg, and that if you would call at some more convenient time he would very likely see you.” That was the message delivered by a servant. I may add that I had called to collect forty-two thousand pounds that he owes us.”

I whistled.

“You can’t get your money?”

“Oh, yes, he is all right about money. I’ll do the old gorilla the justice to say that he is open-handed with money. But he pays when he likes and how he likes, and he cares for nobody.

However, you go and try your luck and see how you like it.” With that he flung himself into his motor and was off.

I waited with occasional glances at my watch until the zero hour should arrive. I am, if I may say so, a fairly hefty individual, and a runner-up for the Belsize Boxing Club middle-weights, but I have never faced an interview with such trepidation as this. It was not physical, for I was confident I could hold my own if this inspired lunatic should attack me, but it was a mixture of feelings in which fear of some public scandal and dread of losing a lucrative contract were mingled. However, things are always easier when imagination ceases and action begins. I snapped up my watch and made for the door.

It was opened by an old wooden-faced butler, a man who bore an expression, or an absence of expression, which gave the impression that he was so inured to shocks that nothing on earth would surprise him.

“By appointment, sir?” he asked.

“Certainly.”

He glanced at a list in his hand.

“Your name, sir?... Quite so, Mr. Peerless Jones.... Ten-thirty. Everything is in order. We have to be careful, Mr. Jones, for we are much annoyed by journalists. The Professor, as you may be aware, does not approve of the Press. This way, sir. Professor Challenger is now receiving.”

The next instant I found myself in the presence. I believe that my friend, Ted Malone, has described the man in his “Lost World” yarn better than I can hope to do, so I’ll leave it at that. All I was aware of was a huge trunk of a man behind a mahogany desk, with a great spade-shaped black beard and two large grey eyes half covered with insolent drooping eyelids. His big head sloped back, his beard bristled forward, and his whole appearance conveyed one single impression of arrogant intolerance. “Well, what the devil do you want?” was written all over him. I laid my card on the table.

“Ah yes,” he said, picking it up and handling it as if he disliked the smell of it. “Of course. You are the expert so-called. Mr. Jones-- Mr. Peerless Jones. You may thank your godfather, Mr. Jones, for it was this ludicrous prefix which first drew my attention to you.”

“I am here, Professor Challenger, for a business interview and not to discuss my own name,” said I, with all the dignity I could master.

“Dear me, you seem to be a very touchy person, Mr. Jones. Your nerves are in a highly irritable condition. We must walk warily in dealing with you, Mr. Jones. Pray sit down and compose yourself. I have been reading your little brochure upon the reclaiming of the Sinai Peninsula. Did you write it yourself?”

“Naturally, sir. My name is on it.”

“Quite so! Quite so! But it does not always follow, does it? However, I am prepared to accept your assertion. The book is not without merit of a sort. Beneath the dullness of the diction one gets glimpses of an occasional idea. There are germs of thought here and there. Are you a married man?”

“No, sir. I am not. “

“Then there is some chance of your keeping a secret. “

“If I promised to do so, I would certainly keep my promise. “So you say. My young friend, Malone”--he spoke as if Ted were ten years of age--“has a good opinion of you. He says that I may trust you. This trust is a very great one, for I am engaged just now in one of the greatest experiments--I may even say the greatest experiment --in the history of the world. I ask for your participation.”

“I shall be honoured.”

“It is indeed an honour. I will admit that I should have shared my labours with no one were it not that the gigantic nature of the undertaking calls for the highest technical skill. Now, Mr. Jones, having obtained your promise of inviolable secrecy, I come down to the essential point. It is this--that the world upon which we live is itself a living organism, endowed, as I believe, with a circulation, a respiration, and a nervous system of its own.” Clearly the man was a lunatic.

“Your brain, I observe,” he continued, “fails to register. But it will gradually absorb the idea.

You will recall how a moor or heath resembles the hairy side of a giant animal. A certain analogy runs through all nature. You will then consider the secular rise and fall of land, which indicates the slow respiration of the creature. Finally, you will note the fidgetings and scratchings which appear to our Lilliputian perceptions as earthquakes and convulsions.”

“What about volcanoes?” I asked.

“Tut, tut! They correspond to the heat spots upon our own bodies.”

My brain whirled as I tried to find some answer to these monstrous contentions.

“The temperature!” I cried. “Is it not a fact that it rises rapidly as one descends, and that the centre of the earth is liquid heat?”

He waved my assertion aside.

“You are probably aware, sir, since Council schools are now compulsory, that the earth is flattened at the poles. This means that the pole is nearer to the centre than any other point and would therefore be most affected by this heat of which you spoke. It is notorious, of course, that the conditions of the poles are tropical, is it not?”

“The whole idea is utterly new to me.”

“Of course it is. It is the privilege of the original thinker to put forward ideas which are new and usually unwelcome to the common clay. Now, sir, what is this?” He held up a small object which he had picked from the table.

“I should say it is a sea-urchin.”

“Exactly!” he cried, with an air of exaggerated surprise, as when an infant has done something clever. “It is a sea-urchin--a common echinus. Nature repeats itself in many forms regardless of the size. This echinus is a model, a prototype, of the world. You perceive that it is roughly circular, but flattened at the poles. Let us then regard the world as a huge echinus. What are your objections?”

My chief objection was that the thing was too absurd for argument, but I did not dare to say so. I fished around for some less sweeping assertion.

“A living creature needs food,” I said. “Where could the world sustain its huge bulk?”

“An excellent point--excellent!” said the Professor, with a huge air of patronage. “You have a quick eye for the obvious, though you are slow in realizing the more subtle implications. How does the world get nourishment? Again we turn to our little friend the echinus. The water which surrounds it flows through the tubes of this small creature and provides its nutrition.”

“Then you think that the water--”

“No, sir. The ether. The earth browses upon a circular path in the fields of space, and as it moves the ether is continually pouring through it and providing its vitality. Quite a

flock of other little world-echini are doing the same thing, Venus, Mars, and the rest, each with its own field for grazing.”

The man was clearly mad, but there was no arguing with him. He accepted my silence as agreement and smiled at me in most beneficent fashion.

“We are coming on, I perceive,” said he. “Light is beginning to break in. A little dazzling at first, no doubt, but we will soon get used to it. Pray give me your attention while I found one or two more observations upon this little creature in my hand.

“We will suppose that on this outer hard rind there were certain infinitely small insects which crawled upon the surface. Would the echinus ever be aware of their existence?”

“I should say not.”

“You can well imagine then, that the earth has not the least idea of the way in which it is utilized by the human race. It is quite unaware of this fungus growth of vegetation and evolution of tiny animalcules which has collected upon it during its travels round the sun as barnacles gather upon the ancient vessel. That is the present state of affairs, and that is what I propose to alter.”

I stared in amazement. “You propose to alter it?”

“I propose to let the earth know that there is at least one person, George Edward Challenger, who calls for attention--who, indeed, insists upon attention. It is certainly the first intimation it has ever had of the sort.”

“And how, sir, will you do this?”

“Ah, there we get down to business.

You have touched the spot. I will again call your attention to this interesting little creature which I hold in my hand. It is all nerves and sensibility beneath that protective crust. Is it not evident that if a parasitic animalcule desired to call its attention it would sink a hole in its shell and so stimulate its sensory apparatus?”

“Certainly.”

“Or, again, we will take the case of the homely flea or a mosquito which explores the surface of the human body. We may be unaware of its presence. But presently, when it sinks its proboscis through the skin, which is our crust, we are disagreeably reminded that we are not altogether alone. My plans now will no doubt begin to dawn upon you. Light breaks in the darkness.”

“Good heavens! You propose to sink a shaft through the earth’s crust?”

He closed his eyes with ineffable complacency.

“You see before you,” he said, “the first who will ever pierce that horny hide. I may even put it in the present tense and say who has pierced it.”

“You have done it!”

“With the very efficient aid of Morden and think I may say that I have done it. Several years of constant work which has been carried on night and day, and conducted by every known species of drill, borer, crusher, and explosive, has at last brought us to our goal.”

“You don’t mean to say you are through the crust!”

“If your expressions denote bewilderment they may pass. If they denote incredulity--”

“No, sir, nothing of the kind.”

“You will accept my statement without question. We are through the crust. It was exactly fourteen thousand four hundred and forty-two yards thick, or roughly eight miles. In the course of our sinking it may interest you to know that we have exposed a fortune in the matter of coal-beds which would probably in the long run defray the cost of the enterprise. Our chief difficulty has been the springs of water in the lower chalk and Hastings sands, but these we have overcome. The last stage has now been reached--and the last stage is none other than Mr. Peerless Jones. You, sir, represent the mosquito. Your Artesian borer takes the place of the stinging proboscis. The brain has done its work. Exit the thinker. Enter the mechanical one, the peerless one, with his rod of metal. Do I make myself clear?”

“You talk of eight miles!” I cried. “Are you aware, sir, that five thousand feet is considered nearly the limit for Artesian borings? I am acquainted with one in upper Silesia which is six thousand two hundred feet deep, but it is looked upon as a wonder.”

“You misunderstand me, Mr. Peerless. Either my explanation or your brain is at fault, and I will not insist upon which. I am well aware of the limits of Artesian borings, and it is not likely that I would have spent millions of pounds upon my colossal tunnel if a six-inch boring would have met my needs. All that I ask you is to have a drill ready which shall be as sharp as possible, not more than a hundred feet in length, and operated by an electric motor. An ordinary percussion drill driven home by a weight will meet every requirement.

“Why by an electric motor?”

“I am here, Mr. Jones, to give orders, not reasons. Before we finish it may happen--it may, I say, happen--that your very life may depend upon this drill being started from a distance by electricity. It can, I presume, be done?”

“Certainly it can be done.”

“Then prepare to do it. The matter is not yet ready for your actual presence, but your preparations may now be made. I have nothing more to say.”

“But it is essential,” I expostulated, “that you should let me know what soil the drill is to penetrate. Sand, or clay, or chalk would each need different treatment.”

“Let us say jelly,” said Challenger. “Yes, we will for the present suppose that you have to sink your drill into jelly. And now, Mr. Jones, I have matters of some importance to engage my mind, so I will wish you good morning. You can draw up a formal contract with mention of your charges for my Head of Works.”

I bowed and turned, but before I reached the door my curiosity overcame me.

He was already writing furiously with a quill pen screeching over the paper, and he looked up angrily at my interruption.

“Well, sir, what now? I had hoped you were gone.

“I only wished to ask you, sir, what the object of so extraordinary an experiment can be?”

“Away, sir, away!” he cried, angrily. “Raise your mind above the base mercantile and utilitarian needs of commerce. Shake off your paltry standards of business. Science seeks knowledge. Let the knowledge lead us where it will, we still must seek it. To know once for all what we are, why we are, where we are, is that not in itself the greatest of all human aspirations? Away, sir, away!”

His great black head was bowed over his papers once more and blended with his beard. The quill pen screeched more shrilly than ever. So I left him, this extraordinary

man, with my head in a whirl at the thought of the strange business in which I now found myself to be his partner.

When I got back to my office I found Ted Malone waiting with a broad grin upon his face to know the result of my interview.

“Well!” he cried. “None the worse? No case of assault and battery? You must have handled him very tactfully. What do you think of the old boy?”

“The most aggravating, insolent, intolerant, self-opinionated man I have ever met, but--”

“Exactly!” cried Malone. “We all come to that “but.” Of course, he is all you say and a lot more, but one feels that so big a man is not to be measured in our scale, and that we can endure from him what we would not stand from any other living mortal. Is that not so?”

“Well, I don’t know him well enough yet to say, but I will admit that if he is not a mere bullying megalomaniac, and if what he says is true, then he certainly is in a class by himself. But is it true?”

“Of course it is true. Challenger always delivers the goods. Now, where are you exactly in the matter? Has he told you about Hengist Down?”

“Yes, in a sketchy sort of way.”

“Well, you may take it from me that the whole thing is colossal colossal in conception and colossal in execution. He hates pressmen, but I am in his confidence, for he knows that I will publish no more than he authorizes. Therefore I have his plans, or some of his plans. He is such a deep old bird that one never is sure if one has really touched bottom. Anyhow, I know enough to assure you that Hengist Down is a practical proposition and nearly completed. My advice to you now is simply to await events, and meanwhile to get your gear all ready. You’ll hear soon enough either from him or from me.”

As it happened, it was from Malone himself that I heard. He came round quite early to my office some weeks later, as the bearer of a message.

“I’ve come from Challenger” said he.

“You are like the pilot fish to the shark.”

“I’m proud to be anything to him. He really is a wonder. He has done it all right. It’s your turn now, and then he is ready to ring up the curtain.”

“Well, I can’t believe it until I see it, but I have everything ready and loaded on a lorry. I could start it off at any moment.”

“Then do so at once. I’ve given you a tremendous character for energy and punctuality, so mind you don’t let me down. In the meantime, come down with me by rail and I will give you an idea of what has to be done.”

It was a lovely spring morning--May 22nd, to be exact--when we made that fateful journey which brought me on to a stage which is destined to be historical. On the way Malone handed me a note from Challenger which I was to accept as my instructions.

“Sir,” (it ran)--

“Upon arriving at Hengist Down you will put yourself at the disposal of Mr. Barforth, the Chief Engineer, who is in possession of my plans. My young friend, Malone, the bearer of this, is also in touch with me and may protect me from any personal contact. We have now experienced certain phenomena in the shaft at and below

the fourteen thousand-foot level which fully bear out my views as to the nature of a planetary body, but some more sensational proof is needed before I can hope to make an impression upon the torpid intelligence of the modern scientific world.

That proof you are destined to afford, and they to witness. As you descend in the lifts you will observe, presuming that you have the rare quality of observation, that you pass in succession the secondary chalk beds, the coal measures, some Devonian and Cambrian indications, and finally the granite, through which the greater part of our tunnel is conducted. The bottom is now covered with tarpaulin, which I order you not to tamper with, as any clumsy handling of the sensitive inner cuticle of the earth might bring about premature results. At my instruction, two strong beams have been laid across the shaft twenty feet above the bottom, with a space between them. This space will act as a clip to hold up your Artesian tube. Fifty feet of drill will suffice, twenty of which will project below the beams, so that the point of the drill comes nearly down to the tarpaulin. As you value your life do not let it go further. Thirty feet will then project upwards in the shaft, and when you have released it we may assume that not less than forty feet of drill will bury itself in the earth's substance. As this substance is very soft I find that you will probably need no driving power, and that simply a release of the tube will suffice by its own weight to drive it into the layer which we have uncovered. These instructions would seem to be sufficient for any ordinary intelligence, but I have little doubt that you will need more, which can be referred to me through our young friend, Malone.

“GEORGE EDWARD CHALLENGER.”

It can be imagined that when we arrived at the station of Storrington, near the northern foot of the South Downs, I was in a state of considerable nervous tension. A weather-worn Vauxhall thirty landaulette was awaiting us, and bumped us for six or seven miles over by-paths and lanes which, in spite of their natural seclusion, were deeply rutted and showed every sign of heavy traffic. A broken lorry lying in the grass at one point showed that others had found it rough going as well as we. Once a huge piece of machinery which seemed to be the valves and piston of a hydraulic pump projected itself, all rusted, from a clump of furze.

“That's Challenger's doing,” said Malone, grinning.

“Said it was one-tenth of an inch out of estimate, so he simply chucked it by the wayside.”

“With a lawsuit to follow, no doubt.”

“A lawsuit! My dear chap, we should have a court of our own. We have enough to keep a judge busy for a year. Government too. The old devil cares for no one. Rex v. George Challenger and George Challenger v. Rex. A nice devil's dance the two will have from one court to another. Well, here we are. All right, Jenkins, you can let us in!”

A huge man with a notable cauliflower ear was peering into the car, a scowl of suspicion upon his face. He relaxed and saluted as he recognized my companion.

“All right, Mr. Malone. I thought it was the American Associated Press.”

“Oh, they are on the track, are they?”

“They to-day, and The Times yesterday. Oh, they are buzzing round proper. Look at that!” He indicated a distant dot upon the sky-line.

“See that glint! That's the telescope of the Chicago Daily News. Yes, they are fair after us now. I've seen 'em in rows, same as the crows, along the Beacon yonder.”

“Poor old Press gang!” said Malone, as we entered a gate in a formidable barbed wire fence. “I am one of them myself, and I know how it feels.

At this moment we heard a plaintive bleat behind us of “Malone! Ted Malone!” It came from a fat little man who had just arrived upon a motor-bike and was at present struggling in the Herculean grasp of the gatekeeper.

“Here, let me go!” he sputtered. “Keep your hands off! Malone, call off this gorilla of yours.”

“Let him go, Jenkins! He’s a friend of mine!” cried Malone. “Well, old bean, what is it? What are you after in these parts? Fleet Street is your stamping ground--not the wilds of Sussex.”

“You know what I am after perfectly well,” said our visitor. “I’ve got the assignment to write a story about Hengist Down and I can’t go home without the copy.”

“Sorry, Roy, but you can’t get anything here.

You’ll have to stay on that side of the wire. If you want more you must go and see Professor Challenger and get his leave.”

“I’ve been,” said the journalist, ruefully. “I went this morning.”

“Well, what did he say?”

“He said he would put me through the window.”

Malone laughed.

“And what did you say?”

“I said, “What’s wrong with the door?” and I skipped through it just to show there was nothing wrong with it. It was no time for argument. I just went. What with that bearded Assyrian bull in London, and this Thug down here, who has ruined my clean celluloid, you seem to be keeping queer company, Ted Malone.”

“I can’t help you, Roy; I would if I could. They say in Fleet Street that you have never been beaten, but you are up against it this time. Get back to the office, and if you just wait a few days I’ll give you the news as soon as the old man allows.”

“No chance of getting in?”

“Not an earthly.”

“Money no object?”

“You should know better than to say that.”

“They tell me it’s a short cut to New Zealand.”

“It will be a short cut to the hospital if you butt in here, Roy. Good-bye, now. We have some work to do of our own.

“That’s Roy Perkins, the war correspondent,” said Malone as we walked across the compound. “We’ve broken his record, for he is supposed to be undefeatable. It’s his fat, little innocent face that carries him through everything. We were on the same staff once. Now there”--he pointed to a cluster of pleasant red-roofed bungalows--“are the quarters of the men. They are a splendid lot of picked workers who are paid far above ordinary rates. They have to be bachelors and teetotallers, and under oath of secrecy. I don’t think there has been any leakage up to now. That field is their football ground and the detached house is their library and recreation room. The old man is some organizer, I can assure you. This is Mr. Barforth, the head engineer-in-charge.”

A long, thin, melancholy man with deep lines of anxiety upon his face had appeared before us. “I expect you are the Artesian engineer,” said he, in a gloomy voice. “I was told to expect you. I am glad you’ve come, for I don’t mind telling you that the

responsibility of this thing is getting on my nerves. We work away, and I never know if it's a gush of chalk water, or a seam of coal, or a squirt of petroleum, or maybe a touch of hell fire that is coming next. We've been spared the last up to now, but you may make the connection for all I know."

"Is it so hot down there?"

"Well, it's hot. There's no denying it. And yet maybe it is not hotter than the barometric pressure and the confined space might account for. Of course, the ventilation is awful. We pump the air down, but two-hour shifts are the most the men can do--and they are willing lads too. The Professor was down yesterday, and he was very pleased with it all. You had best join us at lunch, and then you will see it for yourself."

After a hurried and frugal meal we were introduced with loving assiduity upon the part of the manager to the contents of his engine-house, and to the miscellaneous scrapheap of disused implements with which the grass was littered. On one side was a huge dismantled Arrol hydraulic shovel, with which the first excavations had been rapidly made. Beside it was a great engine which worked a continuous steel rope on which the skips were fastened which drew up the debris by successive stages from the bottom of the shaft. In the power-house were several Escher Wyss turbines of great horse-power running at one hundred and forty revolutions a minute and governing hydraulic accumulators which evolved a pressure of fourteen hundred pounds per square inch, passing in three-inch pipes down the shaft and operating four rock drills with hollow cutters of the Brandt type. Abutting upon the engine-house was the electric house supplying power for a very large lighting installment, and next to that again was an extra turbine of two hundred horse-power, which drove a ten-foot fan forcing air down a twelve-inch pipe to the bottom of the workings.

All these wonders were shown with many technical explanations by their proud operator, who was well on his way to boring me stiff, as I may in turn have done my reader. There came a welcome interruption, however, when I heard the roar of wheels and rejoiced to see my Leyland three-tonner come rolling and heaving over the grass, heaped up with tools and sections of tubing, and bearing my foreman, Peters, and a very grimy assistant in front. The two of them set to work at once to unload my stuff and to carry it in. Leaving them at their work, the manager, with Malone and myself, approached the shaft.

It was a wondrous place, on a very much larger scale than I had imagined. The spoil banks, which represented the thousands of tons removed, had been built up into a great horseshoe around it, which now made a considerable hill. In the concavity of this horseshoe, composed of chalk, clay, coal, and granite, there rose up a bristle of iron pillars and wheels from which the pumps and the lifts were operated. They connected with the brick power building which filled up the gap in the horseshoe. Beyond it lay the open mouth of the shaft, a huge yawning pit, some thirty or forty feet in diameter, lined and topped with brick and cement. As I craned my neck over the side and gazed down into the dreadful abyss, which I had been assured was eight miles deep, my brain reeled at the thought of what it represented. The sunlight struck the mouth of it diagonally, and I could only see some hundreds of yards of dirty white chalk, bricked here and there where the surface had seemed unstable. Even as I looked, however, I saw, far, far down in the darkness, a tiny speck of light, the smallest possible dot, but clear and steady against the inky background.

“What is that light?” I asked.

Malone bent over the parapet beside me.

“That’s one of the cages coming up,” said he. “Rather wonderful, is it not? That is a mile or more from us, and that little gleam is a powerful arc lamp. It travels quickly, and will be here in a few minutes.”

Sure enough the pin-point of light came larger and larger, until it flooded the tube with its silvery radiance, and I had to turn away my eyes from its blinding glare. A moment later the iron cage clashed up to the landing stage, and four men crawled out of it and passed on to the entrance.

“Nearly all in,” said Malone. “It is no joke to do a two-hour shift at that depth. Well, some of your stuff is ready to hand here. I suppose the best thing we can do is to go down. Then you will be able to judge the situation for yourself.”

There was an annexe to the engine-house into which he led me. A number of baggy suits of the lightest tussore material were hanging from the wall. Following Malone’s example I took off every stitch of my clothes, and put on one of these suits, together with a pair of rubber-soled slippers. Malone finished before I did and left the dressing-room. A moment later I heard a noise like ten dog-fights rolled into one, and rushing out I found my friend rolling on the ground with his arms round the workman who was helping to stack my artesian tubing. He was endeavouring to tear something from him to which the other was most desperately clinging. But Malone was too strong for him, tore the object out of his grasp, and danced upon it until it was shattered to pieces. Only then did I recognize that it was a photographic camera. My grimy-faced artisan rose ruefully from the floor.

“Confound you, Ted Malone!” said he. “That was a new ten-guinea machine.”

“Can’t help it, Roy. I saw you take the snap, and there was only one thing to do.”

“How the devil did you get mixed up with my outfit?” I asked, with righteous indignation.

The rascal winked and grinned. “There are always and means,” said he.

“But don’t blame your foreman. He thought it was just a rag. I swapped clothes with his assistant, and in I came.”

“And out you go,” said Malone. “No use arguing, Roy. If Challenger were here he would set the dogs on you. I’ve been in a hole myself so I won’t be hard, but I am watch-dog here, and I can bite as well as bark.

Come on! Out you march!”

So our enterprising visitor was marched by two grinning workmen out of the compound. So now the public will at last understand the genesis of that wonderful four-column article headed “Mad Dream of a Scientist” with the subtitle. “A Bee-line to Australia,” which appeared in The Adviser some days later and brought Challenger to the verge of apoplexy, and the editor of The Adviser to the most disagreeable and dangerous interview of his lifetime. The article was a highly coloured and exaggerated account of the adventure of Roy Perkins, “our experienced war correspondent” and it contained such purple passages as “this hirsute bully of Enmore Gardens,” “a compound guarded by barbed wire, plug-uglies, and bloodhounds,” and finally, “I was dragged from the edge of the Anglo-Australian tunnel by two ruffians, the more savage being a jack-of-all trades whom I had previously known by sight as a hanger-on of the journalistic profession, while the other, a sinister figure in a strange tropical garb, was posing as an Artesian

engineer, though his appearance was more reminiscent of Whitechapel.” Having ticked us off in this way, the rascal had an elaborate description of rails at the pit mouth, and of a zigzag excavation by which funicular trains were to burrow into the earth.

The only practical inconvenience arising from the article was that it notably increased that line of loafers who sat upon the South Downs waiting for something to happen. The day came when it did happen and when they wished themselves elsewhere.

My foreman with his faked assistant had littered the place with all my apparatus, my bellbox, my crowsfoot, the V-drills, the rods, and the weight, but Malone insisted that we disregard all that and descend ourselves to the lowest level. To this end we entered the cage, which was of latticed steel, and in the company of the chief engineer we shot down into the bowels of the earth. There were a series of automatic lifts, each with its own operating station hollowed out in the side of the excavation. They operated with great speed, and the experience was more like a vertical railway journey than the deliberate fall which we associate with the British lift.

Since the cage was latticed and brightly illuminated, we had a clear view of the strata which we passed. I was conscious of each of them as we flashed past. There were the sallow lower chalk, the coffee-coloured Hastings beds, the lighter Ashburnham beds, the dark carboniferous clays, and then, gleaming in the electric light, band after band of jet-black, sparkling coal alternating with the rings of clay. Here and there brickwork had been inserted, but as a rule the shaft was self-supported, and one could but marvel at the immense labour and mechanical skill which it represented. Beneath the coal-beds I was conscious of jumbled strata of a concrete-like appearance, and then we shot down into the primitive granite, where the quartz crystals gleamed and twinkled as if the dark walls were sown with the dust of diamonds. Down we went and ever down--lower now than ever mortals had ever before penetrated. The archaic rocks varied wonderfully in colour, and I can never forget one broad belt of rose-coloured felspar, which shone with an unearthly beauty before our powerful lamps. Stage after stage, and lift after lift, the air getting ever closer and hotter until even the light tussore garments were intolerable and the sweat was pouring down into those rubber-soled slippers. At last, just as I was thinking that I could stand it no more, the last lift came to a stand and we stepped out upon a circular platform which had been cut in the rock. I noticed that Malone gave a curiously suspicious glance round at the walls as he did so. If I did not know him to be amongst the bravest of men, I should say that he was exceedingly nervous.

“Funny-looking stuff,” said the chief engineer, passing his hand over the nearest section of rock. He held it to the light and showed that it was glistening with a curious slimy scum.

“There have been shiverings and tremblings down here. I don’t know what we are dealing with. The Professor seems pleased with it, but it’s all new to me.”

“I am bound to say I’ve seen that wall fairly shake itself,” said Malone. “Last time I was down here we fixed those two cross-beams for your drill, and when we cut into it for the supports it winced at every stroke. The old man’s theory seemed absurd in solid old London town, but down here, eight miles under the surface, I am not so sure about it.”

“If you saw what was under that tarpaulin you would be even less sure,” said the engineer. “All this lower rock cut like cheese, and when we were through it we came on a new formation like nothing on earth. “Cover it up! Don’t touch it!” said the Professor. So we tarpaulined it according to his instructions, and there it lies.

“Could we not have a look?”

A frightened expression came over the engineer’s lugubrious countenance.

“It’s no joke disobeying the Professor,” said he. “He is so damn cunning, too, that you never know what check he has set on you. However, we’ll have a peep and chance it.”

He turned down our reflector lamp so that the light gleamed upon the black tarpaulin. Then he stooped and, seizing a rope which connected up with the corner of the covering, he disclosed half-a-dozen square yards of the surface beneath it.

It was a most extraordinary and terrifying sight. The floor consisted of some greyish material, glazed and shiny, which rose and fell in slow palpitation. The throbs were not direct, but gave the impression of a gentle ripple or rhythm, which ran across the surface. This surface itself was not entirely homogeneous, but beneath it, seen as through ground glass, there were dim whitish patches or vacuoles, which varied constantly in shape and size. We stood all three gazing spell-bound at this extraordinary sight.

“Does look rather like a skinned animal,” said Malone, in an awed whisper. “The old man may not be so far out with his blessed echinus.”

“Good Lord!” I cried. “And am I to plunge a harpoon into that beast!”

“That’s your privilege, my son,” said Malone, “and, sad to relate, unless I give it a miss in baulk, I shall have to be at your side when you do it.”

“Well, I won’t,” said the head engineer, with decision.

“I was never clearer on anything than I am on that. If the old man insists, then I resign my portfolio. Good Lord, look at that!”

The grey surface gave a sudden heave upwards, welling towards us as a wave does when you look down from the bulwarks. Then it subsided and the dim beatings and throbbings continued as before. Barforth lowered the rope and replaced the tarpaulin.

“Seemed almost as if it knew we were here,” said he.

“Why should it swell up towards us like that? I expect the light had some sort of effect upon it.”

“What am I expected to do now?” I asked. Mr. Barforth pointed to two beams which lay across the pit just under the stopping place of the lift. There was an interval of about nine inches between them.

“That was the old man’s idea,” said he. “I think I could have fixed it better, but you might as well try to argue with a mad buffalo. It is easier and safer just to do whatever he says. His idea is that you should use your six-inch bore and fasten it in some way between these supports. “

“Well, I don’t think there would be much difficulty about that,” I answered. “I’ll take the job over as from to-day.”

It was, as one might imagine, the strangest experience of my very varied life which has included well-sinking in every continent upon earth. As Professor Challenger was so insistent that the operation should be started from a distance, and as I began to see a good deal of sense in his contention, I had to plan some method of electric control, which was easy enough as the pit was wired from top to bottom. With infinite care my foreman, Peters, and I brought down our lengths of tubing and stacked them on the rocky ledge. Then we raised the stage of the lowest lift so as to give ourselves room.

As we proposed to use the percussion system, for it would not do to trust entirely to gravity, we hung our hundred-pound weight over a pulley beneath the lift, and ran our

tubes down beneath it with a V-shaped terminal. Finally, the rope which held the weight was secured to the side of the shaft in such a way that an electrical discharge would release it. It was delicate and difficult work done in a more than tropical heat, and with the ever-present feeling that a slip of a foot or the dropping of a tool upon the tarpaulin beneath us might bring about some inconceivable catastrophe. We were awed, too, by our surroundings. Again and again I have seen a strange quiver and shiver pass down the walls, and have even felt a dull throb against my hands as I touched them. Neither Peters nor I were very sorry when we signalled for the last time that we were ready for the surface, and were able to report to Mr. Barforth that Professor Challenger could make his experiment as soon as he chose.

And it was not long that we had to wait. Only three days after my date of completion my notice arrived.

It was an ordinary invitation card such as one uses for "at homes," and it ran thus:

"PROFESSOR G. E. CHALLENGER,

"F.R.S. MD., D.Sc., etc.

"(late President Zoological Institute and holder of so many honorary degrees and appointments that they overtax the capacity of this card)

"requests the attendance of

"MR. JONES (no lady)

"at 11.30 a.m. of Tuesday, June 21st, to witness a

"remarkable triumph of mind over matter at

"HENGIST DOWN, SUSSEX.

"Special train Victoria 10.5. Passengers pay their own fares. Lunch after the experiment or not--according to circumstances. Station, Storrington.

"R.S.V.P. (and at once with name in block letters), 14 (Bis), Enmore Gardens, S.W."

I found that Malone had just received a similar missive over which he was chuckling.

"It is mere swank sending it to us," said he. "We have to be there whatever happens, as the hangman said to the murderer. But I tell you this has set all London buzzing. The old man is where he likes to be, with a pin-point limelight right on his hairy old head."

And so at last the great day came. Personally I thought it well to go down the night before so as to be sure that everything was in order. Our borer was fixed in position, the weight was adjusted, the electric contacts could be easily switched on, and I was satisfied that my own part in this strange experiment would be carried out without a hitch. The electric controls were operated at a point some five hundred yards from the mouth of the shaft, to minimize any personal danger. When on the fateful morning, an ideal English summer day, I came to the surface with my mind assured, I climbed half-way up the slope of the Down in order to have a general view of the proceedings.

All the world seemed to be coming to Hengist Down. As far as we could see the roads were dotted with people. Motor-cars came bumping and swaying down the lanes, and discharged their passengers at the gate of the compound. This was in most cases the end of their progress. A powerful band of janitors waited at the entrance, and no promises or bribes, but only the production of the coveted buff tickets, could get them any farther. They dispersed therefore and joined the vast crowd which was already assembling on the side of the hill and covering the ridge with a dense mass of spectators. The place was like

Epsom Downs on the Derby Day. Inside the compound certain areas had been wired-off, and the various privileged people were conducted to the particular pen to which they had been allotted. There was one for peers, one for members of the House of Commons, and one for the heads of learned societies and the men of fame in the scientific world, including Le Pellier of the Sorbonne and Dr. Driesinger of the Berlin Academy. A special reserved enclosure with sandbags and a corrugated iron roof was set aside for three members of the Royal Family.

At a quarter past eleven a succession of charr-a-bancs brought up specially-invited guests from the station and I went down into the compound to assist at the reception.

Professor Challenger stood by the select enclosure, resplendent in frock-coat, white waistcoat, and burnished top-hat, his expression a blend of overpowering and almost offensive benevolence, mixed with most portentous self-importance.

“Clearly a typical victim of the Jehovah complex,” as one of his critics described him. He assisted in conducting and occasionally in propelling his guests into their proper places, and then, having gathered the elite of the company around him, he took his station upon the top of a convenient hillock and looked around him with the air of the chairman who expects some welcoming applause. As none was forthcoming, he plunged at once into his subject, his voice booming to the farthest extremities of the enclosure.

“Gentlemen,” he roared, “upon this occasion I have no need to include the ladies. If I have not invited them to be present with us this morning it is not, I can assure you, for want of appreciation, for I may say”--with elephantine humour and mock modesty--“that the relations between us upon both sides have always been excellent, and indeed intimate. The real reason is that some small element of danger is involved in our experiment, though it is not sufficient to justify the discomposure which I see upon many of your faces. It will interest the members of the Press to know that I have reserved very special seats for them upon the spoil banks which immediately overlook the scene of the operation. They have shown an interest which is sometimes indistinguishable from impertinence in my affairs, so that on this occasion at least they cannot complain that I have been remiss in studying their convenience. If nothing happens, which is always possible, I have at least done my best for them. If, on the other hand, something does happen, they will be in an excellent position to experience and record it, should they ultimately feel equal to the task.

“It is, as you will readily understand, impossible for a man of science to explain to what I may describe, without undue disrespect, as the common herd, the various reasons for his conclusions or his actions. I hear some unmannerly interruptions, and I will ask the gentleman with the horn spectacles to cease waving his umbrella. (A voice: “Your description of your guests, sir, is most offensive.”) Possibly it is my phrase, “the common herd,” which has ruffled the gentleman. Let us say, then, that my listeners are a most uncommon herd. We will not quibble over phrases. I was about to say, before I was interrupted by this unseemly remark, that the whole matter is very fully and lucidly discussed in my forthcoming volume upon the earth, which I may describe with all due modesty as one of the epoch-making books of the world’s history. (General interruption and cries of “Get down to the facts!” “What are we here for?” “Is this a practical joke?”) I was about to make the matter clear, and if I have any further interruption I shall be compelled to take means to preserve decency and order, the lack of which is so painfully obvious. The position is, then, that I have sunk a shaft through the crust of the earth and

that I am about to try the effect of a vigorous stimulation of its sensory cortex, a delicate operation which will be carried out by my subordinates, Mr. Peerless Jones, a self-styled expert in Artesian borings, and Mr. Edward Malone, who represents myself upon this occasion. The exposed and sensitive substance will be pricked, and how it will react is a matter for conjecture. If you will now kindly take your seats these two gentlemen will descend into the pit and make the final adjustments. I will then press the electric button upon this table and the experiment will be complete.”

An audience after one of Challenger’s harangues usually felt as if, like the earth, its protective epidermis had been pierced and its nerves laid bare. This assembly was no exception, and there was a dull murmur of criticism and resentment as they returned to their places.

Challenger sat alone on the top of the mound, a small table beside him, his black mane and beard vibrating with excitement, a most portentous figure.

Neither Malone nor I could admire the scene, however, for we hurried off upon our extraordinary errand. Twenty minutes later we were at the bottom of the shaft, and had pulled the tarpaulin from the exposed surface.

It was an amazing sight which lay before us. By some strange cosmic telepathy the old planet seemed to know that an unheard-of liberty was about to be attempted. The exposed surface was like a boiling pot. Great grey bubbles rose and burst with a crackling report. The air-spaces and vacuoles below the skin separated and coalesced in an agitated activity. The transverse ripples were stronger and faster in their rhythm than before. A dark purple fluid appeared to pulse in the tortuous anastomoses of channels which lay under the surface. The throb of life was in it all. A heavy smell made the air hardly fit for human lungs.

My gaze was fixed upon this strange spectacle when Malone at my elbow gave a sudden gasp of alarm. “My God, Jones!” he cried. “Look there!”

I gave one glance, and the next instant I released the electric connection and I sprang into the lift. “Come on!” I cried. “It may be a race for life!”

What we had seen was indeed alarming. The whole lower shaft, it would seem, had shared in the increased activity which we had observed below, and the walls were throbbing and pulsing in sympathy. This movement had reacted upon the holes in which the beams rested, and it was clear that a very little further retraction--a matter of inches -- the beams would fall. If they did so then the sharp end of my rod would, of course, penetrate the earth quite independently of the electric release. Before that happened it was vital that Malone and I should be out of the shaft. To be eight miles down in the earth with the chance any instant of some extraordinary convulsion taking place was a terrible prospect. We fled wildly for the surface.

Shall either of us ever forget that nightmare journey? The lifts whizzed and buzzed and yet the minutes seemed to be hours. As we reached each stage we sprang out, jumped into the next lift, touched the release and flew onwards. Through the steel latticed roof we could see far away the little circle of light which marked the mouth of the shaft. Now it grew wider and wider, until it came full circle and our glad eyes rested upon the brickwork of the opening. Up we shot, and up --and then at last in a glad moment of joy and thankfulness we sprang out of our prison and had our feet upon the green sward once more. But it was touch and go. We had not gone thirty paces from the shaft when far

down in the depths my iron dart shot into the nerve ganglion of old Mother Earth and the great moment had arrived.

What was it happened? Neither Malone nor I was in a position to say, for both of us were swept off our feet as by a cyclone and swirled along the grass, revolving round and round like two curling stones upon an ice rink. At the same time our ears were assailed by the most horrible yell that ever yet was heard. Who is there of all the hundreds who have attempted it who has ever yet described adequately that terrible cry? It was a howl in which pain, anger, menace, and the outraged majesty of Nature all blended into one hideous shriek. For a full minute it lasted, a thousand sirens in one, paralysing all the great multitude with its fierce insistence, and floating away through the still summer air until it went echoing along the whole South Coast and even reached our French neighbours across the Channel. No sound in history has ever equalled the cry of the injured Earth.

Dazed and deafened, Malone and I were aware of the shock and of the sound, but it is from the narrative of others that we learned the other details of that extraordinary scene.

The first emergence from the bowels of the earth consisted of the lift cages. The other machinery being against the walls escaped the blast, but the solid floors of the cages took the full force of the upward current. When several separate pellets are placed in a blow-pipe they still shoot forth in their order and separately from each other.

So the fourteen lift cages appeared one after the other in the air, each soaring after the other, and describing a glorious parabola which landed one of them in the sea near Worthing pier, and a second one in a field not far from Chichester. Spectators have averred that of all the strange sights that they had ever seen nothing could exceed that of the fourteen lift cages sailing serenely through the blue heavens.

Then came the geyser. It was an enormous spout of vile treacly substance of the consistence of tar, which shot up into the air to a height which has been computed at two thousand feet. An inquisitive aeroplane, which had been hovering over the scene, was picked off as by an Archie and made a forced landing, man and machine buried in filth. This horrible stuff, which had a most penetrating and nauseous odour, may have represented the life blood of the planet, or it may be, as Professor Driesinger and the Berlin School maintain, that it is a protective secretion, analogous to that of the skunk, which Nature has provided in order to defend Mother Earth from intrusive Challengers. If that were so the prime offender, seated on his throne upon the hillock, escaped untarnished, while the unfortunate Press were so soaked and saturated, being in the direct line of fire, that none of them was capable of entering decent society for many weeks. This gush of putridity was blown southwards by the breeze, and descended upon the unhappy crowd who had waited so long and so patiently upon the crest of the Downs to see what would happen. There were no casualties. No home was left desolate, but many were made odoriferous, and still carry within their walls some souvenir of that great occasion.

And then came the closing of the pit. As Nature slowly closes a wound from below upwards, so does the Earth with extreme rapidity mend any rent which is made in its vital substance. There was a prolonged high-pitched crash as the sides of the shaft came together, the sound, reverberating from the depths and then rising higher and higher until with a deafening bang the brick circle at the orifice flattened out and clashed together,

while a tremor like a small earthquake shook down the spoil banks and piled a pyramid fifty feet high of debris and broken iron over the spot where the hole had been. Professor Challenger's experiment was not only finished, it was buried from human sight for ever. If it were not for the obelisk which has now been erected by the Royal Society it is doubtful if our descendants would ever know the exact site of that remarkable occurrence.

And then came the grand finale. For a long period after these successive phenomena there was a hush and a tense stillness as folk reassembled their wits and tried to realize exactly what had occurred and how it had come about. And then suddenly the mighty achievement, the huge sweep of the conception, the genius and wonder of the execution, broke upon their minds. With one impulse they turned upon Challenger. From every part of the field there came the cries of admiration, and from his hillock he could look down upon the lake of upturned faces broken only by the rise and fall of the waving handkerchiefs. As I look back I see him best as I saw him then. He rose from his chair, his eyes half closed, a smile of conscious merit upon his face, his left hand upon his hip, his right buried in the breast of his frock-coat. Surely that picture will be fixed for ever, for I heard the cameras clicking round me like crickets in a field.

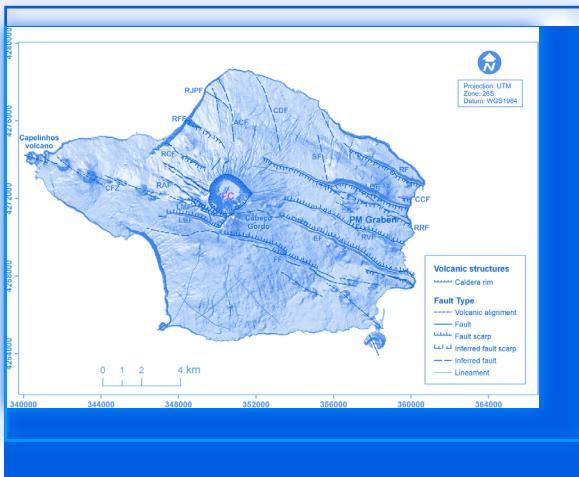
The June sun shone golden upon him as he turned gravely bowing to each quarter of the compass. Challenger the super scientist, Challenger the arch-pioneer, Challenger the first man of all men whom Mother Earth had been compelled to recognize.

Only a word by way of epilogue. It is of course well known that the effect of the experiment was a world-wide one. It is true that nowhere did the injured planet emit such a howl as at the actual point of penetration, but she showed that she was indeed one entity by her conduct elsewhere. Through every vent and every volcano she voiced her indignation. Hecla bellowed until the Icelanders feared a cataclysm. Vesuvius blew its head off. Etna spewed up a quantity of lava, and a suit of half-a-million lira damages has been decided against Challenger in the Italian Courts for the destruction of vineyards. Even in Mexico and in the belt of Central America there were signs of intense Plutonic indignation, and the howls of Stromboli filled the whole Eastern Mediterranean. It has been the common ambition of mankind to set the whole world talking. To set the whole world screaming was the privilege of Challenger alone.

The End

YOU CAN WRITE A POEM
WITH BASALT

Mas eu oiço o vulcão a pulsação
But I hear the volcano the pulse
a linguagem secreta
the secret language
transmitida
transmitted
de poeta a poeta.
from poet to poet.



— Código Manuel Alegre

The Azores archipelago is a Portuguese autonomous region composed by nine islands, several islets and the surrounding seafloor, located in the Atlantic Ocean, between 36° and 41° North Latitude and 24° and 33° West Longitude. It has an administrative area of 2324 sq. km of land surface and 938000 square kilometers of marine area.

São Miguel is the Angel of Portugal (Anjo de Portugal), the Saint Guardian Angel of Portugal (Santo Anjo da Guarda de Portugal), the Custodian Angel (Anjo Custódio) or the Angel of Peace (Anjo da Paz), police officers, military, grocers, mariners, paratroopers, firefighters, paramedics, sickness.

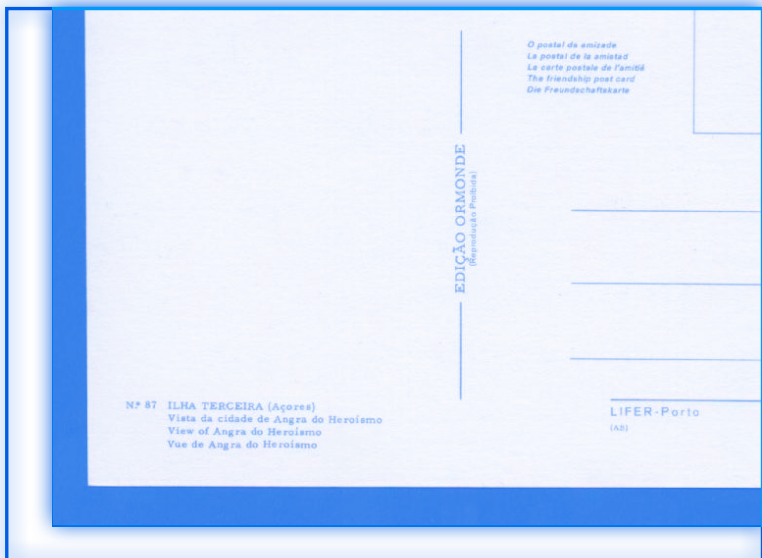


“And, behold, there was a great earthquake:
for the Angel of the Lord descended from
heaven, and came and rolled back the stone
from the door, and sat upon it.

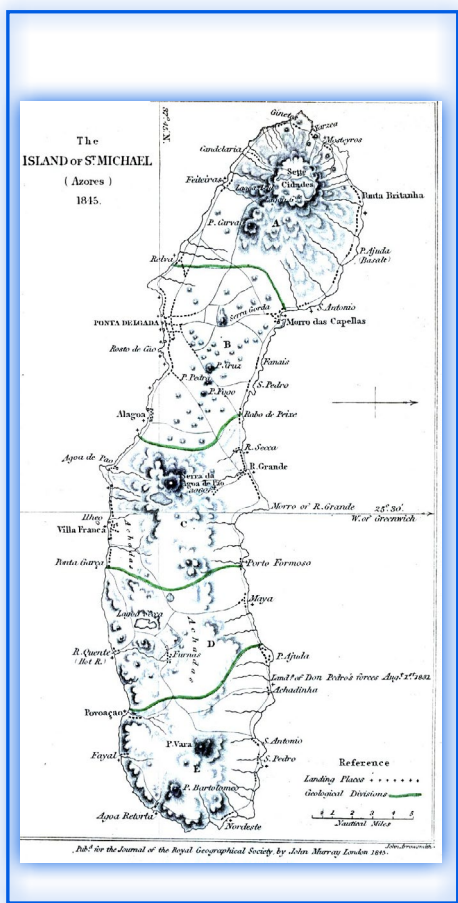
His countenance was like lightning, and his
raiment white as snow:

And for fear of him the keepers did shake,
and became as dead men.”

— (Matthew 28:1-4)



Throughout their history, Azoreans have pleaded for divine attendance and protection from earthquakes and volcanic eruptions, in numerous processions (on all islands), fireworks, and church services. The construction of Holy Ghost chapels (impérios) was common in the Azores during volcanic and seismic crises. As an example, the Holy Ghost Chapel in Horta (Império dos Nobres) was built in remembrance of the eruptions in the Mistério do Capelo, Faial, in 1672. The eruption of Urzelina (São Jorge), in 1808, caused deaths inside the church, shattering the traditional religious belief that churches protected people from the fire rising from the interior of the earth, “a phenomenon never observed in the mainland but found in the Azores beginning with the settlement of São Miguel”.

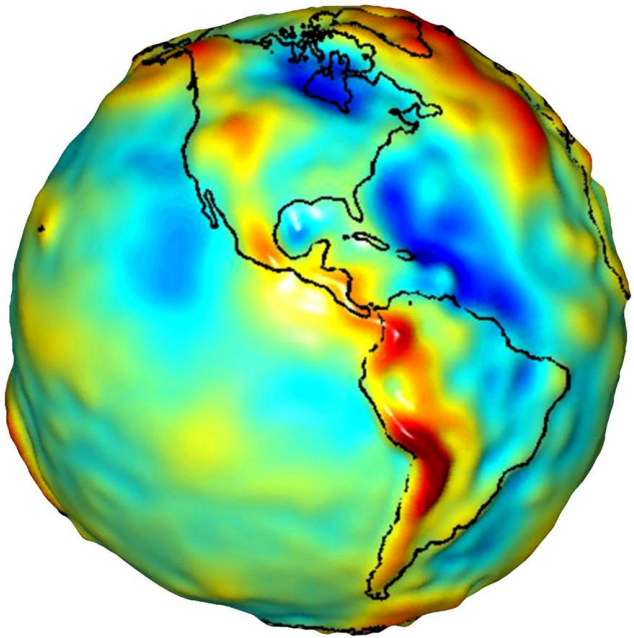


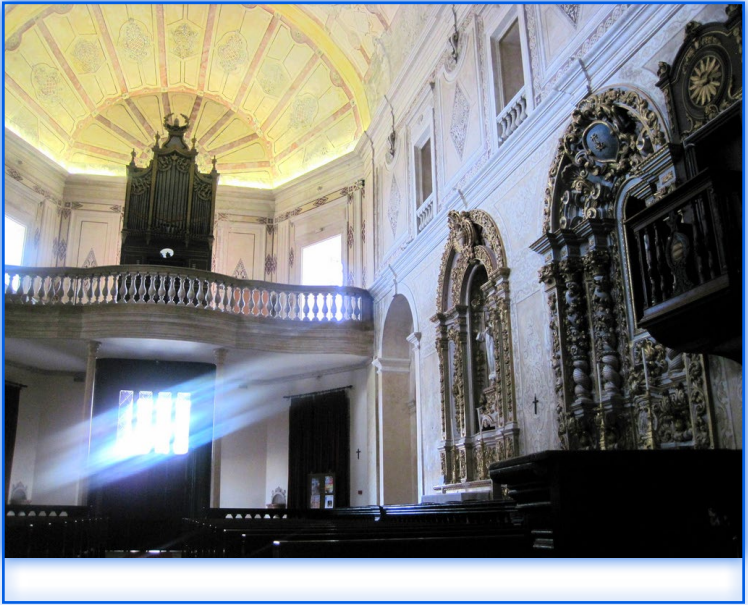
It was priests who often used the religious fervour and folk beliefs of Azorean congregations in order to allow, even encourage “them to believe that the natural disasters that affect the Azores were punishment from God for not staying on the true path. The priest thus becomes His spokesman, gaining and exerting considerable power and control in a society where volcanic activity and earth tremors are very frequent”

— A Portrait of the Azores, Rudolf Beier and Johannes Kramer (2018)

Chronic ingestion of fluoride may cause a number of low-grade symptoms, including loss of appetite, headache, vertigo, and joint pain. The most characteristic effects, however, involve the dentition and skeletal system. Although not directly a result of recent ash leaching, elevated fluoride levels in potable water adjacent to the Furnas volcano in the Azores have resulted in dental fluorosis, a condition characterized by mottling of the teeth.

— Medical Geology, Impacts of the Natural Environment on Public Health (2005)





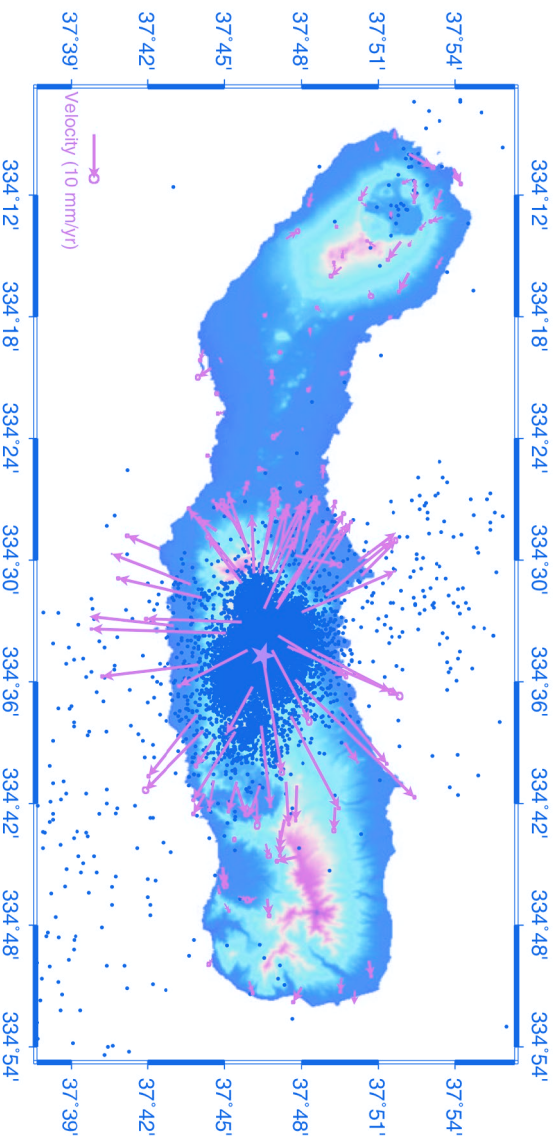
“From that time I began to think of angels. I considered that sights such as I had seen of the silence must have been shared by the people who said they saw angels. I began to review the thing I had seen that morning. My impression now of those fields is of thousands of spirits—spirits trapped, perhaps, by my refusal to call them more fully, or by the paralysis of my own spirit at that time—thousands of spirits, angels in fact, almost discernible to the eye, and whirling. If pressed I would say they were three or four feet from the ground. Only their motion was clear (clockwise, if you insist); that, and their beauty unspeakable.

There are angels in those fields, and, I presume, in all fields, and everywhere else. I would go to the lions for this conviction, to witness this fact. What all this means about perception, or language, or angels, or my own sanity, I have no idea.”

— Annie Dillard, *Teaching a Stone to Talk*

“If we had been to the West of the Azores, the magnet should have declined to the West, but as it declined to the East, we could not have been to the West. Some said that we were in the midst of the Islands, but I demonstrated that this could not be true, as, even though we were at their latitude we did not see them, and that was impossible... Precisely because even before the storm we were to their East. I write this, not so as to praise myself, but so that Your Reverence may see all that I have learned from you, especially in the field of magnetic declination.”

— Martino Martini to Athanasius Kircher, Evora, February 6, 1639
Archivio della Pontificia Università Gregoriana, Rome



Representation of the horizontal velocity field (red arrows) for the period 1999–2007 for the Fogo/São Brás/Congro area, São Miguel Island, interpreted as probable basaltic magma intrusion (Trota et al. 2015). The map also shows all the seismic events for the analyzed period, along with plot of location of the modelled deformation centre. The map shows a strong concentration of events plots enclosing the deformation centre (extracted from Trota 2009)

Geotourism development in the Azores archipelago (Portugal) as an environmental awareness tool

Eva Almeida Lima^{1,2}, Marisa Machado², João Carlos Nunes^{1,2}

e-mail: valima@azoresgeopark.com, marisamachado@azoresgeopark.pt, jcnunes@uac.pt

¹ Azores University, Geosciences Department, Azores Islands, Portugal

² Azores Geopark Association, Azores Islands, Portugal

Lima, E. A., Machado, M., & Nunes, J. C. (2013). Geotourism development in the Azores archipelago (Portugal) as an environmental awareness tool. *Czech Journal of Tourism*, 2(2), 126-142, DOI: 10.2478/cjot-2013-0007.

Abstract

The Azores archipelago is distinguished by its unique natural beauty and marine setting. Thanks to its volcanic origin, the region has a very rich and remarkable geodiversity that includes a diversity of landscapes with innumerable craters, volcanic lakes, fumaroles, hot springs, volcanic caves, marine fossil deposits and thermal water springs. The recognition of this valuable geological heritage came with the recent integration of the Azores Geopark into the European and Global Geopark Networks.

The pressure that the increasing development of tourism have been exerting on these geological sites for the last years, and the need to create alternative forms of tourism, which contribute towards the socio-economic development in rural areas, have highlighted the importance of geotourism as a tool to promote and preserve the geological heritage of the Azores. Geotourism has turned to be an important instrument of environmental awareness through the local and foreign people.

Keywords

Geotourism, Azores archipelago, volcanic islands, geolandscapes, environmental awareness

JEL classification: Q01, L83 / **Accepted:** 5 November 2013

Introduction

The rare nature and its natural and geological heritage are the main ex-libris of the Azores archipelago together with its scenic and aesthetic characteristics and attributes of great attractiveness and a geotouristic potential.

Traditionally, the visitors of this region are looking for the volcanic landscapes and the surrounding sea for mere contemplation, enjoyment or for the practice of different activities in the unique natural environment that the Azores offer. The nature tourism, tourist product defined as strategic for the Azores within the National Strategic Plan for Tourism, is a major one of the main tourist products of the region and is, without doubt, the main component of the Azorean tourist industry (Nunes et al., 2011).

The volcanic landscapes of the Azores are, thus, the main motto of interest and development of geotourism in the archipelago and they present a wide range of possibilities for sustainable use where several activities can be performed and associated tourist products can be developed.

Tourism is one of the sectors with a high development potential in the Azores archipelago. The Azores are in the 3rd place in the ranking of the growth of touristic activity in national terms after Algarve and North Portugal (mainland).

According the Azorean Statistics Regional Service (data available on www.srea.ine.pt), in 2012 there were 360,265 tourism arrivals, which correspond to 1,077,420 tourism nights. About half of them are Portuguese tourists (from the mainland or Madeira archipelago) and the other half are foreigners, with the Germans leading this second group, followed by tourists from Finland, the United States of America, Sweden and the Netherlands.

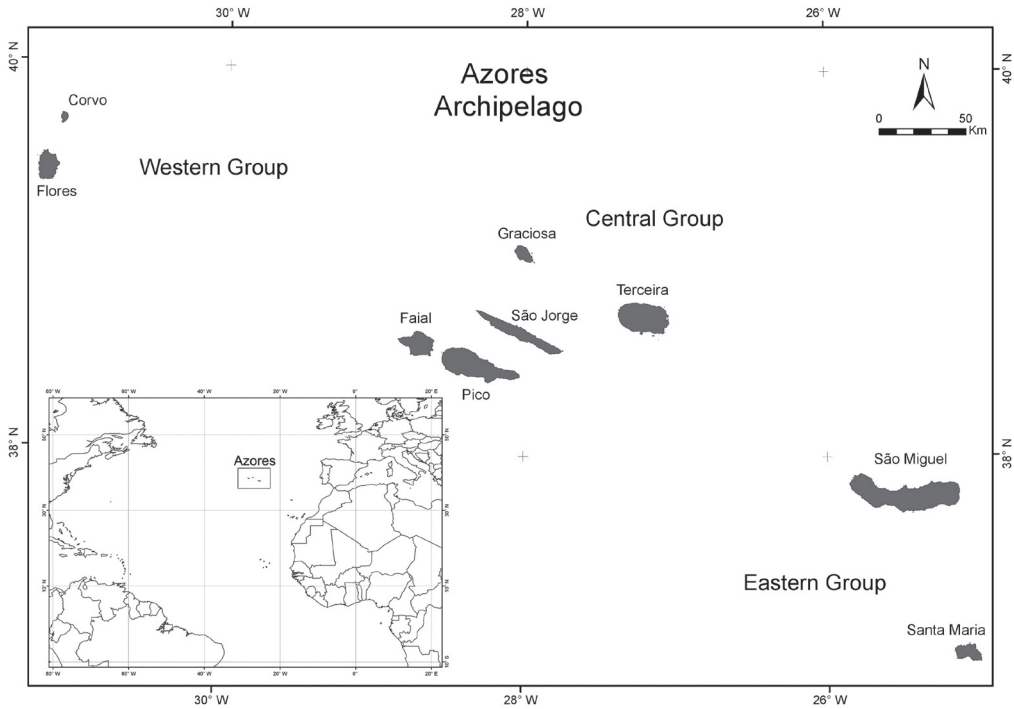
There are presented the natural characteristics of the archipelago that provide the development of geotourism. There are also featured the contributions of the Azores Geopark and partners entities highlighting the opportunity and potential of the development of geotourism in the archipelago has as a tool for environmental awareness

Azores volcanic landscape

The Azores archipelago is a Portuguese autonomous region composed of nine islands, several islets and the surrounding seafloor, located in the Atlantic Ocean between 36° and 41° North Latitude and 24° and 33° West Longitude. It has an administrative area of 2,324 sq. km of land surface and 938,000 sq. km of marine area and it is characterized by the reduced dimension of the islands (between 17 and 745 sq. km), by its dispersion (distributed along approximately 600 km in the Atlantic, between Santa Maria and Corvo islands) and for its distance from the European and American continents (at distances of 1,815 km from mainland Portugal and 2,625 km from Canada). The islands are divided into three groups: the Western Group (Flores and Corvo islands), the Central Group (Terceira, Graciosa, São Jorge, Pico and Faial islands) and the Eastern Group (São Miguel and Santa Maria islands) all of them inhabited (Figure 1). The archipelago has 19 municipalities and 156 parishes with a population of 247,066 inhabitants (year 2011).

The geographic location of the Azores, between the European and American continents, makes this Atlantic territory a true “bridge between two continents”!

Figure 1 Azores geographic setting



Source: Lima, et al. (2009)

The islands emerge from the seafloor at 2,000 meters deep, associated with the triple junction of the Euroasian, North American and African (or Nubian) lithospheric plates (Nunes, 1991; França, et al., 2003; Garcia-Talavera, 2003), and presenting elements closely linked to the dynamics of the Planet Earth, the volcanism and geotectonic.

The Azores archipelago integrates, together with Madeira, Canary and Cape Verde archipelagos, the biogeographic region of Macaronesia, which means “fortunate islands”.

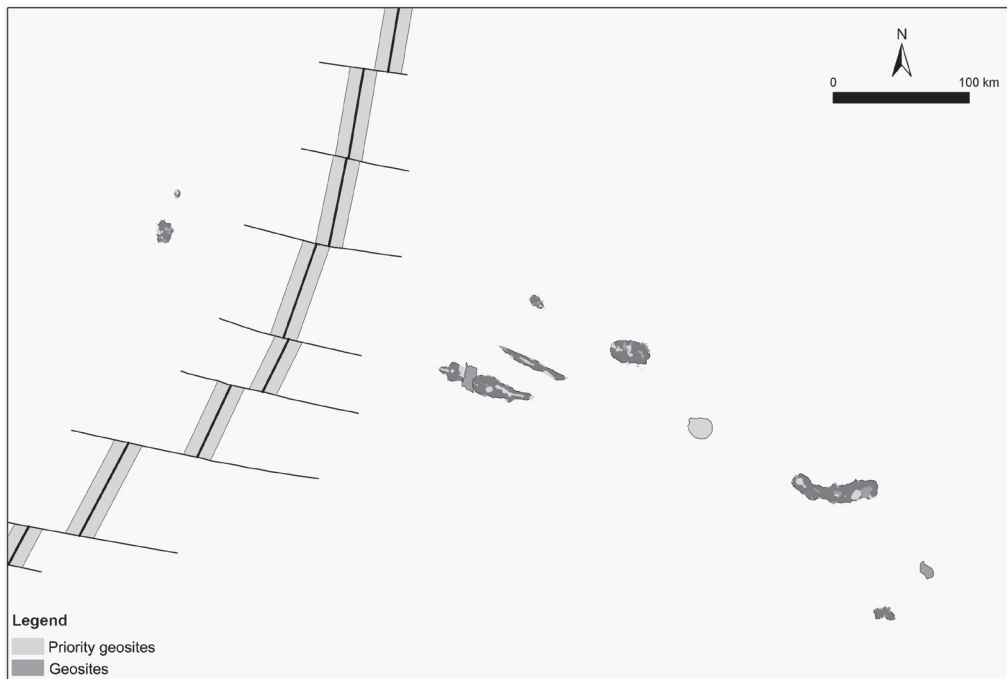
Thanks to its volcanic origin, the archipelago has a very rich and remarkable geodiversity with a wide range of landscapes, forms and structures derived from the types of eruptions, its dynamics and the subsequent actions of weather and erosion (Nunes, 2002). Because of its peculiar geological features and setting, the Azores are a true natural laboratory for volcanic geodiversity (França, et al., 2003).

The recognition of the international relevance of the geological heritage of the territory, its scientific, scenic and educational value, the high number and quality of its geosites and the undoubted importance of its geological heritage, came with the creation of the Azores Geopark, supported with a major effort of the Azores Regional Government to

implement geoconservation and environmental education policies (Costa, et al., 2008; Lima, et al., 2009), and its integration into the European and Global Geopark Networks (EGN and GGN).

The Azores Geopark is based on a network of 121 geosites dispersed by the nine islands and the surrounding seafloor (Figure 2): i) that ensures the representativeness of the geodiversity that characterizes the Azorean territory, ii) that reflects its geological and eruptive histories of about 10 million years, iii) with common conservation and promotion strategies, and iv) based on a decentralized management structure with support in all the islands (Nunes, et al., 2011).

Figure 2 Azores geosites



Source: Nunes, et al. (2011)

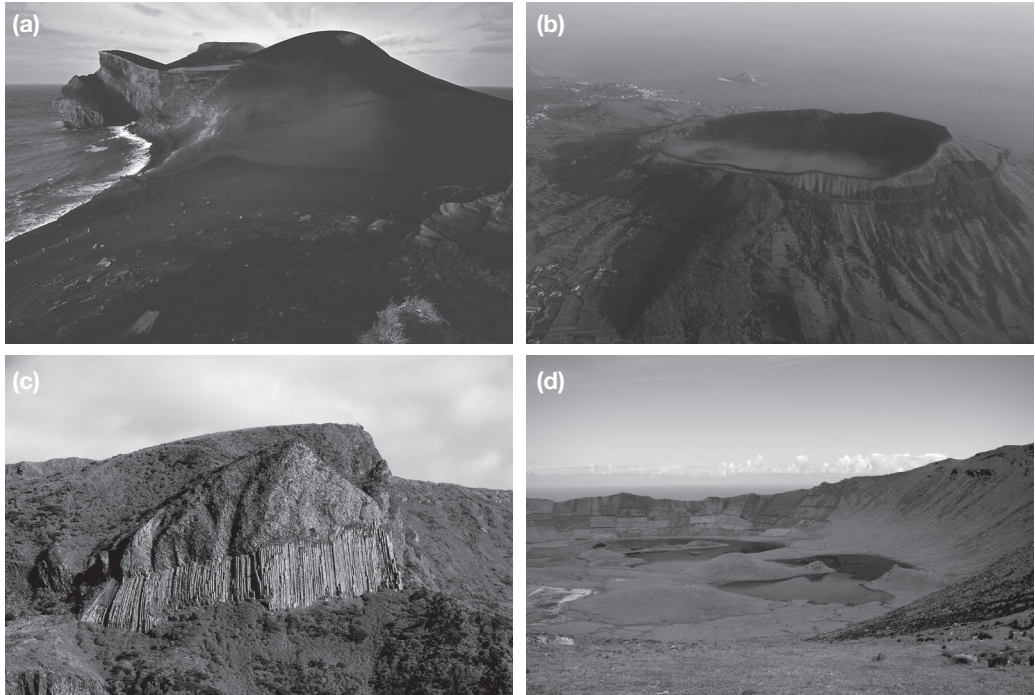
Most of the Azorean geosites are attractive because they are aesthetically appealing and their fantastic and mysterious volcanic phenomena are still active.

The volcanic landscape is the main attraction of the touristic promotion, being the image sold in the touristic campaigns and reflecting the huge geotouristic potential of the archipelago.

Geotouristic potential

The natural landscapes of the archipelago reflect a high geodiversity, associated with a rich biodiversity with an unquestionable aesthetic beauty, which fascinates local population and visitors, being the starting point for the development of geotourism (Figure 3).

Figure 3 Azorean geolandscapes: **(a)** - *Capelinhos* volcano (Faial island), **(b)** - *Caldeira* (Graciosa island), **(c)** - *Rocha dos Bordões* (Flores island), **(d)** - *Caldeirão* (Corvo Island)



Source: Azores Geopark

Since the discovery and settlement of the Azores in the middle of the 15th century the geolandscapes have been important sources of interest and have attracted several visitors and distinguished naturalists and scientists (Lima, 2007), registered in important documents such as “Saudades da Terra” by Gaspar Frutuoso (1583), a Portuguese priest. It is worth mentioning that Charles Darwin, when aboard the *Beagle*, visited briefly the Azores in the summer of 1836, taking opportunity to refer the volcanism as an expression of an Atlantic setting (França, et al., 2003).

According to Lima (2007), important steps were taken to initiate the development of geotourism in the archipelago:

- the opening to the public of some volcanic caves, such as Furna do Enxofre in Graciosa island in 1939, the Algar do Carvão in Terceira island in 1968, and more recently,

Furna da Água and Gruta do Natal, also in Terceira island, Gruta do Carvão in São Miguel island, and Gruta das Torres in Pico island, showing part of the volcano speleological heritage of the archipelago;

- the classification of the first geosites, protected as natural reserves in the 1970's (*Pico Mountain* and *Faial Caldera*), and more recently (1990's) others, such as Natural Monuments (e.g. Pedreira do Campo in Santa Maria island, Gruta do Carvão and *Pico das Camarinhas e Ponta da Ferraria* in São Miguel island, and *Gruta das Torres* in Pico island);
- the volcano speleological museum, opened to the public in the 1980's, a property of the Speleological Association Os Montanheiros (Terceira island);
- the ancient footpaths have been used for many years as tourist walking trails and trekking, with the main points of interest - the volcanism, the presence of water (lagoons, streams, waterfalls), flora and fauna and cultural heritage;
- in different places of the archipelago where there are thermal, mineral and carbonated waters, with recognized therapeutic properties, spas (termas in Portuguese) with treatments, either by ingestion or baths, were established. To mention the most important: Termas das Furnas with the first building constructed in the 17th century and Termas da Ferraria and opened in the middle of the 20th century (both in São Miguel island), Termas do Carapacho (Graciosa island) with the nineteenth century building, and Termas do Varadouro (Faial island) opened in the mid20th century;
- the natural conditions create several bathing areas in special places of geological interest as volcanic craters (e.g. Vila Franca islet, near São Miguel island), hydrothermal zones (e.g. Ribeira Quente and Ferraria in São Miguel island, or Carapacho in Graciosa island), natural swimming pools on the volcanic rocks and black sand beaches.

In recent years geotourism has developed in an organized and systematic way in the Azores archipelago. The nine Azorean islands offer a wide range of experiences and emotions that are linked with other values, such as biodiversity, history and cultural heritage, providing the visitors with unforgettable experiences, corresponding to the motto "Come to visit the Azorean volcanoes and enjoy an eruption ... of flavours, smells and experiences!".

This framework has given an opportunity for the creation of local and regional companies which specialized in geotourism, nature tourism, adventure tourism and rural tourism with the development of products and services of the recognized quality that ensures customer satisfaction. Besides promoting geotourism, the Azores Geopark contributes to the promotion and development of traditional activities related to volcanism of the archipelago (e.g. crafts, gastronomy, traditions and customs) and promotes the dissemination of regional resources.

Therefor nowadays visitors can choose from a variety of geotourism-based products, such as geotours, volcanospeleology, rock climbing, mountain climbing, diving, snorkeling, canyoning, coastering, thermal baths, and walking trails that are offered by several specialized geotouristic companies (Figure 4) (Lima, et al., 2012).

Figure 4 Geotouristic activities: **(a)** - Geotour in *Barreiro da Malbusca* (Santa Maria island), **(b)** - nature photography on the central volcanic ridge (São Jorge island), **(c)** - Walking trail on *Pico Alto* volcano (Terceira island), **(d)** - Guided tour on *Gruta das Torres* lava tube (Pico island)



Source: Azores Geopark

The geotourism strategies in the Azores Geopark are supported by the exploitation, maximization and organization of the existing services and tourist infrastructures, making profit from the available resources and enhancing joint synergies. For this purpose, partnerships with several stakeholders have been set up, such as with the associations responsible for promoting the Azores as a tourist destination and for the qualification of the tourism offer in the region (e.g. the Tourism Association of the Azores and the Regional Association of Tourism-ART). This is done by bearing in mind that the implementation of geotourism requires proper planning to consolidate and develop itself with guarantees of success (Nunes, et al., 2011).

The global strategy of sustainable tourism in the Azores has been successful and its implementation has been recognized. The archipelago is identified as one of the main active volcanic and geothermal touristic destinations of the world (Erfurt-Cooper, 2011), as it is evidenced by several national and international prizes and rewards. In 2007, the National Geographic Traveler magazine considered the archipelago as the second best island in the world for sustainable tourism. In 2008, the publisher Lonely Planet described the region as one of the best destinations worldwide and in 2010 the Forbes magazine distinguished the Azores as “One of the world’s most unique travel

destinations“. In this same year, the Sete Cidades Lake and the Volcanic Landscape of Pico Island were considered two of the „7 Natural Wonders of Portugal“, by public voting integrated in the initiative of the New Seven Wonders Portugal. In the year of 2011, those prizes contained the following classification: (i) the Azores as one of ten best destinations worldwide for summer, given by the National Geographic Traveler; (ii) the walking trail of the Vineyards of Criação Velha, in Pico island, as one of the eight best trails of the World, determined by the Boots n ALL; (iii) Furnas, in São Miguel island, as one of the five more appealing volcanic areas in the world, labelled by the World Travel Guide; (iv) Pico island, as one of the five best secret islands in the world, awarded by the BBC Travel; (v) the Association of the Azorean Municipalities received the Prize “Geoconservation 2011“, attributed by ProGEO Portugal; and (vi) the Faial Island Natural Park received the EDEN Prize, and was confirmed by the European Commission as the first European Destination of Excellence in Portugal (Nunes et al., 2011). In 2013 the archipelago won the QualityCoast Gold Award, an international award for the best sustainable tourism destination.

Man and the volcanoes

Also since the early days of the Azores settlement, the Azorean people have had a strong connection with “their” volcanoes, living through several volcanic eruptions and experiencing many earthquakes.

Therefore, the culture is closely linked with volcanoes, specifically in festivities and architecture. Given the strong Catholic faith of the inhabitants and the lack of scientific knowledge about these catastrophic natural events, the Azoreans created religious events in order to “calm down the wrath of God”, such as processions and pilgrimages. In addition, it is possible to see old manor houses, monasteries, churches and fortresses built from the rocks of each island, and the stone walls that divide some rural terrains help to understand the local history, as well as their toponymy. There are also places and ruins that which eyewitness the occurrence of natural geological phenomena, such as volcanic eruptions and earthquakes (Nunes, et al., 2011) (Figure 5).

The volcanoes and man’s relationship is also imprinted in some ancestral and traditional practices of the local population which are also of high tourist interest, such as the usufruct of the secondary manifestations of volcanism, existing in several islands with a high potential in the health and well-being of this tourism area, taking an advantage of baths in thermal waters of the recognized therapeutic properties, the intake of carbonated and mineral waters and the use of mud as peloides thanks to their medicinal properties. The gastronomy cooked in the steam of the fumarolic field of the Furnas Lake typifies another typical geo-product of the Azores (i.e. the famous Azorean dish *Cozido das Furnas*) (Nunes, et al., 2011; Viveiros, et al., 2012) (Figure 6).

Figure 5 Culture elements linked with the volcanoes: **(a)**- religious procession (São Miguel island), **(b)** – ornamental rocks in the regional architecture (Santa Maria island), **(c)** – *Ribeirinha* lighthouse ruins from the 1998 earthquake (Faial island)



Source: Azores Geopark

Also in the literature the Azoreans volcanoes and geologic processes are not forgotten, with his exponent in the famous Azorean poem by José Ferreira, “*Ilhas de Bruma*”, where he wrote “(...) It’s running into my veins black basalt / At the hearth the blazing of the fumaroles / The immense sea fills my soul / And I have green, so much green showing my hope (...)”. This poem became a song, and it is now the Azores Geopark anthem.

Figure 6 Examples of secondary volcanism usufruct: **(a)**- thermal baths at *Caldeira Velha* (São Miguel island), **(b)** – drinking thermal and mineralized waters (São Miguel island), **(c)** – cooking at Furnas volcano (São Miguel island)



Source: Azores Geopark

Challenges of the Azorean geotourism

The volcanic landscape is the main promotional icon of the archipelago and for the development of geotourism and it offers a wide range of possibilities for sustainable use, where several activities can be performed and associated with different touristic products. The main challenge to this form of tourism is to keep the balance between the management of the touristic operations and the implementation of geoconservation policies (Lima, et al., 2009). The pressure that the increasing development of tourism have been exerting on some geosites over time, and the need to create alternative forms of tourism which contribute towards the socio-economic development in rural areas, have highlighted the importance to protect and promote the geological heritage of the Azores (Viveiros, et al., 2012).

Other important task is the information about the geosites, geolandscapes and geological manifestations through several information and explanatory resources (Figure 7) as a form to discover and understand some secrets of the Earth that are particularly represented in the Azorean geosites; to notice the geological phenomena that gave rise

to the sites that are visited and valued ‘recognize the importance of the natural heritage, its fragility and need for preservation to maintain their natural evolution and ecological balance’ and thus, to contribute to the passage of this legacy for future generations and visitors, in accordance with the definition of geotourism made by Hose (1995). In fact, the need of knowledge makes information an effective tool to provide information in accessible language; it has an important role in the increased interest in geology and geoconservation, and to promote their touristic disclosure and a better environmental awareness and education (Lima, et al., 2009).

Figure 7 Interpretative resources: **(a)** - explanatory panel of *Gruta das Torres* Visitors Center (Pico island), **(b)** - *Capelinhos* volcano Interpretation Center (Faial island), **(c)** - outdoor information panel (Pico island)



Source: Azores Geopark

NOTES

Being an active volcanic archipelago, there is another obvious challenge in the development of geotourism in the region, health and safety issues with a significant risk factor which is often underestimated (Erfurt-Cooper, 2011). The visitors are knowingly approaching potentially dangerous areas. Therefore, it is necessary to work on the risk prevention by building physical barriers and signs or through information and alerts to visitors to raise awareness about a potential dangerous environment, without decreasing the visitor number. In the Azores the principal hazards to a geotourist are thermal burns from hot springs, fumaroles and other degassing vents, or intoxication by inhalation of volcanic gases, in addition to the risks of any outdoor activity (Figure 8).

Figure 8 Geotourists in *Caldeira Velha* fumarolic field (São Miguel island)



Source: Azores Geopark

A point of differentiation of the Azores is the enjoyment of the coastal and submarine geosites through coastering and diving to observe the geomorphology and submarine hydrothermal fields in some shallow geosites.

Another big challenge is to make this niche of tourism accessible to everyone. There are some good examples of inclusive tourism in the archipelago, such as adapted facilities and activities, but it is necessary to generalize them. It is therefore necessary to create conditions to receive people with special needs, such as blind, deaf, handicapped, as well as for seniors and children, and provide a range of activities able to meet the needs of each one, and help to develop their physical and intellectual abilities. It is essential and a priority to create conditions for accessibility and improve the existing ones in order to promote geotourism as an inclusive activity open to all persons.

The Azorean weather sometimes is a constraint and a challenge to the tourist experience, even being just a nature tourist. Thus, there is another challenge which requires having some alternative activities and products in case of unfavourable weather conditions. In the archipelago those alternatives already exist, such as visits to volcanic cavities, the environmental interpretation centres and science centres, for example.

Contributions of the Azores Geopark

The rich geodiversity, complemented by natural and cultural heritage, and together with the existing infrastructures (e.g. viewpoints and visitors, interpretation and science centres) provide good conditions for the development and creation of new touristic products.

It is important to note that the Azores Geopark, as an archipelagic territory, does not offer geotouristic services directly to the public, but works through the partners (tourism companies, interpretation and visitors centres, rural accommodation, and restaurants).

The main contribution of the geopark to the development of the geotourism in the archipelago is its practice in producing information and support materials or actions in order to give support to those who make the activities. However, other aspects were also taken into account, such as the promotion of circulation between the different islands (that present complementary geolandscapes and traditions); an increase in the length of stay (also increasing the revenues to local businesses), and suggest a variety of exciting activities and capability to develop with all weather conditions (as it has been mentioned before, the weather is an important factor in oceanic islands).

The products made by the Azores Geopark include (Viveiros, et al., 2012; Machado, et al., 2013) (Figure 9):

- i) “Geosites Charts” per island, with the areas and information about each geosite and also about some support facilities in the island;
- ii) “Azores geosites leaflet”, with a simple map, identification and photos of the geosites of the archipelago;
- ii) “Thematic routes”, including the Volcanic Caves Route (to “discover the subterranean world of the islands”, valuing the volcanic caves and associated visitors centres), the Belvederes Route (to “discover the Azores volcanic landscapes by car”, valuing the numerous belvederes and panoramic points that exist in all islands of the archipelago, easily accessible, superbly located and with support facilities), the Walking Trails (“discover the Azores geosites on foot”, enhancing the Regional Network of Walking trails with about 100 different options), the Science and Interpretation Centres Route (“to learn and explain the Azorean volcanic phenomena”, valuing 25 science, interpretation and visitors centres existing in all the islands), the Thermal Route (to “discover and enjoy the power of the Azores volcanism”, taking an advantage of the benefits in terms of health and well-being of the thermal waters and mud) and Urban Routes (to “discover the geology of my village/town” that allow local population and visitors to see and learn about the rocks in buildings and monuments and to understand the geology of urban areas);
- iii) “Azores Geotouristic Guide”, to support travellers and tourists that visit the islands, but also to assist the tourism companies to promote their products and services. It

- includes suggestions of places to visit (with an explanation of the geological characteristics and geotouristic potential), leisure activities, and other useful information;
- iv) “Geotours in rural areas” to give rise or improve the local socioeconomic activity in this places, socially depressed; this work has been develop in cooperation with the Local Development Associations (such as ARDE) and with Technical/professional schools (through internships and some final course works);
 - v) “Recycling courses” for the touristic companies staff about the geotourism activites of each island, being a continuous work initiated on the “2011 Meeting of Touristic Activities – Geotourism”, co-organized by the Azores Geopark and Regional Association of Tourism;
 - vi) “Geotourism workshops” targeted at students of technical/professional tourism courses;
 - vii) an “Azores Geopark Passport” is being develop to be launched next season in order to promote the thematic routes and travelling between the islands and the partners of the geopark;
 - viii) a “Geotourist conduct” was defined and disseminated through various tools;
 - viii) and several local products have been recognized as geoproducts of the Azores; this is the case of the wines “Terras de Lava”, “Basalto”, “Magma” or “Pedras Brancas” and the “Cozido das Furnas”, a typical dish cooked in the ground with natural volcano steam.

In addition, visitors can choose from a great variety of geotourism-based products, such as geotours, volcanospeleology, rock climbing, mountain climbing, diving, snorkelling, canyoning, thermal baths, and walking trails that are offered by various tourism companies.

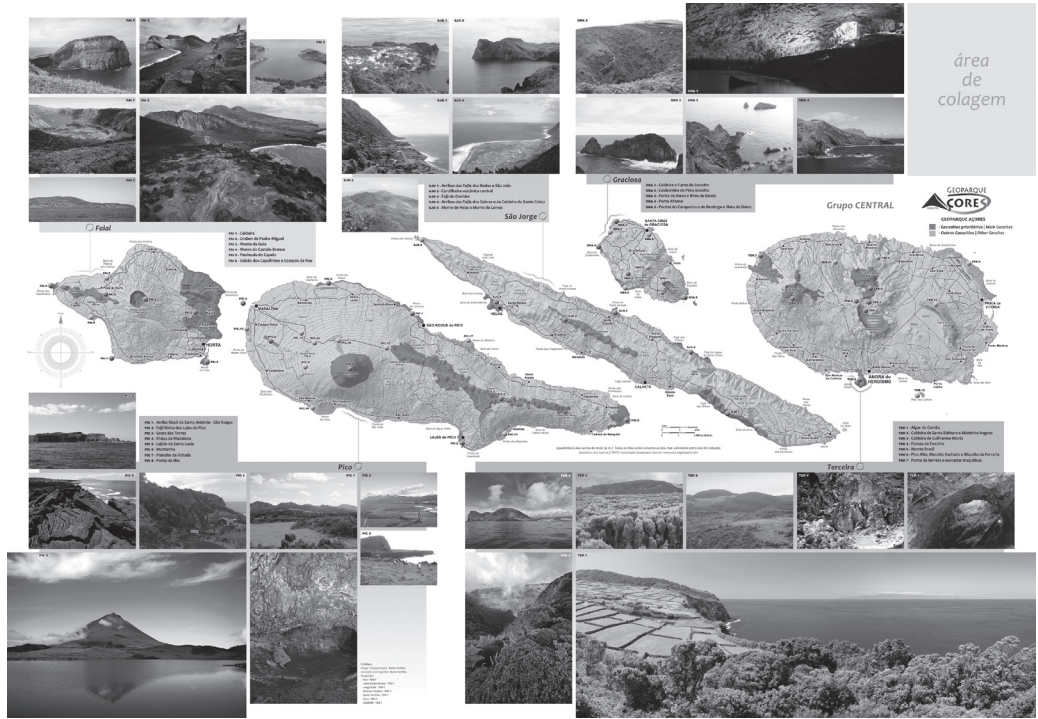
It is important to mention that it is currently a test phase of a monitoring geosites methodology which is going to be applied in the mostly visited places (e.g. belvederes, other viewpoints, or local places where leisure activities can be performed) for the verification of site conditions, their natural evolution and effects of anthropogenic pressure. In addition, this methodology should also help to give an accurate answer when maintenance or changes of the management rules of the site are needed.

Conclusion

Geotourism can be considered as an anthropocentric perspective of the use of the geological heritage and geodiversity. This captivating and promising activity involves learning, exploration and discovery, being also an appealing way of environmental awareness that spread wide through the general public (local and foreign).

Volcanic and geothermal landforms are obviously attractive destinations for geotourism where the special geodiversity offer an extensive range of outdoor direct contact with the volcanic structures and the emotions that they provide, and with including the opportunity for education about geoheritage as well as an insight into their significant value for regional culture, religion and history.

Figure 9 Geotouristic products developed by the Azores Geopark: (a) – Azores geosites leaflet, (b) - Geotourism workshop fieldtrip at Furnas volcano (São Miguel island)



Source: Azores Geopark

In recent years, the Azores Tourism has defined a strategy that includes geotourism as one of the main vectors thanks to the great geological potential of the Azores. The implementation of the Azores Geopark in the archipelago has become an important support for the development of geotourism, and for disclosure and awareness of the importance of the geolandscapes (integrated on the geological heritage, or not) and geoconservation issues, as well as emphasizing the importance of the abiotic part of nature as a basis to all the ecological systems, even to human activities. The creation of various tourism companies, restaurants and accommodations that offer products and services specialized in geotourism also helped to earn its space and marked its strong position in the Azorean nature tourism.

In the Azores archipelago the basic work has been done (e.g. identification and analysis of the geological heritage and geodiversity). As mentioned above, since early days the region has presented appealing characteristics, several ancestral activities and conditions for the practice of geotourism.

The Azores as a nature touristic destination should be built up on the experiences and emotions that tourists can experience and witness. The feedback from geotourists (locals and foreigners, has been positive; they express their satisfaction with the quality of the geosites or geolandscapes sites visited and the available variety of activities, products and services. Also from the tourism stakeholders (companies, environmental interpretation centers, and other partners) there have been requests for cooperation and support to some activities or staff training, resulting in the new partnerships and in the development of new geotouristic products.

With the notion that there are always some issues to improve, it is intended in the near future to: i) work on more assertive communication of the Azorean Geotourism; ii) promote and enhance the quality of the services and products; iii) and work on the consolidation of the archipelago as a nature destination, involving in an articulated and committed way public entities, private sector and the general population.

In order to maintain and improve the quality of geotourism, it is necessary to make this dynamic and accessible to all public by the promoting of a strategy that promotes and safeguards the geological heritage, through a monitoring network of the geosites. Moreover, it is also fundamental to stimulate the geotourists for the environmental awareness so that they can acquire the concern to respect the geosites characteristics and to maintain the geosites visited. It is up to today's geotourists to think about the geotourists of tomorrow.

Acknowledgment

This work is a contribution to the doctoral research project "Definition of a methodology for the management of geological heritage. An application to the Azores archipelago (Portugal)", Ref. M3.1.2/F/033/2011, supported by the Science Regional Fund of the Azores Government, and co-financed by the European Social Fund through the EU Pro-Employment Program.

References

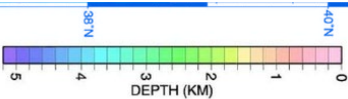
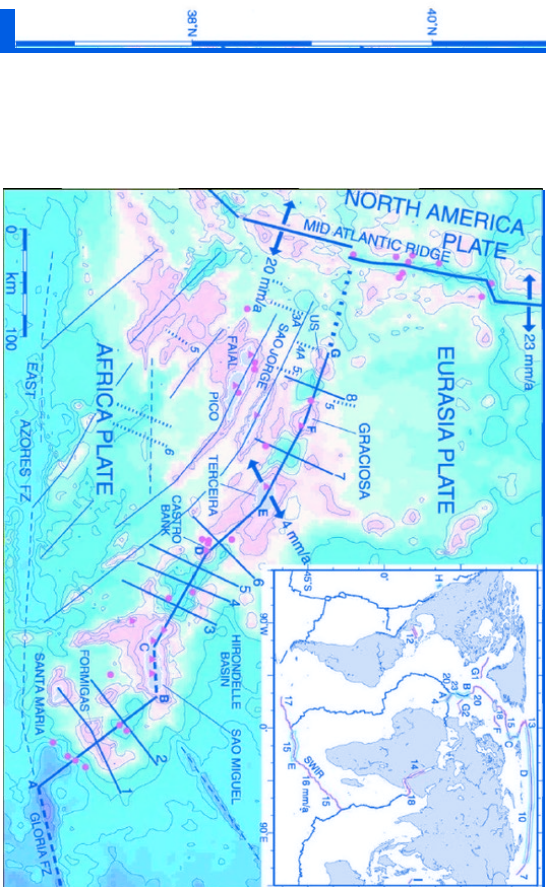
- Costa, M. P., et al. (2008). Geoparque dos Açores – Proposta. In: *V Seminário de Recursos Geológicos, Ambiente e Ordenamento do Território Abstract Book* (pp. 233-238). Universidade de Trás-os-Montes e Alto Douro, Vila Real.
- Decreto Legislativo Regional nº. 38/2008/A, de 11 de Agosto (Azorean Regional Law that approves the Tourism Planning of the Azores archipelago - POTRAA).
- Erfurt-Cooper (2011). Geotourism in Volcanic and Geothermal Environments: Playing with fire? *Geoheritage* 3 (3), 187-194.
- França, Z., et al. (2003). Geologia dos Açores: uma perspectiva actual. *Açoreana*, 10(1), 11-140.
- Fruituoso, G. (1583). *Saudades da Terra*, volume IX (2005). Instituto Cultural de Ponta Delgada, Ponta Delgada.
- García-Talavera, F.C. (2003). La Macaronésia (Consideraciones geológicas, diogeográficas y paleoecológicas). Available at <http://elguanche.net/macaronesiav2003.htm>
- Hose, T. A. (1995). Selling the story of Britain's stone. *Environmental interpretation*, (10), 16-17.
- Lima E. A. (2007). *Património geológico dos Açores: Valorização de Locais com Interesse Geológico das Áreas Ambientais, Contributo para o Ordenamento do Território*. Master Thesis on Land and Environmental Planning. Azores University, Biology Department. Ponta Delgada. 106 pp.
- Lima, E. A., et al. (2009). O geoturismo como instrumento de valorização do “Geoparque Açores”. In Carvalho, C.N., et al (Eds), *Geoturismo e Desenvolvimento Local. Câmara Municipal de Idanha-a-Nova/Geoparque NaturTejo, Lda.*, (pp. 149-160).
- Lima, E. A., et al (2012). Azores Geopark Project: geotouristic Potential. In *1st International Congress on Management and Awareness in Protected Volcanic Awareness Abstract book* (pp. 32-33). Olot (Spain).
- Machado, M., et al. (2013). Contributions of the Azores Geopark to the geotourism development in the archipelago. In Alloia, A., et al. (Eds), *Proceedings of the 12th European Geoparks Conference. National Park of Cilento, Vallo di Diano e Alburni (Italy)*. pp. 165-168.
- Nunes, J. C. (1991). Microssismos e neotectónica - Contribuição para o seu estudo nos Açores. *Provas de Aptidão Pedagógica e Capacidade Científica*. Monografia. Departamento de Geociências. Universidade dos Açores. Ponta Delgada; 245 pp.
- Nunes, J. C. (2002). *Novos Conceitos em Vulcanologia: Erupções, Produtos e Paisagens Vulcânicas*. Geonovas, n.º 16, 5-22.
- Nunes, J. C., et al. (2011). *Azores Geopark application to European Geoparks Network*. Azores Geopark Ed.
- Viveiros, C., et al. (2012). Geotours and the development of rural areas in the Azores islands. In Sá, A. A., et al. (Eds.), *Proceedings of the 11th European Geoparks Conference* (pp. 291-292). Arouca, Portugal: AGA.

The Azores attracted the interest of geoscientists since the beginning of the XX century. In the late 60s, when plate tectonics was established as the basic geodynamic paradigm, the peculiar morphology of the Azores Islands and the surrounding plateau, located close to the Mid-Atlantic ridge, were early interpreted as the result of the separation between the Eurasian and the North-America plates. Nevertheless, a number of particular geological features were targeted for explanation.

- (i) the long active fault going from Gibraltar to the Azores (now called Gloria Fault),
- (ii) the existence of a large but inactive fracture on the North-American plate, offset tenths of kilometres to the north with respect to Gloria Fault,
- (iii) the curvilinear succession of islands marked by pervasive volcanic and seismic activity,
- (iv) the development of a plateau, partially split by the Mid-Atlantic Ridge.

These questions remained elusive for a long time, despite the large amount of geological and geophysical data available, as most of the conventional approaches were not as fruitful as expected, and new identified features raise new unknowns or revealed uncommon geological environments.

—The Tectonic Evolution of the Azores Based on Magnetic Data
J. M. Miranda, J. F. Luis, and N. & Lourenço (2018)



Geology of Three Late Quaternary Stratovolcanoes on São Miguel, Azores

U.S. GEOLOGICAL SURVEY BULLETIN 1900

Prepared in cooperation with the
Regional Government of the Azores



AVAILABILITY OF BOOKS AND MAPS OF THE U.S. GEOLOGICAL SURVEY

Instructions on ordering publications of the U.S. Geological Survey, along with the last offerings, are given in the current-year issues of the monthly catalog "New Publications of the U.S. Geological Survey." Prices of available U.S. Geological Survey publications released prior to the current year are listed in the most recent annual "Price and Availability List." Publications that are listed in various U.S. Geological Survey catalogs (see back inside cover) but not listed in the most recent annual "Price and Availability List" are no longer available.

Prices of reports released to the open files are given in the listing "U.S. Geological Survey Open-File Reports," updated monthly, which is for sale in microfiche from the U.S. Geological Survey Books and Open-File Reports Sales, Box 25425, Denver, CO 80225.

Order U.S. Geological Survey publications by mail or over the counter from the offices given below.

BY MAIL

Books

Professional Papers, Bulletins, Water-Supply Papers, Techniques of Water-Resources Investigations, Circulars, publications of general interest (such as leaflets, pamphlets, booklets), single copies of periodicals (Earthquakes & Volcanoes, Preliminary Determination of Epicenters), and some miscellaneous reports, including some of the foregoing series that have gone out of print at the Superintendent of Documents, are obtainable by mail from

U.S. Geological Survey, Books and Open-File Report Sales
Box 25425
Denver, CO 80225

Subscriptions to periodicals (Earthquakes & Volcanoes and Preliminary Determination of Epicenters) can be obtained ONLY from

Superintendent of Documents
U.S. Government Printing Office
Washington, DC 20402

(Check or money order must be payable to Superintendent of Documents.)

Maps

For maps, address mail order to

U.S. Geological Survey, Map Sales
Box 25286
Denver, CO 80225

Residents of Alaska may order maps from

U.S. Geological Survey, Map Sales
101 Twelfth Ave., Box 12
Fairbanks, AK 99701

OVER THE COUNTER

Books

Books of the U.S. Geological Survey are available over the counter at the following U.S. Geological Survey offices, all of which are authorized agents of the Superintendent of Documents.

- ANCHORAGE, Alaska—4230 University Dr., Rm. 101
- ANCHORAGE, Alaska—605 West 4th Ave., Rm G-84
- DENVER, Colorado—Federal Bldg., Rm. 169, 1961 Stout St.
- LAKEWOOD, Colorado—Federal Center, Bldg. 810
- MENLO PARK, California—Bldg. 3, Rm. 3128, 345 Middlefield Rd.
- RESTON, Virginia—National Center, Rm. 1C402, 12201 Sunrise Valley Dr.
- SALT LAKE CITY, Utah—Federal Bldg., Rm. 8105, 125 South State St.
- SAN FRANCISCO, California—Customhouse, Rm. 504, 555 Battery St.
- SPOKANE, Washington—U.S. Courthouse, Rm. 678, West 920 Riverside Ave.
- WASHINGTON, D.C.—U.S. Department of the Interior Bldg., Rm. 2650, 1849 C St., NW.

Maps

Maps may be purchased over the counter at the U.S. Geological Survey offices where books are sold (all addresses in above list) and at the following Geological Survey offices:

- ROLLA, Missouri—1400 Independence Rd.
- FAIRBANKS, Alaska—New Federal Building, 101 Twelfth Ave.

Geology of Three Late Quaternary Stratovolcanoes on São Miguel, Azores

By RICHARD B. MOORE

Prepared in cooperation with the
Regional Government of the Azores

U.S. GEOLOGICAL SURVEY BULLETIN 1900

U.S. DEPARTMENT OF THE INTERIOR
MANUEL LUJAN, JR., Secretary



U.S. GEOLOGICAL SURVEY
Dallas L. Peck, Director

Any use of trade, product, or firm names in this publication is for descriptive purposes only and does not imply endorsement by the U.S. Government

UNITED STATES GOVERNMENT PRINTING OFFICE: 1991

For sale by the
Books and Open-File Reports Section
U.S. Geological Survey
Federal Center
Box 25425
Denver, CO 80225

Library of Congress Cataloging-in-Publication Data

Moore, Richard B., 1945—
Geology of three late Quaternary stratovolcanoes on São Miguel, Azores / by
Richard B. Moore.

p. cm. — (U.S. Geological Survey bulletin ; 1900)
"Prepared in cooperation with the Regional Government of the Azores."
Includes bibliographical references.

1. Volcanoes—Azores—São Miguel Island. 2. Geology,
Stratigraphic—Quaternary. 3. Geology—Azores—São Miguel Island. I. Title.
II. Series.

QE75.B9 no. 1900

[QE527]

557.3 s—dc20

[551.2'1'094699]

91-12012
CIP

CONTENTS

Abstract	1
Introduction	1
Structure and morphology	2
Sete Cidades volcano	2
Pleistocene units	3
Pre-caldera units	3
Caldera-outflow deposit	3
Post-caldera units	5
Holocene units	5
Trachytic deposits	5
Mafic flank eruptions	7
Agua de Pau volcano	7
Pleistocene units	10
Older caldera-outflow deposit	11
Post-outer caldera units	12
Younger caldera-outflow deposit	12
Post-inner caldera units	12
Holocene units	12
Fogo A	12
Post-Fogo A pumice deposits from vents within and near the inner caldera	13
Eruptions at Lagoa do Congro	13
Mafic flank eruptions	13
Furnas volcano	15
Pleistocene units	16
Pre-caldera units	16
Caldera-outflow deposit	18
Post-caldera units	18
Holocene units	19
Trachytic deposits	19
Mafic deposits	19
Petrography	20
Mafic rocks	20
Intermediate to silicic rocks	20
Syenite xenoliths	20
Xenoliths of mafic and ultramafic rocks	21
Major element chemical compositions	21
Silica-variation diagrams	21
Magnesia-variation diagrams	23
AFM diagram	23
Discussion	23
References cited	25

FIGURES

- 1–3. Maps showing:
 1. Location of Azores fracture zone and other major structures 2
 2. São Miguel, Azores 3
 3. Generalized geology of Sete Cidades volcano 4
4. Composite measured stratigraphic section, western flank of Sete Cidades volcano 6
5. Measured stratigraphic section, western wall of Sete Cidades caldera 7
6. Maps showing generalized geology of Agua de Pau volcano 8
7. Graph showing radiocarbon ages of the Fogo A trachyte pumice deposit 13
8. Map showing generalized geology of Furnas volcano 14
9. Composite measured stratigraphic section, southern flank of Furnas volcano 17
10. Measured stratigraphic section, western wall of Furnas caldera 18
11. Silica-variation diagrams 27
12. Magnesia-variation diagrams 38
13. AFM ternary diagram 46

TABLES

1. Chemical analyses and normative compositions for representative rocks from Sete Cidades, Agua de Pau, and Furnas volcanoes, São Miguel, Azores 22
2. Estimated volumes of different rock types on the three late Quaternary stratovolcanoes of São Miguel 25

Geology of Three Late Quaternary Stratovolcanoes on São Miguel, Azores

By Richard B. Moore

Abstract

Three Quaternary trachytic stratovolcanoes—Sete Cidades, Agua de Pau, and Furnas—are located on the island of São Miguel, Azores. Mafic vent deposits and associated lava flows are between the stratovolcanoes and on their flanks. Each volcano consists of interbedded ankaramite, basanitoid, alkali olivine basalt, hawaiite, mugearite, and tristanite cones and flows, as well as trachyte domes, flows, and pyroclastic deposits. Detailed geologic mapping and new radiocarbon and K-Ar ages indicate that Furnas, constructed entirely within the past 100,000 years, is somewhat younger than the other two volcanoes.

All three volcanoes have calderas that formed in the late Pleistocene as a consequence of voluminous eruption of trachytic pyroclastic flows and fall deposits. The outer caldera of Agua de Pau volcano is the oldest (26,500–46,000 years). The progression then is from west to east: the caldera of Sete Cidades is about 22,000 years old, the inner caldera of Agua de Pau is about 15,000 years old, and the caldera of Furnas is about 12,000 years old. Post-caldera activity has included emplacement of trachyte domes, associated with extensive Plinian and sub-Plinian pumice-fall deposits within the calderas, and eruption of more mafic lavas from vents on the flanks of the volcanoes. Each volcano has erupted during the past 500 years. Holocene eruptions have been most frequent on Sete Cidades and Furnas. Future eruptions present significant risk because a large population (150,000) now inhabits São Miguel. Furnas is particularly dangerous, partly because it has erupted five times during the past 1,100 years, most recently in A.D. 1630.

The three volcanoes range in subaerial volume from about 60 to 80 km³. They were constructed at rates of about 0.02–0.03 km³/century on Sete Cidades, 0.04 km³/century on Agua de Pau, and 0.06 km³/century on Furnas. Trachyte is volumetrically the most abundant rock type, ranging from about 72 percent of the exposed lavas on Sete Cidades to about 93 percent on Agua de Pau. Tristanites are most abundant on Furnas and reflect the generally higher K/Na on that volcano. Potassic hawaiites and mugearites are most abundant (about 18 percent by volume) on Sete Cidades.

New major element chemical and normative data for all mapped rocks from the three volcanoes demonstrate their alkalic (especially potassic) nature and indicate that virtually all mafic and many silicic rocks are nepheline normative. Peralkaline trachytes (including both quartz and nepheline normative types) are particularly abundant on Agua de Pau, where they constitute about 45 percent of the volume of all trachytes. They typically were erupted in large volume during short-lived events, most notably during the two caldera-forming episodes. In contrast, peralkaline trachytes are rare on Sete Cidades and Furnas volcanoes and make up less than 1 percent of their erupted volumes.

Variation diagrams illustrate some chemical differences among the volcanoes and suggest that most of the diverse rock types are related by fractionation of parental basanitoid. Incorporation of silicic material in mafic melts locally has resulted in hybrid lavas, especially on Agua de Pau.

INTRODUCTION

The Azores straddle the Mid-Atlantic Ridge (fig. 1). Historic eruptions have occurred on five islands during the past 500 years (van Padang and others, 1967). Islands east of the Ridge, including São Miguel, are near the Azores fracture zone (called the Terceira Rift or Terceira Ridge by some workers), a seismically active spreading center (Krause and Watkins, 1970; Searle, 1980) near the triple junction of the African, Eurasian, and North American plates. The zone of plate divergence underlying the Azores archipelago changes to one of convergence between the Azores and the Iberian Peninsula (Grimison and Chen, 1986).

This report summarizes information gathered during 1:15,000- and 1:18,000-scale mapping (Moore 1983a, b, 1986) of an area of about 475 km² including Sete Cidades, Agua de Pau, and Furnas volcanoes on the island of São Miguel, Azores (figs. 1–3, 6, 8). New radiocarbon (<40,000 years B.P.; Moore and Rubin, 1991) and K-Ar (>40,000 years B.P.; E.H. McKee, U.S. Geological Survey (USGS),

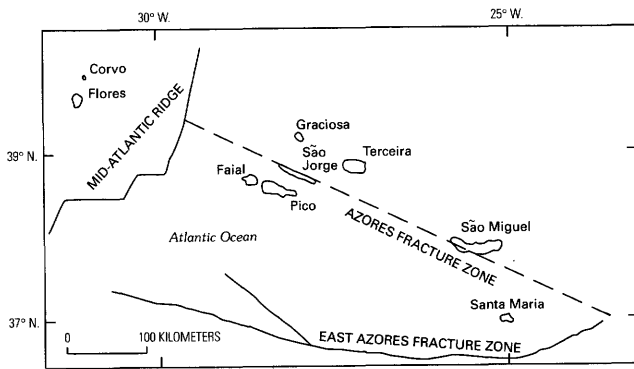


Figure 1. Location of Azores fracture zone and other major structures. Modified from Laughton and Whitmarsh (1975).

written commun., 1986) ages augment the stratigraphic data; all unreferenced ages in this report are from these two sources. Silica- and magnesia-variation diagrams using 357 new chemical analyses of rocks, representing every map unit, from the three volcanoes are presented.

The volcanoes are composed of lava flows, domes, and pyroclastic rocks of the alkali basalt–trachyte suite (Irvine and Barager, 1971). Eruptions of both mafic and trachytic lavas have occurred on Sete Cidades and Agua de Pau during the past 1,000 years, and Furnas has erupted trachyte five times during the past 1,100 years. These volcanoes are the targets of geologic, geophysical, and geochemical investigations by members of the USGS, in cooperation with the Regional Government of the Azores, in an effort to identify and assess the geothermal energy resources of São Miguel.

Zbyszewski and others (1958) and Zbyszewski and Ferreira (1959) published 1:50,000-scale geologic maps showing rock types on São Miguel. Moore (1990, 1991) presented a new geologic map (scale 1:50,000) of all of São Miguel and summarized the geology of the island. Walker and Croasdale (1970) and Booth and others (1978) studied widespread trachyte pumice deposits from the three volcanoes. Chemical analyses are presented by Esenwein (1929), Jeremine (1957), Schmincke and Weibel (1972), Schmincke (1973), Flower and others (1976), and White and others (1979). White and others (1976) described strontium isotope variations, and Hawkesworth and others (1979) evaluated strontium and neodymium isotope data. Storey (1981) discussed the petrologic evolution of the magma reservoir beneath Agua de Pau volcano during the past 4,600 years.

Acknowledgments.—Edward W. Wolfe (USGS) aided considerably with computer generation of the variation diagrams and also critically reviewed the manuscript. Debby Kay (USGS) did the rapid-rock chemical analyses. A.M. Rodrigues da Silva (Laboratório de Geociências e Tecnologia, Ponta Delgada, São Miguel) gave considerable logistical support. Wendell A. Duffield and Donald A. Swanson (USGS) critically reviewed the

manuscript. This work was supported by the Agency for International Development (U.S. Department of State), the Regional Government of the Azores, and the U.S. Geological Survey.

STRUCTURE AND MORPHOLOGY

Normal faults are common on São Miguel; widespread trachyte pumice deposits mask them in most areas. Locally, faults displace unconsolidated pumice deposits as young as 361 (Furnas volcano) and 428 (Agua de Pau volcano) years. Most faults strike northwest or west-northwest and are part of the Azores fracture zone, the axis of which crosses Sete Cidades volcano on the western end of the island. The location of Sete Cidades probably was controlled by the fracture zone; fault scarps about 60 m high on the northwestern and eastern rims of the caldera are truncated by the caldera and apparently experienced major displacement at the time of caldera formation about 22,000 years ago.

Landforms on the three volcanoes are dominantly constructional; significant erosion occurs only on sea cliffs and on pyroclastic deposits in deep canyons cut near contacts between large trachyte domes and lava flows. Oversteepened slopes characterize many of these canyons, and a high probability exists for destructive mudflows during periods of heavy rainfall.

SETE CIDADES VOLCANO

Sete Cidades volcano is located on the western end of São Miguel (figs. 2, 3). Its subaerial volume is about 70 km³, and its lavas have accumulated at an estimated rate of 0.02–0.03 km³/century. An almost circular caldera about 5 km in diameter, with walls as high as 400 m, truncates its summit. Geologic mapping (fig. 3) indicates that pre-caldera rocks crop out chiefly in the caldera walls and in sea cliffs eroded into the flanks of the volcano. Post-caldera units are trachyte cones and pumice rings distributed across the caldera floor, and ankaramite, basanitoid, alkali olivine basalt, hawaiiite, mugearite, and minor trachyte cones and flows erupted from flank fissures radial to the caldera. All trachytic vents on Sete Cidades are within a 7 by 4 km area, the smallest of the three stratovolcanoes, roughly centered on the caldera.

Sete Cidades lacks hot springs, which are prominent on Agua de Pau and Furnas volcanoes. Only two warm springs are known, near Mosteiros on the northwestern coast and at Ponta da Ferraria on the western coast. The latter has a temperature of about 50°C.

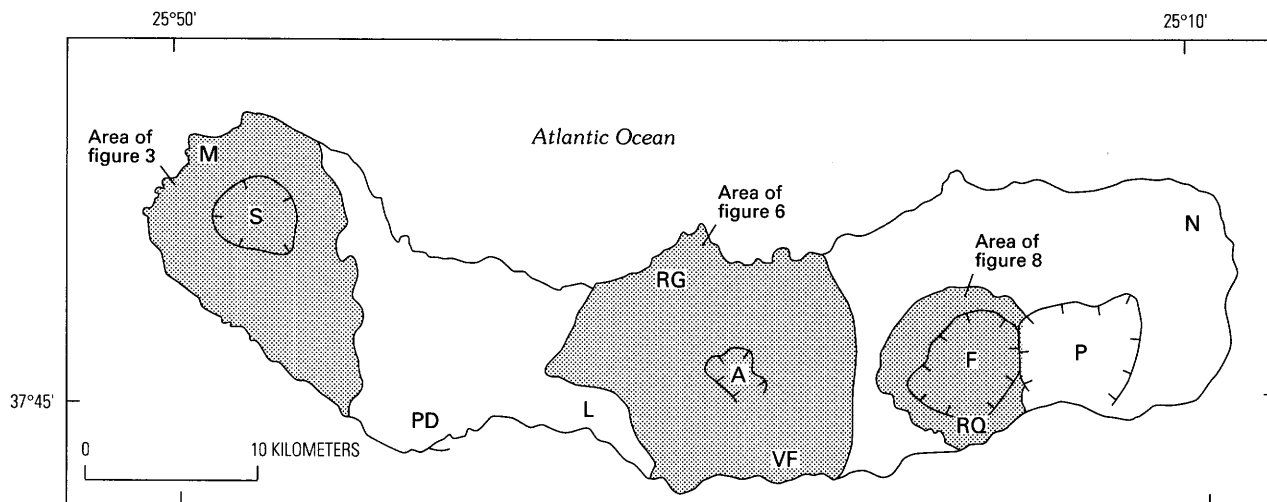


Figure 2. São Miguel, Azores. Hachured lines mark calderas: S, Sete Cidades; A, Agua de Pau; F, Furnas; P, Povoação (extinct). Major towns: M, Mosteiros; PD, Ponta Delgada; L, Lagoa; RG, Ribeira Grande; VF, Vila Franca do Campo; RQ, Ribeira Quente; N, Nordeste. Stippling indicates areas mapped at 1:15,000 scale (figs. 3, 6, 8).

Pleistocene Units

Pre-Caldera Units

The oldest subaerial rocks of Sete Cidades include trachyte and tristanite domes and flows exposed at the base of the caldera wall and in sea cliffs on the western and southern coasts. A trachyte flow at the base of the northwestern caldera wall (fig. 3) has a K-Ar age of $210,000 \pm 8,000$ years, and a tristanite flow at the base of the section at Ponta da Ferraria (fig. 4), on the western coast, has a K-Ar age of $74,000 \pm 6,000$ years. Figure 4 is a composite stratigraphic section in the vicinity of Ponta da Ferraria.

Flows of ankaramite, basanitoid, alkali olivine basalt, hawaiite, mugearite, and tristanite are interbedded with trachyte pyroclastic deposits that overlie the earlier domes and flows; these deposits form the major subaerial part of the stratovolcano. Trachyte pyroclastic deposits include pyroclastic flows, pyroclastic surges, mudflows, and pumice deposited during Plinian and sub-Plinian eruptions. Radiocarbon ages of charcoal recovered from beneath the flows and from within the pyroclastic units are greater than 29,000 years.

Caldera-Outflow Deposit

The caldera of Sete Cidades volcano formed approximately 22,000 years ago after eruption of several cubic kilometers of trachyte pumice. The volume of the caldera is about 6 km^3 . The volume of the caldera-outflow deposit cannot be determined with certainty because of burial by younger lavas. An unknown but probably

significant volume of pumice fell at sea. This eruption produced pyroclastic flows, locally welded, and pyroclastic surges directed primarily southeastward. The resulting composite deposit is more than 60 m thick 13 km southeast of the caldera but only 5 m thick on the western and northern flanks of the volcano. The welded pyroclastic flows crop out chiefly on the western, northern, and southern walls of the caldera.

A new roadcut on the western caldera wall provides the best exposure of the caldera-outflow deposit and overlying units (fig. 5). The caldera-outflow deposit and underlying and overlying deposits up to the Sete A pumice (terminology of Booth and others, 1978) are truncated by the caldera-bounding fault. Truncation of the beds that postdate the caldera-outflow deposit suggests that subsidence of the caldera continued incrementally (Walker, 1984) for some time after the major collapse.

Massive trachyte pumice deposited during an early Plinian phase of the caldera-forming eruption is exposed in the lowest 4 m of the roadcut. Strongly oxidized trachytic pyroclastic flows, 10–12 m thick and characterized by somewhat flattened black obsidian fragments in an orange fine-grained matrix, conformably overlie the Plinian pumice; a welded zone, here only 0.3 m thick and characterized by strongly flattened pumice fragments that are now obsidian, begins about 1 m above the base of this subunit. Above the caldera-outflow deposit is soil 10–30 cm thick that records perhaps several decades or centuries of weathering on the basis of comparison with modern soils developed on historic (A.D. 1563 Agua de Pau and A.D. 1630 Furnas) pumice deposits on São Miguel. A 2-m-thick Plinian deposit, consisting of large (to 0.7 m), dark- and

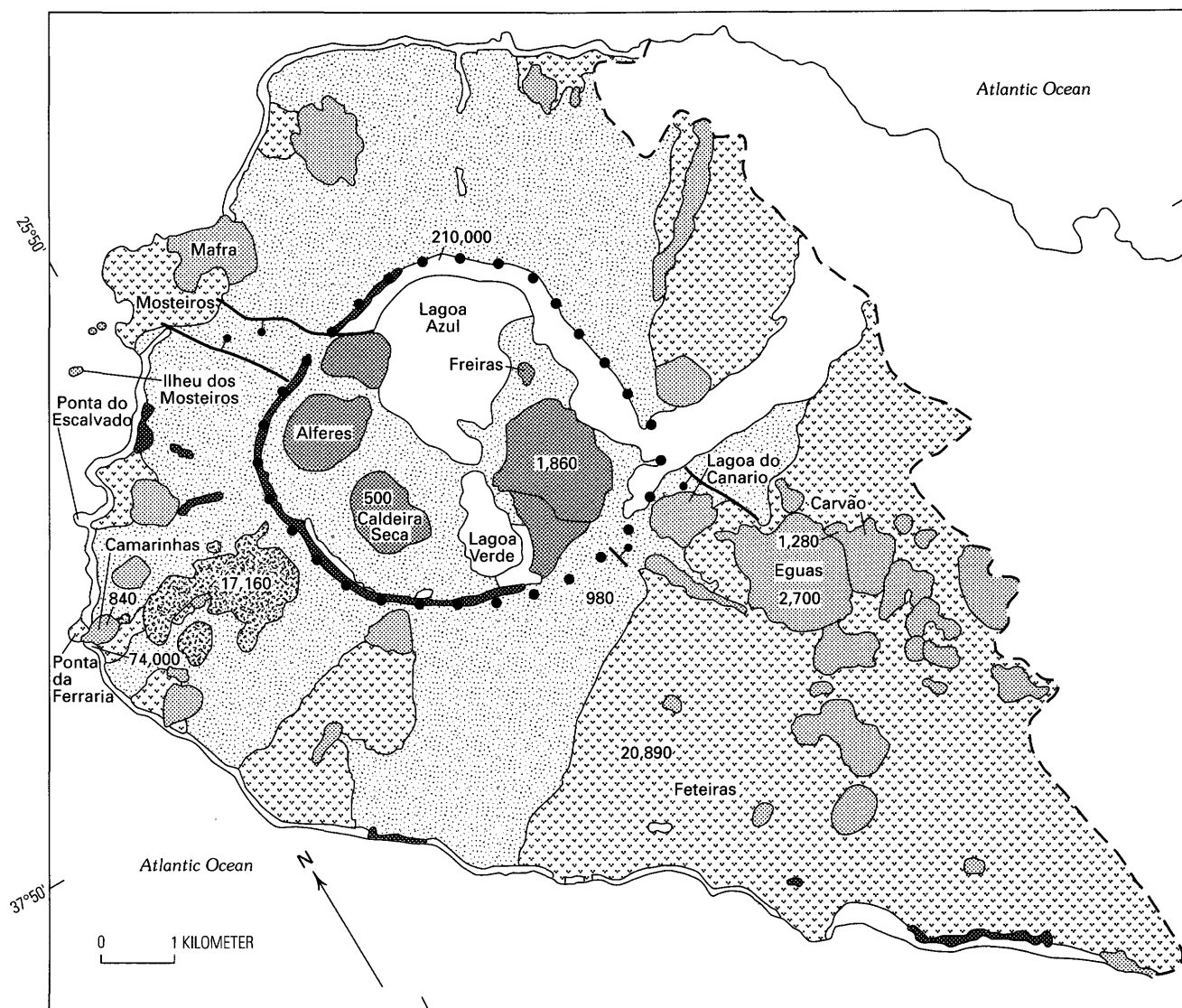


Figure 3 (above and facing page). Generalized geologic map of Sete Cidades volcano.

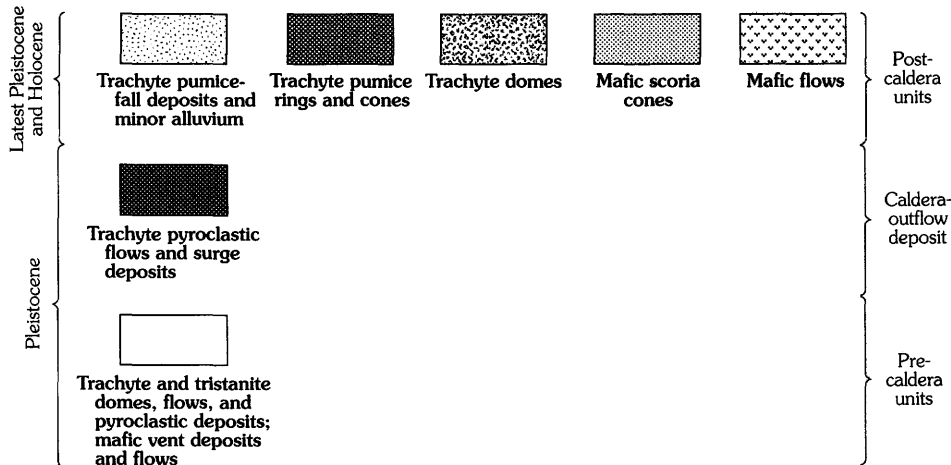
light-gray tristanite pumice fragments that are partly agglutinated and probably close to their source, overlies the soil. A 25–30-cm-thick layer of soil overlies the lower tristanite pumice. The top subunit of this group is coarse tristanite pumice, similar to the lower subunit, that overlies charcoal in the soil dated at $21,160 \pm 180$ years B.P. The thickness of the soils between the dated charcoal and the caldera-outflow deposit suggests that only a few centuries elapsed between these eruptions. The age of the caldera-outflow deposit thus is believed to be about 22,000 years. Voluminous ignimbrites were erupted from Pico Alto volcano on Terceira at about the same time, 23,000 and 19,000 years B.P. (Self, 1976).

Outside of the caldera the caldera-outflow deposit generally is not welded and is recognized chiefly by its

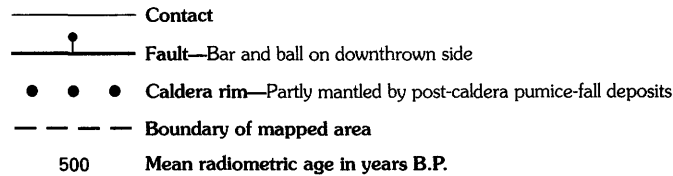
stratigraphic position and by the common occurrence of large (10–40 cm), slightly flattened, black obsidian fragments (formerly pumice) in a light-gray, fine-grained matrix. The thickest exposure of the deposit is about 13 km southeast of the caldera in almost inaccessible sea cliffs. Here, pumice fragments are not flattened to obsidian, the deposit is white to very light gray, and fine-grained cross-bedded surge deposits are common.

In most places (except in the new roadcut on the western caldera wall), the caldera-outflow deposit immediately underlies the Sete A pumice, a Plinian deposit probably from a trachyte cone in the northern part of Sete Cidades caldera (Booth and others, 1978). The caldera-outflow deposit is truncated by the caldera wall, whereas the Sete A pumice mantles it.

EXPLANATION



Mafic rocks include basanitoid, ankaramite, alkali-olivine basalt, hawaiite and mugearite



Post-Caldera Units

At the new roadcut on the western wall of Sete Cidades caldera (fig. 5), the oxidized pyroclastic flows and overlying coarse tristanite pumice are separated from the Sete A pumice by about 6 m of thinly bedded trachyte pumice deposits and soils interbedded with 6–8 m of alkali olivine basalt and potassic mugearite scoria and short flows from a nearby source.

Elsewhere on Sete Cidades, the caldera-outflow deposit is separated from the Sete A pumice by only a few mafic flows and at least one trachyte pyroclastic flow deposit. A potassic mugearite flow near Feteiras (fig. 3) on the southern flank of the volcano has a radiocarbon age of $20,890 \pm 240$ years. A trachyte pyroclastic flow deposit on top of the sea cliff at Ponta do Escalvado, near the western end of the island, has a radiocarbon age of $17,160 \pm 130$ years. This deposit probably is related to post-caldera trachyte domes and flows about 1.5 km southeast of Ponta do Escalvado.

Holocene Units

Trachytic Deposits

Sete Cidades volcano apparently was relatively inactive, except for the few eruptions noted above, during the approximately 17,000 years between formation of the

caldera and deposition of the Sete A pumice. Such relative quiescence following caldera formation characterizes Agua de Pau and Furnas volcanoes as well.

Booth and others (1978) studied the products of 12 trachytic pyroclastic eruptions from Sete Cidades. They considered the age of the oldest eruption, Sete A, to be uncertain; the others, Sete B–L, rest on the 5,000-year-old Fogo A deposit from Agua de Pau volcano. I consider Sete A to be little older than 5,000 years, on the basis of the relatively thin (<20 cm) soil separating Sete A from Sete B.

Six vents, the eruptions of which formed cones or pumice rings, occur on the floor of Sete Cidades caldera in a roughly circular pattern (fig. 3); perhaps magmas rose along a concentric fracture that formed at about the same time as the caldera. Other vents may be submerged beneath Lagoa Azul (Blue Lake) and Lagoa Verde (Green Lake). Four of the six vents were sites of voluminous Plinian and sub-Plinian eruptions of trachyte pumice (Booth and others, 1978) that mantled the western part of São Miguel. The other two vents, Alferes and Freiras (fig. 3), erupted relatively degassed trachyte scoria of only local extent.

Most of the young pumice deposits on Sete Cidades that Booth and others (1978) studied have not been dated. The peralkaline Sete J deposit has a radiocarbon age of $1,860 \pm 120$ years B.P. The next youngest deposit, Sete K, is older than the Carvão basanitoid cone and flow, dated at $1,280 \pm 150$ years B.P.

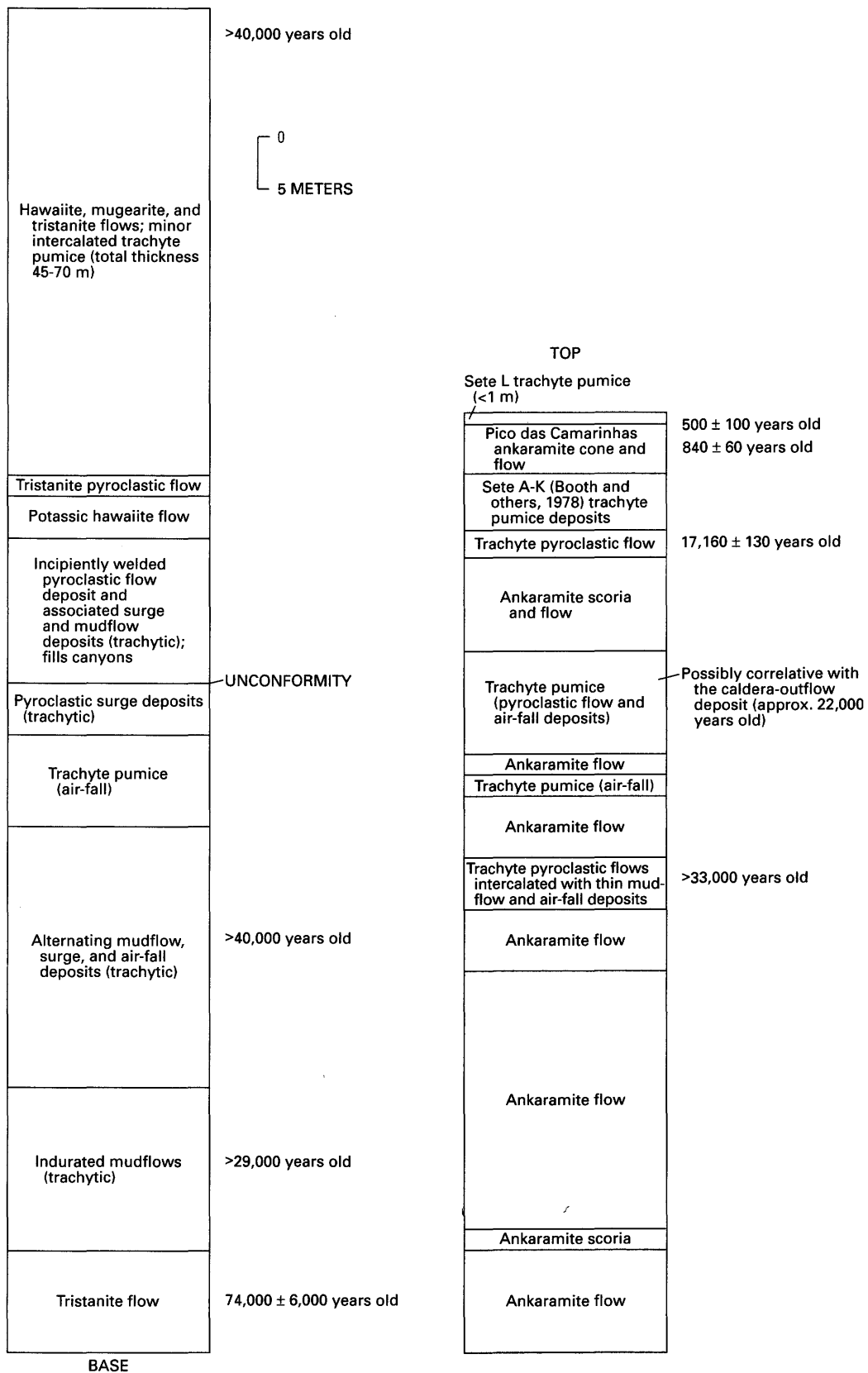


Figure 4. Composite measured stratigraphic section, sea cliff near Ponta da Ferraria on western flank of Sete Cidades volcano. Dips are approximately horizontal except on canyon-filling units.

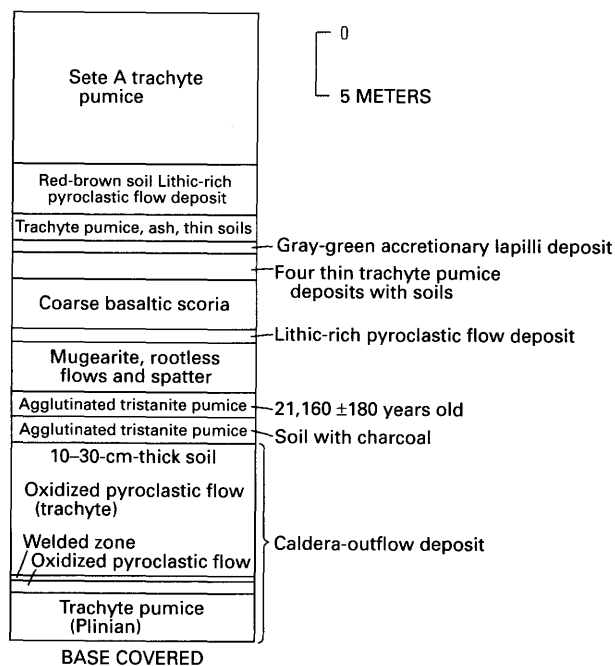


Figure 5. Measured stratigraphic section, roadcut on western wall of Sete Cidades caldera. All units dip approximately 17°W.

The youngest intracaldera eruption formed the Caldeira Seca pumice ring (fig. 3) and produced the peralkaline Sete L deposit. Shotton and Williams (1971) reported a radiocarbon age of 663 ± 105 years B.P. for Sete L; a newly determined radiocarbon age of 500 ± 100 years B.P. is similar to the previous determination and correlates with a reported eruption at the time of Portuguese discovery of the island in the middle of the fifteenth century (van Padang and others, 1967).

Assuming that the Sete A deposit is about 5,000 years old, the average dormant interval for the 12 trachytic pyroclastic eruptions of Sete Cidades that Booth and others (1978) studied is about 409 years. At least 780 years elapsed, however, between the Sete K and L eruptions, and the present dormant interval has lasted at least 540 years.

Mafic Flank Eruptions

Sporadic eruptions of ankaramite, basanitoid, alkali olivine basalt, hawaiiite, and mugearite have occurred on Sete Cidades since formation of the caldera. Most mafic vents are concentrated along the trace of the Azores fracture zone extending southeast from the caldera (volcanic zone 2 of Moore, 1990, 1991). A few vents erupted along radial fissures on the flanks of the volcano.

Four young eruptions on and near Sete Cidades (fig. 3) have recently been dated. The ankaramite cone of Eguas, which forms the highest point on Sete Cidades about 2 km southeast of the caldera, is $2,700 \pm 250$ years old. Pico do Carvão, 1 km southeast of Eguas, and its flow have a

radiocarbon age of $1,280 \pm 150$ years B.P. The basanitoid spatter rampart at Ferrarias, 1 km west of Eguas, is 980 ± 90 years old, and did not form around A.D. 1444, as suggested by Zbyszewski (1961). The Pico das Camarinhas basanitoid cone and Ponta da Ferraria lava delta, products of the most recent subaerial mafic eruption on Sete Cidades, are 840 ± 60 years old. This date and detailed mapping indicate that reports of subaerial eruptive activity on Sete Cidades around A.D. 1713 and perhaps at other times (van Padang and others, 1967) are not correct.

Surtseyan cones, remnants of which form the Ilheudos (Islands of) Mosteiros near the northwestern coast of Sete Cidades (fig. 3), apparently erupted during the time that Sete A and younger trachyte pumice deposits accumulated. Hyaloclastite and deposits of basaltic accretionary lapilli from these vents are interbedded with trachyte pumice near the top of the sea cliff southwest of Mosteiros.

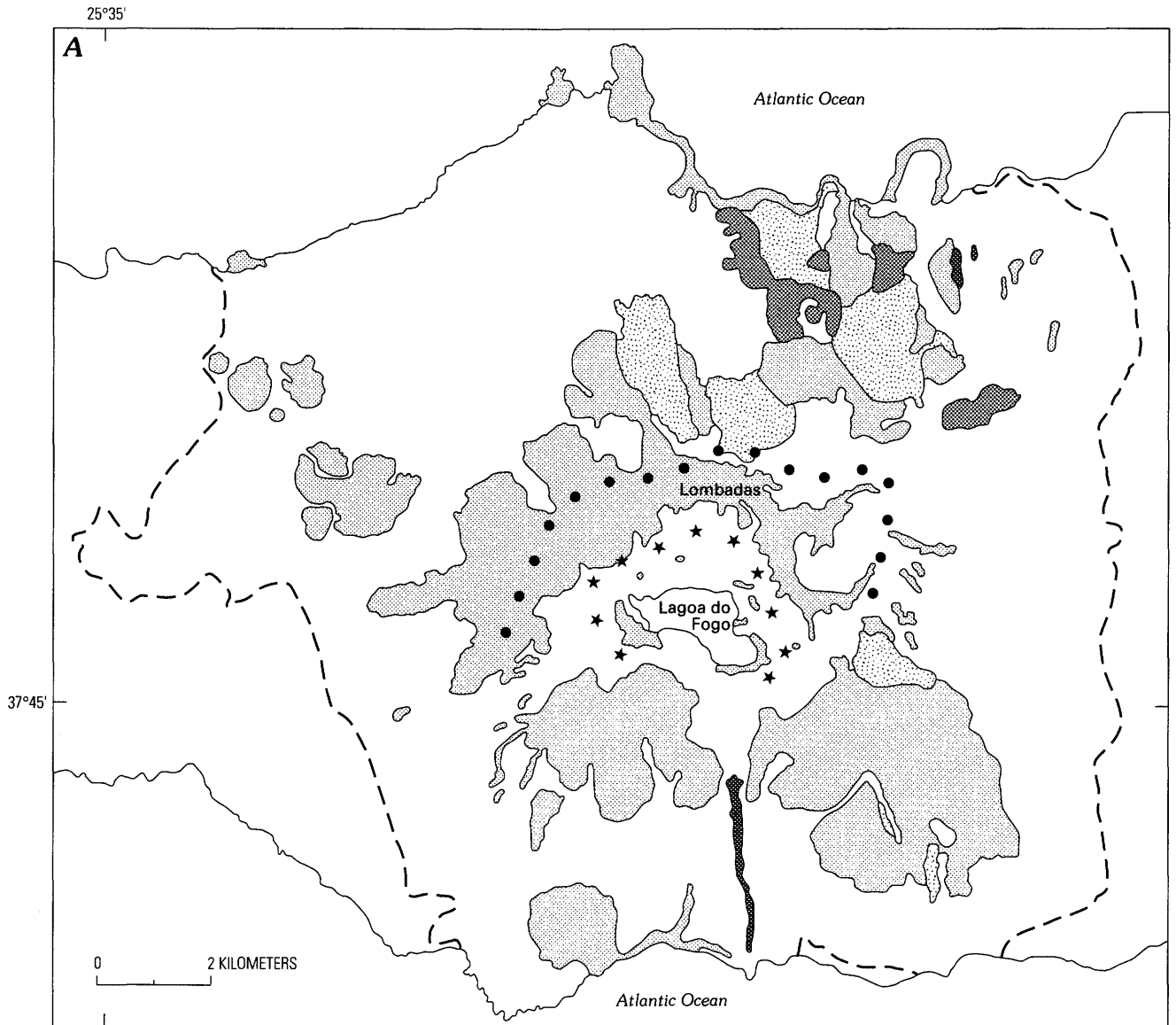
Lagoa do Canario (fig. 3) is a lake within a basanitoid maar about 0.5 km southeast of the southeastern caldera rim. The vent is within 300 m of a major fault marking the trace of the Azores fracture zone. Because the low cone surrounding the vent is thickly mantled by trachyte pumice, the composition of its juvenile material was unknown until it was exposed in roadcuts. These exposures also show that the maar is overlain only by the Sete I-L deposits.

Several vent deposits and associated flows, notably those of Eguas and Camarinhas, contain xenoliths of mafic and ultramafic rocks.

The absence of young mafic deposits within the caldera and the occurrence of recent trachyte eruptions there suggest that trachyte magma may still underlie it.

AGUA DE PAU VOLCANO

Agua de Pau volcano, a stratovolcano whose summit is 947 m above sea level, is located in the central part of São Miguel (fig. 2). Its subaerial volume of about 80 km^3 has increased at an estimated rate of $0.04 \text{ km}^3/\text{century}$. A prominent caldera 3 by 2.5 km across, with walls as high as 300 m, truncates its summit and contains Lagoa do Fogo (Fire Lake). The topographic margin of an older caldera, about 7 by 4 km across, is preserved locally on the western, northern, and eastern sides of the volcano. Stratigraphic relations, especially within the calderas, are generally less obvious on Agua de Pau than on the other two volcanoes because of burial by widespread thick Holocene pumice. Deposits predating both calderas crop out on all flanks of the volcano and in sea cliffs on the northern and southern coasts (fig. 6A). At least five eruptions of trachyte pumice have occurred from vents mostly within the inner caldera during the past 5,000 years (Booth and others, 1978). Mafic and trachytic lavas were erupted from vents on all flanks of the volcano, before and after formation of the calderas. No



EXPLANATION

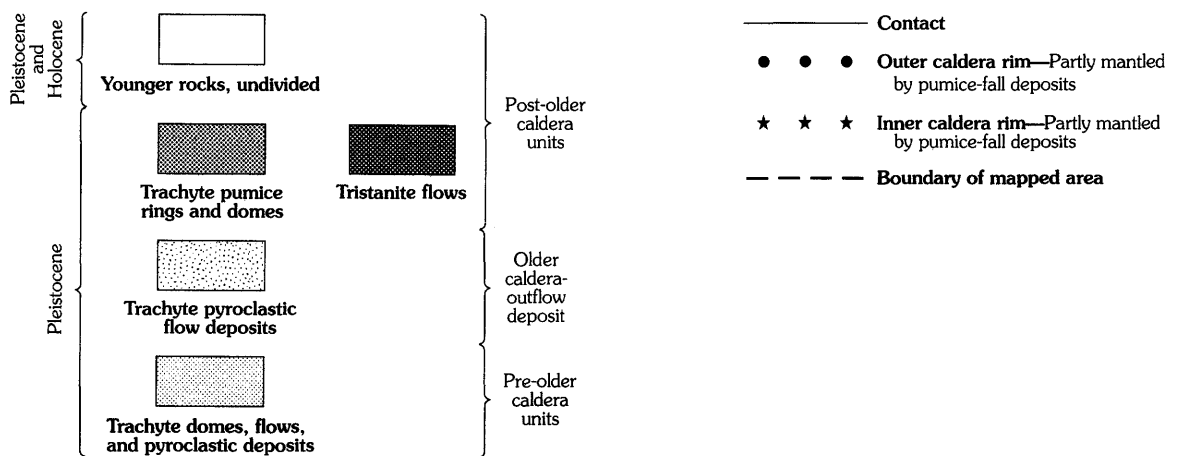
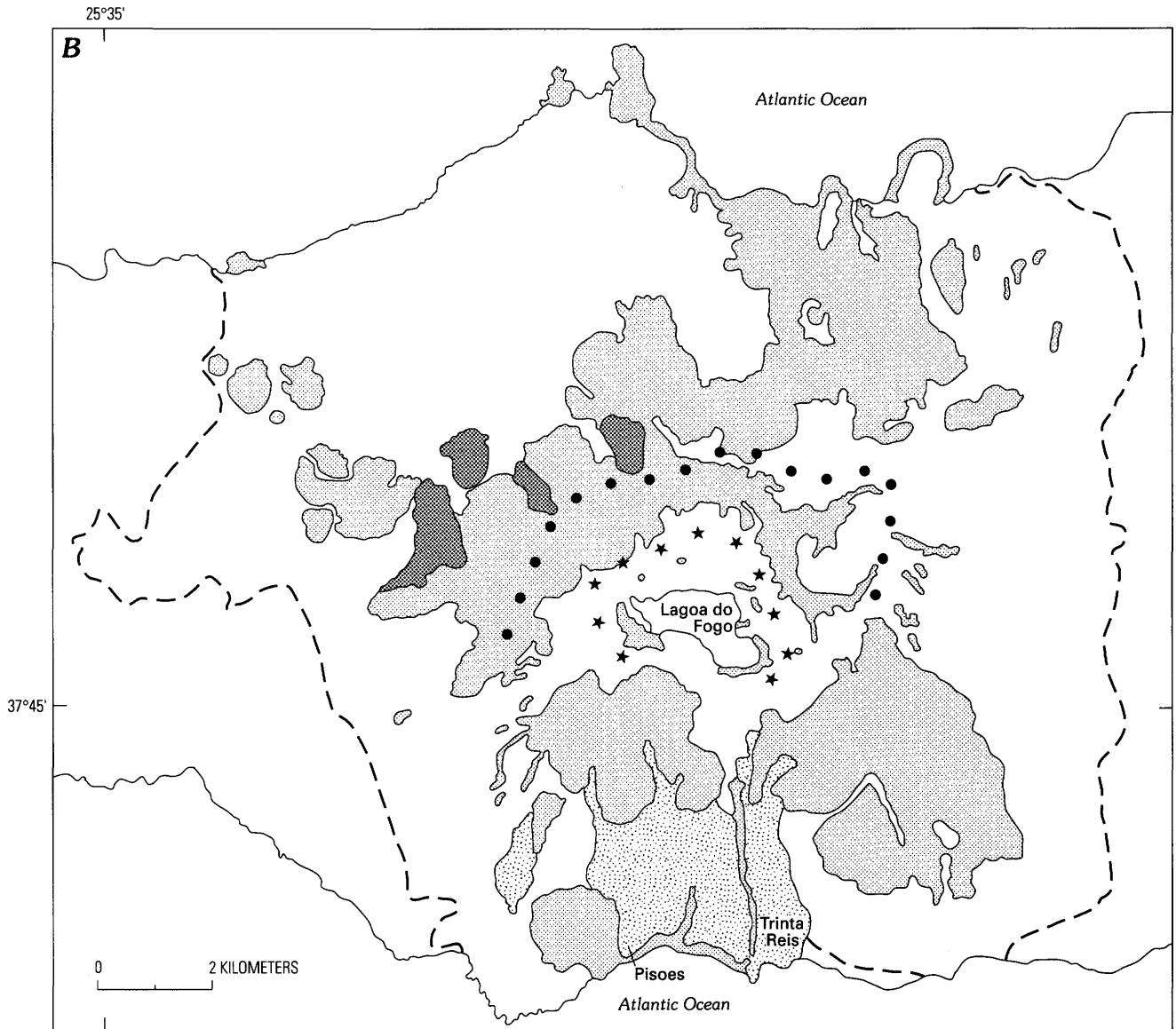


Figure 6 (above and following pages). Generalized geologic maps of Agua de Pau volcano. *A*, Units predating the younger caldera-outflow deposits. *B*, Younger caldera-outflow deposits. *C*, Units postdating the younger caldera-outflow deposits.



EXPLANATION

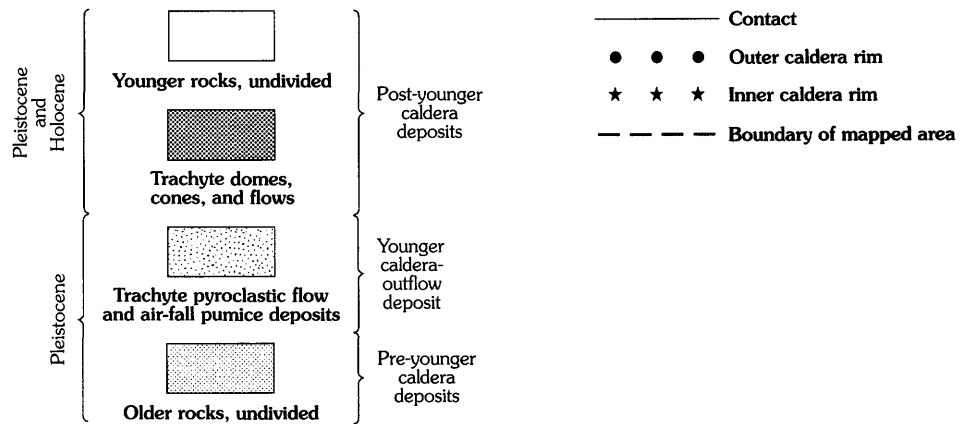


Figure 6. Generalized geologic maps of Agua de Pau volcano—Continued.

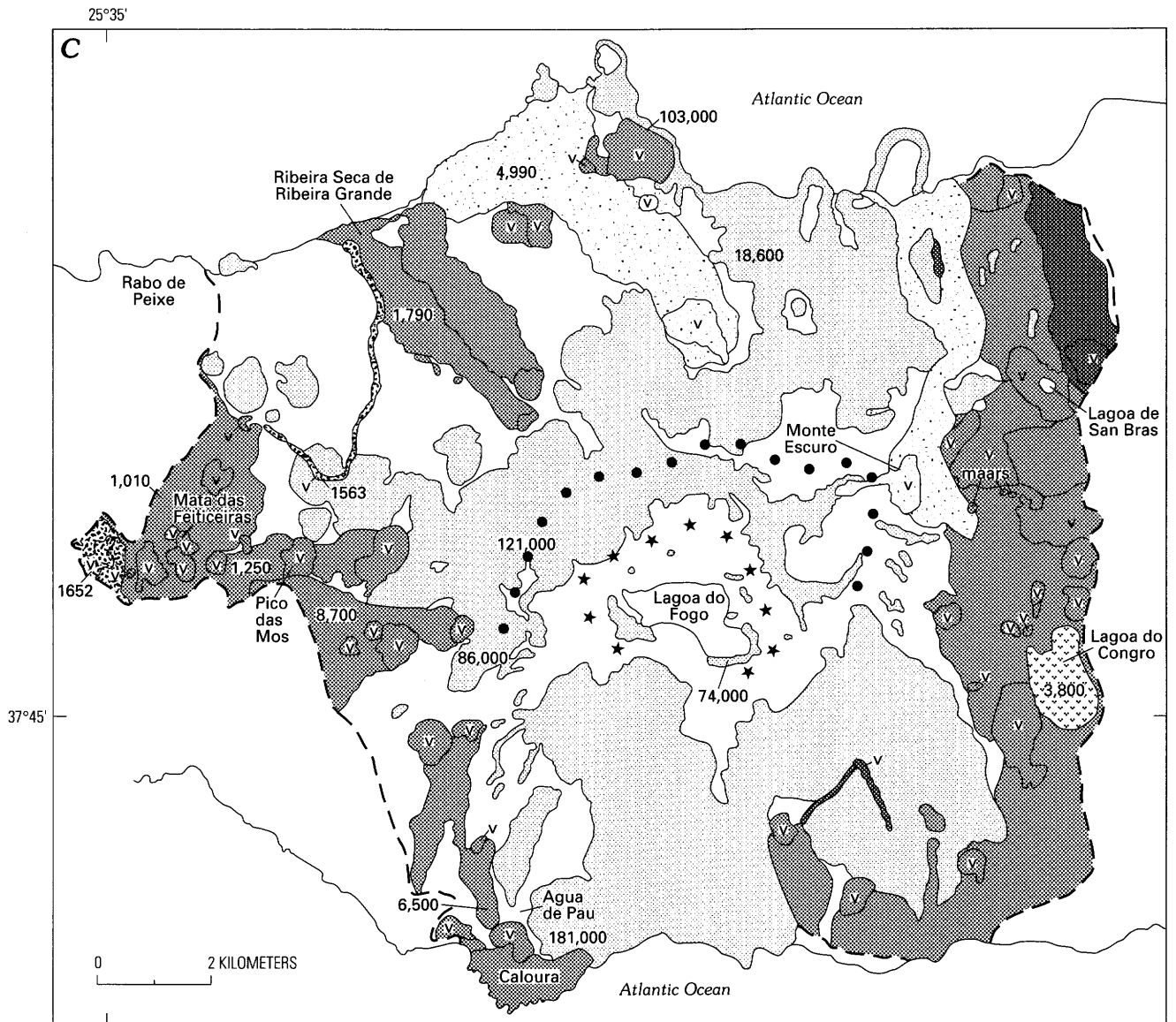


Figure 6. Generalized geologic maps of Agua de Pau volcano—Continued.

mafic vents are known within the calderas. Trachytic vents on Agua de Pau are within an area of about 17 by 14 km (fig. 6A), the largest of the three stratovolcanoes.

Several hot springs, with temperatures commonly near boiling, are on Agua de Pau, mainly on its northwestern flank (Zbyszewski and others, 1958; Zbyszewski and Ferreira, 1959). They are near intersections of northwest-trending faults and the outer caldera boundary. In addition, A.M.R. da Silva (written commun., 1984) recently found an inactive hot spring deposit on the southern flank of the volcano. The hot springs suggest that hot rock or magma associated with the late Pleistocene and Holocene eruptions is close to the surface. Six holes have been drilled to evaluate the geothermal resource, and more are planned.

Pleistocene Units

The oldest subaerial rocks of Agua de Pau volcano (fig. 6A) include a trachyte dome ($181,000 \pm 15,000$ years old; Gandino and others, 1985) on the southern coast, a trachyte flow ($121,000 \pm 5,000$ years old) near the summit, and trachytic welded tuffs (a representative one is $103,000 \pm 7,000$ years old; Gandino and others, 1985) and associated mudflows on the northern coast. Xenoliths of welded tuff possibly correlative with that on the northern coast are common in late Pleistocene and Holocene pumice deposits erupted from within the inner caldera. Muecke and others (1974) obtained K-Ar ages of $117,000 \pm 24,000$ years (57 m depth) and $280,000 \pm 140,000$ years (950 m depth) for

EXPLANATION

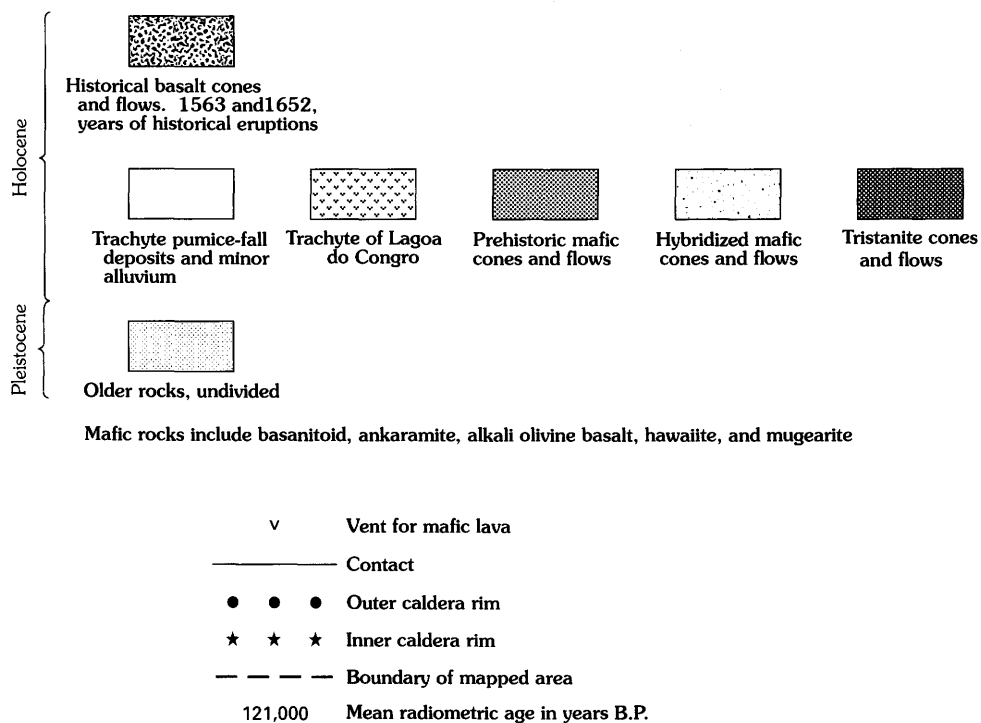


Figure 6. Generalized geologic maps of Agua de Pau volcano—Continued.

samples of drill core on the northwestern flank of Agua de Pau. These deposits formed during a period when Agua de Pau may have been much more active than it has been during the past 100,000 years (Muecke and others, 1974).

The main edifice of the volcano consists of trachytic lava flows, domes, and pyroclastic deposits that probably are about 40,000–100,000 years old (available K-Ar ages are 46,000–86,000 years; Gandino and others, 1985; E.H. McKee, written commun., 1986). Mafic eruptions occurred on the outer flanks of the volcano, outside the area of trachytic activity. One of the best exposures of the early trachytic deposits is in a sea cliff on the southern coast, where Booth and others (1978) recognized products of 65 separate explosive eruptions. Charcoal from soil beneath a trachyte flow near the base of this section (between units 4 and 5 of Booth and others, 1978) has a radiocarbon age greater than 40,000 years. Shotton and Williams (1973) obtained a radiocarbon age of more than 34,200 years for unit 14 of Booth and others (1978).

Older Caldera-Outflow Deposit

Collapse of the summit area may have occurred many times, but only two deposits clearly record such catastrophic events. The outer caldera formed after eruption of several cubic kilometers of welded and nonwelded pumice, now

exposed mainly on the northeastern and southeastern flanks of the volcano (fig. 6A). Any correlative deposits on the eastern or western flanks are deeply buried by younger rocks. The volume of the outer caldera is about 5.5 km³, and the estimated subaerial volume of the caldera-outflow deposit is about 5 km³. An unknown but probably significant volume of pumice fell at sea.

The deposit fills canyons near the margins of the early trachyte flows. Welded tuff of the older caldera-outflow deposit overlies trachyte flows on the northern and southeastern flanks of Agua de Pau and underlies post-outer caldera, pre-inner caldera trachyte domes, pumice rings, and tephra on the northern flank. Along the road to Lombadas (fig. 6A), the welded tuff appears to be faulted at the caldera boundary.

The youngest dated pre-caldera trachyte flow is 46,000±6,000 years old, but stratigraphically younger trachyte flows underlie the older caldera-outflow deposit on the northern flank of the volcano. The deposit underlies a pumice ring and related central dome that have a radiocarbon age of 18,600±300 years B.P. Field relations suggest that the older caldera-outflow deposit predates a basanitoid flow dated at 26,500±500 years B.P., although that flow is outside the mapped areal extent of the caldera-outflow deposit. The deposit has been little eroded; incision of unconsolidated intracanyon pumice-fall deposits amounts to

less than 50 m in a region of relatively heavy rainfall. The age of the older caldera-outflow deposit is thus uncertain but probably is about 30,000–45,000 years on the basis of the above described stratigraphic relations. The deposit may be correlative with a deep-sea tephra unit northeast of São Miguel dated by Huang and others (1979) at about 33,600 years B.P.

The recognizable part of the deposit is dominated by a welded zone, which locally exceeds 80 m in thickness on the northeastern flank of the volcano. In a sea cliff on the northern coast, nonwelded Plinian pumice and associated pyroclastic flows 5 m thick conformably underlie the welded zone. Closer to the caldera, on the northern flank, the thickness of the lower nonwelded pumice increases to about 50 m. Mudflows, which by analogy with younger deposits from major eruptions of Agua de Pau might be expected to overlie the welded zone, have not been found because of either erosional stripping or, more likely, burial by younger pyroclastic deposits.

Post-Outer Caldera Units

No evidence exists of eruptions within the outer caldera for about 15,000–30,000 years; however, a few eruptions of tristanite (fig. 6A) and possibly mafic lavas occurred from vents on the flanks of the volcano.

Three trachyte pumice rings, two with associated central domes, formed along a northwestern trend on the northern and northeastern flanks of the volcano (fig. 6A). The radiocarbon age of the northwestern ring is $18,600 \pm 300$ years B.P. Morphologic expression, stratigraphic relations, and relative lack of erosion suggest that the other two vents are approximately the same age.

Younger Caldera-Outflow Deposit

The inner caldera apparently formed about 15,200 years ago when a large, southward-directed Plinian eruption resulted in deposition of extensive nonwelded pumice and locally welded pyroclastic flows. Emplacement of thick mudflows occurred near the end of this eruption. The welded pyroclastic flows, locally as thick as 3 m, crop out mainly along the southern sea cliff between Pisos and Trinta Reis (fig. 6B). At Trinta Reis, xenoliths of syenite make up 10–20 percent of the rock. Elsewhere, the younger caldera-outflow deposit consists mainly of pumice-fall deposits more than 5 m thick and overlying mudflows commonly more than 50 m thick. Exposed remnants of the deposit are restricted to the southern flank of the volcano. The estimated subaerial volume of this unit is about 1.5 km^3 , slightly more than that of the inner caldera; an unknown, but probably significant volume of pumice fell at sea. Radiocarbon ages of the basal Plinian deposit and of the overlying welded tuff are $15,190 \pm 280$ and $15,180 \pm 150$

years B.P., respectively. The caldera of Santa Barbara volcano on Terceira formed at about the same time (Self, 1976).

The evidence that a caldera formed at this time is less compelling than it is for the other three cases studied, chiefly because of burial by thick pumice deposits. The principal data suggesting that eruption of the 15,200-year-old unit was responsible for formation of the inner caldera are the somewhat greater volume of the deposit compared to the inner caldera, the lack of any other known eruption as a candidate, and the observation that the next major pumice deposit, Fogo A, mantles the caldera wall and rim.

Post-Inner Caldera Units

No significant eruptions within the inner caldera occurred for about 10,000 years; however, six trachyte domes and associated short flows formed just outside the outer caldera rim on the western and northwestern flanks of the volcano (fig. 6B). No deposit older than Fogo A (Walker and Croasdale, 1970) overlies the domes, which therefore could be either latest Pleistocene or Holocene in age.

Holocene Units

Fogo A

The inner caldera of Agua de Pau became active again about 5,000 years ago, when the voluminous Fogo A Plinian fall deposit (fig. 6C), pyroclastic flows, and late mudflows (Walker and Croasdale, 1970) were erupted. The Fogo A deposit rests directly on the 15,200-year-old caldera-outflow deposit on the southern flank of the volcano.

The Fogo A deposit displays complexities not previously recognized by Walker and Croasdale (1970) that indicate Fogo A may be the product of at least five separate eruptions. An artificial exposure about 3 km south of Lagoa do Fogo reveals an approximately 8-m-thick section of syenite-bearing Fogo A that contains four internal soils ranging in thickness from 2.5 to 15 cm, in addition to Plinian fall and pyroclastic surge deposits discussed by Walker and Croasdale (1970). The thicker soils in particular suggest that Fogo A formed over a significant period of time, perhaps several decades or centuries, rather than during a single short-lived event.

Moore and Rubin (1991) reported nine new ages of charcoal collected from pyroclastic surge beds, pyroclastic flow deposits, and the base of the basal Plinian bed of the Fogo A deposit. These samples are from different locations on all flanks of the volcano. The results (fig. 7) show considerable variation. The average of all the ages is 4,936

years, almost 400 years older than the average of two ages (4435, 4672 years) reported by Shotton and others (1968, 1969). The range in mean ages is from 4,480 to 5,380 years, which in itself suggests that more than one eruption occurred. The new ages cluster around 5,000 years, and I suggest that that is a more correct mean age than the ages reported by Shotton and others (1968, 1969). Whatever its age, the Fogo A deposit is a valuable chronostratigraphic marker bed because no other major trachytic eruptions are known on central and eastern São Miguel at this time.

Post-Fogo A Pumice Deposits From Vents Within and Near the Inner Caldera

Booth and others (1978) and Walker and Croasdale (1970) described four post-Fogo A trachyte pumice fall deposits from Agua de Pau volcano, the latest in A.D. 1563. The average dormant interval between the five post-inner caldera eruptions was about 1,150 years (from about 5,000 to about 400 years B.P.), longer than at either Furnas or Sete Cidades volcanoes.

Eruptions at Lagoa do Congro

Lagoa do Congro occupies a maar on the eastern flank of Agua de Pau volcano, about 5.5 km east of Lagoa do Fogo (fig. 6C). Initial activity built a trachyte dome. Explosive eruptions of trachyte pumice destroyed part of the dome and an underlying basalt flow and formed a pyroclastic deposit that is locally more than 13 m thick. An exposure of the lower part of the deposit 250 m west of the crater rim shows three lithic-rich, coarse pumice beds separated by ash and two thin soils, which indicate short time intervals between major explosive events. A quarry 1.5 km southeast of the crater exposes the upper part of the deposit, which consists of 20 coarse pumice beds separated by 20 finer grained ash beds that include surge deposits (Booth and others, 1978). The basal pyroclastic deposit has a radiocarbon age of $3,800 \pm 400$ years B.P., in agreement with the age inferred by Booth and others (1978) on the basis of soil development.

The last eruptive event at Lagoa do Congro was extrusion of a small trachyte dome and short flows on the floor of the crater. Ankaramite aa from a vent 1 km north of Lagoa do Congro later flowed down the northwestern wall of the crater, mantling it with inward-dipping flow units.

Mafic Flank Eruptions

Ankaramite, basanitoid, alkali olivine basalt, hawaiite, and mugearite were sporadically erupted from vents on the flanks of Agua de Pau during the Holocene. Most eruptions occurred west of Agua de Pau, in the zone of dominantly mafic lavas (volcanic zone 2 of Moore, 1990, 1991) that separates Agua de Pau from Sete Cidades volcano. A few eruptions occurred on the northern, eastern, and southern flanks. Dispersal of Holocene air-fall pumice mainly eastward by prevailing westerly winds resulted in thick mantles of pumice on mafic cones and flows (volcanic zone 4 of Moore, 1990, 1991) between Agua de Pau and Furnas volcanoes. A resulting illusion is that these cones are significantly older than the more prominent, thinly mantled cones and flows west of Agua de Pau.

Vents for Holocene mafic lavas, like those of Pleistocene age, are outside the area underlain by the trachytic

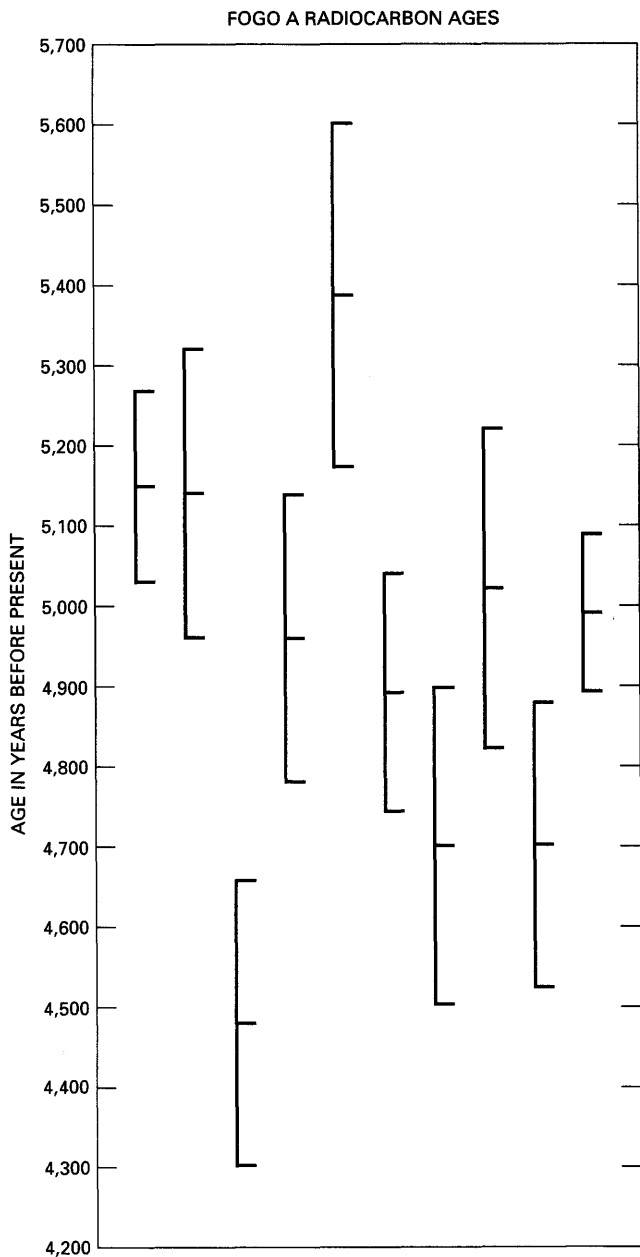


Figure 7. Radiocarbon ages of the Fogo A trachyte pumice deposit (Moore and Rubin, 1991). Brackets indicate one-sigma precision.

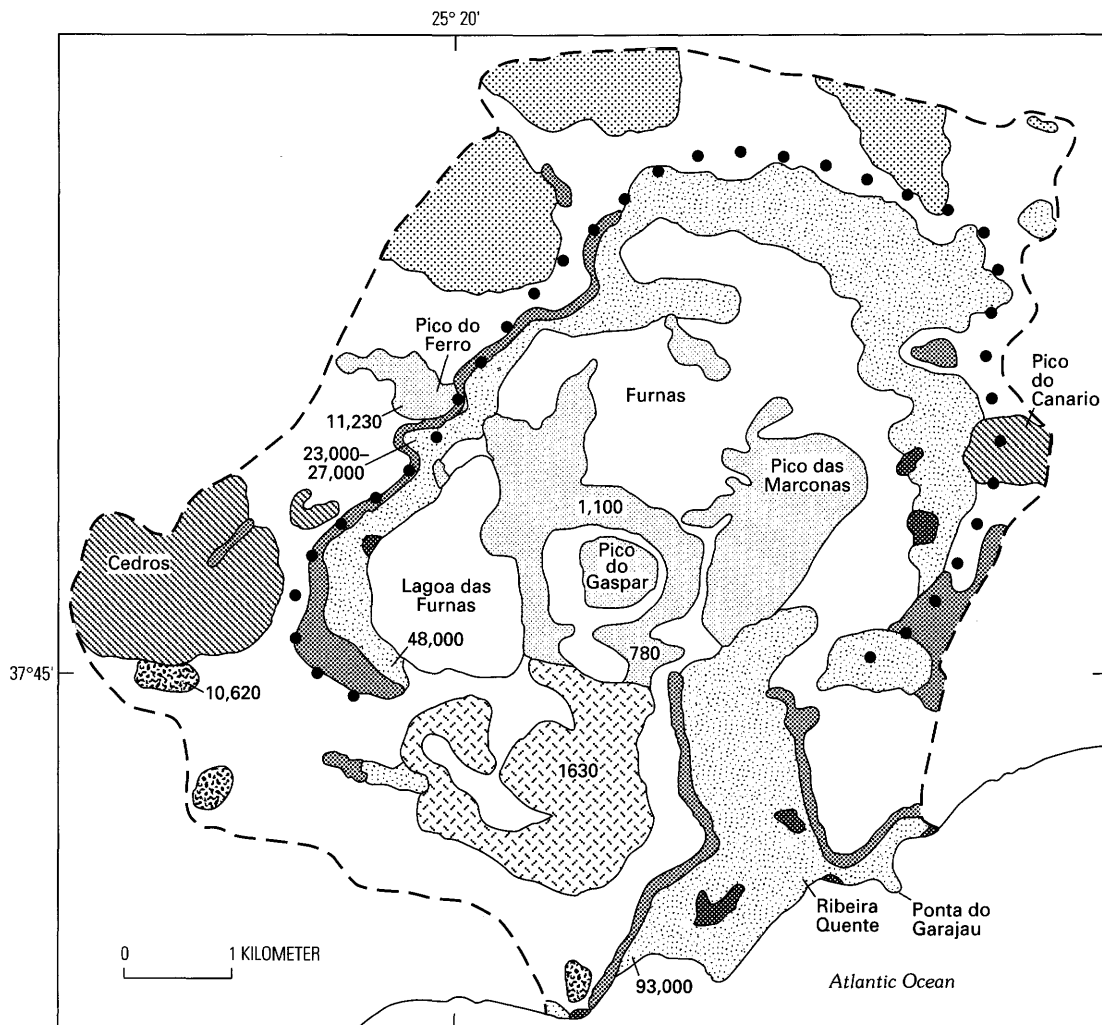


Figure 8 (above and facing page). Generalized geologic map of Furnas volcano.

magma reservoir. As at Sete Cidades, the absence of mafic vents within the caldera suggests that trachytic magma may still underlie it.

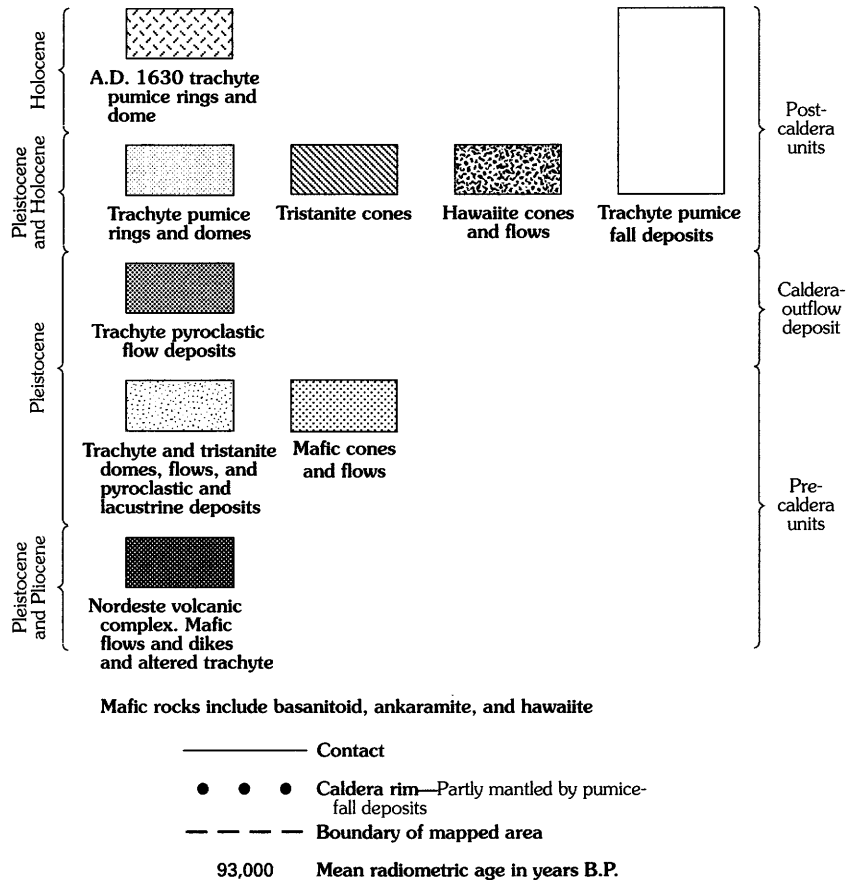
Little systematic spatial or temporal distribution of lava types exists, although concentrations of vents for certain compositions occur locally. For example, vents and flows of ankaramite are concentrated on the western and southwestern flanks of the volcano, although at least three are on the eastern and southeastern flanks. Vents of potassic hawaiite are concentrated on the eastern flank.

Lagoa de San Bras, a maar about 7 km northeast of Lagoa do Fogo (fig. 6C), consists of palagonitic tuff overlying ankaramite spatter and rootless flows. Three other maars occur about 2 km southwest of Lagoa de San Bras. Two of these three vents are on the same west-northwestern trend as a large mafic cone at the eastern edge of the mapped area, and I believe that they formed at the same time in the latest Pleistocene or early Holocene.

At least four vents erupted hybrid lavas that represent a mix of trachytic and more mafic magma (basanitoid at three vents and hawaiite at one vent). The lava of basanitoid parentage has about 58 percent SiO_2 and the lava of hawaiitic parentage (Monte Escuro; fig. 6C) about 55 percent SiO_2 . The basanitoid parentage is identified by titaniferous clinopyroxene in the groundmass, a high bulk-rock TiO_2 content, and ultramafic xenoliths. Three vents are within 1–2 km of the outer caldera boundary; possibly mafic magma rose along the margin of the trachytic magma reservoir and mixed with trachyte prior to eruption.

Ascent of mafic magma has been postulated to trigger eruption of overlying, more silicic melts at many volcanoes (Sparks and others, 1977). The A.D. 1563 trachyte Plinian eruption of Agua de Pau possibly was so initiated because extrusion of basanitoid from a vent 5.5 km west-northwest of Lagoa do Fogo immediately followed the trachyte eruption from the caldera (Weston, 1964). An extensive

EXPLANATION



hybrid flow from a vent about 4 km north of Lagoa do Fogo (fig. 6C) is interbedded with Fogo A trachyte pumice and has a radiocarbon age of $4,990 \pm 100$ years (fig. 7). Ascent of this mafic magma may have triggered the Fogo A eruption.

Several radiocarbon ages of Holocene mafic lavas on the western side (volcanic zone 2 of Moore, 1990, 1991) of Agua de Pau volcano (fig. 6C) have recently been determined (Moore and Rubin, 1991). An ankaramite cone about 4 km west of Lagoa do Fogo is $8,700 \pm 200$ years old. An ankaramite flow on the western side of the village of Agua de Pau, 6 km southwest of Lagoa do Fogo, is $6,500 \pm 100$ years old. A potassic hawaiite flow that forms a lava delta in Ribeira Seca de Ribeira Grande, on the northwestern flank of the volcano, is $1,790 \pm 150$ years old. The quarried basanitoid cone of Mata das Feiticeiras, about 8 km west of Lagoa do Fogo, is $1,010 \pm 120$ years old. Pico das Mos, a basanitoid cone dated at $1,250 \pm 150$ years B.P., is 2 km east of Mata das Feiticeiras.

A young alkali olivine basalt cone and flow in Caloura, on the southern coast of the island, overlies Fogo A trachyte pumice but has not been dated. Its flow formed a lava delta that includes the southernmost part of São Miguel.

Two eruptions of basanitoid have occurred near Agua de Pau volcano since the island was settled in the mid-fifteenth century. The A.D. 1563 eruption formed low spatter ramparts on top of Queimado, a relatively old trachyte dome about 6 km west-northwest of Lagoa do Fogo (fig. 6C). From that source, one small flow moved about 2 km northwest. The main flow went north about 5 km and inundated part of the village of Ribeira Seca de Ribeira Grande (Weston, 1964). In A.D. 1652 (Weston, 1964), Strombolian activity built a cinder cone and extruded flows about 10 km west of Lagoa do Fogo.

FURNAS VOLCANO

Furnas volcano, a stratovolcano about 800 m above sea level, occupies the east-central part of São Miguel (fig. 2). Its subaerial volume of about 60 km^3 has increased at an estimated rate of $0.06 \text{ km}^3/\text{century}$. A region of mafic and minor trachytic vents and associated flows about 8 km long (volcanic zone 4 of Moore, 1990, 1991) separates Furnas and Agua de Pau volcanoes. The Povoação caldera of the

inactive Nordeste volcano adjoins the eastern side of Furnas. A caldera about 6 km in diameter, with walls as high as 0.5 km, truncates the summit of Furnas volcano and contains Lagoa das Furnas (fig. 8). Eruptive units predating the caldera crop out chiefly in the caldera walls and in sea cliffs on the southern coast. At least 10 eruptions of trachyte pumice have occurred from intracaldera vents during the past 5,000 years (Booth and others, 1978); these eruptions formed incomplete pumice rings and associated trachyte domes distributed across the caldera floor. Pre- and post-caldera cones of ankaramite, basanitoid, and hawaiite are outside the caldera, chiefly on its northern and western sides; some pre-caldera mafic flows crop out in the caldera walls. Post-caldera cones, domes, and flows of tristanite erupted just west of the caldera boundary and on the eastern caldera rim.

As at Sete Cidades and Agua de Pau volcanoes, no mafic vents are present within the caldera. The area that encloses only trachytic vents on Furnas volcano is about 8 by 6 km, intermediate in size between Agua de Pau and Sete Cidades. Despite the relatively small size of the volcano, Furnas apparently has a larger subjacent magma reservoir than does Sete Cidades. The relation between the modern Furnas magma reservoir and the apparently extinct Nordeste magma reservoir is unknown; the two volcanoes adjoin, and a connection at depth may once have existed.

Hot springs are prominent at Furnas and, along with its magnificent scenery, serve as the basis for a local tourist industry. The distribution of hot springs is shown by Zbyszewski and others (1958). Those on the northern shore of Lagoa das Furnas probably are related to the nearby caldera-bounding fault. Hot springs in the village of Furnas probably are associated with the Furnas C crater (Booth and others, 1978) or with radial fractures that formed during emplacement of the trachyte domes of Pico das Marconas (fig. 8). Hot springs along the upper Ribeira Quente (Hot River), 1 km southeast of the village, are associated with Pico das Marconas. The other principal location of hot springs is near the village of Ribeira Quente on the southern coast; here, they probably formed near faults associated with the southern caldera boundary. The hot springs suggest that a residual heat source associated with the frequent Holocene eruptions is close to the surface.

Pleistocene Units

Pre-Caldera Units

The Quaternary Furnas volcano overlies the 1- to 4-m.y.-old Nordeste volcanic complex (Fernandez, 1980), exposed near Ribeira Quente on the southern coast and locally at the base of the caldera wall. Roadcuts along the main highway between the villages of Furnas and Povoação expose highly weathered mafic flows and altered trachyte of

the Nordeste complex on the eastern wall of Furnas caldera. Xenoliths of Nordeste mafic rocks are locally common in Plinian fall deposits of Furnas volcano.

The oldest known rocks of Furnas are late Pleistocene trachyte and tristanite flows and domes exposed at the base of the caldera wall and in sea cliffs near Ribeira Quente. A tristanite flow at the base of the section, directly overlying Nordeste basalt, near Ribeira Quente has a K-Ar age of $93,000 \pm 9,000$ years, and a trachyte flow overlying Nordeste basalt near the base of the southwestern caldera wall is $48,000 \pm 4,000$ years old. I conclude that Furnas volcano was built by almost exclusively subaerial eruptions during the past 100,000 years or less.

Sea cliffs west of Ribeira Quente expose pyroclastic units displaying much of the eruptive history of Furnas (fig. 9). Overlying the dated tristanite flow are 30 m of pyroclastic flows and mudflows whose radiocarbon ages are greater than 33,000 years. The next major deposit is a 40-m-thick mudflow whose radiocarbon age is $22,060 \pm 250$ years B.P. The overlying section includes the caldera-outflow deposit, described below, and Holocene pumice-fall deposits.

The western caldera wall exposes a 250-m-thick section of mainly flows and pyroclastic deposits, which, like the southern coastal section, spans much of the eruptive history of the volcano. The sources for many of these units were nearby. Most of the sequence here postdates the $48,000 \pm 4,000$ -year-old flow.

A small canyon eroded into the caldera wall on the southern side of Pico do Ferro (fig. 8) exposes a stratigraphic section (fig. 10) that provides key information about the latest Pleistocene history of Furnas volcano. A basanitoid flow, probably from a vent west of the caldera, crops out at the base of the section. Carbonaceous sedimentary rocks of lacustrine origin, interbedded with thin pumice-fall deposits and pillow lavas of basanitoid and trachyte, overlie the basal flow. The sedimentary rocks include many algal mats containing at least five species of diatoms and a dicot indicative of shallow fresh-water conditions (Chaves, 1908; J. Platt Bradbury, USGS, written commun., 1984). The sediments were deposited in a lake of unknown size that probably was confined within a pumice ring or crater similar to those on the floor of the modern caldera. Radiocarbon ages of three separate lake beds are 23,000–27,000 years B.P. The basanitoid and trachyte pillow lavas apparently flowed into the lake from vents to the west.

Overlying the lacustrine deposits is an 18-m-thick tristanite flow containing ultramafic xenoliths. The caldera-outflow deposit caps this tristanite. Three younger tristanite flows that may have cascaded into the caldera from the top of the Pleistocene section; they came from post-caldera vents to the west and southwest and are overlain by Holocene pumice.

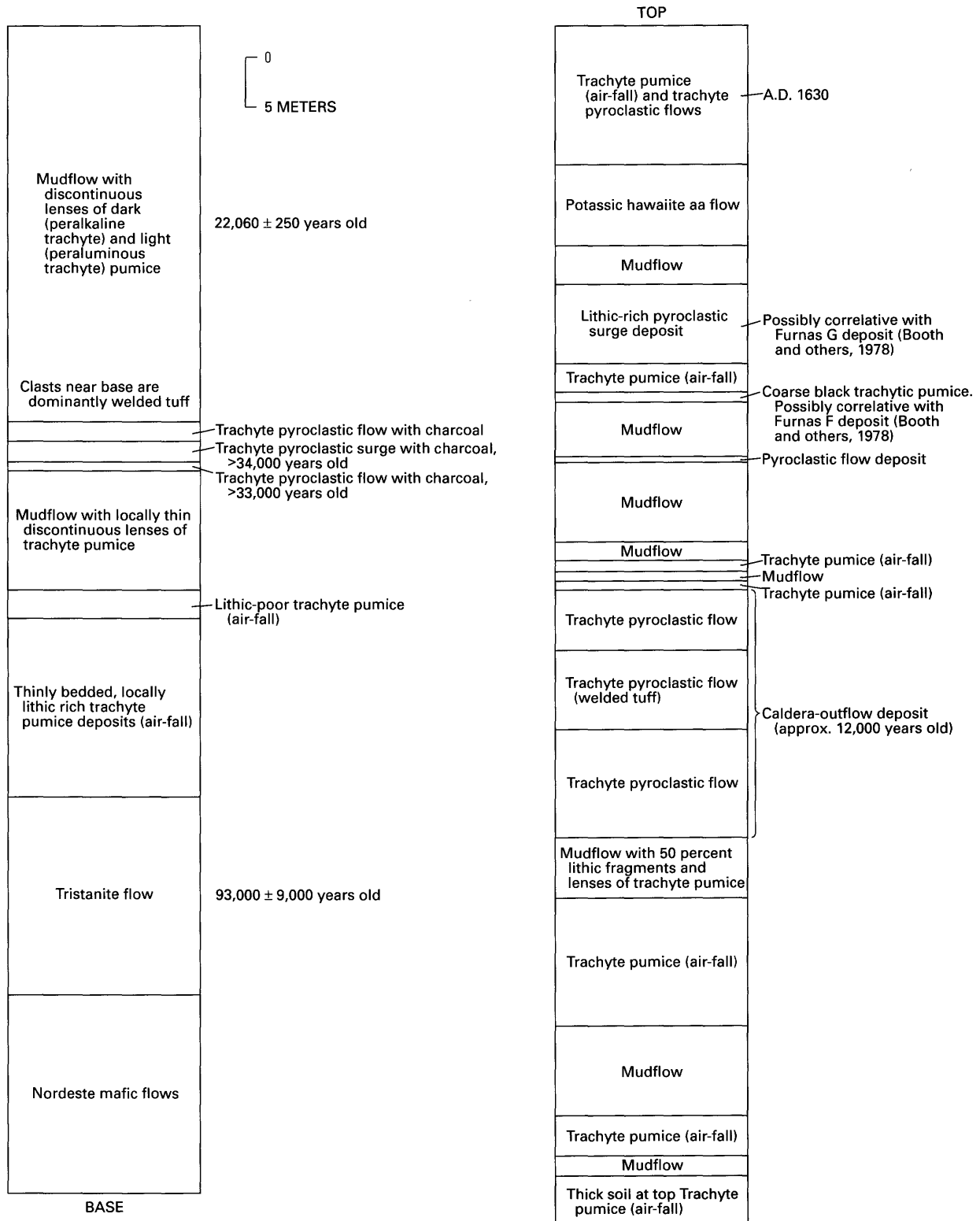


Figure 9. Composite measured stratigraphic section, sea cliff west of Ribeira Quente on southern flank of Furnas volcano. Units dip 0°–26°W.

Other lacustrine deposits, interbedded with potassic hawaiite pillow lava, crop out 2 km northeast of the section shown in figure 10, on the northern side of the village of

Furnas. These deposits are older than the 2,900±120-year-old Furnas C deposit (Shotton and Williams, 1971; Booth and others, 1978), whose crater rim truncates them.

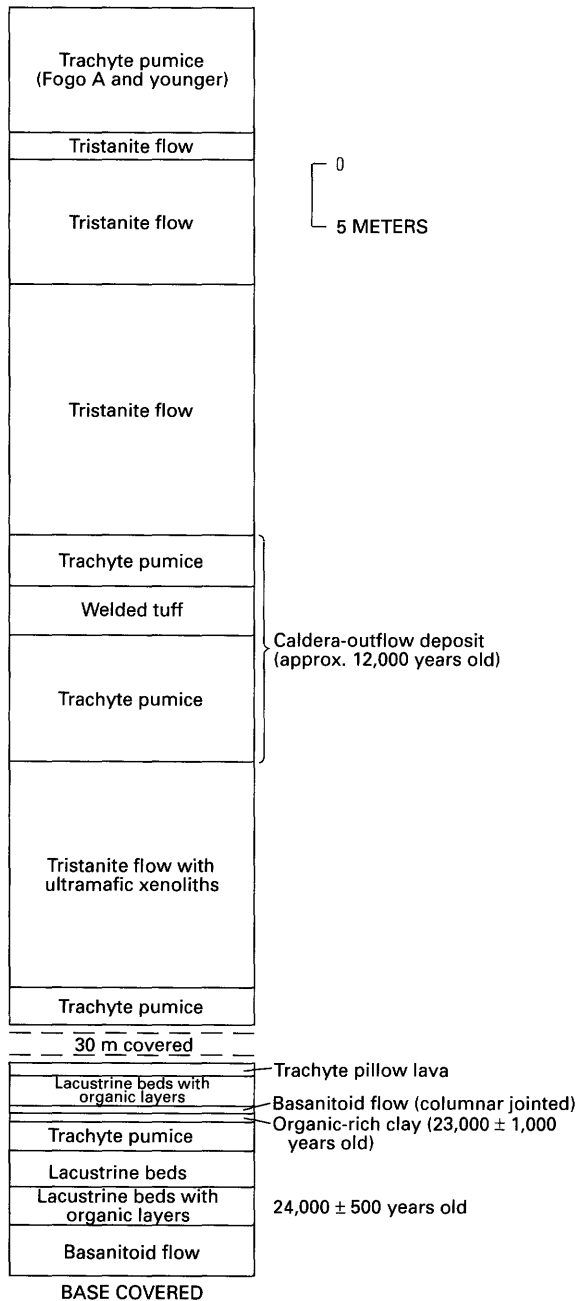


Figure 10. Measured stratigraphic section, western wall of Furnas caldera on southern side of Pico do Ferro. Dips are approximately horizontal.

Other major pre-caldera units exposed on the western and northern caldera walls are chiefly flows of ankaramite, potassic hawaiiite, and tristanite from vents west and north of the caldera. These flows are interbedded with trachytic deposits, chiefly mudflows and pumice of Plinian or sub-Plinian origin.

Caldera-Outflow Deposit

The caldera of Furnas volcano formed about 12,000 years ago in response to ejection of trachyte pumice that

formed a locally welded outflow deposit. This deposit is the uppermost unit truncated by the caldera wall in most places, except in the canyon whose stratigraphy is shown in figure 10; younger pumice-fall deposits mantle the caldera rim and wall. The caldera-forming eruption produced pyroclastic flows directed primarily south and east. A small exposure of the deposit also occurs 10 km north of the village of Furnas.

The caldera-outflow deposit is generally 25–50 m thick but ranges from 1 to 60 m. The welded zone is less than 1 to about 25 m thick. The estimated subaerial volume of the deposit is about the same as that of the caldera (7 km³), but much tephra undoubtedly fell in the ocean.

The outflow deposit is at or just below the western caldera rim and locally is plastered against ankaramite cones just northwest of the caldera (fig. 8). It fills canyons on the southern flank of the volcano, near Ribeira Quente, and covers about half of the older Povoação caldera. This unit is the “Povoação ignimbrite” discussed briefly by Booth and others (1978) and Schmincke and Weibel (1972).

One of the best exposures of welded tuff is in an abandoned quarry on the western side of the Ribeira Quente, about 2 km northwest of the village of Ribeira Quente. The base of the deposit is concealed. The section consists of 9 m of densely welded tuff, 3 m of nonwelded pumice, and 14 m of densely welded tuff to the top of the quarry. Xenoliths of obsidian, trachyte, syenite, and basalt are present. Other good exposures are along trails west and east of the village of Ribeira Quente and at the beach in the village of Povoação.

The age of the caldera-outflow deposit is not known directly, but an overlying cluster of trachyte domes at Pico do Ferro (fig. 8) has a radiocarbon age of 11,230±100 years B.P. The soil separating the outflow deposit from the Pico do Ferro trachyte is only 10–15 cm thick and, by analogy with modern soils formed on historic pumice deposits of São Miguel, probably required only a few centuries to form.

Post-Caldera Units

Three tristanite cones, two with associated flows, and a cluster of seven trachyte domes postdate formation of the caldera; they were erupted from radial and concentric fractures that probably formed during caldera collapse. The cluster of domes, which includes Pico do Ferro, erupted along an arcuate fissure trending from N. 55° W. to due west; the fissure is approximately radial to the caldera but also is approximately parallel with a common regional fracture pattern on São Miguel. Truncation of the eastern dome at the caldera rim suggests either that caldera collapse was not yet complete when the dome formed or that part of the growing dome cascaded into the caldera.

The cone of Pico do Canario consists of tristanite pumice that is locally welded to dense obsidian. It formed atop the eastern Furnas caldera rim, and pumice cascaded into both Furnas and Povoação calderas.

Cones and flows of the Cedros area, about 1.5 km west of Lagoa das Furnas, consist of silica-rich tristanite. Five scoria cones erupted along fractures concentric to the caldera, and associated flows rafted scoria short distances from the vents. This unit overlies the caldera-outflow deposit in a deep canyon on the northeastern side of Cedros.

Tristanite scoria and a thick flow were erupted at another vent 300 m west of the caldera rim. The flow may underlie Pico do Ferro, but the contact is covered.

Except for the Pico do Ferro trachyte dome, the ages of these four post-caldera units are unknown but are either latest Pleistocene or Holocene. A potassic hawaiite cone that may overlie the Cedros tristanite has a radiocarbon age of $10,620 \pm 300$ years B.P. (fig. 8).

Holocene Units

Trachytic Deposits

No known eruptions of Furnas volcano occurred for several thousand years after formation of the caldera; however, the earliest intracaldera eruptions have not been dated.

The oldest dated Holocene unit is a lake deposit about 1 km east of the village of Furnas, 200 m northeast of the junction of the roads to Ribeira Quente and Povoação. Fine-grained, thinly bedded, well-stratified lacustrine beds include lenses of black, fine-grained carbonaceous material. This deposit has not been recognized elsewhere, and it probably formed where a mudflow or pyroclastic flow dammed the ancestral Ribeira Quente. The radiocarbon age of one carbonaceous lens is $6,520 \pm 100$ years B.P., an age not represented by known deposits elsewhere on the volcano.

At least ten Plinian and sub-Plinian eruptions of trachyte pumice, four of which accompanied emplacement of domes, occurred within the caldera during Holocene time. The stratigraphically oldest deposit forms an incomplete pumice ring, with a small central dome, on the northeastern side of Lagoa das Furnas (fig. 8). The lake occupies two adjoining shallow depressions that probably also mark vent locations. The Furnas A or B deposits of Booth and others (1978) possibly came from these vents.

The largest known Holocene pumice eruption produced the Furnas C deposit (Booth and others, 1978) $2,900 \pm 120$ years B.P. (Shotton and Williams, 1971). The incomplete pumice ring that formed during this eruption crops out north and west of the village of Furnas. A late stage of the eruption produced thick mudflows that cover the northern part of the caldera floor.

The next major eruption on the floor of Furnas caldera formed the two trachyte domes of Pico das Marcas and associated pumice rings. Booth and others (1978) suggested that these vents were the sources of their Furnas E and H pumice deposits.

Pico do Gaspar is a trachyte dome about 1 km east of Lagoa das Furnas. Two nested incomplete pumice rings surround the dome. According to Booth and others (1978), these vents produced three widespread pumice deposits, Furnas F, G, and I. Charcoal from the F deposit in a quarry 1.5 km east of Pico do Gaspar has a radiocarbon age of $1,100 \pm 60$ years B.P., and charcoal from the G deposit on the eastern caldera rim is 780 ± 120 years old.

The most recent eruption of Furnas, in A.D. 1630 (Weston, 1964; van Padang and others, 1967), produced three partly nested, incomplete pumice rings and a central dome of trachyte on the southern caldera floor southeast of Lagoa das Furnas (fig. 8). The distribution and relative ages of the pumice rings indicate that the active vent moved west-northwestward about 1 km during the eruption, possibly along a concentric fracture related to collapse of the caldera. These vents lie near the southern caldera boundary, but the proximal deposits cover the rim. Vigorous mudflows swept down the Ribeira Quente and inundated the village at its mouth. Charcoal-rich pyroclastic flows characterize the base of the deposit at many localities. This charcoal yielded a radiocarbon age of 295 ± 40 years B.P., in agreement with the known age of 320 years (before A.D. 1950). Other pyroclastic flows occur higher in the section, where they are interbedded with Plinian fall deposits.

At least 191 people reportedly were killed by the 1630 eruption, but accounts (Weston, 1964; van Padang and others, 1967) vary as to the cause: earthquakes preceding the eruption, hot pumice fall (probably actually pyroclastic flows), or mudflows. All of these events undoubtedly occurred, but mudflows sweeping down the valley to the village of Ribeira Quente likely caused the most deaths. The area of Ribeira Quente has been inundated repeatedly by mudflows and pyroclastic flows, most notably those associated with the caldera-outflow deposit, the Furnas C eruption, and the 1630 eruption.

Radiocarbon ages of the Furnas C and younger deposits permit estimation of the average dormant interval of Furnas volcano. Eight trachytic eruptions occurred between 2,900 and 320 years B.P., an average dormant interval of about 369 years. The interval decreased to only 195 years, however, during the period from 1,100 (Furnas F) to 320 years B.P., when five eruptions occurred. The present quiet interval has now lasted 320 radiocarbon years and 361 calendar years, and Furnas may be overdue for its next eruption.

Mafic Deposits

In contrast to Sete Cidades and Agua de Pau, post-caldera eruptions of mafic lavas have been rare on the flanks of Furnas. Potassic hawaiite cones (fig. 8), one dated at $10,620 \pm 300$ years B.P., are on the southern side of the

Cedros tristanite cones. A potassic hawaiite flow, interbedded with pumice between the Furnas C and A.D. 1630 deposits, is on the southern flank of the volcano. This flow overlies consanguineous cinders from a nearby vent, buried during A.D. 1630 or an earlier eruption, just south of the southern caldera boundary.

PETROGRAPHY

Mafic Rocks

Mafic rocks on the three volcanoes include ankaramite, basanitoid, alkali olivine basalt, hawaiite, and mugearite.

Ankaramite contains abundant olivine and clinopyroxene and minor plagioclase phenocrysts in an intergranular to intersertal groundmass of plagioclase, clinopyroxene, olivine, opaque oxides, and interstitial residuum. Xenocrysts of orthopyroxene and amphibole are present in many samples, and late-stage biotite commonly fills vesicles.

Basanitoid has normative but not modal feldspathoids and thus is not termed basanite. Rocks are commonly aphyric but many contain scattered olivine and rare clinopyroxene and plagioclase phenocrysts in an intersertal to intergranular groundmass of the same minerals, opaque oxides, and interstitial residuum. Clinopyroxene in the groundmass is titaniferous (pleochroic brown or purple), reflecting the high bulk-rock TiO_2 content (generally >3.5 weight percent).

Alkali olivine basalt is less common than the other mafic rock types and is transitional among primitive basanitoid, accumulative ankaramite, and differentiated hawaiite and mugearite. Vent deposits and flows typically have a few volume percent of olivine > clinopyroxene > plagioclase phenocrysts in an intergranular to intersertal groundmass of the same minerals, opaque oxides, and interstitial residuum. Alkali olivine basalt is not easily distinguished in the field from other mafic rocks but is defined here as having less than 5 percent normative nepheline and less than 15 percent olivine and clinopyroxene phenocrysts.

Hawaiite typically has an intersertal to pilotaxitic or hyalophitic texture and is generally almost aphyric. A few samples contain less than 1 percent each of one or more of the following phenocryst minerals: olivine, clinopyroxene, plagioclase, amphibole, and biotite. Amphibole may be xenocrystic, for it invariably has rims of opaque oxides (opacite). Hawaiite is relatively rich in K_2O , as are most of the rocks on São Miguel (Schmincke and Weibel, 1972), and could be called trachybasalt.

Mugearite is relatively uncommon, although it occurs in vent deposits and flows on all three volcanoes. It is most abundant on Sete Cidades, where relatively old (>30,000

years) flows crop out chiefly in sea cliffs on the northern, western, and southern coasts. Mugearite appears completely transitional to hawaiite; samples of both generally have similar phenocryst populations and are indistinguishable in the field. Amphibole is an important phenocryst in the thick section of mugearite in the sea cliff south of Ponta da Ferraria (fig. 4).

Intermediate to Silicic Rocks

Tristanite, which generally has $\text{K}_2\text{O}/\text{Na}_2\text{O} \geq 1$ and SiO_2 of 55–58 percent, is relatively uncommon but occurs throughout the subaerial sequence on all three stratovolcanoes. Many tristanite vent deposits and flows are aphyric; others contain 1 percent or less of one or more of the following phenocrysts: olivine, clinopyroxene, sanidine, plagioclase, amphibole, biotite, and opaque oxides. Some, especially those containing olivine, may be hybrid mixtures of trachytic and more mafic magmas. A thick aphyric tristanite flow underlying the younger caldera-outflow deposit on the southern flank of Agua de Pau (fig. 6A) contains 5–10 percent late-stage biotite in vesicles.

Most trachyte contains phenocrysts of alkali feldspar (generally sanidine or anorthoclase), plagioclase, biotite, opaque oxides, green clinopyroxene, and rare zircon and apatite. Amphibole that is possibly xenocrystic is in several samples. One trachyte flow on the southern flank of Agua de Pau contains 40 volume percent sanidine phenocrysts. Sphene microphenocrysts are unusually abundant (as much as 2–3 percent) in several trachyte flows and domes from Agua de Pau. Storey (1981) reported that clinopyroxenes in young pumice deposits from Agua de Pau are generally salite and have low Al_2O_3 , TiO_2 , and Na_2O . Some trachyte is aphyric or almost so; most is in peralkaline domes on the western and northwestern flanks of Agua de Pau.

Syenite Xenoliths

Xenoliths of syenite as large as 0.5 m in diameter locally are common in trachyte pumice deposits of Furnas and Agua de Pau volcanoes. They are much rarer on Sete Cidades, although several dozen were observed in the sea cliff near Ponta da Ferraria. They are most readily found in alluvial deposits within the calderas and on the flanks of the volcanoes. I found xenoliths of syenite throughout the subaerial sequence on Agua de Pau, including ca. 100,000-year-old welded tuffs on the northern coast of São Miguel. They are particularly abundant in the 15,200-year-old younger caldera-outflow deposit, in which they locally make up 20 percent of the rock.

Cann (1967) discussed the mineralogy of several samples of Agua de Pau syenite; they chiefly contain sanidine, arfvedsonite, quartz, and aegirine, as well as minor biotite and zircon or dalyite. Some lack quartz and contain sodalite. Xenoliths of syenite at Furnas volcano are generally similar to those at Agua de Pau, but most lack quartz and contain sodalite.

E.H. McKee (written commun., 1986) dated a syenite xenolith from a trachyte pumice deposit on Furnas at 0.973 ± 0.029 Ma. This relatively old age suggests that the syenite may have formed within Nordeste volcano.

Cann (1967) and Schmincke (1973) noted that syenite of Agua de Pau may contain either normative nepheline or quartz, and many samples are peralkaline; thus, the syenite generally matches the compositions of the extrusive rocks and is probably cognate.

Xenoliths of Mafic and Ultramafic Rocks

Xenoliths of mafic and ultramafic rocks are in several vent deposits and flows of basalt, basanitoid, and ankaramite on each volcano. The most remarkable sites are on Sete Cidades. The ankaramite cone of Eguas (fig. 3) and its flows contain thousands of xenoliths, including spinel lherzolite and dunite. Some samples have a relatively fine grained, recrystallized groundmass surrounding megacrysts of clinopyroxene, orthopyroxene, and kink-banded olivine. No garnet is known in these rocks or elsewhere on the three volcanoes. Some of these xenoliths may have been carried up from the mantle. Many, however, have cumulate texture and sufficient Na_2O to be nepheline normative; these may have formed in the conduit system of the volcanoes.

Pico das Camarinhas, an 840-year-old ankaramite cone near the western end of São Miguel, and its flow contain abundant xenoliths of hornblende gabbro, hornblendite, and pyroxenite.

The ankaramite cone of Mafra, 1 km east of the village of Mosteiros, and its flow contain common xenoliths of dunite (megacrysts of olivine in a finer grained, recrystallized groundmass of olivine and spinel) of possible mantle origin, wehrlite, olivine clinopyroxenite, green pyroxenite, black pyroxenite, websterite, and gabbro.

One of the most unusual occurrences of xenoliths is in the relatively old tristanite flow that forms Ponta do Garajau, 0.8 km east of Ribeira Quente on Furnas volcano (fig. 8). Xenoliths of olivine clinopyroxenite and syenite are common in a hybridized host that has 59.6 percent SiO_2 and phenocrysts or xenocrysts of sanidine, plagioclase, olivine, clinopyroxene, amphibole, and biotite. The clinopyroxenite contains normative, but not modal, nepheline and leucite; this is the only example of normative leucite among the rocks analyzed for this study.

MAJOR ELEMENT CHEMICAL COMPOSITIONS

Lava flows and pyroclastic materials of Sete Cidades, Agua de Pau, and Furnas volcanoes belong to the alkali basalt-trachyte suite (Irvine and Barager, 1971). Variation diagrams (figs. 11–13) based on 357 new chemical analyses show, for the most part, a continuum in chemical compositions among these rocks. Analytical data and normative compositions of representative rocks from the three volcanoes are given in table 1. A sample from each map unit has been analyzed.

Tholeiitic basalts are on the adjacent Mid-Atlantic Ridge but not on São Miguel (White and others, 1979). A few mafic rocks on all three volcanoes contain normative hypersthene and olivine, but these are either high-silica hawaiite, mugearite, tristanite, and hybrid rocks or ankaramite and basanitoid that have low alkali concentrations, possibly because of post-eruptive leaching. I consider them all to be alkali basalt or its derivatives, consistent with criteria of Poldervaart (1964).

Silica-Variation Diagrams

The Al_2O_3 versus SiO_2 variation diagram (fig. 11A) shows generally increasing alumina with increasing silica through the basalt range, reflecting the lesser abundance of olivine in more silicic compositions. The curve is relatively flat from about 50 to 62 percent SiO_2 . Alumina then decreases with increasing silica in the most silicic rocks, which include peralkaline trachyte. Below about 62 percent SiO_2 , rocks of Agua de Pau have generally lower alumina than do those of Sete Cidades and Furnas volcanoes.

The MgO versus SiO_2 variation diagram (fig. 11B) shows a wide range in magnesia contents of basaltic rocks, in accord with olivine-controlled differentiation. Above about 50 percent SiO_2 , the curve is almost straight; the few deviations represent hybrid rocks, mainly from Agua de Pau, that result from mixing of mafic and trachytic melts.

The $\text{FeO} + 0.9 \cdot \text{Fe}_2\text{O}_3$ versus SiO_2 variation diagram (fig. 11C) shows a fairly straight line. Basaltic lavas surrounding Agua de Pau have slightly higher iron contents than those on the flanks of the other two volcanoes. The greatest scatter is among the most silicic compositions on Agua de Pau, where magnesia abundances are undetectable.

Likewise, the $(\text{FeO} + 0.9 \cdot \text{Fe}_2\text{O}_3) / \text{MgO}$ versus SiO_2 variation diagram (fig. 11D) emphasizes the marked iron enrichment above about 62 percent SiO_2 , most prominent among the trachytic rocks of Agua de Pau.

The CaO versus SiO_2 variation diagram (fig. 11E) shows a fairly straight line. Deviations at the basaltic end are for xenoliths of gabbro and peridotite, as well as for olivine-controlled differentiation and resulting variations in

Table 1. Chemical analyses and normative compositions for representative rocks from Sete Cidades, Agua de Pau, and Furnas volcanoes, São Miguel, Azores
[In weight percent]

	1	2	3	4	5	6	7	8
Chemical analysis								
SiO ₂	44.2	45.0	50.8	54.0	58.2	59.6	61.8	63.4
Al ₂ O ₃	15.9	10.3	18.7	19.2	17.0	18.7	18.3	18.4
Fe ₂ O ₃	2.8	3.4	2.2	1.8	2.9	2.5	2.5	2.4
FeO	10.0	7.4	6.5	4.9	2.8	1.8	1.2	0.76
MgO	5.6	17.2	3.9	2.3	1.5	1.9	0.41	0.45
CaO	10.7	10.0	7.3	4.8	3.0	2.9	0.87	0.68
Na ₂ O	2.6	1.8	4.5	5.7	5.3	5.3	7.9	6.8
K ₂ O	1.9	0.90	2.7	3.6	5.2	5.6	5.5	5.1
H ₂ O ⁺	0.34	0.08	0.19	0.18	0.48	0.19	0.66	0.06
H ₂ O ⁻	0.14	0.31	0.31	0.30	0.59	0.30	0.16	0.43
TiO ₂	4.9	2.1	2.6	1.9	1.6	1.1	0.46	0.60
P ₂ O ₅	0.87	0.44	0.81	0.57	0.51	0.23	0.05	0.08
MnO	0.17	0.14	0.16	0.22	0.14	0.15	0.25	0.21
CO ₂	0.01	0.02	0.04	0.01	0.01	0.02	0.04	0.02
Sum	100.13	99.09	100.71	99.48	99.23	100.29	100.10	99.39
Normative composition								
Q	—	—	—	—	—	—	—	0.71
C	—	—	—	—	—	—	—	0.71
Or	11.29	5.38	15.96	21.51	30.31	33.27	32.86	30.55
Ab	15.09	11.75	31.28	38.70	44.34	44.02	49.90	58.30
An	26.25	17.67	22.85	16.34	9.52	10.76	—	2.75
Ne	3.79	2.02	3.68	5.49	—	0.54	7.72	—
Ac	—	—	—	—	—	—	1.10	—
Ns	—	—	—	—	—	—	0.49	—
Di-Wo	8.91	12.38	3.27	1.62	2.04	0.87	1.58	—
Di-En	4.69	8.67	1.64	0.70	1.03	0.42	0.27	—
Di-Fs	3.96	2.66	1.56	0.92	0.97	0.43	1.44	—
Hy-En	—	—	—	—	1.18	—	—	1.15
Hy-Fs	—	—	—	—	1.10	—	—	4.00
Ol-Fo	6.54	24.43	5.66	3.57	2.74	3.04	0.53	—
Ol-Fa	6.09	8.26	5.94	5.12	2.83	3.37	3.11	—
Mt	2.00	1.70	1.35	1.06	0.78	0.65	—	0.48
Il	9.36	4.05	4.94	3.65	2.53	2.11	0.87	1.16
Ap	2.06	1.07	1.92	1.37	0.64	0.54	0.12	0.19

1. Basanitoid, basal flow on northwestern caldera wall, Furnas volcano.
2. Ankaramite, basal flow on sea cliff below Feteiras, Sete Cidades volcano.
3. Hawaiite, basal flow on sea cliff in Mosteiros, Sete Cidades volcano.
4. Mugarite, flow on sea cliff below Camarinhas cone, Sete Cidades volcano.
5. Hybridized basanitoid, flow on northern flank of Agua de Pau volcano.
6. Tristanite, basal flow on sea cliff east of Ribeira Quente, Furnas volcano.
7. Peralkaline trachyte, welded pumice of the Gaspar ring, Furnas volcano.
8. Trachyte, flow in Feteiras, Sete Cidades volcano.

phenocryst abundances. Ten samples of trachyte from Agua de Pau and one from Sete Cidades have no detectable CaO, another indication of their alkalic nature.

The Na₂O versus SiO₂ variation diagram (fig. 11F) shows considerable variation throughout the compositional range. Three samples of trachyte from Furnas have low

Na₂O and probably are actually altered Nordeste rocks. The rest of the variation likely results from (1) olivine-controlled differentiation in the basaltic range, (2) differences in initial chemical composition or in degree of partial melting of the mantle source, (3) hybridization, (4) post-solidification leaching, or (5) some combination of these processes.

The K_2O versus SiO_2 variation diagram (fig. 11G) resembles the Na_2O - SiO_2 plot, except that (1) the generally higher K_2O in Furnas mafic and trachytic rocks is apparent and (2) above about 63 percent SiO_2 K_2O begins to decrease, mainly in Agua de Pau rocks, because of crystallization and removal of potassium feldspar (Storey, 1981).

The Na_2O+K_2O versus SiO_2 variation diagram (fig. 11H), on which is drawn the line separating alkalic basalts from tholeiites in Hawaii (Macdonald and Katsura, 1964), shows that São Miguel rocks are strongly alkalic. The eight rocks in the tholeiitic field include an altered Nordeste basalt, an olivine clinopyroxenite xenolith from Furnas, and six nepheline normative mafic and ultramafic xenoliths from Sete Cidades. Figures 11E and 11H can be combined to yield a Peacock (1931) index of about 49, further indication of the alkalic nature of the São Miguel rocks.

The K_2O/Na_2O versus SiO_2 variation diagram (fig. 11I) shows that, except for three highly potassic Furnas trachytes, the ratio increases only slightly with increasing silica. Higher K_2O in Furnas mafic and silicic rocks is apparent.

The TiO_2 versus SiO_2 variation diagram (fig. 11J) shows a generally straight line, except among basaltic compositions. Samples of basanitoid have typically high (>3.5 percent) TiO_2 contents, shown modally in titaniferous clinopyroxene phenocrysts and groundmass grains. Fractionation of clinopyroxene, as well as olivine and perhaps iron-titanium oxides, probably accounts for the variable TiO_2 contents in the basaltic range.

The P_2O_5 versus SiO_2 variation diagram (fig. 11K) shows wide scatter, especially below about 56 percent SiO_2 . Two fields of Agua de Pau mafic rocks high and low in P_2O_5 can be distinguished. Apatite needles are present in most mafic rocks of São Miguel, and microphenocrysts of apatite are present in many trachytes. The reason for the wide scatter in figure 11K is not immediately apparent.

Magnesia-Variation Diagrams

The Al_2O_3 versus MgO variation diagram (fig. 12A) shows a relatively straight line throughout most of the compositional range. The exceptions are at the high-magnesia end, where some analyses are of ultramafic xenoliths that may not be cognate, and at the low-magnesia (trachytic) end, where alumina decreases somewhat in the most silicic rocks as feldspar is removed.

The $FeO+0.9*Fe_2O_3$ versus MgO variation diagram (fig. 12B) changes slope abruptly at about 12 percent iron and 5–10 percent MgO. This change reflects the decrease in iron as relatively forsteritic olivine is accumulated in ankaramites and ultramafic xenoliths. Departures from the

general trend reflect, at the high-magnesia end, the analyses of ultramafic xenoliths and, in the basaltic range (about 5–15 percent iron), the effects of hybridization of diverse melts.

The CaO versus MgO variation diagram (fig. 12C) shows a general trend of increasing lime with increasing magnesia; the steep curve in the low-magnesia range flattens above about 8 percent MgO, where accumulation of olivine dominates. The diffuse pattern above about 15 percent CaO represents analyses of gabbroic and ultramafic xenoliths. The small cluster of Agua de Pau mafic compositions at about 6 percent iron and 7 percent MgO are hybrid rocks.

The Na_2O versus MgO (fig. 12D) and K_2O versus MgO (fig. 12E) variation diagrams are similar and show expected trends of decreasing Na_2O and K_2O with increasing magnesia. The Agua de Pau hybridized rocks are most obvious on figure 12E. The K_2O/Na_2O versus MgO variation diagram (fig. 12F) shows the generally higher K_2O in Furnas rocks and the expected trend of slightly decreasing K_2O/Na_2O with increasing magnesia.

The TiO_2 versus MgO variation diagram (fig. 12G) shows a peak in TiO_2 contents (3.5–>5 percent) at about 5–9 percent MgO, corresponding to basanitoid compositions. The scatter of points in this range reflects the dominance of olivine-controlled fractionation, although fractionation of titaniferous clinopyroxene may also be important. The cluster of low- TiO_2 hybrid rocks on the flanks of Agua de Pau is apparent.

The P_2O_5 versus MgO variation diagram (fig. 12H), similar to the TiO_2 versus MgO plot, shows a peak in P_2O_5 (0.7–1.6 percent) in basanitoids. The measurable P_2O_5 (commonly >0.1 percent) in the ultramafic xenoliths suggests they may be cognate to the volcanoes because xenoliths representing fragments of mantle residuum probably would be depleted in incompatible P_2O_5 .

AFM Diagram

The AFM plot (fig. 13) for the newly analyzed São Miguel rocks shows their alkalic nature, especially as compared to alkalic rocks from Hawaii (Macdonald, 1968). Most of the São Miguel mafic compositions are displaced toward the Na_2O+K_2O corner relative to Hawaiian compositions. A small field of four hybrid lava flows on the flanks of Agua de Pau can be distinguished. Several samples of Furnas trachyte and one from Sete Cidades are somewhat more alkalic than other samples of trachyte, although Furnas mafic rocks fall in an intermediate position. No clear distinction among the volcanoes is apparent.

DISCUSSION

The major element chemical data indicate many similarities and some significant differences among the

rocks of Sete Cidades, Agua de Pau, and Furnas volcanoes. One important similarity is that basanitoid of somewhat variable composition is the most likely parental magma from which the other magmas were derived. Perhaps the two most important differences are the common development of peralkaline compositions on Agua de Pau and the generally increasing relative abundance of K_2O from west to east.

Figure 12G indicates that almost aphyric, high- TiO_2 basanitoid occupies a unique position among the analyzed rocks from the three volcanoes. From this composition, one trend leads, with decreasing MgO and TiO_2 , to the more silicic differentiates (hawaiite to trachyte). Another trend is defined by decreasing TiO_2 and increasing MgO because of accumulation of olivine and low-titanium clinopyroxene in ankaramites. TiO_2 is lower in all rocks that trend away from basanitoid and so must be incorporated in minerals that have been removed. The most compelling field and petrographic evidence regarding the distribution of TiO_2 is that it is incorporated, under locally hydrous conditions, in biotite (Storey, 1981), basaltic hornblende-kaersutite, and ilmenite-titanomagnetite. These minerals are abundant and accompany plagioclase, pyroxene, and apatite in the common gabbro and hornblendite xenoliths in ankaramite of the Camarinhas cone.

Magnesia variation diagrams (fig. 12) (Schmincke and Weibel, 1972) suggest that olivine fractionation was important in controlling mafic compositions. However, hawaiite and more silicic rocks have been fractionated beyond olivine control, although olivine commonly is present as scattered microphenocrysts (sometimes xenocrystic) in even the most silicic compositions. The slope of many magnesia variation curves changes near 5 percent MgO, presumably because variation departs from simple olivine control at about that point. The scatter of points at higher magnesia contents suggests, however, that olivine fractionation is not the only process causing variation. The principal alternatives are (1) several parental magmas were generated beneath São Miguel that have different magnesia and other oxide contents resulting from different degrees of partial melting of a homogeneous mantle source or partial melting of an inhomogeneous mantle source, or (2) fractionation of other minerals (chiefly clinopyroxene and plagioclase but also orthopyroxene and opaque oxides) was important. Because microprobe data on mineral compositions are not yet available, quantitative modelling to test these hypotheses has not yet been attempted.

Peralkaline trachyte was erupted throughout the sub-aerial history of Agua de Pau from vents along radial and possibly concentric fractures on the western, southern, and northern flanks of the volcano, as well as from intracaldera vents. The development of volumetrically important peralkaline magmas on Agua de Pau and not on the other two volcanoes may be related to the relatively large subjacent magma reservoir of Agua de Pau, which I infer from the

distribution of trachyte vents (fig. 6) and syenite xenoliths (Booth and others, 1978). In addition, alumina contents generally are lower throughout the compositional range on Agua de Pau as compared to the other two volcanoes (figs. 11, 12) (Schmincke and Weibel, 1972). Self and Gunn (1976) and Storey (1981) found that crystallization and removal of potassium feldspar, biotite, and clinopyroxene was largely responsible for producing peralkaline trachyte on Terceira and among the post-Fogo A pumice deposits on Agua de Pau; fractionation of plagioclase (Schmincke, 1982) must also have been important. Stratigraphic and radiometric data indicate that Sete Cidades, Agua de Pau, and Furnas volcanoes commonly had lengthy repose following major eruptions, especially caldera-forming episodes. Only on Agua de Pau, however, did caldera-forming eruptions produce peralkaline rocks in great volume. It is possible that peralkalinity typically characterized the late stage of magmatic cycles on Agua de Pau, as Storey (1981) found for the post-Fogo A pumice deposits. Perhaps potassium feldspar, biotite, clinopyroxene, and plagioclase were removed during early and intermediate episodes of a cycle, ultimately resulting in development of a peralkaline melt that erupted last in the cycle. Fisher and Schmincke (1984), however, presented evidence of common chemical zonation in silicic magma reservoirs, as shown by compositions of their erupted products; therefore, development of peralkalinity may be a relatively short-term process in large magma reservoirs.

Figure 12F illustrates the general increase of K_2O from west to east across the three volcanoes. This increase somewhat mimics the increase in $^{87}Sr/^{86}Sr$ found by White and others (1976) and Hawkesworth and others (1979) and suggests that increasing distance from the Mid-Atlantic Ridge or from the Azores fracture zone accounts for the increase in K_2O . This explanation does not hold, however, when older rocks are included. For example, Nordeste rocks (Fernandez, 1980) are not enriched in K_2O relative to Furnas rocks. In addition, White and others (1976) found normal (low) $^{87}Sr/^{86}Sr$ in Pliocene basalt from Santa Maria, the next island southeast of São Miguel. I suggest that the higher abundance of K_2O , particularly in Furnas rocks, may result from partial remelting of previously erupted or intruded rocks from Nordeste volcano, such as the ca. 1-m.y.-old syenite that McKee dated, during Furnas magmatic activity. Perhaps K_2O is lowest on Sete Cidades because only a small volume of previously emplaced silicic rock was available for remelting, as suggested by the relative absence of syenite xenoliths.

Preliminary study of available chemical data suggests that a mechanism similar to that proposed by Fernandez (1980) for the origin of Nordeste volcanic rocks produced the melts erupted by the three late Quaternary stratovolcanoes. Partial melting of 5–20 percent of mantle peridotite at depths of 35–70 km (Green and Ringwood, 1967) could produce parental basanitoid of somewhat variable

composition. Crystallization and removal of olivine, pyroxene, and plagioclase in shallow (1–10 km) reservoirs leave more silicic melts (hawaiite, mugearite, tristanite, and trachyte). Accumulation of olivine and pyroxene results in ankaramitic magmas. The biotite- and amphibole-bearing magmas may have formed in reservoirs within 8 km of the surface (Eggler and Burnham, 1973). Evaluation of these processes awaits trace element, electron microprobe, and isotopic data.

The volume of subaerial basanitoid and related basaltic rocks between Sete Cidades and Agua de Pau volcanoes is about 30 km³ and between Furnas and Agua de Pau volcanoes about 22 km³. The volume of exposed trachyte on the three volcanoes is about 100 km³ (table 2). Intrusive complexes of basaltic material may underlie São Miguel in sufficient volume to account for the abundant silicic rocks observed on the volcanoes.

Comparison of stratigraphic and chemical data for São Miguel with those for Terceira, the other Azorean island that has been studied in detail (Self, 1976; Self and Gunn, 1976), shows that:

1. Periods of particularly vigorous eruptive activity, commonly resulting in formation of calderas, occurred about 23,000–19,000 and 15,000–12,000 years B.P.

2. Chemical bimodality (basalt and trachyte) characterizes both islands: trachyte dominates, and intermediate compositions, though present, are volumetrically low.

Table 2. Estimated volumes of different rock types on the three late Quaternary stratovolcanoes of São Miguel

	Cubic kilometers	Percentage
Sete Cidades		
Ankaramite.....	1.14	3
Basanitoid.....	1.4	4
Basalt.....	0.9	2
Hawaiite + mugearite.....	7.3	18
Tristanite.....	0.5	1
Trachyte.....	28.4	72
Agua de Pau		
Ankaramite.....	1.0	2.1
Basanitoid.....	0.5	1.0
Basalt.....	1.0	2.1
Hybrid.....	0.3	0.6
Hawaiite + mugearite.....	0.35	0.7
Tristanite.....	0.5	1.0
Trachyte (peralkaline).....	20.0	41.1
Trachyte (peraluminous).....	25.0	51.4
Furnas		
Ankaramite.....	2.0	6.0
Basanitoid.....	1.0	3.0
Basalt.....	0	0
Hawaiite + mugearite.....	0.5	1.5
Tristanite.....	2.0	6.0
Trachyte.....	28.0	83.5

The output of Azorean volcanoes in general is low, but Sete Cidades, Agua de Pau, and Furnas together have erupted at least five times as much lava as the volcanoes on Terceira (Self, 1976; this paper) during latest Pleistocene and Holocene time. In contrast, volcanoes of somewhat similar composition in the Miocene and younger Canary Islands (Schmincke, 1982) have been constructed at rates 5–10 times greater than the Pliocene and younger Azores.

REFERENCES CITED

- Booth, B., Croasdale, R., and Walker, G.P.L., 1978, A quantitative study of five thousand years of volcanism on São Miguel, Azores: Royal Society of London Philosophical Transactions, ser. A, v. 288, p. 271–319.
- Cann, J.R., 1967, A second occurrence of dalyite and the petrology of some ejected syenite blocks from São Miguel, Azores: Mineralogical Magazine, v. 33, p. 227–232.
- Chaves, F.A., 1908, Gisements de diatomées fossiles a Furnas (Ile de S. Miguel): Lisbon, Bulletin de la Societe Portugueses des Sciences Naturelles, v. II, fasc. 3.
- Eggler, D.H., and Burnham, C.W., 1973, Crystallization and fractionation trends in the system andesite-H₂O-CO₂-O₂ at pressures to 10 kb: Geological Society of America Bulletin, v. 84, p. 2519–2532.
- Esenwein, P., 1929, Zur petrographie der Azoren: Zeitschrift Vulkanologie, v. 12, p. 108–227.
- Fernandez, L.A., 1980, Geology and petrology of the Nordeste volcanic complex, São Miguel, Azores: Geological Society of America Bulletin, v. 91, p. 675–680.
- Fisher, R.V., and Schmincke, H.U., 1984, Pyroclastic rocks. Berlin, Springer-Verlag, 472 p.
- Flower, M.F.J., Schmincke, H.U., and Bowman, H., 1976, Rare earth and other trace elements in historic Azorean lavas: Journal of Volcanology and Geothermal Research, v. 1, p. 127–147.
- Gandino, A., Guidi, M., Merlo, C., Mete, L., Rossi, R., and Zan, L., 1985, Preliminary model of the Ribeira Grande geothermal field (Azores Islands): Geothermics, v. 14, no. 1, p. 91–105.
- Green, D.H., and Ringwood, A.E., 1967, The genesis of basaltic magmas: Contributions to Mineralogy and Petrology, v. 15, p. 103–190.
- Grimison, N.L., and Chen, W.P., 1986, The Azores-Gibraltar plate boundary—Focal mechanisms, depths of earthquakes, and their tectonic implications: Journal of Geophysical Research, v. 91, no. B2, p. 2029–2047.
- Hawkesworth, C.J., Norry, M.J., Roddick, J.C., and Vollmer, R., 1979, ¹⁴³Nd/¹⁴⁴Nd and ⁸⁷Sr/⁸⁶Sr ratios from the Azores and their significance in LIL-element enriched mantle: Nature, v. 280, p. 28–31.
- Huang, T.C., Watkins, N.D., and Wilson, L., 1979, Deep-sea tephra from the Azores during the past 300,000 years; eruptive cloud height and ash volume estimates: Geological Society of America Bulletin, v. 90, p. 131–133.
- Irvine, T.N., and Barager, W.R.A., 1971, A guide to the chemical classification of the common volcanic rocks: Canadian Journal of Earth Sciences, v. 8, p. 523–548.

- Jeremine, E., 1957, Etude microscopique des roches de la region de Furnas (S. Miguel-Acores): Communications de la Service Geologique de Portugal, v. 38, p. 65–90.
- Krause, D.C., and Watkins, N.D., 1970, North Atlantic crustal genesis in the vicinity of the Azores: Geophysical Journal of the Royal Astronomical Society, v. 19, p. 261–283.
- Laughton, A.S., and Whitmarsh, R.B., 1975, The Azores-Gibraltar plate boundary, in Kristjansson, L., ed., Geodynamics of Iceland and the North Atlantic area. Dordrecht, Reidel, p. 63–81.
- Macdonald, G.A., 1968, Composition and origin of Hawaiian lavas: Geological Society of America Memoir 116, p. 477–552.
- Macdonald, G.A., and Katsura, T., 1964, Chemical composition of Hawaiian lavas: Journal of Petrology, v. 5, p. 82–133.
- Moore, R.B., 1983a, Preliminary geologic map of Furnas volcano, São Miguel, Azores: U.S. Geological Survey Open-File Report 83–395, scale 1:15,000.
- _____, 1983b, Preliminary geologic map of Sete Cidades volcano, São Miguel, Azores: U.S. Geological Survey Open-File Report 83–742, scale 1:18,000.
- _____, 1986, Preliminary geologic map of Agua de Pau volcano, São Miguel, Azores: U.S. Geological Survey Open-File Report 86–192, scale 1:18,000.
- _____, 1990, Volcanic geology and eruption frequency, São Miguel, Azores: Bulletin of Volcanology, v. 52, no. 8, p. 602–614.
- _____, 1991, Geologic map of São Miguel, Azores: U.S. Geological Survey Miscellaneous Investigations Series Map I–2007, scale 1:50,000.
- Moore, R.B., and Rubin, M., 1991, Radiocarbon dates for lava flows and pyroclastic deposits on São Miguel, Azores: Radiocarbon, v. 33, no. 1, p. 151–164.
- Muecke, G.K., Ade-Hall, J.M., Aumento, F., MacDonald, A., Reynolds, P.H., Hyndman, R.D., Quintino, J., Opdyke, N., and Lowrie, W., 1974, Deep drilling in an active geothermal area in the Azores: Nature, v. 252, p. 281–285.
- Peacock, M.A., 1931, Classification of igneous rock series: Journal of Geology, v. 39, p. 54–67.
- Poldervaart, A., 1964, Chemical definition of alkali basalts and tholeiites: Geological Society of America Bulletin, v. 75, p. 229–232.
- Schmincke, H.-U., 1973, Magmatic evolution and tectonic regime in the Canary, Madeira, and Azores island groups: Geological Society of America Bulletin, v. 84, p. 633–648.
- _____, 1982, Volcanic and chemical evolution of the Canary Islands, in Geology of the northwest African continental margin. Berlin, Springer-Verlag, p. 273–306.
- Schmincke, H.-U., and Weibel, M., 1972, Chemical study of rocks from Madeira, Porto Santo, and São Miguel, Terceira (Azores): Neues Jahrbuch für Mineralogie, Abhandlungen, v. 117, no. 3, p. 253–281.
- Searle, R., 1980, Tectonic pattern of the Azores spreading centre and triple junction: Earth and Planetary Science Letters, v. 51, p. 415–434.
- Self, S., 1976, The Recent volcanology of Terceira, Azores: Journal of the Geological Society of London, v. 132, p. 645–666.
- Self, S., and Gunn, B.M., 1976, Petrology, volume, and age relations of alkaline and saturated peralkaline volcanics from Terceira, Azores: Contributions to Mineralogy and Petrology, v. 54, p. 293–313.
- Shotton, F.W., Blundell, D.J., and Williams, R.E.G., 1968, Birmingham University radiocarbon dates, II: Radiocarbon, v. 10, p. 204.
- _____, 1969, Birmingham University radiocarbon dates, III: Radiocarbon, v. 11, p. 266.
- Shotton, F.W., and Williams, R.E.G., 1971, Birmingham University radiocarbon dates, V: Radiocarbon, v. 13, p. 141–156.
- _____, 1973, Birmingham University radiocarbon dates, VII: Radiocarbon, v. 15, p. 451–468.
- Sparks, S.R.J., Sigurdsson, H., and Wilson, L., 1977, Magma mixing; a mechanism for triggering acid explosive eruptions: Nature, v. 267, p. 315–318.
- Storey, M., 1981, Trachytic pyroclastics from Agua de Pau volcano, São Miguel, Azores; evolution of a magma body over 4,000 years: Contributions to Mineralogy and Petrology, v. 78, p. 423–432.
- van Padang, M.N., Richards, A.F., Machado, F., Bravo, T., Baker, P.E., and Le Maitre, R.W., 1967, Catalogue of active volcanoes-Atlantic Ocean: International Volcanological Association, pt. 21.
- Walker, G.P.L., 1984, Downsag calderas, ring faults, caldera sizes, and incremental caldera growth: Journal of Geophysical Research, v. 89, p. 8407–8416.
- Walker, G.P.L., and Croasdale, R., 1970, Two Plinian-type eruptions in the Azores: Journal of the Geological Society of London, v. 127, p. 17–55.
- Weston, F.S., 1964, List of recorded volcanic eruptions in the Azores with brief reports: Boletim do Museu e Laboratorio Mineralogico e Geologico da Faculdade de Ciencias, v. 10, fasc. 1, p. 3–18.
- White, W.M., Schilling, J.-G., and Hart, S.R., 1976, Evidence for the Azores mantle plume from strontium isotope geochemistry of the Central North Atlantic: Nature, v. 263, p. 659–663.
- White, W.M., Tapia, M.D.M., and Schilling, J.-G., 1979, The petrology and geochemistry of the Azores Islands: Contributions to Mineralogy and Petrology, v. 69, p. 201–213.
- Zbyszewski, G., 1961, Etude geologique de l'Ile de S. Miguel (Acores): Communications de la Service Geologique de Portugal, v. 45, p. 5–79.
- Zbyszewski, G., de Medeiros, A.C., de Almeida, F.M., and da Veiga Ferreira, O., 1958, Carta geologica de Portugal na escala de 1:50,000 (São Miguel): Servicos Geologicos de Portugal, Lisbon.
- Zbyszewski, G., and da Veiga Ferreira, O., 1959, Carta geologica de Portugal na escala de 1:50,000 (São Miguel): Servicos Geologicos de Portugal, Lisbon.

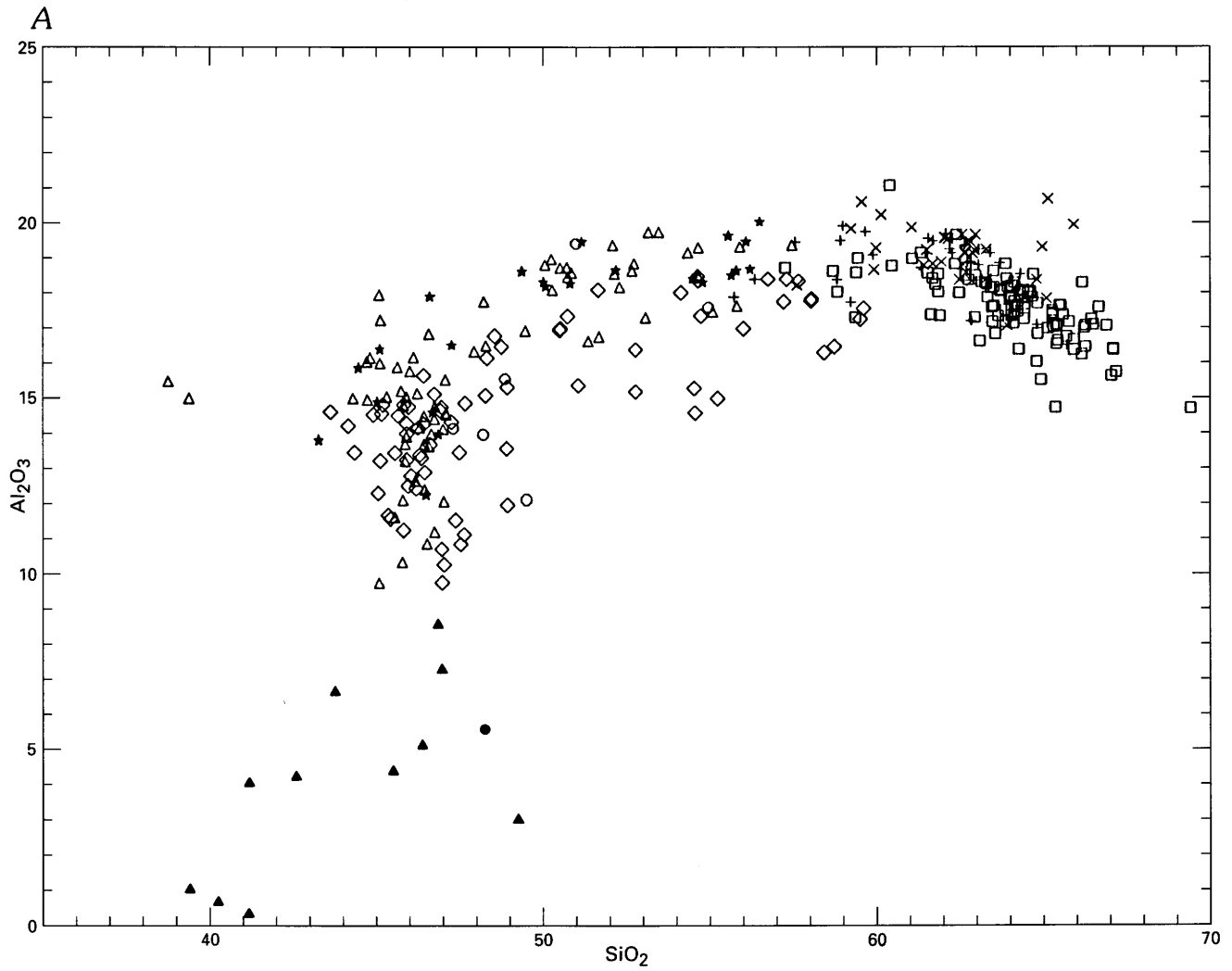


Figure 11 (above and following pages). Silica-variation diagrams (in weight percent). Symbols: \square , trachytes and tristanites of Agua de Pau volcano; $+$, trachytes and tristanites of Sete Cidades volcano; \times , trachytes and tristanites of Furnas volcano (\bullet , ultramafic or mafic xenolith); \diamond , mafic rocks on the flanks of Agua de Pau volcano; \triangle , mafic rocks on the flanks of Sete Cidades volcano (\blacktriangle , ultramafic or mafic xenolith); \star , mafic rocks on the flanks of Furnas volcano; \circ , Nordeste volcano.

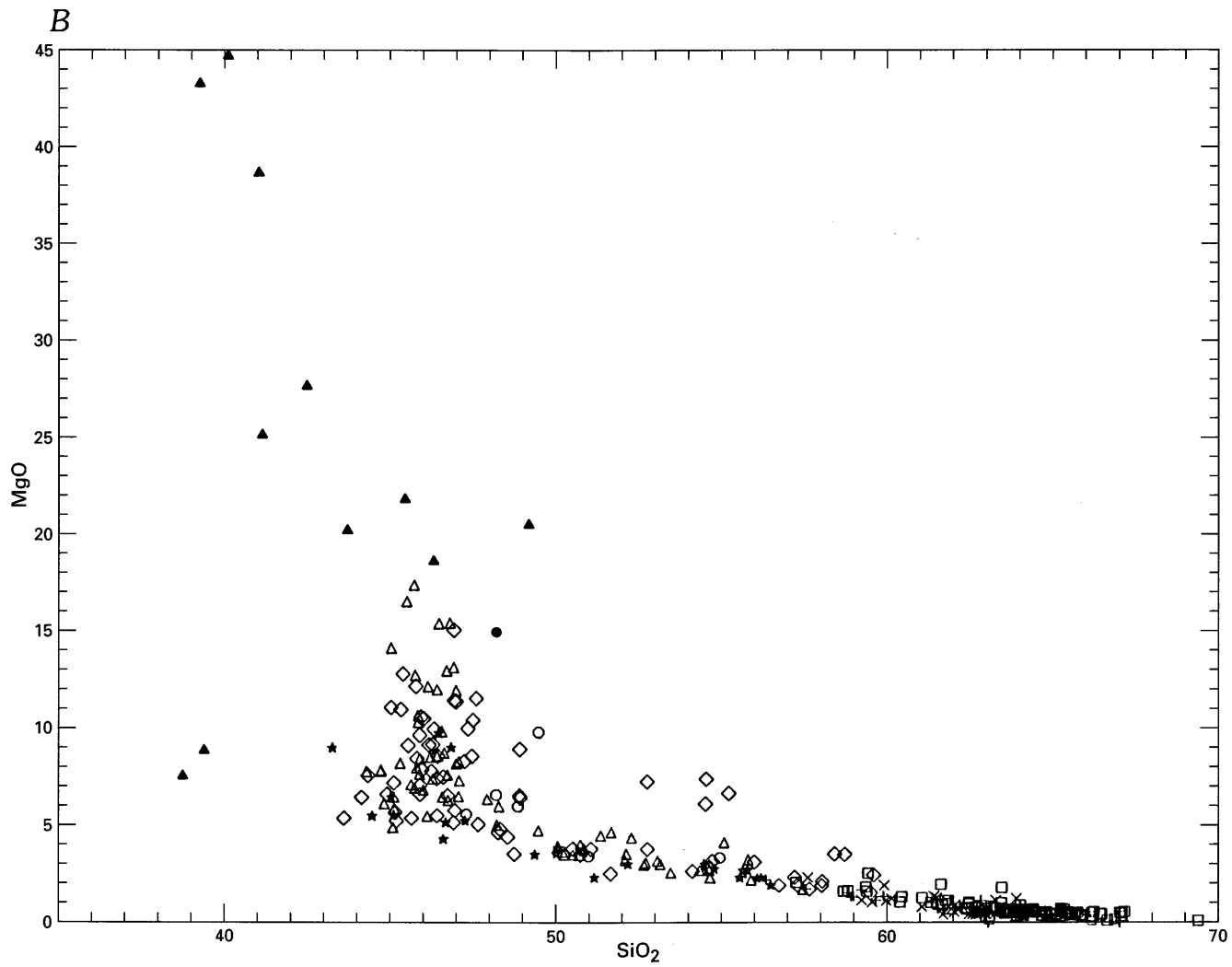


Figure 11. Silica-variation diagrams (in weight percent)—Continued.

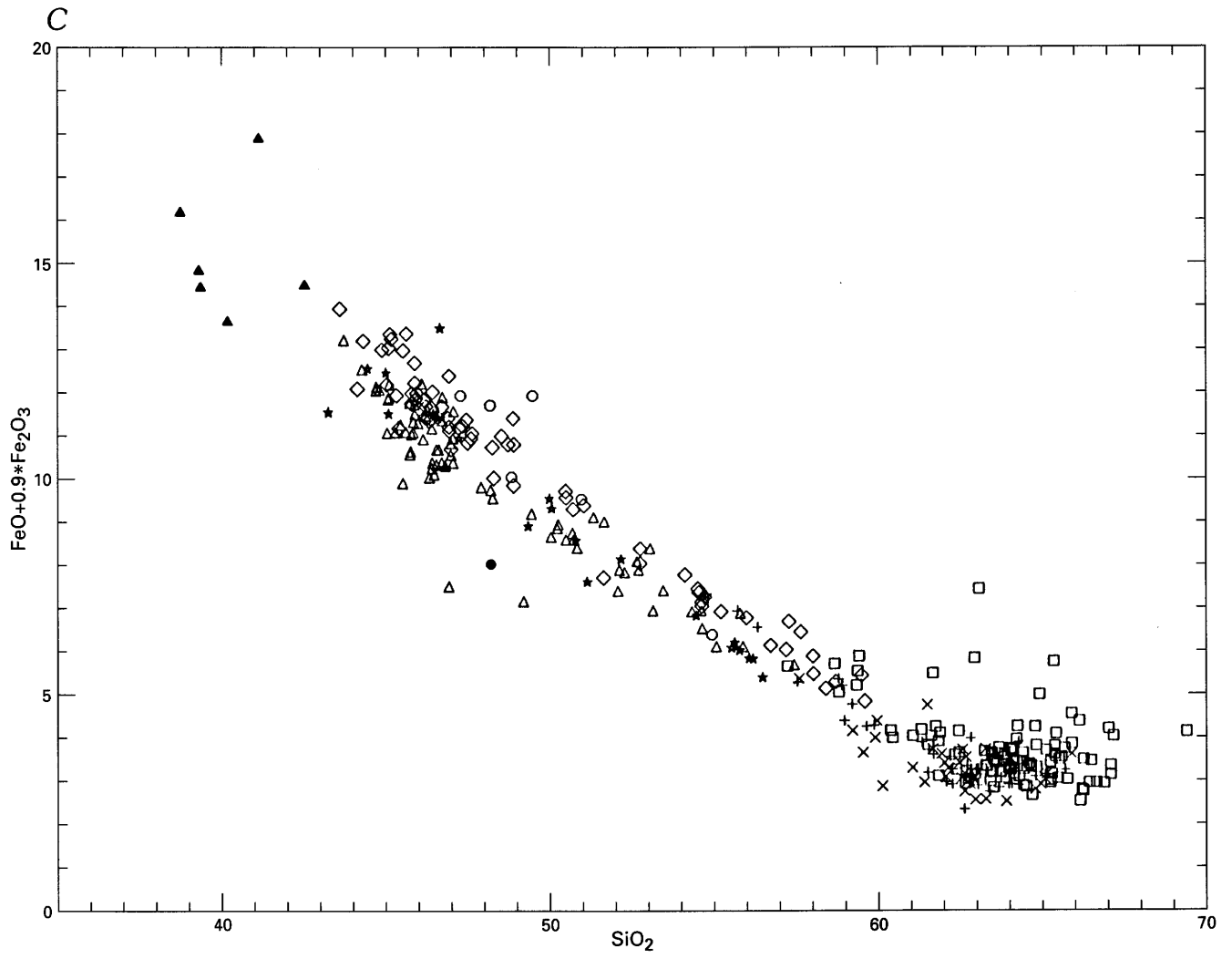


Figure 11. Silica-variation diagrams (in weight percent)—Continued.

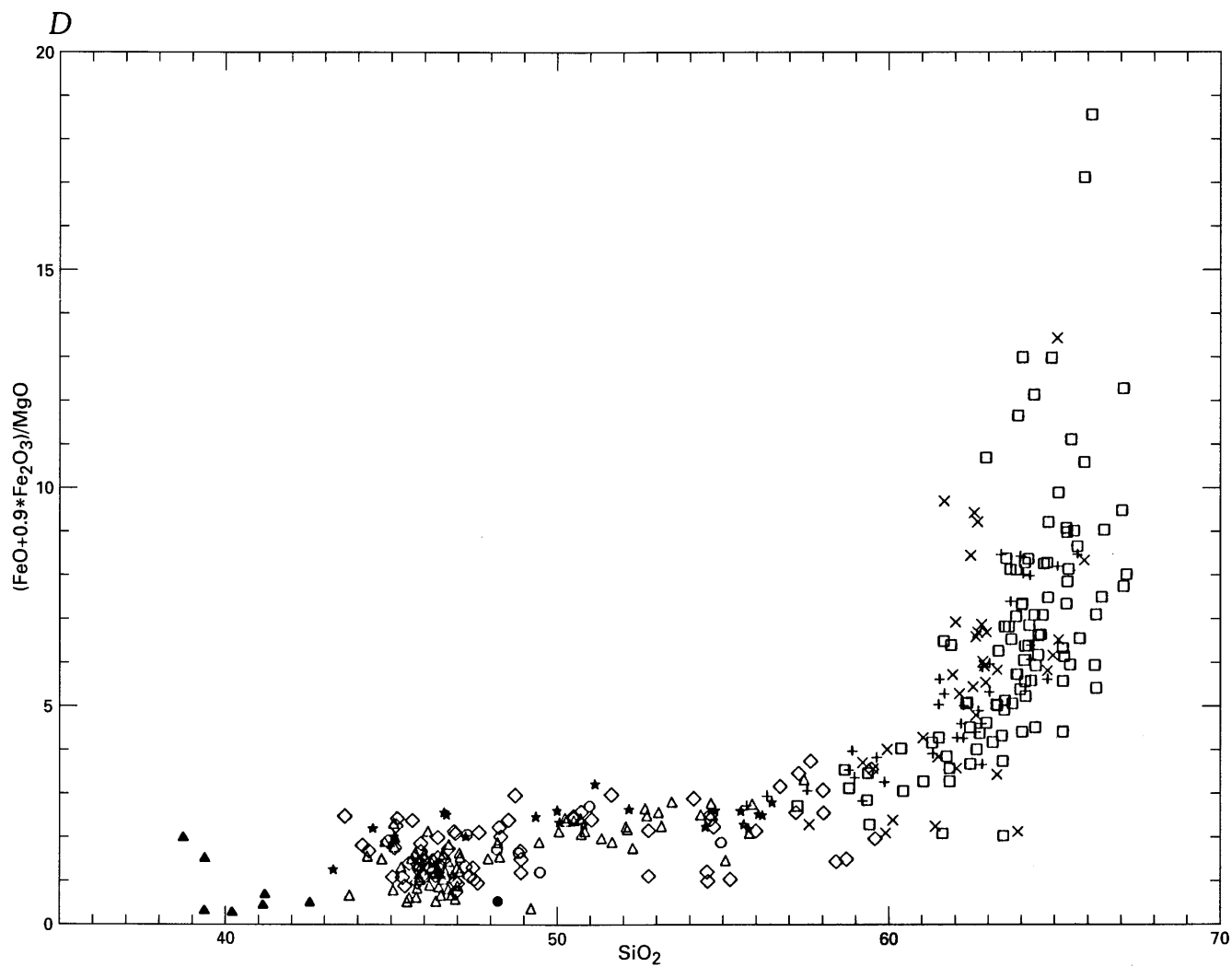


Figure 11. Silica-variation diagrams (in weight percent)—Continued.

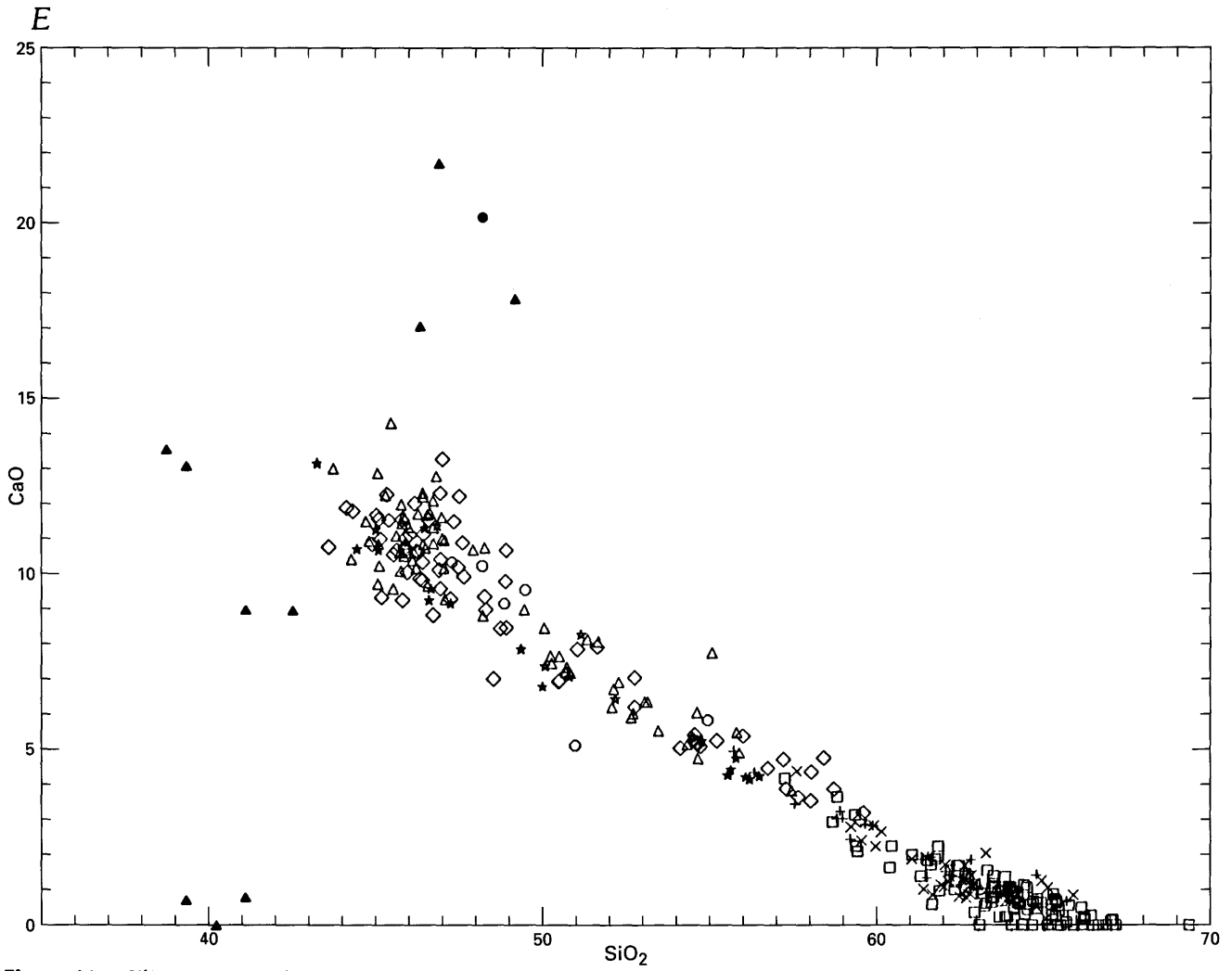


Figure 11. Silica-variation diagrams (in weight percent)—Continued.

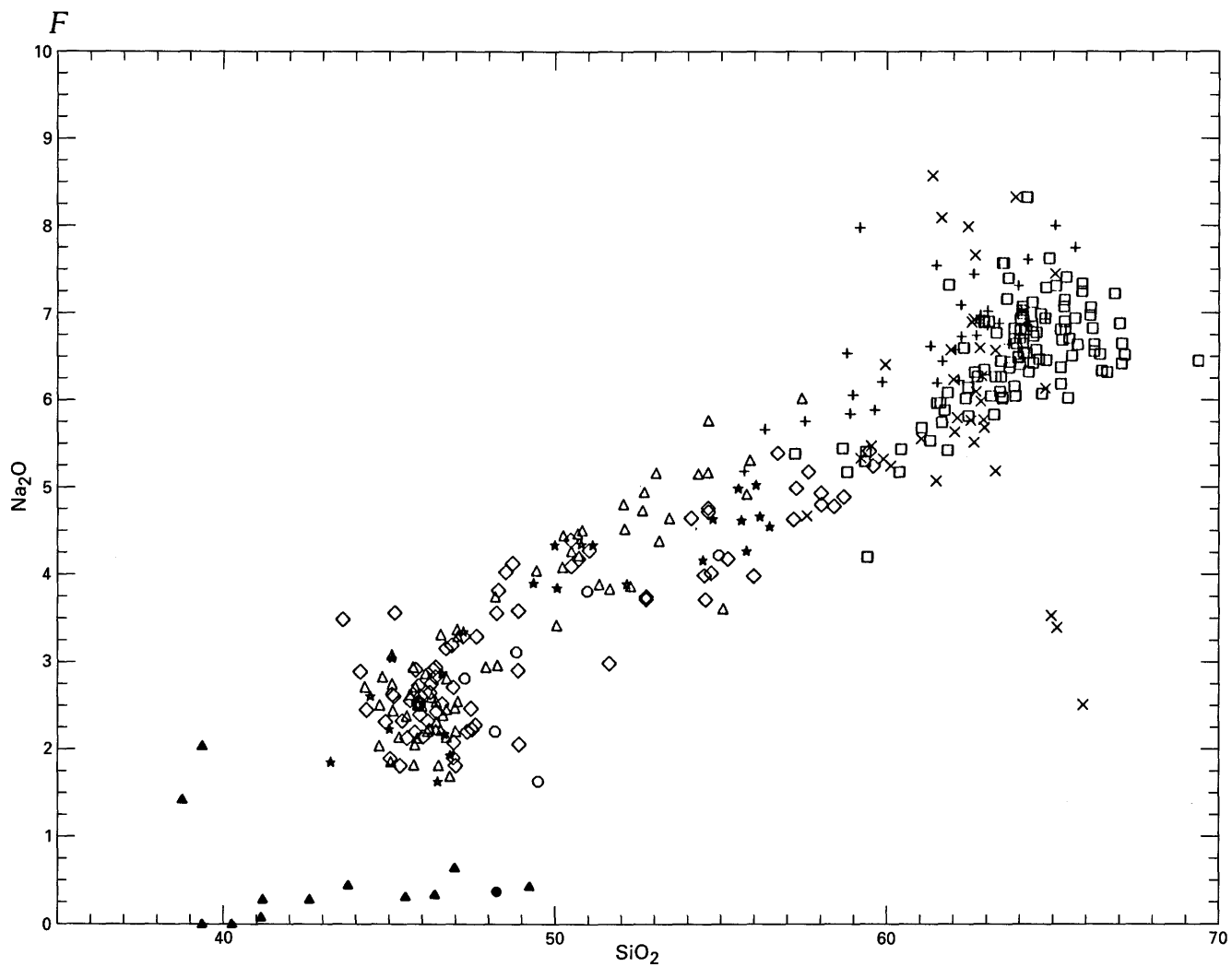


Figure 11. Silica-variation diagrams (in weight percent)—Continued.

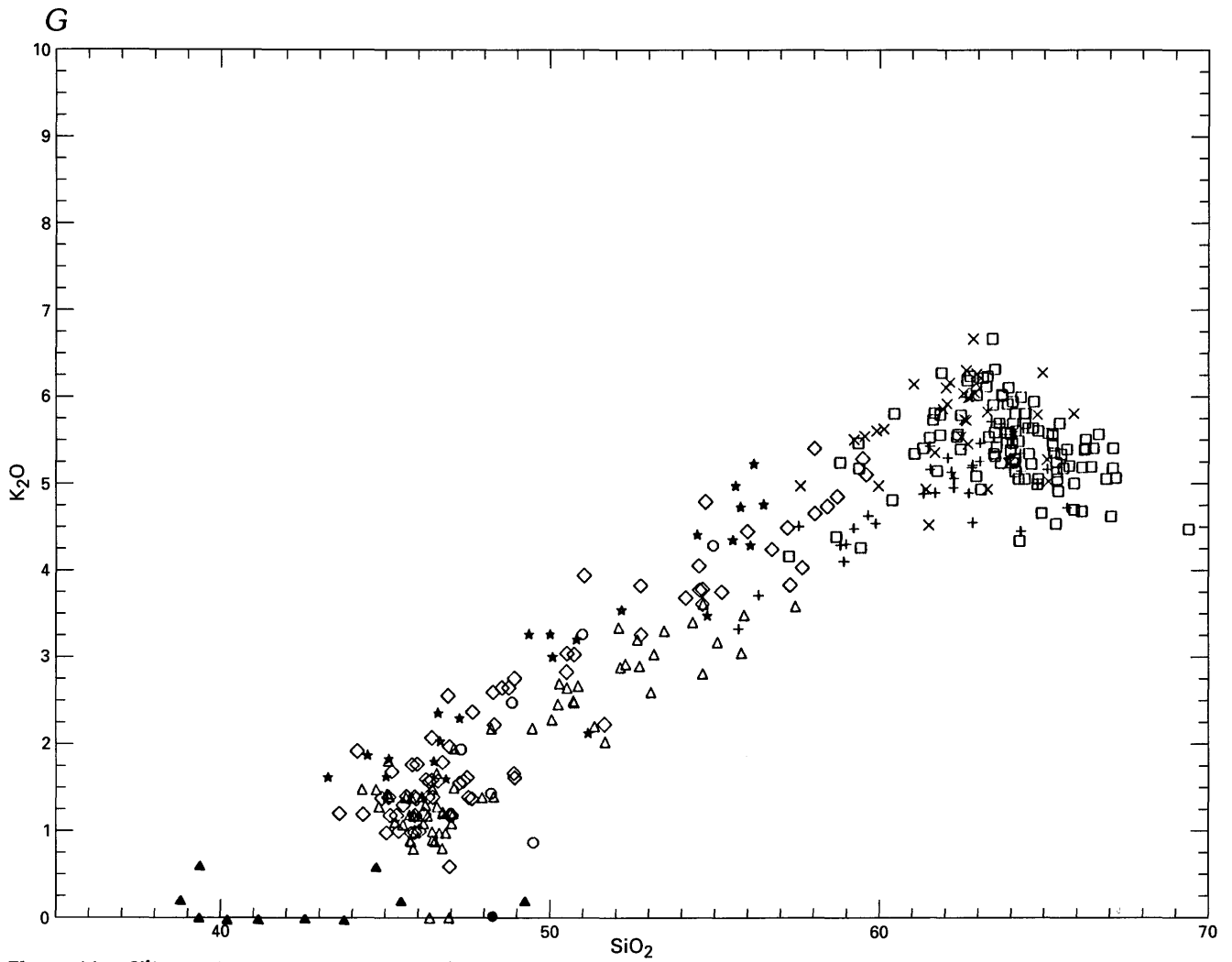


Figure 11. Silica-variation diagrams (in weight percent)—Continued.

H

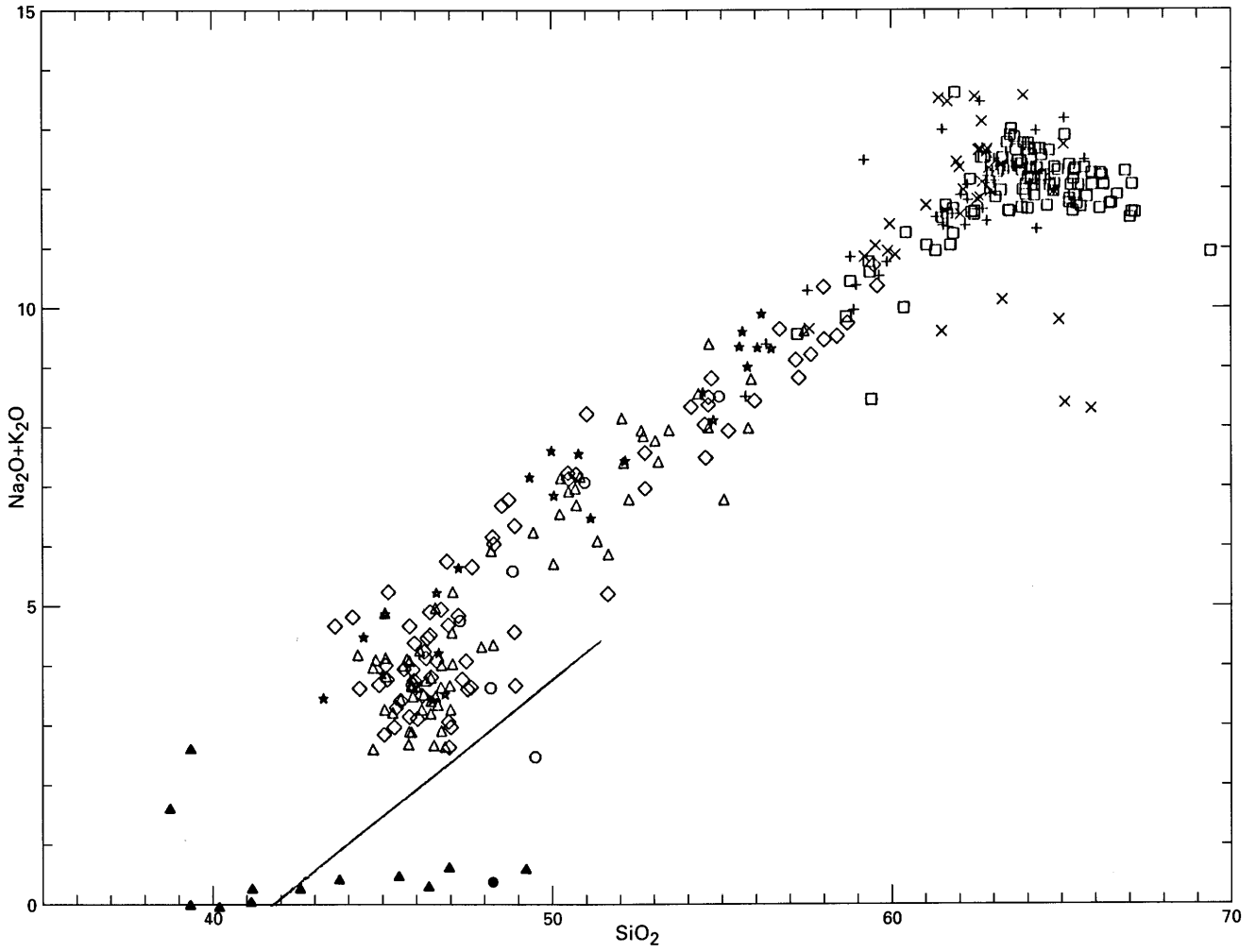


Figure 11. Silica-variation diagrams (in weight percent)—Continued.

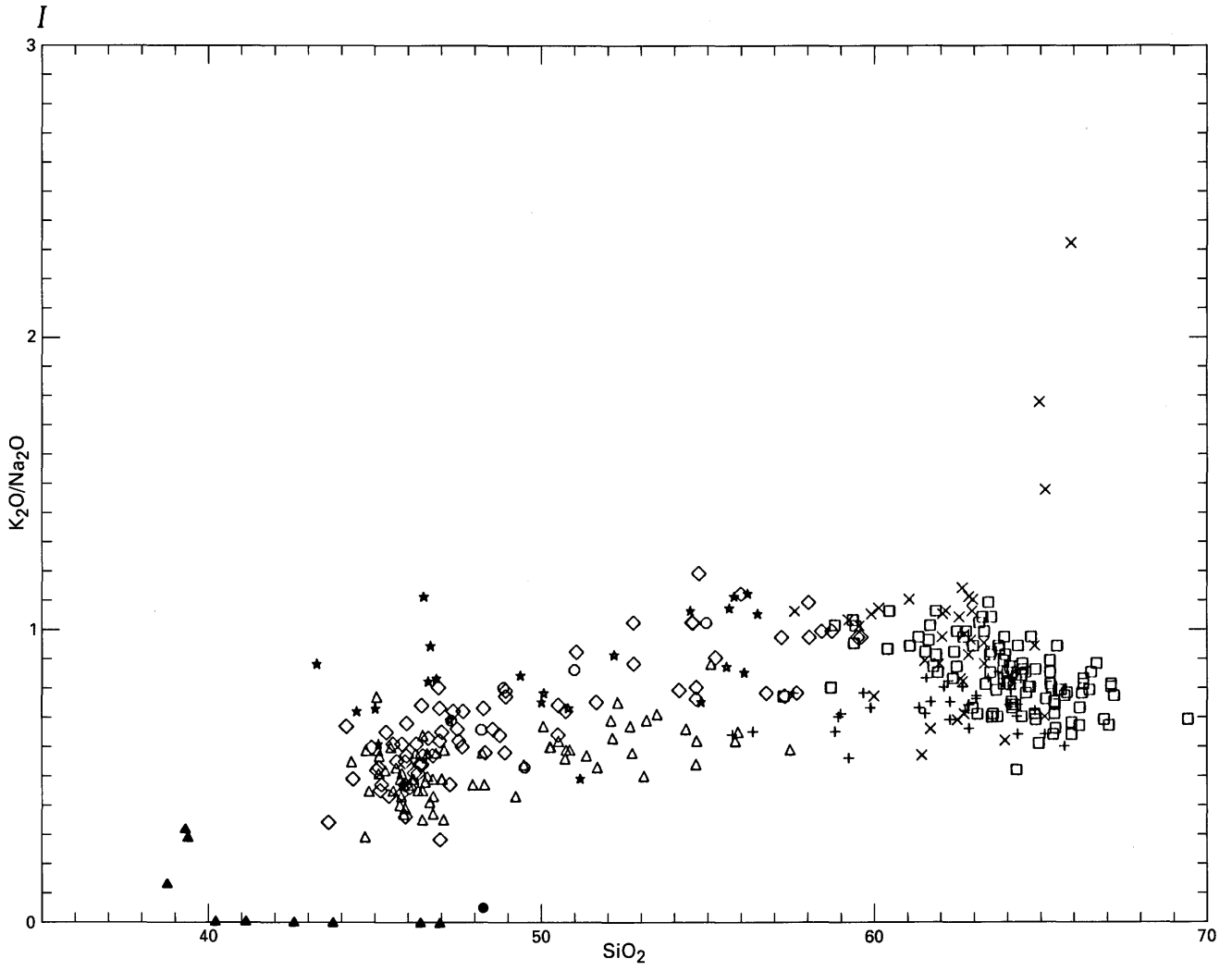


Figure 11. Silica-variation diagrams (in weight percent)—Continued.

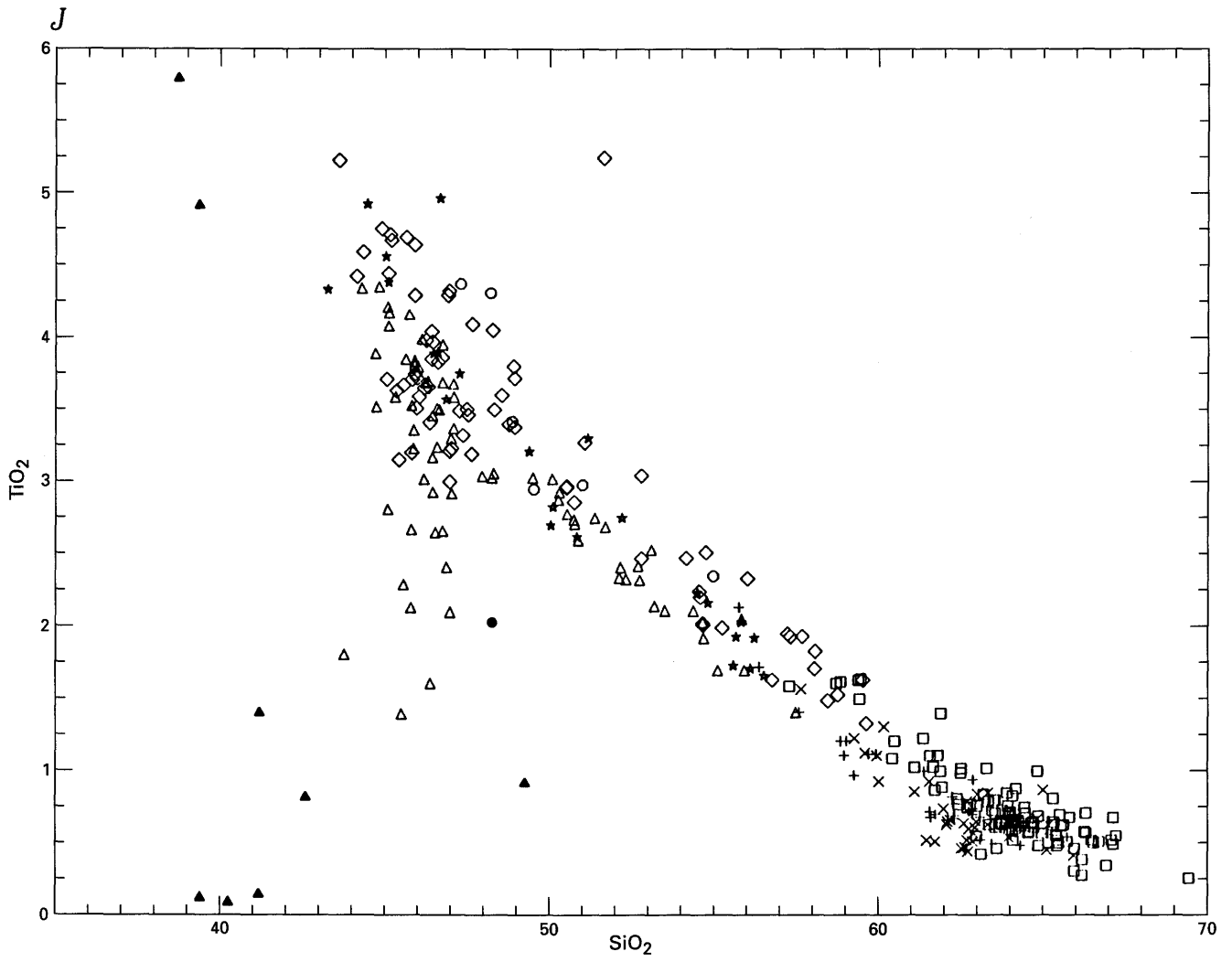


Figure 11. Silica-variation diagrams (in weight percent)—Continued.

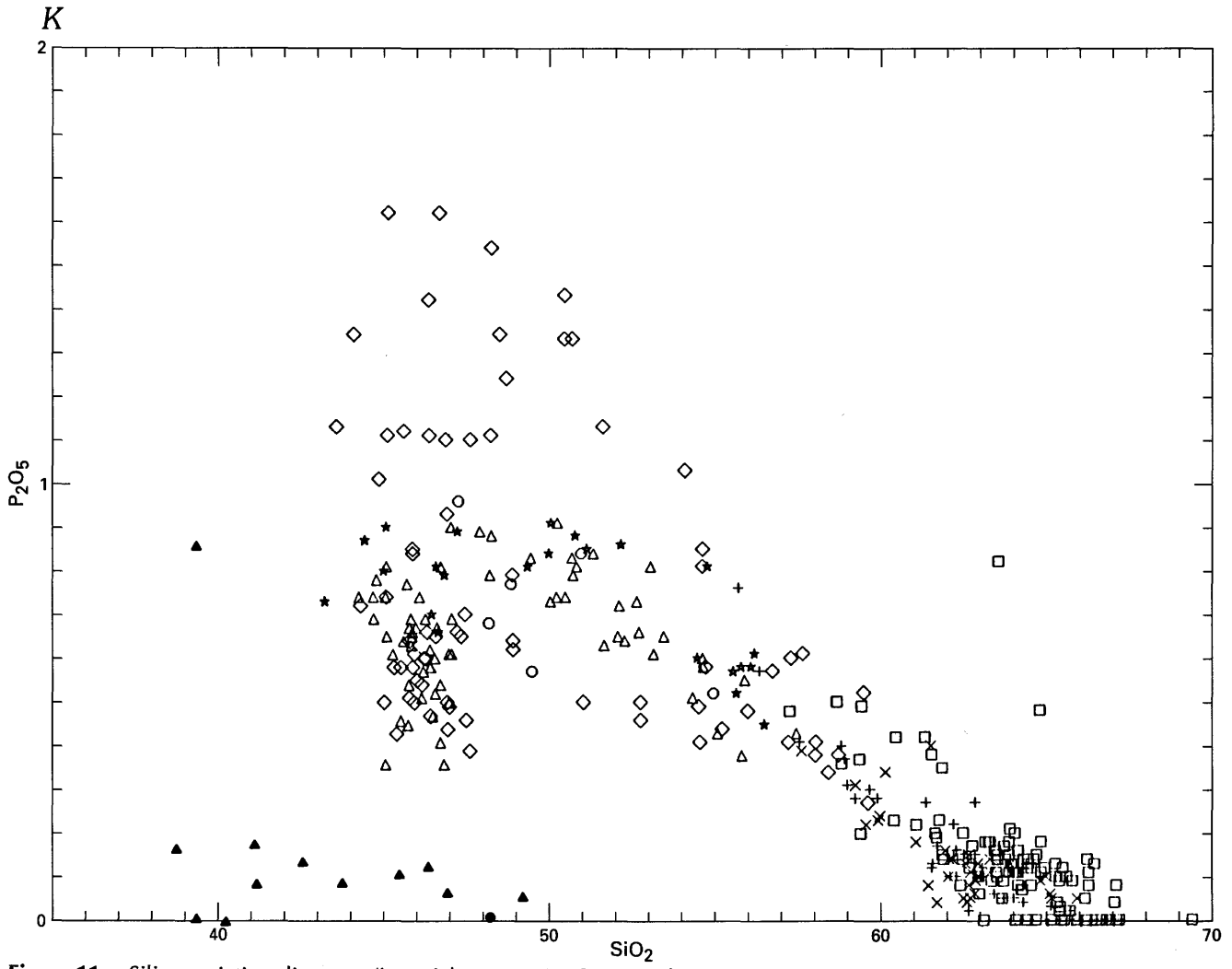


Figure 11. Silica-variation diagrams (in weight percent)—Continued.

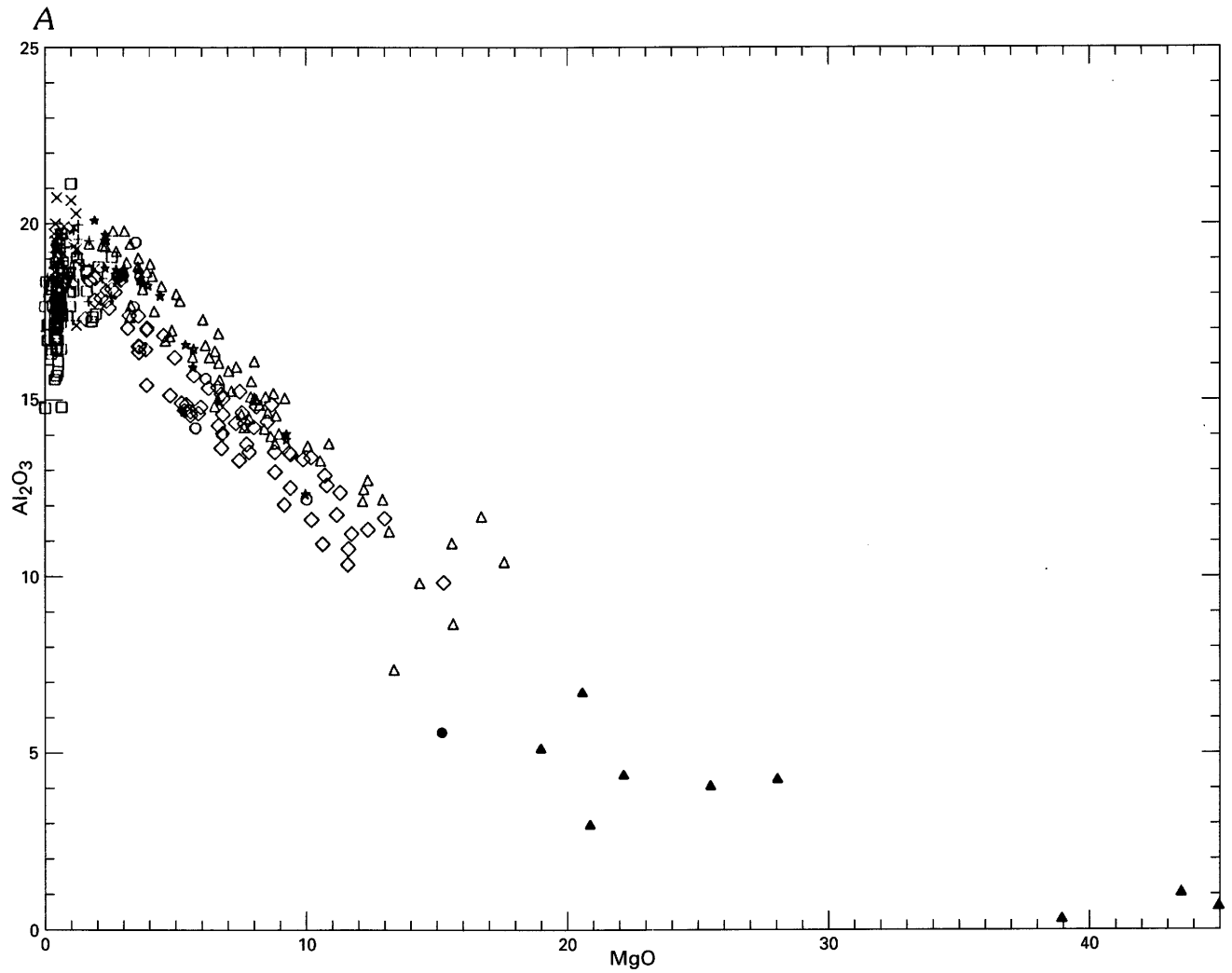


Figure 12. Magnesia-variation diagrams (in weight percent). Symbols as in figure 11. Symbols: □, trachytes and tristanites of Agua de Pau volcano; +, trachytes and tristanites of Sete Cidades volcano; ×, trachytes and tristanites of Furnas volcano (●, ultramafic or mafic xenolith); ◇, mafic rocks on the flanks of Agua de Pau volcano; △, mafic rocks on the flanks of Sete Cidades volcano (▲, ultramafic or mafic xenolith); ★, mafic rocks on the flanks of Furnas volcano; ○, Nordeste volcano.

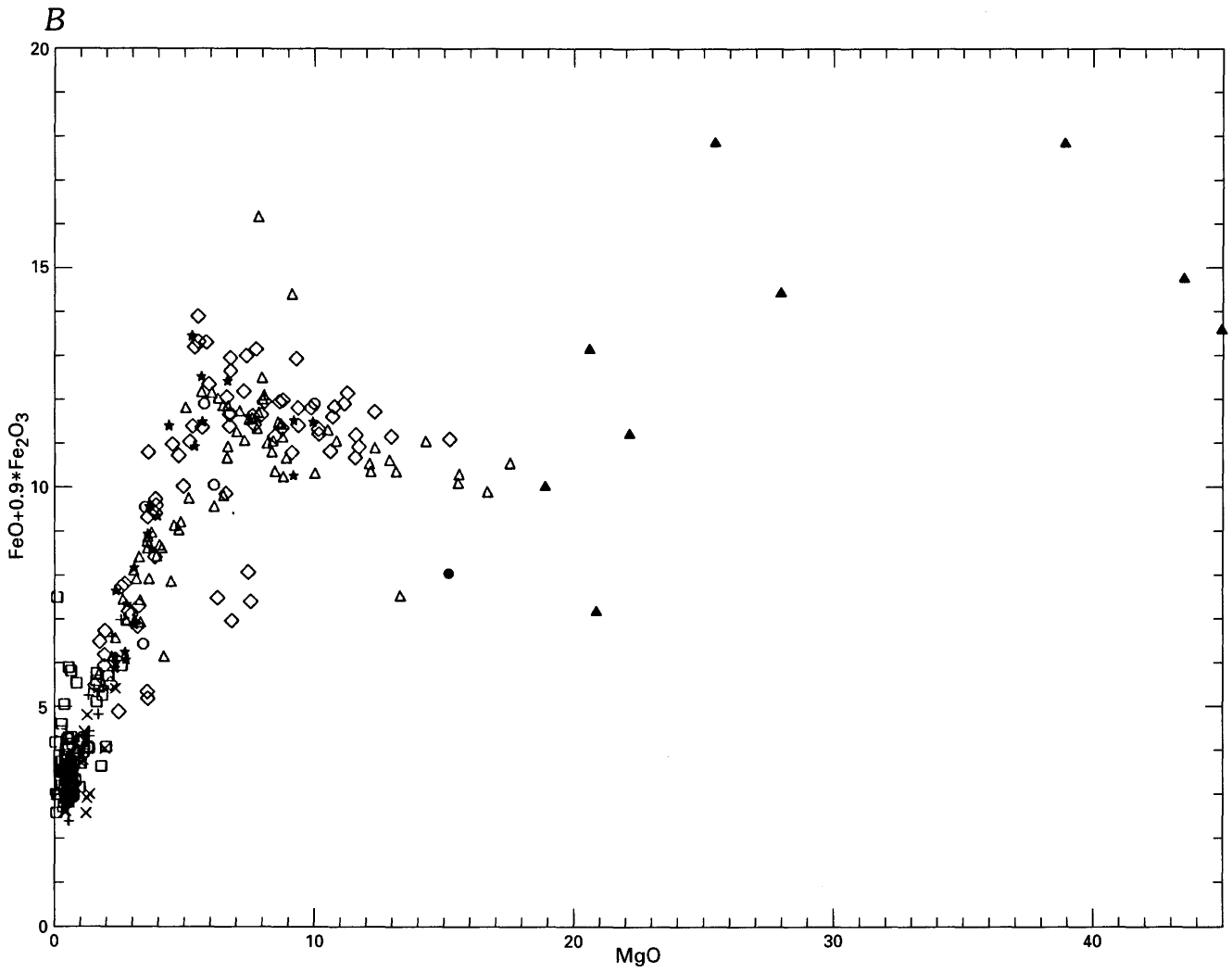


Figure 12. Magnesia-variation diagrams (in weight percent)—Continued.

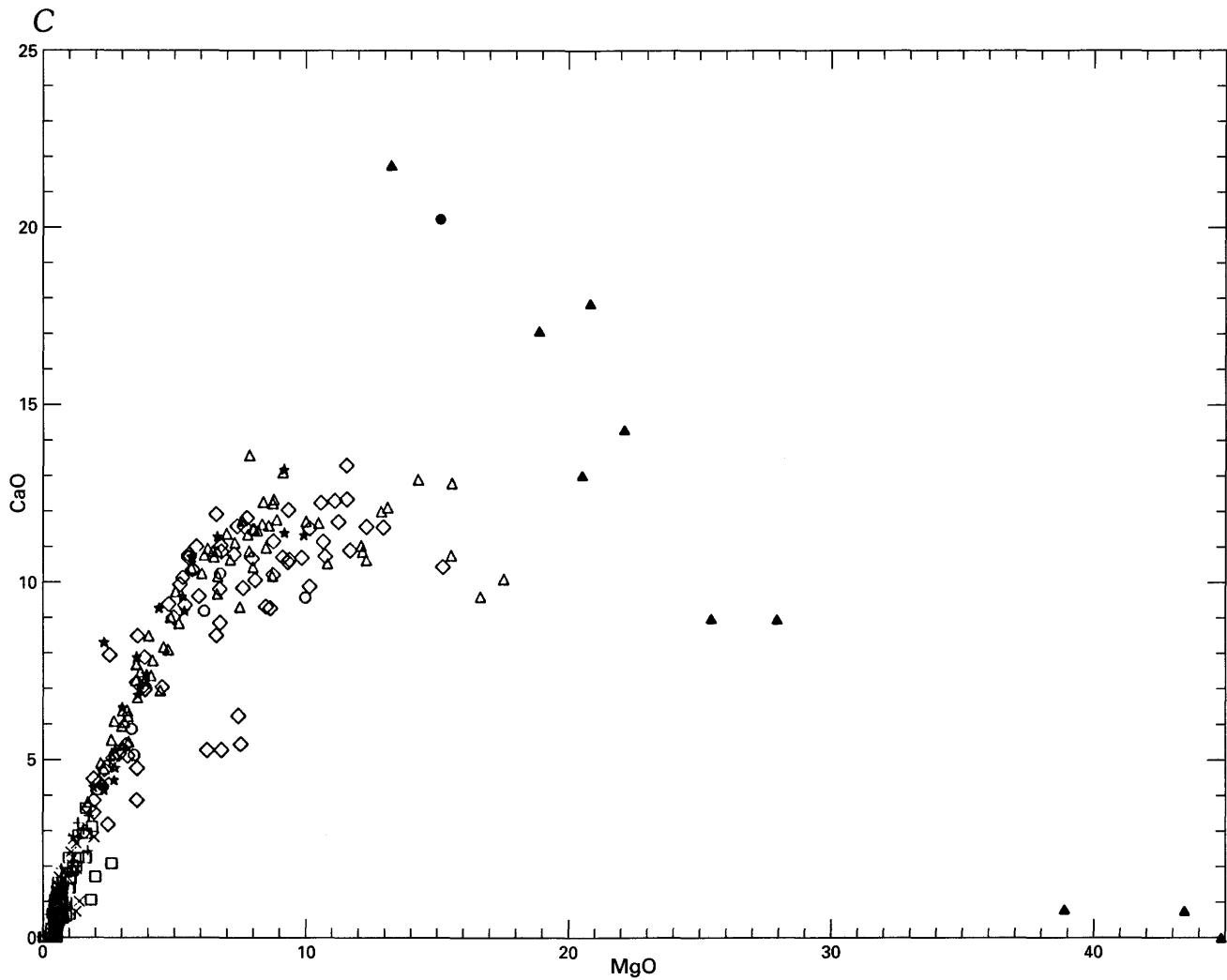


Figure 12. Magnesia-variation diagrams (in weight percent)—Continued.

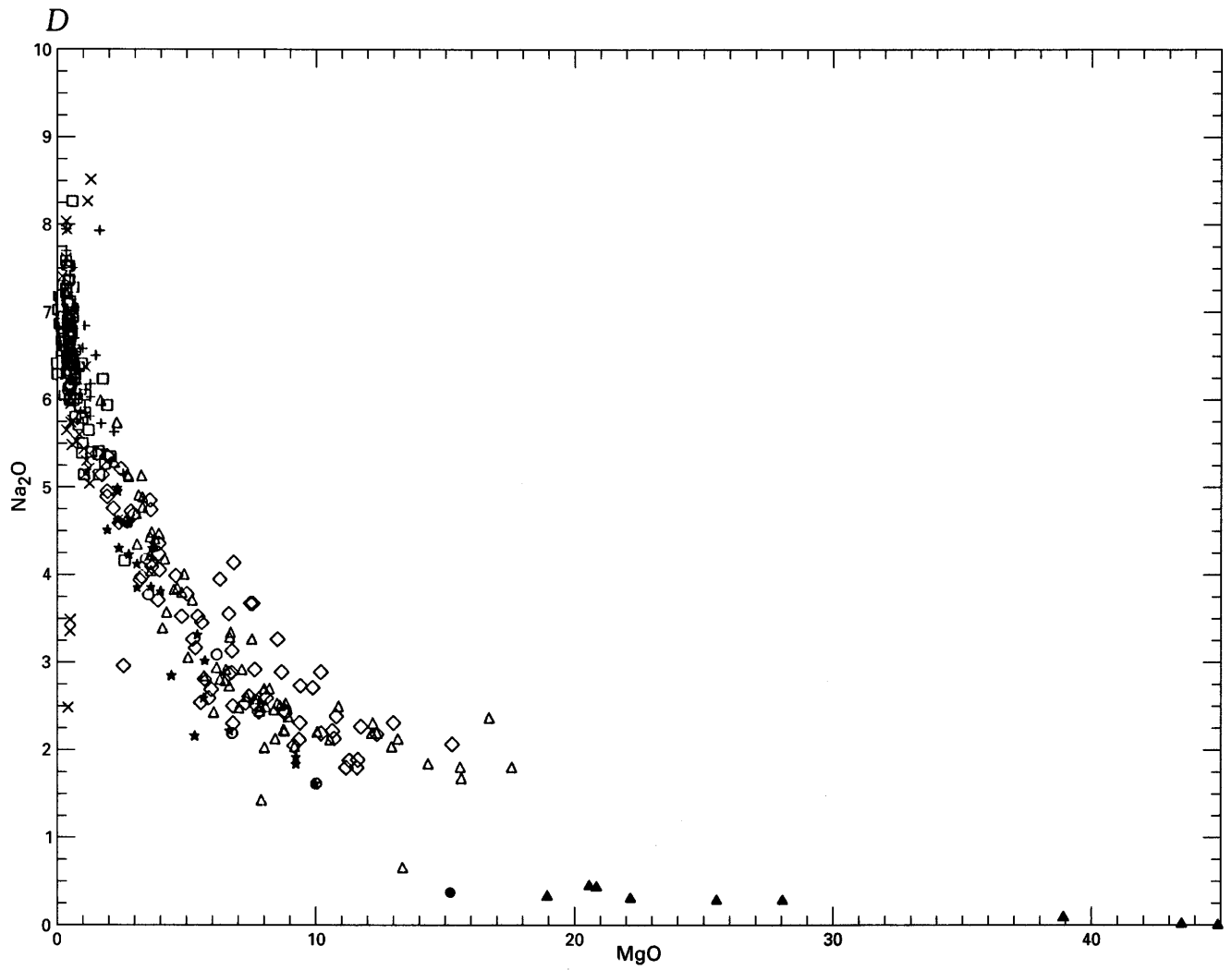


Figure 12. Magnesia-variation diagrams (in weight percent)—Continued.

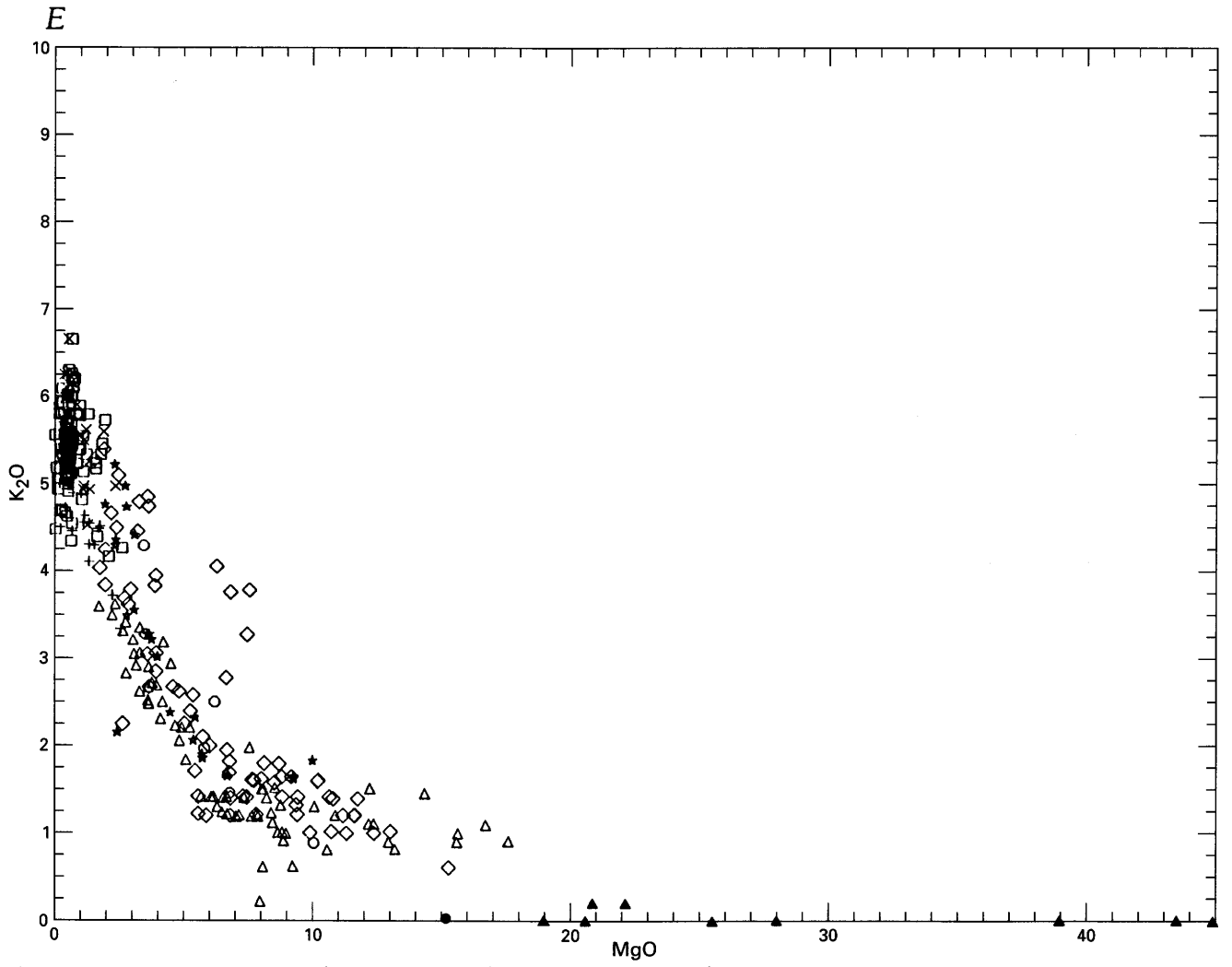


Figure 12. Magnesia-variation diagrams (in weight percent)—Continued.

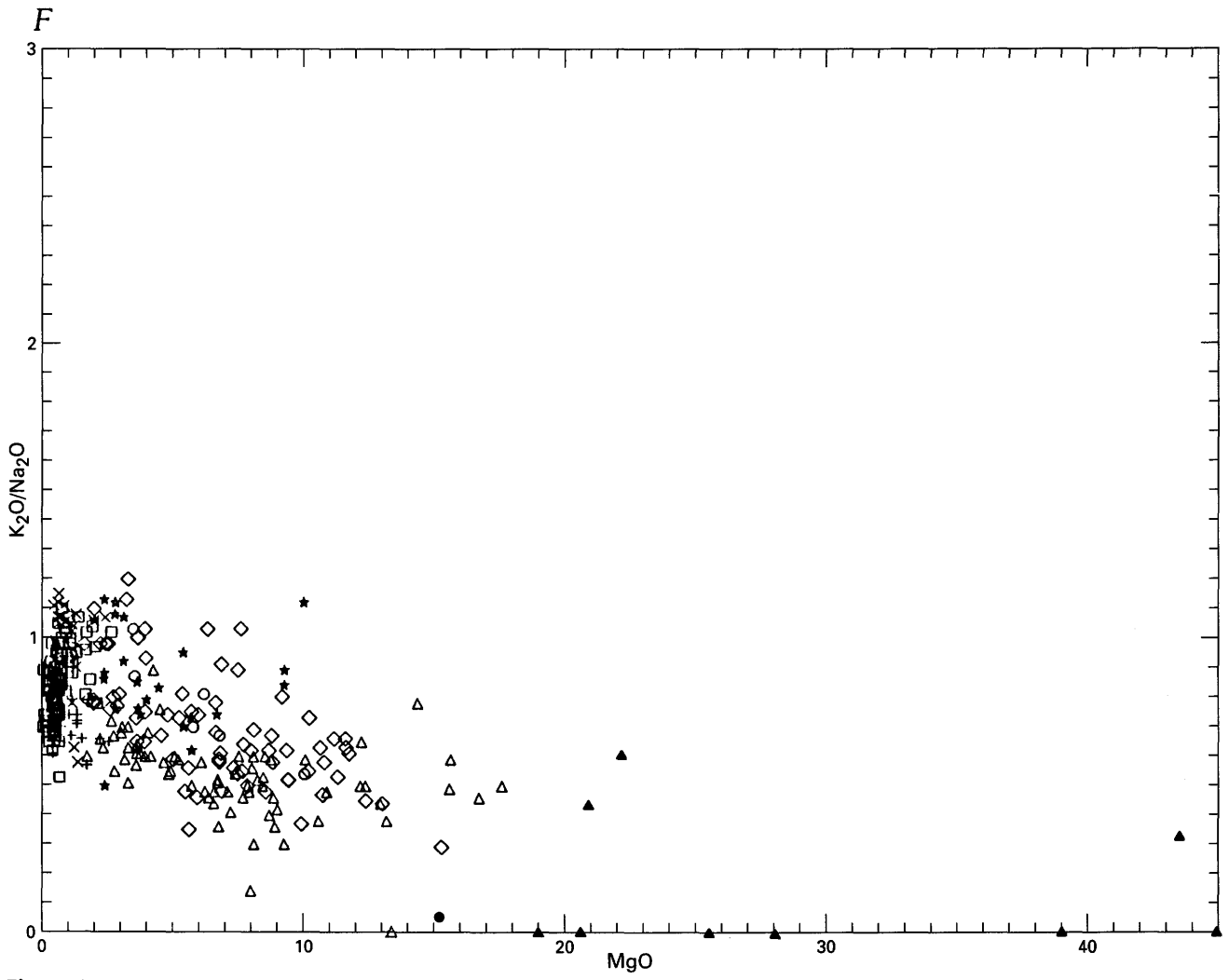


Figure 12. Magnesia-variation diagrams (in weight percent).

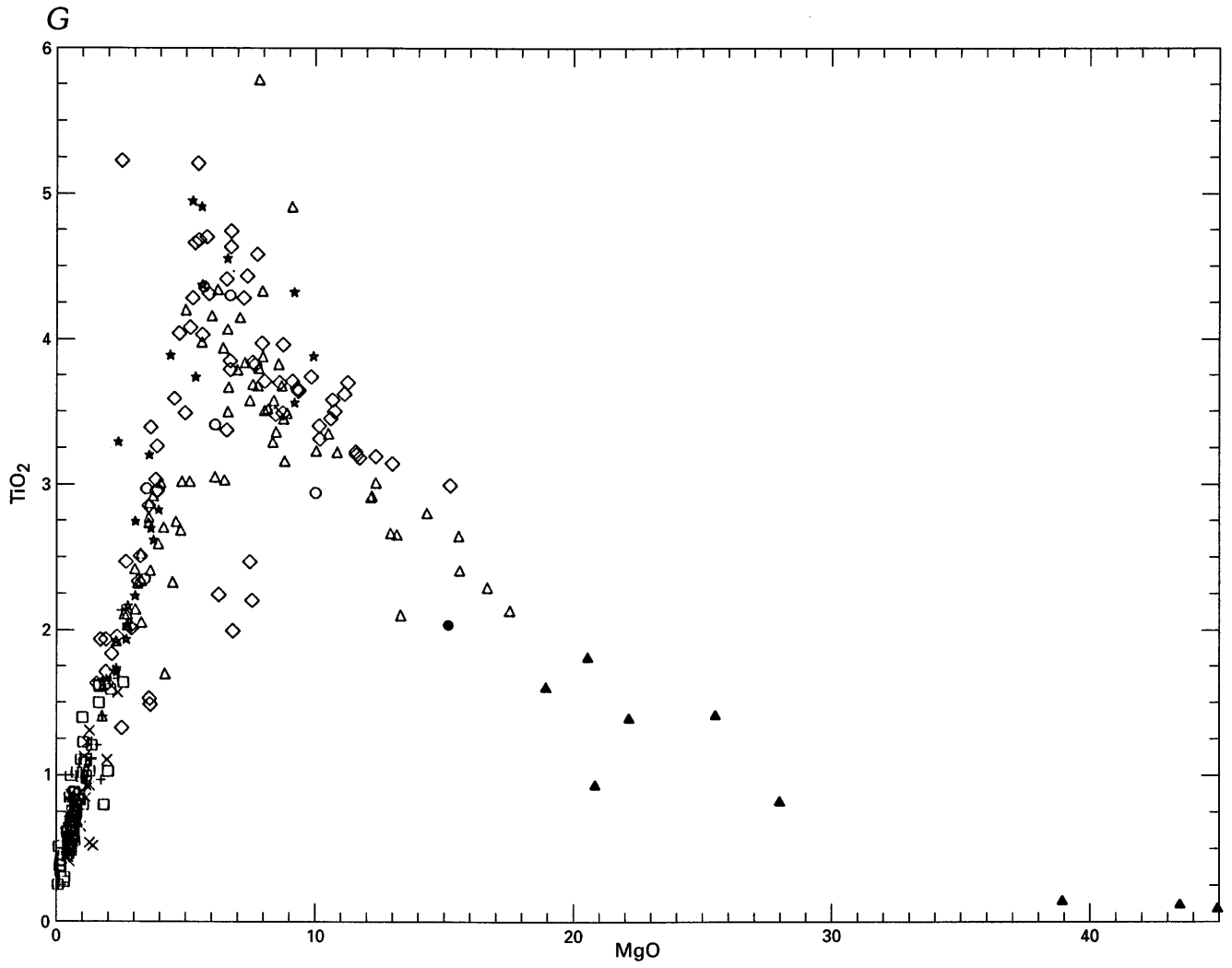


Figure 12. Magnesia-variation diagrams (in weight percent)—Continued.

H

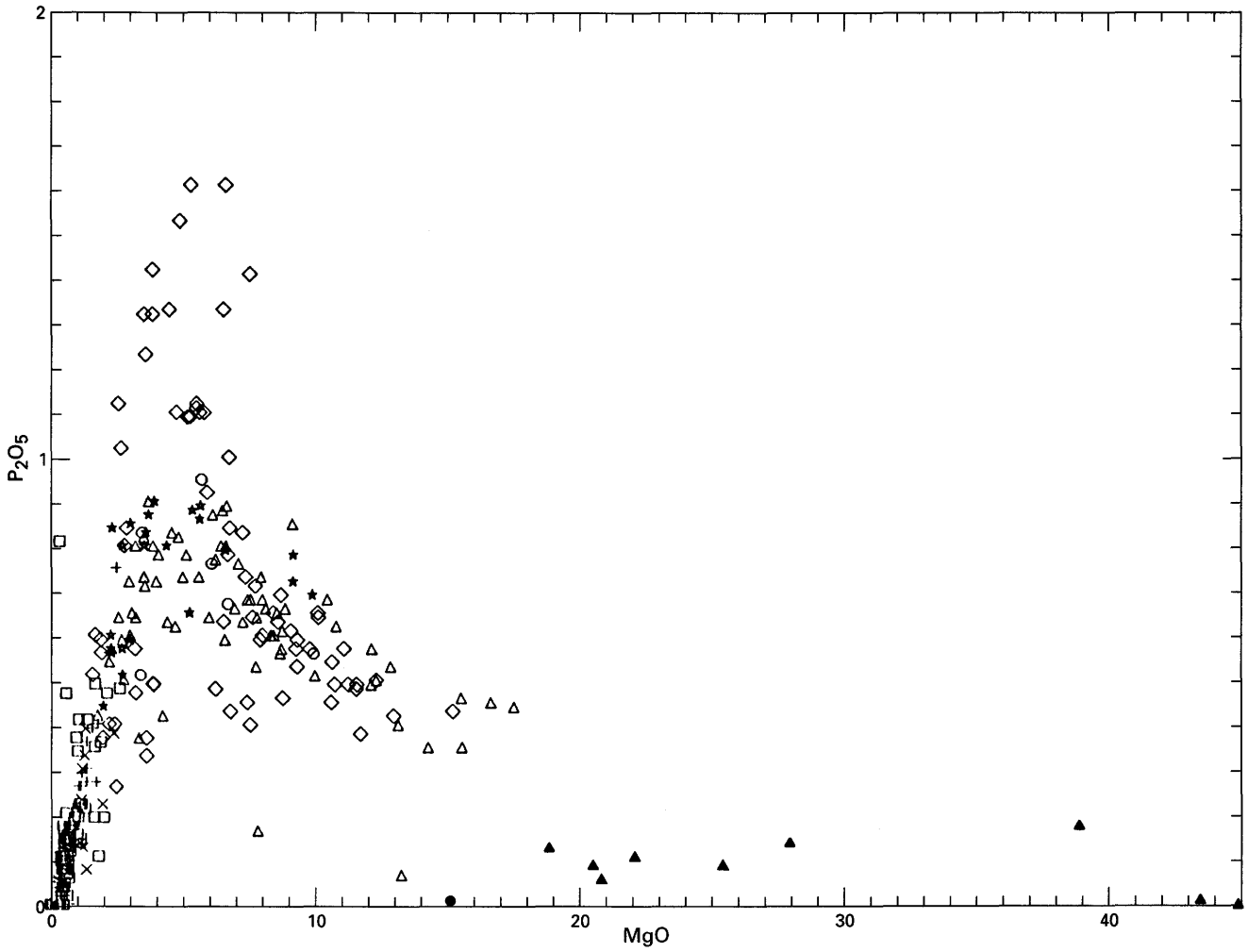


Figure 12. Magnesia-variation diagrams (in weight percent)—Continued.

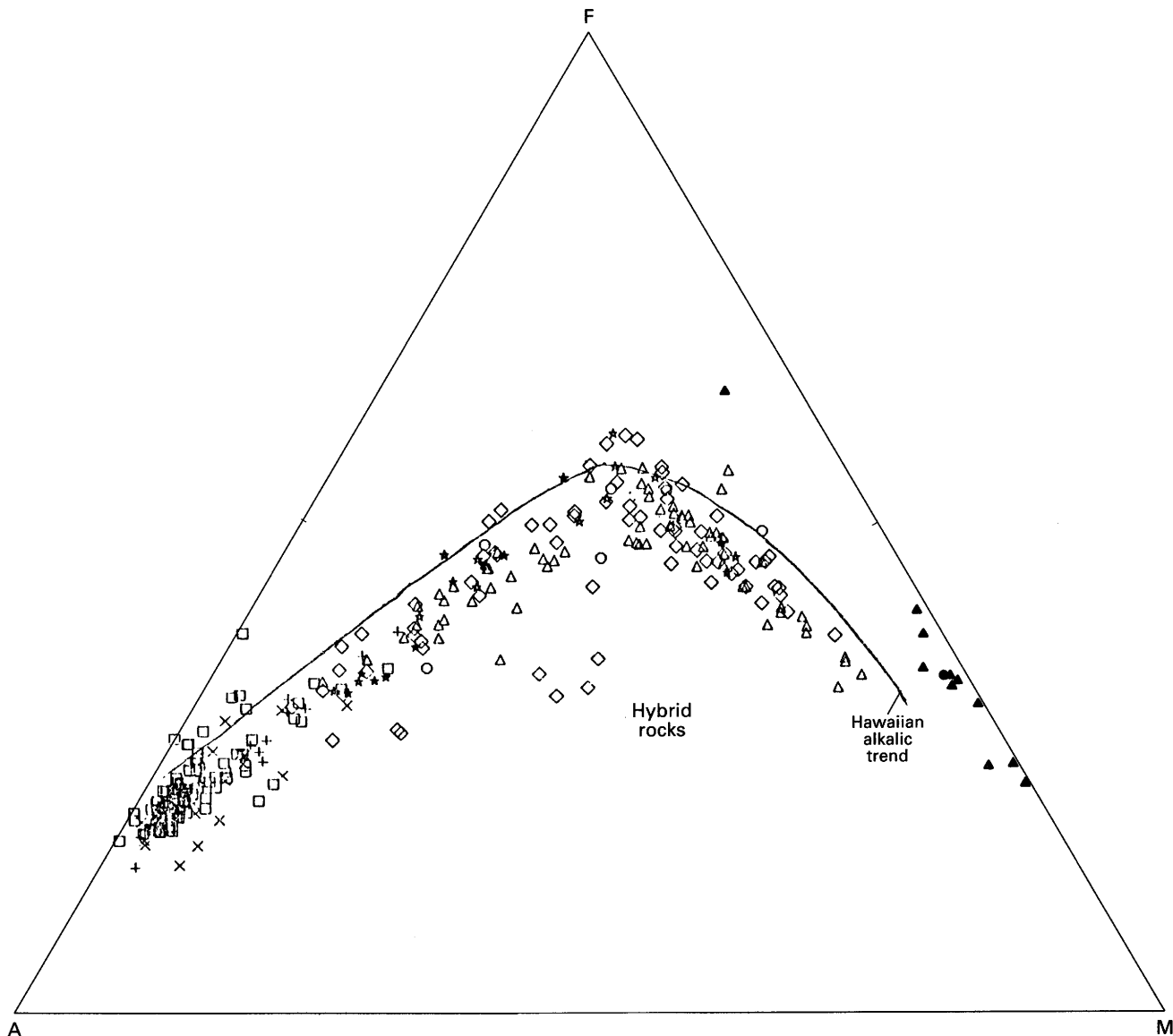


Figure 13. AFM ternary diagram. A, $\text{Na}_2\text{O}+\text{K}_2\text{O}$; F, $\text{FeO}+0.9*\text{Fe}_2\text{O}_3$; M, MgO. Symbols: \square , trachytes and tristanites of Agua de Pau volcano; $+$, trachytes and tristanites of Sete Cidades volcano; \times , trachytes and tristanites of Furnas volcano (\bullet , ultramafic or mafic xenolith); \diamond , mafic rocks on the flanks of Agua de Pau volcano; \triangle , mafic rocks on the flanks of Sete Cidades volcano (\blacktriangle , ultramafic or mafic xenolith); \star , mafic rocks on the flanks of Furnas volcano; \circ , Nordeste volcano.

SELECTED SERIES OF U.S. GEOLOGICAL SURVEY PUBLICATIONS

Periodicals

- Earthquakes & Volcanoes** (issued bimonthly).
- Preliminary Determination of Epicenters** (issued monthly).

Technical Books and Reports

Professional Papers are mainly comprehensive scientific reports of wide and lasting interest and importance to professional scientists and engineers. Included are reports on the results of resource studies and of topographic, hydrologic, and geologic investigations. They also include collections of related papers addressing different aspects of a single scientific topic.

Bulletins contain significant data and interpretations that are of lasting scientific interest but are generally more limited in scope or geographic coverage than Professional Papers. They include the results of resource studies and of geologic and topographic investigations; as well as collections of short papers related to a specific topic.

Water-Supply Papers are comprehensive reports that present significant interpretive results of hydrologic investigations of wide interest to professional geologists, hydrologists, and engineers. The series covers investigations in all phases of hydrology, including hydrology, availability of water, quality of water, and use of water.

Circulars present administrative information or important scientific information of wide popular interest in a format designed for distribution at no cost to the public. Information is usually of short-term interest.

Water-Resources Investigations Reports are papers of an interpretive nature made available to the public outside the formal USGS publications series. Copies are reproduced on request unlike formal USGS publications, and they are also available for public inspection at depositories indicated in USGS catalogs.

Open-File Reports include unpublished manuscript reports, maps, and other material that are made available for public consultation at depositories. They are a nonpermanent form of publication that maybe cited in other publications as sources of information.

Maps

Geologic Quadrangle Maps are multicolor geologic maps on topographic bases in 7 1/2- or 15-minute quadrangle formats (scales mainly 1:24,000 or 1:62,500) showing bedrock, surficial, or engineering geology. Maps generally include brief texts; some maps include structure and columnar sections only.

Geophysical Investigations Maps are on topographic or planimetric bases at various scales, they show results of surveys using geophysical techniques, such as gravity, magnetic, seismic, or radioactivity, which reflect subsurface structures that are of economic or geologic significance. Many maps include correlations with the geology.

Miscellaneous Investigations Series Maps are on planimetric or topographic bases of regular and irregular areas at various scales; they present a wide variety of format and subject matter. The series also includes 7 1/2-minute quadrangle photogeologic maps on planimetric bases which show geology as interpreted from aerial photographs. The series also includes maps of Mars and the Moon.

Coal Investigations Maps are geologic maps on topographic or planimetric bases at various scales showing bedrock or surficial geology, stratigraphy, and structural relations in certain coal-resource areas.

Oil and Gas Investigations Charts show stratigraphic information for certain oil and gas fields and other areas having petroleum potential.

Miscellaneous Field Studies Maps are multicolor or black-and-white maps on topographic or planimetric bases on quadrangle or irregular areas at various scales. Pre-1971 maps show bedrock geology in relation to specific mining or mineral-deposit problems; post-1971 maps are primarily black-and-white maps on various subjects such as environmental studies or wilderness mineral investigations.

Hydrologic Investigations Atlases are multicolored or black-and-white maps on topographic or planimetric bases presenting a wide range of geohydrologic data of both regular and irregular areas; the principal scale is 1:24,000, and regional studies are at 1:250,000 scale or smaller.

Catalogs

Permanent catalogs, as well as some others, giving comprehensive listings of U.S. Geological Survey publications are available under the conditions indicated below from the U.S. Geological Survey, Books and Open-File Reports Sales, Box 25425, Denver, CO 80225. (See latest Price and Availability List.)

"Publications of the Geological Survey, 1879-1961" may be purchased by mail and over the counter in paperback book form and as a set microfiche.

"Publications of the Geological Survey, 1962-1970" may be purchased by mail and over the counter in paperback book form and as a set of microfiche.

"Publications of the U.S. Geological Survey, 1971-1981" may be purchased by mail and over the counter in paperback book form (two volumes, publications listing and index) and as a set of microfiche.

Supplements for 1982, 1983, 1984, 1985, 1986, and for subsequent years since the last permanent catalog may be purchased by mail and over the counter in paperback book form.

State catalogs, "List of U.S. Geological Survey Geologic and Water-Supply Reports and Maps For (State)," may be purchased by mail and over the counter in paperback booklet form only.

"Price and Availability List of U.S. Geological Survey Publications," issued annually, is available free of charge in paperback booklet form only.

Selected copies of a monthly catalog "New Publications of the U.S. Geological Survey" is available free of charge by mail or may be obtained over the counter in paperback booklet form only. Those wishing a free subscription to the monthly catalog "New Publications of the U.S. Geological Survey" should write to the U.S. Geological Survey, 582 National Center, Reston, VA 22092.

Note.—Prices of Government publications listed in older catalogs, announcements, and publications may be incorrect. Therefore, the prices charged may differ from the prices in catalogs, announcements, and publications.



Pode escrever-se um poema com basalto

You can write a poem with basalt

com pedra negra e vinha sobre a lava

with black rock and vine on lava

com incenso mistérios criptomérias

with incense mistérios full of cryptomeria

e um grande Pico dentro da palavra.

and a big Pico in the middle of the word.

Ou talvez com gaviotas e cagarras

Or maybe with seagulls and cagarras

cigarras do silêncio que se trilha

cicadas strangling the silence

sílaba a sílaba até ao poema que está escrito

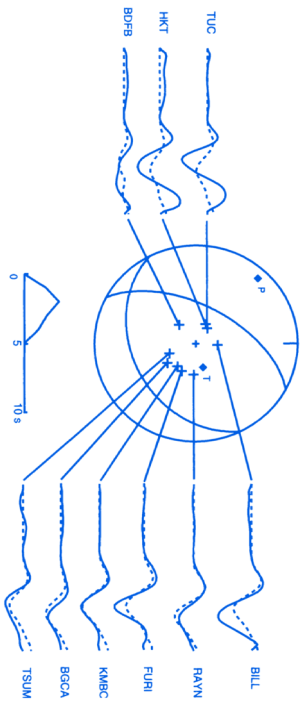
syllable to syllable till the poem is written

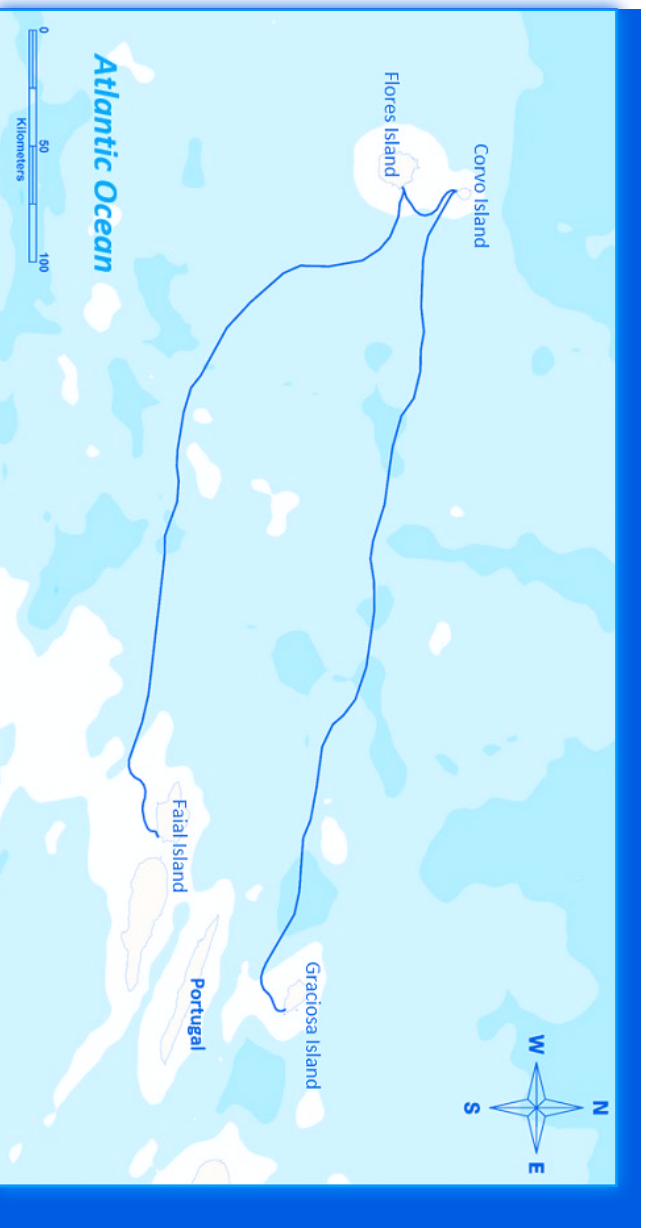
lá em cima no Pico sobre a ilha.

up there on Pico on top of the island.

— Ilha do Pico, Manuel Alegre

Socialist poet and politician and 2006 candidate to the Portuguese presidential election





The fiber optic submarine telecommunications cable system Flores-Corvo Cable System became ready for service around January 2014. Currently, we do not have any information regarding the system's technical specifications. The system has a length of 685 Kilometers and is owned and/or operated by Viatel. Flores-Corvo Cable System has landing points in Portugal.

Unrepeated system, total length 685km

Supper DRZ technology and Enhanced Raman technology

Design capacity: 0.96Tbit/s (16chsx10Gbit/sx6fp), achievable to 80chs x 40/100Gbit/s

RFS: October, 2013

Islands' remote location and geographical landscape

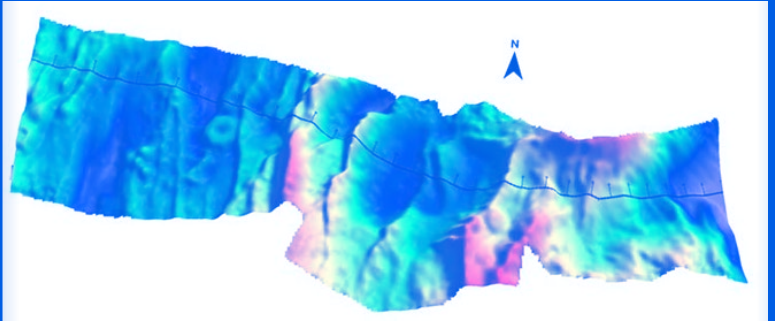
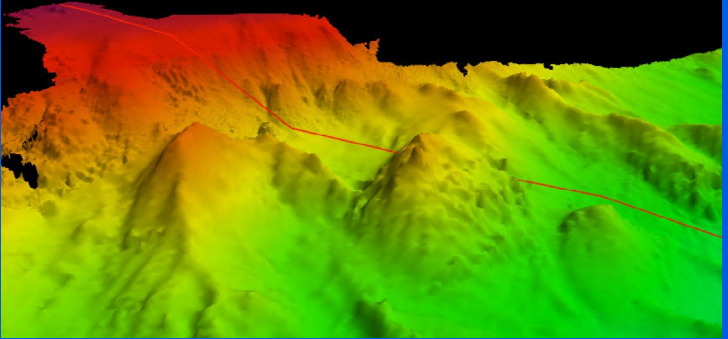
Protect the cable on a 22-meter cliff off the Flores shore

Deliver with in 10 months

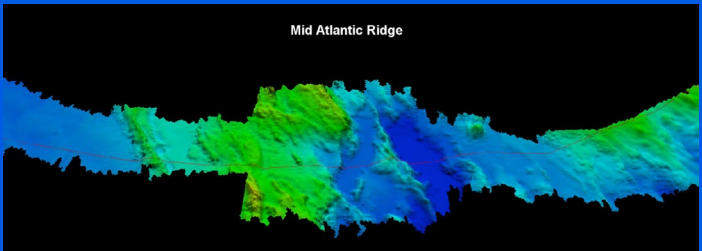


Bathymetric and geophysical surveys were performed in order to obtain the full coverage of the cable route corridor. Data acquisition was finalised to define the seabed geology and bathymetry and the detection and mapping of seabed hazards related to natural or man-made activities. It was a challenging project due to the location close to the Middle Atlantic Ocean Ridge.

Flores



Mid Atlantic Ridge



ONE PERSON'S NOISE IS
ANOTHER PERSON'S SIGNAL

All in all, over eleven million bits a second from the world to our sensory mechanisms.

But we experience far less: Consciousness processes far fewer bits. Over the decades, scientists have measured how much information the human consciousness can take in per second. This has been done in all kinds of ways, one of which is by measuring how many linguistic bits we can process when we read or listen. But language is not the only aspect studied. The ability to see and distinguish flashes of light, sense stimuli to the skin, tell different smells apart, and much more besides can be used in calculating that we consciously perceive about forty bits a second with our consciousness. A figure that may even be exaggerated.

Our sensory perception admits millions of bits a second; consciousness two score. The flow of information, measured in bits per second, is described as the bandwidth or capacity of consciousness. The bandwidth of consciousness is far lower than the bandwidth of our sensory perceptors.

— The User Illusion, Tor Norretranders

How *Much* the Eye Tells the Brain

Kristin Koch,¹ Judith McLean,¹ Ronen Segev,²
Michael A. Freed,¹ Michael J. Berry II,²
Vijay Balasubramanian,³ and Peter Sterling^{1,*}

¹Department of Neuroscience

University of Pennsylvania

Philadelphia, Pennsylvania 19104

²Department of Molecular Biology

Princeton University

Princeton, New Jersey 08544

³Department of Physics

University of Pennsylvania

Philadelphia, Pennsylvania 19104

Summary

In the classic “What the frog’s eye tells the frog’s brain,” Lettvin and colleagues [1] showed that different types of retinal ganglion cell send specific kinds of information. For example, one type responds best to a dark, convex form moving centripetally (a fly). Here we consider a complementary question: how *much* information does the retina send and how is it apportioned among different cell types? Recording from guinea pig retina on a multi-electrode array and presenting various types of motion in natural scenes, we measured information rates for seven types of ganglion cell. Mean rates varied across cell types (6–13 bits · s⁻¹) more than across stimuli. Sluggish cells transmitted information at lower rates than brisk cells, but because of trade-offs between noise and temporal correlation, all types had the same coding efficiency. Calculating the proportions of each cell type from receptive field size and coverage factor, we conclude (assuming independence) that the approximately 10⁵ ganglion cells transmit on the order of 875,000 bits · s⁻¹. Because sluggish cells are equally efficient but more numerous, they account for most of the information. With approximately 10⁶ ganglion cells, the human retina would transmit data at roughly the rate of an Ethernet connection.

Results

Natural Stimuli Differed from White Noise

The information rate for a ganglion cell responding to white noise is proportional to the information rate of a Poisson firing neuron with the same mean spike rate [2]. However, white noise is unsuited for calculating *natural* information rates because it contains all frequencies equally, whereas natural images contain spatio-temporal frequencies that are highly skewed (Figure 1) [3–6]. Therefore, we presented the guinea pig retina with video images of natural scenes to mimic the main categories of biological motion: saccades, optic flow, object

motion, and fixational eye movement. For these stimuli, the intensity distributions and the spatial and temporal spectra differed strikingly from white noise (Figure 1). Instead, like the distributions typical of natural images, they were skewed toward low intensities and low spatial and temporal frequencies.

Responses Depended on Cell Type

Various cell types were recorded simultaneously on a multi-electrode array [7] or singly with a loose patch electrode [2] and identified by their characteristic reverse correlograms and autocorrelograms (see Figure S1 in the Supplemental Data available with this article online) [8–10]. Comparing responses to a given stimulus across seven cell types, we found a characteristic response pattern for each type (Figure 2). For example, in response to the saccade stimulus, brisk-transient cells (both ON and OFF) fired spike bursts that peaked high in the PSTH (>300 spikes · s⁻¹), whereas brisk-sustained cells (both ON and OFF) peaked lower (~150 spikes · s⁻¹) and fired for longer periods (Figure 2). ON-OFF direction-selective cells fired with low jitter in spike timing across trials, whereas local-edge cells fired with considerable jitter (Figure 2 saccade, standard deviation of spike times across trials was 9 ms versus 43 ms).

On the other hand, while comparing responses across four different stimuli, we found that characteristic response patterns were stable (Figure 2). For example, brisk-transient peaks always exceeded 200 spikes · s⁻¹ and ON-OFF direction-selective cells always fired with low jitter in spike timing (Figure 2; 9–17 ms), whereas local-edge cells always fired with considerable jitter (Figure 2; 18–68 ms). We quantified these observations by comparing five basic statistics of the spike train: peak rate, mean rate, temporal jitter (standard deviation of spike timing across repeats [2]), burst fraction (fraction of spikes that occurred <6 ms apart), and firing fraction (fraction of time bins during which a cell fired at ≥ 5% of its peak rate). Spike statistics were constant across stimuli, and this was true for all cell types. Each statistic depended on cell type (two-way analysis of variance, Bonferroni/Dunn post-hoc test, $p < 0.05$), whereas spike statistics generally did not depend on the stimulus ($p > 0.05$). The only exception was that the local-edge cell type fired with significantly greater spike-time jitter to the object motion stimulus than to the fixational stimulus (Figure S2; $p < 0.05$).

Because spike statistics differed between cell types more than between stimuli, the rank ordering of cells was consistent across stimuli and the key response features of each cell type were preserved (Figure S2). Thus, brisk-transient cells always had the largest burst fraction and highest peak rates; brisk-sustained cells usually had the largest firing fraction, and direction-selective cells usually had the smallest firing fraction. Direction-selective and local-edge cells always fired at about half the mean rate of brisk cells; local-edge cells usually had the greatest timing jitter. When pooled

*Correspondence: peter@retina.anatomy.upenn.edu

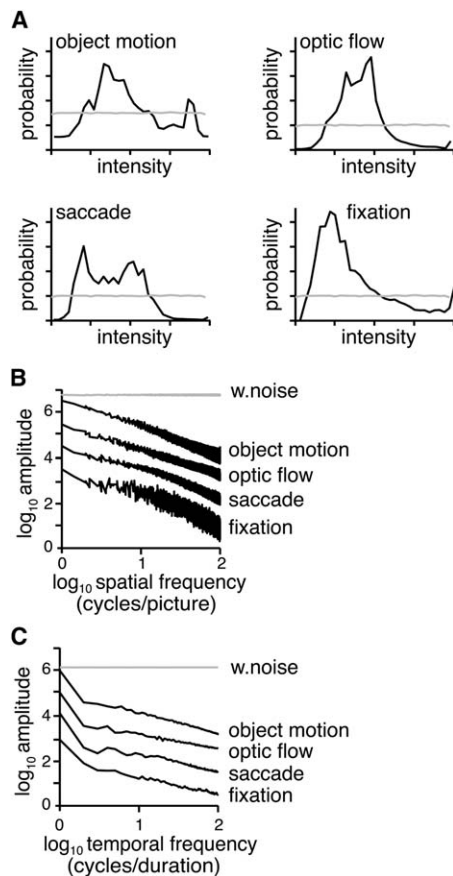


Figure 1. Statistics of Natural Stimuli Differ from Those of White Noise

Natural movies mimicked saccades, optic flow, and object motion [10]. To mimic fixational eye movements, we used Psychophysics toolbox [40, 41] to jitter van Hateren’s images (<http://hlab.phys.rug.nl/archive.html>) randomly over the retina, with step size and velocity matched to that measured for the rabbit [9, 42]. When projected onto the retina, stimuli filled approximately 4 mm × 4 mm with mean luminance corresponding to photopic vision. The photon absorption rates were 2900 and 440 photons · s⁻¹ for the M and S cones, respectively. Each movie lasted 20–27 s and was repeated 60–100 times. Intensity distributions and amplitude spectra were obtained after averaging over all frames.

(A) Intensities in white noise (gray lines) are equally represented, but in natural scenes (black lines), lower intensities are more likely.

(B) Spatial frequencies in white noise have equal amplitude, but in natural scenes, amplitude declines with frequency (slope ~ -1.5). Spectra have been separated (shifted up) for clarity.

(C) Temporal frequencies in white noise have equal amplitude, but in natural motion, amplitude declines with frequency (slope ~ -1.0). Spectra have been shifted up for clarity.

across stimuli and compared with a one-way ANOVA, brisk-transient cells had the highest burst fractions and fired at the highest peak rates (Table 1; $p < 0.05$), and ON-OFF direction-selective cells fired at higher peak rates than local-edge cells ($p < 0.05$). Brisk-sustained cells had higher firing fractions than direction-selective cells ($p < 0.05$). Brisk-transient cells fired at the highest mean rates ($p < 0.05$). Local-edge responses to saccades, optic flow, and object motion showed the highest timing jitter ($p < 0.05$). No other significant differences were found in the responses of the different cell types. Because ON and OFF cells of the same class (brisk-

transient, brisk-sustained) were similar (Table 1), they were pooled in subsequent analyses.

Information Rate Correlated with Mean Spike Rate

The information rate was moderately correlated with peak spike rate and firing fraction (respectively, $r = 0.57$ and 0.48) but strongly correlated with mean spike rate ($r = 0.90$; Figure 3A). Information rate was negatively correlated with timing jitter ($r = -0.29$) because jitter increases noise entropy. Thus, cell types with the highest mean spike rates and lowest jitter (brisk-transient) sent the most bits · s⁻¹ (Figure S2). Information rate depended on cell type ($p < 0.05$) and not on the stimulus ($p > 0.05$). Information rate was constant across stimuli, and this was true for all cell types (Figure S2; $p > 0.05$). Averaged across stimuli, the information rates of brisk-transient cells were highest (Table S1; $p < 0.05$).

Information per Spike Decreased with Mean Spike Rate

The average information per spike (information rate divided by mean spike rate) was highest for the lowest spike rates (~3.5 bits · spike⁻¹ vs. ~1 bit · spike⁻¹ for the highest rate (Figure 3D)). This agrees with the information-theory principle that rarer events carry more information per event [11–13]. Accordingly, cells with lower mean spike rates (typically ON direction-selective cells, ON-OFF direction-selective cells, and local-edge cells) sent approximately 20% more bits · spike⁻¹ than the brisk types (Table S1).

All Cell Types Filled Their Coding Capacities Similarly

Cells with higher spike rates have a greater capacity to encode information, but some cells might make better use of their capacity than others, i.e., might show greater coding efficiency. Coding capacity is the maximum total entropy rate possible at the mean spike rate [2, 11, 14]. It is achieved when spikes are independent (have no temporal correlations) and when the spike train is perfectly reproducible (there is no noise entropy). Coding capacity, C , is calculated as

$$C(R, \Delta t) = \frac{-R\Delta t \log_2(R\Delta t) - (1-R\Delta t) \log_2(1-R\Delta t)}{\Delta t} \text{bits} \cdot \text{s}^{-1} \quad (1)$$

where R = mean spike rate and $\Delta t = 5$ ms, i.e., the time bin used to calculate information. Coding efficiency is a cell’s actual information rate divided by its coding capacity.

Coding capacity differed across types—with means ranging from ~20 bits · s⁻¹ for direction-selective and local-edge cells to ~40 bits · s⁻¹ for brisk cells. However, all types showed the same coding efficiencies (~30% of capacity; Figure 3A and Table S1; $p < 0.05$). Coding efficiency was also the same across stimuli, and this was true for all cell types (Figure S2; $p > 0.05$).

What Sets Coding Efficiency?

Total entropy averaged across cells and stimuli filled 91% of capacity (Figure 3B). This implied that 9% was lost to temporal correlations. The fractional loss depended on cell type: brisk-transient cells lost 15%,

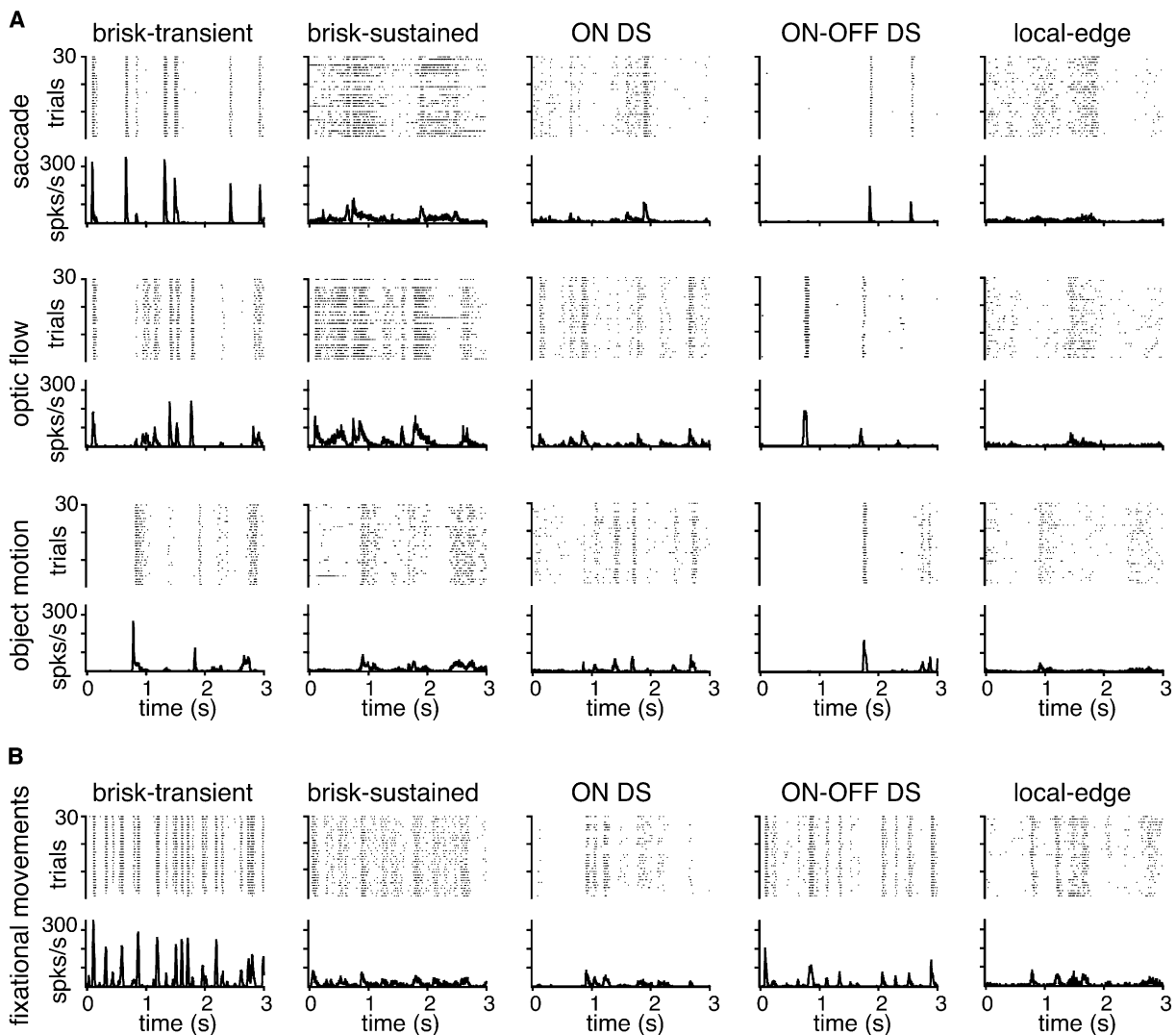


Figure 2. Four Types of Natural Motion Evoked Similar Spike Patterns within a Cell Type But Different Patterns Across Types
(A) All five cells were recorded simultaneously (multi-electrode array). Each cell responded similarly to all three motion stimuli. The brisk-transient and ON-OFF direction-selective (DS) cells responded with high peak rates and low firing fractions, whereas the brisk-sustained, ON DS, and local-edge cells responded with lower peak rates and higher firing fractions. The brisk-transient and ON-OFF DS responses showed the lowest spike-time jitter across trials, whereas the brisk-sustained and local-edge responses showed the highest. As expected for sluggish types, mean firing rates were about half that of the brisk cell types [2].
(B) Cells were recorded singly (loose-patch). Spike patterns to simulated fixational eye movements resembled those of the other types of motion.

whereas local-edge cells lost only 4% (Table S1; $p < 0.05$). Noise entropy averaged across cells and stimuli filled 65% of capacity (Figure 3C). This implies that 65% of capacity was lost to spike train noise. Again, the fractional loss depended on cell type; brisk-transient cells lost 56%, whereas local-edge cells lost 69% ($p < 0.05$). There were no other significant differences across cell types, nor did losses depend on the stimulus ($p > 0.05$). Most cells lost more capacity to spike train noise than to temporal correlations between spikes.

Cell types differing in temporal correlations and noise could transmit with equal efficiency if larger losses due to correlations were offset by smaller losses to noise. This is precisely what we found (Figure 3E; Table S1). For brisk-transient cells, total entropy filled a small fraction of capacity because spikes were strongly correlated, whereas noise entropy was reduced. Conversely,

for local-edge cells, total entropy filled a larger fraction of capacity because spikes were weakly correlated, whereas noise entropy was elevated. Thus, coding efficiency was conserved across cell types because losses due to temporal correlations were finely balanced against losses due to noise.

This balance would be achieved if spike bursts (which inevitably produce correlations) also increase reliability. This is precisely what we found. Spike trains with many bursts (high burst fractions) had much less total entropy compared to their capacities than did spike trains with few bursts (Figure 3F). Bursty spike trains also tended toward lower noise entropy (Figure 3G). This occurs partly because the spike rate during a burst approaches the refractory period; inter-spike intervals are thus regularized, and the spike train's variability is reduced [15].

Table 1. Spike Train Statistics Averaged over All Natural Stimuli

Cell Type	Burst Fraction	Peak Spike Rate (Hz)	Firing Fraction	Mean Spike Rate (Hz)	Jitter (ms)
Brisk-transient (n = 41)	0.26 ± 0.12	171 ± 71	0.22 ± 0.18	8 ± 5	15 ± 7
ON brisk-transient (n = 9)	0.27 ± 0.12	157 ± 77	0.33 ± 0.24	10 ± 6	19 ± 10
OFF brisk-transient (n = 32)	0.26 ± 0.12	175 ± 70	0.19 ± 0.14	7 ± 4	14 ± 6
Brisk-sustained (n = 65)	0.10 ± 0.12	104 ± 38	0.29 ± 0.19	6 ± 4	23 ± 9
ON brisk-sustained (n = 27)	0.11 ± 0.12	119 ± 39	0.29 ± 0.23	6 ± 4	20 ± 8
OFF brisk-sustained (n = 38)	0.08 ± 0.12	93 ± 34	0.30 ± 0.19	6 ± 5	26 ± 9
ON DS (n = 15)	0.07 ± 0.12	90 ± 30	0.15 ± 0.11	3 ± 2	18 ± 5
ON-OFF DS (n = 33)	0.08 ± 0.12	117 ± 36	0.17 ± 0.15	4 ± 3	17 ± 7
Local-edge (n = 19)	0.07 ± 0.12	74 ± 36	0.25 ± 0.14	4 ± 3	40 ± 24

Values are given as mean ± SD.

Discussion

Any study employing natural images faces the concern that only a few of all possible images can be tested. Yet, because natural images share statistical regularities (such as scale-invariant power spectra [4] and skewed intensity distributions [16]), our stimuli resembled each other much more than they resembled white noise (Figure 1). Indeed, the information rates measured here are lower than those reported for white noise [2, 17]. This difference probably arises, at least in part, because white noise lacks spatio-temporal correlations.

Another concern, especially for ganglion cells selective for “trigger features,” is that particular images might fail to excite certain cell types. Yet, we found that all cells responded to all stimuli over much of their dynamic range. Feature-selective types such as the local-edge cell, considered “sluggish” due to its lower peak and average rates [18], fired up to 75 spikes · s⁻¹ and averaged 4 spikes · s⁻¹ over the entire recording. This was only 2-fold less than the peak and average responses to artificial stimuli that are deliberately tuned to the trigger features [2]. Far from being silent, the local-edge type showed larger firing fractions than the less selective brisk-transient type (Figure S2). In general, responses differed more across types than across stimuli.

How Much Information Does the Eye Send the Brain?

The following calculation treats individual ganglion cells as independent channels. Of course, the messages sent by cells of the same and different types are *not* totally independent. Rather, they are partially correlated and the correlations may be important [10]. To calculate the *net* information conveyed about visual stimuli, one would need to evaluate these correlations. Yet, a calculation that excludes them is still useful because it: (i) allows initial estimates of basic parameters, such as power efficiency (bits · erg⁻¹); (ii) reveals how visual information is distributed among the different neural components; and (iii) provides a sense of scale for thinking about the visual system as a whole.

The guinea pig optic nerve sends about 100,000 axons centrally (our unpublished counts [19, 20]). Brisk-transient ganglion cells (ON + OFF) account for about 6% (Kao and P.S., unpublished data; similar estimates are found in cats [21] and primates [22]). The mean information rate for a single brisk-transient cell is about 13 bits · s⁻¹; thus, the brisk-transient component of the guinea pig optic nerve sends approximately 78,000 bits · s⁻¹.

OFF brisk-transient cells are twice as numerous as ON cells in the guinea pig (Borghuis et al., personal communication; see also results for primates [23]). Because OFF and ON transmit at equal rates, the OFF and ON cells contribute, respectively, about 52,000 bits · s⁻¹ and 26,000 bits · s⁻¹. This fits the findings that natural contrast distributions are skewed toward negative contrasts [24, 25] and dark regions in natural images contain more information (Ratliff et al., personal communication).

Next we calculated the density for each cell type, from its dendritic-field area and degree of overlap with its neighbors (Table S2). The ratios of cell densities, plus the fact that there are approximately 6,000 brisk-transient cells, yield numbers for the other types studied here: approximately 24,000 brisk-sustained cells, approximately 7,000 ON direction-selective cells, approximately 12,000 ON-OFF direction-selective cells, and approximately 20,000 local-edge cells. This leaves 30% of optic axons to be apportioned among approximately 5 additional cell types [26]. Because these types are all “sluggish” [18], we assigned them the average information rates for additional sluggish cells that were recorded but not classified by type (9 bits · s⁻¹; n = 18). The total information rate for all components in the optic nerve sums to approximately 875,000 bits · s⁻¹ (Table S2).

Sluggish Cells Transmit Most Information

Most studies of ganglion-cell coding have focused on the brisk types (X and Y in cats, M and P in primates). The sluggish types, despite their similar S/N ratio [27] and large contribution to the optic nerve [18], have been largely ignored. Thus, it is startling to realize that the famous brisk-transient cells contribute only 9% of the information sent down the optic nerve, whereas the more mysterious local-edge cells contribute nearly twice as much! Overall, the non-brisk types contribute 64% of the information; and thus far outscore the brisk types (Table S2).

Correlations in the messages sent by different cells will affect the net information transmitted about visual stimuli relative to the total information and might also affect the proportion carried by each cell type. However, existing measurements suggest comparable redundancies in the responses of different cell classes, with a significant fraction of the “shared information” arising from receptive-field overlap [10, 28]. Thus, when the correlations are accounted for, the sluggish category will probably carry at least as much information as the brisk category—and substantially more than the brisk-transient types.

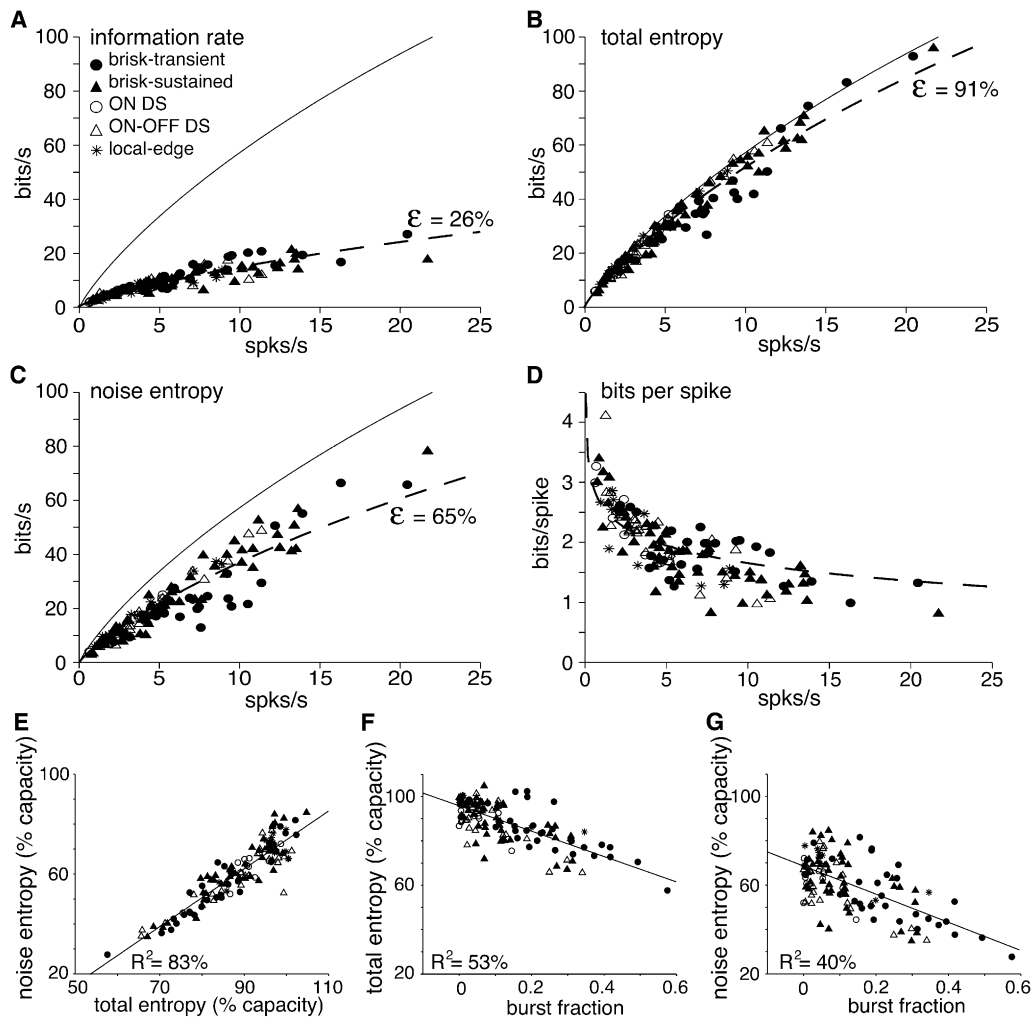


Figure 3. All Cell Types Transmitted Information with Similar Efficiency Because Total Entropy and Noise Entropy were Correlated by Spike Train Bursts

Information rate (total entropy–noise entropy) was estimated by the direct method [43] with bin width (Δt) = 5 ms and spike word-lengths up to eight digits. Bin width was set by the longest refractory period (5 ms for local-edge cells). Estimates of total and noise entropies were extrapolated to infinite data size [44]. Estimated total and noise entropies were within 15% of that calculated for the longest word. A solid line shows the coding capacity of a ganglion cell assuming noiseless firing with no spike correlations ($C(R, \Delta t)$; see text). A dashed line shows the fraction of coding capacity (ϵ) that best fit information rate, total entropy, or noise entropy.

(A) Information rate was 26% of coding capacity ($0.26 C(R, \Delta t)$). K^2 (percent of variation unexplained by coding capacity equation) was 19%.

(B) Total entropy was 91% of coding capacity. $K^2 = 4\%$.

(C) Noise entropy was 65% of coding capacity. $K^2 = 12\%$.

(D) A dashed line indicates the fraction of coding capacity per spike, $(0.26 * C(R, \Delta t))/R$. Lower rates carry more bits per spike.

(E) Line is least squares fit; slope = 1.2 ($R^2 =$ coefficient of determination). Noise entropy is strongly correlated with total entropy.

(F) Burst fraction is the fraction of spikes with interspike intervals <6 ms. Line is least squares fit; slope = -0.6 . Total entropy as a fraction of capacity decreased with burst fraction.

(G) Line is least squares fit; slope = -0.6 . Noise entropy as a fraction of capacity decreased with burst fraction.

Why Are There Many Ganglion Cell Types?

Nerve fibers in the frog auditory nerve are reported to encode naturalistic stimuli with an efficiency sometimes reaching approximately 90% of capacity (4-fold greater than for white noise [29]). This differs strikingly from optic fibers, where coding efficiency to naturalistic stimuli is 3-fold worse than in auditory fibers and where there is little (if any) enhancement compared to white noise. Naturally one wonders why an optic fiber fares so poorly in these comparisons. Our tentative answer bears on the question of why the retina uses so many cell types.

Auditory fibers apparently achieve their high coding efficiency via a “tuned” nonlinear filter that selectively amplifies the anticipated signal [29]. A similar strategy is apparently used by the mammalian rod bipolar cell to encode single photon responses [30]. However, this coding strategy, highly effective when the anticipated signal is sparse and well defined, may serve poorly for ganglion cells because the information of biological interest in natural scenes is so varied that highly tuned, nonlinear filters would either reject too much information or require too many cell types.

Given the ganglion cell strategy of broad tuning and equal coding efficiency, why does the retina not send all visual information over one cell type with a high information rate? This is possibly because the energetic cost of signaling increases nonlinearly with temporal frequency and information rate of individual axons [31–34]. To illustrate, we compare the cost of transmitting $300 \text{ bits} \cdot \text{s}^{-1}$ over a bundle of independent axons with mean spike rates of 4 Hz (local-edge cells), 8 Hz (brisk-transient cells), and 40 Hz (hypothetical high-rate channel). Given approximately 30% efficiency, the 4 Hz neuron sends $2.1 \text{ bits} \cdot \text{spike}^{-1}$, the 8 Hz neuron sends only $1.1 \text{ bits} \cdot \text{spike}^{-1}$ (from Equation 1). Thus, for $300 \text{ bits} \cdot \text{s}^{-1}$, the “local-edge” cable would use $\sim 140 \text{ spikes} \cdot \text{s}^{-1}$, the “brisk-transient” cable would use $\sim 170 \text{ spikes} \cdot \text{s}^{-1}$, and the high-rate cable would use approximately $270 \text{ spikes} \cdot \text{s}^{-1}$. Because the dominant metabolic cost in neural signaling is associated with spiking [35, 36], the cables with lower firing rates would save considerable energy. Likewise, theoretical studies predict that metabolic cost is minimized when signals are distributed over many weakly active cells [37].

Of course, there are other reasons to use multiple cell types [38]. Spatial acuity requires narrow-field cells with a high sampling rate [39]. Because such a type must necessarily distribute densely, its information rate should be relatively low to reduce costs. On the other hand, encoding of high stimulus velocities requires extended spatial summation and thus a broad-field cell—plus the ability to transmit at high bit rates so as not to lose the higher temporal frequencies. Such a cell type must necessarily be expensive, but given the extended dendritic field, this type can be sparse. Consequently energetic considerations probably interact with other constraints to set the number of cell types and a general information rate of roughly $10 \text{ bits} \cdot \text{s}^{-1}$ and $2 \text{ bits} \cdot \text{spike}^{-1}$.

Supplemental Data

Supplemental Data include two figures and two tables and can be found with this article online at <http://www.current-biology.com/cgi/content/full/16/14/1428/DC1/>.

Acknowledgments

We thank Nadiya Tkachuk for assisting with the multi-electrode recordings and Charles Ratliff for analyzing the natural stimuli. This work was supported by National Institute of Health grants T32 EY07035, EY08124, EY013333, and EY014196 and National Science Foundation grant IBN0344678.

Received: May 16, 2006

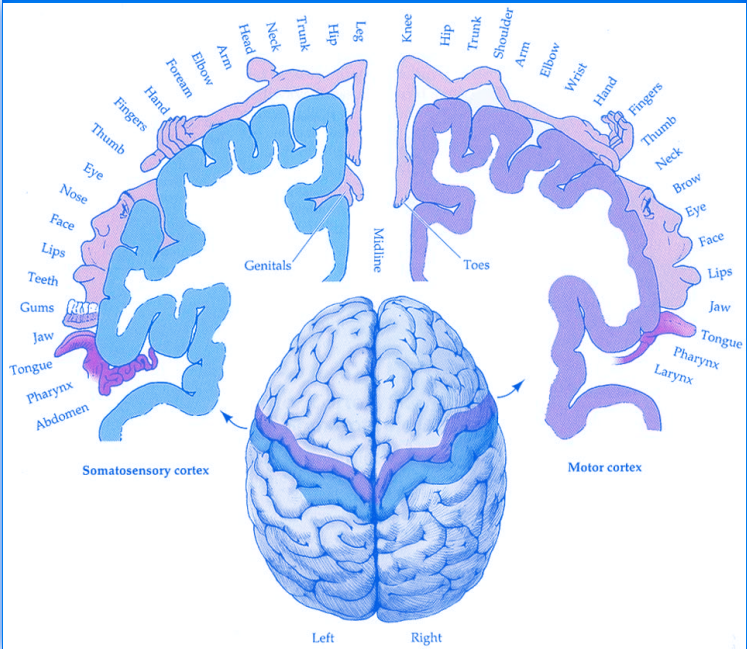
Accepted: May 18, 2006

Published: July 24, 2006

References

1. Lettvin, J.Y., Maturana, H.R., McCulloch, W.S., and Pitts, W.H. (1959). What the frog's eye tells the frog's brain. *Proc. Inst. Radio Engr.* 47, 1940–1951.
2. Koch, K., McLean, J., Berry, M., Sterling, P., Balasubramanian, V., and Freed, M.A. (2004). Efficiency of information transmission by retinal ganglion cells. *Curr. Biol.* 14, 1523–1530.
3. Dong, D.W., and Attick, J.J. (1995). Statistics of natural time-varying images. *Network: Computation in Neural Systems* 6, 345–358.
4. Field, D.J. (1987). Relations between the statistics of natural images and the response properties of cortical cells. *J. Opt. Soc. Am. A* 4, 2379–2394.
5. Simoncelli, E.P., and Olshausen, B.A. (2001). Natural image statistics and neural representation. *Annu. Rev. Neurosci.* 24, 1193–1216.
6. Eckert, M.P., and Buchsbaum, G. (1993). Efficient coding of natural time varying images in the early visual system. *Philos. Trans. R. Soc. Lond. B Biol. Sci.* 339, 385–395.
7. Segev, R., Goodhouse, J., Puchalla, J., and Berry, M.J., 2nd. (2004). Recording spikes from a large fraction of the ganglion cells in a retinal patch. *Nat. Neurosci.* 7, 1154–1161.
8. Devries, S.H., and Baylor, D.A. (1997). Mosaic arrangement of ganglion cell receptive fields in rabbit retina. *J. Neurophysiol.* 78, 2048–2060.
9. Olveczky, B.P., Baccus, S.A., and Meister, M. (2003). Segregation of object and background motion in the retina. *Nature* 423, 401–408.
10. Puchalla, J.L., Schneidman, E., Harris, R.A., and Berry, M.J. (2005). Redundancy in the population code of the retina. *Neuron* 46, 493–504.
11. Rieke, F., Wartland, D., de Ruyter van Steveninck, R., and Bialek, W. (1997). *Spikes: Exploring the Neural Code* (Cambridge, MA: MIT Press).
12. Shannon, C.E., and Weaver, W. (1949). *The Mathematical Theory of Communication* (Urbana, IL: University of Illinois Press).
13. Zador, A. (1998). Impact of synaptic unreliability on the information transmitted by spiking neurons. *J. Neurophysiol.* 79, 1219–1229.
14. MacKay, D., and McCulloch, W.S. (1952). The limiting information capacity of a neuronal link. *Bull. Math. Biophys.* 14, 127–135.
15. Berry, M.J., 2nd, and Meister, M. (1998). Refractoriness and neural precision. *J. Neurosci.* 18, 2200–2211.
16. Richards, W.A. (1982). Lightness scale from image intensity distributions. *Appl. Opt.* 21, 2569–2582.
17. Passaglia, C.L., and Troy, J.B. (2004). Information transmission rates of cat retinal ganglion cells. *J. Neurophysiol.* 91, 1217–1229.
18. Troy, J.B., and Shou, T. (2002). The receptive fields of cat retinal ganglion cells in physiological and pathological states: Where we are after half a century of research. *Prog. Retin. Eye Res.* 21, 263–302.
19. Guy, J., Ellis, E.A., Kelley, K., and Hope, G.M. (1989). Spectra of G ratio, myelin sheath thickness, and axon and fiber diameter in the guinea pig optic nerve. *J. Comp. Neurol.* 287, 446–454.
20. Do-Nascimento, J.L., Do-Nascimento, R.S., Damasceno, B.A., and Silveira, L.C. (1991). The neurons of the retinal ganglion cell layer of the guinea pig: Quantitative analysis of their distribution and size. *Braz. J. Med. Biol. Res.* 24, 199–214.
21. Wässle, H., Levick, W.R., and Cleland, B.G. (1975). The distribution of the alpha type of ganglion cells in the cat's retina. *J. Comp. Neurol.* 159, 419–438.
22. Dacey, D.M. (1994). Physiology, morphology and spatial densities of identified ganglion cell types in primate retina. *Ciba Found Symp* 184, 12–28, discussion 28–34, 63–70.
23. Chichilnisky, E.J., and Kalmar, R.S. (2002). Functional asymmetries in ON and OFF ganglion cells of primate retina. *J. Neurosci.* 22, 2737–2747.
24. Laughlin, S.B. (1981). A simple coding procedure enhances a neuron's information capacity. *Z. Naturforsch. [C]* 36, 910–912.
25. Laughlin, S.B. (1983). Matching coding to scenes to enhance efficiency. In *Physical and Biological Processing of Images*, O.J. Braddick and A. Sleigh, eds. (Berlin: Springer), pp. 42–52.
26. Rockhill, R.L., Daly, F.J., MacNeil, M.A., Brown, S.P., and Masland, R.H. (2002). The diversity of ganglion cells in a mammalian retina. *J. Neurosci.* 22, 3831–3843.
27. Xu, Y., Dhingra, N.K., Smith, R.G., and Sterling, P. (2005). Sluggish and brisk ganglion cells detect contrast with similar sensitivity. *J. Neurophysiol.* 93, 2388–2395.
28. Segev, R., Puchalla, J., and Berry, M.J., 2nd. (2006). Functional organization of ganglion cells in the salamander retina. *J. Neurophysiol.* 95, 2277–2292.
29. Rieke, F., Bodnar, D.A., and Bialek, W. (1995). Naturalistic stimuli increase the rate and efficiency of information transmission by primary auditory afferents. *Proc. Biol. Sci.* 262, 259–265.

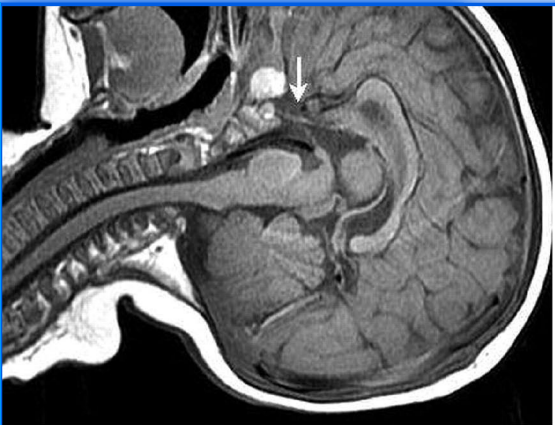
30. Field, G.D., and Rieke, F. (2002). Nonlinear signal transfer from mouse rods to bipolar cells and implications for visual sensitivity. *Neuron* *34*, 773–785.
31. Attwell, D., and Gibb, A. (2005). Neuroenergetics and the kinetic design of excitatory synapses. *Nat. Rev. Neurosci.* *6*, 841–849.
32. Balasubramanian, V., Kimber, D., and Berry, M.J., 2nd. (2001). Metabolically efficient information processing. *Neural Comput.* *13*, 799–815.
33. Laughlin, S.B., de Ruyter van Steveninck, R.R., and Anderson, J.C. (1998). The metabolic cost of neural information. *Nat. Neurosci.* *1*, 36–41.
34. Levy, W.B., and Baxter, R.A. (1996). Energy efficient neural codes. *Neural Comput.* *8*, 531–543.
35. Attwell, D., and Laughlin, S.B. (2001). An energy budget for signaling in the grey matter of the brain. *J. Cereb. Blood Flow Metab.* *21*, 1133–1145.
36. Lennie, P. (2003). The cost of cortical computation. *Curr. Biol.* *13*, 493–497.
37. Sarpeshkar, R. (1998). Analog versus digital: Extrapolating from electronics to neurobiology. *Neural Comput.* *10*, 1601–1638.
38. Sterling, P. (2004). How retinal circuits optimize the transfer of visual information. In *The Visual Neurosciences*, L.M. Chalupa and J.S. Werner, eds. (Cambridge, MA: MIT Press), pp. 234–259.
39. Wässle, H., and Boycott, B.B. (1991). Functional architecture of the mammalian retina. *Physiol. Rev.* *71*, 447–480.
40. Brainard, D.H. (1997). The Psychophysics Toolbox. *Spat. Vis.* *10*, 433–436.
41. Pelli, D.G. (1997). The VideoToolbox software for visual psychophysics: Transforming numbers into movies. *Spat. Vis.* *10*, 437–442.
42. Van der Steen, J., and Collewijn, H. (1984). Ocular stability in the horizontal, frontal and sagittal planes in the rabbit. *Exp. Brain Res.* *56*, 263–274.
43. de Ruyter van Steveninck, R.R., Lewen, G.D., Strong, S.P., Koberle, R., and Bialek, W. (1997). Reproducibility and variability in neural spike trains. *Science* *275*, 1805–1808.
44. Strong, S.P., Koberle, R., de Ruyter van Steveninck, R.R., and Bialek, W. (1998). Entropy and Information in Neural Spike Trains. *Phys. Rev. Lett.* *80*, 197–200.



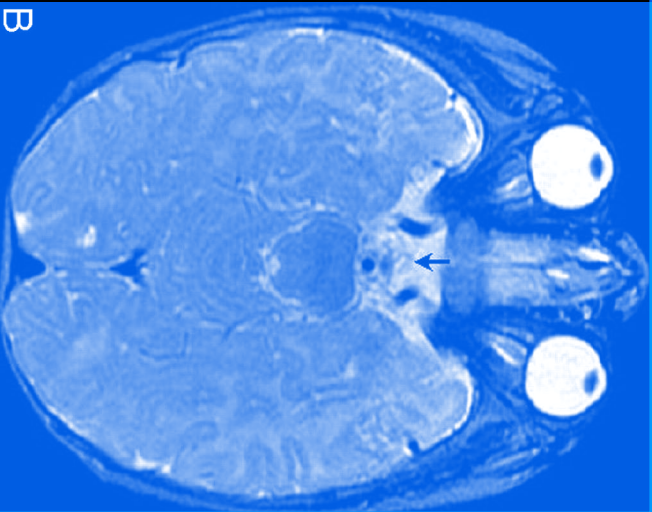
“Of all the information that every second flows into our brains from our sensory organs, only a fraction arrives in our consciousness: the ratio of the capacity of perception to the capacity of apperception is at best a million to one... That is to say, only one millionth of what our eyes see, our ears hear, and our other senses inform us about appears in our consciousness. Metaphorically, consciousness is like a spotlight that emphasizes the face of one actor dramatically, while all the other persons, props, and sets on the vast stage are lost in the deepest darkness. The spotlight can move, certainly, but it takes a long time for all the faces in the chorus to be revealed, one after the other, in the darkness. It goes without saying that this newly discovered fact has the greatest practical significance for all areas of human life.”

— Dietrich Trincker (1965)

Lecture held on the occasion of the three-hundredth anniversary of the University of Kiel



A

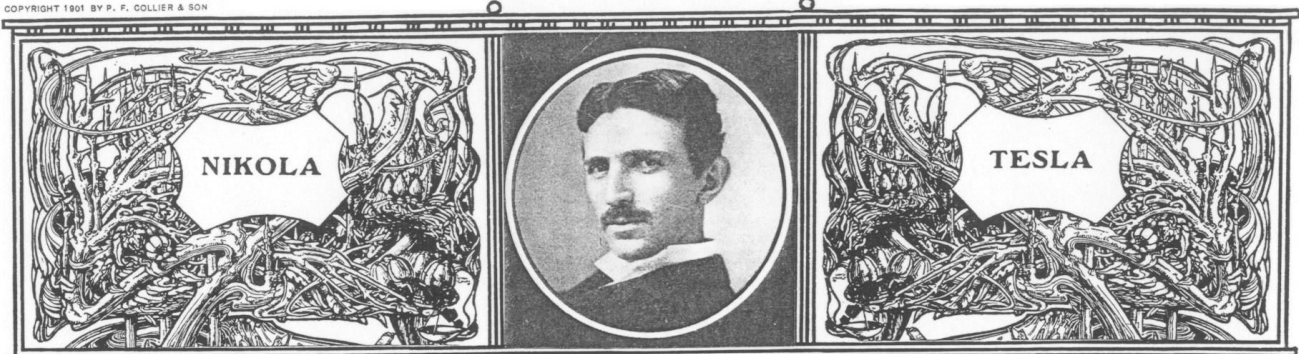


B

B

“Typical frequency range for environmental ground vibrations is 1 – 200 Hz. Waves of lower frequencies (below 1 Hz) are called microseisms, and they are normally associated with natural phenomena, e.g. water waves in the oceans. Environmental ground vibrations generated by rail and road traffic may cause annoyance to residents of nearby buildings both directly and via generated structure-borne interior noise. Very strong ground vibrations, e.g. generated by heavy lorries on bumped roads, may even cause structural damage to very close buildings. Magnitudes of ground vibrations are usually described in terms of particle vibration velocity (in mm/s or m/s). Sometimes they are also described in decibels (relative to the reference particle velocity of 10^{-9} m/s). Typical values of ground vibration particle velocity associated with vehicles passing over traffic calming road humps are in the range of 0.1 – 2 mm/s. Magnitudes of ground vibrations that are considered to be able to cause structural damage to buildings are above 10–20 mm/s.”

COPYRIGHT 1901 BY P. F. COLLIER & SON



TALKING WITH THE PLANETS

By NIKOLA TESLA

EDITOR'S NOTE.—Mr. Nikola Tesla has accomplished some marvellous results in electrical discoveries. Now, with the dawn of the new century, he announces an achievement which will amaze the entire universe, and which eclipses the wildest dream of the most visionary scientist. He has received communication, he asserts, from out the great void of space; a call from the inhabitants of Mars, or Venus, or some other sister planet! And, furthermore, noted scientists like Sir Norman Lockyer are disposed to agree with Mr. Tesla in his startling deductions.

Mr. Tesla has not only discovered many important principles, but most of his inventions are in practical use; notably in the harnessing of the Titanic forces of Niagara Falls, and the discovery of a new light by means of a vacuum tube. He has, he declares, solved the problem of telegraphing without wires or artificial conductors of any sort, using the earth as his medium.

By means of this principle he expects to be able to send messages under the ocean, and to any distance on the earth's surface. Interplanetary communication has interested him for years, and he sees no reason why we should not soon be within talking distance of Mars or of all worlds in the solar system that may be tenanted by intelligent beings.

At the request of COLLIER'S WEEKLY Mr. Tesla presents herewith a frank statement of what he expects to accomplish and how he hopes to establish communication with the planets.

THE IDEA of communicating with the inhabitants of other worlds is an old one. But for ages it has been regarded merely as a poet's dream, forever unrealizable. And yet, with the invention and perfection of the telescope and the ever-widening knowledge of the heavens, its hold upon our imaginations has been increased, and the scientific achievements during the latter part of the nineteenth century, together with the development of the tendency toward the nature ideal of Goethe, have intensified it to such a degree that it seems as if it were destined to become the dominating idea of the century that has just begun. The desire to know something of our neighbors in the immense depths of space does not spring from idle curiosity nor from thirst for knowledge, but from a deeper cause, and it is a feeling firmly rooted in the heart of every human being capable of thinking at all.

Whence, then, does it come? Who knows? Who can assign limits to the subtlety of nature's influences? Perhaps if we could clearly perceive all the intricate mechanism of the glorious spectacle that is continually unfolding before us, and could, also, trace this desire to its distant origin, we might find it in the sorrowful vibrations of the earth which began when it parted from its celestial parent.

But in this age of reason it is not astonishing to find persons who scoff at the very thought of effecting communication with a planet. First of all, the argument is made that there is only a small probability of other planets being inhabited at all. This argument has never appealed to me. In the solar system, there seem to be only two planets—Venus and Mars—capable of sustaining life such as ours; but this does not mean that there might not be on all of them some other forms of life. Chemical processes may be maintained without the aid of oxygen, and it is still a question whether chemical processes are absolutely necessary for

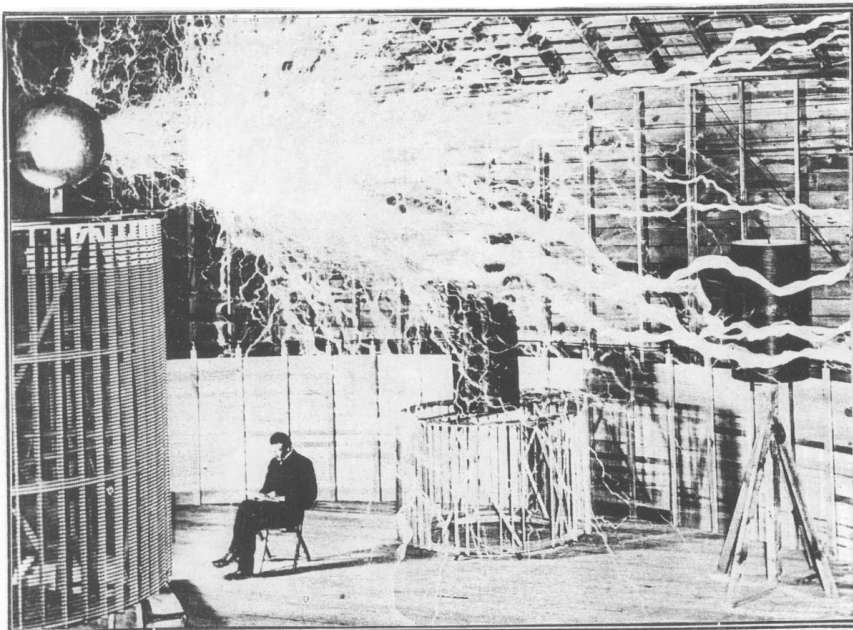
the sustenance of organized beings. My idea is that the development of life must lead to forms of existence that will be possible without nourishment and which will not be shackled by consequent limitations. Why should a living being not be able to obtain all the energy it needs for the performance of its life-functions from the environment, instead of through consumption of food, and transforming, by a complicated process, the energy of chemical combinations into life-sustaining energy?

If there were such beings on one of the planets we should know next to nothing about them. Nor is it necessary to go so far in our assumptions, for we can readily conceive that, in the same degree as the atmosphere diminishes in density, moisture disappears and the planet freezes up, organic life might also undergo corresponding modifications, leading finally to forms which, according to our present ideas of life, are impossible. I will readily admit, of course, that if there should be a sudden catastrophe of any kind all life processes might be arrested; but if the changes, no matter how great, should be gradual, and occupied ages, so that the ultimate results could be intelligently foreseen, I cannot but think that

impossible. By way of illustration, let us suppose that a square mile of the earth's surface—the smallest area that might possibly be within reach of the best telescopic vision of other worlds—were covered with incandescent lamps, packed closely together so as to form, when illuminated, a continuous sheet of light. It would require not less than one hundred million horse-power to light this area of lamps, and this is many times the amount of motive power now in the service of man throughout the world.

But with the novel means, proposed by myself, I can readily demonstrate that, with an expenditure not exceeding two thousand horse-power, signals can be transmitted to a planet such as Mars with as much exactness and certitude as we now send messages by wire from New York to Philadelphia. These means are the result of long-continued experiment and gradual improvement.

Some ten years ago, I recognized the fact that to convey electric currents to a distance it was not at all necessary to employ a return wire, but that any amount of energy might be transmitted by using a single wire. I illustrated this principle by numerous experiments, which, at that time, excited considerable attention among scientific men.



MR. TESLA'S EXPERIMENT TO ILLUSTRATE THE CAPACITY OF HIS OSCILLATOR FOR PRODUCING ELECTRICAL EXPLOSIONS OF GREAT POWER

This being practically demonstrated, my next step was to use the earth itself as the medium for conducting the currents, thus dispensing with wires and all other artificial conductors. So I was led to the development of a system of energy transmission and of telegraphy without the use of wires, which I described in 1893. The difficulties I encountered at first in the transmission of currents through the earth were very great. At that time I had at hand only ordinary apparatus, which I found to be ineffective, and I concentrated my attention immediately upon perfecting machines for this special purpose. This work consumed a number of years, but I finally vanquished all difficulties and succeeded in producing a machine which, to explain its operation in plain language, resembled a pump in its action, drawing electricity from the earth and driving it back into the same at an enormous rate, thus creating ripples or disturbances which, spreading through the earth as through a wire, could be detected at great distances by carefully attuned receiving circuits. In this manner I was able to transmit to a distance, not only feeble effects for purposes of signaling, but considerable amounts of energy, and later discoveries I made convinced me that I shall ultimately succeed in conveying power without wires, for industrial purposes, with high economy, and to any distance, however great.

EXPERIMENTS IN COLORADO

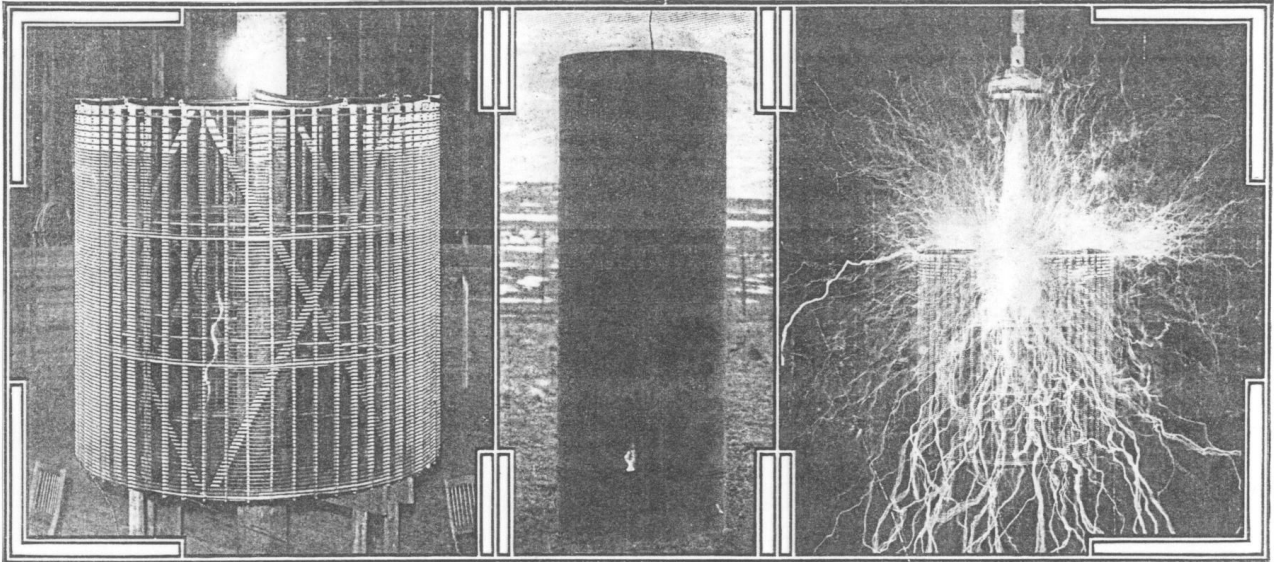
To develop these inventions further, I went to Colorado in 1899, where I continued my investigations along these and other lines, one of which in particular I now consider of even greater importance than the transmission of power without wires. I constructed a laboratory in the neighborhood of Pike's Peak. The conditions in the pure air of the Colorado Mountains proved extremely favorable for my experiments, and the results were most gratifying to me. I found that I could not only accomplish more work, physically and mentally, than I could in New York, but that electrical effects and changes were more readily and distinctly perceived. A few years ago it was virtually impossible to produce electrical sparks twenty or thirty feet long; but I produced some more than one hundred feet in length, and this without difficulty. The rates of electrical movement involved in strong induction

reasoning beings would still find means of existence. They would adapt themselves to their constantly changing environment. So I think it quite possible that in a frozen planet, such as our moon is supposed to be, intelligent beings may still dwell, in its interior, if not on its surface.

SIGNALLING AT 100,000,000 MILES!

Then it is contended that it is beyond human power and ingenuity to convey signals to the almost inconceivable distances of fifty million or one hundred million miles. This might have been a valid argument formerly. It is not so now. Most of those who are enthusiastic upon the subject of interplanetary communication have reposed their faith in the light-ray as the best possible medium of such communication. True, waves of light, owing to their immense rapidity of succession, can penetrate space more readily than waves less rapid, but a simple consideration will show that by their means an exchange of signals between this earth and its companions in the solar system is, at least now,

PHOTOGRAPHS PUBLISHED BY COURTESY OF THE CENTURY COMPANY



SUPPLYING ELECTRICAL ENERGY THROUGH A SINGLE WIRE WITHOUT RETURN

TRANSMITTING ELECTRICAL ENERGY THROUGH THE EARTH WITHOUT WIRE

AN ELECTRICAL OSCILLATOR DELIVERING ENERGY AT A RATE OF 75,000 HORSE-POWER

apparatus had measured but a few hundred horse-power, and I produced electrical movements of rates of one hundred and ten thousand horse-power. Prior to this, only insignificant electrical pressures were obtained, while I have reached fifty million volts.

The accompanying illustrations, with their descriptive titles, taken from an article I wrote for the "Century Magazine," may serve to convey an idea of the results I obtained in the directions indicated.

Many persons in my own profession have wondered at them and have asked what I am trying to do. But the time is not far away now when the practical results of my labors will be placed before the world and their influence felt everywhere. One of the immediate consequences will be the transmission of messages without wires, over sea or land, to an immense distance. I have already demonstrated, by crucial tests, the practicability of signalling by my system from one to any other point of the globe, no matter how remote, and I shall soon convert the disbelievers.

I have every reason for congratulating myself that throughout these experiments, many of which were exceedingly delicate and hazardous, neither myself nor any of my assistants received an injury. When working with these powerful electrical oscillations the most extraordinary phenomena take place at times. Owing to some interference of the oscillations, veritable balls of fire are apt to leap out to a great distance, and if any one were within or near their paths, he would be instantly destroyed. A machine such as I have used could easily kill, in an instant, three hundred thousand persons. I observed that the strain upon my assistants was telling, and some of them could not endure the extreme tension of the nerves. But these perils are now entirely overcome, and the operation of such apparatus, however powerful, involves no risk whatever.

As I was improving my machines for the production of intense electrical actions, I was also perfecting the means for observing feeble effects. One of the most interesting results, and also one of great practical importance, was the development of certain contrivances for indicating at a distance of

many hundred miles an approaching storm, its direction, speed and distance travelled. These appliances are likely to be valuable in future meteorological observations and surveying, and will lend themselves particularly to many naval uses.

It was in carrying on this work that for the first time I discovered those mysterious effects which have elicited such unusual interest. I had perfected the apparatus referred to so far that from my laboratory in the Colorado mountains I could feel the pulse of the globe, as it were, noting every electrical change that occurred within a radius of eleven hundred miles.

TERRIFIED BY SUCCESS

I can never forget the first sensations I experienced when it dawned upon me that I had observed something possibly of incalculable consequences to mankind. I felt as though I were present at the birth of a new knowledge or the revelation of a great truth. Even now, at times, I can vividly recall the incident, and see my apparatus as though it were actually before me. My first observations positively terrified me, as there was present in them something mysterious, not to say supernatural, and I was alone in my laboratory at night; but at that time the idea of these disturbances being intelligently controlled signals did not yet present itself to me.

The changes I noted were taking place periodically, and with such a clear suggestion of number and order that they were not traceable to any cause then known to me. I was familiar, of course, with such electrical disturbances as are produced by the sun, Aurora Borealis and earth currents, and I was as sure as I could be of any fact that these variations were due to none of these causes. The nature of my experiments precluded the possibility of the changes being produced by atmospheric disturbances, as has been rashly asserted by some. It was some time afterward when the thought flashed upon my mind that the disturbances I had observed might be due to an intelligent control. Although I could not decipher their meaning, it was impossible for me to think of them as having been entirely accidental. The feeling is constantly growing on me that I had been the first to hear the greeting

of one planet to another. A purpose was behind these electrical signals; and it was with this conviction that I announced to the Red Cross Society, when it asked me to indicate one of the great possible achievements of the next hundred years, that it would probably be the confirmation and interpretation of this planetary challenge to us.

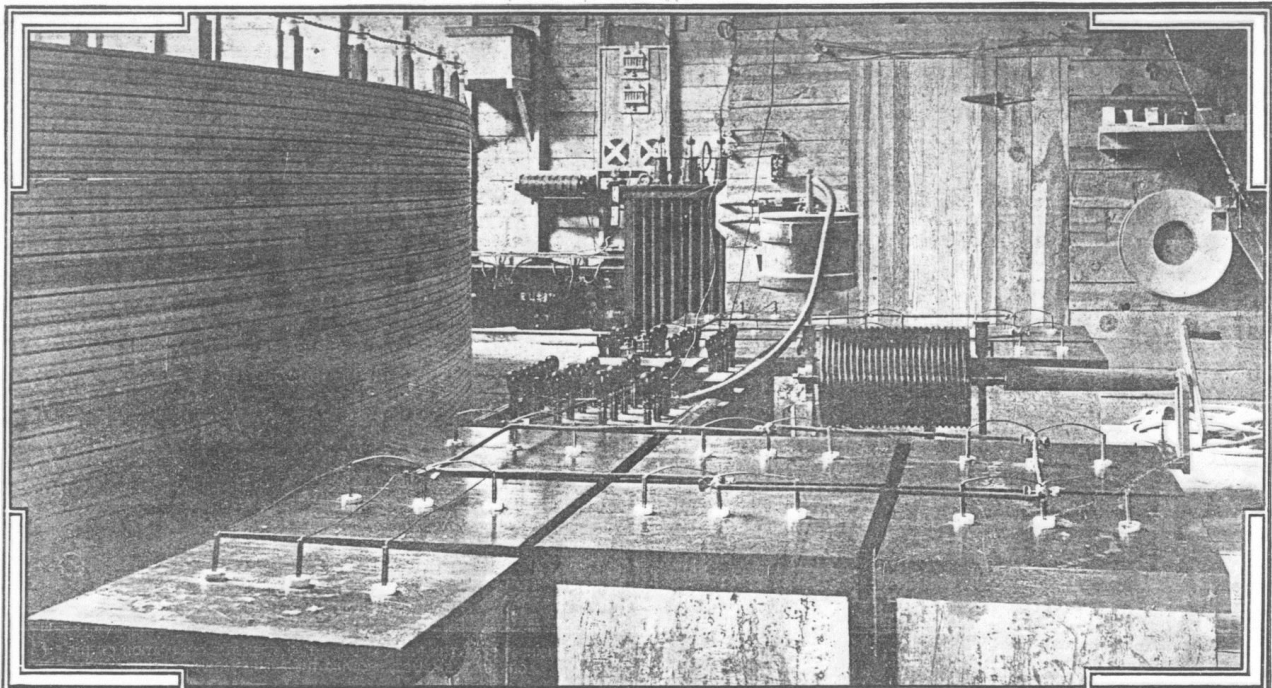
Since my return to New York more urgent work has consumed all my attention; but I have never ceased to think of those experiences and of the observations made in Colorado. I am constantly endeavoring to improve and perfect my apparatus, and just as soon as practicable I shall again take up the thread of my investigations at the point where I have been forced to lay it down for a time.

COMMUNICATING WITH THE MARTIANS

At the present stage of progress, there would be no insurmountable obstacle in constructing a machine capable of conveying a message to Mars, nor would there be any great difficulty in recording signals transmitted to us by the inhabitants of that planet, if they be skilled electricians. Communication once established, even in the simplest way, as by a mere interchange of numbers, the progress toward more intelligible communication would be rapid. Absolute certitude as to the receipt and interchange of messages would be reached as soon as we could respond with the number "four," say, in reply to the signal "one, two, three." The Martians, or the inhabitants of whatever planet had signalled to us, would understand at once that we had caught their message across the gulf of space and had sent back a response. To convey a knowledge of form by such means is, while very difficult, not impossible, and I have already found a way of doing it.

What a tremendous stride this would make in the world! How soon will it come? For that it will some time be accomplished must be clear to every thoughtful being.

Something, at least, science has gained. But I hope that it will also be demonstrated soon that in my experiments in the West I was not merely beholding a vision, but had caught sight of a great and profound truth.



PHOTOGRAPHIC VIEW OF THE ESSENTIAL PARTS OF THE ELECTRICAL OSCILLATOR USED IN MR. TESLA'S EXPERIMENTS



InSAR (Interferometric Synthetic Aperture Radar) uses radar images of Earth's surface to monitor ground surface deformation.



Photogrammetry is a technique that uses imagery collected from airborne and terrestrial platforms, such as drones, to construct high-resolution images of Earth's topography.



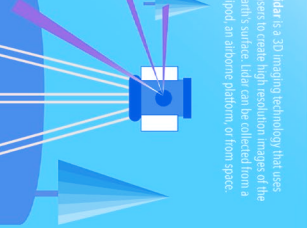
Borehole Strainmeters monitor Earth movement by measuring tiny changes in the dimensions of a borehole at depths of 100 to 250 meters.



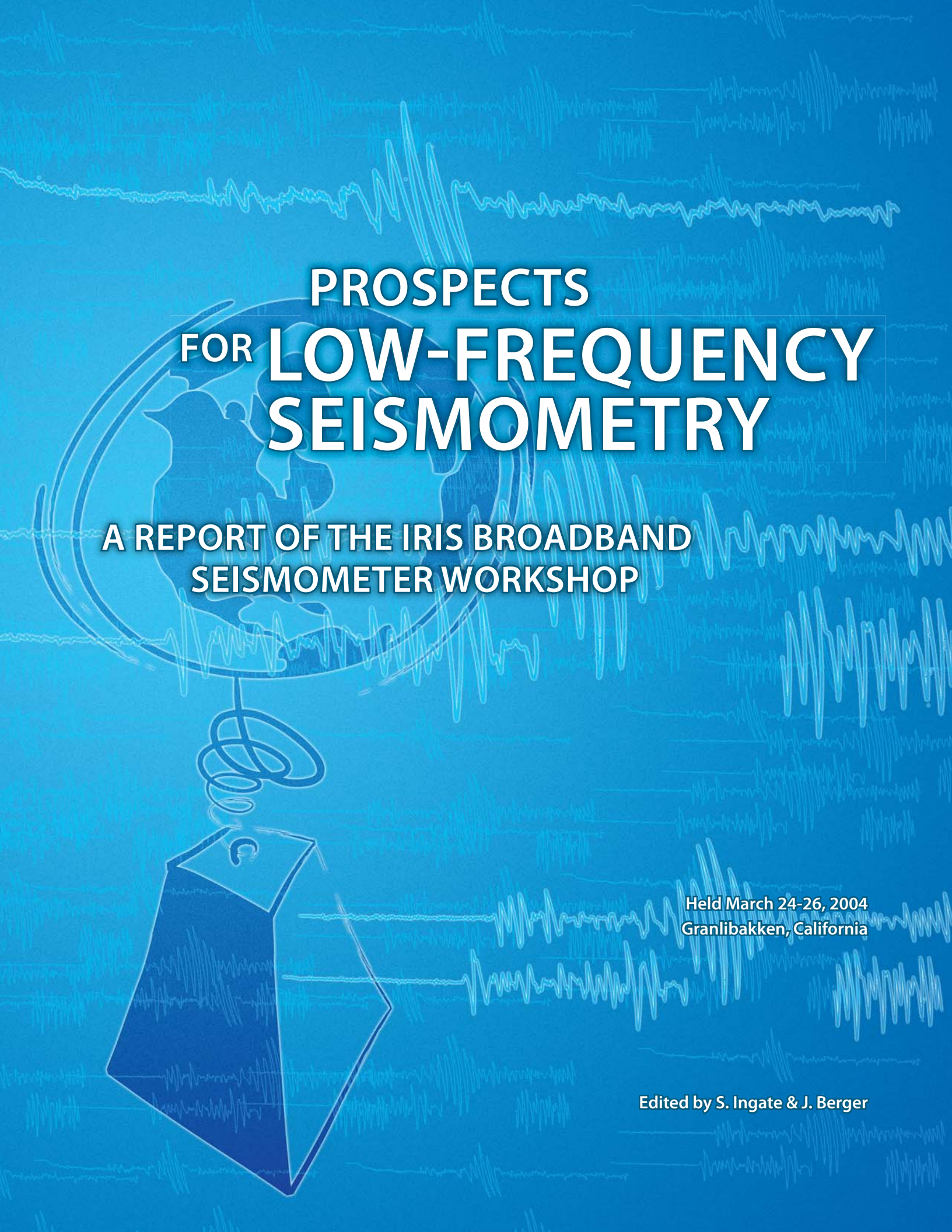
Gravity measurements, some of which are collected by two NASA satellites in paired orbit, allow geodesists to determine how mass is distributed around the planet and how this distribution varies over time.



GPS (Global Positioning System) is the United States's component of GNSS (Global Navigation Satellite System). High precision allows geodesists to detect Earth movements with millimeter-scale accuracy over extended periods of time.



Lidar is a 3D imaging technology that uses lasers to create high-resolution images of the Earth's surface. Lidar can be collected from a tripod, an airborne platform, or from space.



**PROSPECTS
FOR LOW-FREQUENCY
SEISMOMETRY**

**A REPORT OF THE IRIS BROADBAND
SEISMOMETER WORKSHOP**

Held March 24-26, 2004
Granlibakken, California

Edited by S. Ingate & J. Berger

Steering Committee

Jonathan Berger, Co-Chair..... University of California, San Diego
Shane Ingate, Co-Chair IRIS
John Collins..... Woods Hole Oceanographic Institution
William E. Farrell Science Applications International Corporation
Jim Fowler IRIS/PASSCAL Instrument Center
Pres Herrington Sandia National Laboratories
Charles Hutt US Geological Survey
Barbara Romanowicz..... University of California, Berkeley
Selwyn Sacks Carnegie Institution of Washington
Erhard Wieland Universität Stuttgart

Workshop Presentations and Discussion

Background material provided in advance of the workshop, and the record of presentations and discussions may be found on the included CD and also at:
<http://www.iris.edu/stations/seisWorkshop04/seisWorkshop.htm>

**PROSPECTS
FOR LOW-FREQUENCY
SEISMOMETRY**

**A REPORT OF THE IRIS BROADBAND
SEISMOMETER WORKSHOP**

Held March 24-26, 2004
Granlibakken, California

Edited by S. Ingate & J. Berger

Contents

Executive Summary	1
1. Introduction	2
2. Background	4
2.1. The Seismic Spectrum	4
2.2. Seismic Networks	7
2.3. Today's Sensors	8
2.4. Overall Criteria for the GSN Seismometers	10
3. New Ideas and Concepts	12
3.1. Micro Electro Mechanical System (MEMS) Seismometer	12
3.2. Electrochemical Transducer Suspension Design	12
3.3. Magnetic Levitation Seismometer	12
3.4. Ferro-Fluid Suspension	12
3.5. Quartz Seismometer Suspension	13
3.6. Folded Pendulum	13
3.7. Electrochemical Displacement Transducers.....	13
3.8. SQUID Displacement Detector.....	13
3.9. Optical Displacement Transducer.....	13
3.10. Superconducting Gravimeter	14
3.11. SLAC Strainmeter	14
3.12. Feasibility of Using LIGO Facilities as Strainmeters	14
3.13. Ring Laser Gyro.....	14
3.14. New Forcing and Sensing Methods for Seismometers.....	14
3.15. Atomic Fountains for Inertial Sensors	14
4. Testing and Test Facilities.....	15
4.1. Introduction	15
4.2. Test Facilities	15
4.3. Test Procedures.....	16
4.4. Support and Access	16
5. Partnerships between Industry and Academia	17
5.1. Historical Background.....	17
5.2. What is an Appropriate Relationship?.....	17
5.3. Respect for Intellectual Property.....	19
5.4. Student Involvement	19
6. Education and Funding	20
7. Acknowledgements	21
8. References.....	22
Appendix: Workshop Attendees.....	23

Executive Summary

For nearly a quarter of a century, the development of seismic sensors with low noise and high resolution in the normal mode frequency band (0.3-7 mHz) has languished. The seismometer of choice for this field of seismology is now over 20 years old, and is no longer being manufactured. Newer sensors, albeit more portable and physically robust, more energy efficient, and less expensive, are less capable of recording Earth motions in this frequency band. Over the same time period, the training of seismic instrumentalists in departments of Earth science has languished; no longer do academic seismologists design and build new sensors. Outside of traditional science departments, however, a number of innovative ideas have been proposed for novel seismic instruments.

In March 2004, IRIS sponsored a workshop on the future of long-period seismometry, which brought together over 60 participants from government, academic, and business sectors of eight countries. Representatives of groups involved in sensor technology, material sciences, and nanotechnology were all present. The workshop's goals were to assess emerging technologies that may have seismometric applications and formulate a plan to revitalize research and development of techniques in seismometry and related seismographic instrumentation in the United States.

Workshop participants made several important observations and recommendations:

- The cornerstone sensor of the Global Seismographic Network (GSN), the Streckeisen STS-1, is aging and no longer in production. There are no sensors currently in production or in development that match its performance.
- Industry is unwilling to develop a substitute sensor for this frequency band due to the anticipated unfavorable return on investment. (A total production run of 200 units only is projected.)
- Many workshop participants have come to believe that the goal to develop an all-purpose sensor, spanning the frequency band from millihertz to decahertz, should be abandoned, and that two separate transducers should be used to cover this range. Such a decision might ease the technological challenge and reduce the burden on industry.
- An innovative program involving academia, industry, and government is recommended to nurture development of the next generation instruments and to educate the next generation of US seismic system developers.
- A program total of \$10M-\$20M over a period of 5-10 years is envisioned.
- Development needs to commence now to prevent significant deterioration of the GSN over the next 5-10 years.

1. Introduction

Seismology provides the only direct method for measuring the properties of the deep interior of our planet. Seismic sensors range from mass-produced geophones, costing a few hundred dollars and used by the oil industry by the thousands, to low-noise, high-sensitivity instruments that require careful installation in boreholes or underground vaults and cost up to \$75,000 or more.

Seismic sensors are the mechanical or electromechanical assemblies that convert Earth motion into electrical signals that can then be digitized and recorded for later analysis. Here, sensors are distinguished from systems, in that the latter may consist of multiple combinations of the former, coupled to a digitizing and recording apparatus.

Few fundamental advances have been made in seismic sensors since the deployment of force-feedback systems near-

ly a third of a century ago (see Box 1). In the intervening period, academic (and to a lesser extent industrial) research and development of seismographic instrumentation has declined. Today, adequate sensors to meet some important scientific requirements are in short supply (see Box 2). Further, the pool of trained scientists working on seismographic instrumentation in the United States has dwindled to nearly zero.

Following a brief introduction, this report summarizes discussions of the following workshop subjects.

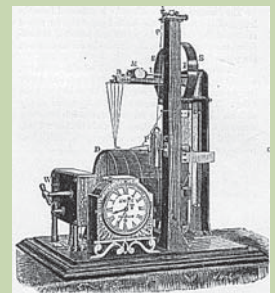
- Seismological Requirements
- Manufacturing Issues
- Testing and Testing Facilities
- Partnerships between Industry and Academia
- Education and Agency Support

Box 1: When Was the First Broadband Seismograph Built?

Dewey and Byerly (1969) credit the Italian Cecchi with building the first recording seismograph around 1875. This sensor recorded on a drum and may well have been the first broadband seismograph. However, it is widely accepted that the Gray and Milne seismograph (see right) is the first successful broadband seismograph. Between 1881-1882, Gray, Ewing, and Milne figured out how to extend the period of a seismometer to about 12 seconds (horizontal "garden-gate" suspension), thus producing a seismograph that had a flat response to Earth displacement from 12 seconds to shorter periods.

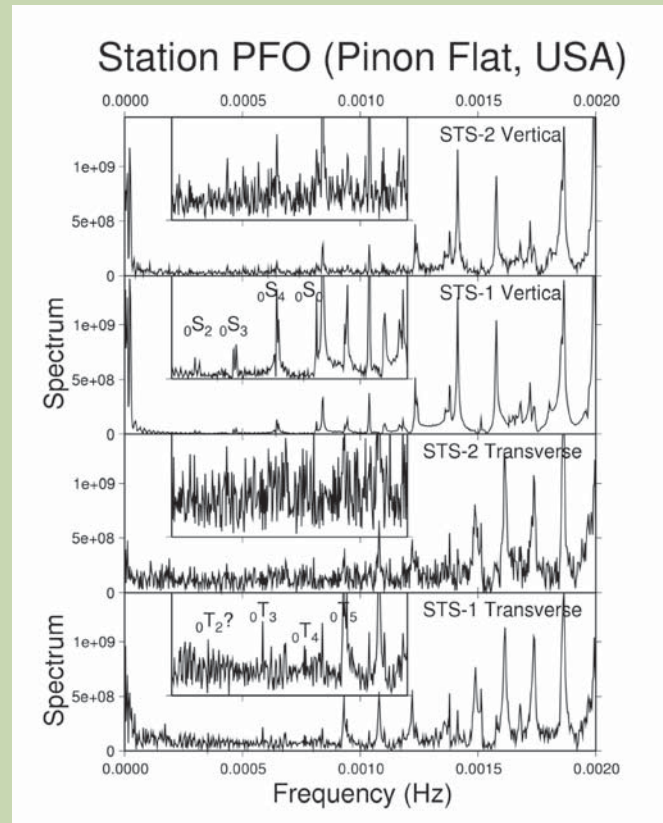
However, the lineage to present broadband or very broadband sensors includes a few other branches. Von Rebeur-Paschwitz introduced continuous photographic recording with a 15-second period, which was responsible for the famous first recorded teleseism in 1889 (see right). One of Milne's students in Japan, Omori in 1899, created a fairly sensitive 60-second mechanical displacement seismograph that recorded some remarkable records of large teleseisms (see the front cover of this report for Omori horizontal recordings in Tokyo of the Alaska 1899 earthquake, showing one-minute period signals that are remarkable in their resemblance to modern very broadband seismograms).

Wiechert introduced viscous damping in 1898. Credit for the first feedback-stabilized broadband sensor probably goes to the remarkable 21-ton de Quervain and Piccard mechanical system at Zurich, 1926, an important development towards force-balance systems. The first direct digital recording seismograph was operational at Caltech around 1961. The Graefenberg array was the first modern digital broadband array in the late 1970s, and prompted development of the Wielandt and Streckeisen 20s STS-1. Plesinger was the first to implement a very broad velocity response, 0.3-300s, although the utility was hampered by analog recording available in the early 1970s. Plesinger's research, however, inspired Wielandt and Steim to develop the digital VBB concept, leading in the mid 1980s to the IRIS/GSN's 360s STS-1/VBB.



Box 2. Science Without Very Broadband Sensors

What if the GSN consisted solely of broadband sensors (such as the STS-2) rather than very broadband sensors (such as the STS-1, which is no longer in manufacture, nor are there any plans to resume production)? Are there any useful signals that would not be recorded? The once-in-a-lifetime Mw 9.3 Sumatran event of 12/26/04 enabled scientists to observe rarely seen gravest free oscillations such as ${}_0S_2$. These signals are rare because smaller sources do not generate the gravest modes with sufficient amplitude to be detected. The plot is a spectrum computed for collocated STS-1 and STS-2 sensors at station PFO in California. The inset boxes are enlargements of the main spectra to show amplitudes of the gravest modes. STS-2 vertical went nonlinear on the first Rayleigh wave for this event, so the first surface wave arrivals were removed before spectrum estimation for the vertical component. The STS-2 did not record the gravest modes below ${}_0S_3$ with sufficient signal-to-noise-ratio, yet the signals are easily seen in the STS-1 spectra. Figure courtesy of J. Park, Yale University.



2. Background

2.1. The Seismic Spectrum

Earthquake-generated elastic waves that are transmitted through the Earth and along its surface range in frequencies from less than a millihertz (the gravest eigenfrequency of the solid Earth has a period of 54 minutes, or 0.31 mHz), to about 30 Hz. Higher frequencies are attenuated so rapidly that they do not travel appreciable distances. These five frequency decades constitute the seismic band; the term broadband is used by seismologists to indicate this entire frequency band.

The seismic source, whether a man-made explosion or earthquake, usually has a duration ranging from milliseconds up to a few minutes only, but the motions excited by the largest events can last days. Although the transient seismic signals radiated by localized sources of finite duration are coherent with a well-defined phase spectrum, this is not the case for ambient seismic noise. The latter is often caused by a diversity of different, spatially distributed, and often continuous sources such as wind, ocean waves, and cultural. Seismic noise thus forms a more or less stationary stochastic process without a defined phase spectrum.

The dynamic range of the seismic spectrum extends from the level of the background ambient noise to the largest signals generated by seismic sources. Both limits are frequency dependant, and the signal levels are also dependant on the distance between source and receiver. The bounds on signals and noise are well established by observation.

2.1.1. Earthquake Signals

Traveling waves from earthquakes are traditionally divided into three categories depending upon the source-receiver distance. Earth's free oscillations, or normal modes, form an-

other category. Due to the effects of internal friction, the frequency content of the signals also varies with source-receiver distance. The categories are roughly described in Table 1.

Figure 1 plots representative earthquake spectra recorded at local, regional, and teleseismic distances for a range of earthquake magnitudes. To make meaningful comparisons between deterministic signals and random noise, the spectral unit is root-mean-square (RMS) acceleration in frequency bands with a width of one octave.

Of particular importance for long-period seismometry are Earth's free oscillations, or normal modes. Following large earthquakes, Earth's free oscillations are observed as spectral peaks in the frequency band of 0.3-7 mHz. The gravest mode of vibration, ${}_0S_2$, has a frequency of 0.3 mHz, and splitting of this peak is frequently observed. At higher frequencies, the split modes overlap, and spectral resolution decreases. Above approximately 7 mHz, normal modes are too closely spaced to be resolvable, and other techniques, based on propagating wave theory, are more appropriate for the analysis of seismograms.

The development of spectral techniques for the analysis of Earth's free oscillations was prompted by the 1960 M 9.6 Chile earthquake. Over the last 40 years, the deployment of global networks of sensors, together with advances in theory, have markedly improved our understanding of the average (1-D) Earth.

For example, measurement of the eigenfrequencies of free oscillations sensitive to Earth's core has confirmed the existence of a solid inner core (Dziewonski and Gilbert, 1971). Eigenfrequency measurements have led to the development of reference 1-D Earth models for elastic-wave velocities,

Table 1.

Category	Distance	Frequencies	RMS Amplitudes
Local Signals	up to ~30 km	.3 to 30 Hz	to ~ 10 ms ⁻²
Regional Signals	~ 1000 km	~10 ⁻¹ to ~10 Hz	to ~10 ⁻¹ ms ⁻²
Teleseismic	~ 10,000 km	~10 ⁻² to ~1 Hz	to ~10 ⁻³ ms ⁻²
Normal Modes	Whole Earth	3x10 ⁻⁴ to ~10 ⁻² Hz	to ~10 ⁻⁵ ms ⁻²

The Earthquake Spectrum

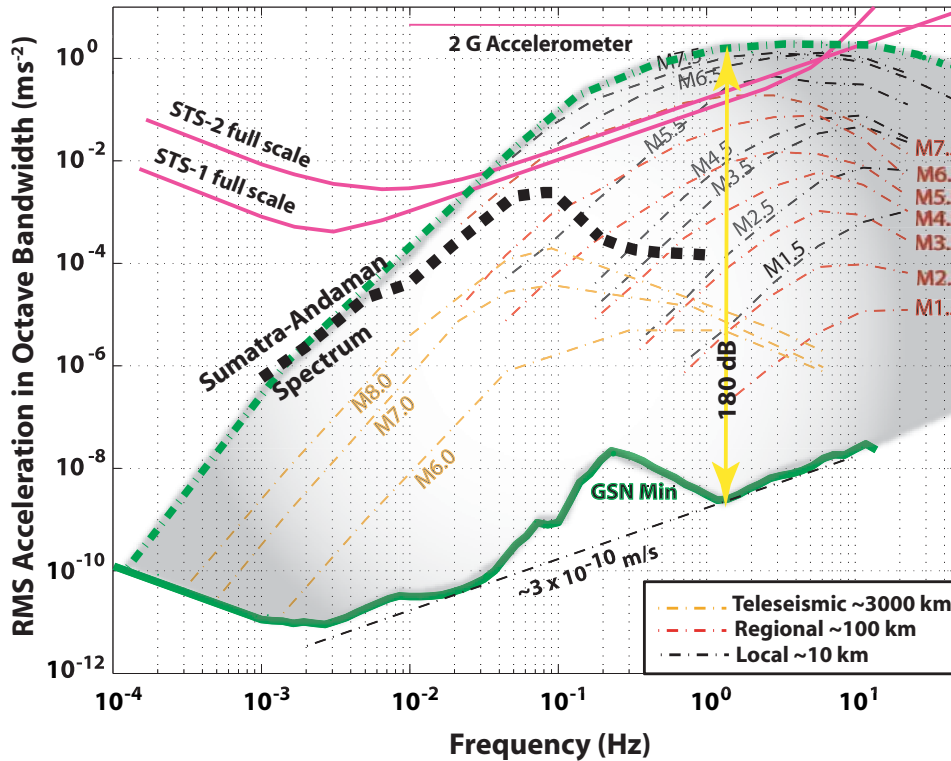


Figure 1. Representative earthquake spectra as recorded at various source distances and for a range of magnitudes. The plot also compares these signal levels to ambient Earth noise. To make meaningful comparisons between deterministic signals and random noise, the spectral unit is RMS acceleration in one-octave bands. The shaded area indicates the spectral range of earthquake signals and includes the signals from the December 26, 2004 Sumatra-Andaman earthquake observed at the closest stations (1585 km to 2685 km). The lower green line illustrates the minimum noise observed on the GSN stations (Berger et al., 2004). The pink lines indicate the full-scale dynamic range of the principal GSN sensors. Figure courtesy of J. Berger, UCSD, after Clinton and Heaton (2002).

density, and attenuation (Q) that are still widely used today (e.g., the Parameterized Reference Earth Model [PREM]) (Dziewonski and Anderson, 1981). Most importantly, the little information we have about Earth's radial density structure comes primarily from normal mode data analysis.

In the last 20 years, attention has shifted to the study of departures from simple spherical symmetry. The earliest indications that free-oscillation data contain important information on heterogeneities were two-fold. Buland and Gilbert (1979) first observed splitting due to lateral heterogeneity in low degree modes, in particular, in the gravest mode ${}_0S_2$. A few years later the "degree-2" geographical pattern in the frequency shifts of fundamental spheroidal modes was discovered, which has been traced back as originating in the upper mantle transition zone (Masters et al., 1982). Anomalous splitting of core sensitive modes was one of the key observations in the discovery of inner-core anisotropy (Woodhouse et al., 1986).

There is now renewed interest in the analysis of normal mode data. This has come with the deployment of dozens of very broadband seismometers along with the advent of digi-

tal, high-quality (low noise and high dynamic range) recording at low frequencies. These advances in observational capability have been coupled with advances in the theory of wave propagation in a 3-D Earth. High-quality data have made it possible to observe the static response to the great 1994 deep Bolivia earthquake (Ekström, 1995). More accurate mode-splitting measurements have helped put definitive constraints on the rate of relative rotation of the inner core with respect to the mantle (Laske and Masters, 1999). These improved splitting measurements have also been used to constrain core structure and anisotropy (e.g., Romanowicz and Breger, 2000; Ishii et al., 2002)

Constraints from normal modes have been used in the development of the latest generations of tomographic models of Earth's mantle (e.g., Masters et al., 1996; Resovsky and Ritzwoller, 1999a). These models provide unique constraints on the longest-wavelength (spherical harmonic degrees 2 and 4) heterogeneity. Normal mode data are the only hope for constraining long-wavelength lateral variations in density in the lower mantle, the subject of recent vigorous debate (e.g., Ishii and Tromp, 1999; Resovsky and Ritzwoller, 1999b; Ro-

manowicz, 2001). Normal-mode constraints on the density jump at the inner core/outer core boundary, critical for the understanding of core formation and dynamics, have been reanalyzed and improved (Masters and Gubbins, 2003).

There is still a wealth of information about low-degree elastic structure, particularly odd-degree structure as well as density, anelastic, and anisotropic structure, to be obtained from free-oscillation data. Making these discoveries requires high-quality, low-noise measurements at the lowest frequencies (i.e., below 0.8 mHz). Large, deep earthquakes that excite the gravest, low angular modes sensitive to Earth's deepest parts are rare (such as the 1994 M 8.3 Bolivia or the 2001 Mw 8.4 Peru events), and each of them provides different and unique constraints due to different source depths, mechanism, and locations. These events need to be observed at many different stations so as to allow the separation of source and propagation effects.

Also notable is the surprising discovery, six years ago, of Earth's "hum"—faint fundamental mode peaks seen even in the absence of recent earthquakes. They were first observed on the vertical component of STS-1 recordings in the period

range 2-7 mHz (Suda et al., 1998; Tanimoto et al., 1998) and on recordings of a superconducting gravity meter in the period range 0.3-5 mHz (Nawa et al., 1998). The mechanism exciting this hum is still the subject of vigorous research, but the existence of seasonal variations in the level of signal suggests an atmospheric or oceanic origin (Tanimoto and Um, 1999; Fukao et al., 2002; Ekström, 2001). Discovery of the "hum" was made by stacking many days' recordings from quiet stations. Recently, an array technique using the properties of propagating surface waves has shown promise in determining that a significant portion of the hum may originate in the ocean (Rhie and Romanowicz, 2004).

2.1.2. Ambient Noise

The most recent study of ambient seismic noise was a comprehensive analysis of a year's worth of data from 118 GSN stations (Berger et al., 2004). The frequency range was divided into many bins, and noise-power histograms were developed for each bin. The position of each station's power in each bin varied from bin to bin. The resulting noise model is illustrated in Figure 2.

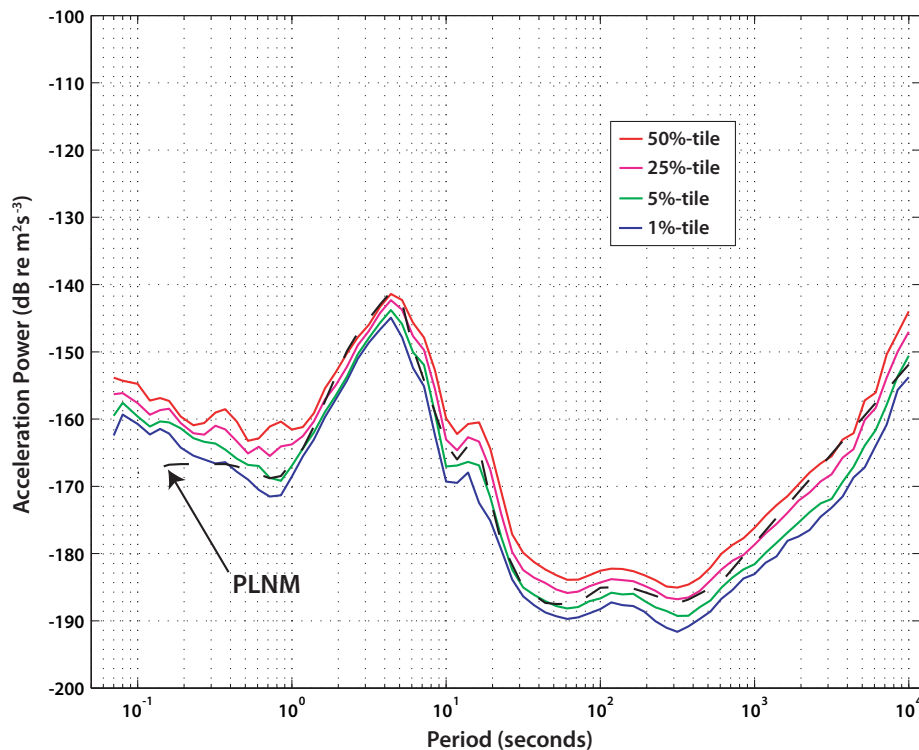


Figure 2. The GSN Low-Noise Model (from Berger, 2004). The plot shows the noise power at the 1st, 5th, 25th, and 50th percentiles for all GSN stations and channels. The dash curve in the figure is the Peterson Low Noise Model, or PLNM (Peterson, 1993). This plot shows that the Earth is even quieter at long periods than previously thought, reinforcing the need for a good long-period seismometer to replace the STS-1. Figure courtesy of J. Berger, UCSD.

2.2. Seismic Networks

The original seismic instrumentation (see Box 1) evolved into a highly specialized sensor, the Streckeisen STS-1. The STS-1 was a very broadband device designed to take fundamental research into Earth's deep internal structure and earthquake physics to new levels of resolution, and yet remain sufficiently sensitive to also record local earthquake activity with a fidelity approaching that of sensors specifically designed to monitor local activity in narrow spectral windows. The STS-1 was the ultimate sensor for probing the internal structure of the whole Earth, representing 100 years of technological advances in thermally stable metallurgical and electronics development.

The primary application for the STS-1 was in global and continental-scale networks deployed to record large earthquakes for studies of deep Earth structure and earthquake physics. Two networks that do use, or intend to use, the STS-1 are:

- The Global Seismographic Network (GSN), which operates and maintains 132 permanent stations globally.
- The USArray Backbone Network, one component of the new EarthScope program (<http://www.earthscope.org>). USArray is a large North American seismographic network currently being constructed under NSF auspices. It will eventually be operated by the US Geological Survey.

2.2.1. The Global Seismographic Network (GSN)

The Federation of Digital Broadband Seismograph Networks (FDSN) (www.fdsn.org) is an international organization for the exchange of data from global seismic observing systems. The Global Seismographic Network (www.iris.edu/about/GSN), operated by the IRIS Consortium and the US Geological Survey, is the largest network within the FDSN. The cornerstone of the GSN, the very broadband STS-1 seismometer, is no longer in production. The GSN is now faced with an aging technology base of equipment that cannot be replaced. Thus, unless steps are taken now to explore new and innovative technologies, the GSN will increasingly be unable to meet the scientific demands of the community.

GSN leadership has been aware of this problem for some time. The following paragraphs, excerpted from "Global Seismic Network Design Goals Update 2002," was prepared by

the GSN ad hoc Design Goals Subcommittee, chaired by T. Lay (http://www.iris.edu/about/GSN/docs/GSN_Design_Goals.pdf):

The design of today's Global Seismographic Network (GSN) dates back to 1985. The original design goals emphasized 20 sample/sec digital recording with real-time or near real-time data telemetry of all teleseismic ground motions (assuming about 20 degrees station spacing) for earthquakes as large as $M_w = 9.5$ (equivalent to the 1960 Chile earthquake) by a uniform global network of about 100 stations, with low noise instrumentation and environment, standardization of system modules, and linearity of response. These design goals were framed within the context of both scientific goals of the research community and by general philosophy of network design and recording system attributes that service the scientific applications of the recorded data. The intent was for total system noise to be less than the ambient Earth noise over the operating bandwidth, and to record with full fidelity and bandwidth all seismic signals above the Earth noise.

Adaptation of GSN design goals to accommodate emerging scientific directions has been, and should continue to be, an ongoing process. However, since 1984 there has not been a community-wide discussion of scientific directions to guide or modify a future vision of GSN instrumentation. Renewal proposals for IRIS funding from NSF have included updated applications of GSN data, but there has not been a forum for broad thinking on expanded roles or capabilities for GSN in the future. Thus, there is a general sense that, at a minimum, the existing instrumentation strategy is serving the community rather well and the original design criteria need to be sustained.

Further, there is increasing scientific interest in ultra-long period signals, such as the Earth's spectrum of continuously excited modes and tides. For example, superconducting gravimeters have demonstrated superior response to existing GSN instrumentation for very long-period free oscillations, and inclusion of a subset of these gravimeters at very quiet sites in the GSN may prove very attractive in the future. The value of high fidelity recording throughout the tidal band is not self-evident, and community discussion of the role GSN should play in data collection at frequencies below the normal mode band (as for some ocean oscillations) should be undertaken.

2.2.2. USArray & EarthScope

EarthScope is a set of integrated and distributed multi-purpose geophysical instrumentation that will provide the observational data needed to significantly advance knowledge and understanding of the structure and dynamics of the North American continent. One element of EarthScope is USArray, a dense array of high-capability seismometers that will improve greatly our resolution of the continental lithosphere and deeper mantle.

USArray's Backbone Network serves as a reference for the continental-scale imaging being performed by USArray's transportable components. As an integrated resource both for EarthScope science and seismic monitoring, the Backbone Network has been designed in close collaboration with the USGS Advanced National Seismic System (ANSS) (see www.ANSS.org). The proposed national broadband network component of the ANSS will consist of approximately 100 stations, of which USArray will contribute 9 new GSN-quality stations and 27 ANSS-quality stations.

USArray has been unable to acquire STS-1 sensors and consequently, the Backbone has been de-scoped and will use enhanced-performance STS-2 broadband sensors instead of the preferred STS-1 sensors.

2.2.3. Other Networks

Seismic sensors find application in a number of other fields; however, the design requirements for these systems are less demanding than for low-frequency sensors, and the engineering and production challenges tend to be driven by cost minimization and environmental factors (size, ruggedness, reliability). Seismic networks to monitor nearby activity require moderate sensitivity, but only at higher frequencies, of order 0.1 to 10.0 Hz. Engineering seismology applications focus on higher signal levels ("strong motion") and frequencies up to 100 Hz. Sensors for the petroleum exploration industry must cover the band from 4 to 500 Hz, be cheap, small, rugged, and easily deployed.

2.3. Today's Sensors

Historically, seismic sensors were separated into two general classes: those with long (15-30 sec) and short (1 sec) free periods. The former were used to measure long-period Earth motion such as those characteristic of surface waves, while

the latter sensors were used to measure high-frequency Earth motions characteristic of body waves (seismic waves that travel through Earth's interior). The widespread application of force feedback has made this distinction less important than in the past. More recent designs favor broadband (from near zero frequency to around 50 Hz) feedback instruments for most applications, but the mechanical sensor can still have either a short free period or a long free period. However, this approach is undergoing reappraisal.

Although the mass-and-spring system is a useful mathematical model for a seismometer, it is incomplete as a practical design. The suspension must suppress five out of the six degrees of freedom of the seismic mass (three translational and three rotational) but the mass must still move as freely as possible in the remaining direction. Furthermore, it must suppress the disturbing influence caused by changes in gravity, magnetic, thermal, and barometric pressure. Careful manufacture is essential in order to reach the Brownian limit in the motion of the suspended mass.

The dynamic range of the signals to be measured is large. Figure 1 showed that an acceleration-sensitive seismometer needs a very large dynamic range in order to resolve with full fidelity signals ranging from those barely above the noise to those from earthquakes of magnitude 9.5.

Excellent reviews of the history of seismometer design are given by Melton (1981a, 1981b), Farrell (1985), and Howell (1989). The design of the so-called very broadband seismometer is well described by Wielandt and Streckeisen (1982) and Wielandt and Steim (1986).

Seismic sensors can be characterized by their frequency response, sensitivity, self-noise, and dynamic range.

2.3.1. Frequency Response

Today's seismometers can be divided into three rough categories. Figure 3 shows the frequency response of a number of seismic sensors.

Short-period (SP) seismometers and geophones measure signals from approximately 0.1 to 250 Hz, with lower corner frequencies between 1 and 10 Hz. Their response is usually flat with respect to ground velocity above this corner frequency. These units are technically simple and are readily available. High-quality units without significant parasitic resonance cost around \$6,000; geophones cost a few hundred dollars.

Velocity Response Comparison of IRIS/USGS GSN Instruments

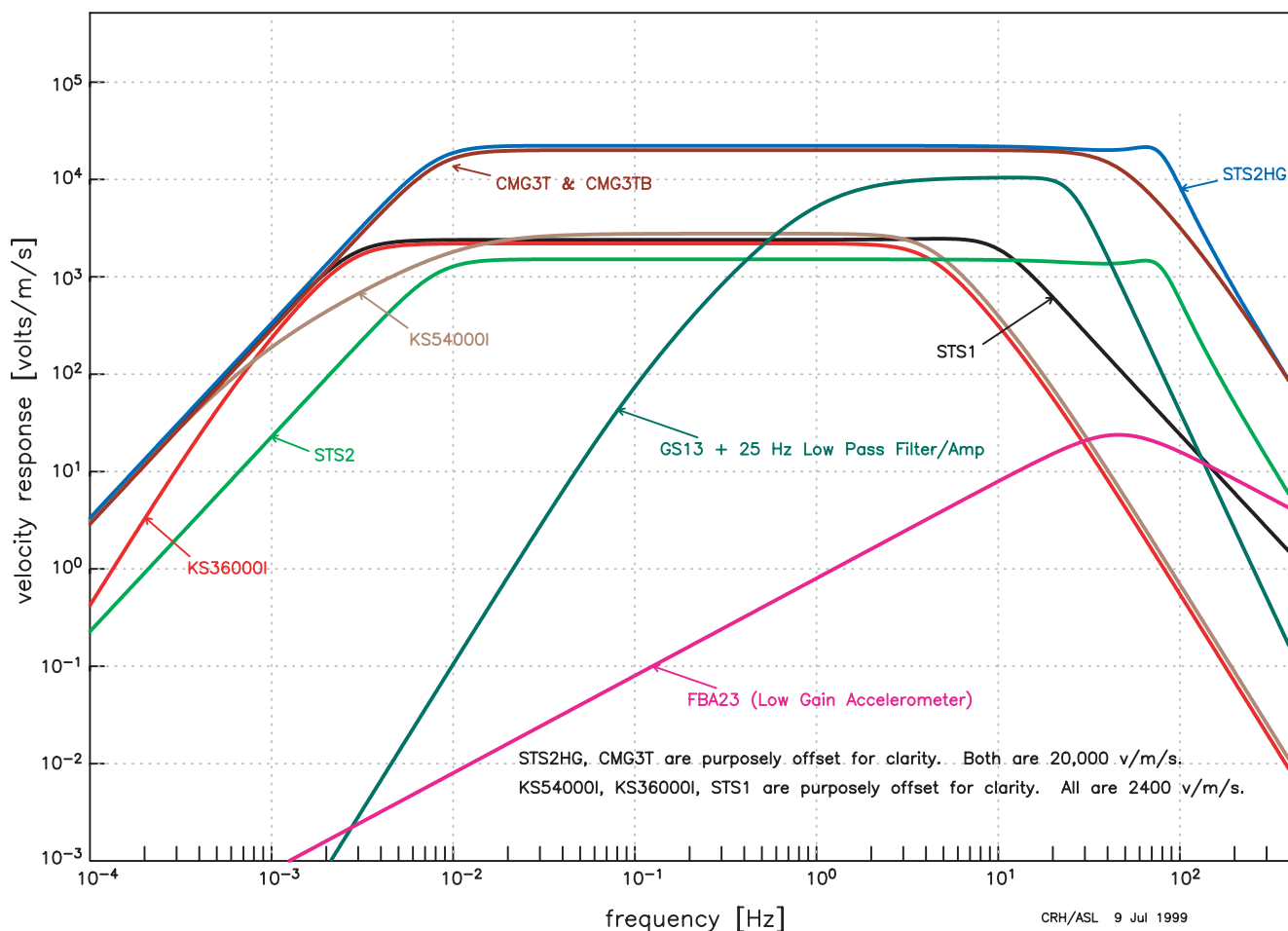


Figure 3. Frequency response of representative seismometers. Figure courtesy of R. Hutt, USGS/ASL.

Broadband sensors (BB) have a response shifted down in frequency by about two decades with respect to SP sensors. Usually, their transfer function is flat to velocity from approximately 0.01 to 50 Hz. Sensors in this class are also readily available, though they are somewhat more expensive (typically \$15,000). They are fragile and require relatively high power (~0.5 W or more).

So-called very broadband seismometers measure ground motion at frequencies from below 0.001 Hz to approximately 10 Hz and are able to resolve Earth's tides. They are extremely fragile and high power consumers (~several watts). They are expensive (typically \$45,000 for a surface sensor, \$100,000 for a borehole sensor and installation).

2.3.2. Sensitivity

Seismometers are weak-motion sensors, usually orders of magnitude more sensitive than accelerometers, though they cannot record as large amplitudes as accelerometers. Seismometers can record local but small events and/or large but distant events. The goal for a VBB seismometer is to measure ground motion smaller than the amplitudes of the lowest natural seismic noise found anywhere in the world.

Accelerometers are strong-motion sensors, and in geophysical and earthquake engineering applications, measure seismic signals between near-DC to up to 50 Hz. However, output voltage of an accelerometer is proportional to ground acceleration, whereas seismometer output is generally pro-

portional to ground velocity. For this reason, accelerometers stress high frequencies and attenuate low frequencies compared with seismometers.

2.3.3. Self-noise

All modern seismographs use semiconductor amplifiers that, like other active (power-dissipating) electronic components, produce continuous electronic noise whose origins are manifold but ultimately related to the quantization of the electric charge. The contributions from semiconductor noise and resistor noise are often comparable, and together limit the sensitivity of the system. Another source of continuous noise, the Brownian (thermal) motion of the seismic mass, may be noticeable when the mass is very small (less than a few grams). Seismographs may also suffer from transient disturbances originating in slightly defective semiconductors or in the mechanical parts of the seismometer when these are subject to stresses. An important goal in constructing a very broadband sensor for Earth studies is for the self-noise to be considerably less than the lowest ambient Earth noise. The GSN Low-Noise Model (Figure 2) summarizes the observed seismic noise levels throughout the seismic frequency band. This model is useful as a reference for assessing the quality of seismic stations, for predicting the presence of small signals, and for the design of seismic sensors.

Comparing self-noise of very broadband and broadband seismometers is instructive. The very broadband STS-1 seismometer has a theoretical noise of around $4 \times 10^{-11} \text{ m/s}^2/\sqrt{\text{Hz}}$ at a period of around 8 sec, and $5 \times 10^{-10} \text{ m/s}^2/\sqrt{\text{Hz}}$ at 1000 sec. The broadband STS-2 can achieve a noise level of $2.5 \times 10^{-9} \text{ m/s}^2/\sqrt{\text{Hz}}$ at 1000 sec.

2.3.4. Dynamic range

In a conventional passive seismometer, the inertial force produced by a seismic ground motion deflects the mass from its equilibrium position, and the displacement or velocity of the mass is then converted into an electric signal. This classical mechanism is now used for short-period seismometers only. Broadband seismometers usually are of a force-feedback design, which provides greater linearity but sometimes at the expense of reduced dynamic range. Here, the inertial force is compensated (or “balanced”) with the electrically generated

force required to constrain the seismic mass. The feedback force is generated with an electromagnetic force transducer. Due to unavoidable delays in the feedback loop, force-balance systems have a limited bandwidth; however, at frequencies where they are effective, they force the mass to move with the ground by generating a feedback force strictly proportional to ground acceleration. When the force is proportional to the current in the transducer, then the current, the voltage across the feedback resistor, and the output voltage are all proportional to ground acceleration. Thus, acceleration can be converted into an electric signal without depending on the precision of the mechanical suspension.

2.4. Overall Criteria for the GSN Seismometers

A characterization of current seismological instrumentation capabilities is shown in Figures 1, 2, and 3. A combination of sensors is often used to realize a full response, and if advances in sensor design can achieve greater performance (while retaining linearity, resolution, bandwidth, and dynamic range) over the full seismic spectrum, it would be attractive to incorporate such instrumentation into the GSN in the future. The GSN design goal is to achieve at least the bandwidth and dynamic range indicated in these figures, as is presently achieved by the current optimal GSN instrumentation. This should guide the development of instrumentation specifications for all future GSN instrumentation.

Table 2 was excerpted from the 2002 GSN ad hoc Design Goals Subcommittee document (www.iris.edu/about/GSN/docs/GSN_Design_Goals.pdf), indicating the functional specification goals of the next-generation GSN sensor. The functional specifications are derived from the design goals by considering detailed limits of the general scientific goals. In general, it's worth making the instrumentation about an order of magnitude better than our ability to model the parameters being measured. Thus, if it is intended to model amplitudes to 20%, the aggregate sources of amplitude error (gain stability, cross-axis coupling, and cross talk) should be less than 2% and individual contributions should be even less.

Table 2. GSN Sensor Requirements.

Dynamic range	On-scale broadband recordings of earthquakes as large as $M_w = 9.5$ (equivalent to the 1960 Chile earthquake) at 4,500 km.
Clip level	5.8 m/s RMS over the band 10^{-4} seconds (or below) to 15 Hz.
Self-noise	Below ambient Earth noise.
Linearity	Total harmonic distortion < 80 dB at 50% maximum acceleration and frequencies within the pass-band of the feedback loop.
Bandwidth	Earth free oscillations to regional body waves (up to 15 Hz for land stations, 100 Hz for ocean-bottom sites).
Calibration	Known to 1% and stable across the bandwidth (adequate for amplitude modeling which at best is good to about 20%).
Cross-axis coupling	Less than about 1% (adequate for amplitude modeling).
Degrees of freedom	Three mutually orthogonal components of motion should be recorded.
Reliability	MTBF of years.
Shock and vibration	Equipment must be robust to survive shipping and installation.
Other environmental	Environmental susceptibility (to temperature, pressure, magnetic fields, electromagnetic and audio fields, etc.) should not constrain site selection or deployment technique.



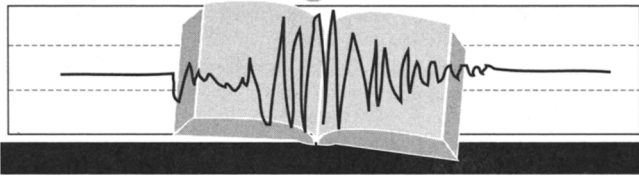
THE INCORPORATED RESEARCH
INSTITUTIONS FOR SEISMOLOGY

WWW.IRIS.EDU/STATIONS/SEISWORKSHOP04/SEISWORKSHOP.HTM

AUGUST 2005

Microseisms at frequencies above about 1 Hz are generally associated with local weather conditions, while below 1 Hz they reflect regional weather and ocean conditions. For seismic stations near the ocean, a particularly strong microseismic signal at a frequency of about .17 Hz (6-second period) apparently is caused by movements of water offshore and against the shoreline.

— Watching the Weather Using a Seismograph, John E. Ebel (2002)
Boston College, Weston Observatory



Larry J. Ruff

E-mail: eduquakes@seismosoc.org
 Dept. of Geological Sciences
 University of Michigan
 Ann Arbor, MI 48109
 Telephone: (734) 763-9301
 Fax: (734) 763-4690

Watching the Weather Using a Seismograph

John E. Ebel

Boston College
 Weston Observatory
 Boston College
 381 Concord Road
 Weston, MA 02493
ebel@bc.edu

Scientists are by nature a curious group of people (in all senses of that phrase!). Seismologists want to know everything they can about earthquakes, physicists about elementary particles, meteorologists about the weather, etc. Most scientists are curious not only about their own disciplines but also about many other scientific subjects as well. For example, I am a seismologist by training, but each fall I teach an introductory meteorology course to non-science majors at Boston College as part of the students' core science requirement.

It is a good thing that scientists are so widely curious, since it helps them in their work. This is because scientific phenomena are inherently interrelated. For example, the study of global climate change does not merely involve an analysis of the atmosphere. The Earth's oceans and its biosphere are intricately linked factors that play roles in controlling global climate. In fact, the movement of continents has likely played a crucial role in determining climatic conditions in the geologic past. Thus, scientists often look outside their own disciplines for ideas to help them understand phenomena they study.

For seismologists who routinely analyze seismograms, the presence of background noise is often a source of frustration, since such noise can partially or even totally obscure earthquake signals they wish to analyze. A study of seismic background noise can be an interesting subject on its own, however. There is a saying among scientists that is quite appli-

cable to the subject of this EduQuakes column: "One person's noise is another person's signal."

If you've ever looked at the traces recorded by a sensitive seismograph, you will see that they are never flat. Rather, the traces indicate that there are always some vibrations that shake the ground. Some of these vibrations are man-made: vehicular traffic, people walking, operating machinery that shakes the ground. Other background vibrations are natural: the wind shaking the ground surface; waves hitting shores; the movement of water in rivers, lakes, and the oceans. Seismologists have a name for natural background vibrations. We call them microseisms. Microseisms are observed at all frequencies on seismograms, although there are some frequencies at which they are especially strong. Microseisms at frequencies above about 1 Hz are generally associated with local weather conditions, while below 1 Hz they reflect regional weather and ocean conditions. For seismic stations near the ocean, a particularly strong microseismic signal at a frequency of about .17 Hz (6-second period) apparently is caused by movements of water offshore and against the shoreline.

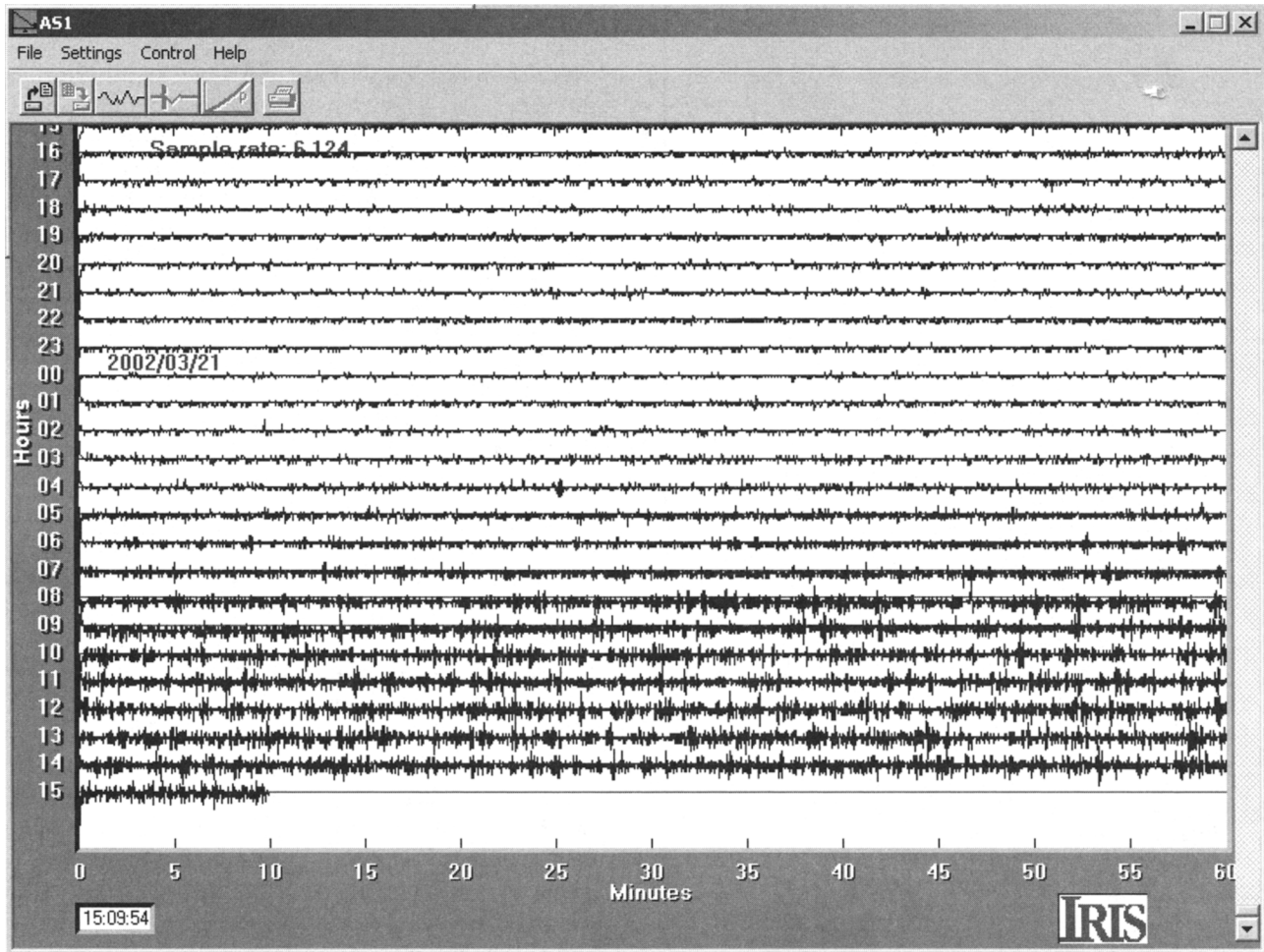
Since microseisms are caused primarily by meteorological conditions, an analysis of microseismic patterns on seismograms can reveal information about current weather conditions or how weather patterns are changing. High-pressure systems generally bring fair skies and light winds, and these are often reflected on seismograms by low levels of background microseismic noise. Low-pressure systems are typically accompanied by stronger winds, clouds, and precipitation. Microseisms on seismograms often are greater at times when low-pressure systems are near a seismic station.

During the fall, winter, and spring, those of us who live along the northeastern North American coast are often visited by storms that New Englanders call "nor'easters." These are low-pressure centers that travel from southwest to northeast along the coast, bringing cold, wind, rain, and higher-than-normal tides. Some can be quite strong, with wind gusts occasionally even exceeding hurricane force. During nor'easters, the microseisms on our seismograms in the New England region can be quite large. It is much more difficult to observe earthquake signals on our seismograms when such storms pass by.

If one studies the microseismic signals during passage of nor'easters at seismic stations in the Boston area, one finds a rather unexpected pattern. The strongest amplitudes for the microseisms do not occur when the low-pressure center is closest to the seismic stations. Rather, it occurs many hours later. In fact, the strongest microseisms can occur as much as half a day after the nor'easter has passed. Why is this?

The answer to this conundrum can be found by a simple, standard scientific investigation. One simply needs to study the passage of a number of nor'easters and then determine the positions of the low-pressure centers when the microseisms are greatest. One also needs to look at the geometry of the land and ocean for hundreds of miles around the seismic station.

The passage of a nor'easter over the Boston area on 20 and 21 March 2002 illustrates the answer to our question.



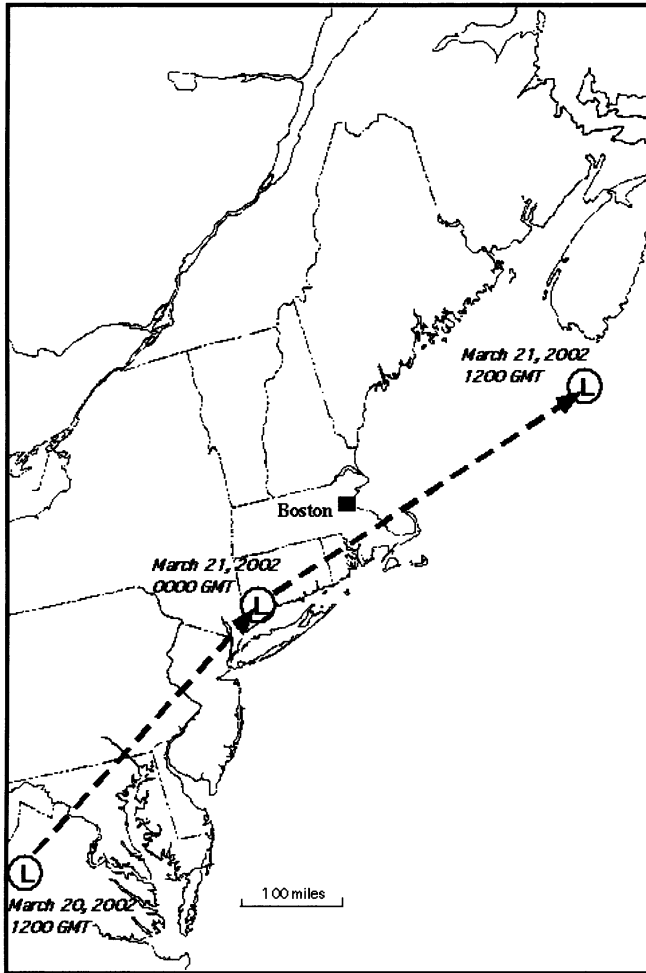
▲ **Figure 1.** Screen image of the Boston College Devlin Hall educational seismograph display for a 24-hour period on 20–21 March 2002. The number at the left side of each line is the hour in GMT. To convert to EST, subtract 5 hours from GMT.

This was a fairly strong nor'easter that brought a substantial amount of rain to Boston during the evening and night of 20–21 March. The strongest rainfall occurred late in the evening on 20 March, and it stopped during the early hours of 21 March. The sky cleared shortly afterward, and by the 6:00 AM EST sunrise on 21 March, the sky was perfectly clear and sunny.

A glance at the display of a home-made AS1 seismograph in Boston College's Devlin Hall (see <http://www.eas.purdue.edu/~braile/news/seisschools.htm> for information about the AS1 seismograph and recording system) on the morning of 21 March showed that the level of microseismic noise did not match the outdoor weather in Boston. During the morning of 21 March, the microseismic noise steadily increased, even though the weather had long since cleared. Figure 1, made at about 10:10 AM EST (1510 GMT) on 21 March, shows a 24-hour display of the ground motions recorded by the seismograph. The rain stopped in Boston between midnight and 3:00 AM on 21 March (0500 to 0800 GMT), but the microseisms were much smaller than they were later in the day. Curiously, as the weather was improving outside, the amplitude of the microseisms in the ground was increasing.

At first glance this might seem strange. But a plot of the center of low pressure from 20 March at 7:00 AM EST (1200 GMT) to 21 March at 7:00 AM EST (1200 GMT), shown in Figure 2, gives a clue to help explain this behavior. Notice the path of the storm from the southwest to the northeast across southern New England and into the Gulf of Maine. It was not until the low-pressure center passed north of Cape Cod and into the Gulf of Maine that the microseisms became strong on the Boston College seismograph. The strongest microseisms occurred at a time when the center of the storm was well out in the Atlantic Ocean and was near Nova Scotia. The low-pressure center was strengthening in intensity in the Gulf of Maine during the day of 21 March, increasing the movements of the surface waters of the ocean there. This probably helped increase the strength of the microseisms at Boston College throughout the day.

It turns out the weather and microseismic trends seen in Boston on 20–21 March are typical. Microseisms in the Boston area are generally weak for storms that stay south of Cape Cod and generally stronger for those low-pressure centers that traverse into the Gulf of Maine. In fact, the microseisms start noticeably increasing only after the low-pressure center



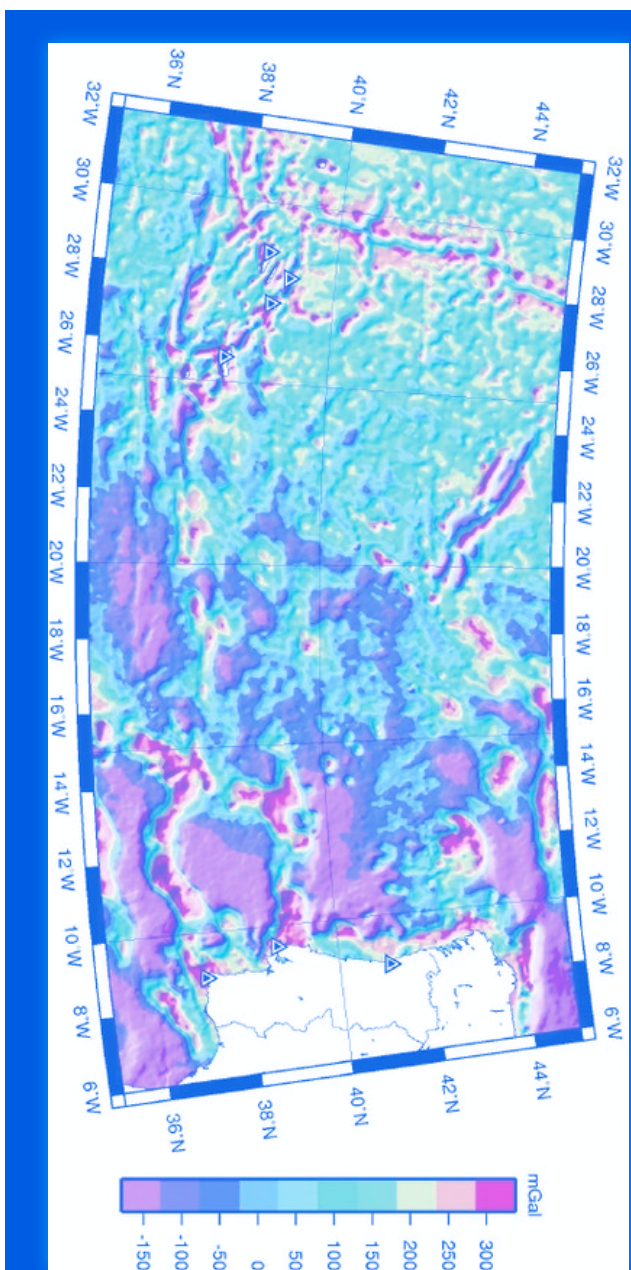
▲ **Figure 2.** Approximate path of the low-pressure center for the nor'easter of 20–21 March 2002. The approximate positions of the low-pressure center on 20 March at 1200 GMT (7:00 AM EST), 21 March at 0000 GMT (7:00 PM EST), and 21 March at 1200 GMT (7:00 AM EST) are shown.

moves out into the Gulf of Maine. Thus, it appears that the strong microseisms at Boston are generated primarily by water movements in the Gulf of Maine and the North Atlantic waters east of there. Also, nor'easters often strengthen when they pass into the Gulf of Maine. In general, the lower the pressure in the storm, the greater the microseisms. Therefore, there appear to be both oceanographic and meteorological reasons that strong microseisms occur when they do in the Boston area.

This example demonstrates that studying microseisms can help determine the movements and strengths of weather systems. While the example I have discussed here pertains to the situation in New England, people in other parts of the world can carry out similar investigations. The relationship of the positions and strengths of weather systems with microseismic levels on seismographs can be investigated by students anywhere. Of course, one needs to pay attention to the possible sources of the microseismic noise. In the Boston area, it appears that the strongest microseisms are caused by ocean movements in the Gulf and Maine and the North Atlantic to the east. In other parts of North America, the sources of microseismic noise will be different. The locations of weather systems relative to oceans, large lakes, mountains, and flatlands all may play a role in controlling the generation of microseisms.

If a school has a seismograph in operation, a study of the variations of microseisms with time and with the positions of weather systems can be an interesting project. It would help students to learn the tie between natural ground vibrations and meteorology. It would encourage students to pay attention to the movement of weather systems across their region. It could even make for an interesting and educational science fair or class project. ✉

SRL encourages guest columnists to contribute to "EduQuakes." Please contact Larry Ruff with your ideas. His e-mail address is eduquakes@seismosoc.org.



Article

Laser-Interferometric Broadband Seismometer for Epicenter Location Estimation

Kyunghyun Lee, Hyungkwan Kwon and Kwanho You *

Department of Electrical and Computer Engineering, Sungkyunkwan University, Suwon 16419, Korea; naman2001@skku.edu (K.L.); ant6565@naver.com (H.K.)

* Correspondence: khyou@skku.edu; Tel.: +82-31-290-7148

Received: 30 August 2017; Accepted: 5 October 2017; Published: 23 October 2017

Abstract: In this paper, we suggest a seismic signal measurement system that uses a laser interferometer. The heterodyne laser interferometer is used as a seismometer due to its high accuracy and robustness. Seismic data measured by the laser interferometer is used to analyze crucial earthquake characteristics. To measure P-S time more precisely, the short time Fourier transform and instantaneous frequency estimation methods are applied to the intensity signal (I_y) of the laser interferometer. To estimate the epicenter location, the range difference of arrival algorithm is applied with the P-S time result. The linear matrix equation of the epicenter localization can be derived using P-S time data obtained from more than three observatories. We prove the performance of the proposed algorithm through simulation and experimental results.

Keywords: seismic wave; laser interferometer; epicenter localization; STA/LTA; range difference of arrival

1. Introduction

The fundamental reasons for earthquakes arise from natural causes and artificial explosions. Natural causes by the movement of tectonic plates bring about energy spouting from the earth's interior, and volcano eruption. Artificial earthquakes are generated by explosions, collapses of large buildings, etc. A seismometer records the vibration caused by natural and artificial earthquakes. Many researchers have used the seismic data measured by seismometer to investigate the features of an earthquake, such as its magnitude, epicenter, and crust pattern. However, despite comprehensive earthquake study, the prediction of earthquake is very difficult since the measurement of seismic wave contains the noise factor during the measurement process [1–4]. The measurement noise occurs inevitably by the imperfection of the measurement environment and the background seismic signals. To investigate earthquake prediction, a precision instrument is needed to measure micro-earthquakes [5–7]. Usually, micro-earthquakes are generated prior to and subsequent to a strong earthquake, and they are termed foreshocks and aftershocks [8], respectively. Therefore, the study of micro-earthquakes is important in seismology. In particular, if a foreshock can be precisely estimated, the damage from a strong earthquake may be lessened.

There have been many efforts to precisely detect and analyze earthquakes. Beyreuther [9] suggested a method to detect and classify earthquakes using hidden Markov modeling, instead of a short-term average over a long-term average (STA/LTA) detector. Botella [10] proposed a real-time earthquake detector with pre-filtering by wavelets. The use of a discrete wavelet transform could increase the detector reliability. Araya [11] suggested a highly sensitive wideband seismometer using a Michelson laser interferometer. This made more exact measurement of the seismic wave than other devices under the noise environment. The epicenter location is very difficult to obtain exactly in spite of its importance [12–14]. Zhu [14] proposed a new estimation algorithm for epicenter location using low frequency seismograms. This is faster than the time domain method, and can also compensate the

error caused by low sampling rate. Gasparini [15] suggested a real-time earthquake location technique for early warning based on an equal differential time formulation and a probabilistic approach for hypocenter estimation.

In this paper, we propose a precision seismometer system with a laser interferometer [16–19]. Contrary to the seismometer based on accelerometers, it can determine the arrival time of a P-S wave and the epicenter location more accurately. The measured seismic wave (I_y) by the heterodyne laser interferometer in the time domain is converted into the time-frequency domain with short-time Fourier transform (STFT) [20–23] and instantaneous frequency (IF) estimation as preprocessing [24,25]. The STFT is a useful tool to analyze non-stationary signals and time-varying systems. In order to more exactly examine the seismic signal with time changes, the IF estimation method is applied to the incoming signal sequences. IF estimation can extract the frequency variation of a seismic wave with time changes. The data in the time-frequency domain is applied and formulated as an STA/LTA ratio to calculate the distance from the epicenter.

In general, the triangulation method is applied to estimate the location of epicenter using three epicentral distances. The triangulation method has weakness about estimation accuracy since it estimates the epicenter location without considering measurement noise. To find the epicenter, the range difference of arrival (RDOA) algorithm [26–29] is used. RDOA method represents the problem in a linear matrix equation and facilitates to apply many kinds of optimization methods. Moreover, the RDOA method has an advantage with the low computational complexity. With the difference of distances that are measured from at least 3 observatories, the origin of the signal spread can be estimated as the epicenter.

This paper is organized as follows. Section 2 describes the seismic wave measurement system with a heterodyne laser interferometer. Section 3 explains P-S time detection with the STFT, IF and STA/LTA method. Section 4 determines the epicenter location with the RDOA algorithm. Section 5 demonstrates the effectiveness of the proposed algorithm through the simulation results, while Section 6 concludes the paper.

2. Heterodyne Laser Interferometer

The measurement of seismic wave is a significant problem since the measurement accuracy is related directly with the accuracy of P-S time computation. In this paper, a heterodyne laser interferometer as a high precision displacement measurement instrument is used for the seismic wave measurement. A heterodyne laser interferometer measures displacement using the orthogonal characteristic of a laser source [30–33]. The laser head emits two polarized beams that have different frequencies. The laser source is divided at the beam splitter (BS) equally into two beams that have the same form. One moves downwards to the detector D_1 , while the other proceeds towards the polarized beam splitter (PBS). The laser sources emitted from the PBS are separated again into two beams. After being reflected by a moving mirror and a fixed mirror respectively, the separated beams are recombined, and collected at the detector D_2 . Figure 1 shows a schematic diagram of seismic detection system based on the heterodyne laser interferometer. The measurement part of seismic detection system needs to be isolated from the seismic wave's effect using the vibration isolation system [34].

The electric fields that are collected at detector D_1 are represented as follows [35]:

$$\begin{aligned} E_{Ap} &= \frac{1}{\sqrt{2}} A e^{j(2\pi f_p t + \phi_A)}, \\ E_{Ao} &= \frac{1}{\sqrt{2}} B e^{j(2\pi f_o t + \phi_B)}, \end{aligned} \quad (1)$$

where A and B are the amplitudes of the electric field, and ϕ_A , ϕ_B are the initial phase values of the given electric field. The laser head emits two-frequency beams of f_p for vertical polarization and f_o for horizontal polarization, respectively. The electric fields measured at detector D_2 are expressed as follows:

$$\begin{aligned} E_{Bp} &= \frac{1}{\sqrt{2}} A e^{j(2\pi f_p t + \phi_A)}, \\ E_{Bo} &= \frac{1}{\sqrt{2}} B e^{j(2\pi f_o t + \phi_B + \Delta\phi)}, \end{aligned} \quad (2)$$

where $\Delta\phi$ is the phase difference occurred by the Doppler effect: $\Delta\phi = 2\pi(f'_o - f_o)t$. f_p and f_o are the frequencies of the two orthogonal polarized beams from a laser head. The intensities of the reference signal and measurement signal that are collected by photo detectors D_1 and D_2 are represented as:

$$\begin{aligned} I_R &\propto (E_{Ap} + E_{Ao})(E_{Ap} + E_{Ao})^* \\ &= \frac{1}{2}(A^2 + B^2) + AB \cos[2\pi\Delta f t + (\phi_B - \phi_A)], \\ I_M &\propto (E_{Bp} + E_{Bo})(E_{Bp} + E_{Bo})^* \\ &= \frac{1}{2}(A^2 + B^2) + AB \cos[2\pi\Delta f t + (\phi_B - \phi_A) + \Delta\phi]. \end{aligned} \quad (3)$$

where Δf means the frequency difference of $f_p - f_o$. The DC components of the measured intensity signals are removed through a high-pass filter. The remaining signals are entered into a lock-in amplifier to obtain the phase value. Then, after passing through a lowpass filter, the intensities of $I_x \propto I_{M,ac} \cdot I_R$ and $I_y \propto I_{M,ac} \cdot I_R e^{j\pi/2}$ are represented as [36]:

$$\begin{aligned} I_x &\propto \frac{AB}{2} \cos(\Delta\phi), \\ I_y &\propto \frac{AB}{2} \sin(\Delta\phi). \end{aligned} \quad (4)$$

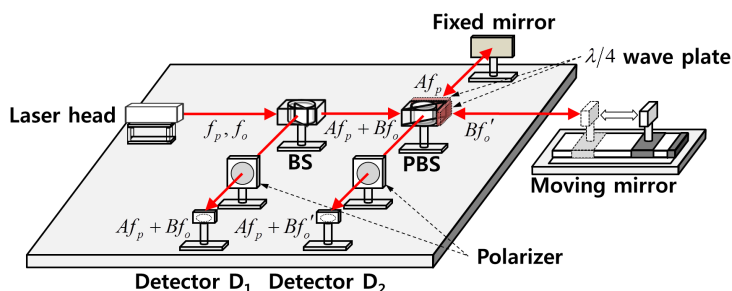


Figure 1. Schematic diagram of seismic wave measurement system using a laser interferometer.

The phase value can then be extracted by solving the trigonometric Equation (4). Moreover, the moving object's displacement can be calculated from the relation between the optical length and the phase value.

3. P-S Time Detection With Instantaneous Frequency

Generally, seismic data that are detected by a seismometer are analyzed in the time-amplitude domain. When an earthquake happens, the seismic signals are measured by observation of the P-wave and S-wave. The P-S time is determined according to the difference of velocity and amplitude between the P-wave and S-wave. However, if the difference of amplitude between the P-wave and S-wave is too small, the measurement of P-S time becomes difficult to calculate. To overcome this problem, we analyze the seismic wave in the time-frequency domain. In order to represent seismic data in the frequency domain, the STFT algorithm is applied. When the seismic signal is transformed into the frequency domain through the STFT, the STFT result represents the frequency change and amplitude value of the seismic signal in frequency with time. Hence, the P-S time is obtained by using the STFT.

With the displacement measurement by the heterodyne laser interferometer, the phase value can be interpreted as proportional to the displacement, as follows:

$$\Delta\phi = \frac{4\pi nD}{\lambda_m}, \quad (5)$$

where n is an air refractive index, and λ_m represents the mean of wavelengths of a laser source. D is the displacement, and $\Delta\phi$ is obtained from Equation (4). The seismic data that are measured by the laser interferometer can be represented as a trigonometric function with the phase information:

$$\begin{aligned} \hat{I}_x &\propto \frac{AB}{2} \cos(\Delta\hat{\phi}), \\ \hat{I}_y &\propto \frac{AB}{2} \sin(\Delta\hat{\phi}), \end{aligned} \quad (6)$$

where \hat{I}_x , \hat{I}_y , and $\Delta\hat{\phi}$ are the measurement values, respectively. With no loss of generality, we use the measured intensity signal (\hat{I}_y) as a seismic data.

Hence, the amplitude change of a seismic signal can be detected with the change of frequency. STFT algorithm is used to represent the detected signal in the time-frequency domain. Fourier transform enables the conversion of a function in the time domain to the frequency domain. However, when data in the time domain is transformed into the frequency domain by the Fourier transform, the time information of the transformed data is lost, and represented in terms of the frequency and amplitude, as the data is calculated for the whole time-interval. The Fourier transform is a function of the angular frequency ω . Therefore, it is impossible to obtain the time-frequency data. To analyze the seismic data in the time-frequency domain, we apply the short-time Fourier transform, which is a modification of the Fourier transform, and has short-term sampling intervals. The STFT of $f(t)$ is defined as follows [37,38]:

$$STFT \{f(t)\} (\tau, \omega) = \int_{-\infty}^{\infty} f(t)h(t-\tau)e^{-j\omega t} dt, \quad (7)$$

where $h(t)$ is a window function for analysis. The shape and the size of the window function affect the resolution of the STFT. When the STFT is applied, the transformed data is represented in time-frequency division as a spectrum, because the STFT is based on the Fourier transform in each time interval. Therefore, we can show the frequency change of the given data as a frequency spectrum. In the STFT method, it is hard to represent the transformed seismic signal in a closed form. To analyze the data as a single value in the time-frequency domain, we use the instantaneous frequency estimation method.

The instantaneous frequency is defined as the derivative of a phase. Generally, the instantaneous frequency is obtained as a single value, by using methods such as counting zero-crossing, and phase differentiation. Other methods for instantaneous frequency estimation are time-frequency distribution with the STFT, wavelet transform, and S-transform. Therefore, the STFT is used for instantaneous frequency estimation to analyze the data in the time-frequency domain. In the time-frequency distribution by the STFT, a single frequency value on time is obtained by an instantaneous frequency estimation. The instantaneous frequency estimation $X(t)$ is defined as follows [39,40]:

$$X(t) = \arg [\max TFD(t, f)], \quad (8)$$

where $TFD(t, f)$ is the time-frequency distribution of a seismic signal that is applied to the STFT. Then, the obtained data is represented in the time-frequency domain, and the arrival time of the P-wave and S-wave can be determined.

STA/LTA is one of the most frequently used methods in seismology to find the P-S time. To determine the arrival time of the P and S wave, the steepness of change rate is an important indicator. STA/LTA uses two moving windows which have different sizes. One has a short-sized window, and the other has a long-sized window. The short-sized moving window is more sensitive to the change of a seismic signal. The long-sized window has a gentle slope. With the characteristic of each window, the variation of seismic data can be detected. The short-term average and the long-term average [41,42] are represented as follows:

$$\begin{aligned}
 A_S(k) &= \sum_{t=k-n_s}^k \frac{X(t)}{n_s}, \\
 A_L(k) &= \sum_{t=k-n_l}^k \frac{X(t)}{n_l},
 \end{aligned}
 \tag{9}$$

n_s and n_l are the short-term window size, and the long-term window size, respectively. Finally, to determine the arrival time of the P-wave and S-wave, we set the threshold value. If v_p, v_s are defined as the velocities of the P-wave and S-wave, respectively, and t_{ps} is the P-S time that is obtained by STA/LTA algorithm, the distance (D_e) from an observatory to the epicenter can be measured by using Equation (10) as follows:

$$D_e = \frac{v_p v_s}{v_p - v_s} t_{ps}. \tag{10}$$

4. Epicenter Localization Based on Range Difference of Arrival

In this section, the RDOA method is used to determine the location of an epicenter. Although the triangulation method has been mostly used for epicenter localization due to its simplicity, there exists a limited accuracy problem caused by not considering the measurement noise. The RDOA method derives the relatively precise location of epicenter with the low computational complexity. The RDOA is the application of the time difference of arrival (TDOA) [43–45]. The TDOA uses the different reaching time from emitter to receiver, and it can be transformed to the RDOA, by multiplying the propagation velocity. The TDOA equation is expressed as follows:

$$t_{ij} = t_i - t_j, \quad i, j \in \{1, 2, \dots, m\}, \tag{11}$$

where t_i is a propagation time, and m is the number of receivers that are considered as observatories. According to the relation between distance and time, the RDOA equation can be expressed as follows:

$$s_i^o = t_i \times v_{sig}, \tag{12}$$

where s_i^o is the distance from the epicenter to each observatory, and v_{sig} is the propagation velocity of the seismic wave.

To determine the epicenter location, we need at least three earthquake observatories. Following the definition of a hyperbola equation, we set the observatory locations as focal points of each hyperbola, and find the point of intersection after depicting two pairs or more hyperbolae. Let us assume that there are m observatories that use the laser seismometer to detect a seismic wave. The measured seismic signals and the arrival time in each observatory are different, because the distances from the epicenter to each observatory are not the same.

RDOA is one of the popular location decision methods. We apply RDOA algorithm based on the least square method. The location of the i -th observatory is defined as $\mathbf{o}_i = [x_i \ y_i]^T, i = 1, 2, \dots, m$. The epicenter location is set as $\boldsymbol{\zeta} = [x \ y]^T$. We set the RDOA measurement value as:

$$\begin{aligned}
 s_i^o &= \|\boldsymbol{\zeta} - \mathbf{o}_i\|, \\
 s_{i1}^o &= s_i^o - s_1^o,
 \end{aligned}
 \tag{13}$$

where s_i^o is the distance between the epicenter and the i -th observatory. s_{i1}^o is the RDOA value between the i -th observatory and the first observatory. Using $s_i^o = \|\boldsymbol{\zeta} - \mathbf{o}_i\|$, the square of the i -th observatory distance from the epicenter can be written as:

$$\begin{aligned}
 (s_i^o)^2 &= \langle \boldsymbol{\zeta} - \mathbf{o}_i, \boldsymbol{\zeta} - \mathbf{o}_i \rangle \\
 &= \|\boldsymbol{\zeta}\|^2 - 2\mathbf{o}_i^T \boldsymbol{\zeta} + \|\mathbf{o}_i\|^2.
 \end{aligned}
 \tag{14}$$

Equation (14) can be rewritten as follows:

$$\begin{aligned} (s_i^o)^2 &= (s_{i1}^o + s_1^o)^2 \\ &= \langle \boldsymbol{\zeta} - \mathbf{o}_1, \boldsymbol{\zeta} - \mathbf{o}_1 \rangle + 2s_{i1}^o s_1^o + (s_{i1}^o)^2. \end{aligned} \quad (15)$$

As Equation (14) is equivalent to Equation (15), we represent the result as a quadratic form:

$$\|\boldsymbol{\zeta}\|^2 - 2\mathbf{o}_1^T \boldsymbol{\zeta} + \|\mathbf{o}_1\|^2 + 2s_{i1}^o s_1^o + (s_{i1}^o)^2 = \|\boldsymbol{\zeta}\|^2 - 2\mathbf{o}_i^T \boldsymbol{\zeta} + \|\mathbf{o}_i\|^2. \quad (16)$$

Then the relation among observatories can be formulated as

$$\|\mathbf{o}_1\|^2 - \|\mathbf{o}_i\|^2 + (s_{i1}^o)^2 = 2 \langle \mathbf{o}_1^T - \mathbf{o}_i^T, \boldsymbol{\zeta} \rangle - 2s_{i1}^o s_1^o. \quad (17)$$

We set the location of the first observatory at the origin of the earthquake coordinate system in order to simplify the equation of epicenter localization. Since the location of the first observatory \mathbf{o}_1 is set as $[0 \ 0]^T$, Equation (17) can be rewritten as the following equation.

$$\bar{\mathbf{A}}\boldsymbol{\zeta} = \mathbf{g}_o + \mathbf{p}_o s_1^o \quad (18)$$

with:

$$\begin{aligned} \bar{\mathbf{A}} &= \begin{bmatrix} \mathbf{o}_2^T \\ \vdots \\ \mathbf{o}_m^T \end{bmatrix}, \quad \mathbf{p}_o = - \begin{bmatrix} s_{21}^o \\ \vdots \\ s_{m1}^o \end{bmatrix}, \quad \mathbf{d} = \begin{bmatrix} \langle \mathbf{o}_2, \mathbf{o}_2 \rangle \\ \vdots \\ \langle \mathbf{o}_m, \mathbf{o}_m \rangle \end{bmatrix}, \\ \mathbf{g}_o &= \frac{1}{2} \begin{bmatrix} \|\mathbf{o}_2\|^2 - (s_{21}^o)^2 \\ \vdots \\ \|\mathbf{o}_m\|^2 - (s_{m1}^o)^2 \end{bmatrix} = \frac{1}{2}(\mathbf{d} - \mathbf{p}_o \bullet \mathbf{p}_o). \end{aligned}$$

where the symbol of (\bullet) means the Hadamard product. However, the epicenter localization formula, denoted by Equation (18), is true only under the ideal condition. In real case, there are some factors that restrict the measurement accuracy.

When we measure the P-S time to calculate the epicenter, STA/LTA algorithm depends on the user selected threshold value for earthquake location. Therefore, the obtained P-S time has a measurement error caused by the limited STA/LTA accuracy. The constrained P-S time data is closely related to finding the epicenter location using the RDOA data. As a result, the RDOA value can be represented as:

$$\begin{aligned} \mathbf{p} &= \text{col} \{s_{k1}^o + \Delta s_{k1}, k = 2, 3, \dots, m\} \\ &= \mathbf{p}_o + \Delta \mathbf{p}, \\ \mathbf{p}_o &= \text{col} \{s_{k1}^o\}, \quad \Delta \mathbf{p} = \text{col} \{\Delta s_{k1}\}, \\ E[\Delta \mathbf{p}] &= 0, \quad \mathbf{Q}_p = E[\Delta \mathbf{p} \Delta \mathbf{p}^T] \end{aligned} \quad (19)$$

where $\Delta \mathbf{p}$ is the epicenter inconsistency error caused by the P-S time measurement error, and $\text{col}\{\cdot\}$ means a column vector. In real environment, the parameter \mathbf{g} is formulated using Equation (19) as follows

$$\mathbf{g} = \mathbf{g}_o + \mathbf{p}_o \bullet \Delta \mathbf{p}. \quad (20)$$

In order to express the formula of the epicenter localization under real environment including the effect of measurement error, the parameters \mathbf{p}_o and \mathbf{g}_o in Equation (18) should be replaced with \mathbf{p} and \mathbf{g} , respectively. Therefore, the epicenter location in real condition can be found as follows [46]:

$$\bar{\mathbf{A}}\zeta = \bar{\mathbf{B}} \quad (21)$$

with:

$$\begin{aligned} \bar{\mathbf{B}} &= \mathbf{b}_o + \mathbf{N}\Delta\mathbf{p}, \\ \mathbf{b}_o &= \mathbf{g}_o + \mathbf{p}_o s_1^o \\ \mathbf{N} &= \text{diag}(\mathbf{p}_o) - s_1^o \mathbf{I} \end{aligned} \quad (22)$$

The vector ζ that denotes the location of epicenter can be obtained using Equation (21). The measurement noise caused by the limited accuracy of STA/LTA method under real environment leads to the discrepancy between the estimated epicenter location and the real epicenter location. By compensating the measurement error using an optimization scheme, the precise location of epicenter (ζ) can be obtained from Equation (21).

5. Simulation and Experimental Results

In this section, we prove the performance of the seismic signal measurement by using a laser interferometer, and obtain the normalized frequency data in the time-frequency domain using STFT algorithm. Moreover, the IF estimation, denoted by Equation (8), is applied to STFT data. Finally, we show the accurate epicenter location detection by using RDOA algorithm from the P-S time that is calculated from IF estimation through STA/LTA algorithm. Figure 2 shows the seismic wave measurement system using a heterodyne laser interferometer. The experiment uses a heterodyne laser interferometer with a He-Ne laser head (Wavetronics: WT-307B). To generate the seismic signal, we use a linear stage driven by a 2-phase stepping motor (Sciencetown: PSA6520) with a 20 mm stroke. Using the linear stage, seismic wave movement is generated to prove the performance of the interferometric seismometer. To compare the performance, we use an accelerometer as a reference since it is currently used as an earthquake motion measurement instrument. The model of JEP-8A3, Mitutoyo, is actively utilized as an acceleration sensor due to its high-performance. The measurement range, dynamic range, and sensitivity of JEP-8A3 are 3000 Gal, 145 dB, and $\pm 3\%$, respectively. The displacement variation caused by the linear stage is measured by the heterodyne laser interferometer. The displacement data can be transformed to the acceleration data using a sample rate (6.7 kHz).

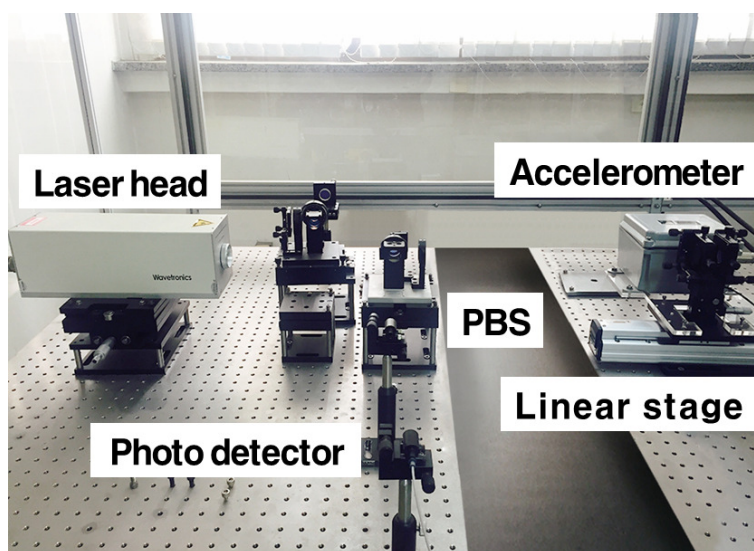


Figure 2. Seismic wave measurement system using a laser interferometer.

We set the mean wavelength (λ_m) from the laser head as 632.9 (nm), and the air refractive index (n) as 1.000000026. Figure 3 shows the seismic wave movement measured by laser interferometer. The amplitude discrepancy in Figure 3 shows the sensitivity to measurement noise.

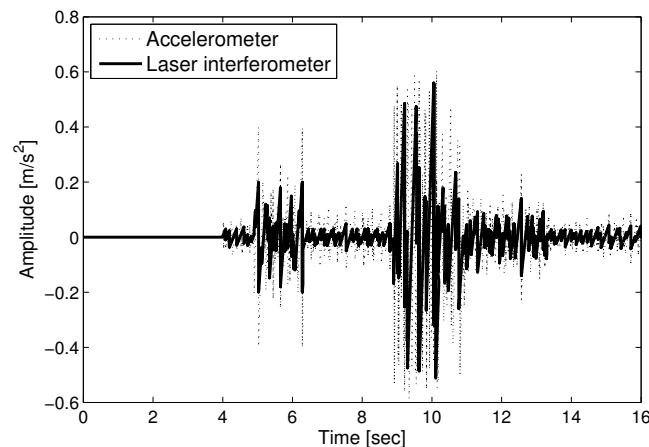


Figure 3. Seismic wave measurement with a laser interferometer.

With the displacement measurement by the heterodyne laser interferometer, the phase value ($\Delta\phi$) is proportional to the displacement (D), as in Equation (5). Figure 4 represents the difference between the true amplitude and the measurement value at each sampling time. The thick solid line and the thin dotted line in Figure 4 denote the root mean square error (RMSE) of the measured seismic wave using a laser interferometer and accelerometer, respectively. The measurement using a laser interferometer is more precise than the accelerometer. Figure 5 shows the intensity signal (I_y) for spectrum analysis with $AB = 2$ in Equation (4). The high-density points of I_y can be interpreted as the arrival time of the P and S waves at 5 and 9 s, respectively. The amplitudes of the P and S waves changing frequently are represented by the highly dense intensities in Figure 5.

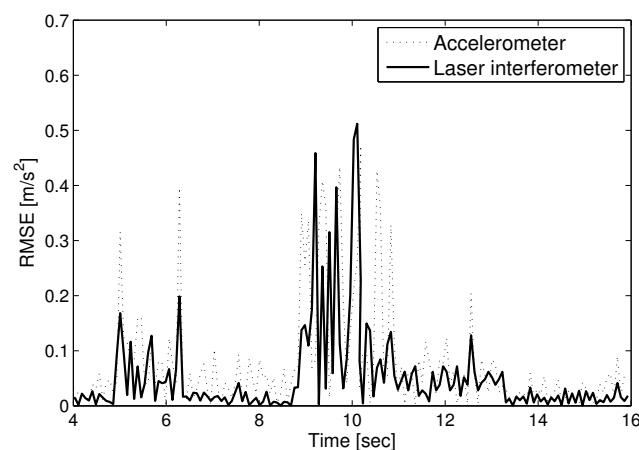


Figure 4. Measurement error comparison between a laser interferometer and accelerometer.

STFT algorithm is used to represent the detected signal in the time-frequency domain. The Fourier transform is adequate to project the data in the time domain into the frequency domain. STFT algorithm is applied to intensity signal (I_y) data that represents high density when P and S wave arrive. The differential phase value is obtained using the STFT data. Figure 6 shows the result of STFT that indicates time, frequency and amplitude distribution. The red color represents a high amplitude value, and the blue color represents a low amplitude value. The figure shows that there are sharp points at 5 and 9 s, respectively. The arrival times of the P-wave and S-wave are confirmed. After the arrival of the P and S waves, the amplitude of the seismic wave changes. Therefore, the peak points at 5 and 9 s mean the arrival time of the P and S waves. With the derived STFT data, IF estimation is performed,

as shown in Figure 7. Using the result of STFT in the time-frequency domain, IF is applied to get the frequency value in each interval time. Similar to the result in Figure 6, the value in Figure 7 represents the arrival time of the seismic signal.

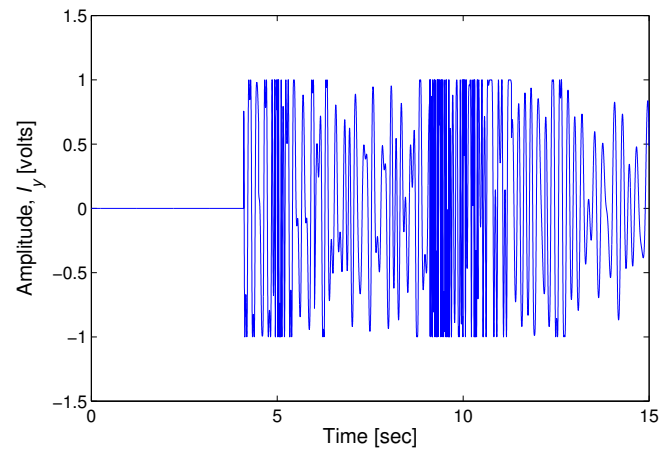


Figure 5. Intensity signal (I_y) for spectrum analysis.

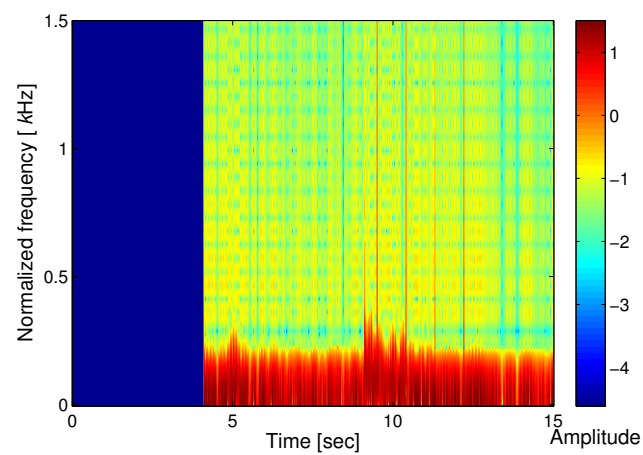


Figure 6. STFT result of the seismic wave.

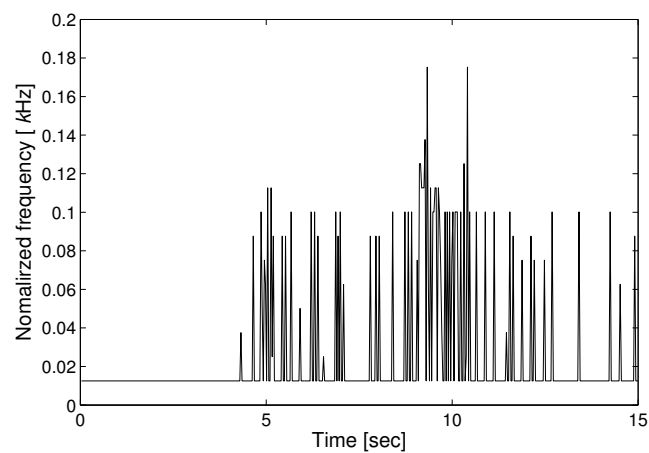


Figure 7. IF analysis of the seismic wave.

Figure 8 shows the seismic wave data with STA/LTA algorithm. We set up the LTA window size with as much as 8 times the STA window size, and set the threshold value as twice the average of the STA/LTA ratio. We can determine the P-S time when the STA/LTA ratio becomes greater than the threshold value. The arrival times of the P-wave and S-wave were measured as 4.65 and 9.12 (s), respectively. If we suppose the velocities of the P-wave and S-wave as 8.2 and 3.7 (km/s) separately, we can calculate the distance to the epicenter as 31.2 (km), according to Equation (10).

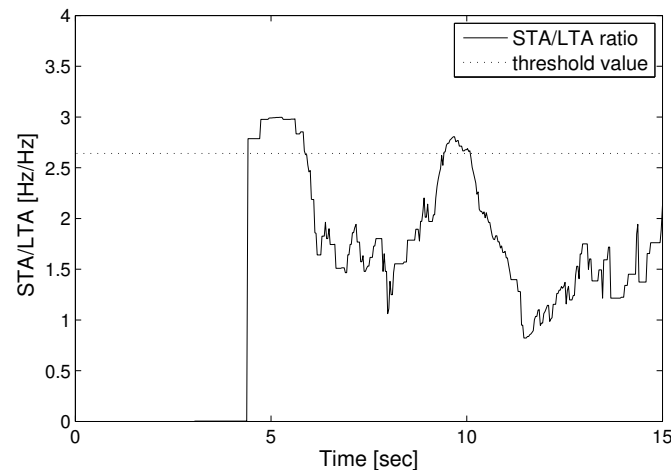


Figure 8. Estimation of the STA/LTA ratio.

Figure 9 shows the estimation of the epicenter location. The circle points represent the observatory locations, while the triangle point represents the epicenter location. We set the epicenter location as (50, 20) (km) when the measurement noise does not exist. We suppose the locations of the observatory as (0, 0), (10, 80), (100, 0), and (100, 80) (km), respectively. The epicenter location found using the RDOA hyperbolae is shown in Figure 9. When the hyperbolae are to be drawn, we set the observatory that is placed at (100, 0) (km) as a reference. With the reference observatory and each separate observatory, the three pairs of hyperbolae were derived. We assume that the measurement noises of epicentral distances at each observatory follow the Gaussian distribution. n_e is the maximum absolute value of the measurement noises. We suppose the parameter n_e as 1 in Figure 9. As a result, we determined the epicenter location using RDOA algorithm as (47.9, 21.2) (km). The asterisk point is the estimated epicenter location using triangulation method that is generally used for location estimation of an epicenter. The estimated result using the triangulation method is (53.7, 17.9) (km). It can be confirmed that the estimated result from RDOA is closer to the actual location. Table 1 shows the RMSE comparison of RDOA based estimation method with the triangulation method for various measurement noises. As the measurement noise represented as n_e increases, the localization accuracy becomes low accordingly. It can be confirmed that the result of RDOA based epicenter estimation is better under the circumstances of measurement noise.

Table 1. RMSE comparison for various measurement noises (n_e).

Methods	RMSE (km)				
	$n_e = 1$	$n_e = 2$	$n_e = 3$	$n_e = 5$	$n_e = 10$
Triangulation	4.25	6.12	7.28	8.92	13.29
RDOA	2.41	3.29	3.93	4.72	7.20

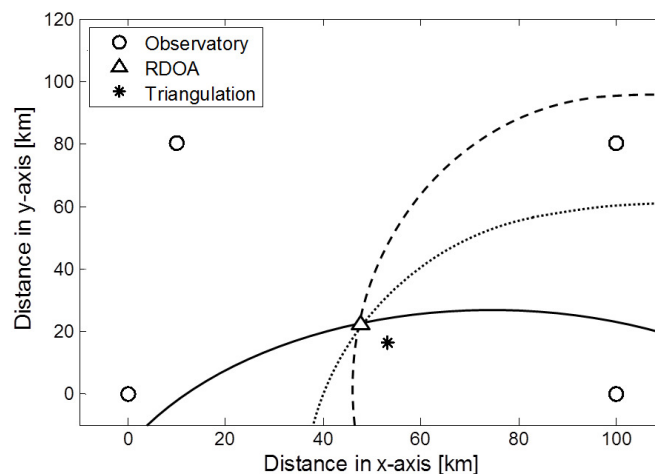


Figure 9. Epicenter location using RDOA algorithm.

6. Conclusions

In this paper, we suggest an epicenter localization method based on RDOA algorithm. The range difference information for RDOA algorithm is obtained from a seismic signal measured by a heterodyne laser interferometer. The laser interferometer uses the Doppler effect to detect movement of the stage. We measure the seismic signal with the use of a laser interferometer. To determine the P-S time, we apply STFT, IF, and STA/LTA algorithms to seismic signal data obtained from the laser interferometer's intensity signal (I_y). Using STFT and IF, the transformed signal of the seismic wave is obtained in the time-frequency domain. With the changes of frequency, we decide the arrival time of the P and S waves. Moreover, we determine the epicenter location with RDOA algorithm. We confirm that RDOA algorithm can more accurately estimate the epicenter location.

Acknowledgments: This work was supported by the National Research Foundation of Korea (NRF) grant funded by the Korea government (MSIP) (NRF-2016R1A2B4011369).

Author Contributions: This paper was accomplished by all the authors with the assignments that Kwanho You and Kyunghyun Lee conceived the idea and performed the analysis and design of the experiment; Kyunghyun Lee and Hyungkwan Kwon carried out the numerical simulation and the experiment; Kyunghyun Lee and Kwanho You co-wrote the manuscript.

Conflicts of Interest: The authors declare no conflict of interest.

References

1. Uyeda, S.; Nagao, T.; Kamogawa, M. Short-term earthquake prediction: Current status of seismo-electromagnetics. *Tectonophysics* **2009**, *470*, 205–213.
2. Zechar, J.; Jordan, T. Testing alarm-based earthquake predictions. *Geophys. J. Int.* **2008**, *172*, 715–724.
3. Keilis-Borok, V.; Ismail-Zadeh, A.; Kossobokov, V.; Shebalin, P. Non-linear dynamics of the lithosphere and intermediate-term earthquake prediction. *Tectonophysics* **2001**, *338*, 247–260.
4. Adeli, H.; Panakkat, A. A probabilistic neural network for earthquake magnitude prediction. *Neural Netw.* **2009**, *22*, 1018–1024.
5. Sileny, J.; Hill, D.P.; Eisner, L.; Cornet, F.H. Non-double-couple mechanisms of microearthquakes induced by hydraulic fracturing. *J. Geophys. Res.-Solid Earth* **2009**, *114*, B08307.
6. Reddy, D.V.; Sukhija, B.S.; Nagabhushanam, P.; Kumar, D. A clear case of radon anomaly associated with a micro-earthquake event in a stable continental region. *Geophys. Res. Lett.* **2004**, *31*, L10609.
7. Collins, D.S.; Pettitt, W.S.; Young, R.P. High-resolution mechanics of a microearthquake sequence. *Pure Appl. Geophys.* **2002**, *159*, 197–219.
8. Ogata, Y.; Utsu, T.; Katsura, K. Statistical discrimination of foreshocks from other earthquake cluster. *J. Geodyn.* **1996**, *65*, 199–217.

9. Beyreuther, M.; Wassermann, J. Continuous earthquake detection and classification using discrete hidden Markov models. *Geophys. J. Int.* **2008**, *175*, 1055–1066.
10. Botella, F.; Rosa-Herranz, J.; Ginger, J.; Monlina, S.; Galiana-Merino, J. A real-time earthquake detector with prefiltering by wavelets. *Comput. Geosci.* **2003**, *29*, 911–919.
11. Araya, A.; Kawabe, K.; Sato, T.; Mio, N.; Tsubono, K. Highly sensitive wideband seismometer using a laser interferometer. *Rev. Sci. Instrum.* **1993**, *64*, 1337–1341.
12. Du, A.; Huang, Q.; Yang, S. Epicenter location by abnormal ULF electromagnetic emissions. *Geophys. Res. Lett.* **2002**, *29*, 1–3.
13. Zhan, Z.; Wei, S.; Ni, S.; Helmberger, D. Earthquake centroid locations using calibration from ambient seismic noise. *B Seismol. Soc. Am.* **2011**, *107*, 1438–1445.
14. Zhu, W.; Sun, L.; Zhu, X. New estimation algorithm for epicenter location of low frequency seismograms. In Proceedings of the 2012 International Conference on Systems and Informatics (ICSAI), Yantai, China, 19–20 May 2012; pp. 1706–1710.
15. Gasparini, P.; Manfredi, G.; Zschau, J. *Earthquake Early Warning System*; Springer: Berlin, Germany, 2007.
16. Deng, Y.; Li, X.; Wu, Y.; Hu, J.; Yao, J. Analysis of frequency mixing error on heterodyne interferometric ellipsometry. *Meas. Sci. Technol.* **2007**, *18*, 3339–3343.
17. Park, T.; Choi, H.; Han, C.; Lee, Y. Real-time precision displacement measurement interferometer using the robust discrete time Kalman filter. *Opt. Laser Technol.* **2005**, *37*, 229–234.
18. Olyae, S.; Yoon, T.; Hamedi, S. Jones matrix analysis of frequency mixing error in three-longitudinal-mode laser heterodyne interferometer. *IET Optoelectron.* **2009**, *3*, 215–224.
19. Hou, W.; Zhang, Y.; Hu, H. A simple technique for eliminating the nonlinearity of a heterodyne interferometry. *Meas. Sci. Technol.* **2009**, *20*, 105303.
20. Lu, W.; Li, F. Seismic spectral decomposition using deconvolutive short-time Fourier transform spectrogram. *Geophysics* **2013**, *78*, 43–51.
21. Wright, P. Short-time Fourier transforms and Wigner-Ville distributions applied to the calibration of power frequency harmonic analyzers. *IEEE Trans. Instrum. Meas.* **1999**, *48*, 475–478.
22. Lu, W.; Zhang, Q. Deconvolutive short-time Fourier transform spectrogram. *IEEE Signal Process. Lett.* **2009**, *16*, 576–579.
23. Auger, F.; Flandrin, P. Improving the readability of time-frequency and time-scale representations by the reassignment method. *IEEE Trans. Signal Process.* **2002**, *43*, 1068–1089.
24. O’Shea, P. A new technique for instantaneous frequency rate estimation. *IEEE Signal Process. Lett.* **2002**, *9*, 251–252.
25. Aboutanios, E.; Mulgrew, B. Iterative frequency estimation by interpolation on Fourier coefficients. *IEEE Trans. Signal Process.* **2005**, *53*, 1237–1242.
26. Cheung, K.W.; So, H.C.; Ma, W.K.; Chan, Y.T. A constrained least square approach to mobile positioning: algorithms and optimality. *EURASIP J. Appl. Signal Process.* **2006**, *2006*, 1–23.
27. Shin, D.H.; Sung, T.K. Comparison of error characteristics between TOA and TDOA positioning. *IEEE Trans. Aero. Elec. Syst.* **2002**, *38*, 307–311.
28. Dogancay, K. Emitter localization using clustering-based bearing association. *IEEE Trans. Aero. Elec. Syst.* **2005**, *41*, 525–536.
29. Zhu, D.; Yi, K. Localization technology research based on particle filter in underground mines. *J. Comput. Inf. Syst.* **2013**, *9*, 3011–3018.
30. Sutton, C.M. Non-linearity in length measurement using heterodyne laser Michelson interferometry. *J. Phys. E: Sci. Instrum.* **1987**, *20*, 1290–1292.
31. Nozato, H.; Kokuyama, W.; Ota, A. Improvement and validity of shock measurements using heterodyne laser interferometer. *Measurement* **2016**, *77*, 67–72.
32. Fu, H.; Hu, P.; Tan, J.; Fan, Z. Simple method for reducing the first-order optical nonlinearity in a heterodyne laser interferometer. *Appl. Opt.* **2015**, *54*, 6321–6323.
33. McRae, T.G.; Hsu, M.T.L.; Freund, C.H.; Shaddock, D.A.; Herrmann, J.; Gray, M.B. Linearization and minimization of cyclic error with heterodyne laser interferometry. *Opt. Lett.* **2012**, *37*, 2448–2450.
34. Yang, J.; Xiong, Y.; Xing, J. Dynamics and power flow behaviour of a nonlinear vibration isolation system with a negative stiffness mechanism. *J. Sound Vib.* **2013**, *332*, 167–183.

35. Wang, Y.; Shyu, L.; Chang, C. The comparison of environmental effects on Michelson and Fabry-Perot interferometers utilized for the displacement measurement. *Sensors* **2010**, *10*, 2577–2586.
36. Lee, K.; Pyo, Y.; You, K. Lagrange multiplier-based error compensation of heterodyne interferometer. *Electron. Lett.* **2016**, *52*, 1692–1694.
37. Quyang, X.; Amin, G. Short-time Fourier transform receiver for nonstationary interference excision in direct sequence spread spectrum communications. *IEEE Trans. Signal Process.* **2001**, *49*, 851–863.
38. Richard, M. Helium speech enhancement using the short-time Fourier transform. *IEEE Trans. Acoust. Speech* **1982**, *30*, 841–853.
39. Katkovnik, V.; Stankovic, L. Instantaneous frequency estimation using the Wigner distribution with varying and data-driven window length. *IEEE Trans. Signal Process.* **1998**, *46*, 2315–2325.
40. Kwok, H.; Jones, D. Improved instantaneous frequency estimation using an adaptive short-time Fourier transform. *IEEE Trans. Signal Process.* **2000**, *48*, 2964–2972.
41. Hara, T. Measurement of the duration of high-frequency energy radiation and its application to determination of the magnitudes of large shallow earthquakes. *Earth Planets Space* **2007**, *59*, 227–231.
42. Svitek, T.; Rudajev, V.; Petruzalek, M. Determination of P-wave arrival time of acoustic events. *Acta Montan. Slovaca* **2010**, *15*, 145–151.
43. Yu, H.; Huang, G.; Gao, J. Constrained total least-squares location algorithm using time difference of arrival measurements. *IEEE Trans. Veh. Technol.* **2010**, *59*, 1558–1562.
44. Hara, S.; Anzai, D.; Yabu, T. A perturbation analysis on the performance of TOA and TDOA localization in mixed LOS/NLOS environments. *IEEE Trans. Commun.* **2013**, *61*, 679–689.
45. Soliman, M.S.; Morimoto, T.; Kawasaki, Z.I. Three-dimensional localization system for impulsive noise sources using ultra-wideband digital interferometer technique. *J. Electromagn. Waves Appl.* **2012**, *20*, 515–530.
46. Oh, J.; Lee, K.; You, K. Hybrid TDOA and AOA localization using constrained least squares. *IEICE Trans. Fund. Electr.* **2015**, *E98-A*, 2713–2718.



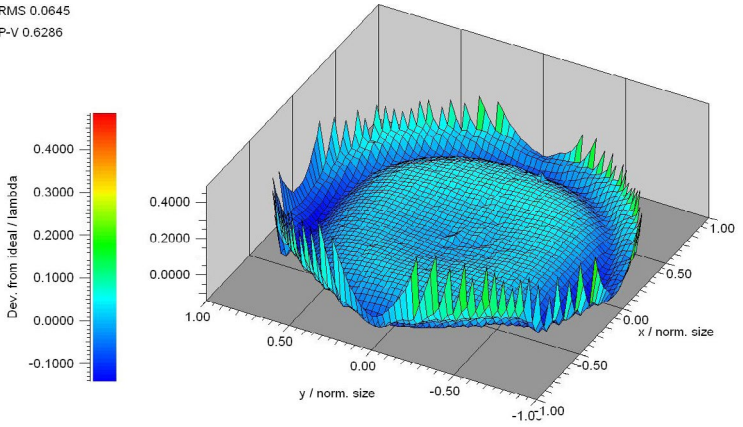
© 2017 by the authors. Licensee MDPI, Basel, Switzerland. This article is an open access article distributed under the terms and conditions of the Creative Commons Attribution (CC BY) license (<http://creativecommons.org/licenses/by/4.0/>).

And connected is
helping people stay in
touch and maintain
empathy for each other,
and bandwidth.

— Marc Zuckerberg

RMS 0.0645

P-V 0.6286



Seismic signals are usually transient waveforms radiated from a localized natural or man-made seismic source. They can be used to locate the source, to analyze source processes, and to study the structure of the medium of propagation. In contrast, the term “seismic noise” designates undesired components of ground motion that do not fit in our conceptual model of the signal under investigation. What we identify and treat as seismic noise depends on the available data, on the aim of our study and on the method of analysis. Accordingly, data treated as noise in one context may be considered as useful signals in other applications.

— Seismic Signals and Noise, Peter Bormann and Erhard Wielandt

RESEARCH LETTER

10.1002/2014GL062782

Key Points:

- The “hum” is caused by the interaction of ocean waves with the bottom slope
- Our model yields maps of seismic sources at all periods from 3 to 300 s
- Sources of the hum are strongest along shelf breaks, on the east side of oceans

Supporting Information:

- Text S1 and Figures S1–S4

Correspondence to:

F. Ardhuin,
ardhuin@ifremer.fr

Citation:

Ardhuin, F., L. Gualtieri, and E. Stutzmann (2015), How ocean waves rock the Earth: Two mechanisms explain microseisms with periods 3 to 300 s, *Geophys. Res. Lett.*, *42*, 765–772, doi:10.1002/2014GL062782.

Received 18 DEC 2014

Accepted 9 JAN 2015

Accepted article online 14 JAN 2015

Published online 10 FEB 2015

How ocean waves rock the Earth: Two mechanisms explain microseisms with periods 3 to 300 s

Fabrice Ardhuin^{1,2}, Lucia Gualtieri³, and Eléonore Stutzmann³

¹Ifremer, Laboratoire d’Océanographie Spatiale, Brest, France, ²Laboratoire de Physique des Océans, CNRS-Ifremer-UBO-IRD, Brest, France, ³Institut de Physique du Globe, PRES Sorbonne Paris-Cité, Paris, France

Abstract Microseismic activity, recorded everywhere on Earth, is largely due to ocean waves. Recent progress has clearly identified sources of microseisms in the most energetic band, with periods from 3 to 10 s. In contrast, the generation of longer-period microseisms has been strongly debated. Two mechanisms have been proposed to explain seismic wave generation: a primary mechanism, by which ocean waves propagating over bottom slopes generate seismic waves, and a secondary mechanism which relies on the nonlinear interaction of ocean waves. Here we show that the primary mechanism explains the average power, frequency distribution, and most of the variability in signals recorded by vertical seismometers, for seismic periods ranging from 13 to 300 s. The secondary mechanism only explains seismic motions with periods shorter than 13 s. Our results build on a quantitative numerical model that gives access to time-varying maps of seismic noise sources.

1. Introduction

Ocean waves provide most of the energy that feeds the continuous vertical oscillations of the solid Earth. In these, three period bands are usually identified. The hum contains periods longer than 30 s, and the primary and secondary peaks are centered around 15 and 5 s, respectively. Motions in all three bands are recorded everywhere on our planet [Webb, 1998; Nishida, 2013] and can provide information on both the solid Earth structure [Shapiro *et al.*, 2005], the ocean wave climate over the past century [Bernard, 1990; Grevemeyer *et al.*, 2000], and the properties of short-period ocean waves [Farrell and Munk, 2010]. Yet the use of seismic data is limited because where and how ocean waves rock the Earth is not known, in particular for the hum. The hum is the least understood part of Earth’s oscillations. Recently discovered in seismometer records [Nawa *et al.*, 1998; Suda *et al.*, 1998], it has been associated with ocean waves for periods shorter than 300 s [Tanimoto, 2005; Rhie and Romanowicz, 2004; Bromirski, 2009; Nishida, 2013]. For any period, a Fourier analysis of the motions in the solid Earth and ocean layer shows that the transfer of energy from ocean waves to seismic waves is significant if ocean wave motions match both the wavelength and periods, and hence the speed, of seismic waves [Hasselmann, 1963]. This necessary matching of the speeds of different wave trains applies to all sorts of wave motions [Hasselmann, 1966], for example, the generation of atmospheric waves by tsunamis [e.g., Artru *et al.*, 2005]. Both primary and secondary mechanisms can be the matchmakers between slow ocean waves and much faster seismic waves. Without any of these two mechanisms, ocean waves propagating over a flat bottom only produce pressure oscillations in the water, at the frequency and wave number of the ocean waves, hence distinct from seismic waves. The crust deformation under such a pressure field is proportional to the local ocean wave amplitude and is known as compliance [e.g., Crawford *et al.*, 1991] and does propagate like seismic waves.

The secondary mechanism is best known, and corresponds to the nonlinear interaction of pairs of ocean wave trains with frequencies f_1 and f_2 and wave number vectors \mathbf{k}_1 and \mathbf{k}_2 . It gives pressure patterns with sum and difference frequencies $f_1 \pm f_2$, wave numbers $\mathbf{k}_1 \pm \mathbf{k}_2$, and thus, phase velocities $C_s = 2\pi|f_1 \pm f_2|/|\mathbf{k}_1 \pm \mathbf{k}_2|$. We will not consider the difference interactions, which have been proposed in other studies [Uchiyama and McWilliams, 2008; Traer and Gerstoft, 2014], because only the sum interactions can yield velocities matching those of seismic waves [Hasselmann, 1963; Webb, 2008] (see also supporting information Text S1). With the secondary mechanism, velocity matching occurs for nearly opposing directions and nearly equal periods (Figure 1a).

In that case, seismic waves have a frequency that is twice the ocean wave frequency [Longuet-Higgins, 1950; Hasselmann, 1963; Ardhuin and Herbers, 2013]. That secondary mechanism explains the most energetic

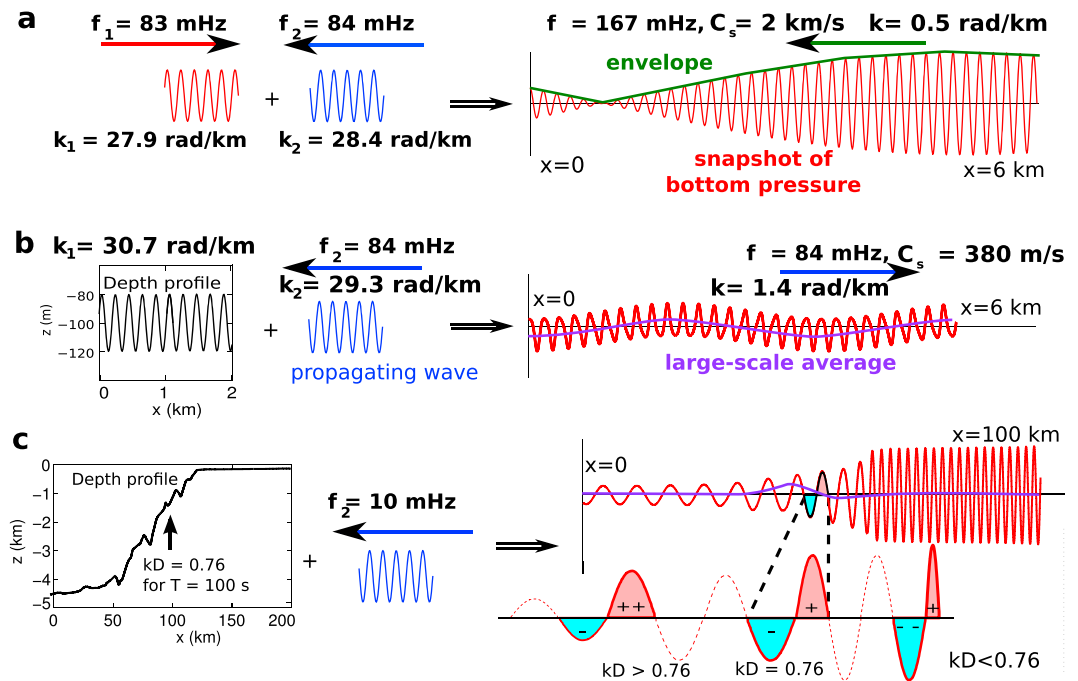


Figure 1. The two mechanisms that produce seismic noise. (a) In the secondary mechanism, opposing waves produce wave groups with fast traveling envelopes, in green. The second-order surface pressure (in red) is proportional to the surface velocity squared; hence, it contains Fourier components that have the same speed as the envelope. (b) The most simple case of the primary mechanism involves a wave with wave number k_1 . The result is a large-scale oscillation of the bottom pressure, here in purple. As $k = k_1 - k_2$ goes to zero, the wavelength and speed of that oscillation go to infinity. (c) A realistic depth profile $D(x)$ contains all possible wavelengths, giving rise to pressure patterns with all possible speeds. The large-scale average of this pressure has a phase which changes sign where $kD = 0.76$, which is where the effect of an increase in wave amplitude toward shallow water is exactly compensated by the effect of a reduction in wavelength. Here the amplitude of the large-scale average was exaggerated for readability. Our choice of an infragravity wave propagating from the shoreline to open ocean corresponds to the most energetic hum sources off west coasts. In Figures 1b and 1c the time series of pressure at each point is a sinusoid.

seismic band with typical periods of 3 to 10 s [Kedar et al., 2008; Ardhuin et al., 2011; Stutzmann et al., 2012; Gualtieri et al., 2013]. At these periods, there is still a debate on the amplitude of the waves transmitted from the oceanic waveguide to the continental crust [e.g., Obrebski et al., 2012; Bromirski et al., 2013], which may vary with the shape of each continental margin.

In the primary mechanism, the bottom topography is like a frozen wave train, with $f_1 = 0$, but it contains wave numbers k_1 that can take any value. Bottom interference with ocean waves of frequency f_2 and wave numbers k_2 gives energy in the bottom pressure spectrum at the same period as the ocean waves (Figures 1b and 1c) but at wave numbers $k_1 \pm k_2$, which can match seismic wavelengths. This mechanism was invoked by Hasselmann [1963] to explain the “primary microseism” peak, with periods usually between 10 and 20 s. The only test of this theory considered periods around 20 s, 6 days of data for a single location [Hasselmann, 1963], and a constant bottom slope that was adjusted to fit seismic observations.

The generation of hum (30 to 300 s) by the primary or the secondary mechanism has been controversial [e.g., Rhie and Romanowicz, 2004; Tanimoto, 2006; Webb, 2007, 2008; Nishida, 2013]. Here we focus on vertical motions which are dominated by Rayleigh waves, but horizontal motions corresponding to Love waves can also be very energetic [Kurrle and Widmer-Schmidrig, 2008]. Saito [2010] and Fukao et al. [2010] have shown how a distributed random array of bottom topographic features could generate both Rayleigh and Love waves, suggesting that bottom slopes can be important. Also, Nishida [2013, 2014] showed that the maximum hum acceleration around 10 mHz suggests a generation by infragravity waves of the same frequency.

Yet without global quantitative information on long-period ocean waves, and a poor resolution of source locations estimated from measurements, both primary and secondary mechanisms appeared plausible [Bromirski, 2009]. Now, with a numerical wave model extended to the infragravity frequencies by Arduin *et al.* [2014], we evaluate the seismic sources predicted by both mechanisms, for all periods, and we model the seismic energy of the fundamental mode of Rayleigh waves, recorded by vertical seismometers.

2. The Primary Mechanism for Realistic Ocean Bottom Profiles

Because the interaction of waves with a sloping bottom has received little theoretical attention, we recall here how pressure fluctuations appear at large wavelengths when short ocean waves propagate over a sloping bottom, following Hasselmann [1963] with minor corrections. Further details are given in the supporting information Text S1. For straight and parallel depth contours, only waves propagating nearly perpendicular to them are able to produce seismic wavelengths. When depth variations occur at scales much smaller than the seismic wavelength, the seismic source amplitude is proportional to the horizontal integral of the ocean bottom pressure field. Decomposing this integral into sums over pairs of neighboring wave trough and crest reveals a particular pattern (Figure 1c). For a monotone bottom slope, the ocean waves shorten and, assuming that the energy is conserved, the wave amplitude increases. Over half a wavelength, the integrated bottom pressure is reduced by the shorter wavelength, corresponding to a higher wave number k , but increased by the larger amplitude. For any wave period, these two opposing effects cancel exactly at the depth D_0 where kD_0 equals 0.76. In deeper water, the amplification dominates over the shortening, with a nearly constant phase shift of the average pressure relative to the local pressure. For shallower water, this phase shift changes sign. As a result, the large-scale averaged pressure field is an oscillating dipole around the depth D_0 , with two poles that do not exactly cancel. For any period, the seismic sources correspond to pressure oscillations at scales of the seismic wavelength, much larger than the ocean wavelength. These sources are thus distributed around D_0 , provided that bottom slopes are significant. For periods of 16, 50, 100, and 200 s, D_0 is 30, 300, 1200, and 4800 m, respectively.

Hence, for periods longer than 50 s, sources are mostly located around shelf breaks. For shorter periods, depth variations on the scale of the ocean wavelength can strongly amplify the seismic source (Figures 1b and S2). Small-scale topographic features on the shallow part of continental shelves are the likely dominant sources of the primary microseismic peak, for periods between 10 and 20 s. In the following applications, the effect of the ocean bottom shape is represented by an effective slope that we take constant at $s = 6\%$, based on calculations for a wide variety of depth profiles (see supporting information Text S1, equation (S21), and Figure S3). The seismic source power is proportional to s .

3. Numerical Modeling and Seismic Data Processing

Four consecutive steps yield modeled spectra of the vertical ground acceleration. First, from analyzed winds over the oceans, we compute ocean wave spectra, with a spatial resolution of half a degree in longitude and latitude [Arduin *et al.*, 2014]. The results of this first step are distributions of wave energy in frequency and direction, every 3 h, at each point of the spatial grid. From these, in a second step, we obtain power spectral densities of pressure in wave number and frequency space at the sea surface [Hasselmann, 1963; Arduin and Herbers, 2013] and bottom [Arduin and Herbers, 2013]. Third, these pressure spectra are converted into sources of seismic Rayleigh waves [Longuet-Higgins, 1950; Hasselmann, 1963; Arduin and Herbers, 2013]. Our fourth and last step is the propagation of the Rayleigh wave energy along great circles, accounting for geometrical spreading and seismic attenuation [Arduin and Herbers, 2013; Stutzmann *et al.*, 2012]. Details about assumptions and technical implementation can be found in the supporting information Text S1.

Our numerical wave model is a global configuration (78°S to 80°N) of the spectral model WAVEWATCH III in its version 5.01 [Tolman *et al.*, 2014]. This configuration has a spatial resolution of half a degree in longitude and latitude, and a spectral grid that contains 36 evenly spaced directions, and 58 frequencies exponentially distributed between 3.3 mHz and 0.72 Hz. The energy reflection coefficient R^2 is parameterized from the wave height, frequency, and the local shoreface slope s_f [Arduin and Roland, 2012]. This parameterization has R^2 increasing with wave period and decreasing with wave height; here we assumed a constant slope $s_f = 10\%$, and R^2 is limited to a maximum value of 80%. This 80% is generally the value applied in the infragravity wave band. The reflected spectrum is defined as the maximum, and not the sum, of the

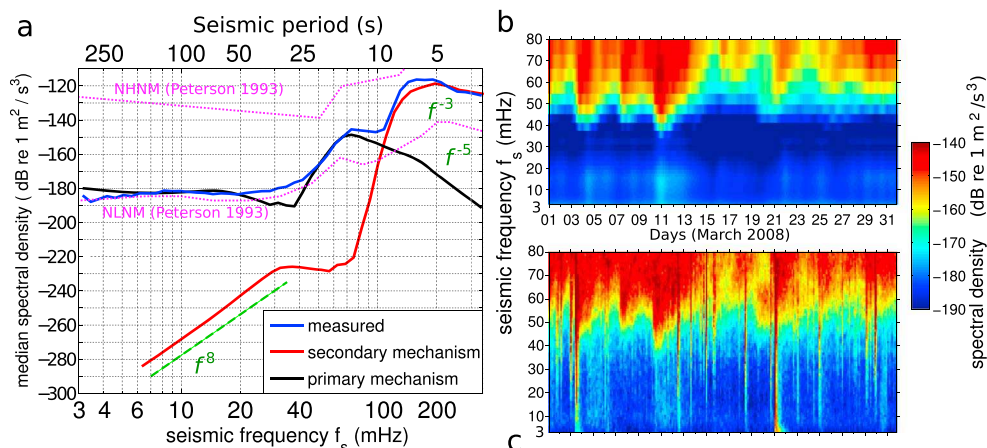


Figure 2. Measured spectra of the vertical ground acceleration, and modeled result for the primary and secondary mechanisms. (a) Median ground acceleration power spectra (LHZ channel) in March 2008 at the SSB seismic station (Geoscope Network) using records uncontaminated by earthquakes with magnitudes 5.6 and larger [Ekström, 2001]. The green dashed lines indicate different power law asymptotes. (b) Spectrogram of modeled ground acceleration and (c) measured spectrogram. Light blue to red vertical stripes correspond to earthquakes. The dotted magenta lines in (a) represent the New Low-Noise Model and New High-Noise Model of Peterson [1993], which is a familiar lower bound of microseismic activity.

reflection of incident waves and the expected local source of free infragravity waves. This procedure allows a smooth transition from the infragravity (IG) to the swell band, and the IG results are consistent with analyses of in situ data [Arduin et al., 2014].

The output of this wave model includes standard parameters such as the significant wave height, used to verify the model against remote sensing data, and frequency-direction spectra of surface elevation $E(f, \theta)$ every 3 h at a selected list of points (10,000 points located every half degree along all the shorelines and the 300 m depth contour, including subgrid islands in the full resolution shoreline database compiled by Wessel and Smith [1996]). On the full model grid, we compute the second-order pressure spectrum at the sea surface and at near-zero seismic wave number.

These pressure spectra are transformed into seismic sources. These seismic sources are added and attenuated along great circles, including multiple orbits around the Earth, as described in the supporting information Text S1. That propagation of seismic energy is controlled by the product of the attenuation Q and the group velocities U . For frequencies above 70 mHz we have used $Q = 240$ with $U = 1.8$ km/s, and a propagation coefficient $P = 1$, already adjusted to measurements at the SSB station [Stutzmann et al., 2012]. For frequencies under 30 mHz and all seismic stations, Q values are given by the QL6 model [Durek and Ekstrom, 1996], and we use seismic group velocities from the Preliminary Reference Earth Model [Dziewonski and Anderson, 1981]. Between 30 and 70 mHz the high-frequency and low-frequency values of UQ are combined as shown in Figure S1. At 3 mHz this gives an e -folding distance of 30,000 km, and 9000 km at 7 mHz. Seismic data from the LHZ channel of the seismometers were obtained from Incorporated Research Institutions for Seismology (IRIS) Data Management Center and corrected for the instrument response. Spectra of the vertical displacement, every 3 h centered on the hour (e.g., from 10:30 UTC to 13:30 UTC), were given by the median of the spectra obtained with 1024 point Fourier transforms with half-overlapping windows. These spectra were automatically edited for earthquakes and glitches, removing all spectra which had a sudden relative increase or drop of power from one 3 h time step to the next, with a fixed threshold. Further removal of earthquake-contaminated records in Figures 2a and 3b uses the empirical editing criterion of Ekström [2001]. Namely, after each earthquake of magnitude greater than $M_w = 5.6$, a time segment was removed of duration

$$T = 2.5 + 40(M_w - 5.6) \tag{1}$$

where T is in hours.

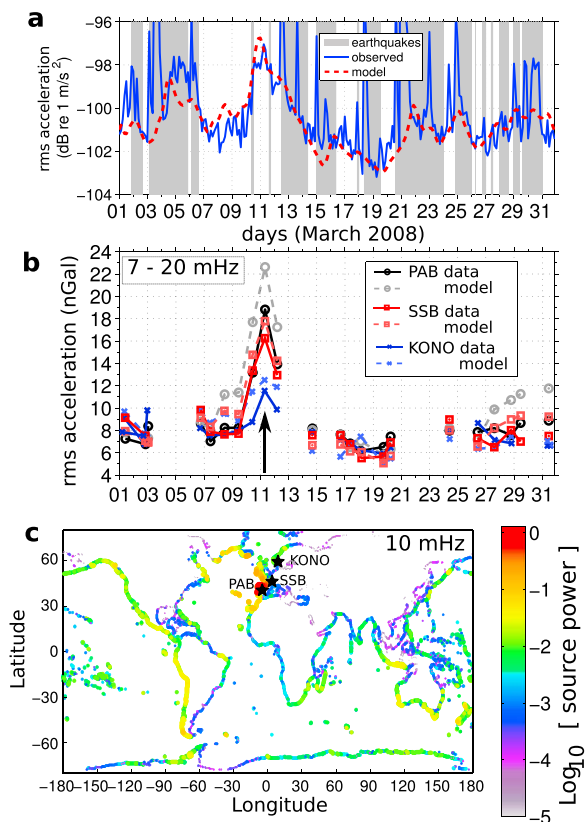


Figure 3. Noise time series and noise source distributions. (a) Measured root-mean-square vertical ground acceleration in the hum frequency band (7–20 mHz) at the SSB seismic station (Geoscope Network), obtained from the data and our hum model. Grey segments correspond to records contaminated by earthquakes with magnitudes $M_w \geq 5.6$ and larger. (b) Daily median root-mean-square acceleration without earthquake at the seismic stations SSB (Geoscope, France, in red), PAB (IU, Spain, in black), and KONO (IU, Norway, in blue). 1 nGal is $10^{-11} \text{ m s}^{-2}$. The arrow marks the noise event of 10–11 March, for which (c) the modeled seismic source distributions are shown. The source power shown here is the value of the spectral density of bottom pressure $F_p(\mathbf{k}_s = 0, f) / (\rho_w g)^2$, evaluated on 11 March at 00:00 UTC with equation (S22) given in the supporting information.

4. Results

We evaluated the primary and secondary mechanisms for the year 2008 at the locations of several seismic stations, with a first focus on the French Geoscope station SSB in March (Figure 2). As already shown [Stutzmann *et al.*, 2012; Gualtieri *et al.*, 2013], the secondary mechanism explains the main microseismic peak for periods between 3 and 10 s. For deep water waves, the predicted seismic acceleration power spectrum grows like the n th power of the frequency, with n close to 8 for periods longer than 25 s (Figure 2a and supporting information Text S1). This slope and the low spectral level are not consistent with measurements at periods longer than 13 s, contrary to previous estimates of deep water sources by Webb [2008]. Ardhuin and Herbers [2013] showed that for vanishing water depths compared to the ocean wave wavelength, the wave-induced pressure at the bottom exactly cancels the pressure at the surface. Because this bottom pressure was ignored by Webb [2007, 2008], it seemed possible that IG waves on the shelf could explain the measured hum levels. Taking bottom pressure into account here, we predict very low energy level at the lowest frequencies.

The primary mechanism, instead, reproduces the main features of the vertical seismic spectra, with a clear peak around 15 s, and a nearly constant acceleration spectrum from 50 s to 250 s

(Figure 2a). A further verification of the theory and model is given by the time evolution of the hum amplitude (Figures 2b and 2c). The resemblance between model (Figure 2b) and measurements (Figure 2c) is clear at frequencies above 40 mHz, but lower frequencies are obscured by the many transient signatures of earthquakes. In particular, two events with magnitude $M_w = 6.9$ and $M_w = 7.1$ occurred on 3 March at 14:11 UTC and on 20 March at 22:33 UTC, according to the centroid moment tensor catalog [Dziewonski *et al.*, 1981; Ekström *et al.*, 2012]. The largest predicted hum event coincides with the strongest infragravity wave event, during the Johanna storm on 10–11 March 2008. That storm generated waves with a peak period of 16 s and significant wave height up to 12.8 m recorded at the Spanish buoy of Estaca de Bares, the highest value in the previous 12 years at that location. That storm also affected the entire Bay of Biscay [e.g., Senechal *et al.*, 2011]. In our model, the strongest source of infragravity waves is predicted along the North-West Spanish coast. The measured spectrogram in Figure 2c exhibits higher energy around 10 mHz at the time of this storm, extending over 36 h. This long duration is not compatible with the expected decay from the largest recent earthquake, a $M_w = 5.6$ event at 9:43 UTC on 10 March. We thus conclude that the measured seismic activity on 11 March around 00:00 UTC corresponds to the modeled infragravity waves and hum caused by the storm.

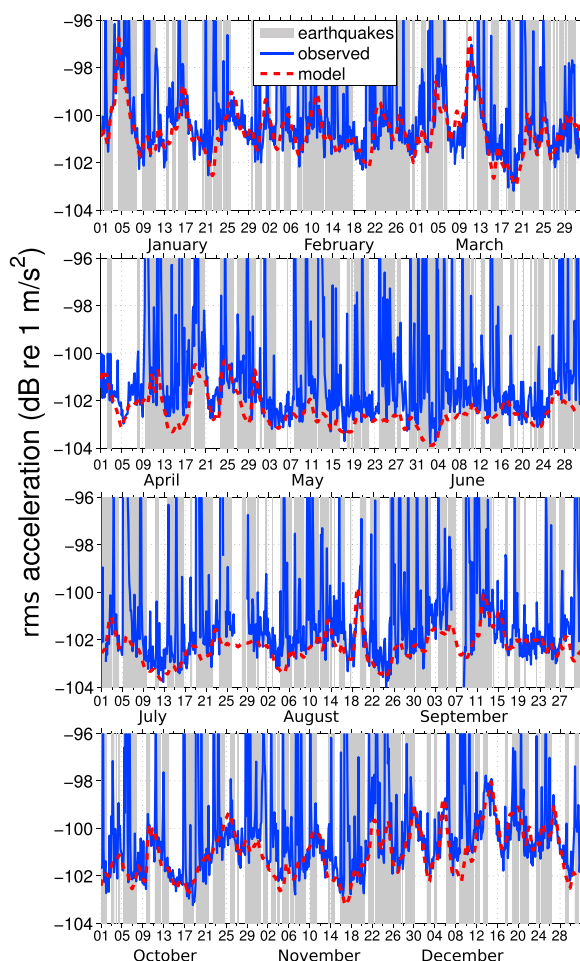


Figure 4. Same as Figure 3a, for the full year 2008: measured root-mean-square vertical ground acceleration in the hum frequency band (7–20 mHz) at the SSB seismic station (Geoscope Network), obtained from the data and our hum model, every 3 h. Grey segments correspond to records contaminated by earthquakes with magnitudes $M_w = 5.6$ and larger, according to Ekström [2001].

the year occurs on 5 and 6 January, with a strong infragravity wave event in the Gulf of Cadiz, described by Rawat et al. [2014].

Because IG waves produce seismic energy over bottom slopes, provided that the depth is shallow enough, mid-oceanic ridges or seamounts [Fukao et al., 2010] may also be significant noise sources for periods larger than 100 s. When considering the average pressure across the mid-Atlantic ridge, we found effective slopes typically 10–100 times smaller than along shelf breaks (Figure S4). A quantitative statistical treatment of seamounts, such as proposed by Saito [2010] and Fukao et al. [2010] will be needed to determine the relative contributions of shelf topography, shelf break, mid-oceanic ridges, and seamounts.

5. Conclusion

Combining the correction for shallow water effects given by Arduin and Herbers [2013] for seismic noise generation by ocean waves, and an extension of a numerical ocean wave model for periods up to 300 s [Arduin et al., 2014], we have shown that the nonlinear interaction of nearly opposing wave trains is a significant source of microseisms for periods shorter than 13 s and is negligible for longer periods. Waves propagating over a sloping bottom can generate the observed microseisms at periods from 13 to 300 s. Together, the two mechanisms provide a realistic model of the full microseism spectrum of Rayleigh waves,

We performed a more quantitative analysis by integrating the acceleration around 80 s period (7 to 20 mHz), the peak of the predicted hum. The hum model provides an accurate lower bound of the seismic record when earthquake activity is low (Figure 3a). We estimated the root-mean-square acceleration for each 3 h record, and the median of these for each day, excluding records contaminated by earthquakes with magnitude $M_w = 5.6$ and larger, as described above [see also Ekström, 2001]. Results of this processing are shown in Figure 3b and extended to other seismic stations. The model reproduces the higher-hum energies during events that are strongest and closest to the seismic station, with a decrease in amplitude from station PAB in Spain, to KONO in Norway (Figure 3b). The infragravity bursts originate at the shoreline when long-period swells arrive there, typically in the eastern part of ocean basins. These infragravity waves propagate offshore from east to west [Rawat et al., 2014], and hum sources are generally lower to the west of ocean basins (Figure 3c).

Model and observations have a similar decrease of hum amplitude by a factor 3 between the peak on 11 March, and the low level on March 19. Thus, observations are consistent with the linear dependence of the hum with infragravity wave height predicted by the primary mechanism. This consistency persists for the entire year (Figure 4). The second largest event of

recorded on vertical seismometers. An important prediction is that most hum sources, with periods 50 to 300 s, are located along the shelf breaks, and are generated by ocean waves of the same period. More work will be needed to expand the present analysis to Love waves and investigate the model-data discrepancies between 20 and 50 mHz. The seismic energy released in this process varies by up to 7 dB on the scale of a few days, associated with predictable infragravity wave events caused by long-period swells. A broadband numerical modeling of both ocean and seismic waves, as described here, should be accurate enough to guide the analysis of seismometer data for Earth-monitoring and tomographic studies.

Acknowledgments

F.A. is supported by European Research Council grant IOWAGA 240009, Labex Mer via grant ANR-10-LABX-19-01, and CNES under the SWOT preparation program. L.G. acknowledges the financial support of QUEST Initial Training Network funded within the EU Marie Curie Program. All seismic data were obtained from GEOSCOPE and IRIS data centers. The wave model code can be obtained from NOAA/NCEP, and the wind forcing fields are provided by ECMWF. The wave model results and reading tools can be found at http://tinyurl.com/iowagaftp/HINDCAST/OTHER_RUNS/GLOBAL_IG_36DIR.

The Editor thanks three anonymous reviewers for their assistance in evaluating this paper.

References

- Ardhuin, F., and T. H. C. Herbers (2013), Noise generation in the solid Earth, oceans and atmosphere, from nonlinear interacting surface gravity waves in finite depth, *J. Fluid Mech.*, *716*, 316–348.
- Ardhuin, F., and A. Roland (2012), Coastal wave reflection, directional spreading, and seismo-acoustic noise sources, *J. Geophys. Res.*, *117*, C00J20, doi:10.1029/2011JC007832.
- Ardhuin, F., E. Stutzmann, M. Schimmel, and A. Mangeney (2011), Ocean wave sources of seismic noise, *J. Geophys. Res.*, *116*, C09004, doi:10.1029/2011JC006952.
- Ardhuin, F., A. Rawat, and J. Aucan (2014), A numerical model for free infragravity waves: Definition and validation at regional and global scales, *Ocean Modell.*, *77*, 20–32.
- Artru, J., V. Ducic, H. Kanamori, P. Lognonné, and M. Murakami (2005), Ionospheric detection of gravity waves induced by tsunamis, *Geophys. J. Int.*, *160*, 840–848, doi:10.1111/j.1365-246X.2005.02552.x.
- Bernard, P. (1990), Historical sketch of microseisms from past to future, *Phys. Earth Planet. Inter.*, *63*, 145–150.
- Bromirski, P. D. (2009), Earth vibrations, *Science*, *324*, 1026–1027, doi:10.1126/science.1171839.
- Bromirski, P. D., R. A. Stephen, and P. Gerstoft (2013), Are deep-ocean-generated surface-wave microseisms observed on land?, *J. Geophys. Res. Solid Earth*, *118*, 3610–3629, doi:10.1002/jgrb.50268.
- Crawford, W. C., S. C. Webb, and J. A. Hildebrand (1991), Seafloor compliance observed by long-period pressure and displacement measurements, *J. Geophys. Res.*, *103*(B5), 9895–9916.
- Durek, J., and G. Ekström (1996), A radial model of anelasticity consistent with long-period surface-wave attenuation, *Bull. Seismol. Soc. Am.*, *86*, 144–158.
- Dziewonski, A. M., and D. L. Anderson (1981), Preliminary reference earth model, *Phys. Earth Planet. Inter.*, *25*(4), 297–356.
- Dziewonski, A. M., T.-A. Chou, and J. H. Woodhouse (1981), Determination of earthquake source parameters from waveform data for studies of global and regional seismicity, *J. Geophys. Res.*, *86*(2), 2825–2852, doi:10.1029/JB086iB04p02825.
- Ekström, G. (2001), Time domain analysis of Earth's long-period background seismic radiation, *J. Geophys. Res.*, *106*(B11), 26,483–26,493.
- Ekström, G., M. Nettles, and A. M. Dziewonski (2012), The global CMT project 2004–2010: Centroid-moment tensors for 13,017 earthquakes, *Phys. Earth Planet. Inter.*, *86*(2), 200–201, doi:10.1016/j.pepi.2012.04.002.
- Farrell, W. E., and W. Munk (2010), Booms and busts in the deep, *J. Phys. Oceanogr.*, *40*(9), 2159–2169.
- Fukao, Y., K. Nishida, and N. Kobayashi (2010), Seafloor topography, ocean infragravity waves, and background Love and Rayleigh waves, *J. Geophys. Res.*, *115*, B04302, doi:10.1029/2009JB006678.
- Grevemeyer, I., R. Herber, and H.-H. Essen (2000), Microseismological evidence for a changing wave climate in the northeast Atlantic Ocean, *Nature*, *408*, 349–351.
- Gualtieri, L., E. Stutzmann, Y. Capdeville, F. Ardhuin, M. Schimmel, A. Mangeney, and A. Morelli (2013), Modelling secondary microseismic noise by normal mode summation, *Geophys. J. Int.*, *193*, 1732–1745, doi:10.1093/gji/ggt090.
- Hasselmann, K. (1963), A statistical analysis of the generation of microseisms, *Rev. Geophys.*, *1*(2), 177–210.
- Hasselmann, K. (1966), Feynman diagrams and interaction rules of wave-wave scattering processes, *Rev. Geophys.*, *4*(1), 1–32.
- Kedar, S., M. Longuet-Higgins, F. Webb, N. Graham, R. Clayton, and C. Jones (2008), The origin of deep ocean microseisms in the north Atlantic ocean, *Proc. R. Soc. London, Ser. A*, *464*, 777–793, doi:10.1098/rspa.2007.0277.
- Kurle, D., and R. Widmer-Schmidrig (2008), The horizontal hum of the Earth: A global background of spheroidal and toroidal modes, *Geophys. Res. Lett.*, *35*, L06304, doi:10.1029/2007GL033125.
- Longuet-Higgins, M. S. (1950), A theory of the origin of microseisms, *Philos. Trans. R. Soc. London, Ser. A*, *243*, 1–35.
- Nawa, K., N. Suda, Y. Fukao, T. Sato, Y. Aoyama, and K. Shibuya (1998), Incessant excitation of the Earth's free oscillations, *Earth Planets Space*, *50*, 3–8, doi:10.1029/2006GC001274.
- Nishida, K. (2013), Earth's background free oscillations, *Annu. Rev. Earth Planet. Sci.*, *41*, 719–740.
- Nishida, K. (2014), Source spectra of seismic hum, *Geophys. J. Int.*, *199*, 416–429.
- Obrebski, M., F. Ardhuin, E. Stutzmann, and M. Schimmel (2012), How moderate sea states can generate loud seismic noise in the deep ocean, *Geophys. Res. Lett.*, *39*, L11601, doi:10.1029/2012GL051896.
- Peterson, J. (1993), Observations and modeling of seismic background noise, *U.S. Geol. Surv. Tech. Rep.*, 93-322, pp. 1–95.
- Rawat, A., F. Ardhuin, V. Ballu, W. Crawford, C. Corela, and J. Aucan (2014), Infra-gravity waves across the oceans, *Geophys. Res. Lett.*, *41*, 7957–7963.
- Rhie, J., and B. Romanowicz (2004), Excitation of Earth's continuous free oscillations by atmosphere-ocean-seafloor coupling, *Nature*, *431*, 552–556, doi:10.1038/nature02942.
- Saito, T. (2010), Love-wave excitation due to the interaction between a propagating ocean wave and the sea-bottom topography, *Geophys. J. Int.*, *182*, 1515–1523.
- Senéchal, N., et al. (2011), The ECORS-Truc Vert 2008 field experiment: Extreme storm conditions over a three-dimensional morphology system in a macro-tidal environment, *Ocean Dyn.*, *61*, 2073–2098, doi:10.1007/s10236-011-0472-x.
- Shapiro, N. M., M. Campillo, L. Stehly, and M. H. Ritzwoller (2005), High-resolution surface-wave tomography from ambient seismic noise, *Science*, *307*, 1615–1617, doi:10.1111/j.1365-246X.2006.03240.x.
- Stutzmann, E., M. Schimmel, and F. Ardhuin (2012), Modeling long-term seismic noise in various environments, *Geophys. J. Int.*, *191*, 707–722, doi:10.1111/j.1365-246X.2012.05638.x.
- Suda, N., K. Nawa, and Y. Fukao (1998), Earth's background free oscillations, *Science*, *279*, 2089–2091.
- Tanimoto, T. (2005), The oceanic excitation hypothesis for the continuous oscillations of the Earth, *Geophys. J. Int.*, *160*, 276–288, doi:10.1111/j.1365-246X.2004.02484.x.

- Tanimoto, T. (2006), Excitation of normal modes by non-linear interaction of ocean waves, *Geophys. J. Int.*, *168*, 571–582, doi:10.1111/j.1365-246X.2008.03801.x.
- Tolman, H. L., et al. (2014), User manual and system documentation of WAVEWATCH-III™ version 4.18, NOAA/NWS/NCEP/MMAB Tech. Rep., 316, 194 pp.
- Traer, J., and P. Gerstoft (2014), A unified theory of microseisms and hum, *J. Geophys. Res. Solid Earth*, *119*, 3317–3339, doi:10.1002/2013JB010504.
- Uchiyama, Y., and J. C. McWilliams (2008), Infragravity waves in the deep ocean: Generation, propagation, and seismic hum excitation, *J. Geophys. Res.*, *113*, C07029, doi:10.1029/2007JC004562.
- Webb, S. C. (1998), Broadband seismology and noise under the ocean, *Rev. Geophys.*, *36*, 105–142.
- Webb, S. C. (2007), The Earth's "hum" is driven by ocean waves over the continental shelves, *Nature*, *445*, 754–756, doi:10.1038/nature05536.
- Webb, S. C. (2008), The Earth's "hum": The excitation of Earth normal modes by ocean waves, *Geophys. J. Int.*, *174*, 542–566, doi:10.1111/j.1365-246X.2008.03801.x.
- Wessel, P., and W. H. F. Smith (1996), A global self-consistent hierarchical, high-resolution shoreline database, *J. Geophys. Res.*, *101*, 8741–8743.



Geophysical Research Letters

Supporting Information for

How ocean waves rock the Earth:

two mechanisms explain microseisms with periods 3 to 300 s

Fabrice Ardhuin^{1,2}, Lucia Gualtieri³, Eleonore Stutzmann³

¹Ifremer, Laboratoire d'Océanographie Spatiale, Brest, France.

²Laboratoire de Physique des Océans, CNRS-Ifremer-UBO-IRD, Brest, France

³Institut de Physique du Globe, PRES Sorbonne Paris-Cité, Paris, France.

Contents of this file

Text S1
Figures S1 to S4

Additional Supporting Information (Files uploaded separately)

none

Introduction

The text S1 gives more details and some corrections on the theory by Hasselmann (1963) as well as the practical implementation. The four figures illustrate various aspects related to the expected seismic sources on realistic bathymetric profiles.

Text S1.

Detailed theoretical aspects of the generation of seismic waves by ocean waves

We give here a few important details and corrections to the general theory laid out by Hasselmann [1963], with a particular attention to its application for long ocean waves with periods larger than 30 s. Both primary and secondary mechanisms enable the short surface gravity waves to generate much longer wavelengths, and thus much faster waves that can couple to seismic waves. The question we address is rather quantitative: how much seismic energy is radiated by each of these mechanism?

After giving the expression for transforming the wave-induced pressure into seismic ground displacement, which is common to both mechanisms, we detail the expressions of the long-wavelength pressure spectrum as a function of the usual ocean wave spectrum, beginning with the secondary mechanism because this is the most studied mechanism. This follows the plan of Hasselmann [1963], with less mathematical detail for some parts, and a final expression in terms of ocean wave spectra, as given by usual numerical models.

For both mechanisms the conversion of pressure in the ocean to seismic amplitudes uses the coupling coefficients that were first determined by Longuet-Higgins [1950, his figure 2], and recomputed by Gualtieri et al. [2013] using normal modes. This follows exactly what has been done for the secondary mechanism by Kedar et al. [2008], Ardhuin et al. [2011], Stutzmann et al. [2012] and others. In the case of the primary mechanism we apply the same formulation to the wave-induced pressure at the bottom because of the shallow water depth. Hence the oscillating bottom elevation is transformed into a flat bottom with a pressure at the sea surface.

1) From the wave-induced pressure spectrum at large wavelengths to seismic waves

For both primary and secondary mechanisms, the source of seismic waves S is a function of the wave-induced pressure spectrum at seismic wavelengths. Since these wavelengths are much larger than those of surface gravity waves, we may practically estimate the pressure spectral density at near-zero wavenumber. For linear waves in a homogeneous ocean (i.e. constant depth and current velocity), this spectral density would be zero. Its non-zero value is due to either nonlinearity (secondary mechanism) or spatial non-

homogeneity (primary mechanism). For a solid half space of density ρ_s and shear wave speed β , Longuet-Higgins [1950] and Hasselmann [1963] give the local seismic source as a function of the seismic frequency f_s and of the wave-induced pressure spectral density near zero wavenumber $F_p(k_x \approx 0, k_y \approx 0, f_s)$,

$$S(f_s) = 4\pi^2 f_s c^2 F_p(k_x \approx 0, k_y \approx 0, f_s) / (\beta^5 \rho_s^2) \quad (S1)$$

where c is a non-dimensional coefficient for microseismic generation [Longuet-Higgins 1950; Ardhuin and Herbers 2013], which is $c=0.2$ for $\beta=2.2$ km/s, $\rho_s = 2.6$ kg/m³, $\rho_w = 1.0$ kg/m³, and $T=200$ s with a water depth of 2000 m. The following sections give the details on how to compute F_p , based on the secondary mechanism considering $F_{p,2}$ (eq. S5) or based on the primary mechanism considering $F_{p,1}$ (eq. S22).

The pressure spectrum in eq. (S1) corresponds to the wave-induced spectrum at the sea surface. However, in the case of the primary mechanism, the water depth at the source is small compared to the acoustic wavelength and the bottom pressure is equivalent to a surface pressure.

This source S has S.I. units of m/Hz. Here we integrate these sources along great circle paths for all azimuths ϕ , and all epicentral distances Δ , taking into account the seismic attenuation and geometrical spreading [e.g. eq. (4.36) in Ardhuin and Herbers 2013]. The integral over Δ goes from zero to 2π , covering one full orbit around the Earth in each direction. The power spectral density of the seismic displacement is

$$F_\delta(f_s) = \int_0^{2\pi} \int_0^{2\pi} S(\Delta, \phi, f_s) \frac{\exp(-2\pi f_s \Delta R_E / UQ)}{(1-b) R_E \sin \Delta} R_E^2 \sin \Delta d \Delta d \phi, \quad (S2)$$

where b is the attenuation over one orbit around the Earth,

$b = \exp(-2\pi f_s 2\pi R_E / UQ)$, hence the factor $1/(1-b) = 1+b+b^2+b^3\dots$ corresponds to the incoherent sum of the energies of all the orbits. This incoherent sum for epicentric distances larger than one orbit is consistent with the coarse spectral resolution used in figure 2, in which the normal mode structure is not resolved. For spectra with frequency resolution finer than $U / (2\pi R_E)$ [e.g. Webb 2007], one could first perform a coherent sum over the orbits. Values of U and Q are discussed in the article and illustrated in figure S1.

A simple estimation of the shape and order of magnitude of the expected microseismic response to the ocean wave forcing in any water depth is provided by assuming a uniform source distribution S . In this case S reduces to a function of the seismic frequency f_s only. Under these assumptions the frequency spectrum of ground vertical displacement F_δ is uniform, and eq. (S2) writes,

$$F_{\delta}(f_s) = S(f_s) \int_0^{2\pi} \frac{\exp(-2\pi f_s \Delta R_E / UQ)}{(1-b)R_E \sin \Delta} R_E^2 2\pi \sin \Delta d\Delta = S U Q / f_s (1-b), \quad (S3)$$

where U is the group speed of the considered seismic mode, Δ is the epicentric distance between the source and the seismic station, R_E is the radius of the Earth and Q is the non-dimensional seismic attenuation factor.

Eq. (S3) is strictly valid for underwater measurements, within a region of homogeneous sea state. This was shown by Ardhuin et al. [2013] to apply for microseisms with periods of 3 s and less. For the general case of a variable sea state, we expect this equality to hold only for time and spatial averages. Since the measurements discussed here are generally made on land, and the oceans only cover part of the Earth surface, eq. (S3) is only expected to provide a reasonable order of magnitude. This approach is consistent the analysis in Webb [2007]. In this context we may neglect the $(1-b)$ factor, with $b = 0.35$ at 3 mHz, decreasing rapidly towards higher frequencies, with $b=0.01$ at 7 mHz.

Combining (S1) and (S3), for either the primary or secondary mechanism, we thus note that the seismic displacement power spectrum F_{δ} is directly proportional to the wave-induced pressure power spectrum F_p , and the f_s term in (S1) cancels the $1/f_s$ in (S3). This will be important for the asymptotic shapes of the seismic acceleration power spectrum for the primary and secondary mechanisms.

2) **How short ocean waves make long seismic waves: Secondary mechanism**

The seismic noise source given by the secondary mechanism is proportional to the square of the wave-induced orbital velocity at the sea surface [eq. 2.11 in ref Hasselmann 1963]. As a result, any pair of wave trains with velocities given by $u_1 \cos(k_1 x - 2\pi f_1 t)$ and $u_2 \cos(k_2 x - 2\pi f_2 t)$ will yield a surface pressure pattern that contain the term

$$u_1 u_2 \{ \cos[(k_1 + k_2)x - 2\pi(f_1 + f_2)t] + \cos[(k_1 - k_2)x - 2\pi(f_1 - f_2)t] \}. \quad (S4)$$

This nonlinear interaction of waves involves sum and difference interactions, which are given by the two parts of this interaction term.

2.a) *Why the difference interaction of ocean waves cannot produce seismic waves in a horizontally homogeneous environment.*

It is well known that difference interactions, the second part of eq. (S4) with the frequency $(f_1 - f_2)$ can have very long periods. Recent publications by Uchiyama and McWilliams [2008] and Traer and Gerstoft [2014] have used that result to suggest this interaction could directly generate seismic noise in the hum frequency band. However, only sum interactions, the first part of eq. (S4) with $(f_1 + f_2)$, were considered for seismic wave generation theory. The reason for neglecting difference interactions, is that they cannot produce fast traveling waves in a horizontally homogeneous environment. This was already mentioned by Hasselmann [1963], and discussed in Webb [2008].

Namely, the difference interactions cannot match the wavenumbers of seismic

components. This is clearly established by considering any pair of frequencies f_1 and f_2 , with $f_2 > f_1$. The speed $C_2 = 2\pi(f_2 - f_1)/|\mathbf{k}_2 - \mathbf{k}_1|$ is fastest for \mathbf{k}_1 and \mathbf{k}_2 aligned and in the same direction. For a constant depth D , these frequencies f_i are functions of the norms k_i of \mathbf{k}_i given by the linear dispersion relation $f_i = h(k_i) = g k_i \tanh(k_i D)/(2\pi)$, where g is the acceleration of gravity. Applying the Taylor-Lagrange formula, there is a wavenumber k_3 such that

$$[f_2 - f_1]/(k_2 - k_1) = h'(k_1) + (k_2 - k_1)h''(k_3)/2.$$

The group speed of ocean waves is $2\pi h'(k_1)$, known to be slower than the ocean phase speed. Because $h''(k)$ is strictly negative, then C_2 is less than this ocean phase speed, itself much slower than the seismic waves.

2.b) Surface and bottom pressure induced by sum interactions

Ocean wave properties are usually represented by a wave frequency-directional spectrum $E(f, \theta)$, where f is the wave frequency, and θ is the azimuth of ocean waves. Only the direction-integrated spectrum $E(f)$ is really well known,

$$E(f) = \int_0^{2\pi} E(f, \theta) d\theta.$$

Very few estimates [Ardhuin et al., 2012; Ardhuin et al. 2013] are available for the directional “overlap integral”, defined here using the convention of Webb [2008], which is twice the value used in Ardhuin and Herbers [2013],

$$I(f) = \int_0^{2\pi} E(f, \theta) E(f, \theta + \pi) d\theta / E^2(f).$$

In deep water, the spectral density at $k_x = k_y = 0$ of the equivalent second order pressure at the sea surface that generates seismo-acoustic noise is given by Hasselmann [1963] and Ardhuin and Herbers [2013],

$$F_{p,2}(k_x = 0, k_y = 0, f_s) = (\rho_w g)^2 f E^2(f) I(f) \quad (S5)$$

where $f_s = 2f$ is the seismic frequency, equal to twice the ocean wave frequency f , g is the acceleration of gravity and ρ_w is the water density.

Finite depth effect in the secondary mechanism

Because we are also dealing with very long waves that also modify directly the bottom pressure, we need to consider the effect of wave-induced bottom pressure together with the wave-induced pressure at the sea surface. That additional bottom pressure term was not considered in previous investigations on the hum by Webb [2007, 2008].

On the full model grid we compute the second order pressure spectrum at the sea surface and at near-zero seismic wavenumber k_s . This is given by eq. (2.29) in Ardhuin and Herbers [2013]. Ardhuin and Herbers [2013] showed that considering the wave-induced pressure at the ocean bottom gives a reduction by a factor

$$G(kD) = [\tanh(kD)]^2 [1 + 2kD/\sinh(2kD)], \quad (S6)$$

where the ocean wavenumber k is related to the wave frequency f by the linear wave

dispersion relation

$$(2 \pi f)^2 = gk \tanh(kD),$$

with D the water depth. For long periods and shallow water, $kD \ll 1$, and $G(kD)$ can be replaced by $2 \tanh^2(kD)$. In practice, this correction has no significant effect for seismic waves with periods around 5s, for which most of the sources are in deep enough water for the approximation $G \approx 1$ to be accurate as used by Stutzmann et al. [2012], but it changes the results for the hum by several orders of magnitude.

Because the orbital velocities induced by ocean waves are much larger for a given height when waves are in shallow water, it was expected by Webb [2007] that microseismic sources would be amplified compared to deep water. Instead, the reduction in bottom pressure is fundamentally related to the Bernoulli effect, in which the pressure drops proportionally to the square of the velocity. Applied at the bottom and in the limit $kD \rightarrow 0$, this effect exactly cancels the surface velocity effect. This cancellation is a well known property in the incompressible context [Herbers et al. 1991; Ardhuin and Herbers 2013] and is supported by bottom pressure observations that resolve both the short and long ocean waves [Herbers et al. 1991]. The consistency between the compressible and incompressible theories is detailed in the appendix A of Ardhuin and Herbers [2013], with the sum of surface and bottom contributions given there by eq. (A4).

Power law behavior of wave and microseismic spectra for the secondary mechanism

Combining eqs. (S1), (S3) and (S5) gives a dependence of the vertical displacement power spectrum on the seismic frequency that is proportional to f_s if $E(f, \theta)$ is constant, giving a power spectrum of the acceleration proportional to f_s^5 . In our model, $E(f, \theta)$ increases like f_s around $f_s = 10$ mHz. That increase and the factor $G(kD)$ combine to give an acceleration power spectrum that is closer to f_s^8 . At higher wave frequencies $f = 0.15$ Hz, the wave spectrum typical decreases like f^{-n} with n between 4 and 5. Taking $n=4$ gives the observed shape of the acceleration power spectrum, decreasing like $f_s^{4+1-2n} = f_s^{-3}$ (Figure 2a).

3) How short ocean waves make long seismic waves: Primary mechanism

This mechanism is a linear transformation of ocean waves into seismic waves of the same frequency f . For a practical application we use the wave model output of $E(f, \theta)$ along shorelines, and more particularly its value in the direction perpendicular to shore. The primary mechanism was previously explored in the case of constant bottom slopes by Hasselmann [1963]. We give here a few more details and show general results for realistic bottom profiles. We estimate the spectral density at $k_x = k_y = 0$ in order to give, for the primary mechanism, the equivalent of the secondary source of eq. (S5).

We estimate a similar pressure spectrum at large wavelengths, for the first order pressure field in the presence of a sloping bottom. The final result is eq. (S22). We first characterize the bottom pressure field for a monochromatic wave train, and then apply that result to random waves and express the pressure spectrum as a function of the wave spectrum $E(f, \theta)$.

3.a) Bottom pressure for monochromatic waves

A monochromatic wave train propagating over depths varying only in direction x gives field of surface elevation and bottom pressures, with amplitudes that are modulated as shown in figure 1.c. In order to normalize all the wave-related fields, we use the wave amplitude a_A for a reference depth that we set at $D_A = 4000$ m. The assumption of alongshore uniformity is appropriate if the depth varies alongshore on scales much larger than the seismic wavelength. For cases where the depth varies in the y direction at scales comparable or shorter than the seismic wavelength, we only expect a qualitative agreement, which is supported by preliminary tests with a phase-resolving refraction-diffraction model. We note that for linear ocean waves over a flat bottom, the dispersion relation is

$$(2 \pi f)^2 = gk \tanh(kD), \quad (S7)$$

where k is the wavenumber, f is the frequency, D is the water depth, and g is the vertical acceleration due to gravity.

We will see that one effect of the bottom slopes is to put a very small fraction of the ocean wave energy at wavenumbers that are very far from this linear dispersion relation. With an alongshore wavenumber k_y we consider the bottom pressure $P_0(x, k_y, f)$ induced by our monochromatic wave train, normalized by the wave amplitude a_A . Because of this normalization, P_0 has units of Pa/m. Its Fourier transform in the x dimension over a distance L_x is

$$K(f, k_x, k_y) = \frac{1}{2\pi} \int_{-L_x}^0 P_0(x, k_y, f) e^{ik_x x} dx,$$

(S8) which has units of Pa. This spectrum K is used with the same definition by Hasselmann [1963]. The actual bottom pressure spectrum is $a_A K$, with units of Pa.m. In Hasselmann, the eq. (4.23) is an integral from minus infinity to plus infinity. Here we have defined our Fourier transforms over a finite domain because this is how it is used for practical applications in the next section. Because the shoreline is at $x=0$, P_0 is zero for $x > 0$. As a result our definition of K is the same as Hasselmann's, in the limit $L_x \rightarrow \infty$. Figure S2 shows examples of the pressure field at the bottom for waves propagating in one dimension.

If k_y is smaller than the magnitude of seismic Rayleigh wavenumbers, then the broad spectrum of K overlaps with wavenumbers of seismic Rayleigh waves. In practice the spectrum K is nearly white, i.e. weakly dependent on wavenumbers near $k_x = k_y = 0$. We can thus replace K by its value at $k_x = 0$, which corresponds to the x -average of the pressure signal, and $k_y = 0$, which corresponds to waves exactly perpendicular to the depth contours.

The alongshore wavenumber k_y is the same for ocean and seismic waves, and is unchanged during cross-shore propagation. Since we are considering only the spectral components of the ocean wave field that can couple to seismic Rayleigh waves, with a typical phase speed $C_s = 3$ km/s, the ocean waves must have propagation angles that are nearly perpendicular to the depth contours, namely the ratio of the alongshore wavenumber k_y to the wavenumber magnitude k should be less than the ratio of the ocean wave to seismic wave phase speeds C / C_s , which is always less than 0.1.

3.b) Theoretical expression for the pressure spectrum

The bottom pressure power spectral density is, by definition, the ratio of the bottom pressure variance and the spectral increment,

$$F_{p,1}(f, k_x, k_y) = \frac{|a_A K(k_x, k_y, f) \Delta k_x|^2}{\Delta k_x \Delta k_y \Delta f}. \quad (\text{S9})$$

Mathematically, eq. (S9) is correct in the limit of small spectral increments, which correspond to spectra estimated over long times and distances. In practice, due to the spatial inhomogeneities and temporal variability of the sea state, we estimate (S9) with finite spectral increments $\Delta k_x = 2\pi/L_x$, $\Delta k_y = 2\pi/L_y$, $\Delta f = 1/\tau$, where L_x , L_y , and τ are the lengths over which the Fourier transform is computed in the three dimensions. The definition of the wave directional spectral density is again the ratio of the variance (this time of the surface elevation) divided by the spectral increment,

$$E_A(f, k_y) = \frac{|a_A|^2}{\Delta k_y \Delta f}. \quad (\text{S10})$$

We now change the spectral coordinates ($f, k_y = k \sin \theta$) to the more usual (f, θ) where θ is the azimuth of the ocean waves. The Jacobian of this spectral coordinate transform is $k \cos \theta$. For $\theta=0$, $\cos \theta=1$ and eq. (S10) gives

$$E_A(f, \theta=0) = k_A E_A(f, k_y=0), \quad (\text{S11})$$

where, at location A, the depth is D_A , and the norm of the wavenumber vector is k_A , as given by eq. (S7), namely $(2\pi f)^2 = g k_A \tanh(k_A D_A)$.

We can now replace the wave amplitude a_A in eq. (S9) by the wave spectrum (S11), using (S10), and we arrive at the first order bottom pressure spectrum. We particularly consider the power spectral density relevant for seismic wave generation, with $k_x = 0$, $k_y = 0$,

$$F_{p,1}(k_x=0, k_y=0, f) = \frac{E_A(f, \theta=0)}{k_A} |K^2(k_x=0, k_y=0, f)| \frac{2\pi}{L_x}. \quad (\text{S12})$$

This expression is inversely proportional to L_x , the length over which the spectrum is evaluated. This is so because the relevant pressure perturbation is localized at a scale much smaller than L_x .

For an alongshore distance L_y , and a frequency bandwidth df the bottom pressure spectrum given by (S12) is equivalent, for small k , to the one produced by a vertical force oscillating with a frequency f and an amplitude F [Hasselmann 1963, Gualtieri et al. 2013]. This amplitude is simply the area $L_x L_y$ multiplied by the square root of twice the corresponding pressure variance,

$$F = 2\pi \sqrt{2 L_x L_y F_{p,1}(k_x=0, k_y=0, f) df}. \quad (\text{S13})$$

Given (S12), this force F does not depend on L_x , and varies like the square root of L_y

which corresponds to an incoherent sum of sources in the y direction. For $k_x = 0, k_y = 0$, eq. (S8) becomes a spatial average

$$K(k_x=0, k_y=0, f) = \frac{1}{2\pi} \int_{-L_x}^0 P_0(x, k_y=0, f) dx. \quad (\text{S14})$$

The usual spectral density is obtained when the length L_x goes to infinity, but for practical estimates, this length is always finite. Without any wave dissipation, the pressure field at the bottom is given by the following equations. First the local group speed is defined from the local water depth D and the frequency f

$$C_g = \frac{2\pi f}{k} \left(0.5 + \frac{kD}{\sinh(2kD)} \right) \quad (\text{S15})$$

in which k is estimated from D and f using eq. (S6). The conservation of the energy flux gives the local surface elevation amplitude a ,

$$C_g a^2 = C_{gA} a_A^2. \quad (\text{S16})$$

The phase is obtained by integrating the local ocean wavenumber k , [e.g. Mei 1989],

$$S(x) = \int_0^x k(x') dx'. \quad (\text{S17})$$

These amplitudes and phase can be used to determine the surface elevation,

$$\zeta(x, k_y=0, f) = a_A \sqrt{\frac{C_g}{C_{gA}}} e^{iS}.$$

Using linear wave theory gives the conversion factor from surface elevation to the bottom pressure, which, divided by the amplitude a_A gives

$$P_0(x, k_y=0, f) = \frac{\rho_w g}{\cosh(kD)} \sqrt{\frac{C_g}{C_{gA}}} e^{iS}. \quad (\text{S18})$$

All this is enough to estimate the pressure spectrum defined by (S12). We have used this eq. (S18) to compute the pressure field over the bottom, as shown by the red curve in figure 1.c.

3.c) Practical calculation

In general there is no simple expression for the pressure integral (S14). For a constant bottom slope D' , Hasselmann [1963] has evaluated (S14), and proposed that

$$|K|^2 = \frac{\rho_w^2 g^4}{(2\pi f)^4 64\pi} D'. \quad (\text{S19})$$

we will in particular use his value for $D' = 1\%$,

$$|K_1|^2 = \frac{0.01 \rho_w^2 g^4}{(2\pi f)^4 64\pi}. \quad (\text{S20})$$

We now revise this analytical expression, which is not exact but is still a good

approximation of (S14), for slopes D' between 1.5 and 4%. Near the shoreline, where $x=0$ and $S=0$, the integrand in (S14) is proportional to $\sqrt{S} e^{iS}$. Under the incorrect assumption that the integral of $\sqrt{S} e^{iS}$ from $S=0$ to infinity is defined, eq. (S19) was obtained by Hasselmann [1963] using contour integration on the complex plane [Hasselmann, personal communication 2013]. In practice, the integrand for large S is very different from $\sqrt{S} e^{iS}$ and goes to zero, which keeps the integral (S14) defined. For D' between 1.5 and 4% we found that (S19) is within 10% of our numerical estimates using the full expression for (S14). We also verified that (S8), with the non-zero wavenumber components k_x and k_y expected for Rayleigh waves, gives similar results.

We now consider any bottom depth profile, with the only assumption that the depth is constant in the y direction. To simplify the notations, we introduce a normalized seismic source s , using eqs. (S14) and (S20),

$$s = |K|^2 / |K_1|^2. \quad (\text{S21})$$

This parameter s contains all the effects of the bottom topography and is an “effective slope”. s is a non-dimensional parameter that depends on the depth profile and the wave frequency f . We finally use a wave-induced pressure power spectrum expressed as follows,

$$F_{p,1}(k_x=0, k_y=0, f) = s \frac{E_A(f, \theta=0)}{k_A} \frac{\rho_w^2 g^4}{(2\pi f)^4 3200 L_x}.$$

This equation is directly used to compute seismic sources in figure 3, with the direction $\theta=0$ replaced by the local shore-normal direction θ_n , and, to take into account waves propagating towards the shore and away from the shore we replace $E(f, \theta=0)$ by $[E(f, \theta_n) + E(f, \theta_n + \pi)]$,

$$F_{p,1}(k_x=0, k_y=0, f) = s \frac{\rho_w^2 g^4 [E_A(f, \theta_n) + E_A(f, \theta_n + \pi)]}{k_A (2\pi f)^4 3200 L_x}. \quad (\text{S22})$$

Estimates of s for different bottom profiles are shown in Figure S3.

Eq. (S22) can be combined to eq. (S3) to estimate the shape of the seismic response. Taking A in 4000 m depth, then k_A is proportional to f for f smaller than 10 mHz. A constant spectrum E_A gives a pressure spectrum $F_{p,1}$ predicted by the primary mechanism that decreases like f^{-5} . Combined with eq. (S3) this gives a vertical displacement power spectrum that decreases like f^{-5} and an acceleration power spectrum that follows f^{-1} . Since our numerical model in the infragravity wave band actually predicts a spectrum E_A that grows like f from 5 to 15 mHz, this explains the nearly constant acceleration spectrum in that frequency range. At higher frequencies, a decrease of the wind wave spectrum like f^{-4} around $f=0.1$ Hz gives a f^{-5} seismic acceleration power spectrum.

3.d) Interpretation of the source dependence on the bottom profile

Eq. (S22) is interesting because it gives a practical expression for the pressure spectral density. However, the use of Fourier transforms removes the spatial resolution, and

prevents us from understanding which is the part of the depth profile that is responsible for the seismic source. In order to discuss spatial distribution of sources, we thus define a partial spatial integration $s(x)$,

$$s(x) = \frac{1}{(2\pi)^2 |K_1|^2} \left| \int_x^0 P_0(x', k_y, f) dx' \right|^2.$$

(S23)

Combining eqs. (S13) and (S20), this definition gives $s(-L_x) = s$, namely, the limit of $s(x)$ when reaching the end of the depth profile is the noise source previously defined. The quantity $s(x)$ is plotted in figures S1g and S1h. The locations where $s(x)$ varies most rapidly can be interpreted as the locations where the seismic sources are strongest.

3.e) Surf zone parameterization

An important detail for wave periods between 10 and 50 s is the treatment of the surf zone.

The ocean wave height decreases rapidly to zero for wave periods shorter than 30 s, and becomes roughly constant in the infragravity wave band. Hasselmann [1963] had proposed to represent the effect of wave dissipation in shallow water by an abrupt reduction of the bottom pressure to zero at a position x_b . Such a sharp jump in bottom pressure would give an order of magnitude increase of s . Instead, we prefer to reduce gradually the wave amplitude, and thus the bottom pressure, by a factor proportional to the water depth, giving the more realistic amplitude and pressure distribution shown in Fig. (S1.f). In the case of a smooth bottom topography, this treatment of the surf zone reduces s by one order of magnitude. Using a constant amplitude, more appropriate for the infragravity wave band (i.e. $T > 30$ s), did not significantly change the results.

3.f) Effects of unresolved bathymetric features

By taking into account realistic depth variations on the scale of the ocean wavelength for sandy bottoms, the value of s is typically increased by an order of magnitude, for periods in the range 10 to 30 s. Here we have used an empirical spectrum of the bottom elevation,

$$F_B(k_b) = 1.5 \times 10^{-4} k_b^{-3}, \quad (\text{S24})$$

which is consistent with depth soundings over sandy continental shelves [Hino 1968; Ardhuin and Magne 2002]. This impact of the depth oscillations, on the scale of the ocean wavelength, can be interpreted as a classical wave-wave interaction process [Hasselmann 1966] with the ocean waves of wavenumber vector \mathbf{k}_1 coupling to bottom depth perturbations of wavenumber vector \mathbf{k}_b to generate seismic waves of the same frequency but wavenumber $\mathbf{k}_1 + \mathbf{k}_b$.

In practice we have estimated the ratio $s = |K|^2/|K_1|^2$ for many different bottom profiles and wave periods. Our simple choice $s = 6$ is consistent with these calculations, within one order of magnitude (figures S2 and 2), and gives a reasonable fit to the measured hum, as shown in figures 2, 3 and 4. We have used east-west depth profiles at a 1 degree interval around 41° N [mid-Atlantic ridge, Lourenco et al. 1998], and 0.2° intervals around 46.47°N [Bay of Biscay, Anonymous 2008], 41.473°N [Oregon shelf, U.S. DoC NOAA/NGDC 2006], and north-south profiles around 157.8°W across the Oahu north

shore, Hawaii [Anonymous 2011].

3.g) Choice of s for our calculations

When evaluating the integral (S14) with the linear wave-induced bottom pressure (S18) we generally found a slightly larger value of s for frequencies below 10 mHz, with a maximum value obtained for the Hawaii bathymetry profile $s=40$ at 5 mHz. The fundamental reason why s is larger at these low frequencies, is that there are no strong enough slopes for depth such that $kD > 0.76$. Indeed, for $f=5$ mHz, $kD = 0.76$ corresponds to $D=4800$ m.

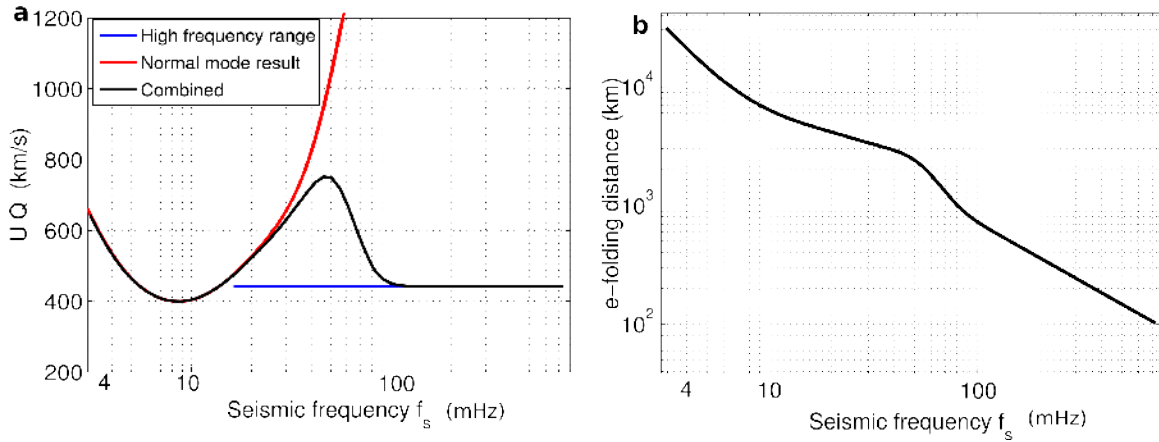
For short periods (typically less than 30 s), the value of s critically depends on the magnitude of the bottom depth perturbations at wavelengths similar to the ocean surface wavelength (around 100 m), and would otherwise be as low as 0.1 for a smooth bottom on these scales. The constant value $s = 6$, gives good results for the hum amplitude (Fig. 2). The good amplitude for the primary peak also should not be overstated. At these shorter periods we would expect s to be lower (figure S2) and we know that the seismic attenuation model is not well constrained. Finally we also expect that the alongshore variation in water depth lead to quantitative deviations from the previous result. This aspect has not been explored in the present paper.

References:

- Anonymous, A 500 m resolution bathymetry of the Bay of Biscay and Channel. <http://diffusion.shom.fr/produits/bathymetrie/mnt-golfe-de-gascogne-manche-500m.html> (2008).
- Anonymous, a 50 m resolution synthesis bathymetry and topography map of the Hawaiian islands, <http://www.soest.hawaii.edu/HMRG/multibeam/> (2011)
- Ardhuin, F., and Magne, R. Current effects on scattering of surface gravity waves by bottom topography. *J. Fluid Mech.*, **576**, 235 (2007).
- Ardhuin, F., Balanche, A., Stutzmann, E., and Obrebski, M.. From seismic noise to ocean wave parameters: General methods and validation, *J. Geophys. Res.* **117**, C05002 (2012).
- Ardhuin, F., and Herbers, T. H. C. Noise generation in the solid Earth, oceans and atmosphere, from nonlinear interacting surface gravity waves in finite depth. *J. Fluid Mech.*, **716**, 316-348 (2013).
- Ardhuin, F., Lavanant, T., Obrebski, M., Marié, L., Royer, J.-Y., d'Eu, J.-F., Howe, B. M., Lukas R., and Aucan, J. A numerical model for ocean ultra-low frequency noise: Wave-generated acoustic-gravity and Rayleigh modes. *J. Acoust. Soc. Am.* **134**, 3242–3259 (2013).
- Hasselmann, K. A statistical analysis of the generation of microseisms. *Rev. Geophys.*, **1**, 177 (1963).
- Hasselmann, K. Feynman diagrams and interaction rules of wave-wave scattering processes. *Rev. Geophys.*, **4**, 1 (1966).
- Herbers, T. H. C., Guza, R. T. Wind-wave nonlinearity observed at the sea floor. Part I: Forced-wave energy. *J. Phys. Oceanogr.*, **21**, 1740–1761 (1991).
- Gualtieri, L., Stutzmann, E., Capdeville, Y., Ardhuin, F., Schimmel, M., Mangeney, A., and Morelli, A. Modelling secondary microseismic noise by normal mode summation, *J. Int.*, **193**, 1732–1745 (2013).

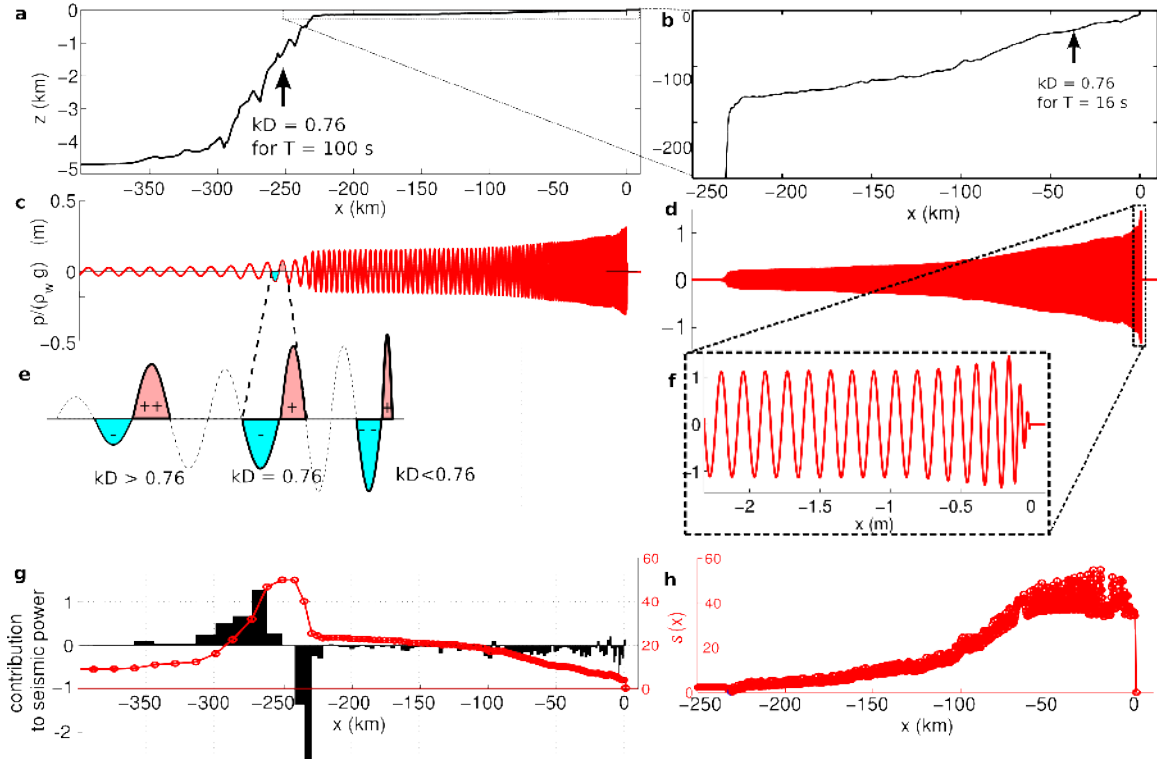
- Hino, M. Equilibrium-range spectra of sand waves formed by flowing water. *J. Fluid Mech.*, **34**, 565 (1968).
- Longuet-Higgins, M. S. A theory of the origin of microseisms. *Phil. Trans. Roy. Soc. London*, **A243**, 1–35 (1950).
- Lourenço, N. , Miranda, J.M., Luis, J.F., Ribeiro, A., Mendes Victor, L.A., Madeira, J., and Needham, H.D. Morpho-tectonic analysis of the Azores volcanic plateau from a new bathymetric compilation of the area, *Marine Geophysical Researches*, **20**,141-156 (1998).
- Mei, C. C. Applied dynamics of ocean surface waves. World Scientific, 2nd ed. (1989).
- Stutzmann, E., Arduin, F., Schimmel, M., Mangeney, A., and Patau, G. Modelling long-term seismic noise in various environments. *Geophys. J. Int.*, **191**, 707 – 722 (2012).
- U.S. Department of Commerce, National Oceanic and Atmospheric Administration, National Geophysical Data Center. *2-minute Gridded Global Relief Data (ETOPO2v2)*, (2006).

Figure S1.



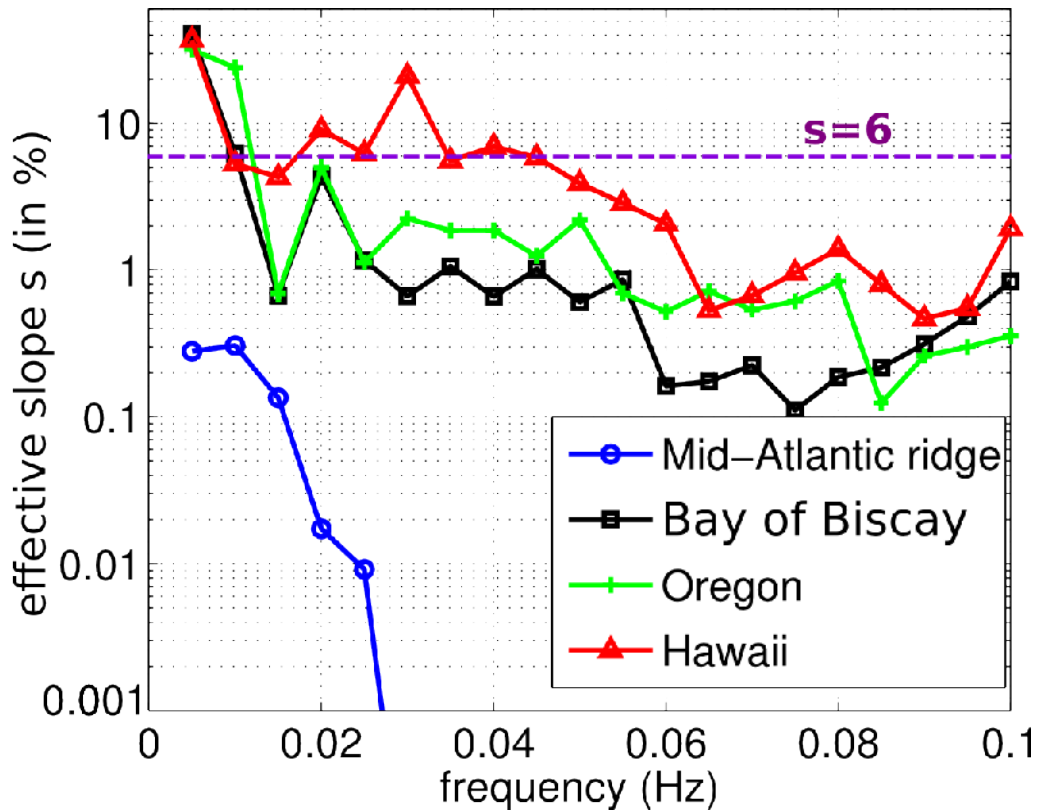
Supporting information, figure S1. Attenuation of seismic waves in our model. a, Values of UQ obtained by combining QL6 for Q and PREM for U (computed with a water depth of 2 km), for periods larger than 30 s with a constant $U=1.8$ km/s and $Q=240$ for shorter periods. **b,** Corresponding distance over which the seismic energy is reduced by a factor 2.7. For a period of 250 s ($f_s=4$ mHz) this distance is half-way round the globe, which allows the constructive interference that yields the modal structure seen in high-resolution spectra (e.g. Webb 2007).

Figure S2.



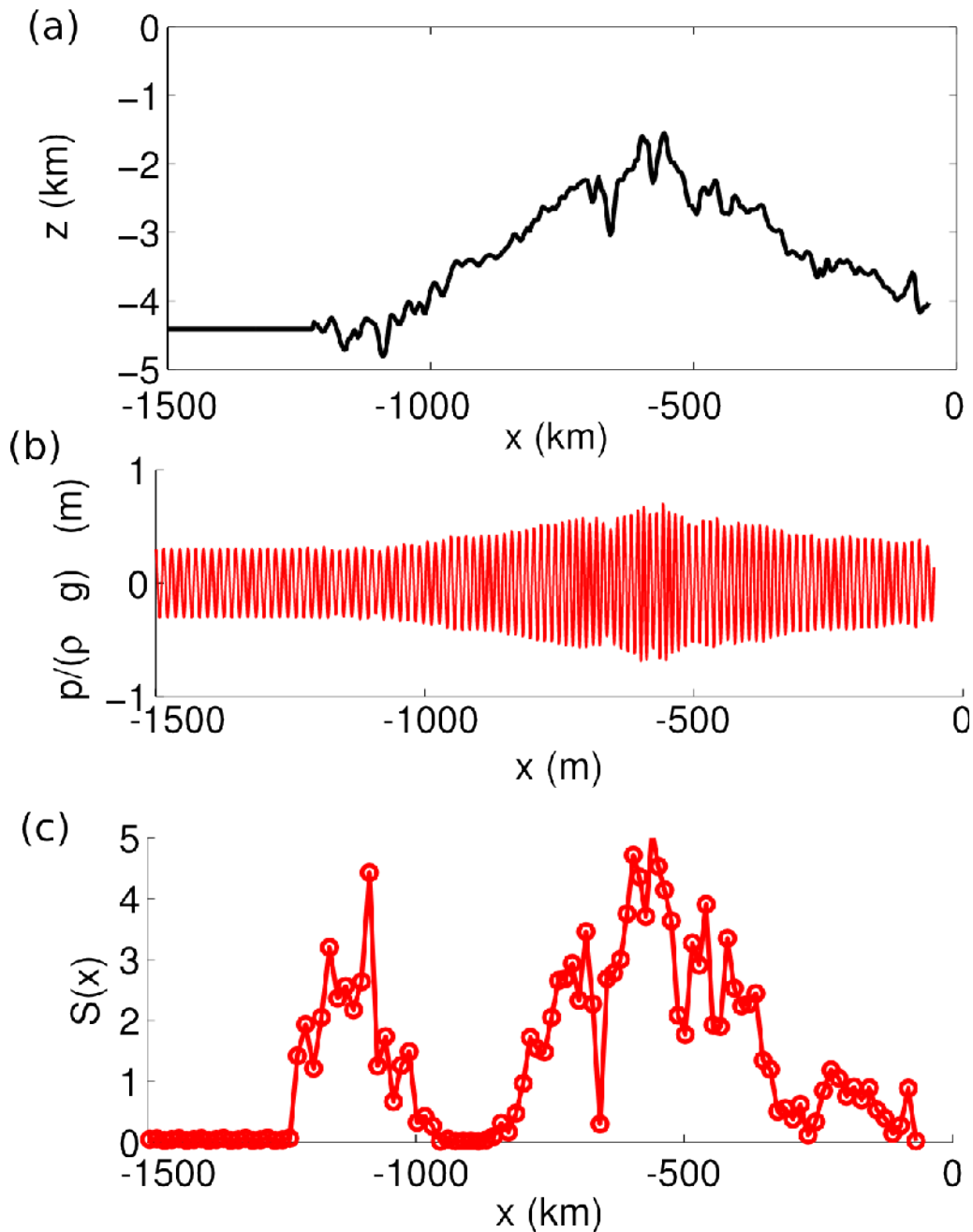
Supporting information, figure S2. How ocean waves propagating over a sloping bottom produce very long wavelength components capable of coupling to seismic Rayleigh waves. Example with waves of period 100 s and 16 s, over a continental shelf. **a,b** Example bottom topography in the Bay of Biscay at 47° N. **c** Snapshot of the bottom pressure computed using linear wave theory and energy conservation – except in the surf zone, for a period of 100 s and **d**, 16 s. **e**, Schematic showing how the pressure in a trough, with negative values, does not exactly cancel the pressure in the adjacent crest, due to a combination of wavelength shortening and increase in wave amplitude, giving a systematic phase shift between the wavelength-averaged pressure and the local pressure. For a non-dimensional depth $kD > 0.76$, corresponding to $x > 250$ km in **c,e,g**, the amplitude changes dominate. In shallower water the shortening dominates, giving opposing contributions to the mean pressure. **f**, close-up on the surf zone and reduction in wave amplitude due to breaking near the shore. **g,h**, In red, expected normalized seismic source power $s(x)$ due to waves between the shoreline and the local position x as defined in eq. (S22). In **g** the areas of black bars are proportional to the increment in source power over one ocean wavelength.

Figure S3.



Supporting information, figure S3. Amplification factors for primary seismic sources. The effective bottom slope s defined by eq. (S22, Supporting information text) is shown for different bottom depth profiles and for frequencies ranging from 5 to 100 mHz. These estimates are median values over 11 contiguous depth profiles taken from (28-31). For the calculations shown in figures 1 and 2, we have used a constant $s = 6$. The exact location of east-west depth profiles are a 1 degree interval around 41° N (mid-Atlantic ridge), and 0.2° intervals around 46.47°N (Bay of Biscay), 41.473°N (Oregon shelf), and north-south profiles around 157.8°W across the Oahu north shore, Hawaii. The seismic source power is proportional to s .

Figure S4.



Supporting information, figure S4. Primary seismic sources over the mid-Atlantic ridge. Results for 100 s infragravity waves over a depth profile taken from the mid-Atlantic ridge, north of the Azores, at 41°N . **a**, Bottom topography, **b**, bottom pressure computed using linear wave theory and energy conservation. **c**, seismic source power due to waves between the local position x and $x=1500$ km, estimated from the variance of the spatially-averaged bottom pressure.

RESEARCH ARTICLE

10.1002/2015JB012478

Key Points:

- Vertical displacement spectra of buried geophones is predicted from measured wind spectra
- The surface fluctuating wind shear stress may be as large as the pressure fluctuations
- Large wind noise reduction is achieved by mounting the geophone flush with the ground

Correspondence to:

V. Naderyan,
Vahid.nad@gmail.com

Citation:

Naderyan, V., C. J. Hickey, and R. Raspet (2016), Wind-induced ground motion, *J. Geophys. Res. Solid Earth*, 121, 917–930, doi:10.1002/2015JB012478.

Received 26 AUG 2015

Accepted 19 JAN 2016

Accepted article online 22 JAN 2016

Published online 18 FEB 2016

Wind-induced ground motion

Vahid Naderyan¹, Craig J. Hickey¹, and Richard Raspet¹

¹National Center for Physical Acoustics, Department of Physics and Astronomy, University of Mississippi, University, Mississippi, USA

Abstract Wind noise is a problem in seismic surveys and can mask the seismic signals at low frequency. This research investigates ground motions caused by wind pressure and shear stress perturbations on the ground surface. A prediction of the ground displacement spectra using the measured ground properties and predicted pressure and shear stress at the ground surface is developed. Field measurements are conducted at a site having a flat terrain and low ambient seismic noise. Triaxial geophones are deployed at different depths to study the wind-induced ground vibrations as a function of depth and wind velocity. Comparison of the predicted to the measured wind-induced ground displacement spectra shows good agreement for the vertical component but significant underprediction for the horizontal components. To validate the theoretical model, a test experiment is designed to exert controlled normal pressure and shear stress on the ground using a vertical and a horizontal mass-spring apparatus. This experiment verifies the linear elastic rheology and the quasi-static displacements assumptions of the model. The results indicate that the existing surface shear stress models significantly underestimate the wind shear stress at the ground surface and the amplitude of the fluctuation shear stress must be of the same order of magnitude as the normal pressure. Measurement results show that mounting the geophones flush with the ground provides a significant reduction in wind noise on all three components of the geophone. Further reduction in wind noise with depth of burial is small for depths up to 40 cm.

1. Introduction

Wind noise significantly limits seismic measurements and can obscure seismic signals sensed by geophones and other seismic sensors. Wind turbulence over the ground generates pressure and shear stress distributions at the ground surface that result in deformation of the ground. These wind-induced ground deformations are measured by seismic sensors.

The effect of wind noise on seismic measurements has been the subject of many investigations. The studies can be grouped into three areas: wind noise on geophones [Withers *et al.*, 1996; Stewart, 1998; Dey *et al.*, 2000; Bland and Gallant, 2001, 2002; Alcudia and Stewart, 2008], wind noise on very long period seismograms [Ewing and Press, 1953; Sorrells, 1971; Sorrells *et al.*, 1971; Savino and Rynn, 1972; Sorrells and Goforth, 1973; Beauduin *et al.*, 1996; Kroner *et al.*, 2005], and wind noise effects on the horizontal-to-vertical spectral ratio [Cara *et al.*, 2003; Mucciarelli *et al.*, 2005]. Most investigations of wind noise on geophones (except Withers *et al.* [1996]) study the wind noise on the geophones during a seismic survey and do not record the wind noise geophone data in the absence of other seismic sources.

Literature applicable to wind-ground coupling studies is very limited. Current understanding is limited to observational and qualitative conjectures for particular cases. There are no quantitative and testable physical models to calculate displacements in the ground from the measured velocity fluctuations outdoors. In the literature, there is an agreement on using elastic rheology and quasi-static assumptions for ground modeling. Also, there is an agreement on the significance of the wind coupling effects on the horizontal and vertical seismic sensors and increase of the noise with increasing wind velocity. However, there is a wide variation in measurements of the ground vibrations as a function of depth of burial and wind velocity. None of the previous works has accounted for the effect of shear stress at the ground surface on the wind-induced ground displacements. This research seeks to develop an effective theory to predict ground displacements associated with turbulent wind outdoors and to introduce experiments to study wind noise on geophones. Understanding the physics of this coupling phenomenon is necessary for the development of practical solutions to the problem of wind noise on seismic sensors.

Section 2 presents a summary of the theory of the wind pressure and shear stress generated by the atmospheric turbulence at the ground surface, as well as the solution of the deformations in an infinite

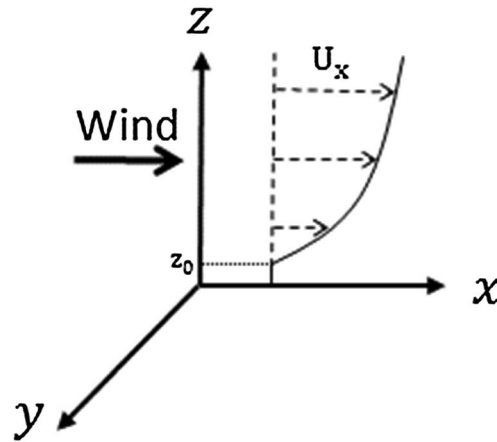


Figure 1. Coordinate system for wind and the mean longitudinal velocity profile.

elastic half-space. These theories are then applied to develop a theoretical model for wind-induced ground displacements.

Section 3 describes the field measurement setup and presents the results of the measurements. The induced ground displacements are studied as a function of depth and wind velocity by deploying multiple three-component geophones at different depths.

Section 4 compares predictions of the power spectra of the ground displacements to geophone measurements. The prediction and the measurement agree very well for the vertical displacement. The model, however, underestimates the horizontal displacements. A controlled test measurement is designed to verify the ground motion model. The results show that the ground motion measurements can be used to measure the wind shear

stress at the surface and indicate that the fluctuating shear stress is much larger than expected. Section 5 presents the conclusions of this research.

2. Theory

2.1. Wind Pressure and Shear Stress at the Ground Surface

Wind turbulence generates pressure and shear stress distributions at the ground surface. *Yu et al.* [2011] developed a theoretical model for the prediction of the wind pressure spectrum at the ground surface from the measured atmospheric turbulence spectra and wind velocity using the mirror flow model of anisotropic turbulence developed by *Kraichnan* [1956]. *Raspet et al.* [2008] showed that a revised von Karman form,

$$F_{11}^1(k_x) = \frac{C}{[1 + (k_x \lambda)^2]^{5/6}}, \tag{1}$$

provides a good fit to the measured longitudinal velocity spectrum above the surface outdoors, where C and λ are fit parameters, and k_x is the wave number in the direction of flow. Figure 1 shows the coordinate system used for wind throughout this paper. x is the direction of the wind, z is the vertical direction, and y is the transverse direction.

In the surface layer, the relation between the outdoor wind velocity and height is approximately logarithmic [*Panofsky and Dutton*, 1984]. The mean wind velocity for a logarithmic profile satisfies the form

$$U_x(z) = a \ln\left(\frac{z}{z_0}\right), \tag{2}$$

where a is the friction velocity (u_*) divided by the von Karman constant ($\kappa=0.41$), and z_0 is the roughness length of the ground surface. The corresponding mean velocity gradient is

$$s(z) = \begin{cases} \frac{a}{z} & z \geq z_0 \\ 0, & z < z_0. \end{cases} \tag{3}$$

The average wind velocity is assumed to be zero under the roughness length ($0 \leq z < z_0$). Finally, the predicted power spectral density (PSD) of the surface pressure fluctuation due to the turbulence-shear interactions is given by

$$|\rho(0, k_x)|^2 = \frac{440a^2 \rho^2 k_x^2 C \lambda^4}{9\pi} \int_0^\infty \int_0^\infty \frac{dk_z dk_y}{[1 + (k\lambda)^2]^{17/6}} \times \left[\int_{z_0}^\infty \frac{e^{-kz} \sin(k_z z)}{z} dz \times \int_{z_0}^\infty \frac{e^{-kz'} \sin(k_z z')}{z'} dz' \right], \tag{4}$$

where ρ is the density of air.

Much of the previous research leading to equation (4) was associated with understanding the ambient background noise in acoustic outdoor environments. *Yu et al.* [2011] showed that the predictions from this theory agree closely with the measurements of a flush microphone at the ground surface, indicating that turbulence-shear interaction pressure is the dominant source of wind noise at the surface. Detailed explanation of the derivation, meaning, and sensitivity of this equation and the starting point for a vast amount of literature of wind noise can be found in *Yu et al.* [2011].

Mathis et al. [2013] developed a model for predicting the surface shear stress fluctuations in turbulent boundary layers, based on the Schumann-Grötzbach (SG) model. However, no predictive model for the surface shear stress fluctuation at a rough ground surface under unsteady wind conditions was found in the literature. The SG model, *Mathis et al.'s* [2013] model, and other models in the literature are proposed and have been verified for shear stress at smooth surfaces with boundary layer flows. From the SG model, the PSD of the surface shear stress will be

$$|\tau(0, k_x)|^2 = \left[\frac{\langle \tau_w \rangle^2}{\langle u(t) \rangle^2} \right] |u(k_x)|^2, \quad (5)$$

where $\langle u(t) \rangle$ is the mean wind velocity, and $\langle \tau_w \rangle$ is the mean shear stress calculated from

$$\tau_w = \rho u_*^2. \quad (6)$$

Detailed explanation of this equation can be found in *Marusic et al.* [2001].

2.2. Deformation of an Infinite Elastic Half-Space Caused by a Surface Point Force

In this work the ground is modeled as an infinite elastic half-space. The deformation of an elastic medium bounded by an infinite plane on one side, i.e., occupying a half-space, due to forces applied to its free surface is determined. The free surface of the elastic medium is taken as the xy plane, and the medium is in the positive z direction. The equation of equilibrium of the medium has the form

$$\nabla(\nabla \cdot \mathbf{u}) + (1 - 2\sigma)\Delta \mathbf{u} = 0, \quad (7)$$

where σ is Poisson's ratio of the medium, and \mathbf{u} is the three-component displacement vector. Since the unit outward normal vector is in the negative z direction, the boundary conditions which must be satisfied at the free surface of the medium are

$$\sigma_{iz} = -P_i, \quad (8)$$

where σ_{iz} are components of the stress tensor inside the medium, and P_i are components of the external forces per unit area applied to the surface and are functions of x and y .

Assuming that a concentrated force \mathbf{F} is applied to a very small area, so it can be regarded as a point, and applying the boundary conditions, the resulting equations for the displacements in the medium are [*Landau and Lifshitz*, 1986]:

$$u_x = \frac{1 + \sigma}{2\pi E} \left\{ \left[\frac{2(1 - \sigma)r + z}{r(r + z)} + \frac{(2r(\sigma r + z) + z^2)}{r^3(r + z)^2} x^2 \right] F_x + \left[\frac{(2r(\sigma r + z) + z^2)}{r^3(r + z)^2} xy \right] F_y + \left[\frac{xz}{r^3} - \frac{(1 - 2\sigma)x}{r(r + z)} \right] F_z \right\} \quad (9a)$$

$$u_y = \frac{1 + \sigma}{2\pi E} \left\{ \left[\frac{(2r(\sigma r + z) + z^2)}{r^3(r + z)^2} xy \right] F_x + \left[\frac{2(1 - \sigma)r + z}{r(r + z)} + \frac{(2r(\sigma r + z) + z^2)}{r^3(r + z)^2} y^2 \right] F_y + \left[\frac{yz}{r^3} - \frac{(1 - 2\sigma)y}{r(r + z)} \right] F_z \right\} \quad (9b)$$

$$u_z = \frac{1 + \sigma}{2\pi E} \left\{ \left[\left(\frac{1 - 2\sigma}{r(r + z)} + \frac{z}{r^3} \right) x \right] F_x + \left[\left(\frac{1 - 2\sigma}{r(r + z)} + \frac{z}{r^3} \right) y \right] F_y + \left[\frac{2(1 - \sigma)}{r} + \frac{z^2}{r^3} \right] F_z \right\}, \quad (9c)$$

where E is Young's modulus of the ground, and $r = \sqrt{(x^2 + y^2 + z^2)}$. This representation of the point source will be used to model the complete excitation of the ground by integrating over a distribution of such sources due to the interaction of the wind with the ground.

2.3. Wind-Ground Coupling Theory

The wind excitations over the ground surface are assumed to be slowly moving fluctuations of pressure and shear stress. Very little wave energy is induced. Since the accelerations are small, the ground displacements are mainly quasi-static. This is very different from rapidly moving acoustic excitations.

Consider the solutions for the displacement of points in the medium due to a point force \mathbf{F} applied to the surface. If the force is applied to the origin, its effect is the same as that of surface stresses given by $\mathbf{P} = \mathbf{F}\delta(x)\delta(y)$. Then the solution for any stress distribution $\mathbf{P}(x, y)$ can be obtained from the solution for a concentrated point force. If the displacement due to the action of a concentrated force \mathbf{F} applied at the origin is

$$u_i = G_{ij}(x, y, z)F_j, \tag{10}$$

then according to Green's theory the displacements caused by $\mathbf{P}(x, y)$ are given by the integral

$$u_i = \iint G_{ij}(x - x', y - y', z)P_j(x', y')dx'dy'. \tag{11}$$

Here \mathbf{G} is the Green's tensor for the equations of equilibrium of a semi-infinite elastic medium, which is the 3×3 matrix of the coefficients in equations (9a)-(9c).

The PSD of the i component of the displacement at the point $(0, 0, z)$ due to point forces applied at $(x, y, 0)$ and $(x', y', 0)$ and integrating over the entire surface area is

$$|u_i(0, 0, z, k)|^2 = \int_{-\infty}^{\infty} \int_{-\infty}^{\infty} \int_{-\infty}^{\infty} \int_{-\infty}^{\infty} G_{ij}(x, y, z)G_{ij}(x', y', z) \langle P_j(x, y, k)P_j(x', y', k) \rangle dx dy dx' dy'. \tag{12}$$

A correlation function, $R(x - x', y - y')$, must be considered in order to have a realistic distribution of sources associated with wind turbulence over the ground surface. *Priestley* [1965] experimentally verified that the wind correlation function can be approximated by

$$R(x - x', y - y') \approx R(x - x')R(y - y'). \tag{13}$$

Shields [2005] used a three-axis orthogonal pressure sensor array to study wind correlation. The correlation of the pressure and shear stress is assumed to be the same as the wind correlation, because pressure and shear stress spectra are proportional to the wind velocity spectra. In this work, it is assumed that wind pressure and shear stress have the same correlation behavior as measured by *Shields* [2005]. Therefore, his wind noise correlations are used as turbulence correlation functions of the wind pressure and shear stress at the surface.

The wave number-dependent correlation function of the wind noise in the downwind and crosswind directions from *Shields* [2005] are

$$R(\text{downwind}) = \exp\left[-\alpha \frac{k_x}{2\pi} |x - x'|\right] \cos(k_x |x - x'|) \tag{14}$$

$$R(\text{crosswind}) = \exp\left[-\beta \frac{k_x}{2\pi} |y - y'|\right]. \tag{15}$$

His measurements showed that α and β over a range of wind velocities (from 4 to 8 m/s) and atmospheric and environmental conditions are approximately 3.2 and 7.0, respectively. He determined that within experimental error and over the limited range of velocities measured, the correlation is independent of wind velocity and the terrain. The cross correlations are assumed to be negligible as *Shields* [2005] experimentally verified.

Finally, substituting the correlation functions, equations (14) and (15), and the Green's tensors components from equations (9a) to (9c) into equation (12), the power spectra of the three components of the wind-induced ground displacements are [Naderyan, 2015]

$$\begin{aligned}
 |u_x(0, 0, z, k)|^2 &= \left(\frac{1 + \sigma}{2\pi E}\right)^2 \\
 &\times \int_{-\infty}^{\infty} \int_{-\infty}^{\infty} \int_{-\infty}^{\infty} \int_{-\infty}^{\infty} \left\{ \left[\frac{2(1 - \sigma)r + z}{r(r + z)} + \frac{(2r(\sigma r + z) + z^2)}{r^3(r + z)^2} x^2 \right] \left[\frac{2(1 - \sigma)r' + z}{r'(r' + z)} + \frac{(2r'(\sigma r' + z) + z^2)}{r'^3(r' + z)^2} x'^2 \right] \tau_x^2(k) \right. \\
 &+ \left. \left[\frac{(2r(\sigma r + z) + z^2)}{r^3(r + z)^2} xy \right] \left[\frac{(2r'(\sigma r' + z) + z^2)}{r'^3(r' + z)^2} x'y' \right] \tau_y^2(k) + \left[\frac{xz}{r^3} - \frac{(1 - 2\sigma)x}{r(r + z)} \right] \left[\frac{x'z}{r'^3} - \frac{(1 - 2\sigma)x'}{r'(r' + z)} \right] p_z^2(k) \right\} \\
 &\exp \left[-\alpha \frac{k_x}{2\pi} |x - x'| \right] \cos(k_x |x - x'|) \exp \left[-\beta \frac{k_x}{2\pi} |y - y'| \right] dx dy dx' dy'
 \end{aligned} \tag{16a}$$

$$\begin{aligned}
 |u_y(0, 0, z, k)|^2 &= \left(\frac{1 + \sigma}{2\pi E}\right)^2 \\
 &\times \int_{-\infty}^{\infty} \int_{-\infty}^{\infty} \int_{-\infty}^{\infty} \int_{-\infty}^{\infty} \left\{ \left[\frac{(2r(\sigma r + z) + z^2)}{r^3(r + z)^2} xy \right] \left[\frac{(2r'(\sigma r' + z) + z^2)}{r'^3(r' + z)^2} x'y' \right] \tau_x^2(k) \right. \\
 &+ \left. \left[\frac{2(1 - \sigma)r + z}{r(r + z)} + \frac{(2r(\sigma r + z) + z^2)}{r^3(r + z)^2} y^2 \right] \left[\frac{2(1 - \sigma)r' + z}{r'(r' + z)} + \frac{(2r'(\sigma r' + z) + z^2)}{r'^3(r' + z)^2} y'^2 \right] \tau_y^2(k) \right. \\
 &+ \left. \left[\frac{yz}{r^3} - \frac{(1 - 2\sigma)y}{r(r + z)} \right] \left[\frac{y'z}{r'^3} - \frac{(1 - 2\sigma)y'}{r'(r' + z)} \right] p_z^2(k) \right\} \\
 &\exp \left[-\alpha \frac{k_x}{2\pi} |x - x'| \right] \cos(k_x |x - x'|) \exp \left[-\beta \frac{k_x}{2\pi} |y - y'| \right] dx dy dx' dy'
 \end{aligned} \tag{16b}$$

$$\begin{aligned}
 |u_z(0, 0, z, k)|^2 &= \left(\frac{1 + \sigma}{2\pi E}\right)^2 \\
 &\times \int_{-\infty}^{\infty} \int_{-\infty}^{\infty} \int_{-\infty}^{\infty} \int_{-\infty}^{\infty} \left\{ \left[\left(\frac{1 - 2\sigma}{r(r + z)} + \frac{z}{r^3} \right) x \right] \left[\left(\frac{1 - 2\sigma}{r'(r' + z)} + \frac{z}{r'^3} \right) x' \right] \tau_x^2(k) \right. \\
 &+ \left. \left[\left(\frac{1 - 2\sigma}{r(r + z)} + \frac{z}{r^3} \right) y \right] \left[\left(\frac{1 - 2\sigma}{r'(r' + z)} + \frac{z}{r'^3} \right) y' \right] \tau_y^2(k) + \left[\frac{2(1 - \sigma)}{r} + \frac{z^2}{r^3} \right] \left[\frac{2(1 - \sigma)}{r'} + \frac{z^2}{r'^3} \right] p_z^2(k) \right\} \\
 &\exp \left[-\alpha \frac{k_x}{2\pi} |x - x'| \right] \cos(k_x |x - x'|) \exp \left[-\beta \frac{k_x}{2\pi} |y - y'| \right] dx dy dx' dy',
 \end{aligned} \tag{16c}$$

where p_z , τ_x , and τ_y are surface wind pressure, downwind shear stress, and crosswind shear stress, respectively. The displacements at the ground surface result from setting $z = 0$.

Since linear elastic rheology is used, the loading effects due to different components of the driving force are superimposed. If τ_y and p_z are set to zero, the displacement in the x direction is much larger than the displacements in the y and z direction. Similarly, setting τ_x and p_z to zero yields a predominating y displacement, and setting τ_x and τ_y to zero yields a predominant z displacement. This means that a one-directional force on the surface is expected to mainly induce a motion in its own direction.

In the model the source distribution is integrated over the entire ground surface area up to infinity. It is worthwhile to investigate the effect of the source area integration as a function of wave number to determine the effective source area for each wave number range. The integration over smaller radii is computed to investigate the sensitivity of the model to the source area. Figure 2 displays the effect of the radius of integration area on the vertical displacement power spectra for radii of 10 cm, 1 m, and 10 m. The horizontal components (x and y) are at the same level.

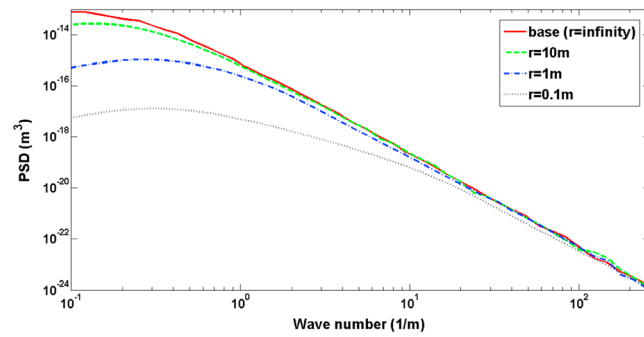


Figure 2. Influence of integration area on the wind-induced ground displacements.

Larger wavelengths, corresponding to lower wave numbers, cover larger surface area. Hence, as Figure 2 displays, at lower wave numbers the displacements are sensitive to the wind force load over larger areas. At short wavelengths (large wave numbers), the ground displacements are dominated by the wind force load over a smaller surface area surrounding the observation point. The displacement for wave numbers above 10 m^{-1} is determined by wind over a region of roughly 0.1 m in radius. For wave numbers of about

1 m^{-1} the displacement is determined by wind over a region of roughly 1 m in radius. At very small wave numbers, ($\sim 0.1 \text{ m}^{-1}$), the displacement is determined by wind over a region of roughly 10 m in radius.

3. Field Measurements and Results

3.1. Site Location and Ground Truth

All measurements were acquired in an agricultural field near Locke Station, MS. The terrain was flat and open around the location of measurements for about 25.0 m to the east and west, 4.0 m to the north, and 10.0 m to the south. Beyond these points, the site consists of mowed grass and harvested fields with a fetch of about 180 m to the west, 600 m to the east, and 1.5 km to the north. The wind often blew from south to north. This field was chosen for several reasons: proximity and ease of access for experimentation, distance from main roads, highways, and trees, and consequently low seismic ambient noise. Eleven sets of measurements were conducted from 19 December 2013 to 7 February 2015, under different wind conditions. All measurements were performed at times in which there were no farming or other human activities in the vicinity. The only possible source of induced seismic noise was a wind fence placed 35 m away from the measurements location. The porous wind fence was 10 sided and cylindrically shaped, 2.9 m high and 5.0 m diameter with an open top. Figure 3 is an aerial photo from Google Maps that shows the location of the measurements and the fence.

A set of standard seismic refraction measurements was performed to provide the ground truth and characterization at the site. Measuring the velocity of the ground using seismic methods results in an average value associated with wavelengths of the seismic waves being used and the natural heterogeneity

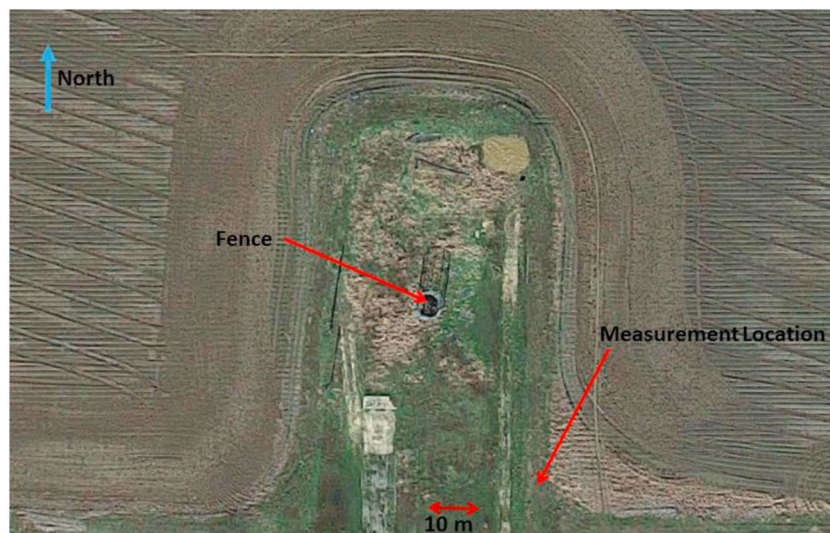


Figure 3. Image from Google Maps of the measurement site showing the relative locations of the measurement and the fence.

of the ground. The measured compressional velocity (V_p) and shear velocity (V_s) were 285 ± 5 m/s and 140 ± 5 m/s, respectively. These values would most likely be less if the measurements were performed at higher frequencies. The density of the ground (ρ_g) was measured to be 1995 ± 10 kg/m³ using a soil core. The relations for Poisson's ratio (σ) and Young's modulus (E) in terms of compressional velocity and shear velocity are given by

$$\sigma = \frac{V_p^2 - 2V_s^2}{2(V_p^2 - V_s^2)} \quad (17)$$

$$E = \frac{\rho_g V_s^2 (3V_p^2 - 4V_s^2)}{V_p^2 - V_s^2}. \quad (18)$$

The values are $\sigma = 0.34$ and $E = 1.03 \times 10^8$ Pa.

3.2. Anemometer

Wind velocity measurements were obtained simultaneously with the geophone measurements. The turbulence spectrum data were collected using a Gill Instrument R3A-100 Ultrasonic Research Anemometer mounted 1.0 m above the ground surface.

The wind velocity power spectra are calculated and converted from frequency to wave number space using Taylor's frozen turbulence hypothesis following the method of *Yu et al.* [2011]. The coefficients C and λ are determined by fitting the measured velocity spectrum in the wind direction to equation (1).

In *Yu* [2009] and *Yu et al.* [2011], multiple anemometers at different heights were used to measure the wind velocity profile and determine the friction velocity (u_*). In this work only one anemometer was employed, so the velocity profile could not be directly measured. Instead, the friction velocity is calculated from the measured three-dimensional wind spectrum using the method described in *Garratt* [1994]. In this method, the coordinate system is rotated so that in the new reference frame the mean of the vertical component of the velocity becomes zero. The friction velocity is then calculated from the fluctuating parts of the velocity components calculated using Reynolds decomposition (equations (2.5) and (2.6) of *Naderyan* [2015]).

The roughness length, z_0 , used in equation (4) is calculated using the measured average velocity and parameter a in equation (2). The average calculated roughness length is $z_0 = 0.0056$ m, which is found to be on the order of that listed for open flat terrain with no vegetation (0.005 m) [*Panofsky and Dutton*, 1984]. Finally, *Yu's* prediction for the pressure fluctuation spectrum at the ground surface, equation (4), is used to predict the spectrum of the pressure fluctuations at the ground surface.

3.3. Geophones

Four three-component 4.5 Hz, RTC Geophones with 375 ohm windings were used for the ground displacement measurements. Each geophone box contains two perpendicular horizontal and one vertical geophone element. Each geophone has three 7 cm steel spikes on the bottom for coupling to the ground. The acquisition hardware system had an internal low-cut filter at 1.75 Hz.

The four geophones were planted at the corners of two adjacent equilateral triangles. The spacing between each two geophones was 65 cm, far enough so that wind noise generated by one geophone would not be detectable by adjacent geophones and close enough so that the wind would not vary greatly over the area of the experiment. The first geophone was planted at the ground surface. The second geophone was mounted flush to the ground surface. The third and the fourth geophones were buried at depths of 20 cm and 40 cm, respectively. All the holes were dug with a shovel and made as small as practical. All the holes were backfilled and covered with the same soil after planting the geophones. The geophones were oriented with the x component approximately along the dominant wind direction, the y component along the horizontal crosswind direction, and the z component in the vertical direction. Figure 4 shows a diagram of the relative location of the geophones and the anemometer with respect to wind direction. Figure 5 shows a photograph of the geophones and the anemometer setup in the field.

The PSDs for three components of the ground velocities measured by the geophones are generated following the same procedure as for the wind velocity spectra. The PSDs in frequency space are divided by

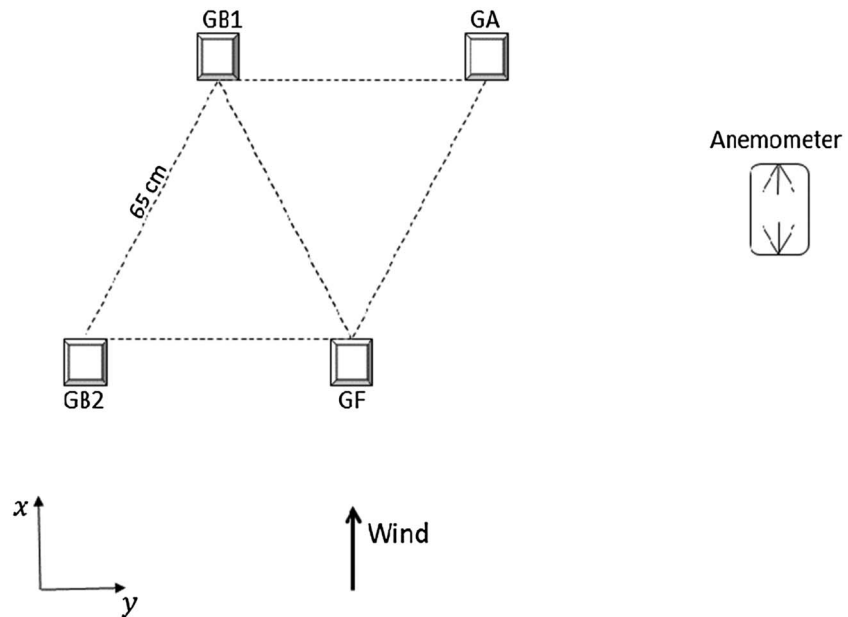


Figure 4. Plan view diagram of the relative location of the geophones and the anemometer with respect to wind direction. “GA” represents the geophone above the ground, “GF” represents the geophone mounted flush to the ground, and “GB1” and “GB2” represent the geophones buried 20 and 40 cm, respectively.

the square of the frequency response function of the geophone to convert from voltage (V^2s) to velocity ($\frac{m^2}{s^2}$). The PSDs are then divided by $(2\pi f)^2$ to convert from velocity ($\frac{m^2}{s^2}$) to displacement (m^2s).

3.4. Wind Velocity Effect

Comparison of the spectral levels under high and low wind conditions verifies that the observed displacements are due to the wind. Figure 6a displays a comparison between the displacements at high wind velocity (7.1 m/s), medium wind velocity (4.8 m/s), and low wind velocity (2.2 m/s) for the geophone at the ground surface. Figure 6b displays the displacements on the geophone mounted flush to the ground, and Figures 6c and 6d display data for the geophones buried at 20 cm and 40 cm, respectively. Unwanted noise peaks at 60 Hz, 120 Hz, and 180 Hz on the low wind velocity data are due to electrical interference.

The results show that for all three components there is a significant difference between the displacements due to high wind velocity and low wind velocity. Even for the geophone buried at 40 cm, the differences in the displacements are large. This assures that what is measured is actually the wind coupled to the ground and the geophones. The mechanism and structure stay the same for high wind and low wind velocities, but the displacement amplitudes are bigger for higher wind velocity and the bumps at 6–13 Hz vanish at low wind velocity independent of geophone burial depth.



Figure 5. Experimental setup for the geophones and the anemometer.

The horizontal components of the displacements are larger than the vertical component for the geophone at the ground surface. The direct interaction of the wind with the geophone shakes it more in the horizontal directions. The displacement on the x component of the geophone, along the wind direction, is larger than the crosswind horizontal

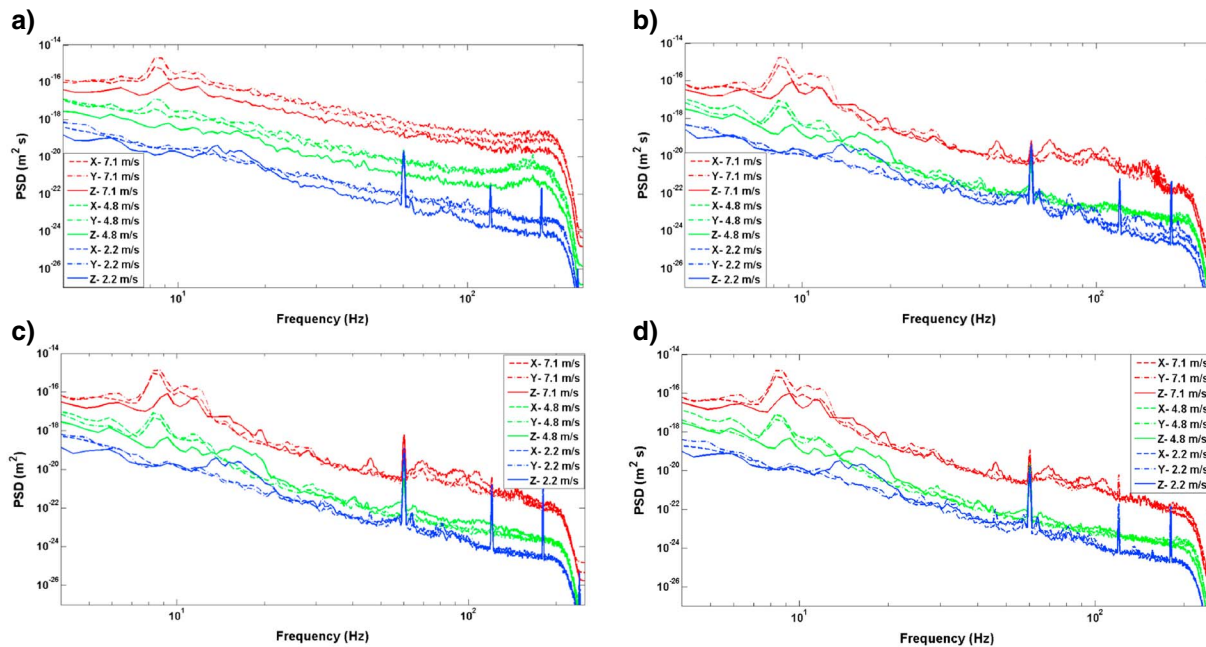


Figure 6. Displacements at different wind velocities for (a) the ground surface geophone, (b) the flush mounted geophone, (c) the geophone buried at 20 cm, and (d) the geophone buried at 40 cm.

component, y , because it is exposed to the wind direction. For the buried geophones the three components of the displacements are at the same level.

3.5. Depth Effect

To investigate whether the wind noise can be reduced by burying the geophones, the effect of depth on the reduction of the displacements on each component is studied. Figure 7a displays the displacements of the horizontal in-line component, x , of the geophone at the ground surface, the geophone mounted flush to the ground, and the geophones buried at 20 cm and 40 cm. Figures 7b and 7c display the data for the horizontal cross-line, y , and the vertical, z , components of the geophones. The mean wind velocity for this measurement was 6.6 m/s.

Burying the geophone drastically reduces the amount of noise on all three components of the geophone, since it eliminates the direct interaction of wind with the geophone case. Noise reduction afforded by 20 cm and 40 cm burial of the geophone beyond the flush mounted is small.

4. Analysis and Discussion

4.1. Comparison of Measurements and Predictions

Yu's model, equation (4), for normal pressure at the ground surface is used in this work as p_z in equations (16a)-(16c). In Yu [2009] and Yu *et al.* [2011] the results of the prediction model were compared to measurements of wind noise on a flush microphone in a surface beneath a foam covering. The theory provided reliable predictions of the measurements.

The direct measurement of the surface shear stress fluctuations is largely inaccessible in field measurements. The shear stress fluctuation predicted from the SG model, equation (5), and other models in the literature (such as Mathis *et al.* [2013] and Orlu and Schlatter [2011]) is 2 orders of magnitude smaller than the normal pressure fluctuations predicted from Yu's model. Our calculations show that for shear stresses of this magnitude, the contribution of τ_x and τ_y terms in the ground displacements will be negligible compared to the contribution of the normal pressure p_z in equations (16a)-(16c).

Figure 8 displays predicted and measured ground displacement spectra for three components of the geophone mounted flush to the ground surface, i.e., $z=0$. The mean wind velocity for this measurement

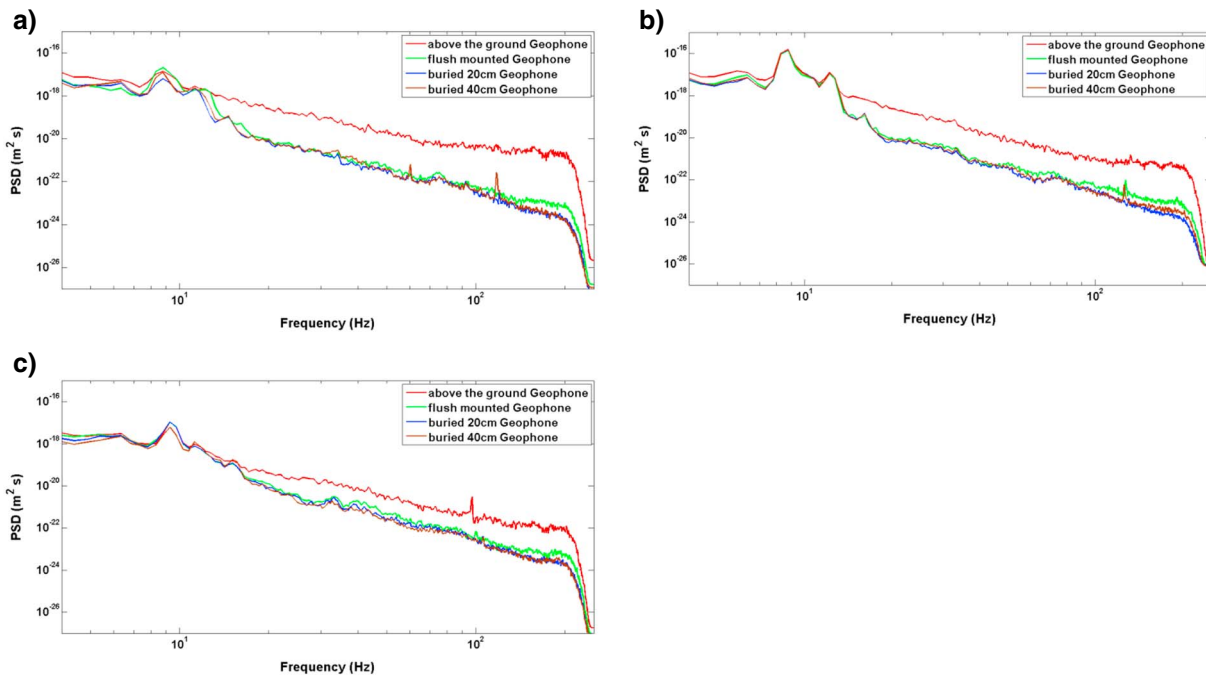


Figure 7. The effect of depth on (a) the horizontal in-line, *x*, component of the displacement, (b) the horizontal cross-line, *y*, component of the displacement, and (c) the vertical, *z*, component of the displacement.

was 6.3 m/s, and the measured coefficients to predict the pressure at the ground surface were $C = 1.99$, $\lambda = 2.68$, and $a = 1.66$.

The measurements and the predictions for the vertical component of the displacement match very well, but the horizontal displacements are significantly underpredicted. The measured displacements at frequencies between 6 to 13 Hz are larger than predicted, and the horizontal displacements are larger than the vertical displacement. The displacements in this frequency range increase with wind velocity (Figure 6) but are independent of geophone depth (Figure 7). That the displacements are sensitive to wind speed but independent of geophone depth suggests that the displacements are not associated with direct wind interaction or the burial of the individual geophones. An increase in displacement is not observed at low wind speeds (Figure 6) suggesting that this phenomena is not associated with resonant amplification of ambient seismic noise due to ground layering. One possibility is that the interaction of the wind with the nearby wind fence induces vibrations into the ground which are sensed by the geophones; however, a suitable explanation of this part of the spectra requires further investigation.

It is well known that there are important differences between the turbulent flow behavior in indoor wind tunnels over a smooth surface and outdoor wind fluctuations over a rough ground surface. In the fluctuations of the pressure and shear stress at the ground surface the roughness characteristics of the ground play an important role. Also, surface pressure and shear stress under steady wind are different from the turbulent wind outdoors.

The disagreement in the predicted and measured horizontal components casts doubt on the validity of the existing predictive models for the amplitude of shear stress fluctuations for field measurements over ground rough surface. To investigate this, a test experiment is

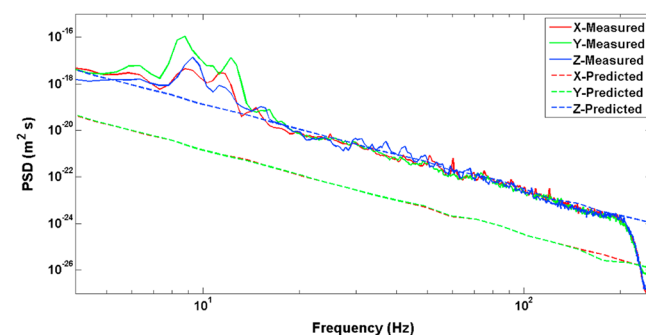


Figure 8. The measured and predicted displacements for a wind speed of 6.3 m/s.



Figure 9. (left) Vertical mass-spring apparatus to exert controlled normal pressure on the ground, and (right) horizontal mass-spring apparatus to exert controlled shear stress on the ground.

designed to check the validity of the calculation of ground’s quasi-static displacements from the pressure and shear stress distribution.

4.2. Test Experiment: Controlled Pressure and Shear Stress to the Ground

A test experiment with controlled pressure and shear stress exerted on the ground surface was conducted to test the ground model of the proposed theoretical model. The vertical and horizontal mass-spring apparatuses built to apply controlled normal and tangential forces are shown in Figure 9. In both apparatuses, a mass was attached between two identical springs. If the mass is moved from its initial equilibrium position and released, it will vibrate at the resonance frequency of the system. The force due to this vibration will be exerted on the ground under the plate.

The measured resonance frequency for both systems was $f = 12.33$ Hz. This frequency can be altered by changing the mass or springs. The mass between the springs was $m = 0.304$ kg and the mass of each spring was $m_s = 0.232$ kg. The effective mass of the system is given by

$$m_{\text{eff}} = m + \left(\frac{1}{3} \times 2 \times m_s\right) = 0.458 \text{ kg.} \tag{19}$$

The force due to the mass-spring system vibration is given by

$$F = m_{\text{eff}} x \omega^2, \tag{20}$$

where x is the amplitude of the mass displacement, and $\omega = 2\pi f$ is the angular frequency of the vibration. Normal pressure, for vertical spring, and tangential stress, for horizontal spring, for uniform loads are calculated from

$$P = \frac{F}{A}, \tag{21}$$

where A is the surface area of the plate. For the vertical spring $A_{\text{vert}} = 0.212 \text{ m}^2$ and for the horizontal spring $A_{\text{hor}} = 0.135 \text{ m}^2$.

Table 1. Average Results of the Vertical Mass-Spring System Over Four Sets of Measurements

Component	Prediction (m)	Measurement (m)
u_x	3.0×10^{-9}	2.5×10^{-9}
u_y	3.0×10^{-9}	2.6×10^{-9}
u_z	8.5×10^{-7}	8.2×10^{-7}

The experiment was conducted on a very calm, nonwindy day, at the same site where the wind-ground measurements were conducted. A three-component geophone was buried 1.0 cm below the surface of the ground, and the spring apparatus

Table 2. Average Results of the Horizontal Mass-Spring System Over Four Sets of Measurements

Component	Prediction (m)	Measurement (m)
u_x	4.7×10^{-7}	4.3×10^{-7}
u_y	2.6×10^{-9}	2.3×10^{-9}
u_z	2.4×10^{-9}	2.1×10^{-9}

plate was placed on the ground centered on the geophone. The mass-spring was excited to vibrate, and the geophone recorded the motion of the soil. The recording length was 30 s to allow for large enough vibration (i.e., force) before

damping. To measure the amplitude of vibration, a fixed scale was placed behind the vibrating mass and a video was recorded with a high-speed camera. The average amplitude of vibration was assumed as the value of x .

To predict the displacements associated with the vertical spring apparatus above the ground from equations (16a)-(16c), the integration limits are set to the plate dimensions, the correlation functions are set to one, because the pressure is uniform over the plate, and τ_x and τ_y are set equal to zero. Similarly, the displacements for the horizontal spring apparatus aligned with the x component of the geophone is given by setting the integration limits to the plate dimensions, the correlation functions to one, and τ_y and P_z equal to zero.

Tables 1 and 2 show an ensemble average of four sets of the calculations and measurements for each of the vertical and horizontal systems, respectively. Individual sets of the measurements are within $\pm 7.0 \times 10^{-10}$ m of the predictions.

Several different sets of measurements with different configurations were conducted. The reasonable match between the predictions and measurements for the ground displacements verifies the predictive theoretical model for the ground deformation. This verification confirms that the linear elastic rheology is appropriate for this model. It was observed that having only a vertical force on the ground surface produces much larger vertical displacements than horizontal displacements. Similarly, having only a tangential shear force on the ground produces mainly horizontal displacements in the direction of the tangential force.

4.3. Ground Displacement Measurement as a New Tool for Surface Wind Shear Stress Measurement

The measured ground properties, \mathbf{G} , and the predicted pressure and shear stress, \mathbf{P} , have been used to predict ground displacements, \mathbf{u} , using equations (16a)-(16c). The test experiment verified the theoretical model of the ground, using known driving forces. Therefore, an inverse approach can be used to measure the wind driving forces, \mathbf{P} , from the measured \mathbf{G} and \mathbf{u} . It was shown in Figure 8 that for the buried geophones, the three components of the wind-induced displacements are almost at the same level. The predicted displacement for the vertical component agreed with the measured displacement. However, for the horizontal components the predictions underestimated the displacements.

From equations (16a)-(16c), since each load component mainly induces a motion in its own direction, the mismatch of the horizontal ground displacement in Figure 8 must be due to fluctuating shear stress at the rough ground surface. The fluctuating wind shear stress at the ground surface must be of the same order of magnitude as the wind normal pressure to produce the measured levels. Figure 10 displays the comparison of the predicted and the measured ground displacements

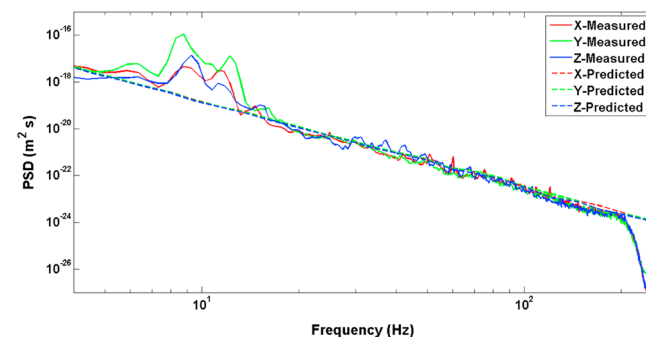


Figure 10. The measured and the predicted displacements using the new estimate of surface shear stress.

if the surface shear stresses (τ_x and τ_y) are set equal to the pressure (P_z) in equations (16a)-(16c).

Figure 11 compares the prediction of the vertical displacement at the ground surface ($z=0$), and 20 cm and 40 cm depths, from equations (16a)-(16c). The reduction afforded by 20 cm and 40 cm depths compared to the surface displacement is small, which is in agreement with the measurement results shown in Figure 7. This behavior is the same for horizontal displacements.

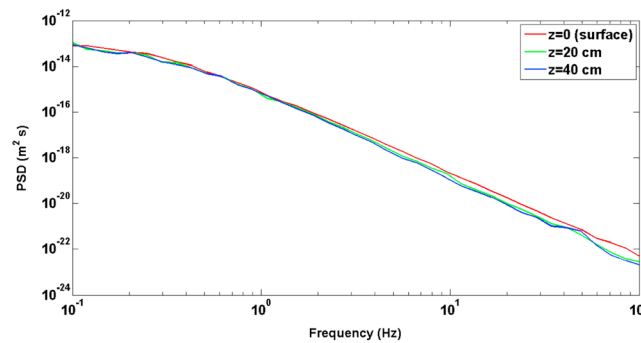


Figure 11. Predicted vertical displacement at the surface and 20 cm and 40 cm depths.

4.4. Variation of Model Parameters

It is important to understand the contributions from different parameters to the displacement spectrum prediction to investigate the effect of error in the measurements of the ground parameters on the results. The sensitivity of calculated displacements to each parameter is investigated by changing one parameter value, calculating the new response, and comparing the new displacement levels to that obtained with the “base” parameter set.

Compressional velocity (V_p) and shear velocity (V_s) are varied both above and below their base values.

4.4.1. Compressional Velocity (V_p)

To maintain reasonable values for Poisson’s ratio (σ), the compressional velocity (V_p) is varied 20% both above and below its base value. The base compressional velocity is 285 m/s, so the compressional velocity 20% above the base is 342 m/s, corresponding to $\sigma = 0.40$, and 20% below the base is 228 m/s, corresponding to $\sigma = 0.19$. Decreasing the compressional velocity by 20% results in 40% increase in displacement levels. Increasing the compressional velocity by 20% results in 20% reduction in displacement levels.

4.4.2. Shear Velocity (V_s)

To maintain reasonable values for Poisson’s ratio (σ), the shear velocity (V_s) is varied 20% both above and below its base value. The base shear velocity is 140 m/s, so the shear velocity 20% above the base is 168 m/s, corresponding to $\sigma = 0.23$, and 20% below the base is 112 m/s, corresponding to $\sigma = 0.41$. Decreasing the shear velocity by 20% results in 100% increase in displacement levels. Increasing the shear velocity by 20% results in 80% reduction in displacement levels.

The displacement spectra are more sensitive to variations in shear velocity than compressional velocity. Since the variation in parameters has the same effect in the amplitude of both horizontal and vertical displacements, it would not change the conclusion that all three components of the displacements are about the same magnitude and the conclusion about the magnitude of the wind shear stress at the surface of the ground. The experimental error in compressional and shear velocities was ± 5 m/s, which is equivalent to 2%–4% change in parameters. The effect of this experimental range in the displacements spectra is negligible.

Natural grounds are inhomogeneous, and the seismic velocity usually increases with depth. The influence of depth dependent ground properties on the wind-induced ground motion is the topic of a future study.

5. Conclusions

This paper provides predictions of three components of the ground displacements induced by wind noise fluctuations over the ground surface. The theoretical model transfers the driving pressure and shear stress perturbations on the ground surface to the ground vibrations. The measurements show that all three components of the displacement are about the same magnitude for buried geophones. The predictions are in good agreement for the vertical ground displacements. However, the horizontal ground displacements are significantly underpredicted. Comparison of the predictions and the measurements shows that the existing surface shear stress models significantly underpredict the amplitude of the fluctuating shear stress on the ground. The results indicate that the shear stress must be of the same order of magnitude of the normal pressure on the ground surface.

The existing surface shear stress models were developed and calibrated for turbulent boundary layer flow over smooth surfaces. The discrepancy between these results and the existing surface shear stress predictive models is likely due to roughness effects of the ground surface and unsteadiness of turbulent wind outdoors. Further work is necessary to develop a model for fluctuating surface shear stress to account for roughness effect and other additional effects of turbulent outdoor flows.

An experimental setup was introduced to measure ground displacements under controlled pure normal and tangential forces to the ground surface. This experiment verified the linear elastic rheology and the quasi-static displacement assumptions for the ground model. With this calibration, the measured seismic displacements can be used to determine the amplitude of the wind shear stress at the ground surface associated with wind-induced forces. This result can have important implications in prediction of the surface shear stress in environmental studies such as erosion studies and sediment transport studies.

The effect of the burial depth and wind velocity on the displacements has shown that the wind noise on the geophone above the ground is mainly dominated by the direct interaction of the wind with the geophone box. The wind noise increases by roughly 8 dB for an increase of 1 m/s in wind velocity. Mounting the geophone flush to the ground provides roughly 20–25 dB reduction in wind noise. However, only a very small additional reduction in wind noise with deeper burial (down to 40 cm) is realized.

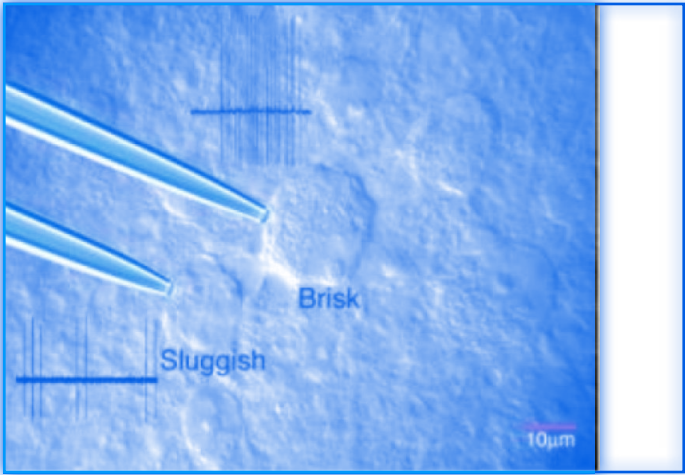
Acknowledgments

This research was funded by the United States Department of Agriculture (USDA) under research award 58-6408-1-608. We appreciate the assistance of Jeremy Webster, Gregory Lyons, Maryam Landi, Saeed Arab, Alessandra Conti, and Leti Wodajo in the measurement program. The data published in this article can be obtained by contacting the corresponding author directly.

References

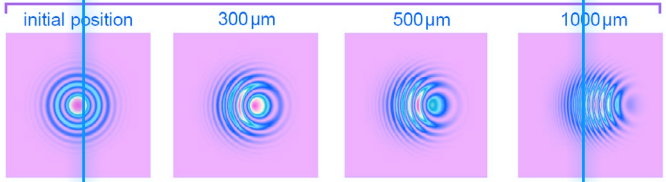
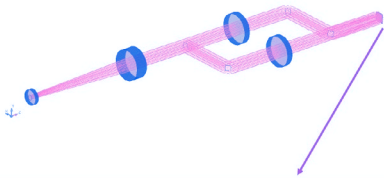
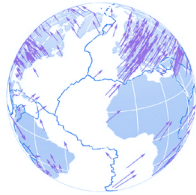
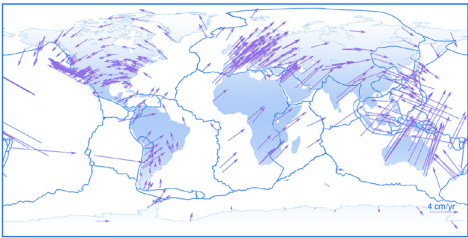
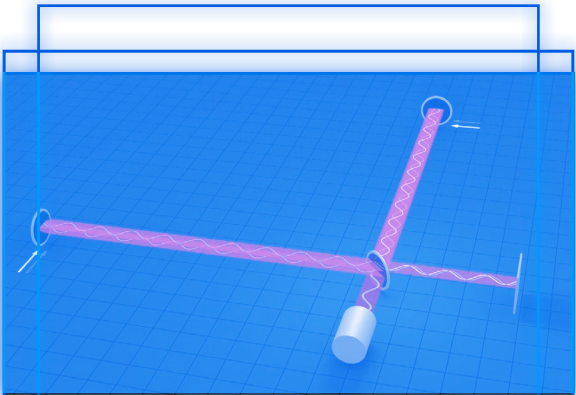
- Alcudia, A., and R. R. Stewart (2008), Microphone applications in seismic exploration, paper presented at CSPG CSEG CWLS Convention.
- Beauduin, R., P. Lognonné, J. P. Montagner, S. Cacho, J. F. Karczewski, and M. Morand (1996), The effects of the atmospheric pressure changes on seismic signals or how to improve the quality of a station, *Bull. Seismol. Soc. Am.*, *86*(6), 1760–1769.
- Bland, H. C., and E. V. Gallant (2001), Wind noise abatement for 3-C geophones, *CREWES Res. Rep.*, *13*, 1–15.
- Bland, H. C., and E. V. Gallant (2002), Avoiding wind noise: How helpful is geophone-burying, paper presented at CSEG Geophysics.
- Cara, F., G. Di Giulio, and A. Rovelli (2003), A study on seismic noise variations at Colfiorito, central Italy: Implications for the use of H/V spectral ratios, *Geophys. Res. Lett.*, *30*(18), 1972, doi:10.1029/2003GL017807.
- Dey, A. K., R. R. Stewart, L. R. Lines, and H. C. Bland (2000), Noise suppression on geophone data using microphone measurements, *CREWES Res. Rep.*, *12*, 1–12.
- Ewing, M., and F. Press (1953), Further study of atmospheric pressure fluctuations recorded on seismographs, *Eos Trans. AGU*, *34*(1), 95–100, doi:10.1029/TR034i001p00095.
- Garratt, J. R. (1994), *The Atmospheric Boundary Layer*, 41 pp. Cambridge Univ. Press, Cambridge, U. K.
- Kraichnan, R. H. (1956), Pressure fluctuations in turbulent flow over a flat plate, *J. Acoust. Soc. Am.*, *28*(3), 378–390.
- Kroner, C., T. Jahr, S. Kuhlmann, and K. D. Fischer (2005), Pressure-induced noise on horizontal seismometer and strainmeter records evaluated by finite element modelling, *Geophys. J. Int.*, *161*(1), 167–178, doi:10.1111/j.1365-246X.2005.02576.x.
- Landau, L. D., and E. M. Lifshitz (1986), *Theory of Elasticity, Course of Theor. Phys.*, vol. 7, 3 ed., Butterworth-Heinemann, Oxford.
- Marusic, I., G. J. Kunkel, and F. Porte-Agel (2001), Experimental study of wall boundary conditions for large-eddy simulation, *J. Fluid Mech.*, *446*, 163–180, doi:10.1017/S0022112001005924.
- Mathis, R., I. Marusic, S. I. Chernyshenko, and N. Hutchins (2013), Estimating wall-shear-stress fluctuations given an outer region input, *J. Fluid Mech.*, *446*, 309–320, doi:10.1017/jfm.2012.508.
- Mucciarelli, M., M. R. Gallipoli, D. Di Giacomo, F. Di Nota, and E. Nino (2005), The influence of wind on measurements of seismic noise, *Geophys. J. Int.*, *161*(2), 303–308, doi:10.1111/j.1365-246X.2004.02561.x.
- Naderyan, V. (2015), Wind Induced Ground Motion, MSc thesis, Univ. of Miss.
- Orlu, R., and P. Schlatter (2011), On the fluctuating wall-shear stress in zero pressure-gradient turbulent boundary layer flows, *Phys. Fluids*, *23*(2), 021704, doi:10.1063/1.3555191.
- Panofsky, H. A., and J. A. Dutton (1984), *Atmospheric Turbulence: Models and Methods for Engineering Applications*, pp. 119–143, Wiley, New York.
- Priestley, J. T. (1965), Correlation studies of pressure fluctuations on the ground beneath a turbulent boundary layer, MS thesis, Univ. of Md.
- Raspet, R., J. Yu, and J. Webster (2008), Low frequency wind noise contributions in measurement microphones, *J. Acoust. Soc. Am.*, *123*(3), 1260–1269, doi:10.1121/1.2832329.
- Savino, J. M., and J. M. Rynn (1972), Quasi-static loading of the Earth by propagating air waves, *J. Geophys. Res.*, *77*, 5033–5041, doi:10.1029/JB077i026p05033.
- Shields, F. D. (2005), Low-frequency wind noise correlation in microphone arrays, *J. Acoust. Soc. Am.*, *117*(6), 3489–3496, doi:10.1121/1.1879252.
- Sorrells, G. G. (1971), A preliminary investigation into the relationship between long-period seismic noise and local fluctuations in the atmospheric pressure field, *Geophys. J. Int.*, *26*(1-4), 71–82, doi:10.1111/j.1365-246X.1971.tb03383.x.
- Sorrells, G. G., and T. T. Goforth (1973), Low-frequency earth motion generated by slowly propagating partially organized pressure fields, *Bull. Seismol. Soc. Am.*, *63*(5), 1583–1601.
- Sorrells, G. G., J. A. McDonald, Z. A. Der, and E. Herrin (1971), Earth motion caused by local atmospheric pressure changes, *Geophys. J. Int.*, *26*(1-4), 83–98, doi:10.1111/j.1365-246X.1971.tb03384.x.
- Stewart, R. R. (1998), Air-noise reduction on geophone data using microphone records, *CREWES Res. Rep.*, *10*, 5.1–5.8.
- Withers, M. M., R. C. Aster, C. J. Young, and E. P. Chael (1996), High-frequency analysis of seismic background noise as a function of wind speed and shallow depth, *Bull. Seismol. Soc. Am.*, *86*(5), 1507–1515.
- Yu, J. (2009), Calculation of wind noise measured at the surface under turbulent wind fields, PhD dissertation, Univ. of Miss.
- Yu, J., R. Raspet, J. Webster, and J. Abbott (2011), Wind noise measured at the ground surface, *J. Acoust. Soc. Am.*, *129*(2), 622–632, doi:10.1121/1.3531809.

A GUINEA PIG RETINA
TRANSFERS DATA AT ABOUT
875 KILOBITS PER SECOND.
HUMAN RETINAS HAVE
ABOUT TEN TIMES AS MANY
GANGLION CELLS, GIVING
A BANDWIDTH OF 8.75
MEGABITS PER SECOND.

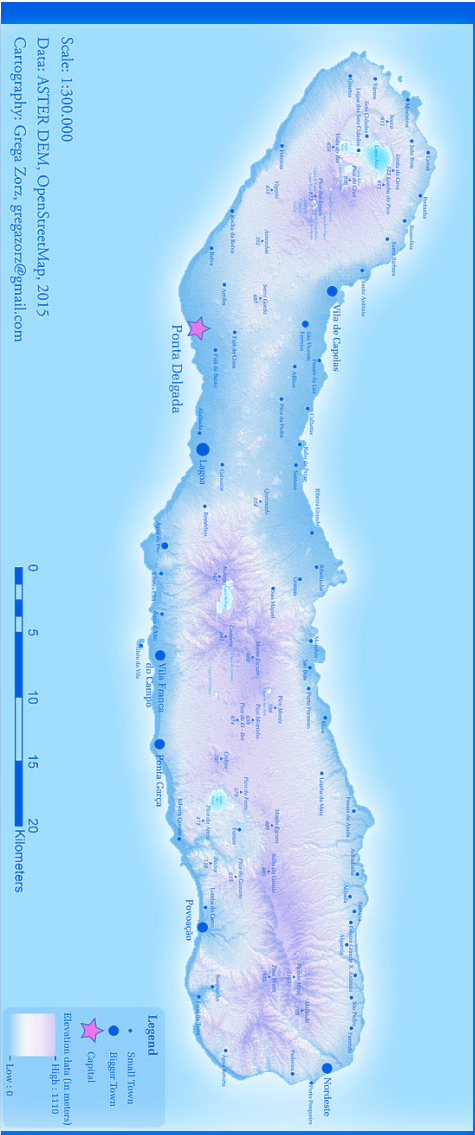


The two broad classes of ganglion cell types in the guinea pig retina: brisk cells, which are larger and transmit electrical impulses faster, and sluggish, which are smaller and slower.





Most special thanks to Rob Adamson, researcher in optical, ultrasonic and acousto-optic technologies for biomedical imaging and therapy, Assistant Professor, Biomedical Engineering and Electrical Engineering, Dalhousie University, Halifax, Nova Scotia and founder of Daxsonics Ultrasound Inc. Thanks to Luis Brum and the team at Walk&Talk, São Miguel Island and the ever brilliant Dani Admiss for her care, accord and kind attentions.



Published by **Shift Register, Basel 2018**
www.shiftregister.info

Edited by Jamie Allen, Martin Howse
 Designed by Merle Ibach

**Critical
 Media
 Lab
 Basel**

Institute of
 Experimental
 Design and Media
 Cultures

